Volume 133 Numbers 1–4(1992)

FEROA8 133(1–4) 1–312 (1992)
ISSN: 0015-0193

AD-A263 427

# FERROELECTRICS

[redacted]

DISTRIBUTION STATEMENT A
Approved for public release;
Distribution Unlimited

DTIC
ELECTE
APR 21 1993
S E D

GORDON AND BREACH SCIENCE PUBLISHERS
SWITZERLAND • AUSTRALIA • BELGIUM • FRANCE • GERMANY • GREAT BRITAIN
INDIA • JAPAN • MALAYSIA • NETHERLANDS • RUSSIA • SINGAPORE • USA

# FERROELECTRICS
## and related materials


**EDITOR: George W. Taylor**

*Princeton Resources, P.O. Box 211, Princeton, New Jersey 08540, U.S.A*

**ASSOCIATE EDITORS**

**Peter Günter**
*Institut für Quantenelektronik*
*ETH,*
*CH 8093 Zürich, Switzerland*

**Sidney B. Lang**
*Department of Chemical Engineering*
*Ben Gurion University of the Negev*
*Beer Sheva 84120, Israel*

**Koichi Toyoda**
*Research Institute of Electronics*
*Shizuoka University*
*Hamamatsu 432, Japan*

**Bibliographers**

**Koichi Toyoda** (Ferroelectrics)
**S. B. Lang** (Pyroelectrics)

**Book Review Editor**

**S. C. Abrahams**, *Ashland, Oregon*

**EDITORIAL BOARD**

Ryuji Abe, *Nagoya, Japan*
F. Ainger, *Northhampton, United Kingdom*
K. S. Aleksandrov, *Krasnoiarsk, Russia*
A. S. Bhalla, *State College, Pennsylvania*
R. Blinc, *Ljubljana, Yugoslavia*
L. E. Cross, *State College, Pennsylvania*
V. Dvorak, *Prague, Czechoslovakia*
J. Fousek, *Prague, Czechoslovakia*
V. M. Fridkin, *Moscow, Russia*
A. M. Glass, *Murray Hill, New Jersey*
J. A. Gonzalo, *Madrid, Spain*
G. H. Haertling, *Clemson, South Carolina*
W. Heywang, *Munich, Germany*
B. Hilczer, *Poznan, Poland*
Sadao Hoshino, *Yokohama, Japan*
V. Janovec, *Prague, Czechoslovakia*
Jinzo Kobayashi, *Tokyo, Japan*
S. K. Kurtz, *University Park, Pennsylvania*
S. Lagerwall, *Göteborg, Sweden*
C. E. Land, *Albuquerque, New Mexico*
W. J. Lawless, *Westerville, Ohio*
R. LeBihan, *Nantes, France*
V. V. Lemanov, *St. Petersburg, Russia*
K. A. Müller, *Zürich, Switzerland*
H. E. Müser, *Saarbrücken, Germany*
Terutaro Nakamura, *Tokyo, Japan*
C. F. Pulvari, *Washington, DC*
G. A. Samara, *Albuquerque, New Mexico*
Shozo Sawada, *Iwaki, Japan*
H. Schmid, *Geneva, Switzerland*
G. Shirane, *Brookhaven, New York*
L. A. Shuvalov, *Moscow, Russia*
W. A. Smith, *Arlington, Virginia*
J. Stankowski, *Poznan, Poland*
E. C. Subbarao, *Pune, India*
Kenji Uchino, *Tokyo, Japan*
F. G. Ullman, *Lincoln, Nebraska*
Yu. N. Venevtsev, *Moscow, Russia*
Zhi-wen Yin, *Shanghai, Peoples Republic of China*
I. S. Zheludev, *Moscow, Russia*


## GENERAL INFORMATION

**Aims and Scope** *Ferroelectrics* is designed to provide a forum for people working in ferroelectrics and related materials such as ferroelastics, ferroelectric-ferromagnetics, electrooptics, piezoelectrics, pyroelectrics, nonlinear dielectrics, and liquid crystals. *Ferroelectrics* publishes experimental and theoretical papers aimed at the understanding of ferroelectricity and associated phenomena and applied papers dealing with the utilization of these materials in devices and systems. An important aspect of *Ferroelectrics* is to provide a vehicle for the publication of interdisciplinary papers involving ferroelectricity.

The editor invites original papers and short communications on the theory, fabrication, properties, and applications of ferroelectrics and related materials. In addition to research papers, *Ferroelectrics* publishes appropriate and timely review articles. There are no charges to authors or to institutions.

Notes for contributors can be found at the back of the journal.

**Please see inside back cover for information on subscription rates and ordering information.**


© 1992 Gordon and Breach Science Publishers S.A. All rights reserved.
No part of this publication may be reproduced or utilized in any form or by any means, electronic or mechanical, including photocopying and recording, or by any information storage or retrieval system, without permission in writing from the Publisher.

LICENSE TO PHOTOCOPY This publication is copyrighted and protected under the Universal Copyright Convention, The Berne Convention, and is also registered for copyright in the United States of America. The subscription rate for academic and corporate subscribers includes the Publisher's licensing fee which allows the subscriber photocopy privileges beyond the "fair use" provisions of the U.S.A. and most other national copyright laws. Please note, however, that the license does not extend to other kinds of copying, such as copying for general distribution, for advertising or promotion purposes, for creating new collective works, or for resale. If the subscriber wishes to apply to the Publisher for a waiver of the license fee, the subscriber further agrees that, upon acceptance and confirmation from the Publisher for the waiver, any copies which exceed the "fair use" provisions will require payment to the Copyright Clearance Center. It is expressly forbidden, through use of the Publisher's license or Copyright Clearance Center, for any individual or company to copy any article as agent, either express or implied, of another individual or company. For licensing information, please write to Gordon and Breach Science Publishers S.A., Y-Parc, Chemin de la Sallaz, 1400 Yverdon, Switzerland.

REPRINTS OF INDIVIDUAL ARTICLES Copies of individual articles may be obtained from the Publisher's own document delivery service at the appropriate fees. Write to: SCAN, P.O. Box 786, Cooper Station, New York, NY 10276, U.S.A. or P.O. Box 90, Reading, Berkshire RG1 8JL, Great Britain. Special Fax Service: U.S.A.: (212) 645-2459 or Great Britain: (0734) 568211.

Permission to reproduce and/or translate material contained in this journal must be obtained in writing from the Publisher. Please contact Rights and Permissions Officer, Gordon and Breach Science Publishers S.A., Y-Parc, Chemin de la Sallaz, 1400 Yverdon, Switzerland.



Distributed for Gordon and Breach Science Publishers S.A. by STBS Ltd., P.O. Box 90, Reading, Berkshire RG1 8JL, Great Britain. Printed in the United States of America.

FERROELECTRICS, ISSN 0015-0193, is published monthly for U.S. $298.00 per volume by Gordon and Breach Science Publishers S.A., Y-Parc, Chemin de la Sallaz, 1400 Yverdon, Switzerland. Second-class postage paid at New York, NY and additional mailing offices. POSTMASTER: Send address changes to FERROELECTRICS, c/o Gordon and Breach Science Publishers S.A., P.O. Box 786, Cooper Station, New York, NY 10276.

AUGUST 1992

PROCEEDINGS OF

# THE SECOND EUROPEAN CONFERENCE ON THE APPLICATION OF POLAR DIELECTRICS

TO CELEBRATE

**The 25th Anniversary of the Dielectric Society**

**incorporating**

**1st International Workshop on Integrated Ferroelectrics**

Part I of II Parts

12–15 April 1992
London, United Kingdom

**Guest Editors**

J. M. Herbert
R. W. Whatmore

DTIC QUALITY INSPECTED 4


| Accesion For | | |
|---|---|---|
| NTIS CRA&I | X | |
| DTIC TAB | ☐ | |
| Unannounced | ☐ | |
| Justification per DLW | | |
| By | | |
| Distribution / | | |
| Availability Codes | | |
| Dist | Avail and / or Special | |
| A-1 | | |


93-06205

93 3 25 150

# REPORT DOCUMENTATION PAGE

Form Approved
OMB No 0704-0188

Public reporting burden for this collection of information is estimated to average 1 hour per response, including the time for reviewing instructions, searching existing data sources, gathering and maintaining the data needed, and completing and reviewing the collection of information. Send comments regarding this burden estimate or any other aspect of this collection of information, including suggestions for reducing this burden, to Washington Headquarters Services, Directorate for Information Operations and Reports, 1215 Jefferson Davis Highway, Suite 1204, Arlington, VA 22202-4302, and to the Office of Management and Budget, Paperwork Reduction Project (0704-0188), Washington, DC 20503.

| 1. AGENCY USE ONLY (Leave blank) | 2. REPORT DATE | 3. REPORT TYPE AND DATES COVERED |
|---|---|---|
| | 1 April 1993 | Final |

**4. TITLE AND SUBTITLE** Proceedings of the Second European Conference on the Application of Ferroelectrics Ferroelectrics Vol. 133 (1-4), Vol. 134 (1-4), 1992

**5. FUNDING NUMBERS**
N00014-92-J-1497
R-T Project:
Conf 1032 --- 01

**6. AUTHOR(S)**
Conference Attendees

Editors: J. M. Herbert, R. W. Whatmore

**7. PERFORMING ORGANIZATION NAME(S) AND ADDRESS(ES)**
The Pennsylvania State University
Sponsored Programs and Contracts Office
248 Calder Way, Suite 300
University Park, PA 16802

**8. PERFORMING ORGANIZATION REPORT NUMBER**
FE 133, 134 (1-4) 1992

**9. SPONSORING/MONITORING AGENCY NAME(S) AND ADDRESS(ES)**
Wallace A. Smith
Code 1131, ONR
800 North Quincy Street
Arlington, VA 22217-5000

**10. SPONSORING MONITORING AGENCY REPORT NUMBER**
N/A

**11. SUPPLEMENTARY NOTES**
Prepared in cooperation with other sponsoring agencies and the ECAPD-2 committee.

**12a. DISTRIBUTION/AVAILABILITY STATEMENT**
The proceedings are available to all those attending the conference and to subscribers of the journal Ferroelectrics.

**12b. DISTRIBUTION CODE**

**13. ABSTRACT** *(Maximum 200 words)*

The Second European Meeting on the Applications of Polar Dielectrics was held in April 1992 to celebrate the 25th Anniversary of the Dielectric Society. Recognising the rising importance of thin films of ferroelectrics for a wide range of applications, the meeting also incorporated the 1st International Workshop on Integrated Ferroelectrics. To facilitate international participation the meeting was held at Imperial College, London.

Over 150 delegates registered for the meeting from 27 countries. Unfortunately, attendance from Eastern Europe was limited by the present economic and political problems. However, the generous financial support provided by our sponsors enabled the organisers to assist the attendance of many from this region and to provide reduced attendance costs for students.

Reflecting the current extent of interest in dielectric materials, 175 abstracts were submitted. Topics ranged from stable ceramics for microwave applications to organic crystals and polymers with high non-linear electro-optical coefficients. About one sixth of the contributions were concerned with the preparation and properties of thin films, particularly those involving ferroelectric materials.

**14. SUBJECT TERMS**
Ferroelectrics, Thin Films, Piezoelectrics, Pyroelectrics, Dielectrics, Electro-optics, Crystals, Ceramics

**15. NUMBER OF PAGES**
688

**16. PRICE CODE**

| 17. SECURITY CLASSIFICATION OF REPORT | 18. SECURITY CLASSIFICATION OF THIS PAGE | 19. SECURITY CLASSIFICATION OF ABSTRACT | 20. LIMITATION OF ABSTRACT |
|---|---|---|---|
| unclassified | unclassified | unclassified | SAR |

NSN 7540-01-280-5500

Standard Form 298 (Rev. 2-89)
Prescribed by ANSI Std. Z39-18
298-102

## GENERAL INSTRUCTIONS FOR COMPLETING SF 298

The Report Documentation Page (RDP) is used in announcing and cataloging reports. It is important that this information be consistent with the rest of the report, particularly the cover and title page. Instructions for filling in each block of the form follow. It is important to ***stay within the lines*** to meet ***optical scanning requirements***.

**Block 1.** Agency Use Only *(Leave blank)*.

**Block 2.** Report Date. Full publication date including day, month, and year, if available (e.g. 1 Jan 88). Must cite at least the year.

**Block 3.** Type of Report and Dates Covered. State whether report is interim, final, etc. If applicable, enter inclusive report dates (e.g. 10 Jun 87 - 30 Jun 88).

**Block 4.** Title and Subtitle. A title is taken from the part of the report that provides the most meaningful and complete information. When a report is prepared in more than one volume, repeat the primary title, add volume number, and include subtitle for the specific volume. On classified documents enter the title classification in parentheses.

**Block 5.** Funding Numbers. To include contract and grant numbers; may include program element number(s), project number(s), task number(s), and work unit number(s). Use the following labels:

| | | | |
|---|---|---|---|
| C | - Contract | PR | - Project |
| G | - Grant | TA | - Task |
| PE | - Program Element | WU | - Work Unit Accession No. |

**Block 6.** Author(s). Name(s) of person(s) responsible for writing the report, performing the research, or credited with the content of the report. If editor or compiler, this should follow the name(s).

**Block 7.** Performing Organization Name(s) and Address(es). Self-explanatory.

**Block 8.** Performing Organization Report Number. Enter the unique alphanumeric report number(s) assigned by the organization performing the report.

**Block 9.** Sponsoring/Monitoring Agency Name(s) and Address(es). Self-explanatory.

**Block 10.** Sponsoring/Monitoring Agency Report Number. *(If known)*

**Block 11.** Supplementary Notes. Enter information not included elsewhere such as: Prepared in cooperation with ...; Trans. of ...; To be published in ... When a report is revised, include a statement whether the new report supersedes or supplements the older report.

**Block 12a.** Distribution/Availability Statement. Denotes public availability or limitations. Cite any availability to the public. Enter additional limitations or special markings in all capitals (e.g. NOFORN, REL, ITAR).

- DOD - See DoDD 5230.24, "Distribution Statements on Technical Documents."
- DOE - See authorities.
- NASA - See Handbook NHB 2200.2.
- NTIS - Leave blank.

**Block 12b.** Distribution Code.

- DOD - Leave blank.
- DOE - Enter DOE distribution categories from the Standard Distribution for Unclassified Scientific and Technical Reports.
- NASA - Leave blank.
- NTIS - Leave blank.

**Block 13.** Abstract. Include a brief *(Maximum 200 words)* factual summary of the most significant information contained in the report.

**Block 14.** Subject Terms. Keywords or phrases identifying major subjects in the report.

**Block 15.** Number of Pages. Enter the total number of pages.

**Block 16.** Price Code. Enter appropriate price code *(NTIS only)*.

**Blocks 17. - 19.** Security Classifications. Self-explanatory. Enter U.S. Security Classification in accordance with U.S. Security Regulations (i.e., UNCLASSIFIED). If form contains classified information, stamp classification on the top and bottom of the page.

**Block 20.** Limitation of Abstract. This block must be completed to assign a limitation to the abstract. Enter either UL (unlimited) or SAR (same as report). An entry in this block is necessary if the abstract is to be limited. If blank, the abstract is assumed to be unlimited.

13. ABSTRACT (Continued)

A wide range of sol-gel and vapour phase methods are still under development for piezoelectric, pyroelectric, electro-optic and information storage devices.

The main objective of such occasions is the interchange of ideas between individuals and encouragement of a feeling of common purpose among scientists and engineers. This was enhanced by the informal atmosphere at the poster sessions, the introductory buffet and banquet.

FERROELECTRICS
Volume 133 (1992)

# CONTENTS—PART I

**Note on Pagination, Author Index and Table of Contents**

*The Proceedings of The Second European Conference on the Application of Polar Dielectrics are being published in two volumes of* **Ferroelectrics** *(Volumes 133 and 134). To facilitate indexing and referring to these Proceedings, the page numbers of Volume 134 run continuously from the end of Volume 133. The complete Table of Contents and an Author Index appear in both Volumes 133 and 134.*

**ORGANIZING COMMITTEE** xvii

**LIST OF PARTICIPANTS** xix

**GUEST EDITORIAL** xxiii

## Section I: PLENARY PAPERS

**EoX1. MOLECULAR CRYSTALS AND LANGMUIR-BLODGETT FILMS FOR NON-LINEAR OPTICS**
P. GUNTER 1

**TfX2. A CRITICAL REVIEW OF VAPOUR PHASE DEPOSITION METHODS FOR FERROELECTRIC THIN FILMS**
A. I. KINGON, A. AUCIOLLO, D. LICHTENWALNER AND K. Y. HSIEH 3

**PyX3. IR BOLOMETERS AND THERMAL IMAGING: THE ROLE OF FERROELECTRIC MATERIALS**
R. WATTON 5

**PdX4. CERAMIC SENSORS AND ACTUATORS FOR SMART MATERIALS AND ADAPTIVE STRUCTURES**
L. E. CROSS 11

## Section II: INVITED PAPERS

**DeI6. THE INFLUENCE OF DEFECTS ON THE ELECTRICAL PROPERTIES OF PEROVSKITE AND PEROVSKITE-RELATED MATERIALS**
D. M. SMYTH 13

**EoI13. FERROELECTRIC POLYMER LIQUID CRYSTALS**
H. F. GLEESON 15

**Pcl2. NEW PIEZOELECTRIC COMPOSITES FOR ULTRASONIC TRANSDUCERS**
K. LUBITZ, A. WOLFF, G. PREU, R. STOLL AND B. SCHULMEYER 21

**Pdl1. PIEZO-ELECTRIC MOTORS AND THEIR APPLICATIONS**
H.-P. SCHÖNER 27

**Pyl11. PYROELECTRIC PROPERTIES OF THIN FILM LEAD SCANDIUM TANTALATE**
N. SHORROCKS, A. PATEL AND R. WHATMORE 35

**Pyl12. PYROELECTRIC SINGLE-ELEMENT DETECTORS AND ARRAYS BASED ON MODIFIED TGS**
G. HOFMANN, N. NEUMANN AND H. BUDZIER 41

**Tdl10. FERROELECTRIC THIN FILMS IN INTEGRATED MICROELECTRONIC DEVICES**
J. F. SCOTT, C. A. PAZ de ARAUJO, L. D. McMILLAN, H. YOSHIMORI, H. WATANABE, T. MIHARA, M. AZUMA, T. UEDA, T. UEDA, D. UEDA AND G. KANO 47

**Tdl18. PROCESS INTEGRATION OF THE FERROELECTRIC MEMORY FETs (FEMFETs) FOR NDRO FERRAM**
D. R. LAMPE, D. A. ADAMS, M. AUSTIN, M. POLINSKY, J. DZIMIANSKI, S. SINHAROY, H. BUHAY, P. BRABANT AND Y. M. LIU 61

**Tdl9. THIN FILMS FOR FERROELECTRIC DEVICES**
R. BRUCHHAUS 73

**Tfl7. ELECTRICAL PROPERTIES OF MOCVD-DEPOSITED PZT THIN FILMS**
Y. SAKASHITA, T. ONO, H. SEGAWA, K. TOMINAGA AND M. OKADA 79

**Tfl8. PULSED PLASMA DEPOSITION OF LEAD LANTHANUM ZIRCONATE TITANATE(PLZT) AND LEAD LANTHANUM TITANATE(PLT)**
I. P. LLEWELLYN, R. A. HEINECKE, K. L. LEWIS AND K. F. DEXTER 85

**Tfl14. FERROELECTRIC THIN FILMS FOR MEMORY APPLICATIONS: SOL-GEL PROCESSING AND DECOMPOSITION OF ORGANO-METALLIC COMPOUNDS**
M. KLEE AND P. K. LARSEN 91

**TfI15. DOMAIN ORIENTATION CHANGE INDUCED BY FERROELECTRIC FATIGUE PROCESS IN LEAD ZIRCONATE TITANATE CERAMICS**
W. PAN, C.-F. YUE AND S. SUN 97

**ThI3. THERMODYNAMIC PHENOMENOLOGY OF SELECTED COMPOSITIONS IN THE LANTHANUM-MODIFIED LEAD ZIRCONATE-TITANATE SOLID SOLUTION SYSTEM**
G. A. ROSSETTI, JR. 103

**TrI4. THE ROLE OF GRAIN BOUNDARIES IN CONDUCTION AND BREAKDOWN OF PEROVSKITE-TYPE TITANATES**
R. WASER 109

## Section III: CONTRIBUTED PAPERS
### IIIa. Dielectrics/Domains/Microstructure

**DiC7. AN ORIENTATIONAL GLASS MODEL OF ELECTROSTRICTION IN RELAXOR DIELECTRICS**
A. J. BELL, F. CHU AND M. DAGLISH 115

**DiC9. MODIFICATION OF THE RELAXOR PROPERTIES OF PLZT-1/95/5 BY THERMAL AND ELECTRICAL TREATMENT**
G. E. KUGEL, M. HAFID, J. HANDEREK, Z. UJMA AND D. DMYTROW 121

**DiC12. MAGNESIUM TITANATE MICROWAVE DIELECTRIC CERAMICS**
V. M. FERREIRA, F. AZOUGH, J. L. BAPTISTA AND R. FREER 127

**DiC14a. NEW BARIUM TITANATE BASED MATERIAL FOR MLCs WITH Ni ELECTRODE**
Y. SAKABE, Y. HAMAJI AND T. NISHIYAMA 133

**DiC15a. MULTILAYER CAPACITORS WITH COPPER INNER ELECTRODES**
K. HIRAKATA, S.-I. SATO, F. UCHIKOBA, Y. KOSAKA AND K. SAWAMURA 139

**DiC16a. PLASMA POLYMERISED THIN INSULATING FILMS**
A. SMITH AND C. W. SMITH 145

**DiC16b. DIELECTRIC RELAXATION SPECTROSCOPY OF A MODEL ANAEROBIC ADHESIVE**
B. P. McGETTRICK AND J. K. VIJ 151

**DiC17. HIGH DIELECTRIC CONSTANT CERAMICS IN THE $PbSc_{0.5}Ta_{0.5}O_3$-$PbZrO_3$ SYSTEM**
P. C. OSBOND AND R. W. WHATMORE 159

**DiP219. LINEARIZATION OF DIELECTRIC NONLINEARITY BY INTERNAL BIAS FIELDS**
U. ROBELS, CH. ZADON AND G. ARLT 163

**DiP222. MACROSCOPIC BEHAVIOUR OF THE DIFFUSE PHASE TRANSITIONS IN FERROELECTRIC RELAXORS**
R. P. S. M. LOBO, R. L. MOREIRA AND N. D. S. MOHALLEM 169

**DiP223. STRONGLY TEMPERATURE DEPENDENT ELECTRO-OPTIC COEFFICIENTS IN $BaTiO_3$**
F. ABDI, M. D. FONTANA, M. AILLERIE AND G. GODEFROY 175

**DiP224. NEODYMIUM TITANATE ($Nd_2Ti_2O_7$)CERAMICS**
G. WINFIELD, F. AZOUGH AND R. FREER 181

**DiP227. MICROWAVE DIELECTRIC PROPERTIES OF COMPLEX PEROVSKITE $Ba(Mg_{1/3}Ta_{2/3})O_3$**
E. S. KIM AND K. H. YOON 187

**DiP228. TIME DEPENDENCES OF DIELECTRIC CONSTANT IN $Ba(Ti_{0.95}Sn_{0.05})O_3$**
C. KAJTOCH 193

**DiP229. MICROWAVE AND MILLIMETRE WAVE DIELECTRIC SPECTROSCOPY OF FUNDAMENTAL DIELECTRIC DISPERSION IN FERROELECTRICS**
J. GRIGAS, J. BANYS AND R. SOBIESTIANSKAS 199

**DiP230. DIELECTRIC SPECTROSCOPY OF SOME $Ba(B'_{1/2}B''_{1/2})O_3$ COMPLEX PEROVSKITES IN THE $10^{11}$ - $10^{14}$ Hz RANGE**
J. PETZELT, R. ZURMÜHLEN, A. BELL, S. KAMBA, G. V. KOZLOV, A. A. VOLKOV AND N. SETTER 205

**DiP233. DIELECTRIC LOSS OF FERROELECTRIC LITHIUM TRIHYDROGEN SELENITE UNDER HYDROSTATIC PRESSURE**
S. FUJIMOTO AND K. KANAI 211

**DiP256. THE TEMPERATURE COEFFICIENT OF THE RELATIVE PERMITTIVITY OF COMPLEX PEROVSKITES AND ITS RELATION TO STRUCTURAL TRANSFORMATIONS**
E. L. COLLA, I. M. REANEY AND N. SETTER 217

**DoP234. DOMAIN WALL TRAPPING AS A RESULT OF INTERNAL BIAS FIELDS**
U. ROBELS, L. SCHNEIDER-STÖRMANN AND G. ARLT 223

**MsP145. ANOMALOUS TWIN STRUCTURES IN FERROIC CRYSTALS**
I. SHMYT'KO, I. BDIKIN AND N. AFONIKOVA 229

## Section III: CONTRIBUTED PAPERS
### IIIb. Transport Phenomena/Switching

**TrC10. ELECTRON EMISSION FROM FERROELECTRICS AND ITS APPLICATIONS**
G. ROSENMAN 235

**TrP140. POLARONIC TRANSPORT IN $LiNbO_3$ AT ELEVATED TEMPERATURES**
W. BAK, K. KRZYWANEK, C. KUŚ AND W. S. PTAK 241

**TrP141. PECULIARITIES OF POLARON ELECTRONICS OF COMPLEX OXIDES**
A. MYASNIKOVA 247

**TrP142. ELECTRON EMISSION AND SPONTANEOUS POLARIZATION DISTRIBUTION OF PROTON-EXCHANGED $LiNbO_3$**
S. B. LANG, G. ROSENMAN, S. RUSHIN, V. KUGEL AND D. NIR 253

**SwP218. ON THE POSSIBILITY OF AMPLITUDE AND DURATION OF ELECTRIC PULSE REGISTRATION BY MEANS OF FERROELECTRICS**
I. G. TOLSTIKOV AND E. Z. NOVITSKII 259

## Section III: CONTRIBUTED PAPERS
### IIIc. Sintering

**ThP152. COMPUTER SIMULATION OF SINTERING AND FRACTURE OF THE FERROELECTRIC MATERIALS**
D. KARPINSKY, I. PARINOV AND L. PARINOVA 265

**SmC5. HYDROTHERMALLY PROCESSED PIEZOELECTRIC AND ELECTROSTRICTIVE CERAMICS**
C. E. MILLAR, L. PEDERSEN AND W. W. WOLNY 271

**SmC11. EFFECT OF $V_2O_5$ ON DIELECTRIC PROPERTIES OF $Pb(Mg_{1/3}Nb_{2/3})O_3$ - $PbTiO_3$ CERAMICS**
K. H. YOON, J. H. CHUNG AND D. H. KANG 277

**SmP104. EFFECT OF THE INITIAL PARTICLE SIZE ON THE DIELECTRIC PROPERTIES OF $Pb(Fe_{1/2}Nb_{1/2})O_3$ CERAMICS**
K. B. PARK AND K. H. YOON 283

**SmP105. GROWTH OF RARE-EARTH MOLYBDATE CRYSTALS**
B. RED'KIN, V. KURLOV, I. PET'KOV AND S. ROSSOLENKO 289

**SmP108. EFFECT OF SUBSTITUTION $Ba^{2+}$ ION ON SINTERING AND DIELECTRIC PROPERTIES OF CERAMICS IN THE SYSTEM $Pb_{1-x}Ba_x(Cd_{1/3}Nb_{2/3})O_3$**
H.-J. JUNG, J.-H. SOHN, J.-G. BAEK AND S.-H. CHO 295

**SmP109. STUDY ON THE PREPARATION OF PZT CERAMIC MATERIAL FOR MEDIUM HIGH FREQUENCY SAW DEVICES BY LOW VACUUM ATMOSPHERE SINTERING**
M. M. WEI, F. GU AND W. Y. XIE 301

**SmP110. SYNTHESIS OF ELECTRONIC CERAMICS BY USING $CO_2$ LASER**
S. SUGIHARA AND T. FUKUYAMA 307

**AUTHOR INDEX** i

**ANNOUNCEMENTS**

FERROELECTRICS
Volume 134 (1992)

# CONTENTS—PART II

**Note on Pagination, Author Index and Table of Contents**

*The Proceedings of The Second European Conference on the Application of Polar Dielectrics are being published in two volumes of* ***Ferroelectrics*** *(Volumes 133 and 134). To facilitate indexing and referring to these Proceedings, the page numbers of Volume 134 run continuously from the end of Volume 133. The complete Table of Contents and an Author Index appear in both Volumes 133 and 134.*

**ORGANIZING COMMITTEES** xvii

**LIST OF PARTICIPANTS** xix

**GUEST EDITORIAL** xxiii

## Section III: CONTRIBUTED PAPERS
## IIId. Electro-Optics/Other Optical

**EoC21. STRONGLY TEMPERATURE DEPENDENT ELECTRO-OPTIC COEFFICIENTS IN $BaTiO_3$**
F. AFDI, M. D. FONTANA, M. AILLERIE AND G. GODEFROY 1/[313]

**EoC21a. PHOTOCONDUCTING FERROELECTRIC POLYMERS**
K. A. VERKHOVSKAYA, V. M. FRIDKIN, A. V. BUNE AND J. F. LEGRAND 7/[319]

**EoP202. SPATIAL RESOLUTION OF A PHASE-CONJUGATE RING-RESONATOR**
G. BALZER, T. KOBIALKA AND T. TSCHUDI 17/[329]

**EoP203. CIRCULAR PHOTOGALVANIC EFFECT OF SOME OPTICALLY ACTIVE CRYSTALS**
H. TOMIYASU, Y. FUKUSHIMA, Y. UESU AND S. TOYODA 23/[335]

**EoP250. RECENT ADVANCES IN TRANSPARENT FERROELECTRIC CERAMICS RESEARCH AND APPLICATIONS**
A. STERNBERG 29/[341]

**EoP254. THE ANALYSIS OF ELECTRIC FIELD FOR A PERIODIC ELECTRODE WITH A DIELECTRIC BUFFER-LAYER**
G.-S. LIN, J.-J. LIANG, W.-Y. LEE, P.-O. CHEN AND C.-C. CHEN 35/[347]

**EoP261. A NUMERICAL TECHNIQUE FOR ANALYSIS OF ARBITRARILY SHAPED INHOMOGENEOUS OPTICAL WAVEGUIDES**
H.-M. WANG, W.-Y. LEE, J.-J. LIANG AND S.-J. HWANG 41/[353]

**EoP264. LATTICE SITE OF TRANSITION METAL AND RARE-EARTH IMPURITIES IN $LiNbO_3$ SINGLE CRYSTALS. AN EXAFS STUDY**
C. ZALDO AND C. PRIETO 47/[359]

**PmP154. NEWLY DEVELOPED MULTICOMPONENT PIEZOCERAMIC SYSTEM FOR ALTERNATING PRESSURE SENSORS**
S. A. GRIDNEV, N. G. PAVLOVA, V. V. GORBATENKO AND L. A. SHUVALOV 53/[365]

## Section III. CONTRIBUTED PAPERS
### IIIe. Piezoelectric Composites

**PcC2. 1.3.1 PZT-POLYMER COMPOSITES FOR HIGH PRESSURE HYDROPHONE APPLICATION**
C. RICHARD, P. EYRAUD, L. EYRAUD, Ms. M. RICHARD AND G. GRANGE 59/[371]

**PcC3. 0–3 PIEZOELECTRIC—GLASS COMPOSITES**
S. SHERRIT, H. D. WIEDERICK, B. K. MUKHERJEE AND S. E. PRASAD 65/[377]

**PcC15b. NON-POLAR POLYMER/FERRO AND ANTIFERROELECTRIC CERAMIC COMPOSITE FILMS FOR HIGH ENERGY STORAGE CAPACITORS**
D. K. DAS-GUPTA AND Z. SHUREN 71/[383]

**PcP123. MICROSTRUCTURAL DEPENDENCE OF PIEZOELECTRIC PROPERTIES OF CERAMIC-GLASS COMPOSITES**
L. PARDO, F. CARMONA, C. ALEMANY AND B. JIMENEZ 77/[389]

## Section III. CONTRIBUTED PAPERS
### IIIf. Piezoelectric Devices and Materials

**PdC1. PIEZOELECTRIC MICRO-MOTOR**
M. KANNO, H. OKABE AND S. SAKANO 83/[395]

**PdC4a. THE ACTIVE CONTROL OF SOUND REFLECTION/TRANSMISSION COEFFICIENTS USING PIEZOELECTRIC COMPOSITE MATERIALS**
A. J. SALLOWAY, R. C. TWINEY, R. W. WHATMORE AND R. LANE 89/[401]

**PdC13. INVESTIGATIONS INTO PIEZOELECTRIC SPARK GENERATORS**
P. GONNARD, C. GARABEDIAN, H. OHANESSIAN AND L. EYRAUD 93/[405]

**PdP131. LOW SIGNAL ANALYSIS OF PIEZOELECTRIC TRANSFORMERS**
R. PÉREZ, L. BENADERO, A. ALBAREDA, M. TRESANCHEZ, J. A. GORRI AND J. L. VILLAR 99/[411]

**PdP133. ACCURACY OF THE FORMULAS USED FOR THE CHARACTERIZATION OF PIEZOELECTRIC THICKNESS MODE RESONATORS WITH IMPEDANCE ANALYZERS**
J. L. SAN EMETERIO PRIETO 105/[417]

**PdP135. NON-ITERATIVE EVALUATION OF THE REAL AND IMAGINARY MATERIAL CONSTANTS OF PIEZOELECTRIC RESONATORS**
S. SHERRIT, H. D. WIEDERICK AND B. K. MUKHERJEE 111/[423]

**PdP136. APPLICATION OF PIEZOELECTRIC ACTUATOR TO BURR-FREE BLANKING**
Y. KAWAMURA AND KOZO MATSUMOTO 121/[433]

**PdP152. THE INFLUENCE OF THE ELECTRIC STIFFENING ON THE RESONANT FREQUENCY TEMPERATURE DEPENDENCE OF QUARTZ RESONATORS**
J. ZELENKA 127/[439]

**PmC4. PIEZOELECTRIC PROPERTIES OF $Pb(Zn_{1/3}Nb_{2/3})O_3$-$(PbTiO_3)$ PREPARED BY HIP**
T. TAKENAKA, K. MURAMATSU AND T. FUJIU 133/[445]

**PmC6. GIANT ELECTROSTRICTION OF FERROELECTRICS WITH DIFFUSE PHASE TRANSITION—PHYSICS AND APPLICATIONS**
V. V. LEMANOV, N. K. YUSHIN, E. P. SMIRNOVA, A. V. SOTNIKOV, E. A. TARAKANOV AND A. YU. MAKSIMOV 139/[451]

**PmC6a. MAXIMAL ELECTROMECHANICAL COUPLING IN PIEZOELECTRIC CERAMICS—ITS EFFECTIVE EXPLOITATION IN ACOUSTIC TRANSDUCERS**
W. A. SMITH 145/[457]

**PmP111. EFFECTS OF DOPANT $Nb^{+5}$ ON LEAD ZIRCONATE-TITANATE**
T. KATO, N. YAMADA AND A. IMAI 151/[463]

**PmP113. FREQUENCY DEPENDENCE OF THE PIEZOELECTRIC $d_{31}$ COEFFICIENT AS A FUNCTION OF CERAMIC TETRAGONALITY**
J. M. VICENTE AND B. JIMÉNEZ 157/[469]

**PmP114. PROPERTIES OF SUBSTITUTED $PbNb_2O_6$ CERAMICS AND MEASUREMENT OF THEIR LGW ELECTROMECHANICAL COEFFICIENTS**
R. BRIOT, N. GLISSA AND M. TROCCAZ 163/[475]

**PmP116. STUDIES ON FLAWS IN PZT CERAMICS USED IN UNDERWATER DETECTION TRANSDUCERS**
M. M. GUILLEMOT-AMADEI, P. GONNARD AND M. TROCCAZ 169/[481]

**PmP118. PIEZOELECTRIC CERAMICS FOR HIGH-TEMPERATURE TRANSDUCERS**
L. KORZUNOVA 175/[487]

**PmP262. THE TRANSIENT PIEZOELECTRIC RESPONSE OF IMPACT LOADED PZT CERAMICS**
J. A. CLOSE AND R. STEVENS 181/[493]

## Section 3. CONTRIBUTED PAPERS
### IIIg. Pyroelectrics

**PcP151. THIN-FILM PYROELECTRIC INORGANIC/ORGANIC COMPOSITES**
C. E. MURPHY, T. RICHARDSON AND G. G. ROBERTS 189/[501]

**PyC18. PYROELECTRIC PROPERTIES OF RAPID GROWTH ATGSP CRYSTALS**
F. CHANGSHUI, W. QINGWU, Z. HONGSHENG AND W. MIN 195/[507]

**PyP214. INFLUENCE OF SURFACE LAYERS AND ELECTROTHERMAL COUPLING ON DIELECTRIC LOSS OF THIN CHIPS MADE FROM MODIFIED TRIGLYCINE SULPHATE**
N. NEUMANN AND G. HOFMANN 201/[513]

**PyP216. PYROELECTRIC RESPONSE OF PIEZOELECTRICS**
YU. M. POPLAVKO, M. E. ILCHENKO AND L. P. PEREVERZEVA 207/[519]

**PyP217. THE ELECTROCALORIC COEFFICIENT OF LATGS CRYSTALS**
F. JIMENEZ-MORALES 213/[525]

**PyP247. STUDIES ON THE DIELECTRIC, PIEZOELECTRIC, PYROELECTRIC AND STRUCTURAL PROPERTIES OF $(Pb_{1-x}Gd_x)(Zr_{.6}Ti_{.4})O_3$**
A. GOVINDAN, H. D. SHARMA, A. K. TRIPATHI, P. K. C. PILLAI AND T. C. GOEL 217/[529]

**PyP261. CHARACTERIZATION OF FERROELECTRIC $LiTaO_3$ THIN FILM**
A. KANDUŠER, Đ. MANDRINO, M. KOSEC, P. PANJAN AND B. B. LAVRENČIČ 223/[535]

## Section III. CONTRIBUTED PAPERS
### IIIh. PVDF and Copolymers

**PvP127. EFFECT OF MOISTURE ON THE ELECTRICAL PROPERTIES OF BIAXIALLY STRETCHED POLYVINYLIDENEFLUORIDE (PVDF) FILMS**
P. A. RIBEIRO, M. RAPOSO AND J. N. MARAT-MENDES 229/[541]

**PvP128. INTERACTION OF CORONA DISCHARGE SPECIES WITH TEFLON-FEP (FLUOROETHYLENEPROPYLENE) FOILS**
M. RAPOSO, P. A. RIBEIRO AND J. N. MARAT-MENDES 235/[547]

**PvP129. STUDY OF THE POLARIZATION OF VDF-TrFE 75%–25% COPOLYMER FILMS USING THE PRESSURE WAVE PROPAGATION METHOD**
C. LABURTHE TOLRA, C. ALQUIE AND J. LEWINER 241/[553]

**PvP150. DIFFUSE PHASE TRANSITION IN FERROELECTRIC POLYMERS**
R. L. MOREIRA AND B. V. COSTA 247/[559]

## Section III. CONTRIBUTED PAPERS
### IIIi. Phase Transitions/General

**PtP240. PHASE TRANSITIONS IN PLZT CERAMICS**
U. BÖTTGER, A. BIERMANN AND G. ARLT 253/[565]

**PtP242. FLUCTUATIONS OF INCOMMENSURATE WAVE NEAR PARAELECTRIC-MODULATED PHASE TRANSITION IN $Rb_2ZnCl_4$**
M. P. TRUBITSYN AND V. V. SAVCHENKO 259/[571]

**PtP251. PHASE TRANSITIONS IN HIGHLY DISORDERED FERROELECTRICS**
N. K. YUSHIN AND S. N. DOROGOVTSEV 265/[577]

**FgP244. PRESSURE-ELECTRIC EFFECT IN POLAR DIELECTRICS**
R. POPRAWSKI 271/[583]

## Section III. CONTRIBUTED PAPERS
### IIIj. Ferroelectric Thin Films (Materials and Devices)

**TfC13. RAPID THERMAL PROCESSING OF PZT THIN FILMS**
Y. HUANG, I. M. REANEY AND A. J. BELL 285/[597]

**TfC14. GROWTH OF PARA- AND FERROELECTRIC EPITAXIAL LAYERS OF $KTa_{1-x}Nb_xO_3$ BY LIQUID PHASE EPITAXY**
R. GUTMANN, J. HULLIGER AND H. WÜEST 291/[603]

**TfC16. GROWTH OF PEROVSKITE PLZT THIN FILMS BY DUAL ION BEAM SPUTTERING**
D. A. TOSSELL, N. M. SHORROCKS, J. S. OBHI AND R. W. WHATMORE 297/[609]

**TfC17. MICROSTRUCTURAL, COMPOSITIONAL AND ELECTRICAL CHARACTERIZATION OF FERROELECTRIC LEAD ZIRCONATE TITANATE THIN FILMS**
M. HUFFMAN, F. D. GEALY, L. KAMMERDINER, P. ZURCHER, J. G. ZHU, M. AL-JASSIM AND C. ECHER 303/[615]

**TfC23. PHASE TRANSITIONS IN FERROELECTRIC FILMS**
D. R. TILLEY AND B. ZEKS 313/[625]

**TfP205. PREPARATION OF LEAD TITANATE THIN FILMS BY REACTIVE ELECTRON BEAM COEVAPORATION USING OZONE**
S. MOCHIZUKI, T. MIHARA, S. KIMURA AND T. ISHIDA 319/[631]

**TfP210. THIN-FILM ZnO ULTRASONIC TRANSDUCER ARRAYS FOR OPERATION AT 100 MHz**
Y. ITO, K. KUSHIDA, H. KANDA, H. TAKEUCHI, K. SUGAWARA AND H. ONOZATO 325/[637]

**TfP253. 53/47 PZT FILMS BY METALLO-ORGANIC DECOMPOSITION TECHNOLOGY FOR NON-VOLATILE MEMORY APPLICATIONS**
W. ZHU AND R. W. VEST 331/[643]

**TfP255. MAGNETOELECTRIC EFFECTS IN FERROELECTROMAGNETIC FILMS**
I. E. CHUPIS 337/[649]

**TfP258. PHYSICOCHEMICAL PROPERTIES OF SOL-GEL DERIVED LEAD SCANDIUM TANTALATE $Pb(Sc_{0.5}Ta_{0.5})O_3$ THIN FILMS**
A. PATEL, N. SHORROCKS AND R. WHATMORE 343/[655]

**TfP259. GROWTH OF PLZT THIN FILMS USING CLUSTER MAGNETRON TECHNIQUES**
K. F. DEXTER, K. L. LEWIS AND J. E. CHADNEY 349/[661]

**TdC20. HIGH SPEED OPTO-ELECTRONIC NON-DESTRUCTIVE READOUT FROM FERROELECTRIC THIN FILM CAPACITORS**
S. THAKOOR 355/[667]

**TdP213. FERROELECTRIC THIN FILMS FOR MICROELECTRONIC APPLICATIONS**
E. V. ORLOVA, V. I. PETROVSKY, E. F. PEVTSOV, A. S. SIGOV AND K. A. VOROTILOV 365/[677]

**AUTHOR INDEX** i

**ANNOUNCEMENTS**

# THE SECOND EUROPEAN CONFERENCE ON THE APPLICATION OF POLAR DIELECTRICS

12–15 April 1992
London, United Kingdom

## ORGANIZING COMMITTEE

| | |
|---|---|
| F. W. Ainger | Conference Chair and Treasurer of the Dielectric Society |
| R. W. Whatmore | Programme Chair |
| K. J. Humphrey | Secretary |
| R. C. Twiney | Exhibition |
| P. Groves | Programme |
| A. J. Bell | European Co-ordinator |
| R. Freer | University Liaison |
| J. H. Calderwood | Chairman of the Dielectric Society |
| R. M. Hill | The Dielectric Society |
| B. C. H. Steele | Local Representative |
| G. W. Taylor | Editor *Ferroelectrics* |
| S. B. Lang | Associate Editor *Ferroelectrics* |

## IWIF-1

| | |
|---|---|
| R. Panholzer | Chairman |
| J. Alexander | Programme |
| J. F. Scott | Representing ISIF |
| C. A. P. Araujo | Representing ISIF |
| F. W. Ainger | Co-ordinator |

J. M. Herbert, Guest Editor

The Organizers wish to thank the following for their generous support:

Defence Advanced Research Projects Agency, DARPA, ONREUR, Gordon and Breach Science Publishers, The Dielectric Society, Cooksons Plc, and GEC-Marconi Materials Technology Group.

*Ferroelectrics*, 1992, Vol. 133, pp. xix–xxi
Reprints available directly from the publisher
Photocopying permitted by license only

© 1992 Gordon and Breach Science Publishers S.A.
Printed in the United States of America

# LIST OF PARTICIPANTS

**AUSTRALIA**
CHAN, H. L. W.

**BRAZIL**
MOREIRO, R. L.

**CANADA**
MUKHERJEE, B. K.

**CHINA**
FANG, C. S.

**CZECHOSLOVAKIA**
KAMBA, S.
PETZELT, J.

**DENMARK**
MILLAR, C. E.

**FINLAND**
JANTUNEN, H.
TURUNEN, A.

**FRANCE**
ACHARD, H.
AILLERIE, M.
FONTANA, M.
GARABEDIAN, C.
GAUCHER, P.
GONNARD, P.
HADNI, A.
KUGEL, G. E.
LE BIHAN, R.
LE MOËL, A.
LEWINER, J.
RICHARD, C.
TROCCAZ, M.

**GERMANY**
BALZER, G.
BÖTTGER, U.
BRUCHHAUS, R.
HOFMANN, G.
KLEE, M.
KLIEM, H.
KOBIALKA, T.
KUNTZ, M.
LUBITZ, K.
NEUMANN, N.
QUAD, R.
ROBELS, U.
SCHÖNER, H. P.
SIMON, M.
WASER, R.

**INDIA**
BHANUMATHI, A.
PILLAI, P. K. C.
RAMANA MURTY, K. V.

**IRELAND**
McGETTRICK, B. P.
SESHADRI, A. T.

**ISRAEL**
LANG, S. B.
ROSENMAN, G.

**ITALY**
WATTS, B.

**JAPAN**
FUJIMOTO, S.
HAMAJI, Y.
HIRAKATA, K.
HIRAKATA, M.
ITOU, Y.
KANNO, M.
KATO, T.
KAWAMURA, Y.
MOCHIZUKI, S.
SAKASHITA, Y.
SEGAWA, H.
SUGIHARA, S.
TAKENAKA, T.
TOMIYASU, H.

UESU, Y.

**KOREA**
CHO, S. H.
SOO, K. E.
YOON, K. H.

**LATVIA**
STERNBERG, A.

**LITHUANIA**
BANYS, J.

**MOROCCO**
ELAMMARI, L.
OUCHETTO, M.

**POLAND**
POPRAWSKI, R.

**PORTUGAL**
FERREIRA, V. M.
MARAT-MANDES, J. N.
RAPOSO, M.
RIBEIRO, P. A.

**RUSSIA**
FRIDKIN, V.
LEMANOV, V. V.
PARINOV, I. A.
SHUVALOV, L. A.
SIGOV, A. S.
VERKHOVSKAYA, K. A.

**SLOVENIA**
LAVRENCIC, B. B.

**SPAIN**
BENADERO, A.
JIMENEZ, B.
SAN EMETERIO PRIETO, J. L.
ZALDO, C.

**SWITZERLAND**
BELL, A. J.
BICHSTEL, R.
COLLA, E. L.
DAMJANOVIC, D.
FORSTER, M.
GÜNTER, P.
GUTMANN, R.
HUANG, Y.
VAN DER KLINK, J.
LUTHIER, R.
REANEY, I. M.
ROLAND, G.
SREENIVAS, K.
STURZENEGGER, M.
ZURMUHLEN, R.

**THE NETHERLANDS**
FEINER, L. F.
LARSEN, P. K.

**TAIWAN**
LEE, W. Y.
WANG, H. M.

**UNITED KINGDOM**
AINGER, F. W.
ANIS, M. K.
AZOUGH, F.
BUTCHER, S.
CALDERWOOD, J. H.
CALZADA, M. L.
CANNELL, D. S.
CHILTON, J.
CLOSE, J. A.
DAS-GUPTA, D. K.
DEXTER, K. F.
FOTHERGILL, J.
FREER, R.
GARNER, G.
GLEESON, H.
GROVES, P.
HALL, D. A.
HERBERT, J.
HUMPHREY, K. J.
KINSMAN, B.
LEWIS, T. J.
LLEWELLYN, I. P.
MAGILL, J. H.
MURPHY, C. E.
MURRAY, S.

OSBOND, P.
PATEL, A.
SALLOWAY, A. J.
SHORROCKS, N. M.
SIMPSON, J. A.
SIRISOON-THORN, S.
SMITH, C. W.
TILLEY, D.
TODD, M.
TONTRAKOON, J.
TOSSELL, D.
TWINEY, R. C.
WANG, H. W.
WATTON, R.
WHATMORE, R.
WILLIAMS, M.

**UKRAINE**
POPLAVKO, Y. M.

**USA**
ALEXANDER, J.
BECKER, R.
CROSS, L. E.
DEY, S. K.
GRABOWSKI, J.
HUFFMAN, M.
KINGON, A. I.
LAMPE, D. R.
McMILLAN, L.
PAN, W.
PANHOLZER, R.
RANDALL, C. A.
ROSETTI, JR., G. A.
SCOTT, J.
SMITH, W. A.
SMYTH, D. M.
TAYLOR, G. W.
THAKOOR, S.

# GUEST EDITORIAL

The Second European Meeting on the Applications of Polar Dielectrics was held in April 1992 to celebrate the 25th Anniversary of the Dielectric Society. Recognising the rising importance of thin films of ferroelectrics for a wide range of applications, the meeting also incorporated the 1st International Workshop on Integrated Ferroelectrics. To facilitate international participation the meeting was held at Imperial College, London.

Over 150 delegates registered for the meeting from 27 countries. Unfortunately, attendance from Eastern Europe was limited by the present economic and political problems. However, the generous financial support provided by our sponsors enabled the organisers to assist the attendance of many from this region and to provide reduced attendance costs for students.

Reflecting the current extent of interest in dielectric materials, 175 abstracts were submitted. Topics ranged from stable ceramics for microwave applications to organic crystals and polymers with high non-linear electro-optical coefficients. About one sixth of the contributions were concerned with the preparation and properties of thin films, particularly those involving ferroelectric materials. A wide range of sol-gel and vapour phase methods are still under development for piezoelectric, pyroelectric, electro-optic and information storage devices.

In the case of thin films for electro-mechanical applications, processes are sought which will yield multilayer structures that give large movements for small applied voltages. For information storage, it is already possible to deposit high permittivity layers on silicon, but it is proving more difficult to produce materials exhibiting switchable polar states that retain this property after prolonged exposure to the large variety of switching pulse sequences that may be experienced in storage systems. The great improvements already achieved promise eventual success.

For electro-optical applications, the possibilities of non-linear behaviour have been expanded by the use of organic compounds for which the Langmuir Blodgett technique remains an important means of obtaining large areas of oriented molecules.

The uses of ferroelectric ceramics in electro-mechanical transducers continue to expand with, for instance, the possibility of efficient small motors based on surface waves. New compositions offering improved electrostrictive and piezoelectric properties are being developed. The behaviour of domain walls underlying such phenomena as the poling of ceramics and the changes in dielectric properties with time are under scrutiny. Models explaining the interaction of lattice defects with walls are increasingly successful. High permittivity dielectric ceramics that can be sintered with base-metal electrodes *in situ* are being further improved by combining donor with acceptor substituents so as to minimise the concentration of vacant oxygen sites and thereby prolong life at high temperatures under high fields. High stability dielectrics continue to be studied for microwave applications and thin organic polymer films as constituents of silicon circuits.

The main objective of such occasions is the interchange of ideas between individuals and the encouragement of a feeling of common purpose among scientists

and engineers. This was enhanced by the informal atmosphere at the poster sessions, the introductory buffet and banquet.

The organisers would particularly like to thank the financial sponsors (DARPA, ONR Europe and Gordon and Breach Science Publishers) for their support and the Dielectric Society for sponsoring and underwriting the conference, and allowing the occasion of their 25th anniversary to be used for ECAPD-2.

Grateful thanks are also due to all those who gave their time in the organisation and execution of the meeting and to their partners for patient forebearance and, in many cases, active assistance on registration desks, poster assembly, etc.

Finally, the programme chair would like to add a personal word of thanks to his friends and colleagues who assisted with the production of the abstract book and spent much time refereeing and commenting upon manuscripts.

We all look forward to ECAPD-3, to be held in Germany in 1996.

J. M. Herbert
R. W. Whatmore

# SECTION I
# PLENARY PAPERS

*Ferroelectrics*, 1992, Vol. 133, p. 1
Reprints available directly from the publisher
Photocopying permitted by license only

© 1992 Gordon and Breach Science Publishers S.A.
Printed in the United States of America

# EoX1

## MOLECULAR CRYSTALS AND LANGMUIR-BLODGETT FILMS FOR NON-LINEAR OPTICS

P Gunter, Non-Linear Optics Laboratory, Institute of Quantum Electronics, ETH-Honggerber 8093, Zurich

Organic materials with extended, delocalized π-electron systems and functional groups acting as electron donors and acceptors have been shown to have non-linear optical and electro-optical effects which can be more than one order of magnitude larger than in any other material. Non-linear optical bulk single crystals and crystalline thin films, crystal cored optical fibres, Langmuir-Blodgett films as well as poled polymers have been prepared. The non-linear optical effects observed in these materials will be described, the relationship between the molecular arrangement and the functional properties outlined and the main materials requirements for optoelectronic and photonic applications will be given.

Recent results on the preparation of novel molecular crystals and Langmuir-Blodgett films and the measurement of their optical and non-linear optical properties will be discussed. First guided-wave non-linear optics experiments in DCANP Langmuir-Blodgett films will be presented[1,2].

Ref [1] G Decher, B Tieke, Ch Bosshard and P Gunter, Ferroelectrics 91, 193 (1989).

[2] Ch Bosshard, M Flosheimer, M Kupfer and P Gunter, Opt Commun 85, 247 (1991)

*Ferroelectrics*, 1992, Vol. 133, p. 3
Reprints available directly from the publisher
Photocopying permitted by license only

© 1992 Gordon and Breach Science Publishers S.A.
Printed in the United States of America

# TfX2

## A CRITICAL REVIEW OF VAPOUR PHASE DEPOSITION METHODS FOR FERROELECTRIC THIN FILMS

A I Kingon, A Auciollo[1], D Lichtenwalner and K Y Hsieh, Department of Materials Science and Engineering, North Carolina State University, Raleigh, NC 27695-7919, USA

[1]Microelectronics Center of North Carolina, Research Triangle Park, NC

The paper presents a brief critical view of vapour phase deposition techniques, which are currently being utilized for the deposition of ferroelectric thin films. These techniques include chemical vapour deposition (CVD) and plasma enhanced (PE) CVD, sputtering (plasma and ion beam) and pulsed laser ablation deposition (PLD).

In each case, the technique is briefly described, the sources of development referenced, and mention is made of the ferroelectric materials systems deposited. More particularly, critical advantage and disadvantages of each technique are discussed, and process issues which require attention by reserach groups are emphasized.

Special attention is paid to stoichiometry control, film homogeneity, Pb-based systems, deposition rates, scale and epitaxial versus polycrystalline films.

A general conclusion is made that advantages and disadvantages of each technique need to be understood in relation to the application.

*Ferroelectrics*, 1992, Vol. 133, pp. 5–10
Reprints available directly from the publisher
Photocopying permitted by license only
© 1992 Gordon and Breach Science Publishers S.A.
Printed in the United States of America

# PyX3

## IR BOLOMETERS AND THERMAL IMAGING: THE ROLE OF FERROELECTRIC MATERIALS

REX WATTON
Defence Research Agency, Electronics Division, St Andrews Road, Malvern, Worcs WR14 3PS.

Abstract Large arrays of bolometer elements have considerable potential for thermal imaging applications, offering uncooled operation, and a performance which challenges the cooled semiconductor detectors. A hybrid array technology, exploiting pyroelectric materials, is the basis of a successful range of linear and 2-D arrays. Ceramic uniformity for large area arrays is good but wafer processing is demanding. Other technologies will compete for cost-effectiveness in large area devices. Ferroelectric thin films have recently shown marked improvement in the merit figures and, if compatible with the silicon IC, may allow a more direct array fabrication. Thin film resistance bolometers have advantages in ease of fabrication, but there are also some inherent disadvantages, when compared with the ferroelectric operation.

## INTRODUCTION

Research programmes investigating arrays of bolometer elements for thermal imaging reflect the drive towards low cost, uncooled technologies to satisfy both military and commercial applications. The requirements are for infrared images with television quality, ie for very large arrays of moderate to good performance backed up by increasingly sophisticated signal processing as this becomes available at low cost.

Ferroelectric detectors will satisfy many of these applications[1,2]. However, the present technology utilises a hybrid design involving solder bump bonding of the detector wafer to the silicon readout IC. An element of the array is shown in section in figure 1. The solder bond, provides the electrical connection to the input pad on the IC while maintaining a high degree of thermal isolation between the element and silicon surface due to its small diameter. This design involves features affecting cost through processing time or yield, eg the preparation of the thin ceramic wafer to high polishing tolerances, and the solder bond processing[3]. Wafer processing may also lead to some degradation from the bulk properties.

A monolithic technology based on direct integration of the detector array onto the silicon IC should offer large array sizes and substantial cost reductions in array production. The design of the thermal structure will reflect the recent advances made in silicon micro-engineering, including micro pellicle and bridge structures. For the detector layer, thin film resistance and ferroelectric bolometers are contenders, the merit depending not only on performance but on the compatibility of the deposition with the underlying silicon IC technology.

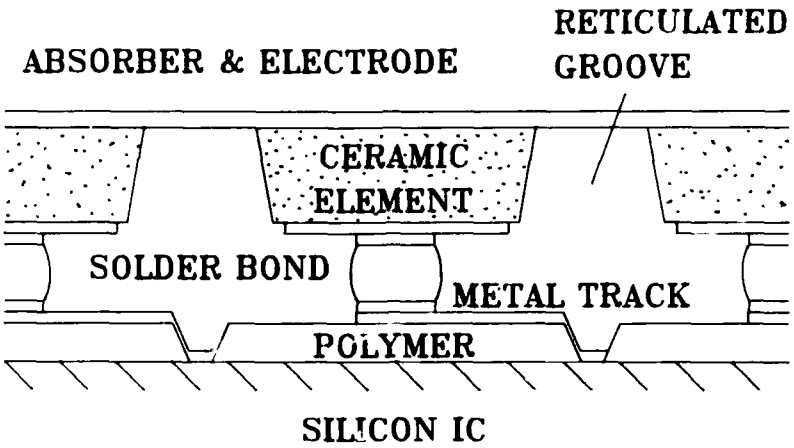


FIGURE 1 Element Structure for a Ferroelectric Hybrid Array

THERMAL MICRO-STRUCTURE DESIGN

The solder bonded hybrid design and technology[1] sets a base line for performance in terms of the thermal conductance from the element to the IC and to its neighbours. At an element pitch of 50 µm, the design of figure 1, which includes a thick polyimide layer and thin interconnecting metallisation, results in a thermal conductance to the silicon of 10 µW/K. The reticulation grooves between the elements are etched by a laser assisted process[4] and this limits the effective inter-element (left/right) conductance to 5 µW/K.

Micro-wells and Micro-bridges on Silicon

Microbridge construction over active circuitry has been demonstrated[5,6] using a phosphosilicate oxide/glass (PSG) layer as a sacrificial under-layer, etched out by buffered HF. A 100 nm thick layer of $Si_3N_4$ may be used to protect the structures already in place on the silicon IC. Figure 2 illustrates a typical micro-bridge. These structures are preferable to pellicles on wells etched into the silicon, since the competition in area for readout circuitry forces a poor pixel fill factor. A high degree of control on leg angle and dimensions can be obtained by using thin masking layers or ion induced surface damage to alter the etch rates.

The conductance offered by this technology depends on the leg dimensions and materials, and on the temperature variation across the bridge due to its thermal characteristics. Total leg cross-sectional area/length ratios of ≈ 0.2 µm are possible, and with low conductivity amorphous silicon or silicon nitride pellicles, allow averaged conductances of 0.3-7 µW/K. Even lower conductance could be derived by further isolation of the bridge legs from the silicon IC surface.

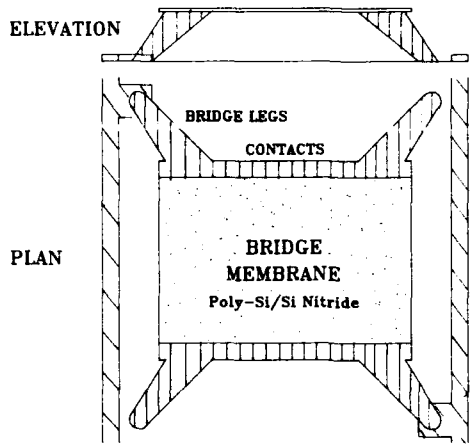


FIGURE 2 Microbridge for Integrated Arrays on the Silicon IC

DETECTOR OPTIONS - FERROELECTRIC AND RESISTANCE BOLOMETERS

Infrared detectivity ($D^*$) measures signal to noise performance in a unit noise bandwidth. It is not therefore a suitable measure for array performance, where noise bandwidth is associated with the sampling and multiplexing requirements. The comparisons made here are based on the NETD performance using the LAMPAR, low noise, readout design for thermal detector arrays[7]. This design defines and limits the array noise, by using both low and high frequency cut-off filtering. The dominant noise contributions within the pixel for a ferroelectric array are; - the limiting noise due to the fundamental temperature fluctuations in the element, - the dielectric loss or tan delta noise from the detector material, - the current or leakage noise at the preamplifier input, - the voltage noise due to the preamplifier.

In order to achieve the limiting NETD, the temperature fluctuation noise must be the largest noise term. Since the temperature noise is proportional to the responsivity, high response is desirable. On the other hand measures to reduce the noise from the other sources are a key feature. It is in this latter aspect that the ferroelectric detectors exhibit a large advantage over the other bolometers.

Noise and Performance in Ferroelectric Arrays[7]

In the ferroelectric arrays, the high capacitance of the detector element acts as its own filter for the important noise sources, and a low integrated noise can be achieved for these. However, design measures must be taken to ensure that the flat, unfiltered, preamplifier voltage noise is also limited. In the LAMPAR design a filter is placed at the output of the column sense line to limit this noise. With the LAMPAR design and the present ceramic ferroelectrics, the effective dielectric loss in the array elements results in a noise which dominates both the preamp noise and the fundamental temperature noise.

The requirement that the dielectric loss noise is less than the temperature noise, can be written (as mean squares);

Integrated Dielectric Loss Noise < Integrated Temperature Noise

$$3JkTC\tan\delta/\pi(C+C_a)^2 < (kT^2/2G\tau_t)\ [pA/(C+C_a)]^2\ (1-e^{-\beta})(3-e^{-\beta}) \quad (1)$$

p is the pyroelectric coefficient, C and A the element capacitance and area, $C_a$ is the preamp input capacitance, J≃7-10 is an integration factor dependent on array size, G is the thermal conductance to the element, $\tau_t$ is the effective thermal time constant, and $\beta=\tau_f/\tau_t$ ( ≃ 1) where $\tau_f$ is the field time. Rearranging, the inequality can be written in terms of the ferroelectric material Merit Figure $M_D = p/c(\varepsilon\varepsilon_o\tan\delta)^{\frac{1}{2}}$, (c is the effective volume specific heat for the element);

$$M_D > [6J/\pi c\tau(1-e^{-\beta})(3-e^{-\beta})]^{\frac{1}{2}} \simeq 10\text{-}15\ 10^{-5}\ Pa^{-\frac{1}{2}} \quad (2)$$

Recently, several ceramic ferroelectric materials[1,2,8], with transitions near ambient and operating with an applied bias, have achieved on bulk samples, Merit Figures which approach this requirement. These are shown Table 1.

TABLE 1 Properties of Pyroelectric Materials (with applied bias)

| | $T_c$ degC | Field V/μm | ε | tanδ % | $p.10^4$ $C/m^2K$ | $M_D.10^5$ $Pa^{-\frac{1}{2}}$ |
|---|---|---|---|---|---|---|
| Doped lead magnesium niobate | -20 | 6 | 1650 | 0.1 | 8.5 | 8.3 |
| Barium strontium titanate | 17 | 4 | 1500 | 0.4 | 18 | 9.2 |
| Lead scandium tantalate (PST) | 25 | 4 | 3400 | 0.4 | 43 | 14.6 |
| RF sputtered PST (1.5μm) | 6 | 4 | 4100 | 0.48 | 32 | 9.1 |
| RF sputtered $PbTiO_3$ (2.1μm) | 540 | 0 | 200 | 1.0 | ~5 | 4.8 |

Despite the high bulk Merit Figure for PST, limiting performance has not been achieved due to an excess detector noise experienced in fabricated arrays, and to the significant levels of preamplifier noise. Both these features will improve with research and design.

However, PST thin films for direct deposition on the thermal microstructures described above now offer properties approaching the bulk ceramic as shown in the Table[9]. Figure 3 illustrates the permittivity and loss at zero field and 4V/μm for this film. The sharp characteristics indicate strong first order properties. However these properties are obtained only after an anneal to 900°C, which may be incompatible with deposition on the silicon IC, unless the films can be annealed by laser beam irradiation, already demonstrated for films of lead titanate. Sputtered lead titanate offers an alternative to PST for thin film arrays. It demands lower deposition/anneal temperatures[10,11], ≃ 550°C, but operates as a conventional pyroelectric, ie in zero bias, and has a lower merit figure, (Table 1, p estimated from responsivity).

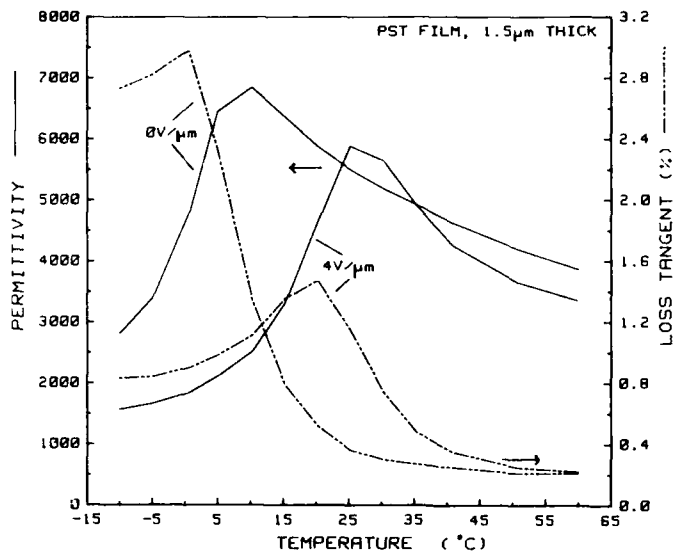


FIGURE 3 Permittivity and Loss for a Sputtered PST Film (1.5μm)

Noise and Performance in Resistance Bolometer Arrays

A major difference with resistance bolometer elements, compared with ferroelectric elements, is the absence of the large capacitance in the pixel. The important noise terms for these elements are therefore not filtered at the pixel level. The bandwidth applicable to the key noise terms, ie the resistor Johnson noise, is determined by the LAMPAR filter time constant $\tau_b=\tau_f/(10N)$, for a NxN array. A second major difference is that the resistance bolometer elements require a current bias, i, or bias power $P=i^2R$. The responsivity of the element is proportional to $P^{\frac{1}{2}}$. The responsivity is also proportional to the temperature coefficient of resistance, $\alpha=(1/R)(dR/dT)$. High values may be obtained in lightly doped poly or amorphous silicon. At a resistivity of $10^5$ ohm cm, $E_g \simeq 042$eV, and $\alpha=qE_g/kT^2 \simeq 6\%$.

As with the ferroelectrics, the largest noise component can be examined against the temperature or limiting noise, with the aim of reducing it to below this level. The largest noise is the Johnson noise, and ignoring any excess noise, the limiting performance is obtained when the integrated noise levels meet the criterion,

Integrated Johnson Noise<Integrated Limiting Temperature Noise

$$(4kTR)(3/8\tau_b) < (kT^2/2G\tau_t)\ (iR\alpha)^2\ (1-e^{-\beta})\ (3-e^{-\beta}) \qquad (3)$$

or,

$$G < \alpha^2\ (\tau_b/\tau_t)\ PT \simeq 10^{-3}\ P, \text{ with } \alpha=6\%,\ \tau_b \simeq 10^{-5}\text{sec},\ \tau_t \simeq \tau_f. \qquad (4)$$

From the discussion of micro-structures on the silicon IC, thermal conductance values down to a minimum of a few tenths of a microwatt/K may be available. Therefore in the above inequality, element power levels approaching a milliwatt will be required for limiting performance. In

large arrays, >100x100, a dc bias at this level would be prohibitive, but using a bias pulsed for a fraction of the field time reduces the averaged array power. For example, a bias voltage and current of 5V and 50 μa, pulsed for $\tau_f/10$, and a resistor of 0.1 Mohm gives an element bias of 0.25 mW and an array power of 2.5W ($10^5$ elements). Although the criterion for limiting performance is unlikely to be met, full calculations of the array NETD indicate that value of 0.2K should be achieved for large arrays (7 $10^4$) elements at 2.5 watts total power. This performance still demands a thermal conductance of ≈1μW/K in the microbridge on the silicon IC.

## CONCLUSIONS

The major points of the comparison of integrated thermal imaging arrays using either ferroelectric or resistance bolometers are as follows.

Temperatures required in the deposition and annealing of the bolometer layer onto the silicon IC. Silicon resistive bolometers will present a less severe problem than the ferroelectric oxides which require research into low growth temperatures and special annealing techniques.

Bias. Ferroelectrics do not require a dissipative bias. In resistance bolometers, bias power controls the performance. A limit must be specified.

Noise. Noise sources for the ferroelectric pixel are reduced due to shunting by the self capacitance.

Imaging performance. With the properties as observed on deposited thin films, ferroelectric arrays should approach the limiting performance. Considerable flexibility in the thermal structure design is possible. Resistance bolometers are unlikely to achieve limiting performance and require very low levels of thermal conductance in the structures to satisfy moderate imaging requirements in large arrays.

Crown Copyright 1992.

## REFERENCES

1. R. Watton, ECAPD-1/ISAF 1988, Ferroelectrics, 91, 87 (1989).
2. R. W. Whatmore, P. C. Osbond and N. M. Shorrocks, Ferroelectrics, 76, 351 (1987).
3. D. J. Pedder, Hybrid Circuits, 15, 4 (1988).
4. M. A. Todd and R Watton, SPIE Vol 1320, 95 (1990).
5. G. Rebeiz, Y. Guo, P. Stimson and D. Rutledge, SPIE Vol 1039, 31 (1988).
6. R. T. Howe and R. S. Muller, IEEE Trans. Elec. Devices, ED-33, 499 (1986).
7. R. Watton and P. A. Manning, SPIE Vol 807, 98 (1987).
8. N. M. Shorrocks, R. W. Whatmore and P.C. Osbond, Ferroelectrics, 106, 1223 (1990).
9. R. Watton and M. A. Todd, Ferroelectrics, 118, 279 (1991).
10. M. Okuyama, Y. Matsui, H. Nakano and Y. Hamakawa, Ferroelectrics, 33, 235 (1981).
11. Y. Matsui, M. Okuyama, N. Fujita and Y. Hamakawa, J Appl Phys, 52, 5107, (1981).

*Ferroelectrics*, 1992, Vol. 133, p. 11
Reprints available directly from the publisher
Photocopying permitted by license only

© 1992 Gordon and Breach Science Publishers S.A.
Printed in the United States of America

# PdX4

## CERAMIC SENSORS AND ACTUATORS FOR SMART MATERIALS AND ADAPTIVE STRUCTURES

L E CROSS, MRL, Penn State University, University Park, PA 16802-4800, USA

Over the last several years there has been rapidly increasing interest in 'smart' materials which can self-adjust some of their properties in response to changing ambient conditions, and in adaptive structures which modify their shape and function to address changing needs. For highly energetic changes in the environmental stimulus, the energy needed to effect property change can be drawn directly directly from the stimulus in a completely passive system. Currently, however, what are of more interest are composite systems, with independent power supply, which incorporate high sensitivity sensors, solid state electronics for control and actuators to effect the required property changes. In these smart composites, the keenest interest appears to be in using the 'smarts' of electronics to control the shape and elastic response of materials and structures.

Piezoelectric and electrostrictive ceramics are highly competitive in the elastic 'smarts' for both sensing and actuation function and current applications in both vibration and shape control will be briefly reviewed. For large area systems, polymer ceramic piezoelectric composite offer interesting possibilities, and the achievable properties will be reviewed. For many of the most important needs, inadequacy of the present solid state actuators is probably the 'Achilles heel' in the smart systems and efforts to improve will be discussed.

Recently, it has become possible to mate thin film ferroelectric ceramics with silicon technology. The very high piezoelectric energy densities in the films open up a whole new arena for micro-mechanical (MEMS) systems which make the inexpensive replication of silicon technology available for miniature integrated micro motors and actuators in a new generation of micro robots.

# SECTION II
# INVITED PAPERS

*Ferroelectrics*, 1992, Vol. 133, p. 13
Reprints available directly from the publisher
Photocopying permitted by license only

© 1992 Gordon and Breach Science Publishers S.A.
Printed in the United States of America

# DeI6

## THE INFLUENCE OF DEFECTS ON THE ELECTRICAL PROPERTIES OF PEROVSKITE AND PEROVSKITE-RELATED MATERIALS

D. M. Smyth, Materials Research Center, Bldg. 5, Lehigh University, Bethlehem, PA 18015, U. S. A.

Oxides having perovskite or perovskite-related structures are used in an extraordinary variety of electrical and optical applications. These materials include insulators, semiconductors, metallic conductors, superconductors, ionic conductors, and mixed electronic-ionic conductors. Most of the interesting compounds contain transition metal elements with variable oxidation states, and, as a result, have variable oxygen contents that profoundly affect their electrical conductivities. The oxygen nonstoichiometry also interacts with charged impurity centers in ways that give additional degrees of design freedom. Common themes in the defect chemistry of perovskite-related systems will be reviewed, and examples will be given to illustrate the use of these principles to obtain desired properties.

*Ferroelectrics*, 1992, Vol. 133, pp. 15–20
Reprints available directly from the publisher
Photocopying permitted by license only
© 1992 Gordon and Breach Science Publishers S.A.
Printed in the United States of America

**EoI13**

# FERROELECTRIC POLYMER LIQUID CRYSTALS.

HELEN F GLEESON
The Physics Department, The University, Manchester, M13 9PL, UK.

Abstract. Prior to their introduction in the early 1980's, polymeric ferroelectric liquid crystals were thought likely to be a much slower analogue of their low molar mass counterparts. However, side-chain ferroelectric liquid crystal polymers have proved to have extremely interesting and in some cases unexpected properties. These include fast electro-optic switching, high spontaneous polarisation, multiple switching mechanisms, extended electroclinic-like switching, and enhanced second order optically non-linear properties. This paper reviews these novel materials, their physical properties, and some of their applications.

## INTRODUCTION.

Ferroelectricity in liquid crystals was first proposed in 1975 by Meyer et al[1] and demonstrated several years later by Clark and Lagerwall[2] who developed the surface stabilised device. An enormous research effort has since been directed towards low molar mass ferroelectric liquid crystals (FELCs) with the aim of capitalising on their promise for electro-optic display devices. Their switching speed (typically ~10μs), potential for bistability and good optical characteristics make their performance theoretically far better than nematic liquid crystal displays. A wide variety of materials and driving schemes suitable for FELC display devices have existed for some years. Nevertheless, it is only recently that a company announced the pilot production of these displays (Canon, late 1991).

The major obstacles to the development of ferroelectric displays have been the occurrence of defects combined with lack of ruggedness, problems which are inherent in all low molar mass smectic displays. Given the problems related to lack of ruggedness, the advent of side-chain polymeric ferroelectrics was surprisingly slow. It had been shown in the early 1980's that side-chain smectic-A polymers produced extremely rugged, high optical contrast displays[3] though the response times were slow (>100ms). The increase in response time over the analogous low molar mass systems was attributed to the high viscosity of the polymers. It was thought initially that the same disadvantage would haunt polymeric FELCs, and that their electro-optic response times would be too slow to be of interest. However, the electro-optic switching in ferroelectric systems is related to a rotation of the mesogenic group rather than the reorientation of the bulk fluid observed in

nematic and smectic-A systems. Thus, the electro-optic response times of ferroelectric polymers can be similar to those of low molecular mass systems.

Structurally, the composition of ferroelectric polymer liquid crystals can be summarised as comprising a backbone (usually polyacrylate or polysiloxane) and one or more mesogenic side groups decoupled from the backbone by a long (typically ~10 carbon) alkyl or alkoxy spacer unit. The mesogenic units contain a permanent transverse electronic dipole and at least one chiral centre. It is advantageous if the transverse dipole and the chiral centre are strongly coupled to the rigid portion of the molecule. This paper will not consider the finer details of structural variations in ferroelectric polymers; in fact there are sufficiently few examples of these materials to make a summary of structure/property correlations rather difficult. It should, however, be noted that structural variations define the physical properties of the system, as has been shown in detail for low molar mass FELCs. We consider here the physical properties of ferroelectric polymer liquid crystals in detail.

## PHYSICAL PROPERTIES.

A variety of techniques exist which allow the measurement of the physical properties (spontaneous polarisation, tilt angle,, response times etc.) of FELCs. The different methods each have their own advantages and disadvantages, including for example, susceptiblity to electrical conductivity of the sample. However, almost all of the techniques require that the liquid crystal exists in a fully unwound state as the natural helicoidal structure of the $S_c^*$ phase will negate ferroelectricity in the sample. The helix is usually suppressed by surface forces in the surface stabilised device configuration. In addition, a monodomain sample is required and in low molar mass systems this is achieved by surface alignment techniques, together with the use of pitch compensated mixtures which allow the surface alignment layers to fully orient the system in the chiral nematic phase. It is known that polymeric materials react poorly to surface alignment techniques and the production of unwound, monodomain samples is therefore much more difficult than in the equivalent low molar mass systems. Measurement of the physical properties of the polymeric systems, without contributions due to misalignment of the sample, is consequently far more difficult than for low molar mass materials.

### Measurements of spontaneous polarisation.

The first polymeric FELCs were synthesised by Shibaev et al[4-5], followed by Decobert et al[6,7]. These first materials were not electro-optically active, and there were therefore no measurements of spontaneous polarisation in these systems. The phases were

characterised by X-ray scattering and polarising microscopy techniques which together verified the existence of the $S_C^*$ phase, and ferroelectricity was inferred.

It was only later that switchable polymers were reported[8,9]. Uchida et al[8] gave the first measurements of spontaneous polarisation ($P_s$) for a side-chain FELC polymer. The polymer structure and phase sequence are shown in figure 1. The $P_s$ measurements were made using the current reversal technique and values were obtained within the $S_C^*$ phase range. No results were gained below 45°C though in principle the lower temperature phase is also ferroelectric and should exhibit higher $P_s$ values than the $S_C^*$ phase. The $P_s$ values obtained were the lowest which have been quoted for a polymeric system (~ 3nC $cm^{-2}$). The authors hinted at difficulties in measuring the $P_s$ as the result depended on the frequency of the applied field - we return to this point later.

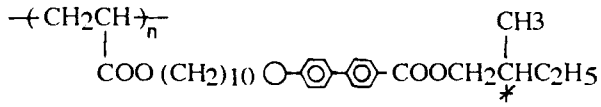

**Glass 15 $S_I^*$ 38 $S_C^*$ 50 $S_A$ 119 I**

FIGURE 1. The phase transition temperatures and structure of the polymer (30 repeat units) studied by Uchida et al[8].

The next measurements of $P_s$ were made on an acrylate polymer[9] and extremely high values were reported (~1000nC $cm^{-2}$). Measurements were made using a Sawyer-Tower bridge. These data were again obtained with difficulty, though the samples were well aligned and good hysteresis curves were recorded. It was speculated that conductivity in the samples may have contributed to the results.

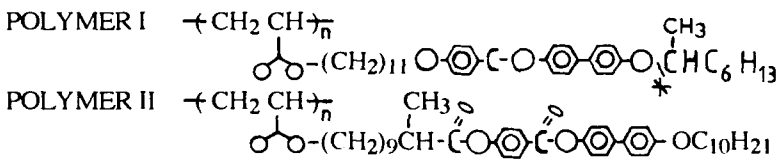


FIGURE 2. The acrylate polymers studied by Coles et al[10].

It is only very recently that the discrepancy between obtaining very large and very small values of $P_s$ in similar polymers has been understood. Work by Coles[10] on acrylate polymers (shown in figure 2) showed that provided the samples were sufficiently well aligned (usually by use of a combination of surface forces and shear flow effects), and that the measurement technique employed used sufficiently large electric fields (in excess of a threshold field characteristic of the material and the temperature), then straightforward,

reproducible measurements of $P_s$ may be made. In the absence of these conditions, experiments may not be reliable. Data taken by Coles et al for $P_s$ in a ferroelectric polymer are shown in figure 3; it can be seen that typical values of ~100 nC $cm^{-2}$ were obtained. Similar values for a different ferroelectric polymer have been reported very recently by Naciri et al[12]. The threshold field which had to be exceeded to give reliable data was also observed in the measurement of other physical properties, and its origin is discussed in further detail below.

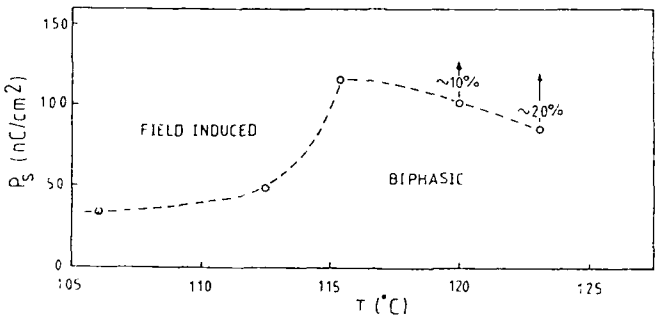


FIGURE 3. Temperature dependence of the $P_s$ of polymer II (figure 2[10]).

Electro-optic responses (tilt angles and response times)

Again, electro-optic response times and tilt angles have only been measured for the most recently synthesised polymers[8-12]. The response times are all of the order of milliseconds or less thus achieving the expected rapid responses of ferroelectric polymers. The tilt angle measurements show a threshold field effect similar to that observed for $P_s$. The electro-optic effects in ferroelectric polymers show two distinct switching regimes, characterised by electroclinic like (low field, low temperature) and ferroelectric like (higher field, higher temperature) switching. The measurements carried out by Coles et al[10] clearly illustrate the different responses observed in each regime (figure 4). It can be seen that there is a field threshold between the two regimes which may be readily measured by optical hysteresis techniques, as shown. At low fields, switching is electroclinic-like, and only at higher fields is the response ferroelectric. These switching data may be interpreted in terms of helical unwinding, with the threshold occurring where the applied field is sufficiently large to unwind the $S_c^*$ helix. Coles[10,11] was the first to give this explanation which applies not only to his data, but which is of relevance to correct measurements in ferroelectric polymer systems.

Similar switching effects have been reported recently by Skarp et al[13], who favour an alternative explanation involving an anti-ferroelectric phase. In this case, there is a threshold field corresponding to the anti-ferroelectric/ferroelectric phase transition. As the structure of the anti-ferroelectric phase may be considered in terms of two interleaving

helices of opposite handedness, it is easy to comprehend the difficulty in distinguishing between the two possible explanations. The discussion between anti-ferroelectric switching and helical unwinding is likely to continue for some time.

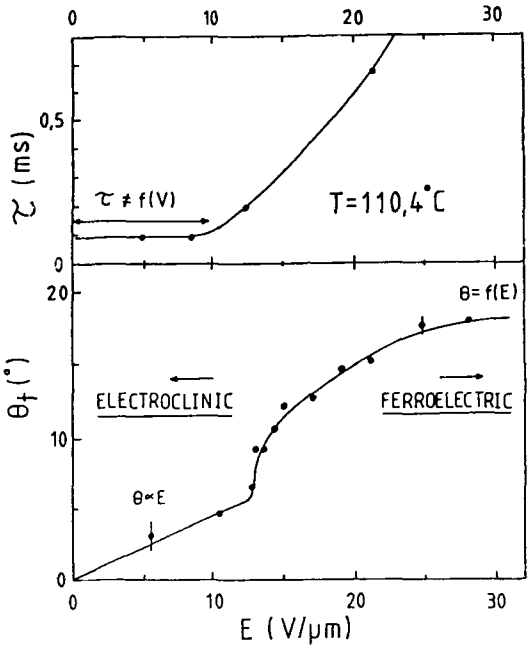


FIGURE 4. Electro-optic switching data showing tilt angle and response time measurements at constant temperature (Coles et al[11])

Finally, we note that many of the polymers[10-12] show enhanced electroclinic (field-induced) tilt angles at the $S_C^*$-$S_A$ phase transition. As the electroclinic effect is linear in the field and switching is generally faster than ferroelectric switching, this may also be of importance technologically.

## APPLICATIONS.

Currently, the most interesting applications for ferroelectric polymers are electro-optic switching applications and second order non-linear optical (NLO) effects. In addition, though, there are some interesting non-display devices possible including pyro-electric and piezzo-electric transducers. In the case of electro-optics, the current polymers will probably not be used in displays as they are difficult to align and are relatively slow compared with low molar mass systems. However, there are several important advantages which exist in the polymeric systems; they are rugged, show extremely good true bistability, and can contain large proportions of dichroic dyes as side groups in copolymer

systems[14]. This final property makes the materials potentially very useful in ferroelectric dye guest-host systems[15].

Once it has been recognised that the symmetry of the permanent dipoles in the $S_C^*$ phase is equivalent to that required for the observation of second order NLO effects, it is clear that FELCs have great potential for use in this area. Organic systems are already clear favourites for use in NLO devices because of their low laser damage thresholds and high non-linear coefficients. The combination of the advantages of an organic system with a 'self-poling' structure having the correct symmetry should lead to an extremely useful system. It was shown recently that low molar mass FELCs produced exciting NLO effects[16]. With the intrinsic advantages of polymeric systems (ruggedness, high order, the possibility of copolymer materials, etc.), it is likely that the use of ferroelectric polymer liquid crystals for this type of application will be of great interest in the future.

ACKNOWLEDGEMENTS. I would like to thank Prof. Harry Coles for the use of diagrams and both he and Dr. Garry Lester for their help in the preparation of this article.

REFERENCES.

1. R B Meyer, L Liebert, L Strzelecki and P Keller, J. de Phys. 36 69 (1975).
2. N A Clark and S T Lagerwall, Appl. Phys. Lett. 36, 899 (1980), and Ferroelectrics, 59 , 25, (1984).
3. H J Coles, Faraday Discuss. Chem. Soc.79, 201, (1985).
4. V P Shibaev, M V Kozlovskii, L A Berensev, L M Blinov and N A Platé, Polymer Bulletin 12, 299 (1984).
5. M V Kozlovskii, L A Berensev, C G Kononov, V P Shibaev, and L M Blinov, Solid State Phys., 29 1470 (1987).
6. G Decobert, J C Dubois, S Esselin and C Noël, Liquid Crystals, 1(4), 307 (1986).
7. S Esselin, L Bosio, C Noël, G Decobert and J C Dubois, Liquid Crystals, 2(4), 505, (1987).
8. S Uchida, K Morita, K Miyoshi, K Hashimoto and K Kawasaki, Mol. Cryst. Liq. Cryst. 155, 93, (1988).
9. H J Coles, H F Gleeson, G Scherowsky and A Schliwa, Mol. Cryst. Liq. Cryst. (Letts.) 7(4), 117 (1990).
10. H J Coles, R Simon, H F Gleeson, J Bone, G Scherowsky, A Schliwa and U Müller, Polymer Preprints , Japan (English Edition), 39(1-4) (Supplement), S5, (1990).
11. H J Coles, The 2nd International Ferroelectric Liquid Crystal Conference, Boulder, Colorado, (1991).
12. J Naciri, S Pfeiffer and R Shashidhar, Liquid Crystals 10(4), 585 (1991).
13. K Skarp, G Andersson, S T Lagerwall, H Kapitza, H Poths and R Zentel, Ferroelectrics, 122(1-4), 127 (1991).
14. H J Coles, H F Gleeson, G Scherowsky and A Schliwa, Mol. Cryst. Liq. Cryst. (Letts.) 7(4) 125, (1990), and G Scherowsky, A Schliwa and H J Coles, Liquid Crystals, 10,809, (1991).
15. H J Coles, H F Gleeson and J Kang, Liquid Crystals 5(4), 1243 (1989).
16. D M Walba, M Blanca Ros, T Sierra, J Rego, N A Clark, R Shao, M Wand, R Vohra, K Arnett and S Velsco, Ferroelectrics (in press).

*Ferroelectrics*, 1992, Vol. 133, pp. 21–26
Reprints available directly from the publisher
Photocopying permitted by license only
© 1992 Gordon and Breach Science Publishers S.A.
Printed in the United States of America

**PcI2**

# NEW PIEZOELECTRIC COMPOSITES FOR ULTRASONIC TRANSDUCERS

K. LUBITZ, A. WOLFF, G. PREU
Siemens AG, Munich, Germany
R. STOLL, B. SCHULMEYER
Du Pont de Nemours (Deutschland) GmbH, Neu-Isenburg, Germany

Abstract The combination of photolithographic processes and green ceramic body structuring methods allow the fabrication of 1-3 or 2-2 composites with very fine structures and a free geometric design. Two suitable methods - named lost mould resp. jet machining - are presented with their potential to make new transducer geometries in the frequency range ≥ 5 MHz.

## INTRODUCTION

1-3 piezocomposites consisting of long thin PZT (leadzirconatetitanate) rods embedded in a polymer matrix are a very favourable material for the construction of acoustic transducers used in hydrophones, nondestructive testing and medical ultrasound[1,2]. Depending on the frequency, the aspect ratio of the rods and the desired volume fraction of PZT different manufacturing methods[3-6] have been developed. The mostly used dice-and-fill technique is limited to intermediate frequencies and rectangular structures.

For frequencies up to 20 MHz a lost mould technique has been developed[7-9] which is described below with respect to the generation of a 1-3 composite made of PZT rods with hexagonal cross section. Concerning the demands of annular transducers also a new technique is presented called jet machining. Here it is possible to make 2-2 composites with a periodic structure of fine PZT rings and decoupling polymer rings. The methods, the resulting transducers and some of their piezoelectric properties are shown.

## JET MACHINING

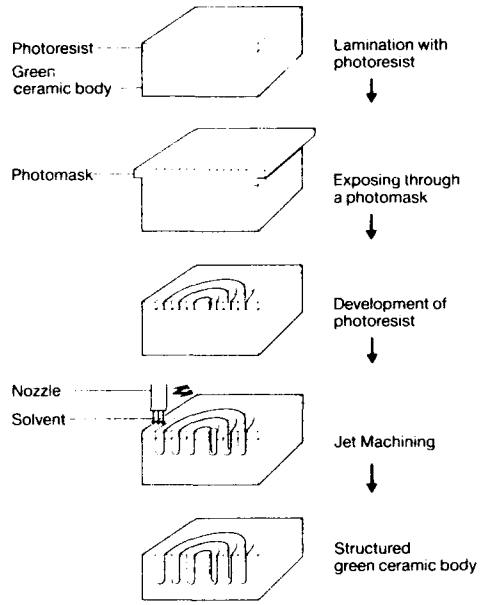


Fig.1 Jet machining of green piezoelectric ceramics

A green ceramic tape with about 1 mm thickness consisting of PZT powder and binder is laminated with a photoresist. After a photolithographic process, the tape is structured by repeated scanning with a solvent-air jet (see Fig.1). The tape binder is dissolved, the PZT particles become free and are removed by the air stream. Annular grooves with a width of 140 µm can be etched to a maximum depth of 650 µm. Subsequently, the structure (see Fig.2) is sintered at 1250 °C for 1 hour. After filling the grooves with polymer, the top and bottom of the structured ceramic are grinded, electroded and poled (3 kV/mm at RT).

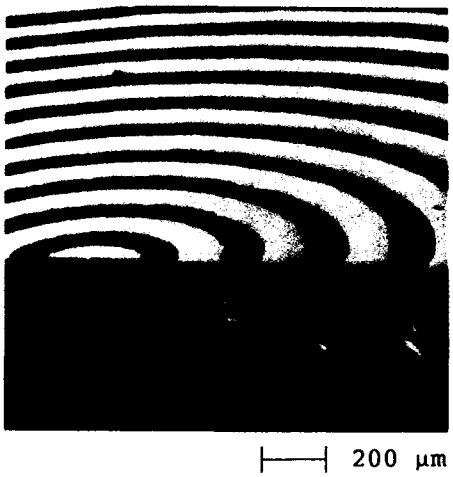


Dimensions of the structure:

| | green | sintered |
|---|---|---|
| ridge width | 170 µm | 160 µm |
| groove width | 140 µm | 130 µm |
| groove depth | 650 µm | 550 µm |
| total diameter | 23.6 mm | 19.7 mm |
| thickness | | 260 µm |
| active area | | 60 % |
| number of PZT rings | | 34 |

Fig.2 Cross section of an annular green ceramic structure (2-2 composite) fabricated by jet machining

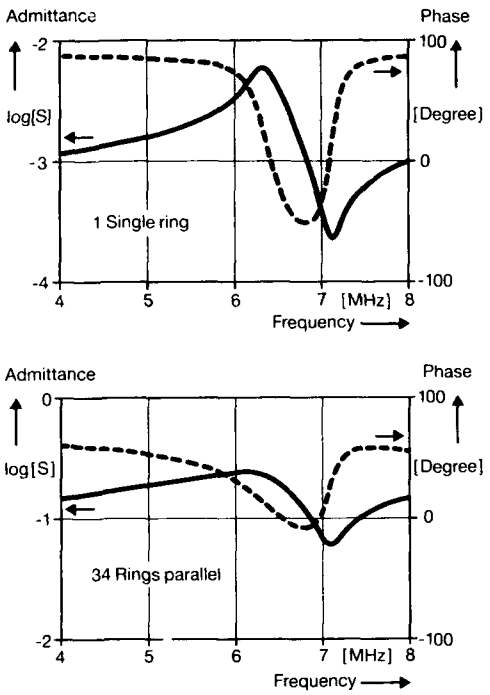


Fig.3 Admittance versus frequency of an annular transducer

For a transducer with all 34 rings connected in parallel electric resonant measurements (see Fig.3) show a coupling factor $k_t$ of 0.51, a resonance frequency of 6 MHz, a mechanical quality factor of 3 and no lateral modes. The relative permittivity of the ceramic is 1300 with a loss factor $\tan \delta = 0.017$. When contacting all single PZT rings with a self aligned technique isolated of each other, a pure thickness resonance without radial harmonics and very small crosstalk to the next neighbouring PZT elements (> 20 dB) can be observed.

## LOST MOULD METHOD

The basis of this method is a plastic mould which contains the desired structure as a negative, for instance a honeycomb like structure. This mould can be fabricated using an X-ray lithography technique called LIGA[10]. A ceramic slurry is poured into this mould (Fig.4). After casting the slurry is dried and the plastic mould is burned out. Next, the green PZT ceramic is sintered (Fig.5) and the structure is filled with a passive polymer. After removing the ceramic base and the additional polymer by grinding, opposite sides are metallized. After poling with 3 kV/mm at RT, electric resonant measurements of the 1-3 composites (Fig.6) show a high coupling factor $k_t$ of 0.64 and a mechanical quality

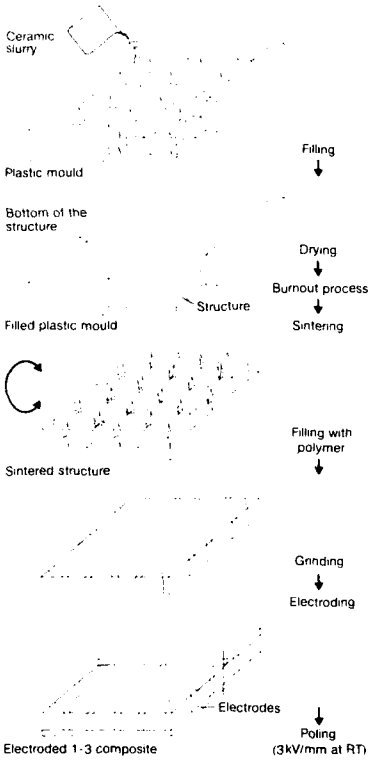


Fig.4 Block diagramm of the lost mould method

factor of 33. The coupling factor $k_t$ and the mechanical quality factor of the bulk PZT sample with the same resonant frequency are 0.47 and 61 respectively. In comparison to the bulk PZT sample lateral modes are completely suppressed. The relative permittivity of the structured ceramic is 1200 with a loss factor of 0.02.

| | |
|---|---|
| rod width | 115 µm |
| groove width | 45 µm |
| rod heigth | 400 µm |
| total diameter | 16 mm |
| active area | 52 % |

100 µm

Fig.5 SEM Picture of hexagonal rods after sintering

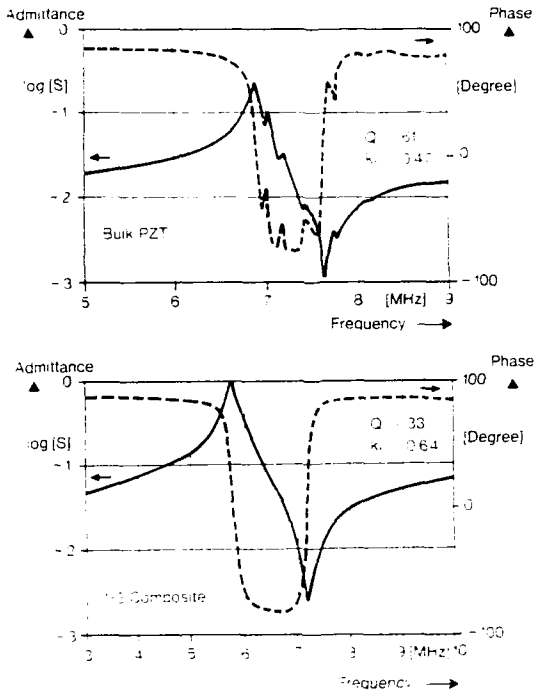


Fig.6 Admittance versus frequency of a 1-3 composite transducer in comparison to bulk PZT

## DISCUSSION

The present microstructuring of green ceramics for both methods results in an undamaged sintered ceramic surface inside the composites. Together with the hexagonal structure of the PZT rods a very good adhesion between the filler polymer and the PZT is given and allows a defectfree grinding process. The fluctuations of the wall thickness in the case of jet machining (see Fig.2) and of the thickness and position of the hexagonal rods (see Fig.5) due to the structuring process and the shrinkage during sintering are favourable for an additional suppression of harmonics and stopband modes.

The annular structure shows a $k_t$ of 0.5 which is smaller than in optimized 1-3 composites and which is due to a circumferential clamping of the PZT rings. The large active

area of 60% nevertheless gives enough acoustic power and sensitivity. By combining several active rings with one electrode in a Fresnel like manner annular acoustic arrays can be realized. Only by changing the mask in the photolithographic process the dimensions of grooves and ridges can be varied and optimized for special purposes.

The lost mould technique is more and more easier to use with increasing frequencies. Even at 20 MHz an ideal 1-3 composite structure can be realized with an active area of 50 %, an optimized aspect ratio of the PZT rods and almost vertical small grooves. An additional important potentiality of this method is not only the free choice of PZT rod geometries but also the choice of statistical fluctuations or systematic variations of the rod geometry over the transducer area by changing the lithography mask. In combination with an optimized electrode design transducers with lower spurious modes and a better acoustic behaviour can be expected.

## REFERENCES


1. W. A. Smith, Proceedings of the 1991 IEEE International Symposium on Applications of Ferroelectrics, 145-152, (1991).
2. W. A. Smith, Proceedings of the 1989 IEEE Ultrasonics Symposium, 755-766, (1989).
3. K. A. Klicker, J. V. Biggers, R. E. Newnham, Journal of the American Ceramic Society, 64(1), 5-9, (1981).
4. T. R. Gururaja, W. A. Schulze, L. E. Cross, Ferroelectrics, 54, 183-186, (1984).
5. J. Zola, U.S. Patent 4,572,981, (1986).
6. H. Takeuchi, H. Masuzawa, C. Nakaya, Y. Ito, Proceedings of the 1989 IEEE Ultrasonics Symposium, 705-708, (1989).
7. W. Wersing, Proceedings of the 1986 IEEE International Symposium on Applications of Ferroelectrics, 212-223, (1986).
8. U. Bast, D. Cramer, A. Wolff, Proceedings of the 7th CIMTEC (Montecatini, Italy), 2005-2015, (1991).
9. G. Preu, A. Wolff, D. Cramer, U. Bast, Proceedings of the 2nd ECERS (Augsburg, Germany), (1991), in press.
10. E. W. Becker, W. Ehrfeld, P. Hagman, A. Maner, D. Münchmeyer, Microelectronic Engineering, 4, 35-56, (1986).

*Ferroelectrics*, 1992, Vol. 133, pp. 27–34
Reprints available directly from the publisher
Photocopying permitted by license only
© 1992 Gordon and Breach Science Publishers S.A.
Printed in the United States of America

# PdII

## PIEZO-ELECTRIC MOTORS AND THEIR APPLICATIONS

HANS-PETER SCHÖNER
Daimler-Benz AG, Research Institute Frankfurt, D-6000 Frankfurt 71

**Abstract** General properties of piezo-electric motors are explained. A short review of their historical development is given. Limiting factors for the power of piezo-electric motors are discussed in comparison to standard electromagnetic motors. Aspects for the choice of piezo-electric materials for motor applications result from these limits.

## 1. INTRODUCTION

Ever since the discovery of the piezo-electric effect people have been challenged to design and construct actuators and continuously operating motors using the motion produced by electric fields when applied to piezo-electric materials.

Nowadays with the availability of powerful and quickly acting materials in conjunction with fast electronic power control for excitation of mechanical oscillations as well as increased knowledge in the design of mechanical multimode-resonators, piezoelectric motors become a more and more attractive alternative to conventional electromagnetic motors. Although magnetostrictive materials can be used in a similar manner for the construction of motors and although they offer bigger displacements, their use has been restricted to very few experimental setups because of the much higher costs compared to piezo-electric materials.

## 2. PRINCIPLE OF OPERATION

In contrast to the well-known electromagnetic motors (as well as to new designs with electrostatic motors), which base on forces in magnetic (or electric) fields, the piezo-electric effect produces forces in conjunction with deformation of shape. Hence, the fixed and the moving part of a piezo-electric motor have to be in contact with each other while the force is acting. Thus, at the location where the force is transmitted to the moving part, the motion of the moving part is limited by the elastic properties of the motor. In order to produce a steady motion, the force-transmission can only be one part of a complete working cycle; during a second part of the cycle a retraction of the piezo-electrically elongated part of the motor has to take place without (or with little) transmission of force.

In general, this is achieved by superimposing a second - at best orthogonal - cyclical deformation over the first one in such a manner that the contact pressure between fixed part and moving part is high during forward movement - thus allowing high forward forces to be transmitted - and low or even zero during retraction (fig. 1, [14]). This process can be called a mechanical rectification of motion.

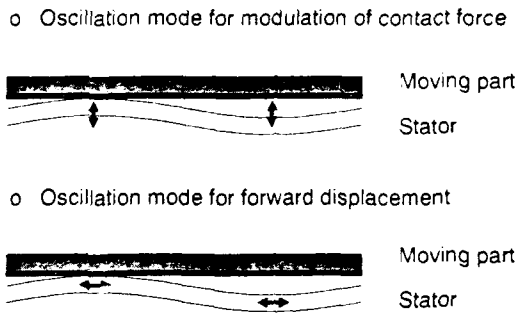


FIGURE 1 Orthogonal modes of oscillation in piezo-electric motors

In order to achieve a more or less continuous transmission of force to the moving part of the motor, several general solutions are possible:

A) A single force-transmitting location can act with a very short cycle time (high frequency), such that the gaps in force transmission are overcome by the inertia of the moving part.

B) A multiple number of force-transmitting locations can be used during alternate phases of a complete operating cycle.

C) In the extreme case of B), the location of force-transmission can vary continuously with time, thus producing a really continuous transmission of force.

High motor speed and motor power need large displacements during one cycle of operation and short cycle times. Large displacements can be achieved by use of mechanical resonances for the deformation modes. In this case the deformations become more or less sinusoidal. Both have to take place at the same frequency (in special cases an integer frequency ratio is possible), the phase shift of the two deformations being approximately 90° for maximum speed. Operating frequencies in the ultrasonic range are advantageous not only with respect to power output, but they are also necessary with respect to the noise emission of the motor. Thus resonant piezo-electric motors are often called ultrasonic motors.

## 3. SHORT HISTORICAL REVIEW OF PIEZO-ELECTRIC MOTORS

The best known and readily available piezo-electric motor is the "Inchworm-Motor" of Burleigh Instruments [1]. This motor uses a piezoelectric elongator for forward movement and two piezoelectric clamps on either side of the elongator, using the principle B of possibilities mentioned above. This motor is designed for exact positioning purposes, not for high speed operation. Thus it does not utilize mechanical resonances for its operation. Maximum speed is 0.002 m/s, maximum mechanical power output 30 mW. Many other, similar constructions using the same non-resonant principle of operation have been designed; output-power is limited by the relatively long cycle time in combination with the small displacements per cycle.

The first patent concerning piezo-electric motors seems to be the US-Patent [2] of Williams and Brown from 1942. They proposed several ways to produce rotatory movements, using a multitude of piezoelectric bending elements. They already recognized the importance of using resonances for high drive speeds; the use of power line frequency as operating frequency was proposed. Ultrasonic operating frequencies were beyond the technological possibilities of that time.

In the seventies with the advent of high power piezo-electric ceramics new activities on piezo-electric motors started, concentrating first on motors using simple oscillators which move to and fro in an acute angle to a surface, thus driving the surface forward by frictional force and gliding back on the surface during retraction (principle A of the list above). The principle being first mentioned by Barth [3], it was discussed in detail by a very comprehensive patent of Vishnevsky e.al. [4] of the Kiew Polytechnical Institute, which also covered other types of usable oscillators. As one problem of the motors the limited lifetime of the contact surface due to gliding friction was recognized.

By 1980 a book on piezo-electric motors was published in Russia by the same group of authors [5], dealing with many theoretical and practical aspects of the design of such motors. Unidirectional and bidirectional motors are discussed, driving circuits for these motors are presented.

Little later, Sashida in Japan proposed several patents [6] on the use of travelling waves in a rotatory motor, the waves being produced through superposition of two bending modes excited by piezoelectric ceramics. One big advantage of this motor is the continuous force transmission between stator and rotor, since the location of the force transmission rotates continuously with the travelling wave (principle C of the list above). This principle significantly reduces the problems of lifetime of the contact surface between stator and rotor. Sashida's motor produces up to 4 W mechanical power; forward displacement speeds at the contact surface are in the range of 0.4 m/s.

Probably triggered by the work of Sashida, many Japanese activities started in the following years. Researchers at Matsushita, Hitachi, Canon and many other companies tried different configurations of oscillators. Akiyama gave a review [7] of different ultrasonic motors realized up to 1986. The same author published a book [8] on ultrasonic motors in 1986. Tomikawa published a systematical review of possible combinations of oscillation modes to be applied in oscillatory motors [9].

Especially three Japanese publications should be mentioned: Kumada [10] designed a motor with a torsional mode of oscillation; 2 W mechanical power and 0.2 m/s speed at the contact surface can be calculated from the given motor data. Kuribayashi [11] uses travelling waves in a rod to produce a linear motor; he only achieved 15 mW and a speed of 0.1 m/s. A more powerful drive for linear motors is investigated by Tomikawa e.al. [12]; several Watts are reached, and speeds of 0.3 m/s.

In Europe two research teams have published results concerning piezo-electric motors. Siemens [13] reports on a motor using a bar-resonator as driving element. 2.5 W mechanical power are reached, and speeds of 0.3 m/s. Daimler Benz [14] uses the travelling wave principle and reports a maximum power of more than 8 W and speeds of 0.3 m/s.

## 4. General Properties of Piezo-electric Motors and Typical Applications

Piezo-electric motors offer several positive features, which make them attractive for a lot of applications:

- Much higher torque compared to conventional drives of the same volume
- Generation of low speeds, adjustable down to zero, without the need for gearing
- Large holding torque at rest without additional elements and without energy supply
- Extremely high dynamics and excellent controllability
- Quiet running in the audible range
- Compact design possible
- Simple mechanical components
- No magnetic fields and hence no electromagnetic disturbance

As seen from this list, piezo-electric motors are especially well suited for fast positioning applications, where high dynamics, no need for gearing and inactive holding torque are advantageous. Piezo-electric motors are relatively simple in their mechanical parts, but in addition they need electronic circuits. With the necessity of electronic motor control for variable speed drives and bus-controlled drives even with standard electromagnetic motors, this is not a disadvantage for piezo-electric motors.

Conceivable applications for piezo-electric motors are all kind of positioning motors in cars, office technology and consumer goods, but also in satellites and medical equipment. Power demands of 2 W up to 50 W are typical. Window winders, gearless window-wipers, seat adjustors, heating and ventilation flap operation, drives for paper feeders and writing head adjustment of printers, and lens focus motors are just some examples of first applications.

## 5. Limits of Force

The following considerations are meant to give some insight into the possibilities of piezo-electric motors compared to conventional electromagnetic motors.

The force acting on a lead carrying the current I for a length l within a magnetic field B is given by the equation

$$F = I\,l\,B\,.$$

The total active area A of electromagnetic motors is given by the length l and the circumference $\pi d$ of the airgap. Thus the motor force per active area is given by

$$F / A = i\,B \qquad \text{with } i = I / (\pi\, d).$$

The one-dimensional current density i of the motor is limited by the necessary cooling of the motor to values of 500 .. 1000 A/cm, the flux density B is limited by the material properties of the flux conducting iron core to values of 0.8 .. 1 T. Hence the motor force per active area is limited to values of

$$F / A = 4\ \mathrm{N/cm^2} \,..\, 10\ \mathrm{N/cm^2}\,,$$

which can be achieved only in big machines with special cooling. In small machines of the power range typical for actuators only values of

$$F / A = 0.1 \text{ N/cm}^2 .. 0.15 \text{ N/cm}^2$$

are reached.

For piezo-electric motors a similar force per active area can be defined, if the motor force and the contact area between stator and the moving part is considered. For state-of-the-art piezo-electric motors a value of

$$F / A = 3.5 \text{ N/cm}^2 .. 10 \text{ N/cm}^2$$

is obtained from experimental results. This value is strongly dependent on the properties of the contact material between stator and moving part. The value is comparable to the upper limit for electromagnetic motors, and it is 30 to 100 times larger than the value for small electromagnetic motors.

The active area between stator and moving part of the motor does not consider either the necessary volume to produce the magnetic flux and to conduct the current (in electromagnetic motors) or the necessary volume to induce and perform the two modes of oscillation (in piezo-electric motors). State-of-the-art piezo-electric motors only need about one tenth of the volume of electromagnetic motors of the same torque. Considering the relatively young development of piezo-electric motors, further improvements may still be possible.

## 6. LIMITS OF SPEED

Speed of piezo-electric motors is proportional to the operating frequency and the amplitude of oscillation at the location of force transmission. The frequency may not be chosen freely, since oscillatory energy losses are proportional to frequency. By choice of a mechanical resonance, normally somewhere between 20 kHz and 50 kHz, the frequency is more or less fixed even with varying motor load.

The attainable amplitude of oscillation strongly depends on the available power of excitation, as well as on the damping of the oscillator. Damping is due to losses in the (metal) oscillator itself as well as in the piezo-electric element attached to the oscillator for excitation. A third source of damping is the mechanical power output of the motor. Thus piezo-electric materials with high power conversion and low damping are needed.

If very little damping or very strong excitation is present, the amplitude of oscillation can reach large values. In this case, the amplitude may be limited by the maximum allowable strain in the oscillator. Piezo-electric ceramics as part of the oscillator fail at much lower strains than metals; by proper design of the oscillator the maximum strain of the piezo-electric element can be made much less than the maximum strain at the force transmitting location of the oscillator.

Experimental results show, that a speed of 0.6 m/s at the contact surface between stator and moving part can be achieved at low motor forces. There are indications that the technological limit is at least by a factor of 2 or 3 higher.

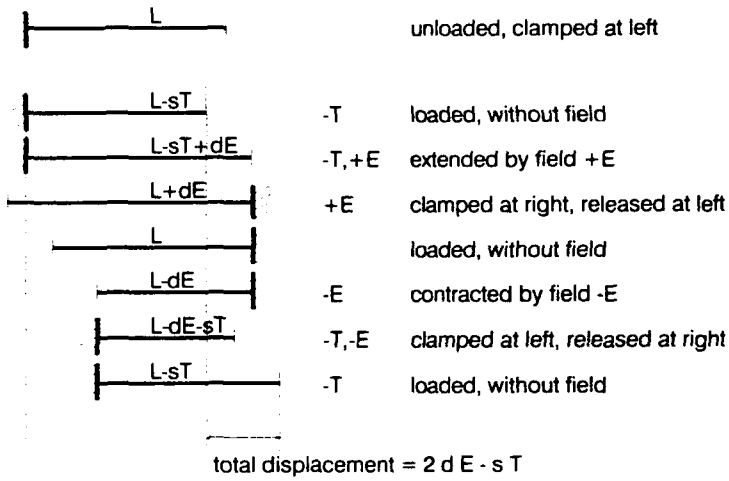


FIGURE 2 One motion cycle of a loaded Inchworm-motor

## 7. MOTOR CHARACTERISTICS

As mentioned before, the amplitude of oscillation and thus the speed of the motor depends on the damping due to the mechanical power output. Thus, the speed-over-torque curve of a resonant piezo-electric motor is a tilted line with highest speed at zero-load. Using piezo-electric sensors, the amplitude of oscillation can be detected and controlled to maintain a given value. By this means the motor characteristics can be made much less dependent on motor load. Nevertheless, the speed-over-torque curve still remains tilted. The reason for this fact shall be explained for the Inchworm-motor:

Figure 2 shows the different phases of a working cycle of an Inchworm-motor. From top to bottom, first the unloaded center part of length L is shown, being clamped on the left side. Next, a load T is applied, reducing the length of the elongator by sT. An electric field E now increases the length by dE to become L-sT+dE. Clamping on the right side releases the elongator from the load; thus the unclamping on the left side results in an increase in length to L+dE. Reversing the electric field shortens the elongator from L+dE to L-dE. Clamping again on the left side and unclamping on the right side puts the load back onto the elongator, which reduces its length by sT. Without electric field the situation becomes equivalent to the starting situation, again with a length of L-sT. The resulting total displacement during the cycle is 2dE-sT. Since motor speed is frequency times displacement per cycle, the speed depends linearly on the load T. The slope of the speed-over-torque curve is proportional to the elasticity of the material which transmits the force between stator and moving part of the motor.

Although in this example the inchworm-motor was used because of the easy understanding of the single steps, the same principle is valid, however, for resonant piezo-electric motors. Thus in resonant piezo-electric motors the speed-over-torque curve is (even with control of the oscillation amplitude, s. fig. 3) linearly decreasing with torque, the slope of the curve being proportional to the shear-elasticity of the contact material.

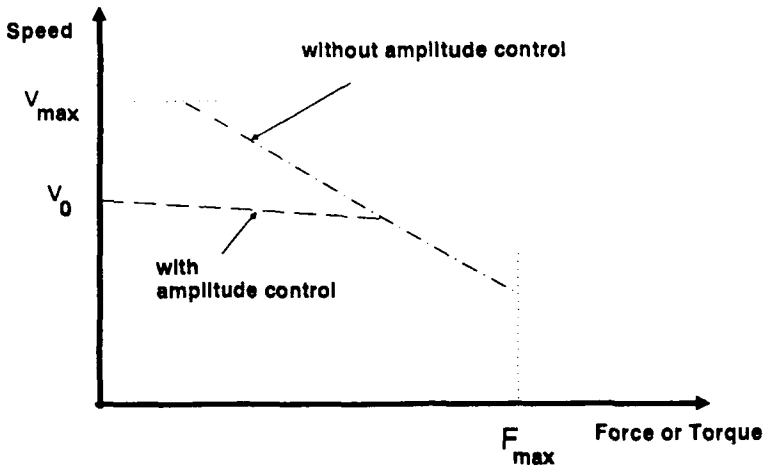


FIGURE 3 Characteristics of a piezo-electric motor

## 8. LOSSES AND OPERATING TEMPERATURE

In order to achieve high motor efficiencies, resonant piezo-electric motors must be designed for as little oscillatory losses as possible. These losses are proportional to the excitation frequency and the loss factor of the oscillating material. Loss factors of metals used for mechanical resonators are in the range of $10^{-4}$; piezo-ceramics have loss factors in the range of $10^{-3}$. Thus, a considerable amount of oscillatory losses is due to losses in the ceramics, although the amount of ceramics is in general only the smaller part of the resonator.

The operating temperature range required for many applications of piezo-electric motors extends from -40°C up to +90°C. Motor temperatures of 120°C are easily reached at high ambient temperatures. Losses in piezo-ceramics increase with temperature at least in the upper part of this temperature range. For this reason there is a certain risk of thermal runaway. When selecting piezo-ceramics for motor applications this fact should be considered.

## 9. FURTHER ASPECTS OF PIEZO-ELECTRIC MOTORS

Piezo-electric motors need power electronics for the control of voltage and frequency to be applied to the piezo-ceramics. Operation of the motor has to be stabilized close to a resonance frequency which, however, shifts with motor load and with temperature. The use of piezo-electric sensors provides an easy means to monitor the oscillations in the motor. Signals from the sensors may be used for closed loop control of the oscillation. Often the integration of such sensors is possible in the same piece of ceramics which is used for the excitation of the oscillation.

The core of the electronic control is a converter which supplies the two phased supply voltages for the excitation of the piezoelectric oscillators. Capacitance of the piezo-ceramics and converter inductivity form an electric resonance circuit precisely

matched to the stator resonance in order to reduce the reactive power demands of piezo-electric motors.

In the future piezo-electric motors with reduced losses, higher motor powers and larger motor dimensions will be possible. A large market for piezo-electric motors is anticipated. However, further development work needs to be done before piezo-electric motors will be implemented in many products. Temperature extremes are still a problem, caused not only by ceramics but also by the contact material between stator and moving part of the motor. Overloading of the motor has negative effects on the operational lifetime of the motor; suitable control methods will solve this problem. In a few years piezo-electric motors will be serious competitors to standard electromagnetic motors in many applications.

## 10. REFERENCES

[1] Burleigh Instruments, Inc.: 'Micropositioning Systems', 1989, Burleigh Park, Fishers, NY 14453

[2] Williams, A.; Brown, W.: 'Piezoelectric Motor', United States Patent 2 439 499, Aug. 1942

[3] Barth, H.V.: 'Ultrasonic Driven Motor', IBM Technical Disclosure Bulletin Vol. 16, No.7, p.2263, Dec. 1973

[4] Wischnewski e.a., Kiew Polytechn. Institut: 'Elektrostriktiver Motor', Patent DE 25 30 045 C2, July 1975

[5] Labrinenko; Kartaschew; Wischnewski: 'Piezoelektrische Motoren', Verlag Energie, Moskau, 1980

[6] Sashida, Toshiiku: 'Motor device utilizing ultrasonic oscillation', United States Patent 4 562 374, Feb. 1983

[7] Akiyama, Y.: 'Present State of Ultrasonic Motors in Japan', JEE, April 1987, pp.76-80

[8] Akiyama, Y.: 'Ultrasonic Motors/Actuators', Triceps Co., Tokyo, 1986

[9] Tomikawa,Y.; Ogasawara,T.; Sugawara,S.; Konno,M.; Takano,T.: 'Construction of Ultrasonic Motors and their Application', Proc. 8th Symp. on Ultrasonic Electronics, Tokyo 1987, Jap. J. Applied Physics, Vol.27 (1988), Suppl. 27-1, pp.195-197

[10] Kumada, A.: 'A Piezoelectric Ultrasonic Motor', Proc. 6th Int. Meeting on Ferroelectricity, Jap. J. Applied Physics Vol.24 (1985) Suppl. 24-2, pp.739-741

[11] Kuribayashi, Minoru; Ueha, Sadayuki; Mori, Eiji: 'Excitation conditions of flexural travelling waves for a reversible ultrasonic linear motor', J. Acoust. Soc. Am. 77 (4), pp.1431-1435, April 1985

[12] Endo, A.; Sasaki, N.; Tomikawa, Y.: 'Linear type ultrasonic motor using two-dimensionally positioned piezoelectric elements', Ferroelectrics 112, 1990, pp.165-170

[13] Fleischer, M.; Stein, D.; Meixner, H.: 'Novel Ultrasonic Motors with Mono- and Bimodal Drives', Sensors and Actuators, A21-A23 (1990), pp.357-361

[14] Salomon, B.; Schadebrodt, G.; Schöner, H.P.: 'Travelling Wave Ultrasonic Motor', Actuator 90, Paper 1.4, pp.28-31, Bremen, June 1990

*Ferroelectrics*, 1992, Vol. 133, pp. 35–40
Reprints available directly from the publisher
Photocopying permitted by license only

© 1992 Gordon and Breach Science Publishers S.A.
Printed in the United States of America

**PyI11**

# PYROELECTRIC PROPERTIES OF THIN FILM LEAD SCANDIUM TANTALATE

NICHOLAS SHORROCKS, ANIL PATEL & ROGER WHATMORE
GEC-Marconi Materials Technology Ltd, Caswell, Towcester, Northants, NN12 8EQ, UK

Abstract Electrical measurements on thin film ferroelectric lead scandium tantalate, deposited from solution, are described. It has good pyroelectric properties, approaching those of the bulk ceramic material. Its potential for thermal imaging applications is discussed. A theoretical specific detectivity of 4 x $10^8 cmHz^{1/2}W^{-1}$ has been calculated using measured film properties in a simple detector array structure.

## INTRODUCTION

Lead scandium tantalate ($Pb(ScTa)_{1/2}O_3$, PST) is a ferroelectric with the perovskite structure, with its transition ($T_c$) close to room temperature. PST ceramic has been reported to have excellent pyroelectric properties when operated at or above $T_c$ with a dc bias field applied to stabilise the polarisation[1]. This mode of operation results in very high pyroelectric coefficients, which are useful for applications requiring very small area detectors, for example, a 2d thermal imaging array[2]. Such a device could need, for high spatial resolution, a close-packed array of about $10^5$ detectors, each 5-10μm thick on a sub-100μm pitch. This could be made from bulk ceramic material, successively sliced, lapped and polished to the final thickness. However, it would be more convenient to produce the required thickness directly with good uniformity by thin film growth. This paper discusses the electrical properties of thin film PST, comparing them with the bulk ceramic data. Its potential for pyroelectric applications is discussed.

## FILM PREPARATION

Thin film PST has been produced by deposition from metal-organic solutions. Reference 3 discusses this in detail. The maximum processing temperature is about $900^0C$, so an inert substrate with a good thermal expansion match to PST is required. Sapphire has been used successfully. Deposition onto metallised substrates has proved impossible, because of the reactivity of the lead in the film. Samples of up to 5.8μm thick have been produced. X-ray analysis has shown that 100% perovskite can be obtained, but that there is only a small amount of ordering of the Sc and Ta cations on the lattice B-site.

## ELECTRICAL MEASUREMENTS

In order to assess the potential detector performance of PST films, it is necessary to measure their electrical properties: the permittivity and dielectric loss, the pyroelectric coefficient and the resistivity. This has been achieved using an interdigitated electrode (IDE) pattern, defined in evaporated chrome-gold on the top surface. As the inter-electrode gap (about 11μm) was significantly greater than the film thicknesses, the measuring field was mostly parallel to the film surface. As the films have been grown directly on insulating substrates, through-film measurements could not be made routinely.

Film permittivity and loss were calculated from measurements made with a Wayne Kerr 6425 Multi Bridge for bias voltages of up to 50V. The stray capacitance from the substrates had been measured separately and was subtracted. The resistivity was measured using a Keithley 602 electrometer. The pyroelectric response, also with up to 50V bias, was derived from the ac current produced by modulating the substrate temperature, typically by 0.2Krms at 0.01Hz. As the films were measured under bias,

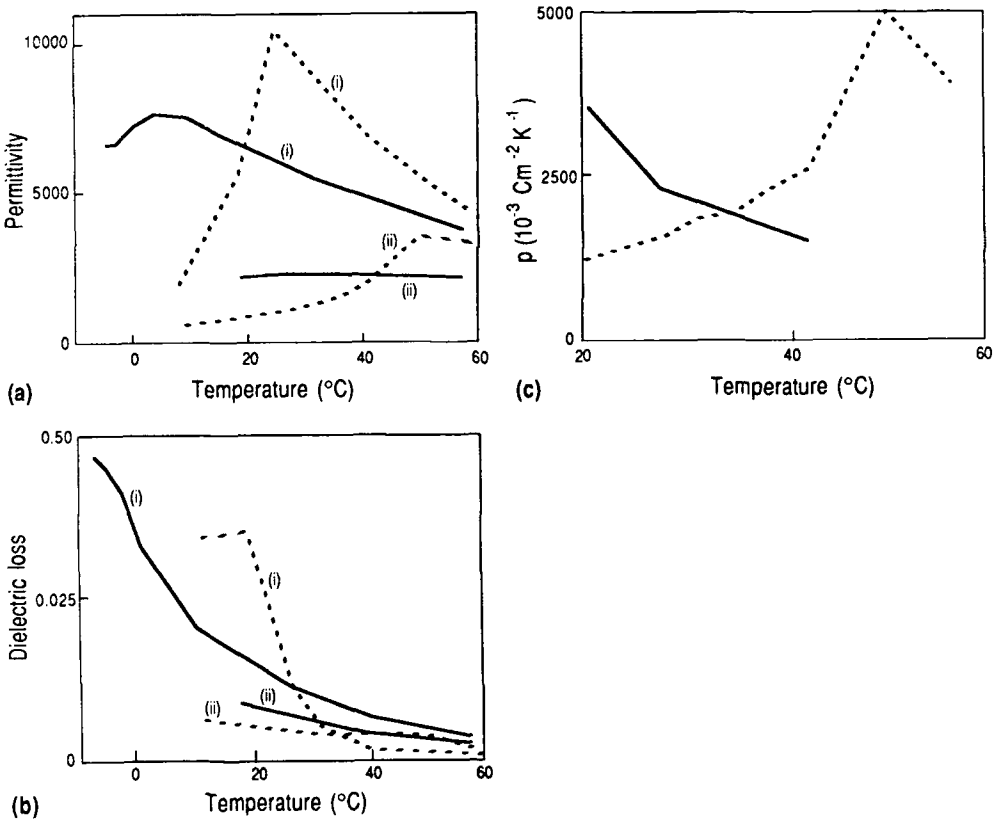


Figure 1 Thin Film (—) and bulk ceramic (---) PST dielectric properties

| | | | |
|---|---|---|---|
| i) | at zero bias | a) | Relative permitittivity |
| ii) | at 4.2 x $10^6$Vm$^{-1}$ | b) | Dielectric loss |
| | | c) | Pyroelectricity (p) |

there were additional, spurious signals proportional to the temperature coefficient of the resistivity. These have been calculated and the results corrected accordingly. The use of interdigitated electrodes resulted in a non-uniform distribution of the bias field for both capacitance and pyroelectricity measurements. In particular, there was significant field enhancement at the edges of the electrodes and reduced fields elsewhere. Therefore, the measurements under bias only approximate the film properties in a uniform field.

Figure 1 shows dielectric data from a 3μm thick film with grain size from 0.3 to 0.8μm. For comparison, the equivalent data is included for ceramic PST, which had been produced by hot pressing to near full theoretical density with a 1 to 2μm grain size. There is general agreement on the magnitude of the properties. $T_c$ of this film, estimated from the permittivity peak, is low; typically the films have $T_c$ 5 to 30K below the ceramic value. The zero bias permittivity curves show that the ferroelectric transition of the thin film is much less sharp than that of the ceramic. This is expected, because of the degree of ordering of the Sc and Ta cations on the B-site of the lattice[4]; X-ray data indicates less than 10% ordering for the film, about 60% for the ceramic.

For both samples, the strong bias field reduces the dielectric peak and shifts it up by 30K as expected for a first order transition[1]. Their dielectric losses are similar, comparatively high at and below their transitions, lower in the paraelectric phase or under bias. The pyroelectric responses under bias, Figure 1(c), have similar magnitude. With the ceramic, there is a response peak associated with the biassed permittivity peak. This is absent from the thin film data, because its transition is so much broader. This, together with the reduced $T_c$, accounts for much of the difference between the two.

The major difference between the samples occurs in the resistivity, ranging from 0.3 to 3 x $10^{10}\Omega$m for most of the thin films, but over $10^{12}\Omega$m for the ceramic. The thin films have also shown less consistency, with, for example, the peak relative

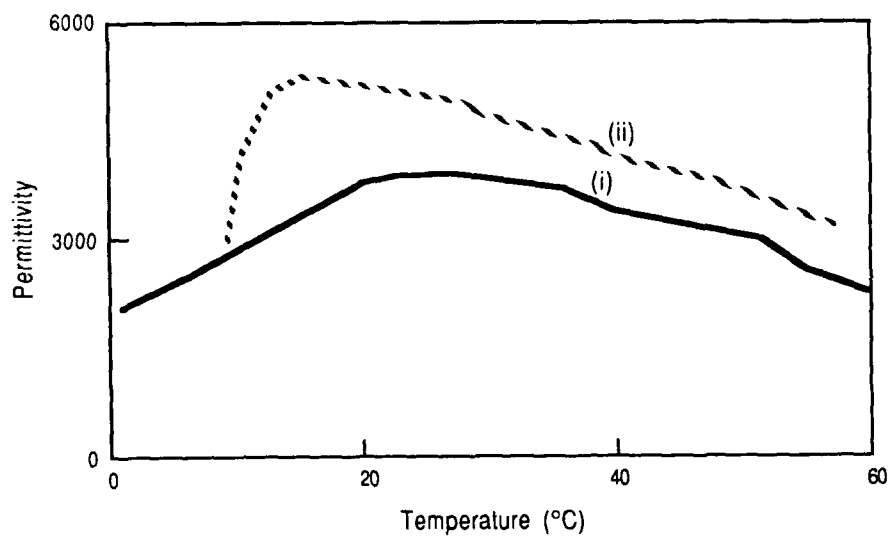


Figure 2 Relative permittivity of thin film PST (i) before and (ii) after release from substrate

permittivities spread over the range 1500 to 9000. There has, however, been no correlation of these spreads with either film thickness, which has varied from 0.4 to 5.8μm or with the 0.3 to 1.5μm range in average grain size. This suggests that no significant property degradation has been caused either by the inter-grain boundaries or by surface layer effects. The former would have been observed in poorer properties for fine grain material with a higher grain boundary density, the latter in poorer properties for thin layers, where any surface layer would be proportionally more significant.

A single measurement has been made on a 4μm thick piece of film, released by chemical etching of an MgO interlayer from its substrate, with both surfaces electroded. The peak permittivity, Figure 2, was close to the value measured pre-release, but the peak was sharper. This might be the result of separating the film from the mechanical clamping of the rigid substrate, which would inhibit the dimensional changes associated with a ferroelectric transition. Alternatively, X-ray analysis revealed that the film had a preferred (100) orientation. This would favour the released measurement, made through the film thickness, over the unreleased, made parallel to the surface, where there is no consistent orientation of grains.

## PYROELECTRIC DETECTOR PERFORMANCE

For high resolution 2d imaging array, the thin film PST permittivity ($\varepsilon$) would give an element capacitance of a few picofarads. This would be a reasonable match to a MOSFET pre-amplifier, resulting in a detector noise dominated by the Johnson noise of the dielectric loss (D). In this case, the detector signal-to-noise would be proportional to the material figure of merit[2], $F_D = p/\sqrt{(\varepsilon D)}$, where p is the pyroelectric coefficient. Table (1) compares the relevant properties of a range of pyroelectric materials. Though the thin film PST does not match the bulk ceramic, it is superior to most other bulk materials, especially in applications for small area detectors where low permittivity is undesirable. It is also not known whether the bulk materials would retain all their properties if thinned down to match the PST film thicknesses.

TABLE 1 Comparison of PST ($4 \times 10^6 Vm^{-1}$ bias) with conventional bulk pyroelectric materials

| | Pyroelectric Coefficient | Relative Permittivity | Dielectric Loss | $F_D$ |
|---|---|---|---|---|
| PST Ceramic | 4.9 | 3760 | 0.0042 | 410 |
| PST Thin Film | 3.16 | 2170 | 0.0064 | 280 |
| Triglycine Sulphate[5] | 0.55 | 55 | 0.025 | 160 |
| $Sr_{0.5}Ba_{0.5}Nb_2O_6$[6] | 0.55 | 400 | 0.003 | 170 |
| Doped $PbTiO_3$[7] | 0.38 | 220 | 0.011 | 80 |
| $LiTaO_3$[8] | 0.23 | 47 | 0.001 | 360 |
| Units | $10^{-3}Cm^{-2}K^{-1}$ | - | - | $J^{1/2}m^{-3/2}K^{-1}$ |

Further development is required before these thin film properties can be utilised. As PST is operated under bias, the finite resistivity results in a leakage current and an associated shot noise term. As yet, only the best films reach the minimum acceptable resistivity for which $F_D$ is the appropriate figure of merit. Secondly, the films must be detached from their insulating substrates, as these both block electrical connection to

one face and act as large unwanted heatsinks. This has been demonstrated over small areas by growing PST with a chemically etchable layer of MgO between it and the substrate. This needs to be extended to areas of the order of $10^{-3}m^2$, removing the PST intact on a support structure suitable for 2d array processing techniques.

Figure 3 illustrates a possible, schematic structure, suitable for a linear, rather than 2d, array.The process steps needed include: definition of the top face electrode, ion beam milling[9] of the PST to define the detector volumes and deposition of a polymer support film, which together with a resistive metal coating produces efficient infra-red absorbing structures[10]. The PST would then be released by chemical etching from its sapphire substrate and transferred to a temporary support substrate. The second face is thus exposed for metallisation with split-electrodes, which remove the need for a top contact, and for solder bonding[11] to an appropriate carrier substrate. Removal of the temporary support and connection to FET pre-amplifiers would complete the array. The only non-standard process steps would be the release and transfer to the temporary support. Simple calculations indicate that, provided the unreleased film properties are maintained, a high specific detectivity ($D^*$) of above $4 \times 10^8 cmHz^{1/2}W^{-1}$ over 30 to 300Hz could be achieved for 100μm square detectors, 5μm thick.

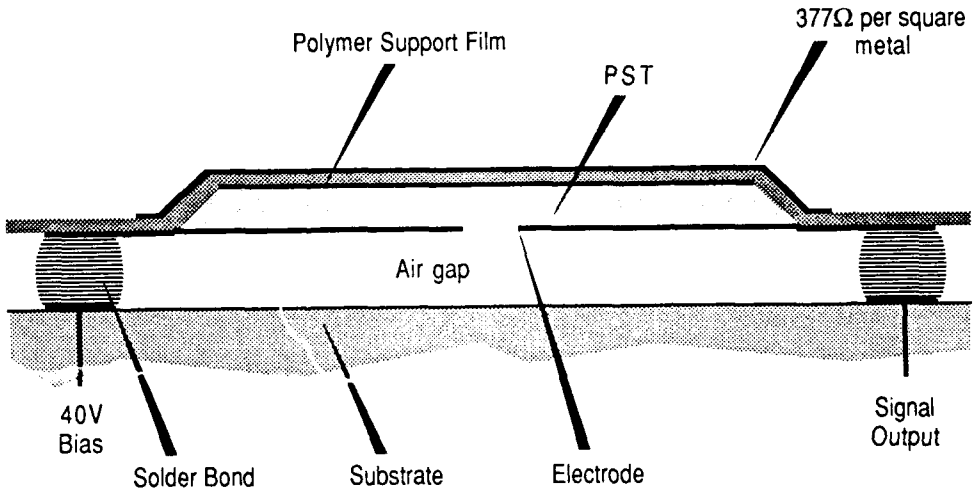


Figure 3 Schematic cross-section of a thin film PST thermal detector

## CONCLUSIONS

PST thin films, deposited from solution, have been characterised electrically. Their pyroelectric properties approach those measured on bulk PST ceramic. The combination of controlled low thickness and very large pyroelectric charge coefficients make them suitable for large 2d imaging arrays. Their properties appear to be independent of both grain size and film thickness. A release layer technique using MgO has been demonstrated, which is a necessary step in the fabrication of a detector array.

ACKNOWLEDGEMENT

This work has been carried out with the support of the Procurement Executive, Ministry of Defence.

REFERENCES

1. N.M. Shorrocks, R.W. Whatmore and P.C. Osbond, Ferroelectrics, 106, pp1223-8 (1990).
2. R. Watton and M.V. Mansi, SPIE, 865, pp78-85 (1987).
3. A. Patel, N.M. Shorrocks and R.W. Whatmore, this conference proceedings.
4. L.S. Kamzina, N.N. Krainik. L.M. Sapozhnikova, I.S. Barash and N.V. Zaitseva, Sov. Tech. Phys. Lett., 14, pp764-5 (1988).
5. P. Felix, P. Gamat, P. Lacheau and Y. Rowerdy, Ferroelectrics, 17, pp543-51 1978).
6. S.T. Liu and R.B. Maciolek, J. Electron. Mater., 4, pp91-100 (1975).
7. N. Ichinose, Am. Ceram. Soc. Bull., 64, pp1581-5 (1985).
8. E.H. Putley, Infra-Red Phys., 20, pp149-56 (1980).
9. R.A.C. Bache, C. O'Hara, A.D. Parsons, N.M. Shorrocks and D.J. Pedder, J. Vac. Sci. Tech. A, 7, pp2988-91 (1989).
10. A.A. Turnbull, SPIE Proc., 588 (1985).
11. D.J. Pedder, Hybrid Circuits, 15, pp4-7 (1988).

*Ferroelectrics*, 1992, Vol. 133, pp. 41–45
Reprints available directly from the publisher
Photocopying permitted by license only

© 1992 Gordon and Breach Science Publishers S.A.
Printed in the United States of America

# Py112

## PYROELECTRIC SINGLE-ELEMENT DETECTORS AND ARRAYS BASED ON MODIFIED TGS

GÜNTER HOFMANN, NORBERT NEUMANN and HELMUT BUDZIER
Technische Universität Dresden, Institut für Festkörperelektronik,
Dresdner Institut für angewandte Sensorik (DIAS)
O - 8027 Dresden, Mommsenstraße 13, Germany

Abstract Pyroelectric detectors based on modified triglycine sulphate are described. Single-element detectors reach D*(500 K, 10 Hz, 25 °C) values up to $2 \times 10^9$cm $Hz^{1/2}$/W. Linear arrays (128 elements, 100 $\mu$m pitch) and two-dimensional arrays (128x128 elements, 50 $\mu$m pitch) with NEP (500 K, 40 Hz, 25 °C) values up to 1 nW (0.16 nW/ $Hz^{1/2}$) and NEP (500 K, 10 Hz, 25 °C) values of 0.4 nW respectively were also realized.

## INTRODUCTION

With modified triglycine sulphate (TGS) high-sensitive pyroelectric infrared detectors may be realized. In Fourier interferometers, for example, pyroelectric single-element detectors based on modified TGS are commonly used. In the last few years we also developed some types of linear and two-dimensional TGS-arrays. In this paper some results of pyroelectric single-element detectors and arrays based on modified TGS are described. The measured properties are compared with the results of also realized detectors and arrays based on lithium tantalate ($LiTaO_3$) manufactored at our institutes too.

## DESIGN

The TGS-modifications used are deuterated and L-alanine doped TGS (DTGS:L-A) or L-alanine and chromium doped TGS ( TGS:L-A+$Cr^{3+}$ ) respectively[1]. Single domain crystals of high purity, good homogeneity and stability up to 70 °C were grown. DTGS:L-A-crystals were produced by use of a {001} area seed by box method[2]. Figure 1 shows the lateral distribution of the internal bias-field of a DTGS:L-A-crystal. In table 1 the values of some figures of merit of the crystals used are listed.

TABLE 1 Figures of merit at 25 °C

| material | DTGS:L-A | TGS:L-A+$Cr^{3+}$ | $LiTaO_3$ |
|---|---|---|---|
| $M_U$ in $10^{-10}$ Ccm/J | 5.3 | 4.7 | 1.4 |
| $M_I$ in $10^{-8}$ Ccm/J | 1.0 | 1.5 | 0.6 |

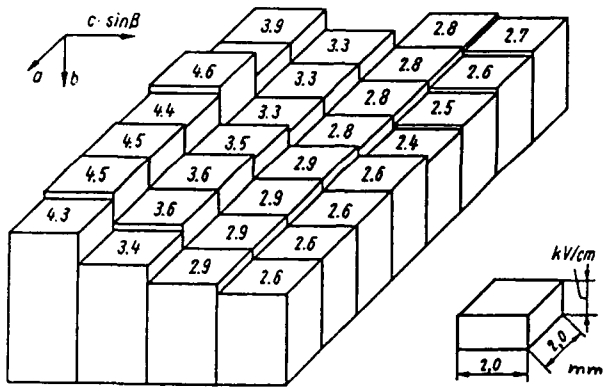


FIGURE 1 Lateral distribution of bias-field $E_B$ of a DTGS:L-A-crystal at 25°C

The figures of merit $M_U$ and $M_I$ are given by

$$M_U = p/(c'_P \varepsilon_r) \quad (1)$$

$$M_I = p/c'_P \quad (2)$$

where p is the pyroelectric coefficient, $c'_P$ is the volume specific heat and $\varepsilon_r$ is the dielectric constant.

Pyroelectric chips with NiCr/Au-electrodes and a thickness $d_P$ = 10...30 $\mu$m in the region of the sensitive area were made by means of mechanical, chemical, photolithographical, evaporating and ion-beam milling processes.

Pyroelectric single-element detectors contain the pyroelectric chip with a sensitive area $A_S$ = 2x2 $mm^2$, a high-megohm resistor (2...4 x $10^{11}$ Ω) and a low-noise JFET, which are mounted in a TO5-transistor package with an IR-transparent window (KRS5, coated Ge or Si ).

The pyroelectric chips of linear arrays contain 128 sensitive elements (element size 90 x 100 $\mu m^2$, 100 $\mu$m pitch). By means of ion beam milling techniques it is possible to produce insulating grooves between the sensitive elements to reduce the thermal and capacitive cross-talk[1]. The read-out circuit used contains FILL-SPILL gate modulation input structures for every sensitive element, a common 1 1/2 phase BCCD shift register and a floating gate output[3]. An integrated thermoelectric element was used to hold the array components at a stable temperature. Pyroelectric chip, read-out circuit and thermoelectric element were mounted in a special metallic package with coated Ge window (Figure 2).

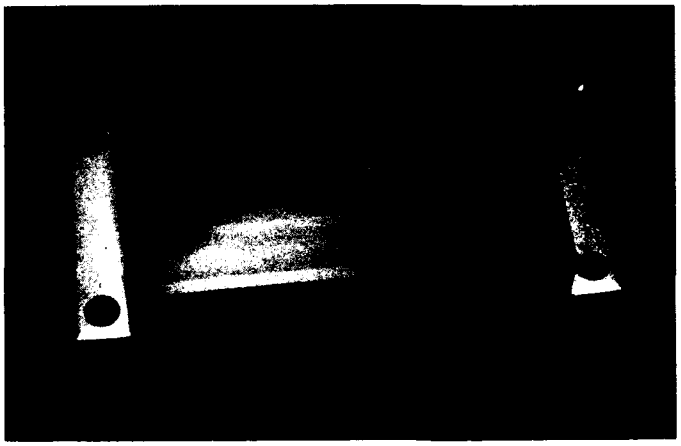

FIGURE 2 Pyroelectric linear array (128 elements, 100 μm pitch). (See Color Plate I).

Pyroelectric two-dimensional arrays contain a sandwich-structure of pyroelectric chip and CCD read-out circuit. The pyroelectric chip with 128 x 128 sensitive elements ( 50μm pitch) is shown in Figure 3. Ion beam milled grooves between the sensitive elements were produced to reduce the thermal and capacitive cross-talk . The thickness of the pyroelectric chip is about 50 μm. To improve the thermal insulation between the pyroelectric chip and the read-out circuit electrical conductive polymeric bumps were used. The hight of the bumps amounts to about 15 μm. Figure 4 shows the read-out circuit with bumps including Al contacting areas. The coupling between the pyroelectric chip and the bumps was realized by a dielectric PMMA layer. The components of the two dimensional array were mounted in a metallic package with coated Ge window.

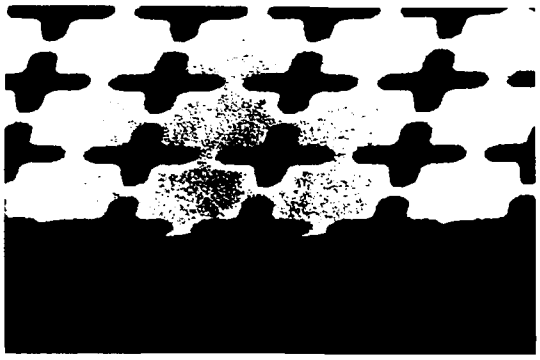

FIGURE 3 DTGS:L-A chip of the two dimensional array (128 x 128 elements, 50μm pitch)

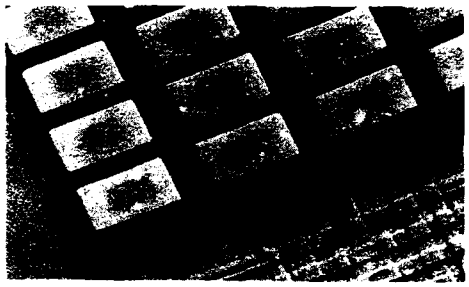

FIGURE 4 Read-out circuit with bumps of the two-dimensional array (128 x 128 elements)

## PROPERTIES

Important properties of single-element detectors realized are summerized in table 2. The responsivity $S_V$ and specific detectivity $D^*$ were measured for a sinusoidal modulated incident radiation. $D^*$ values up to $2 \times 10^9$ $cmHz^{1/2}/W$ were reached.

In tables 3 and 4 properties of linear and two-dimensional arrays are given. The values were measured for a rectangular modulated radiation. Linear arrays with NEP values up to 1 nW were realized. By integration to a frame rate of 1 Hz the NEP values at a chopping frequency of 40 Hz were decreased up to 0.16 nW/ $Hz^{1/2}$.By use of digital filters it is possible to increase the modulation transfer function MTF of about 80% at 3 lp/mm. Two-dimensional arrays reach NEP values up to 0.4 nW.

The results are in good agreement with theoretical calculations[4,5] and measured properties of similar detectors and arrays[6].

TABLE 2 Properties of pyroelectric single-element detectors with KRS5-window at 25 °C
( *) with additional black coating)

| material | DTGS:L-A | TGS:L-A+$Cr^{3+}$ | $LiTaO_3$ |
|---|---|---|---|
| responsivity $S_V$(500 K, 10 Hz) in V/W | 1 500 | 1 350 | 260<br>390 *) |
| specific detectivity D*(500 K, 10 Hz) in $cmHz^{1/2}/W$ | $10^9$<br>($d_P = 30\ \mu m$)<br>$2 \times 10^9$<br>($d_P = 10\ \mu m$) | $10^9$<br>($d_P = 30\ \mu m$) | $3 \times 10^8$<br>$5 \times 10^8$ *)<br>($d_P = 20\ \mu m$)<br>$6 \times 10^8$<br>$8 \times 10^8$ *)<br>($d_P = 5\ \mu m$) |

TABLE 3 Properties of pyroelectric linear arrays (128 elements, 100$\mu$m pitch) at 25 °C
( *) with additional insulating grooves between the sensitive elements)

| material | DTGS:L-A or TGS:L-A+$Cr^{3+}$ | $LiTaO_3$ |
|---|---|---|
| responsivity $S_V$(500K, 40 Hz) in V/W | 470 000...700 000 ($d_p$ = 30...10 $\mu$m) | 180 000 ($d_p$= 20 $\mu$m) |
| $S_V$-variations among the 128 elements | 2...5% | 2...5% |
| noise equivalent power NEP(500K, 40Hz) in nW | 1.0...1.7 ($d_p$ = 10...30 $\mu$m) | 4 ($d_p$= 20 $\mu$m) |
| modulation transfer function MTF(3 lp/mm, 40Hz) | 0.5 0.6 *) | 0.2 |

TABLE 4 Properties of pyroelectric two-dimensional arrays (128 x 128 elements, 50$\mu$m pitch) at 25 °C

| responsivity $S_V$(500K, 10 Hz) in V/W | noise equivalent power NEP(500K, 10Hz) in nW | modulation transfer function MTF(3 lp/mm, 10Hz) |
|---|---|---|
| 2.5 x $10^6$ | 0.4 | 0.5 |

This work has been carried out with the support of the Bundesministerium für Forschung und Technologie (13 I 30160).

## REFERENCES

1. V. Norkus, N.Neumann, L. Walther, G. Hofmann, J. Schieferdecker, M. Krauß, H. Budzier and N.Heß, SPIE Vol. 1484, 98 (1991).
2. B. Brezina, CSSR patent, PV-7276-80 (1980).
3. J. Schieferdecker, L. Walther, G. Hofmann, G. Heine, V. Norkus, M. Krauß, H. Budzier, W. Titel, N. Neumann and P. Banse, radio fernsehen elektronik, 39, 221 (1990).
4. G. Hofmann, L. Walther, J. Schieferdecker, N. Neumann, V. Norkus, M. Krauß and H. Budzier, Sensors ans Actuators A, 25-27, 413 (1991).
5. H. Budzier, G. Hofmann and N. Heß, Infrared Physics, 33, 263 (1992).
6. N. M. Shorrocks, S. G. Porter, R. W. Whatmore, A. D. Parsons, J. N. Gooding and D. J. Pedder, SPIE Vol. 1320, 88 (1990).

*Ferroelectrics*, 1992, Vol. 133, pp. 47–60
Reprints available directly from the publisher
Photocopying permitted by license only

© 1992 Gordon and Breach Science Publishers S.A.
Printed in the United States of America

**TdI10**

# FERROELECTRIC THIN FILMS IN INTEGRATED MICROELECTRONIC DEVICES

J. F. SCOTT, C. A. PAZ de ARAUJO, L. D. McMILLAN
Symetrix Corporation, 5055 Mark Dabling Blvd., Colorado Springs, CO and University of Colorado, Depts. of Physics and Electrical Engineering, Boulder, CO and Colorado Springs, CO

H. YOSHIMORI, H. WATANABE, and T. MIHARA
Olympus Optical Co.
Hachioji, Japan

M. AZUMA, TOSHIYUKI UEDA, TETSUKO UEDA, D. UEDA, and G. KANO
Matsushita Electronics Corp.
Osaka, Japan

## ABSTRACT

We present results on four integrated ferroelectric projects: 1) An integrated barium strontium titanate thin-film on GaAs MMIC (monolithic microwave integrated circuit) with dielectric constant of 450 and loss tangent of $10^{-3}$ at 2.2 GHz operation, done as a Symetrix/Matsushita Electronics Corp. joint development; 2) A low-density (1 Kb) ferroelectric RAM (random access memory) done with PZT (lead zirconate titanate) and other ferroelectrics on CMOS (complementary metal oxide semiconductor) Si, carried out as a joint development with Olympus Optical Co.; 3) A liquid-source CVD (chemical vapor deposition) machine and its deposition of strontium titanate and barium strontium titanate films of exceptionally low d.c. leakage current (1 nA/cm$^2$ at 120 nm thickness and 3V operation) for DRAM (dynamic RAM) applications; and 4) performance parameters of a proprietary material for RAM application which is totally fatigue-free up to at least $5 \times 10^{11}$ cycles.

## INTRODUCTION

This year ferroelectric thin-film technology for integrated memory devices[1-3] has finally moved out of the laboratory and into production of commercially useful, albeit prototype, devices. Ramtron/Seiko-Epson has given objective test results[4] on their 256 kbit RAM; Symetrix/Matsushita Electronics have presented results[5] of the first ferroelectric integrated onto a MESFET GaAs MMIC; and NEC has shown parameters[6] of sputtered ferroelectric films for high density (64 and 256 Mb) planarized DRAMs.

Although work on GaAs JFETs (junction FETs) at McDonnell-Douglas[7] and on silicon bipolar ICs at Raytheon[8] has slowed, the development of $BaMgF_4$ ferroelectric FETs (field effect transistors with ferroelectric gates) has accelerated at Westinghouse;[9] and some progress has been made on thin-film ferroelectric CCD (charge coupled device) infrared focal-plane arrays and related pyroelectric detectors at both GEC-Marconi[10] and a Mitsubishi-Osaka University collaboration.[11] Thus, in contrast to previous years, when such conferences emphasized the materials science and engineering physics of ferroelectric films (microstructure, electrical characteristics, deposition and processing, electrodes, etc.), we are finally able at this meeting to discuss half a dozen different, real devices capable of reaching commercial volume fabrication this year. Below we describe four such projects or devices from our own group: 1) A 2.2 GHz ferroelectric-on-GaAs MMIC; 2) A low-density (1 kb) RAM; 3) DRAM films produced by liquid-source CVD; 4) Films of a new material that exhibit no degradation over $5 \times 10^{11}$ switching cycles (not only does the switched charge remain constant, but more importantly, the exact shape of the hysteresis curve remains unaltered).

## $Ba_xSr_{1-x}TiO_3$ on GaAs MESFET MMIC

By relacing the $SiO_2/Si_3N_4$ capacitors in a standard integrated circuit with barium strontium titanate, one achieves a reduction in size of the capacitors by x50.

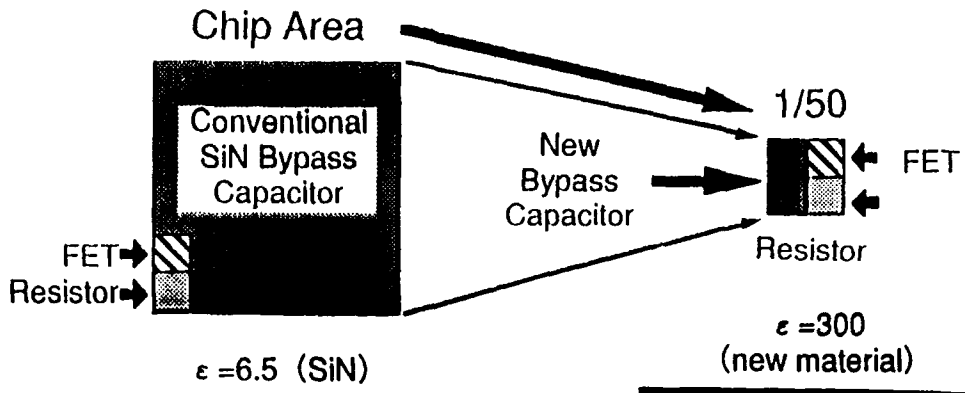


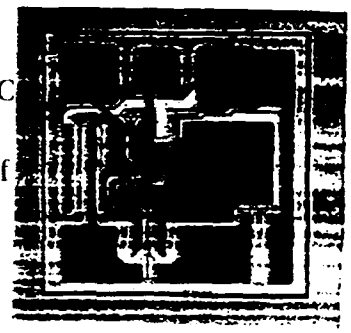

1.) Photo of 2.2 GHz GaAs MESFET MMIC with barium strontium titanate sol-gel capacitor (MEC/Symetrix). Actual size of this MMIC tuner is 0.6 x 0.6 mm.

This permits putting the capacitor on the chip for GaAs MMIC devices. A 0.6 x 0.6 mm GaAs 0.8-2.2 GHz tuner is shown in Fig. 1 from Matsushita Electronics Corp. that utilizes barium strontium titanate films from our group that achieve dielectric constant $\varepsilon = 450$, loss tangent $\delta = 0.001$ at frequency f = 2.2 GHz, and d.c. conductivity $\sigma = 1\ \mu A/cm^2$ (1 $nA/cm^2$ is obtainable with 1% Nb doping), thickness d = 120 nm, and voltage V = 3V. Four different devices have been made from this ferroelectric-on-GaAs MMIC technology by Matsushita/Symetrix: An automatic gain control for TV; a frequency mixer; and 0.8-2.2 GHz tuners for both satellite telephone systems and cable TV.

Fig. 2 shows that the FET characteristics of the GaAs MESFET remain virtually unaffected by the barium strontium titanate processing, while Figs.3-5 show respectively the thickness dependence of d.c. breakdown voltage, the C(V) characteristics, and the frequency dependence of the capacitance (flat at 10 pF until about 2.5 GHz).

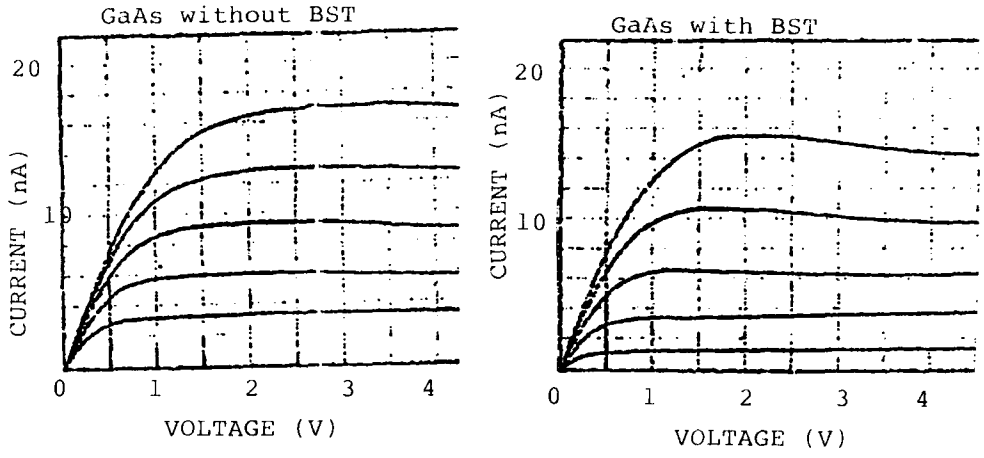


2.) I(V) characteristics of a GaAs MESFET before and after deposition of barium strontium titanate film, showing preservation of electrical characteristics.

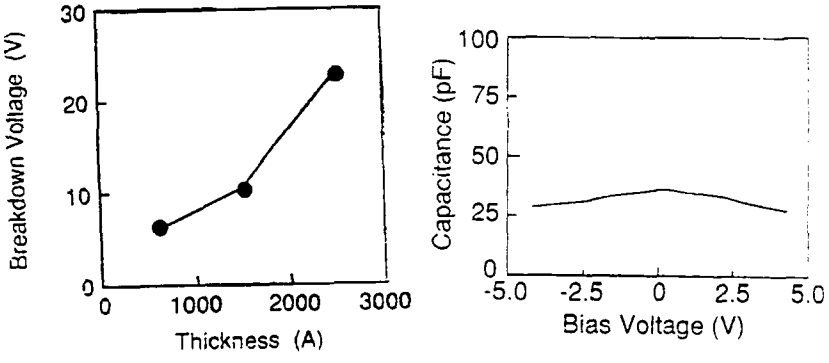


3.) Breakdown voltage versus film thickness for $Ba_{0.70}Sr_{0.30}TiO_3$ spin-on films; 700°C anneal.
4.) C(V) characteristics of one of the films in Fig.3 (250 nm thickness).

5.) C(f) characteristics of the film in Fig. 4.

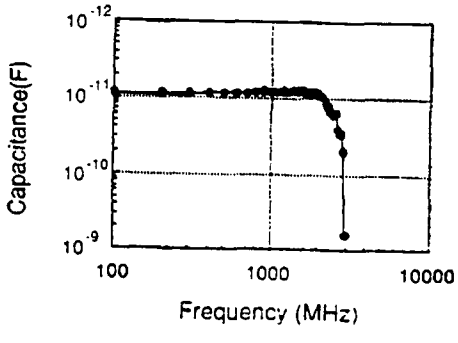

$PbZr_xTi_{1-x}O_3$ on CMOS Si RAM

Fig. 6 illustrates a the block diagram of a low-density memory made by Olympus Optical Co. with sol-gel, spin-on PZT from our group. The cross-sectional structure of this 1K x 1 chip is shown in Fig. 7. The memory circuit is given in Figs. 8; and the processing flow chart for producing this device with PZT is illustrated in Fig. 9. A processing problem that is often encountered in integrated PZT devices is lift-off of the Pt electrode from the PZT; an air gap results and the device fails (a Ti-layer does not eliminate the problem). However, when our new proprietary material (discussed below) replaces the PZT, there is no lift off.

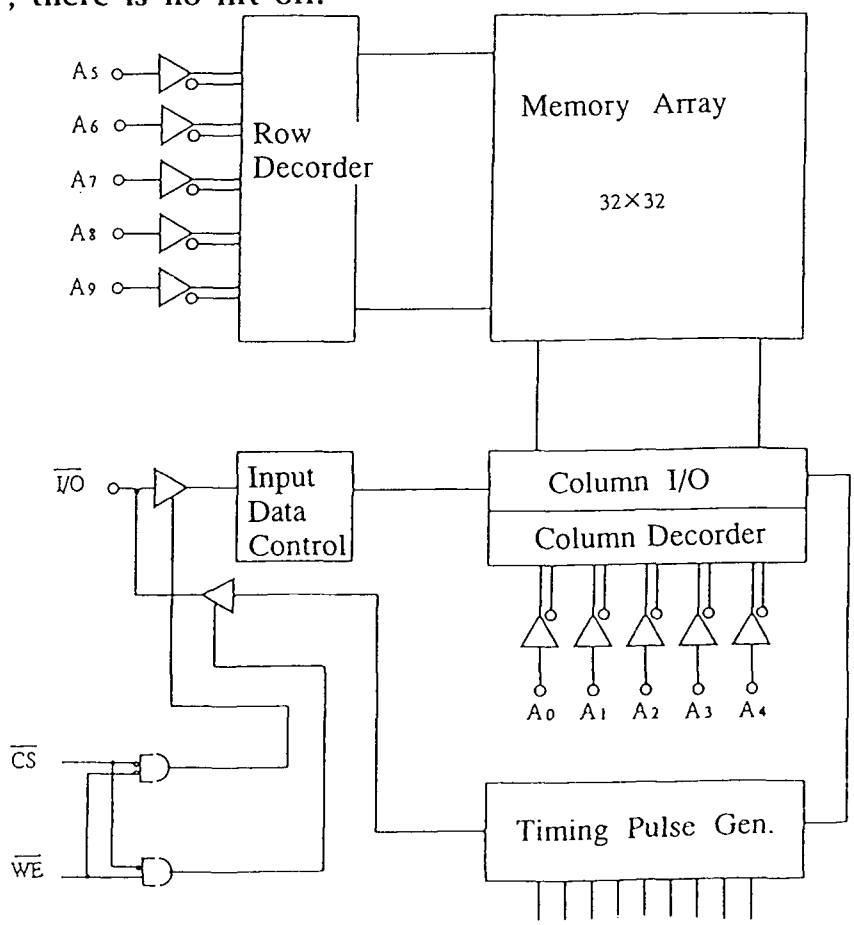


6.) Block diagram of the Olympus/Symetrix 1K x 1 ferroelectric RAM.

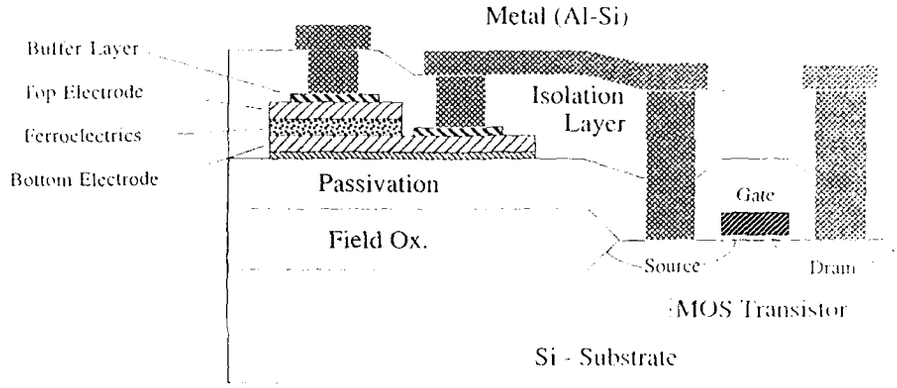


7.) Cross-sectional cell structure of the RAM in Fig.6.

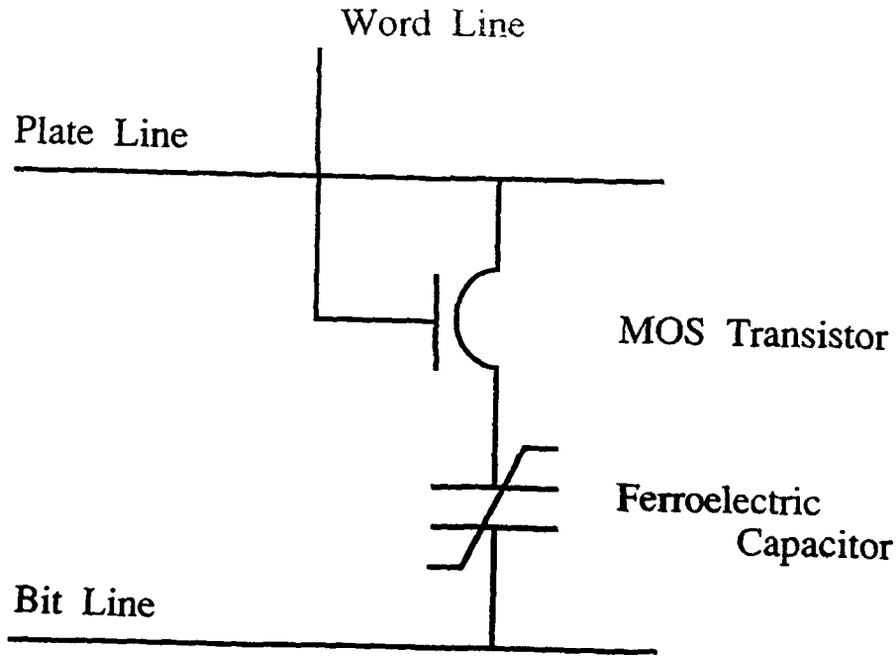


8.) Memory cell circuit for the device in Figs.6,7.

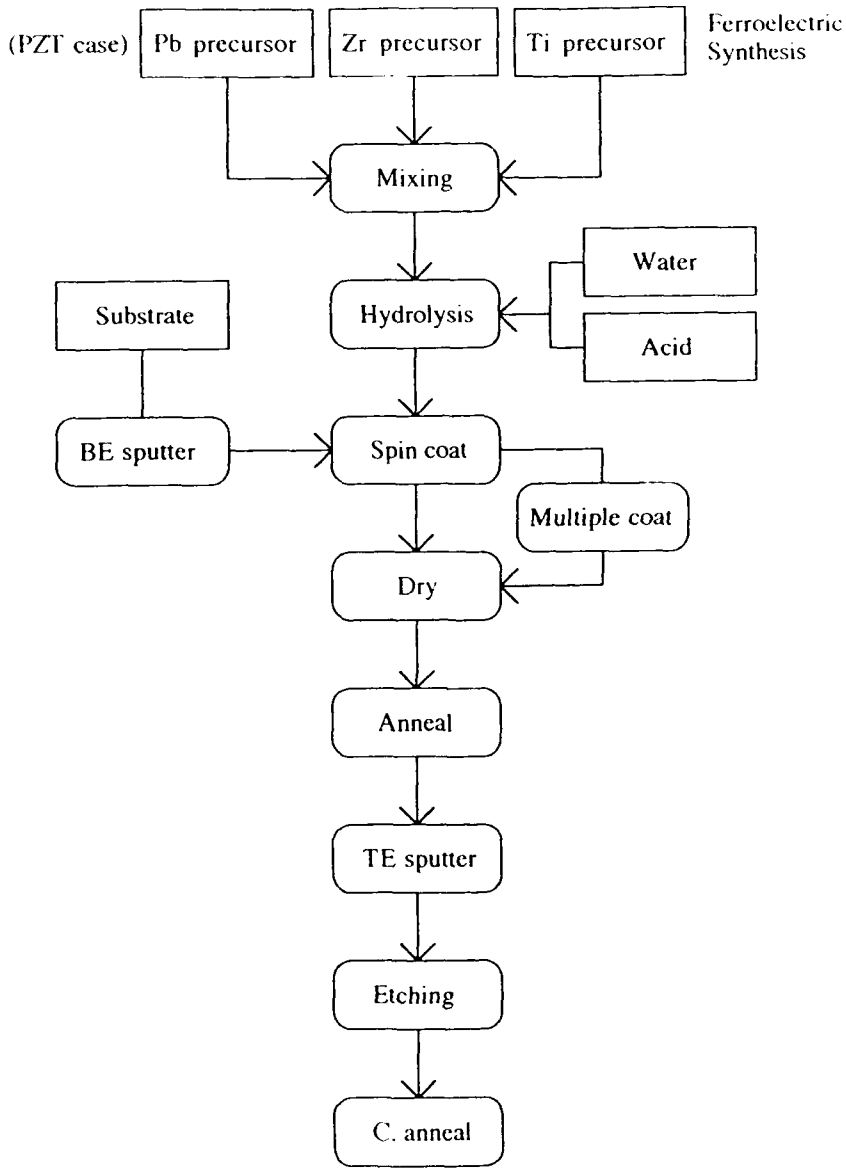


9.) Process flow chart for the 1K x 1 memory with PZT as the ferroelectric material.

LIQUID-SOURCE CVD MACHINE

In 1991 we demonstrated the use of a deposition machine that injected liquid sol-gel material into a vacuum at room temperature for the production of high-quality PZT. Fig. 10 shows schematically the actual machine. This year we have modified the machine to produce excellent strontium titanate and barium strontium titanate films for DRAM applications. Typically it operates from 20 to 50°C. The pressure is set to 1 μm prior to deposition and 500-600 mm Hg during deposition. The substrate is not heated. Dep rates of 3.5 - 10 nm/minute are obtained. The dielectric constants achieved by this deposition technique are summarized in Fig. 11; and Fig. 12 shows d.c. leakage [note that unlike our earlier results on PZT, the leakage current behavior in strontium titanate is dominated by Schottky barrier phenomena at the electrode interface, not by space charge injection]. Fig. 13 illustrates excellect step coverage obtained over a 0.22 μm wide Pt line.

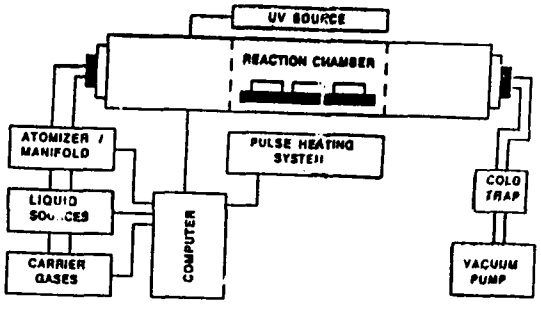


10.) Block diagram of Symetrix' liquid-source, room-temperature CVD machine for deposition of strontium titanate or barium strontium titanate.

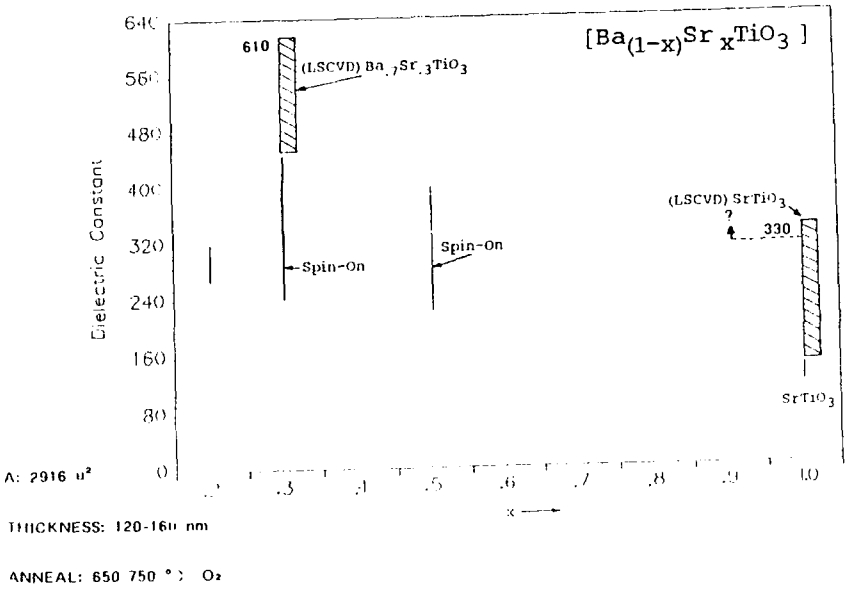


11.) Achieved dielectric constants ε(x) in $Ba_xSr_{1-x}TiO_3$ from the Symetrix liquid-source CVD machine.

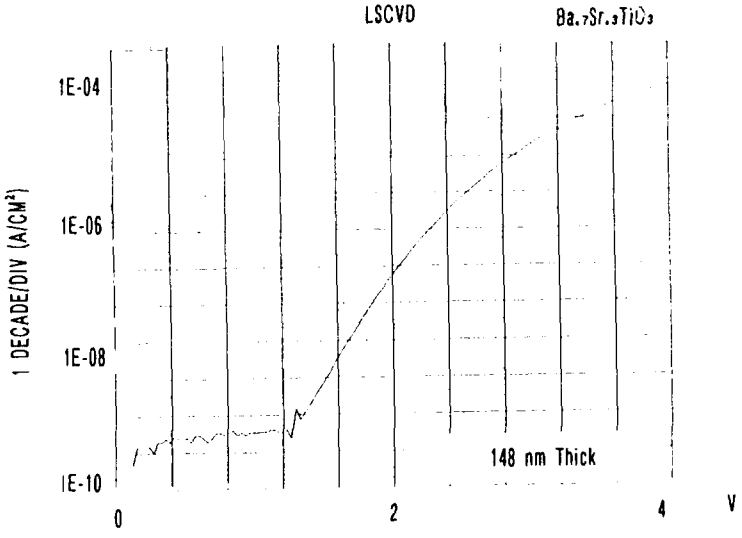


12.) d.c. leakage current in liquid-source CVD strontium titanate film 122 nm thick. At the 3V GaAs operating voltage the current is ca. 2 $\mu A/cm^2$ [by doping barium strontium titanate we achieve 1 $nA/cm^2$]. Note that the general I(V) shape is Schottky-like.

13.) Step-coverage of liquid-source CVD barium strontium titanate ($Ba_{0.80}Sr_{0.20}TiO_3$) over a 0.22 μm Pt line.

DRAMs

The use of our barium strontium titanate has been made already in DRAMs. This structure has stacking but no trenching. It consists of three intermediate sub-devices, referred to as "cylindrical", "fin", and "crown". This was originally a $Ta_2O_5$ device with W metallization, modified to substitute barium strontium titanate and platinum. Details of this device are available in Matsushita Electronics Corp. publications.

NEW FATIGUE-FREE MATERIAL

It is possible to make PZT and other ferroelectrics by doping such that they exhibit no change in switched charge over many ($10^{11}$) cycles, as shown in Fig. 14. However, as Fig. 15 makes clear, there is actually substantial degradation over that number of cycles: The hysteresis curve becomes less square; the coercive field changes; the loops no longer saturate, etc. This makes it difficult for the sense amplifiers in a RAM to read the sense of the stored charge in the ferroelectric cell.[12] By comparison, the new material we have discovered exhibits no change in either switched charge or hysteresis shape after100 billion cycles (Fig. 16).

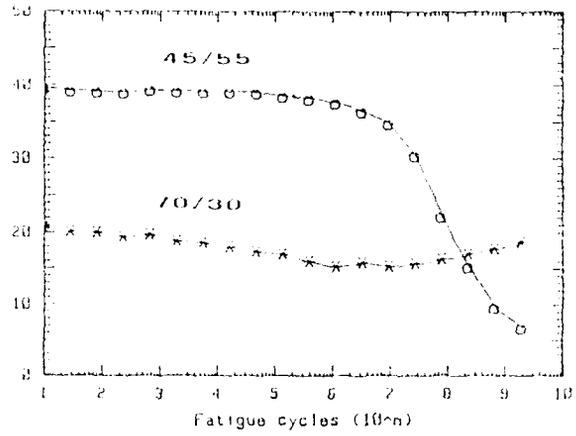


14.) Switched charge versus number of polarization-reversing cycles in PZT (70% Zr), giving the illusion of no fatigue.

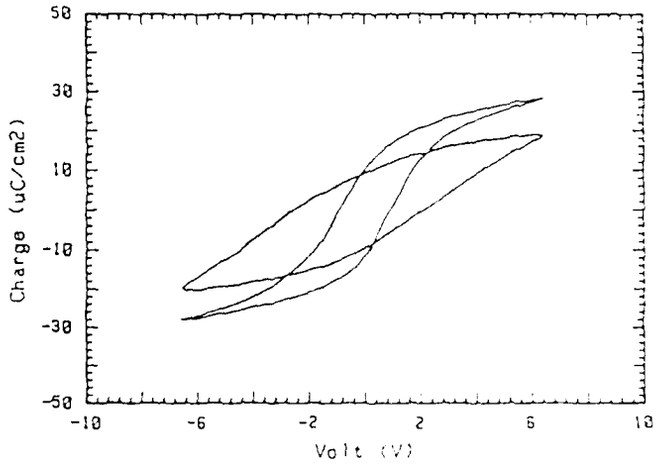


15.) Hysteresis curves for the PZT (70% Zr) specimen in Fig.14, showing that the capacitor actually degrades substantially -- the loop becomes unsaturated; the coercive field changes; and the sense amplifiers find it more difficult to discriminate between stored "1" and stored "0".

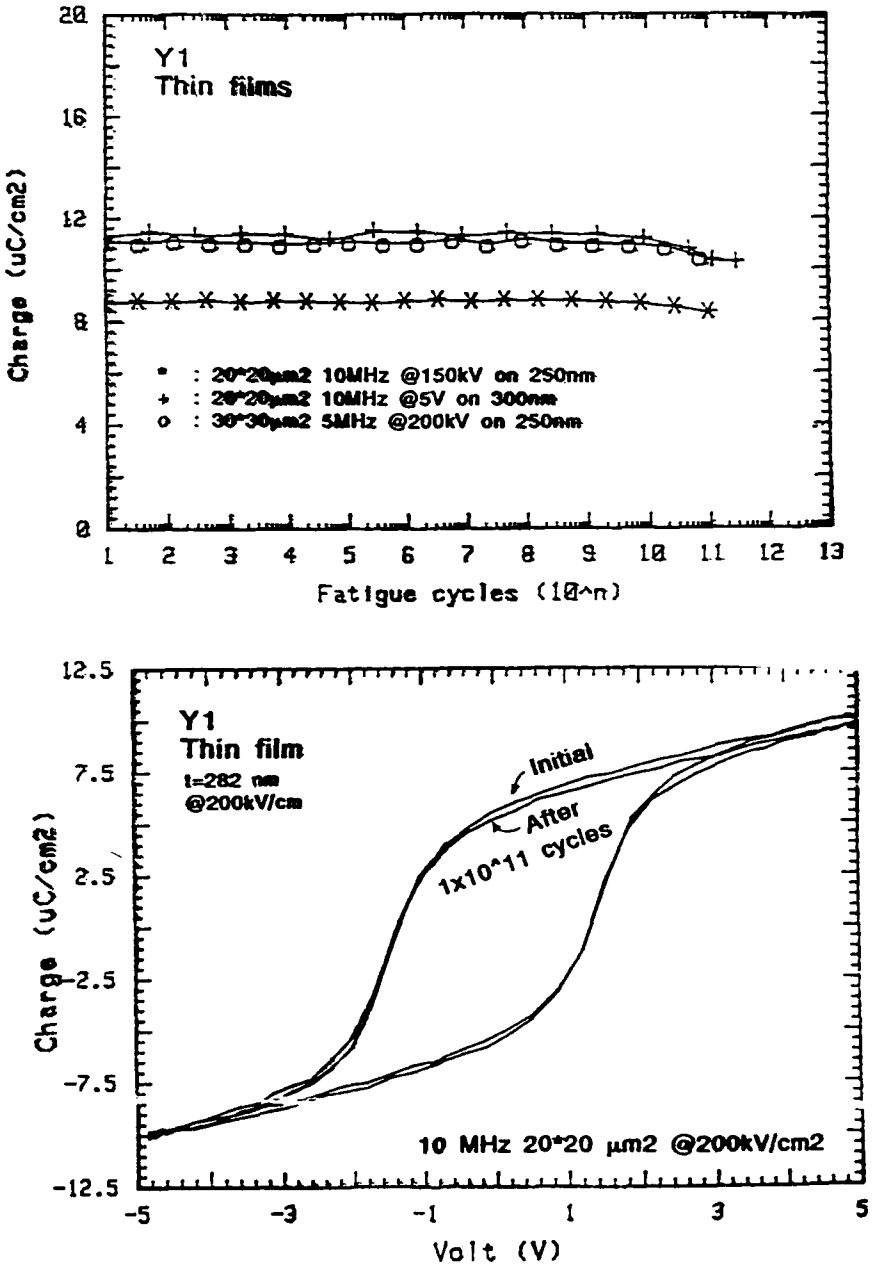


16.) Switched charge (a) and hysteresis curves (b) for the proprietary new material "Y1" showing no fatigue up to 5 x $10^{11}$ switching cycles.

This material has already been put into the 1 kb Symetrix/Olympus RAM shown in Figs.6-8 as a replacement for PZT. It appears compatible with standard CMOS processing.

## SUMMARY

We have summarized briefly four integrated ferroelectrics projects carried out in our laboratories at Symetrix Corp. and the University of Colorado. These have resulted in the first ferroelectric-GaAs MMIC, in a 1 kb RAM with fatigue-free material, in 0.2 micron step coverage with a liquid-source CVD deposition of barium strontium titanate suitable for immediate DRAM applications, and with a new fatigue-free material for ferroelectric RAMs with DRO (destructive read-out).

## ACKNOWLEDGMENTS

The work summarized here was supported by Matsushita Electronics Corp., Olympus Optical Co., and grants or contracts from the NSF (DMR89-18900), ARO (DAAL-0390-G0002), DARPA, and DNA. Our collaborators included M. C. Scott, B. M. Melnick, J. D. Cuchiaro, and T. Roberts at Symetrix, A. Noma, H. Ishida, T. Tanaka at Matsushita Electronics Corp. (MEC), and others at Olympus Optical Co.

## REFERENCES

1.) J. T. Evans and R. Womack, IEEE J. Sol. St. Circ. 23, 1171 (1988).
2.) D. Bondurant and F. Gnadinger, IEEE Spectrum 30, 1 (1989).
3.) J. F. Scott and C. A. Paz de Araujo, Science 146, 1400 (1989).
4.) K. Takenaka, M. Shimada, K. Kato, Y. Haga, T. Stodart, W. Larson, B. Meadows, P. McClure, S. Traynor, and B. Mueller Proc. ISIF '92 (Monterey, CA, 11 March 1992; Ferroelectrics, in press).
5.) Toshiyuki Ueda, M. Azuma, Tetsuzo Ueda, A. Noma, H. Ishida, T. Tanaka, D. Ueda, M. Kazumura, G. Kano, and C. A. Paz de Araujo, Ibid.

6.) K. Takemura, S. Matsubara, T. Sakuma, S. Yamamichi, and Y. Miyasaka et al., Ibid.; T. Sakuma et al., Appl. Phys. Lett. 57, 2431 (1990).
7.) W. Geidemann, Int. Meeting Ferroelectrics, Sept. 1989, Saarbrucken; Proc. ISIF '91 (Colorado Springs, CO, April 1991; Ferroelectrics, in press).
8.) S. E. Bernacki et al., Ibid.
9.) D. R. Lampe, D. A. Adams, S. Sinharoy, and H. Buhay, Ref. 4; S. Sinharoy, H. Buhay, D. R. Lampe, and M. H. Francombe, Ref. 4.
10.) D. A. Tossell, A. Patel, N. M. Shorrocks, and R. W. Whatmore, Ref. 4.
11.) M. Okuyama, Y. Togami, Y. Hamakawa, M. Kimata, and M. Denda Ref. 4.
12.) J. M. McGarrity, J. M. Benedetto, and R. A. Moore, Ref. 4.

*Ferroelectrics*, 1992, Vol. 133, pp. 61–72
Reprints available directly from the publisher
Photocopying permitted by license only

© 1992 Gordon and Breach Science Publishers S.A.
Printed in the United States of America



# Td118

## *PROCESS INTEGRATION OF THE FERROELECTRIC MEMORY FETs (FEMFETs) FOR NDRO FERRAM* *

D.R.Lampe°, D.A.Adams°, M.Austin°, M.Polinsky°, J.Dzimianski°, S.Sinharoy[‡], H.Buhay[‡], P.Brabant°, Y.M.Liu°
Westinghouse Electric Corporation
° Advanced Technology Division, Baltimore, Md.
[‡] Science & Technology Center, Pittsburgh, Pa.

**Abstract** Experimental results derived from early lots made with modified EEPROM masks are described. MIS structures formed with ferroelectric (FE) films grown on lightly doped silicon substrates have yielded FE switching properties demonstrated by hysteresis in capacitance vs voltage (CV) characteristics as the first step required to show suitability for use in high performance FEMFETs. In particular, switching attributable to polarization charge reversal inside the FE layer is observed, as opposed to tunnel injection of carriers from the silicon into the gate dielectric. Barium magnesium fluoride (BMF) and bismuth titanate FE films are currently under evaluation. Recent FEMFETs have achieved a 9.5V memory window using 20V programming, with $I_{on}/I_{off} \geq 10^5$ for W/L = 12μm/3μm, ***after complete fabrication ~ including Scratch-Protection.*** Some data loss is apparently associated with the BMF films having their primary $\underline{P}_r$ vector nearly in the plane of the film and only a small component of $\underline{P}_r$ experiencing reversal during memory hysteresis programming, as well as the reversable polarization lacking a definite coercive field.

## INTRODUCTION

Most programs aimed at incorporating FE films into VLSIC nonvolatile memories make use of the destructive readout (DRO) configuration closely resembling DRAM operation. The goal of the effort described herein is a nondestructive readout (NDRO) ferroelectric random access memory (FERRAM) closely resembling SONOS (Semiconductor-Oxide-Nitride-Oxide-Semiconductor) or other EEPROMs. This resemblance to SONOS EEPROMs results in significant benefits. Most of the design and performance features in existing high-speed EEPROM or flash EPROM can be carried almost directly into the high-speed NDRO FERRAM.

## DEVELOPMENTAL APPROACH

The approach used to develop this technology is typical of many evolutionary very large scale integrated circuit (VLSIC) inventions, relying on synergism between previous projects and the

* This work partially sponsored by contract #N00014-90-C-0159 via USN/ONR, Dr. Wallace Smith (COTR), from Dr. Jane Alexander (DARPA,MTO).

desired new devices. Prior experience with the earliest bismuth titanium oxide (BTO) FEMFETs[1], continuing with numerous MNOS/SONOS EEPROM programs, provided abundant background for such innovation. Routine SONOS EEPROM process monitors are ideal vehicles for economical FEMFET memory gate-stack investigations. Short-loop experiments use gridded-wafers to make CV dots that are virtually identical to the FEMFET memory gate-stack, as illustrated in Figure 1. Fabrication process parameters, including various layer thicknesses and materials, can easily be changed. The gridded-wafer memory stack CV dots can also demonstrate threshold hysteresis, endurance, and polarization switching speed.

The integration compatibility, accelerated lifetime (ICAL) test vehicle involves the complete fabrication process. It includes numerous variations of FEMFETs and capacitor

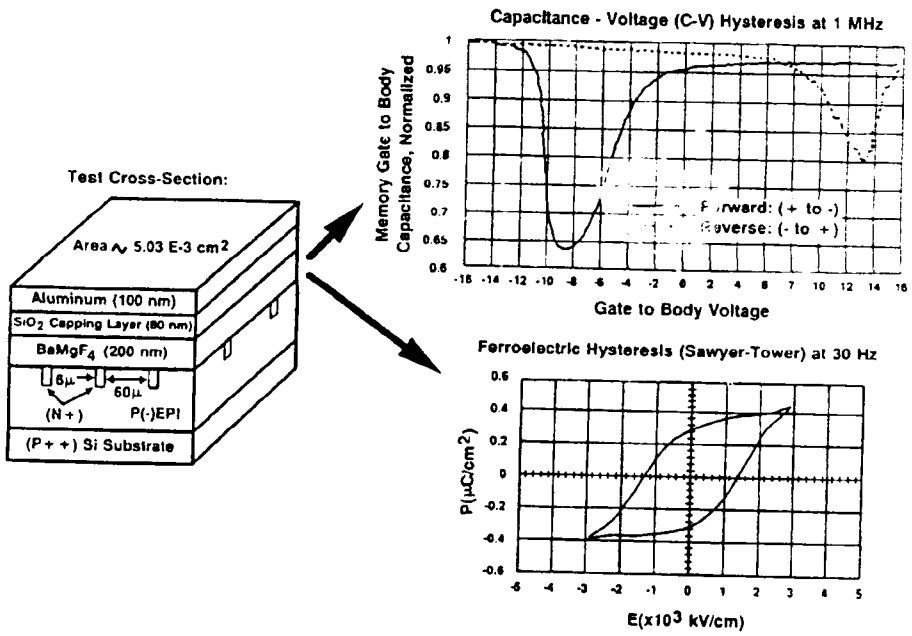


**FIGURE 1** Gridded-wafer, Capacitance-Voltage (CV) Dot Short Loop Experiments.

structures, as well as an 8K, fully-decoded, demonstration NDRO FERRAM. After a particular memory gate-stack has been partially optimized using short-loop, gridded-wafer CV dots, further development continues via the ICAL test vehicle. The ICAL test vehicle incorporates the complete double metal interconnect structure overlaying the FE to insure the associated processing and stresses are accurately emulated.

## FABRICATION PROCESS SEQUENCE

The steps required to make the FEMFETs are best described as a Fabrication Process Module that is added to the Westinghouse CMOS baseline process. The FEMFET fabrication module is summarized in Table 1. All the regular CMOS circuits, excluding the nonvolatile elements that exhibit hysteresis, are made as per the usual fabrication process. The baseline CMOS processing continues through the deposition of the normal dielectric sandwich used between the polysilicon gates and the first metal layer.

Table 1 FEMFET Fabrication Process Module

| Step | Fabrication Operation |
|---|---|
| 1 | Baseline CMOS VLSIC Process, Up To Metal-1 Contact Definition. |
| 2 | Open Contacts & FEMFET Sites. |
| 3 | Deposit FE Gate Dielectric Sandwich/Stack. |
| 4 | Pattern FE Dielectric Sandwich (FE Removal). |
| 5 | Deposit VLSIC Metal-1. |
| 6 | Pattern Memory Gate/VLSIC Metal-1. |
| 7 | Sinter/Anneal Memory Gate/VLSIC Metal-1. |
| 7T | Test & Evaluate FEMFETs & Key Circuitry. |
| 8 | Resume Baseline CMOS VLSIC Fabrication. |

In step 2, the contact windows and the sites for the FEMFETs are opened through the borophosphosilicate glass (BPSG) down to the underlying nitride layer. Then the BPSG is reflowed to give the smoothly tapered edge, shown in Figure 2, greatly facilitating subsequent

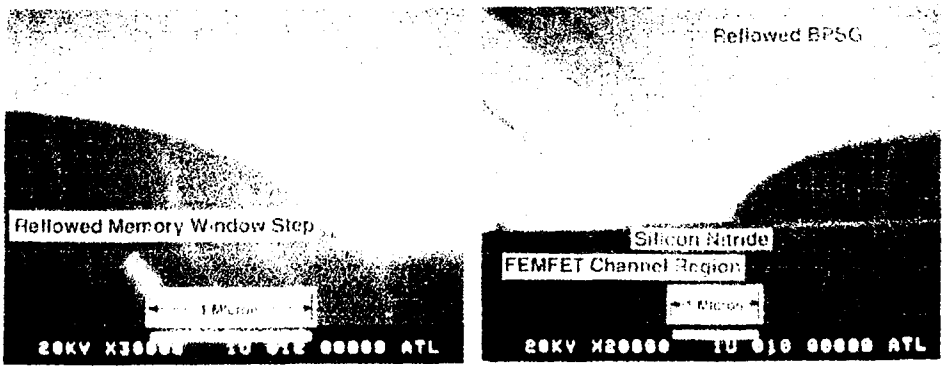


**FIGURE 2** Edges of FEMFET Site: Smooth Reflowed BPSG for Improved Metal Step Coverage.

metal step coverage. Next the contact windov only are opened and silicide deposited therein. To finish step 2, the remaining thin layers of nitride and $SiO_2$ are removed from the FEMFET sites in preparation for deposition of the FE memory gate dielectric stack. Step 3 starts with the growth of a high quality thermal gate oxide ($SiO_2$). This $SiO_2$ layer functions as a barrier

to charge injection, i.e. charge tunnelling and trapping. Next the FE itself is deposited[2,3]. The end of step 3 is the deposition of 50nm of LTO (LPCVD $SiO_2$). This capping layer serves multiple purposes: First is the mutual protection of the FE and the fabrication apparatus, each one from the other. Second is the known common surface for photoresist and the help in masking for the FE removal step (#4). Third is the known common interface onto which to deposit the conductive memory gate material. Step 4 is to remove the FE sandwich from all the areas where contact must be made to the sources, drains, and poly gates. The capping layer is etched with a dry plasma, followed by a wet etch for the FE material itself. The results are shown in Figure 3, for a BTO gate-stack. The usual premetal dip/clean is performed

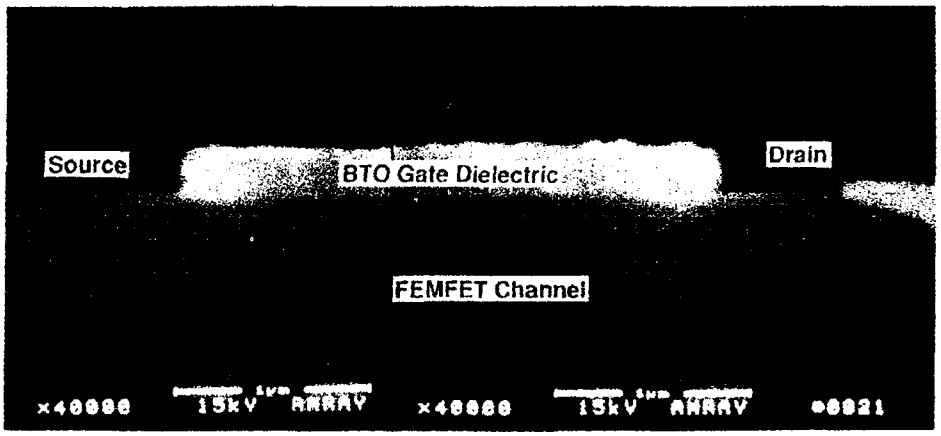


**FIGURE 3** SEM of The Bismuth Titanate FEMFET Gate Before Metal.

immediately before the VLSIC Metal-1 conductive memory gate is deposited (step 5). Figure 4 shows the result of dry plasma etching the memory gate (step 6) for a BMF FEMFET. Notice that this FEMFET has the gate-stack completely enclosed on top and sides with first metal. Although test FETs can be measured at this point, better characteristics are usually recorded after the sinter and anneal operation of step 7. Finally, the remainder of the Baseline CMOS Process for double metal is executed (step 8): intermetal dielectric, vias, second metal, scratch-protect dielectric, bonding pad openings.

## RECENT RESULTS: Gridded Wafer, CV Dots

Figures 5 & 6 are FEMFET CV-dot hysteresis curves from gridded wafers illustrating significant developmental progress toward actual FEMFETs. The memory stack giving the results of Figure 5 is BMF deposited at 200°C, annealed in forming gas at 480°C for 1hr., with capping of 49nm LTO and 1$\mu$m thick aluminum dots. Notice that 10V programming gives an 11.1V hysteresis window. Likewise for BTO, Figure 6 shows a 6.6V FEMFET CV-dot

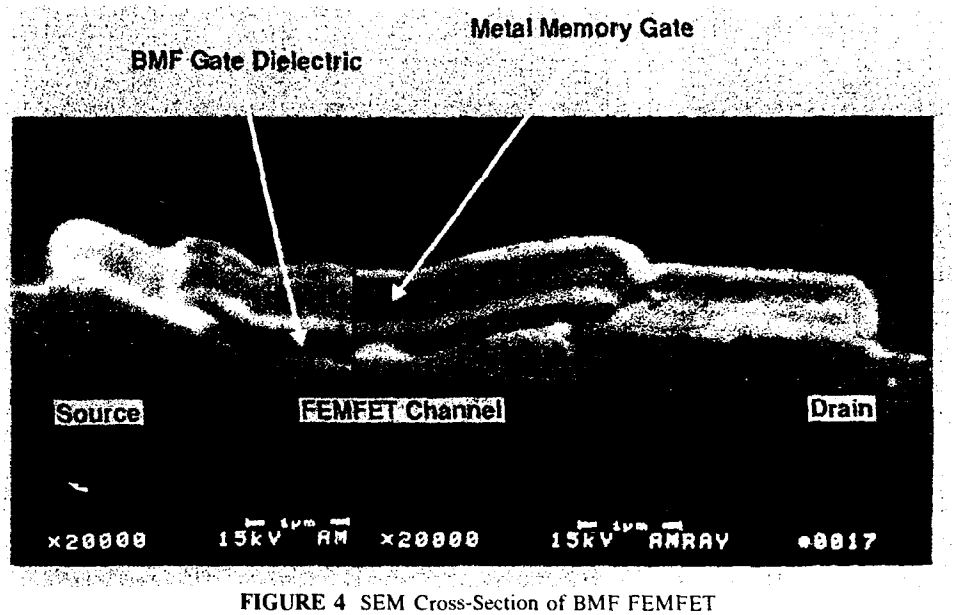


**FIGURE 4** SEM Cross-Section of BMF FEMFET

hysteresis window from 10V programming, for a pulsed laser deposition (PLD) BTO film grown on 10nm $SiO_2$ buffer barrier with 50nm LTO capping. Results like these indicated

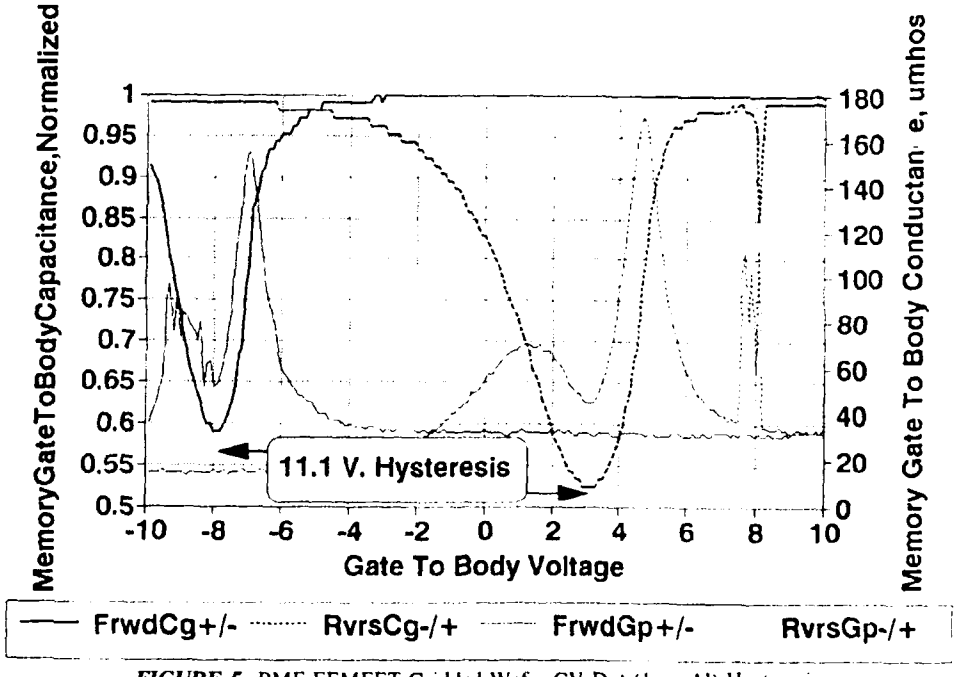


**FIGURE 5** BMF FEMFET Gridded-Wafer CV Dot (1$\mu$m Al) Hysteresis
Sample: BMF122 (920130)

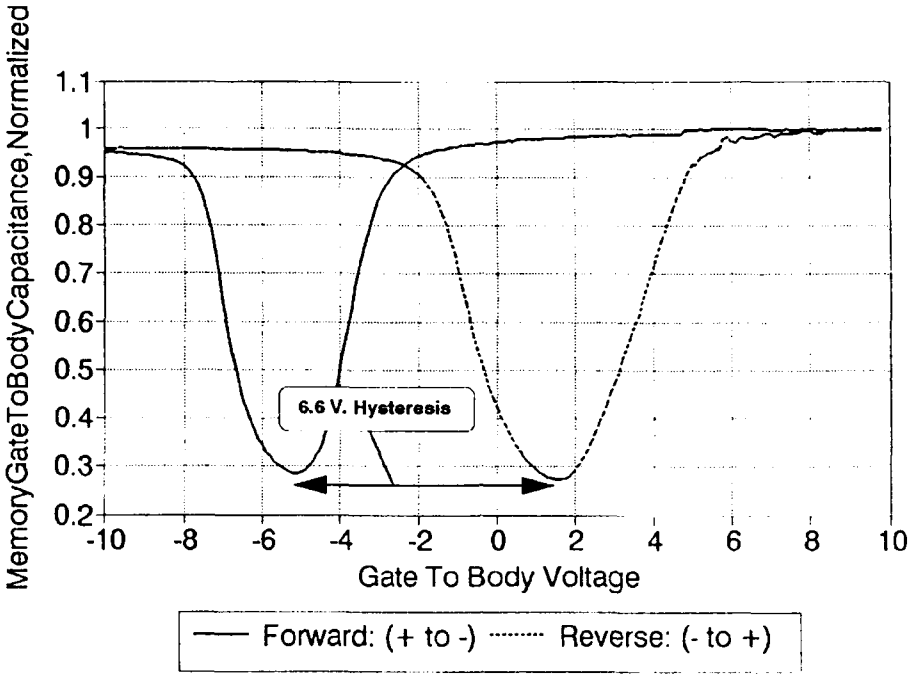


**FIGURE 6** BTO FEMFET CV Dot (0.1$\mu$m Al) Hysteresis
Sample: FN07 BTO-4-2 (920219)

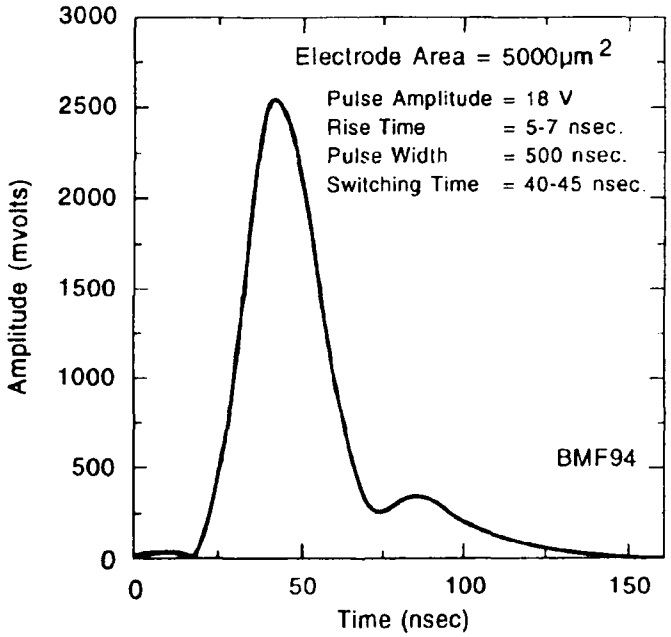


**FIGURE 7** BMF Memory Stack Ferroelectric Polarization Reversal.

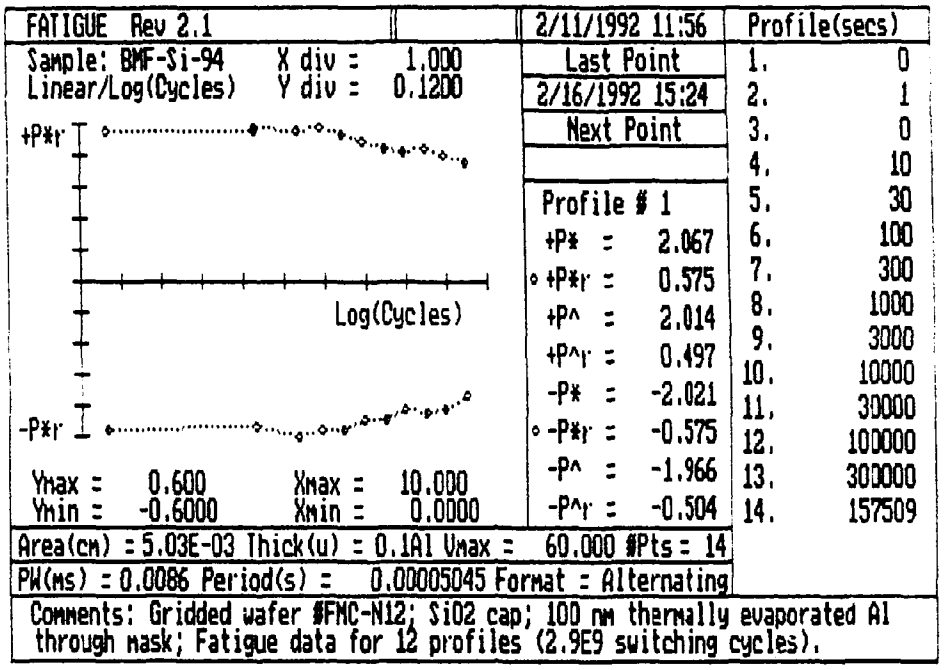


**FIGURE 8** Gridded-Wafer BMF FEMFET CV Dot Endurance
Sample BMF 94; RT-66A Measured at $V_{max}$ = 60 V

readiness to incorporate these memory stacks into actual ICAL transistor wafers. Further evidence supporting incorporation of the BMF memory stack into ICAL transistor wafers was a measurement of a ferroelectric polarization reversal time of less than 50ns[2] (Figure 7) recorded at various spots around the wafer. Endurance or fatigue measurements using the RT-66A tester[2] showed only a 22% reduction in $P^*$, after 2.9 x $10^9$ switching cycles at 60V, as in Figure 8 (limited by continuous test-equipment use-time).

**FEMFET (NDRO FERRAM) Wafers** The BMF memory stack like that of Figure 5 having BMF deposited at 200°C, annealed in forming gas at 480°C for 1hr., with capping of 49nm LTO, was incorporated into the fabrication process of Table 1. Figure 9 shows electrical results for individual transistors on wafer #6083-7806-1. For each FEMFET $I_{ds}$-$V_{gs}$ hysteresis curve, the source and body were grounded and the drain was held constant as indicated, while the gate was cycled through the programming voltage range. Figure 9 shows the same FEMFET (#7/5) after sintering but in response to both 15V and 20V programming. In each case, the apparent threshold hysteresis window at 10nA is a significant fraction of the programming voltage.

Figure 10-a shows a nearby FEMFET (#7/9) immediately after sintering the metal memory gate, and Figure 10-b after the full fabrication including scratch-protection. Notice that the

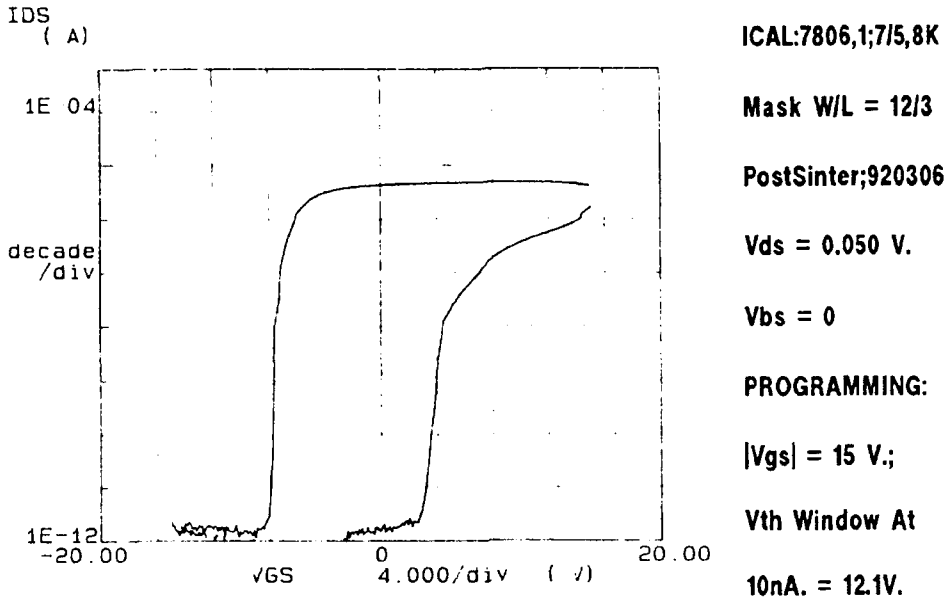


**FIGURE 9-a** ±15 V Programming of the BMF FEMFET Sample: 6083-7806-1 (7/5,8K)

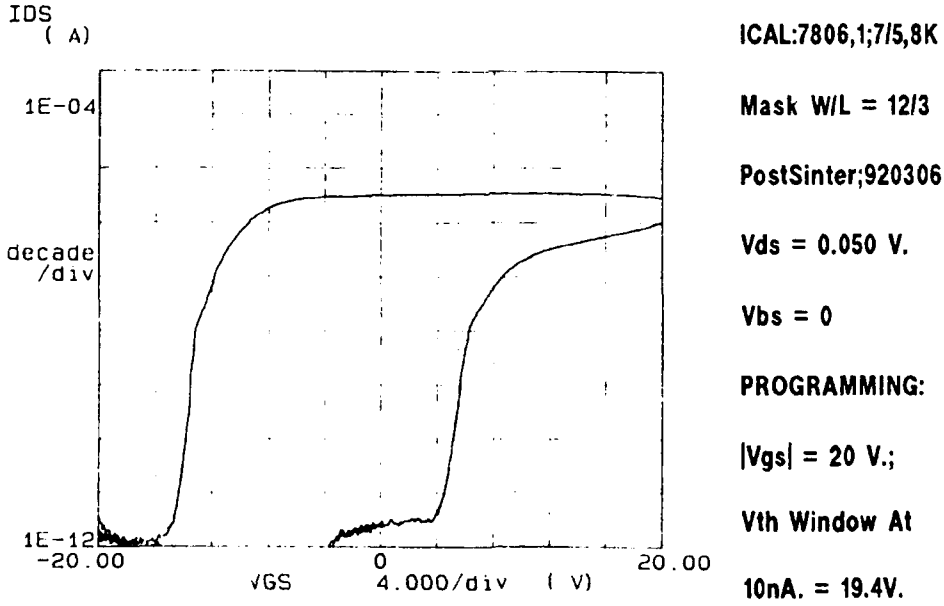


**FIGURE 9-b** ±20 V Programming.
BMF FEMFET $I_{ds}$-$V_{gs}$ Hysteresis
Sample: 6083-7806-1 (7/5,8K)

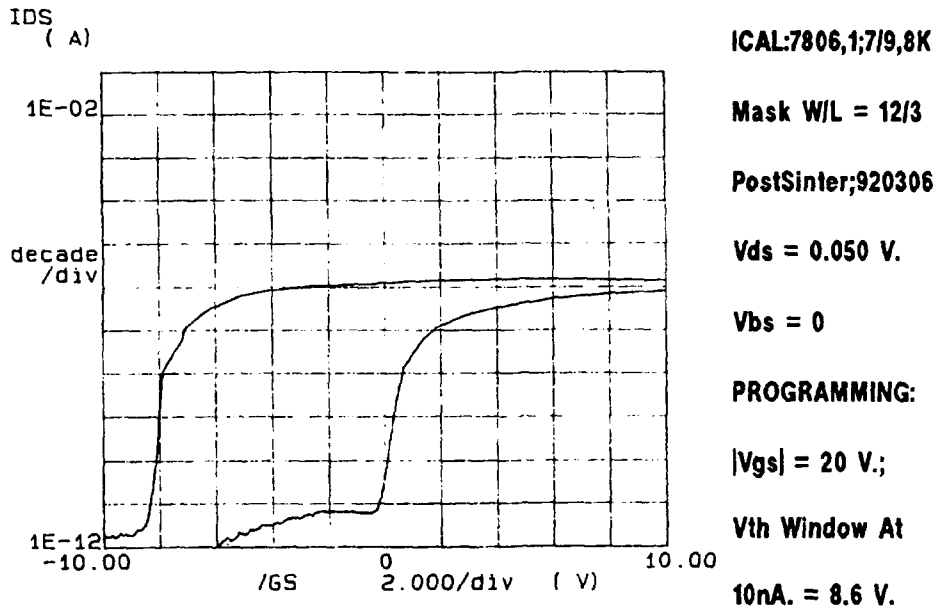


**FIGURE 10-a** After Sintering First Metal Memory Gate.
BMF FEMFET Sample: 6083-7806-1 (7/9,8K)

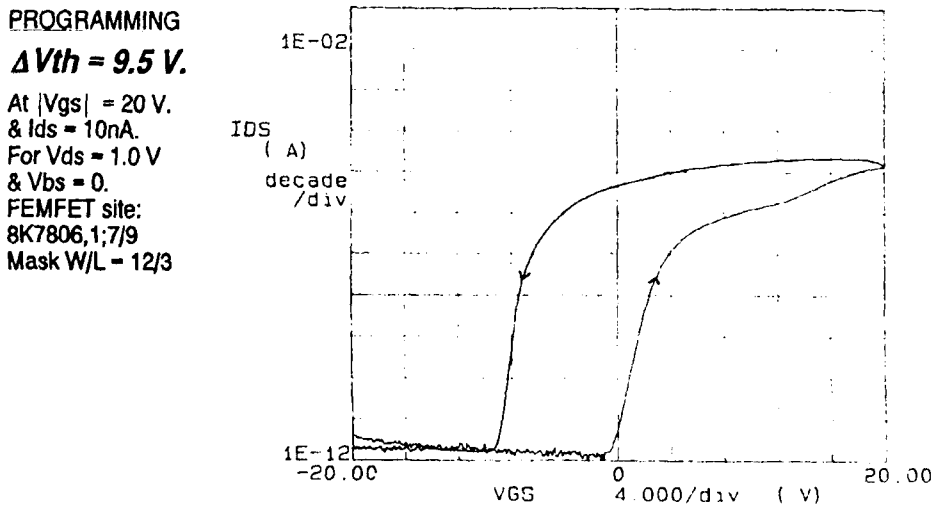


**FIGURE 10-b** After *FULL Scratch-Protect Fabrication.*
$I_{ds}$-$V_{gs}$ Hysteresis BMF Sample: 6083-7806-1 (7/9,8K)

memory threshold hysteresis measured at 10nA actually increased slightly from 8.6V to 9.5V, while the ratio $I_{on}/I_{off}$ also seemed to increase somewhat.

One of the basic attributes of any nonvolatile memory is the retention of the programmed data for some acceptably long period of time, such as years. Thus one of the first measurements on the early BMF FEMFETs was ***memory retention***. FEMFET retention is best measured in a manner emulating the way the FEMFET is incorporated into the "READ" circuitry of the memory. Modern EEPROMs typically connect the gate, the source, and the body in common and use the drain current as the input to the high-speed sense amplifier. This configuration generally gives a temporary voltage from gate to drain that is a sizable fraction of the power supply. In some memory devices, such a temporal bias may cause a "read disturb" effect. An alternate but somewhat slower scheme uses the "source follower" approach, wherein a very large source resistor and a small transistor current effectively give a transistor memory threshold voltage readout to the sense amplifier. The low-current source-follower approach more nearly approximates the flat-band situation, with a very low electric field at the critical silicon/dielectric interface. Consequently this pseudo-flat-band condition should greatly reduce any possible "read disturb" effects. BMF FEMFET retention measurements of both types were made for purposes of comparison, with no significant difference between the results.

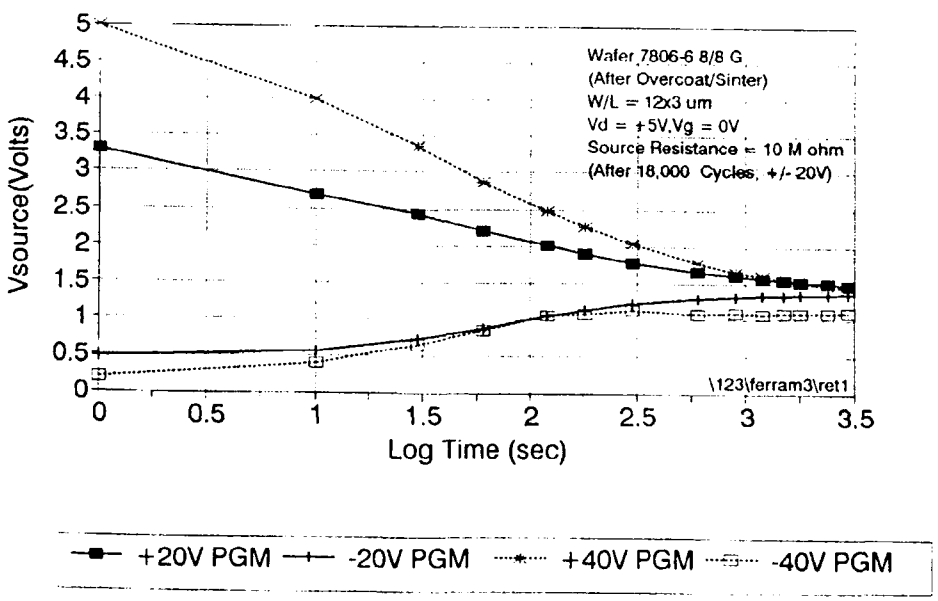


**FIGURE 11** Initial source-follower BMF FEMFET retention.

The BMF film[4] has its spontaneous polarization vector, $\underline{P}$, within 30° of the plane of the film. Thus, not the primary $\underline{P}$ vector itself, but only a small component of $\underline{P}$ experiences

reversal during memory hysteresis programming, and without a well defined coercive field. Figure 11 shows retention results measured with the source-follower scheme, where the effective BMF FEMFET threshold voltage is plotted as a function of time. Notice the memory window starts around 2.7 V, dropping to about 0.25 V at 1,000 sec., for an average drift rate of 0.82V/decade of time. Retention measurements by means of the drain current gave similar loss of data for these early BMF FEMFETs after full fabrication, including scratch-protection. To investigate whether the additional overlying layers impacted that behavior, measurements were also made on both BMF FEMFETs and CV dots immediately after first metal memory gate sinter, again giving similar data loss or threshold drift. ***Notice again that this data loss is apparently associated with the BMF films having their primary P vector nearly in the plane of the film and only a small component of P experiencing reversal during memory hysteresis programming, as well as the reversable polarization lacking a definite coercive field.***

## SUMMARY

Using CV dots on gridded wafers, BMF FEMFET gate-stacks have exhibited endurance of at least 2.9 x $10^9$ cycles, a ferroelectric polarization reversal time not exceeding 50ns, and an 11V threshold hysteresis window at 10V programming. Early BTO CV-dot gate-stacks show 6.6V threshold hysteresis windows at 10V programming. Integration of the FEMFET gate-stack into CMOS VLSICs has included very smooth slopes at the openings for the FEMFETs, dry/wet pattern etch techniques for the FE sandwiches, and use of the standard VLSIC metal-1 for the FEMFET conductive gate material. ***After complete fabrication ~ including Scratch-Protection,*** the resultant BMF FEMFETs have shown hysteresis windows as large as 9.5 V at 10nA for 20 V programming with $I_{on}/I_{off}$ ratios exceeding $10^5$. While these initial BMF FEMFETs displayed good hysteresis windows, their limited data retention constrained their application to strategic circumvention situations or power outages of modest duration. The retention of only hours is assumed to be associated with ***the BMF films having their primary P vector nearly in the plane of the film and only a small component of P experiencing reversal during memory hysteresis programming, as well as the reversable polarization lacking a definite coercive field.*** Experiments are underway to better orient the primary P vector of the BMF films. Gate-stack CV-dot threshold drift as a function of time is the preferred method to rapidly survey additional FE films, prior to incorporation into FEMFETs for programming and retention measurements. Various other ferroelectric films having their primary P vector nearly perpendicular to the plane of the film are actively under investigation as candidates for this application.

**ACKNOWLEDGEMENTS**

The authors wish to thank Prof. S. B. Krupanidhi and his graduate students at Penn State University for the switching speed measurements.

**REFERENCES**

1. S. Y. Wu,"A New Ferroelectric Memory Device: Metal-Ferroelectric-Semiconductor Transistor," IEEE Trans. Electron Devices, Vol. ED-21, p.499 (1974). Also: S. Y. Wu, "Memory Retention and Switching Behavior of Metal-Ferroelectric-Semiconductor Transistors," Ferroelectrics Vol. 11, p.379 (1976).

2. S. Sinharoy, H. Buhay, D. R. Lampe, M. H. Francombe, "$BaMgF_4$ Thin Film Development and Processing for Ferroelectric FETs," Proceedings of the Fourth International Symposium on Integrated Ferroelectrics, March 1992, Monterey, Calif., (to be published).

3. H. Buhay, S. Sinharoy, D. R. Lampe, D. A. Adams, M. H. Francombe, "Large-Area Pulsed Laser Deposition (PLD) & Integration of Ferroelectric Bismuth Titanate Thin Films for FEMFET Applications," Fourth International Symposium on Integrated Ferroelectrics, March 1992, Monterey, Calif.

4. M. H. Francombe, S. Sinharoy, H. Buhay, "Influence of Orientation Effects on Polarization Switching in Bismuth Titanate and Barium Magnesium Fluoride Films," Fourth International Symposium on Integrated Ferroelectrics, March 1992, Monterey, Calif.

*Ferroelectrics*, 1992, Vol. 133, pp. 73–78
Reprints available directly from the publisher
Photocopying permitted by license only

© 1992 Gordon and Breach Science Publishers S.A.
Printed in the United States of America

# TdI9

# THIN FILMS FOR FERROELECTRIC DEVICES

RAINER BRUCHHAUS
SIEMENS AG, Corporate Research and Development, Dept. ZFE BT MR 21,
Otto-Hahn-Ring 6, W-8000 München 83, Germany

Abstract The article reviews the materials and deposition methods for ferroelectric thin films. The electrical results of PZT films deposited with six different deposition methods combined with two different routes to process the films are compared. Planar multi target sputtering of PZT and lead titanate is discussed in more detail.

## INTRODUCTION

Ferroelectric materials provide a unique blend of electrical and electro-optic properties. However, the bulk form is not suitable for integration on substrates used in the microelectronic industry such as Si and GaAs. The use of thin films with thicknesses in the submicrometer range permits this integration and the operation at low voltages of 2.5 to 5 V.

Numerous devices based on ferroelectric thin films have been proposed and made at least in prototype form. They include nonvolatile ferroelectric RAMs in which the switchable remanent polarization in conjunction with select transistors is used for non volatile data storage[1], ferroelectric FETs in which the ferroelectric film is deposited in the gate region of a field effect transistor (FET)[2], integrated pyroelectric detector arrays[3], microsensors and microactuators[4] and optical modulators[5]. The high permittivity of the ferroelectric thin film materials make them potential candidates as capacitor dielectric in future generations of very high density DRAMs (dynamic random access memories).

## MATERIALS

Lead zirconate titanate (PZT) is the material currently used for the ferroelectric RAM. It offers high remanent polarization, sufficiently low coercive field strength to switch the ferroelectric with 5 V and very small intrinsic switching time below 1 ns[6]. However, for optimized ferroelectric RAMs there are a number of issues to be solved. The processing temperatures for PZT of 550°C and above make this material difficult to integrate with the underlying Si and GaAs integrated circuit and the metallic interconnects. PZT exhibits degradation effects, so called "fatigue", after continuous swit-

ching of the ferroelectric capacitor. Since in ferroelectric RAMs every read operation is destructive and must be followed by a write operation, the ferroelectric memory devices should withstand at least $10^{12}$ (better $10^{15}$) read/write operations to guarantee a life time of 10 years.

$BaMgF_4$ and $Bi_4Ti_3O_{12}$ are the two ferroelectric materials under development for a ferroelectric FET at Westinghouse. In this device the ferroelectric film is deposited in the gate region of a field effect transistor. The polarization state of the ferroelectric modifies the magnitude of the source to drain current. The ferroelectric FET permits nondestructive readout by sensing the source-to-drain-current without the reversal of the polarization state.

For room temperature pyroelectric detector arrays pure or lanthanum doped lead titanate (PT) are attractive materials. They offer a large pyroelectric coefficient p, small dielectric constant $\varepsilon$, and small temperature coefficient of p. Especially c-axis oriented PT gives a large figure of merit $F_V = p/c_V\varepsilon$ ($c_V$ = volume specific heat) for voltage responsivity. Oriented PT films in combination with surface micromachined polysilicon membranes as a mechanical support structure with low thermal mass and conductivity resulted in integrated pyroelectric detectors with good electrical properties.

For micropressure sensors, microactuators and micromotors again PZT is an interesting material because of its large piezoelectric coupling factor.

## DEPOSITION METHODS

Application of thin films in integrated ferroelectric devices put very high demands on the quality of the films. The deposition methods should in principle be able to produce thin, dense, homogenous and crystalline films of a given composition in the submicrometer range and over large areas. The deposition technique must be compatible with the semiconductor technology used for the production of integrated circuits.

Methods so far used to deposit high quality ferroelectric films on large area substrates are the sol-gel spin-on method, sputtering, OM CVD, and, for $BaMgF_4$, evaporation in an UHV deposition system. Also pulsed laser deposition of thin ferroelectric films, such as $Bi_3Ti_4O_{12}$[7], $BaTiO_3$[8], and also PZT[9] has produced films of good quality. However, PLD is mainly used for film deposition on substrates with smaller area.

There are in principle two routes to process the ferroelectric films. In the so called "one step" process the substrate is heated to elevated temperatures and a well crystallized (and on suitable substrates oriented or even epitaxial films) can be grown ("in-situ" growth). The processing temperatures are usually lower with the one step process compared to the "two step" process. In this processing route in the first step an amorphous or partly crystalline film is deposited at room temperature or slightly ele-

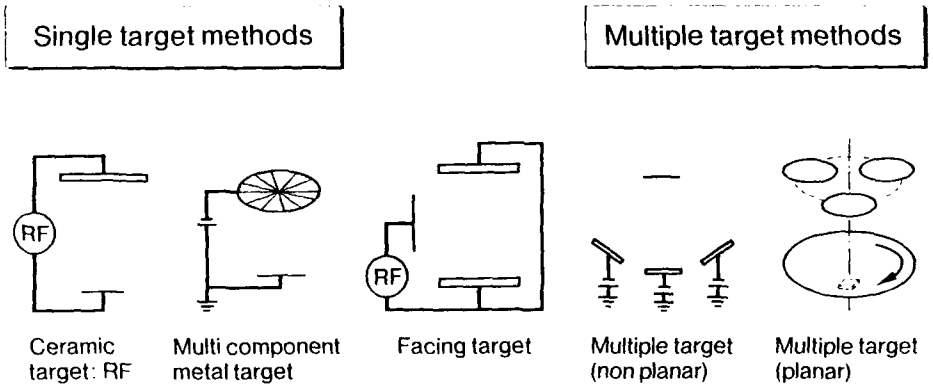


FIGURE 1 Plasma sputtering geometries and targets for PZT deposition

vated temperature. The second step is a postdeposition annealing to crystallize the ferroelectric phase within a conventional furnace or via rapid thermal processing (RTP). Very recently Kumar et al.[10] have described the crystallization of sputtered PZT films by RTP. It has been shown that RTP yields improved ferroelectric properties compared to films annealed in conventional furnaces.

Sputtering is a deposition method compatible with standard IC-technology. In most of the earlier work on sputtering of PZT films ceramic targets have been used for rf sputtering. The experience with these targets indicated several disadvantages. Using elevated substrate temperatures the films usually are deficient in lead. This problem was solved in part by adding excess of lead oxide to the target. However, it is difficult and expensive to press large diameter ceramic disks, ceramic targets tend to crack due to localized heating and exhibit stoichiometric variations on the target surface after repeated use[11]. On the other hand reactive sputtering of metal targets offers a number of advantages, such as possibility to use higher input powers and fabricating targets with high purity and very large areas and maintaining the composition constant throughout the target lifetime.

Different kinds of sputtering geometry have been used to deposit PZT thin films[12-15], Figure 1. One can divide into single target and multiple target methods. With the multi target methods the stoichiometry can be varied by changing the power on the different targets whereas in the single target methods for every different stoichiometric composition a new target has to be manufactored. As the electrical properties of PZT films vary with the Zr/Ti stoichiometric ratio the multi target approach is more flexible for the deposition of this materials family.

This flexibility can be demonstrated by our own results on deposition of PZT and PT thin films with the planar multi target sputtering geometry. The deposition

TABLE I Sputtering conditions for PZT and PT thin films

| | | PZT | PT |
|---|---|---|---|
| Gas ($Ar/O_2$) | | 1:1 | 1:1 |
| Pressure | | 1.4 Pa | 1.5-2.8 Pa |
| Power | Pb | 500 W | 300 W |
| | Zr | 560 W | - |
| | Ti | 830 W | 1840 W |
| Deposition rate | | 4.75 nm/min | 3 nm/min |
| Substrate temperature | | about 450°C | about 450°C |

system is described elsewhere[16]. Table 1 gives the deposition conditions both for PZT and PT films. The deposition conditions are very much the same, solely the power at the targets has to be adjusted to deposit either PZT or PT. Figure 2 shows the X-ray Röntgen diffraction spectra of the films deposited on a Si wafer with thin Pt bottom electrode. Both films are single phase perovskite. PZT exhibits a lattice constant of 409.3 +-0.2 pm. The PT film is (111) oriented.

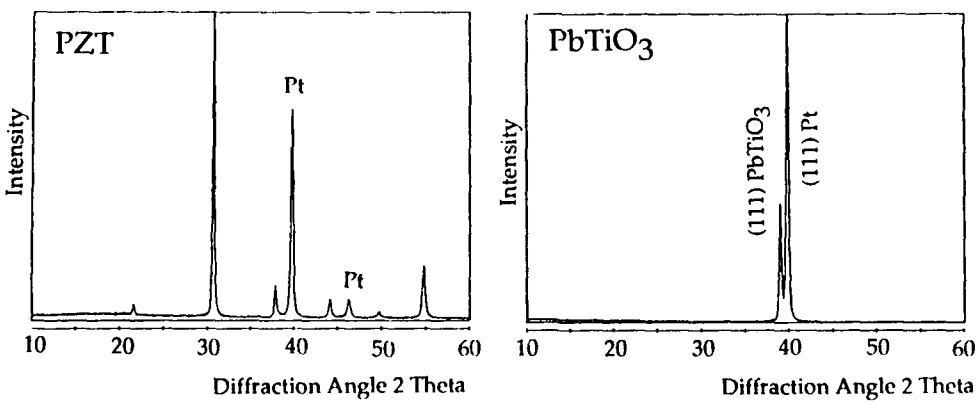


FIGURE 2 X-ray Röntgen diffraction spectra of "in-situ" deposited PZT and PT films

Table II gives an overview of the electrical properties of PZT films fabricated by different deposition methods. Compared to the early results in the 1960s and 70s, with all techniques high quality films could be obtained. The remanent polarization of the films with compositions on the rhombohedral side of the phase diagramm ranges from about 20 to 50 $\mu C/cm^2$. The large variations in the coercive field strength may be attributed to the different thicknesses of the films and different grain sizes. It has been shown that the fabrication of the bottom electrodes also strongly influences the electri-

Table II: Electrical properties of PZT thin films fabricated by different deposition methods and processing routes

| Deposition Method [Ref] | Processing Temp. [°C] | Zr/Ti ratio | Film Thickness [nm] | Remanent Polarization [μC/cm$^2$] | Coercive Field Strength [kV/cm] | Dielect. Permittivity $\varepsilon_r$ |
|---|---|---|---|---|---|---|
| OM CVD, one step, [17] | 700 | 23/77<br>57/43 | 220<br>350 | 60<br>50 | 170<br>75 | 400<br>870 |
| Single target sputter., two step, [10] | 650 | 58/42 | 350 | 24 | 32 | 950 |
| Planar Multi-Target, one step, [16] | 450 | 52/48 | 520 | 20 | 70 | 610 |
| Sol-Gel, [18] | 700 | 53/47 | 390 | 18 | 79 | 570 |
| Pulsed Laser Deposition, two step [19] | 650 | 52/48 | - | 32 | 130 | 850 |
| Multi Target Ion beam, one step [20] | 480 | 50/50 | 90 | 20 | 110 | 900 |
| Multi Ion Beam, two step [21] | 650 | 56/44 | 800 | 20 | 60 | 1150 |

cal properties of the films[18,22]. Substrate temperatures range from about 450°C for the "in-situ" deposited films with sputtering and ion-beam deposition to about 700°C for the OM CVD deposited films and the films processed via the two step route.

## SUMMARY AND CONCLUSION

The advances in the growth techniques for deposition of submicron thick films it has become possible to produce ferroelectric films of high quality. Based on these films numerous ferroelectric devices have been proposed and made at least in prototype form. They include ferroelectric RAMs, ferroelectric field effect transistors, integrated pyroelectric detector arrays, on chip capacitors, microsensors, microactuators, and optical modulators. So far, PZT seems the material of choice for the ferroelectric RAMs and the microactuators, whereas for the ferroelectric field effect transistor $BaMgF_4$ and $Bi_4Ti_3O_{12}$ are being used. For integrated pyroelectric detector arrays pure or modified lead titanate is under investigation. At least six different deposition methods combined with two possible processing routes are capable to deposit PZT thin films with

good quality. Planar multi target sputtering of PZT and lead titanate are described in more detail. Simply by changing the power at the targets this method is capable to poduce single phase thin films of these materials.

## ACKNOWLEDGEMENT

The author wish to acknowledge the help of D. Pitzer, H. Huber, and B. Pachaly for preparing the ferroelectric films and patterned test capacitors, B. Jobst for measuring the XRD patterns and W. Wersing for helpfull discussions.

## REFERENCES

1. D.W. Bondurant and F.P. Gnadinger, IEEE Spectrum 26, 30, 1989.
2. S. Sinharoy, H. Buhay, D.R. Lampe, and M.H. Francombe, to be published in J. Vac. Sci. Techn. A.
3. D.L. Polla, Chiang-ping Ye, and. T. Tamagawa, Appl. Phys. Lett., 57, 3539 (1991).
4. C.C. Hsueh, T. Tamagawa, C. Ye, A. Helgeson, and D.L.Polla, to be published in Ferroelectrics.
5. H. Adachi and K. Wasa, IEEE Trans. Ultrasonics, Ferroelectrics and Frequency Control, 38, 645 (1991).
6. P.K. Larsen, G.L.M. Kampschöer, M.J.E. Ulenaers,G.A.C.M. Spierings, and R. Cuppens, Appl. Phys. Lett., 59, 611(1991).
7. R. Ramesh, K. Luther, B. Wilkins, D.L. Hart, E. Wang,J.M. Tarascon, A. Inam, X.D. Wu, and T. Venkatesan, Appl. Phys. Lett., 57, 1505 (1990).
8. H. Buhay, S. Sinharoy, W.H. Kasner, M.H. Francombe, D. Lampe, and E. Stepke, Appl. Phys. Lett., 58, 1 (1991).
9. J.S. Horowitz, K.S. Graboswski, D.B. Chrisey, and R.E.Leuchtner, Appl. Phys. Lett., 59, 1565 (1991).
10. C.V.R. Vasant Kumar, R. Pascual, and M. Sayer, J. Appl. Phys., 71, 864 (1992).
11. K. Iijima, Y. Tomita, R.Takayama, and I. Ueda, J. Appl. Phys., 60, 361 (1986).
12. A. Okada, J. Appl. Phys., 48, 2905(1977).
13. K. Sreenivas and M.Sayer, J. Appl. Phys., 64, 1484 (1988).
14. R.A. Roy, K.F. Etzold, and J.J. Cuomo in Ferroelectric Thin Films, edited by E.R. Myers and A.I. Kingon (Mater. Res. Soc. Proc. 200, Pittsburgh, PA, 1990), pp. 77-82.
15. H. Adachi, T. Mitsuyu, T. Yamazaki, and K. Wasa, Ipn. J. Appl. Phys., 24, Suppl. 24-3,13(1985).
16. R. Bruchhaus, H. Huber, D. Pitzer, and W. Wersing, submitted to Ferroelectrics.
17. G.J.M. Dormans, M. deKeijser, and P.J. van Veldhoven,to be published in Mater. Res. Soc. Proc., 243.
18. G.A.C.M. Spierings, M.J.E. Ulenaers, G.L.M. Kampschöer, H.A.M. van Hal, and P.K. Larsen, J. Appl. Phys., 70, 2290 (1991).
19. D. Roy, S.B. Krupanidhi, and J.P. Dougherty, J. Appl. Phys., 69, 7930 (1991).
20. A.I. Kingon, private communication.
21. S.B. Krupanidhi, H. Hu, and V. Kumar, J. Appl. Phys., 71, 376(1992).
22. R. Bruchhaus, D. Pitzer, O. Eibl, U. Scheithauer, and W. Hoesler, to be published in Mater. Res. Soc. Proc., 243.

*Ferroelectrics*, 1992, Vol. 133, pp. 79–84
Reprints available directly from the publisher
Photocopying permitted by license only
© 1992 Gordon and Breach Science Publishers S.A.
Printed in the United States of America

# Tf17

## ELECTRICAL PROPERTIES OF MOCVD-DEPOSITED PZT THIN FILMS

YUKIO SAKASHITA, TOSHIYUKI ONO, HIDEO SEGAWA
Materials Res. Lab., Nippon Mining Co., Ltd., Saitama, Japan

KOUJI TOMINAGA and MASARU OKADA
Faculty of Engineering, Chubu University, Aichi, Japan

Abstract Strongly c-axis oriented epitaxial PZT thin films have been successfully grown on (100)MgO and (100)Pt/(100)MgO substrates by using the MOCVD method. The epitaxial relation is (001)PZT ‖ (001)MgO and [010]PZT ‖ [010]MgO. Their dielectric constants, remanent polarizations and coercive fields are relatively in good agreement with those of PZT single crystals. This indicates that the MOCVD-deposited films have good crystallinity.

## INTRODUCTION

It is known that ferroelectric $Pb(Zr_xTi_{1-x})O_3$ (PZT) ceramics show superior piezoelectric and pyroelectric properties. Recently, several studies on making use of these advantages for $PbTiO_3$ and PZT thin films have already been reported.[1-4] Their applications are included in many devices such as nonvolatile memories, thermal or ultrasonic image sensors and surface acoustic wave (SAW) filters.

It is anticipated that the electrical properties of PZT thin films greatly depend on many factors, such as their composition, microstructure and stress, analogous to bulk ceramics. Therefore, we should judge the quality of deposition techniques by comparing the electrical properties of the obtained thin films with those of perfect PZT single crystals. The RF-magnetron sputtering technique, which is generally used to prepare ferroelectric thin films, has certain disadvantages, such as defect formation due to sputtering damage. Because of less defects expected from the absence of high-energy particles, the authors considered that the metal-organic chemical vapor deposition (MOCVD) method is preferable, and thus have continued the studies on the preparation of ferroelectric thin films by this method.[5,6] In this paper, it is reported that PZT thin films can be epitaxially grown on MgO single crystal substrates by using the MOCVD method, and that the electrical properties of the films show good agreement with those of single crystals.

## EXPERIMENTAL TECHNIQUE

The details of deposition and evaluation technique were explained in the previous papers.[5,6] Briefly, PZT thin films were deposited on 15×15×0.4 mm polished (100)MgO single crystal substrates or on those coated with approx. 0.1 μm-thick (100) oriented platinum film as an electrode; by using the MOCVD method with precursors of tetraethyllead ($Pb(C_2H_5)_4$), zirconium tetradipivaloylmethane ($Zr(DPM)_4$) and titanium tetraisopropoxide ($Ti(i\text{-}OC_3H_7)_4$).

## RESULTS AND DISCUSSION

By observing surface and cross sectional morphologies using SEM (scanning electron microscopy), the approx. 2 $\mu$m-thick $Pb(Zr_xTi_{1-x})O_3$ (PZT) thin films obtained by this method are composed of regularly ordered large grains with diameter of 1-2 $\mu$m. Surface morphologies become smooth with increasing composition x. The columnar structure usually observed in typical CVD films is not found. The x-ray diffraction patterns show that the films have c-axis oriented tetragonal perovskite structure and that the crystal structure changes from tetragonal to rhombohedral at a value of approx. x=0.52.[6]

FIGURE 1 (a) shows the crystal lattice image of the interface between the PZT thin film (x=0.48) and MgO substrate using TEM (transmission electron microscopy) and FIGURE 1 (b) shows electron diffraction pattern of the same region in a diameter of 300 nm. The epitaxial growth of the PZT thin film on the MgO substrate is apparently seen in the crystal lattice image, in FIGURE 1 (a). The lattice constant "a" calculated from the crystal lattice image is approx. 4.0 Å, which is almost the same value as that of PZT bulk ceramics.[7] In the 20 Å-thick interface layer between film and substrate, edge dislocations are observed. The origin of the edge dislocations is considered to exist in the difference between the lattice constant of MgO substrate (4.21 Å) and that of the PZT thin film (approx. 4.0 Å). As is seen in FIGURE 1 (b), the electron diffraction pattern of the PZT thin film greatly coincides with that of MgO substrate, showing that the epitaxial relation is (001)PZT ‖ (001)MgO and [010]PZT ‖ [010]MgO. The lattice constant "a" calculated from the diffraction pattern is approx. 4.0 Å, which is in accordance with that obtained from the crystal lattice image.

All the electrical properties described here are measured at room temperature. The relative dielectric constants along the a-axis ($\varepsilon_a$) and c-axis ($\varepsilon_c$) of the PZT thin films were measured separately without poling treatment: $\varepsilon_a$ of the films deposited directly on (100)MgO substrates with interdigital electrodes (700 $\mu$m in length and 10$\mu$m in width) are calculated from the electrical capacitances measured at 1 kHz with the application of 1V by an impedance-analyzer HP4192A; $\varepsilon_c$ of the films deposited on the (100)Pt/(100)MgO substrates with 2mm$\phi$ Au top electrode are calculated from the electrical capacitances measured at 1 kHz with the application of 0.1V.

FIGURE 2 shows the relative dielectric contants, $\varepsilon_a$ and $\varepsilon_c$, of the PZT thin films (2$\mu$m in thickness) and PZT single crystals as a function of composition x. Both open and filled squares in FIGURE 2 represent experimental values of the films by our MOCVD method, while the continuous line and the dotted line are the values of PZT single crystals with single-domain calculated by M.J.Haun et. al.[7] $\varepsilon_a$ of the films are, within the experimental error range, similar to those of single crystals which have a peak around x=0.5. On the other hand, $\varepsilon_c$ of the films are almost independent of composition x: over the range of 0.2<x<0.4, $\varepsilon_c$ of the films are larger than those of single crystals; in the range of 0.4<x<0.6, $\varepsilon_c$ of the films are smaller than those of single crystals. The difference in 0.2<x<0.4 might be related to the influence of $\varepsilon_a$, by judging from the experimental results that the degree of c-axis orientations[6] for the films in this composition range are lower (f=0.8-0.9) than those of the films in 0.4<x<0.6 (f≒1) and that the $\varepsilon_c$ decrease to approx. 150 after poling treatment. The difference in 0.4<x<0.6 might be originated from some kind of clamping effects. According to Tsuzuki et. al.[8], who measured the electrical properties of PZT single crystals with nearly morphotropic phase boundary (MPB, x≒0.5), clamped $\varepsilon_c$ are smaller than free $\varepsilon_c$ and independent of composition x, although free $\varepsilon_c$ increase at MPB. Therefore in the case of the thin films, it might be considered that some kind of clamping effects, such as thermal stress caused by the difference of thermal expansion

coefficient between PZT thin films and MgO substrates, make $\varepsilon_c$ smaller and independent of composition x.

FIGURE 3 shows the relationship between film thickness d and the relative dielectric constants along c-axis ($\varepsilon_c$) of the PZT thin films in the range of 0.45<x<0.52. Below d=0.5$\mu$m, $\varepsilon_c$ decreases drastically. This phenomenon might be caused by the internal stress generated from the frequent aggregation of crystal grains. Further studies have been performed and the results will be reported elsewhere. $\varepsilon_c$ is, however, almost constant above d=0.5$\mu$m and independent of film thickness. The data in FIGURE 2 are obtained from 2$\mu$m-samples, which $\varepsilon_c$ are within this range independent of film thickness. Therefore, the decrease in $\varepsilon_c$ at MPB in FIGURE 2 might not be attributed to some kind of the effect caused by thinning, such as the size effect.

FIGURE 4 shows the remanent polarizations $P_r$ and the coercive fields $E_c$ as a function of composition x. $P_r$ and $E_c$ decrease with increasing composition x, as do PZT single crystals[7], and are almost the same values as the experimental data of PZT single crystals[9] which have $P_r$=50 $\mu$C/cm$^2$ and $E_c$=40 kV/cm at x=0.4, respectively.

The electrical properties of PZT thin films near the MPB deposited by the sputtering method were reported by Iijima et. al.[10] The $\varepsilon_c$ of the sputter-deposited films are approx. 500 and larger than those of the MOCVD-deposited films. The $P_r$ of sputter-deposited films are approx. 10$\mu$C/cm$^2$ and smaller than those of the MOCVD-deposited films. Considering differences in $\varepsilon_c$ and $P_r$, the sputter-deposited films seem to have worse crystallinity than the MOCVD-deposited films because of sputtering damage, dislocation or some kind of stress. Judging from the electrical properties that are closely related to crystallinity of the films, the MOCVD method seems to be superior to the sputtering method in preparing PZT thin films.

## SUMMARY

Strongly c-axis oriented epitaxial PZT thin films with good surface morphology have successfully been grown on (100)MgO and (100)Pt/(100)MgO substrates by using the MOCVD method. The epitaxial relation is found to be (001)PZT ‖ (001)MgO and [010]PZT ‖ [010]MgO. The dielectric constants, remanent polarizations and coercive fields of the films show better agreements with those of PZT single crystals than those of sputter-deposited films. This indicates that the MOCVD-deposited films have better crystallinity than sputter-deposited films.

## REFERENCES

1) M.Okuyama and Y.Hamakawa, Ferroelectrics 63, 243(1985)
2) R.Srivastava and A.Mansingh, Ferroelectrics 108, 1627(1990)
3) P.D.Beale and H.M.Duiker, Ferroelectrics 116, 111(1991)
4) R.Takayama, Y.Tomita, K.Iijima and I.Ueda, Ferroelectrics 118, 325(1991)
5) M.Okada, K.Tominaga, T.Araki, S.Katayama and Y.Sakashita, Jpn.J.Appl.Phys. 29, 718 (1990)
6) Y.Sakashita, T.Ono, H.Segawa, K.Tominaga and M.Okada, J.Appl.Phys. 69, 8352(1991)
7) B.Jaffe, R.S.Roth and S.Marzullo, J.Res.Natl.Bur.Stds. 55, 239(1955)
8) M.J.Haun, E.Furman, S.J.Jang and L.E.Cross, Ferroelectrics 99, 63(1989)
9) K.Tsuzuki, K.Sakata and M.Wada, Ferroelectrics 8, 501(1974)
10) K.Iijima, I.Ueda and K.Kugimiya, Jpn.J.Appl.Phys. 30, 2149(1991)

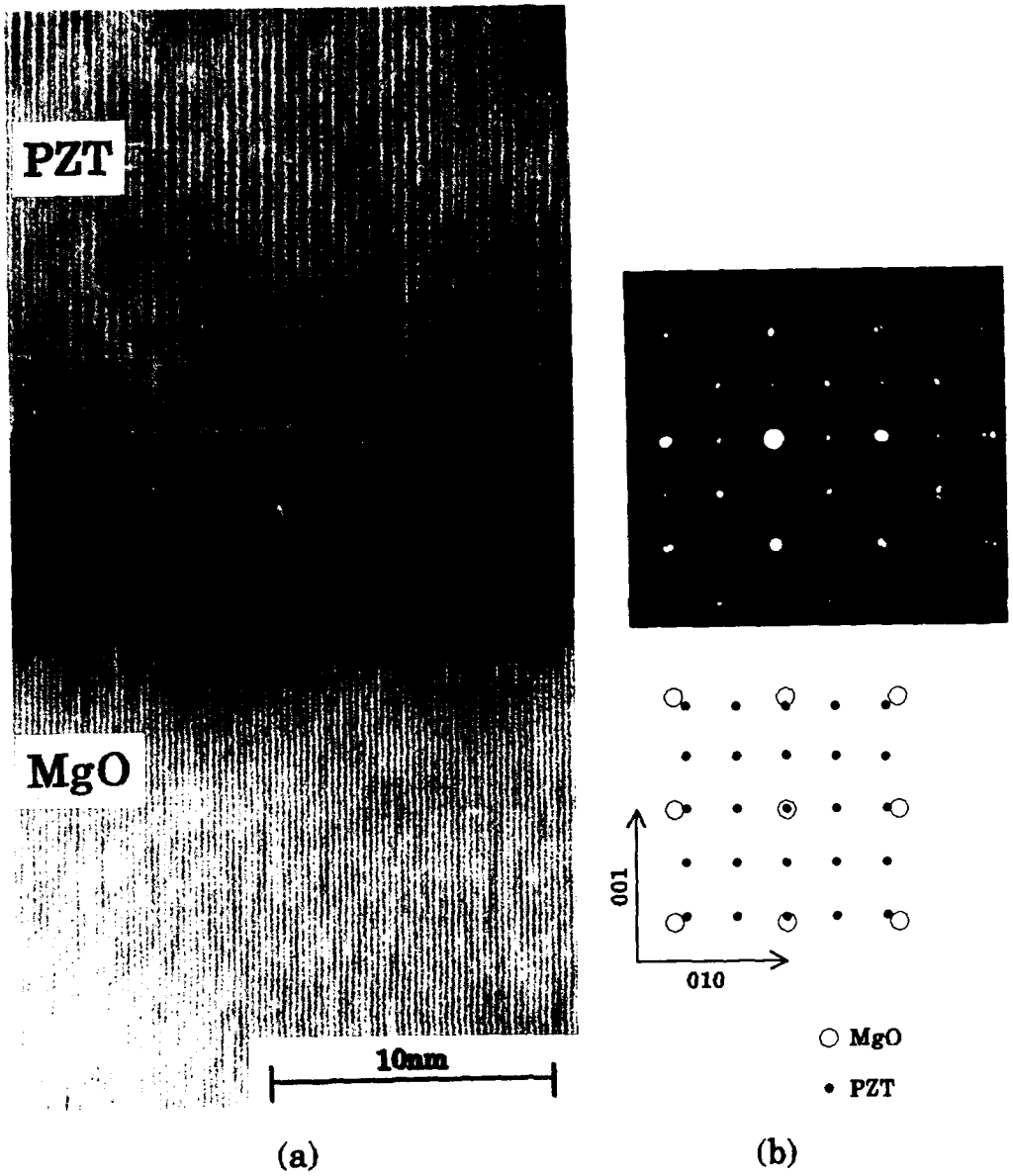


**FIGURE 1** Epitaxial growth of PZT thin film (x=0.48): (a); crystal lattice image, (b); electron diffraction pattern.

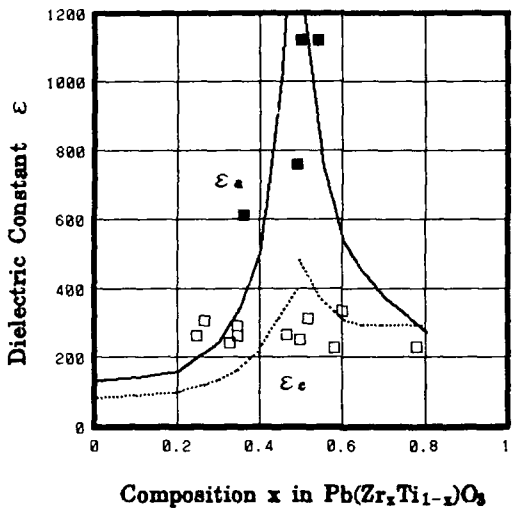


**FIGURE 2** Dielectric constants $\varepsilon$ as a function of composition x (■: $\varepsilon_a$ of PZT films, □: $\varepsilon_c$ of PZT films, —: calculated $\varepsilon_{11}$ of PZT single crystals, ···: calculated $\varepsilon_{33}$ of PZT single crystals)

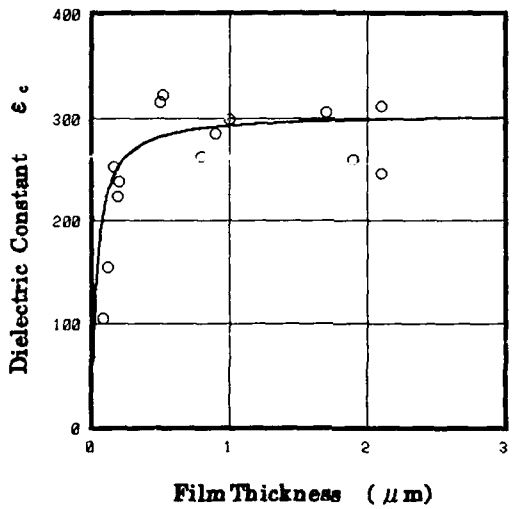


**FIGURE 3** Relationship between film thickness and dielectric constants along c-axis $\varepsilon_c$ of PZT thin films

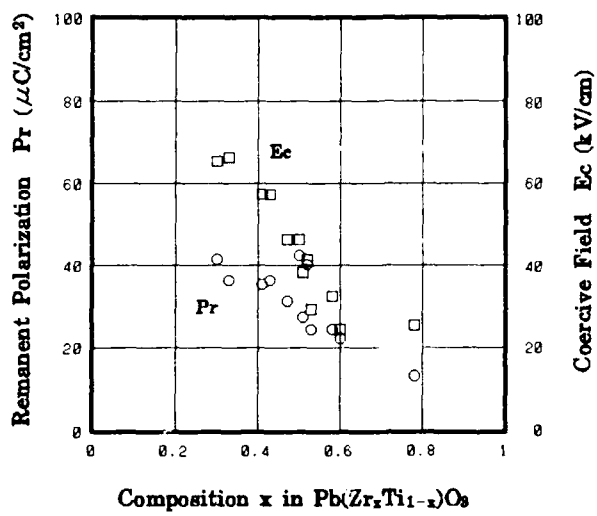


**FIGURE 4** Remanent polarization $P_r$ and coercive field $E_c$ as a function of composition x (○: remanent polarization $P_r$, □: coercive field $E_c$)

*Ferroelectrics*, 1992, Vol. 133, pp. 85–90
Reprints available directly from the publisher
Photocopying permitted by license only

© 1992 Gordon and Breach Science Publishers S.A.
Printed in the United States of America

# Tf18

## PULSED PLASMA DEPOSITION OF LEAD LANTHANUM ZIRCONATE TITANATE(PLZT) AND LEAD LANTHANUM TITANATE(PLT)

IAN P. LLEWELLYN, RUDOLF A. HEINECKE
BNR Europe Limited, London Road, Harlow, Essex, U.K.

KEITH L. LEWIS, KATHLEEN F. DEXTER
DRA Electronics Division, RSRE, Malvern, Worcester, U.K.

Abstract Thin films of ferroelectric lanthanum-modified lead zirconate titanate (PLZT) and lanthanum-modified lead titanate (PLT) have been prepared using a novel high-powered pulsed plasma deposition technique. This method uses a microwave-induced intense discharge in a low pressure gas containing organometallic precursors of each of the required metal atoms, together with carbon dioxide and argon. In the discharge, the precursors dissociate to produce atoms which then recombine on the substrate to form the oxide film. Results are presented on the composition and crystal form of the films as the deposition conditions are varied. By careful control of deposition temperature, it is shown that a microcrystalline perovskite phase may be grown on a wide variety of substrate materials.

## INTRODUCTION

Lanthanum-doped lead zirconate titanate (PLZT) and lanthanum- doped lead titanate (PLT) are well known as ferroelectric materials, which exhibit a number of interesting electrical and optical effects. Recently, attention has been focused on using these materials in thin film form, and thin film devices have been proposed for applications in optics[1], sensors[2], displays[3] and non-volatile memory storage[4]. In particular, the high electro-optical coefficient of PLZT has led to it being used in flat-panel displays which can be refreshed at pixel rates in excess of 500 MHz[5].

To date, sputtering has been the preferred method for depositing PLT and PLZT thin films[6]. In order to achieve the desired perovskite structure and to eliminate the unwanted pyrochlore phase, the sputtering (or a later post-growth anneal) must be performed at temperatures in excess of 550°C. This can cause a change in stoichiometry of the deposited film from that of the sputtering target, due to the different volatility of the metal oxides in the film. Since the film stoichiometry is critical to many of the optical and electrical applications considered, this has led to the development of multi-target sputtering techniques in order to adjust the film stoichiometry[7]. This is difficult to control accurately, and has been a significant handicap in the production of PLZT devices.

This paper presents an alternative method of preparing PLT and

PLZT using a plasma-assisted chemical vapour deposition method. This uses a high-powered, pulsed, microwave discharge of a mixture of volatile organometallic precursors in an oxidising plasma atmosphere at low pressure. The discharge breaks the precursors into atoms which deposit onto a heated substrate. The oxygen atoms released from the oxidising gas in the discharge remove the carbon and hydrogen in the depositing film as carbon dioxide and water respectively, leaving behind a pure oxide film. By varying the concentration of the precursors in the discharge, the stoichiometry of the film can be readily controlled to any value required, while allowing the deposition temperature to be adjusted to produce the desired perovskite phase.

## PULSED PLASMA DEPOSITION OF PLZT

The use of the pulsed plasma process to deposit dielectrics, metals, and compound semiconductors has been described elsewhere[8,9,10]. However, the use of this technique to deposit crystalline metal oxides produces a number of unique problems that need to be overcome. First, and in common with all chemical vapour deposition techniques, suitable volatile precursor compounds have to be identified. Second, it is necessary to control the flow of these compounds into the reactor with great accuracy. Third, due to the different mobilities of ions and electrons in the discharge, high negative bias is developed on the discharge electrode which is connected to the RF. This causes preferential sputtering of some metal atoms from the depositing film, leading to a loss of stoichiometry. In the present work, this has been avoided by the use of a novel microwave discharge technique, in which the frequency of the excitation is high enough to limit electron mobility in the discharge.

### Identification and Control of Precursors

By careful study of the available literature, suitable precursor compounds for the lead, lanthanum, zirconium, and titanium have been identified. These are shown in Figure 1. In all cases, compounds of the metal containing only carbon, oxygen and hydrogen have been used, since these atoms have readily volatile oxides. Several halogen containing compounds have substantially higher vapour pressures, but have been avoided in this work due to the possibility forming the metal halide in the film. Apart from the lanthanum precursor, which is a solid, the other compounds are liquids.

| | |
|---|---|
| $Pb(C_2H_5)_4$ | Tetra ethyl lead |
| + $La((CH_3)_3\text{-}C\text{-}CO\text{-}CH\text{-}CO\text{-}C\text{-}(CH_3)_3)_3$ | Lanthanum tetramethylheptanedionate |
| + $Zr(OC_4H_9)_4$ | Zirconium tert-butoxide |
| + $Ti(OCH(CH_3)_2)_4$ | Titanium(IV) iso-propoxide |

$$+\ CO_2 + Ar \xrightarrow[\text{Plasma discharge}]{} PLZT + CO + H_2O + Ar$$

FIGURE 1 Precursor compounds used in this work.

Controlling the flow of the precursor into the deposition chamber required different techniques for the solid lanthanum compound than for the liquids. The latter was controlled by means of bubblers, the control of the compound flow being achieved by varying the flow of the argon carrier gas. Since the pressure in the deposition chamber (300 mtorr) was lower than the typical pressure in the bubbler (10 torr), it was necessary to control the bubbler pressure as well as the carrier gas flow, in order to achieve reproducible results. This was done by placing a throttle valve between bubbler and chamber and throttling the valve to keep a constant pressure in the bubbler. By lowering the bubbler pressure, the flow of compound into the chamber could be increased, and this allowed the film stoichiometry to be adjusted.

The lanthanum compound flow was controlled by placing it inside a heated cell with a pinhole orifice at the top. The compound escaping from the cell through the orifice was transported to the deposition chamber in argon through a heated pipe. The flow of lanthanum compound could be varied by increasing the temperature of the cell. Typically temperatures were in the range of 180°C to 200°C.

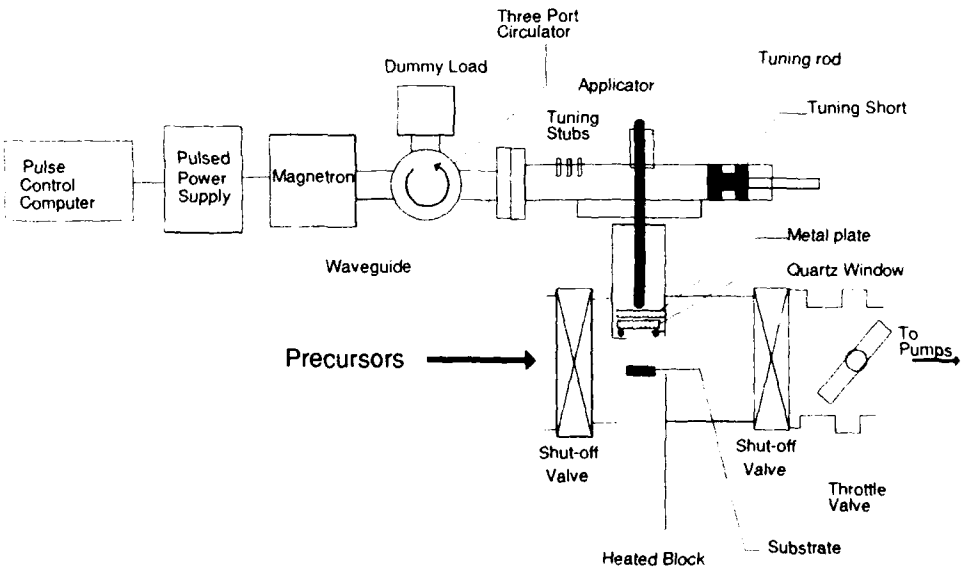


FIGURE 2 Schematic of deposition equipment.

Microwave Deposition Technique

The microwave deposition equipment is shown in Figure 2. The discharge power is supplied by a high powered magnetron (Hitachi 2M130), pulsed to give 50 kW pulses by switching the high voltage supply using a triode valve. The rise time of the pulse is less than 1 μs. Output from the waveguide is taken along a 9A waveguide to a three-port circulator arranged so that any reflected power from the discharge is taken to a 50 Ω dummy load. From here, the microwave energy is taken through power samplers to the applicator. This consists of a three-stub reflector and a short total reflector between which a standing wave is

generated. A co-axial section leads to a metal plate sitting above a quartz window. The metal plate, which is isolated from ground by a Teflon sheath, absorbs and re-emits the microwave energy to the plasma and, in this way, improves the microwave energy distribution in the discharge. At a distance of 25 mm below the window, in the deposition chamber, lies the substrate on a grounded, heated, metal plate. Since the magnetron becomes hot during operation, it is necessary to cool it by using nitrogen blown directly into the waveguide.

The microwaves are tuned into the discharge by altering the position of the short and the length of the coaxial section. Typical matching ratios give a reflected power of 2 kW for 50 kW forward power into the discharge. A discharge can be sustained using this technique at pressures of 100 mtorr to in excess of 20 torr, but most work has been performed within a pressure range of 200 mtorr to 400 mtorr. The reactant gases flow across the substrate and are pumped using a 500 $m^3h^{-1}$ roots/rotary combination. Typical gas flows (precursors, argon and carbon dioxide) are in the region of 2000 sccm.

## PROPERTIES OF DEPOSITED FILMS

Films of PLT and PLZT have been deposited over a wide range of compositions, and on a wide range of substrates, including c-plane sapphire, which is known to be a good crystal match to perovskite PLZT[11], silicon, silica, and conductive tin oxide coated sapphire. Typical deposition rates are 1-2 µm per hour. In this publication, the physical properties of the films will be described; a future publication will discuss electrical and optical properties of the films in some detail.

### Film Stoichiometry

Films of a wide range of compositions have been formed using the technique, by varying the reagent flows, and have been analyzed by X-ray photoelectron spectroscopy and SEM microanalysis. For substrate temperatures less than 700°C, the composition of the deposited film is proportional to the partial pressure of the precursor in the gas phase. Using the standard formulation for PLZT of $Pb_{100-x}La_x(Zr_yTi_z)_{100-x/4}O_3$, films have been deposited over the range $2<x<30$, $0<y<70$, and $30<z<100$ by varying the flow of the precursors.

At temperatures >500°C, the films show loss of lead which needs to be compensated for by increasing the partial pressure of the lead precursor in the gas phase. At higher temperatures, on silicon and silica substrates, the film tends to absorb silicon from the substrate and form an amorphous glassy phase. When the surface of the film is analysed by XPS, up to 20% of silicon can be incorporated into the film when deposited at 700°C, suggesting the formation of a silicate phase. It is suspected this reaction occurs between the substrate and one of the precursors, since it is possible to sputter PLZT onto silica at these temperatures quite successfully[6].

### Film Structure

Under high magnification in the SEM, the films deposited onto sapphire and onto tin oxide coated substrates are observed to grow in a columnar fashion, with column diameters of 50 nm near the substrate growing to 0.2 µm at the top of a 1 µm film (Figure 3). Films deposited on tin oxide are similar to those deposited on sapphire. However, films deposited on silicon and silica substrates tend not to show well-developed columns, but exhibit a fine (0.01 µm) grainy structure. The film microstructure is the same on all substrates and does not appear

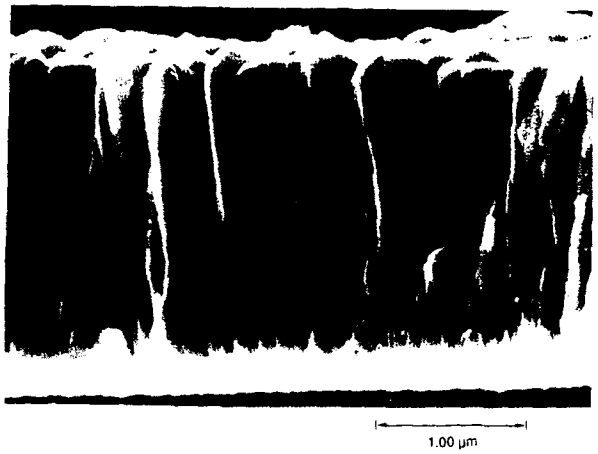


FIGURE 3 SEM micrograph of PLZT film on sapphire

to vary greatly between deposition temperatures of 500°C and 700°C.

PLZT can exist in several crystalline states depending on the composition and the temperature. A phase diagram for the compound has been published[12]. Films with the correct stoichiometry to form the perovskite phase have been studied by X-ray diffraction in order to determine the crystal phase of the films with the temperature of the deposition. Films deposited at temperatures less than 550°C are largely amorphous, with weak peaks of both the pyrochlore and the perovskite phases. Films deposited at 600°C show strong perovskite peaks in the X-ray diffraction pattern. This is shown for PLT (9/0/100) grown at 600°C in Figure 4. Films grown at temperatures greater than 750°C show other peaks, which appear to occur from crystals of binary oxides forming in the films. By annealing films grown at temperatures of 500°C or below in an inert gas at 600°C for 6 hours, the amorphous phase can be replaced by the perovskite phase. However, heating the films in this

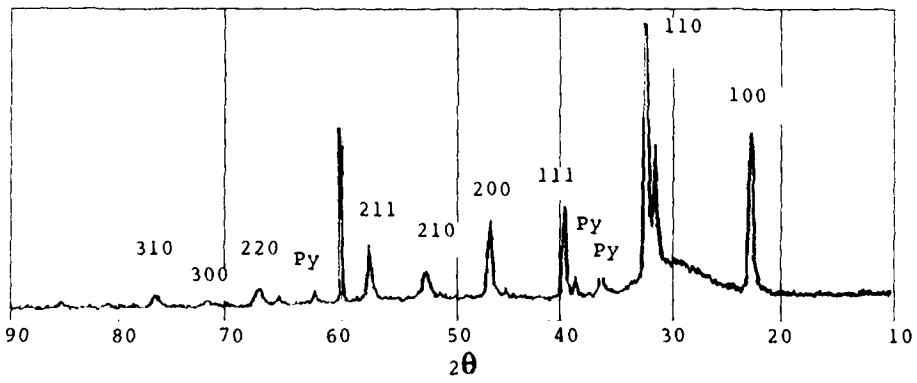


FIGURE 4 X-Ray diffraction spectrum of PLT (9/0/100), showing the principle lines from the perovskite lattice. Lines due to the pyrochlore phase are marked Py. Other peaks are due to the sapphire substrate and a thin aluminium metallisation deposited on top of the film.

fashion produces a substantial loss of lead from the films and, consequently, the film has to be deposited lead rich in order to arrive at a specific film stoichiometry after annealing.

## CONCLUSIONS

The pulsed plasma process has been shown to be capable of depositing PLZT over a wide range of compositions and at a wide range of deposition temperatures. Depending on the deposition temperature used, either an amorphous film, the pyrochlore phase, or the perovskite phase can be produced.

## ACKNOWLEDGEMENTS

The authors would like to thank the Materials Evaluation Centre at BNR Europe for X-ray analysis and SEM work. The work has been supported and sponsored by the Defence Research Agency, Electronics Division, RSRE.

## REFERENCES

1. T. Lin, A. Ersen, J. H. Wang, S. Dasgupta, S. Esener and S. H. Lee, Appl. Optics, 29 1595 (1990).
2. R. Takayama, Y. Tomita, K. Iijima and I. Ueda, J. Appl.Phys., 61, 411 (1987).
3. K. Sreenivas, M. Sayer, D.J. Baar and M. Nishioka, Appl.Phys.Lett., 52, 709 (1988).
4. Y. Hamakawa, Y. Matsui, Y. Higuma and T. Nakagawa, Tech. Digest, IEEE Int. Electron Devices Meeting, Washington, D.C., 148 (1977).
5. A.Y. Wu, F. Wang, C. Juang, and C. Bustamante, Ferroelectric Thin Films Symposium, San Francisco, CA, USA, 16-20 April 1990, 261.
6. H. Volz, K. Koger and H. Schmitt, Ferroelectrics, 51, 87 (1983).
7. H. Adachi, T. Mitsuyu, O. Yamazaki, and K. Wasa, J. Appl Phys, 60, 736 (1986).
8. G. Scarsbrook, I.P. Llewellyn, S.M. Ojha and R.A. Heinecke, Vacuum, 38, 627 (1988).
9. G. Scarsbrook, I.P. Llewellyn and R.A. Heinecke, J.Vac.Sci.Technol.A , 7, 1099 (1989).
10. I.P. Llewellyn, N. Rimmer, G.A. Scarsbrook and R.A. Heinecke, Thin Solid Films, 191, 135 (1990).
11. H. Adachi, T. Mitsuyu, O. Yamazaki, and K. Wasa, J.Appl. Phys, 60, 736 (1986).
12. G.H. Haertling and C.E. Land, J.Am.Cer.Soc., 54, 1 (1971).

*Ferroelectrics*, 1992, Vol. 133, pp. 91–96
Reprints available directly from the publisher
Photocopying permitted by license only

© 1992 Gordon and Breach Science Publishers S.A.
Printed in the United States of America

**TfI14**

# FERROELECTRIC THIN FILMS FOR MEMORY APPLICATIONS: SOL-GEL PROCESSING AND DECOMPOSITION OF ORGANO-METALLIC COMPOUNDS

MAREIKE KLEE AND POUL K. LARSEN*
Philips GmbH Forschungslaboratorium Aachen, Aachen, Germany
*Philips Research Laboratories, P.O. Box 80.000, 5600 JA Eindhoven, The Netherlands

Abstract $Pb(Zr_xTi_{1-x})O_3$ (PZT), $Bi_4Ti_3O_{12}$ and $BaTiO_3$ films as well as $SrTiO_3$ films are considered for nonvolatile memory applications and high density dynamic random access memories. These perovskite systems are frequently deposited by a sol-gel or MOD technique. Processing and the properties of the thin films are summarized.

## INTRODUCTION

Thin perovskite films have attracted the attention of the microelectronics industry in recent years due to their potential uses in binary memories. The reversible polarization of some ferroelectric perovskite films, e.g. $Pb(Zr_xTi_{1-x})O_3$ (PZT) and $Bi_4Ti_3O_{12}$, can be applied in non-volatile (ferroelectric) random access memories (FERAMs).[1] The dielectric properties of thin films of $SrTiO_3$ and $(Sr,Ba)TiO_3$ are considered for high density dynamic random access memories (DRAMs).[2]

The deposition of the perovskite films is realized by many groups using spin-coating techniques based on either sol-gel[3-5], modified sol-gel processing[6-9] or by decomposition of organometallic compounds (MOD).[7,8,10-13] In all cases a solution containing a mixture of precursors is spun onto a substrate and is followed by a heat treatment. The process is repeated until the desired film thickness is obtained. The last step is a final anneal treatment. The sol-gel and the modified processes are based on the hydrolysis and condensation of complex precursors such as metal alkoxides, while in the MOD process a decomposition of the organometallic compounds occurs. For both methods the use of different precursors and heat treatments are being widely studied. For non-volatile memory applications evaluations are made on basis of performances such as the influence of the number of polarization reversals on the magnitude of polarization (i.e. fatigue behaviour). The dielectric $(Ba,Sr)TiO_3$ films for DRAM applications are investigated with respect to high permittivities and low leakage currents.

This paper summarizes our spin-coating processes for the preparation of PZT films of various compositions. More recently developed spin-coating deposition methods for $BaTiO_3$, $SrTiO_3$ and $Bi_4Ti_3O_{12}$ will also briefly be discussed. Finally, electrical properties of the films will be presented.

## THIN FILM PREPARATION

### Lead zirconate-titanate (PZT)

For the PZT thin film deposition we have investigated a sol-gel, a modified

Table 1 Details and properties of three precursor systems

| Precursor system | Precursors | Solvent | Concentration | Weight loss | Exothermic reactions (K) | XRD analysis |
|---|---|---|---|---|---|---|
| I (Modified sol-gel) | Pb-acetate-tri-hydrate<br>Ti-tetra-n-butylate<br>Zr-tetra-n-butylate | methyoxy-ethanol | 0.5 M | 20% | 553-573, 673, 743 | 773 K: Pyrochlore / perovskite<br>873-973 K: Perovskite |
| II (MOD) | Pb-2ethylhexanoate<br>Ti-tetra-n-butylate<br>Zr-acetylacetonate | butanol | 0.2-0.5 M | 45% | 593-623 | ≥ 773 K: Perovskite |
| III (Sol-gel) | Pb-acetate<br>Ti-tetra-i-propylate<br>Zr-tetra-n-butylate | methoxy-ethanol<br>$HNO_3/H_2O$ | 0.5 M | 19% | 493, 553-583, 743 | 773 K: Pyrochlore / perovskite<br>873-973 K: Perovskite |

sol-gel and an MOD process (see Table 1). In the MOD process, metal carboxylates such as Pb-2ethylhexanoate are mixed with metal alkoxides and acetylacetonates of Ti and Zr. Formation of the PZT films occurs by decomposition and subsequently reaction of these compounds. In the sol-gel and the modified sol-gel processes a hydrolysis and condensation of metal alkoxides are carried out. In the precursor system III complex alkoxides are prepared as described in Refs.(3-4) and subsequently hydrolized with $HNO_3/H_2O$. In the modified sol-gel process precursor system I the Ti- and Zr-alkoxides are hydrolized with water, which is introduced by the lead-acetate-tri-hydrate. In Table 1 the precursor systems are indicated together with some properties derived from investigations of powders made by evaporation of the solutions.[8] It is noteworthy that the exothermic reactions occur in a smaller temperature range for precursor system II than for I and III and that for this system a single perovskite phase is formed at low temperatures of 773 K. For precursor systems I and III the pyrochlore phase is formed together with the perovskite phase at that temperature, so that 873-973 K are necessary to form a single perovskite phase. Although perovskite films are formed at low temperatures with precursor system II they have a lower density than higher temperature fired films due to the high carbon content of this precursor system.

Films were deposited by spin-coating (2000-3000 rpm) on platinated $SiO_2/Si$ substrates provided with a thin Ti adhesion layer.[13] The firing of the films to form the perovskites can be carried out in alternative ways. A standard technique is to use a furnace anneal after each coating in an $O_2$ atmosphere at 573-973 K.[7,8] Another method uses a hot-plate treatment (373-623 K) for the evaporation of the solvents after each spin-coating, followed by a final furnace annealing at 873-973 K. Investigations of rapid thermal annealing processes indicate that this method is an interesting alternative.[14]

Figure 1 SEM micrograph of a PZT(53/47) film made by process III

The crystallization of the PZT films is found to depend on the substrate, e.g. on the pretreatment of this, on the precursor system used, on the lead excess in the precursor solution and on the details of the

heating procedure. In general, it is found that, especially for the sol-gel and the modified sol-gel processes, the lead excess and the fast heating procedure (to 873-973 K) are necessary to form the perovskite films without any intermediate growth of the pyrochlore phase. The fast heating processes are either realized by ramping of the layers into the hot zone of the furnace held at 873-973 K or by using a rapid thermal annealing process at 923-973 K. The excess of the lead in the solutions, which is usually in the order of 10%, acts probably as a sintering (densifying) aid, so that homogeneous and fine-grained films with grain sizes of 50-150 nm are obtained (see Fig. 1). Wet chemical and X-ray fluorescence analyses show that some excess lead remains in the film even after firing at 973 K.

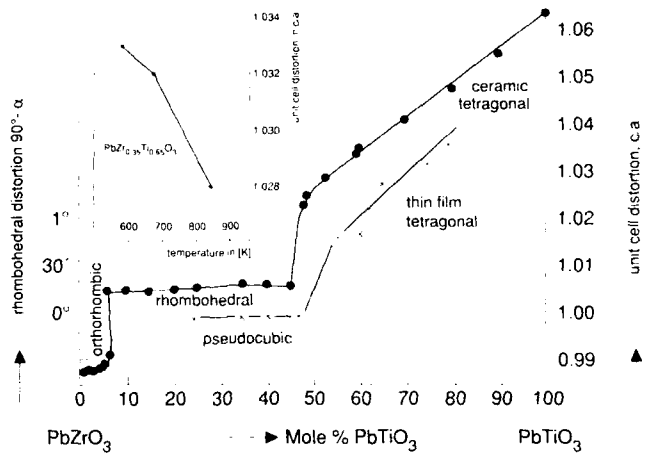


FIGURE 2 Unit cell distortion c/a as a function of the zirconium concentration x for thin PZT films (-x-) and bulk PZT ceramics (-•-).

Using precursor system I PZT films were prepared with various compositions in the range 0.2<x<0.75. The PZT films with 0.2<x<0.53, crystallizing tetragonally, exhibit a gradual decrease of the tetragonal distortion with increasing zirconium content similar to bulk data.[15] This is shown in Fig. 2. The smaller distortion of the unit cell for films with x<0.53 compared to bulk ceramics is probably due to the extremely fine grains within the films.[16] The unit cell distortion is furthermore a function of firing conditions. This is shown in the insert in Fig. 2 giving the c/a ratio for films having different firing temperatures and a subsequent anneal at 973 K. Higher firing temperatures apparently lead to a smaller c/a ratio, probably related to a smaller grain size.

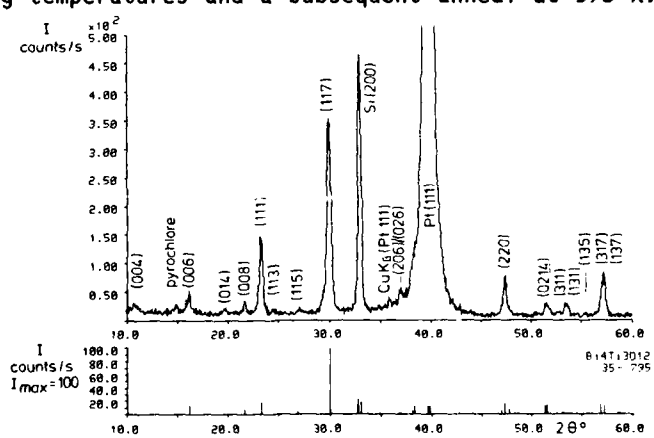


FIGURE 3 XRD pattern of a $Bi_4Ti_3O_{12}$ film deposited on a $Pt/Ti/SiO_2/Si$ substrate.

## Other oxides

Similar to the lead zirconate-titanates, the alkaline earth titanates and the $Bi_4Ti_3O_{12}$ films have been deposited by both sol-gel[5,9] and MOD methods.[17,18] Our investigations have shown that these films always grow randomly oriented.[17] In

Fig. 3 an XRD pattern of a $Bi_4Ti_3O_{12}$ film prepared by the MOD process is shown. Small amounts of $Bi_2Ti_2O_7$ as second phase are found. In contrast, the earth alkaline films are always grown single phase. Similar to the PZT films all these oxide films are very fine-grained.

XRD pattern of the $BaTiO_3$ films show a pseudocubic and not a tetragonal crystal structure with an axis of a=0.400 nm. This is probably caused by the fine-grained morphology. For the $SrTiO_3$ films a cubic lattice constant of a=0.3906 nm was determined. The $Bi_4Ti_3O_{12}$ films have an orthorhombic crystal structure with the axes a=0.544 nm, b=0.541 nm and c=3.284 nm.

## ELECTRICAL PROPERTIES

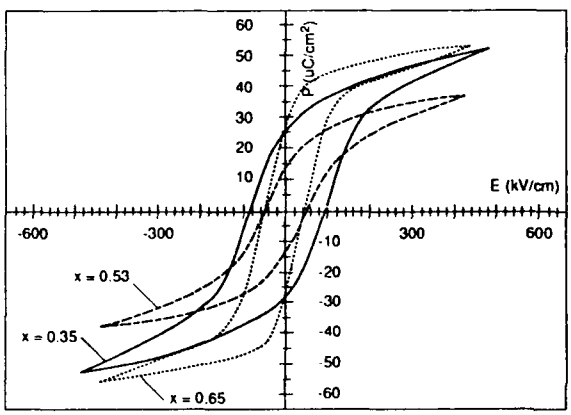


FIGURE 4 Hysteresis loops obtained for PZT films with various compositions.

For non-volatile memory applications the ferroelectric film should meet a number of device-oriented requirements. The minimum switching polarization, estimated from typical charge detection threshold, is of the order of 1 $\mu C/cm^2$. The switching should be possible with pulse amplitudes at or below standard IC voltages (3-5 V). The number of allowed read and write cycles ('endurance') should be at least $10^{10}$ and ultimately up to $10^{15}$. The switching time should be smaller than 100 ns.

In Fig. 4 we show hysteresis measurements for PZT films of various compositions prepared by precursor system I. The thickness of the films is approximately 0.44 $\mu m$. A high Ti content which leads to a high c/a ratio also gives a high coercive field strength. Thus PZT films with x=0.2-0.35 need a field strength exceeding a threshold strength of $E_{th}$=140 kV/cm to obtain high polarizations. Switching with pulses having 5 V amplitudes therefore require thicknesses below 0.3 $\mu m$ for these compositions. The curves further demonstrate that if the pulse amplitude has to be minimized it is more advantageous to select a composition with a higher Zr content.

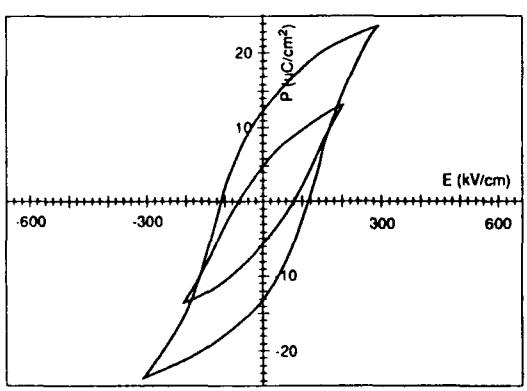


Figure 5 Hysteresis loops for a $Bi_4Ti_3O_{12}$ film.

In Fig. 5 hysteresis loops for $Bi_4Ti_3O_{12}$ films are shown. These randomly oriented layers have a lower remanent polarization and a lower coercive field

strength than those of laser deposited layers.[19]

Studies of the switching kinetics for PZT films as well as La doped $PbTiO_3$ films have revealed switching times in the range 10-100 ns[20] and below 2 ns.[21] This demonstrates that these materials fulfil by far the requirements on the switching time for memory applications.

The endurance is determined by the fatigue properties, e.g. the degradation of the ferroelectric properties caused by repeated reversals. The fatigue behaviour of the switched and non-switched polarizations ($\Delta P_s$ and $\Delta P_{ns}$, resp.) is shown in Fig. 6 for PZT films (x=0.53) prepared by the precursor systems I and II, respectively, together with measurements for a $Bi_4Ti_3O_{12}$ film. The measuring procedure has been described in Ref.(7). Due to long measuring times the measurements were stopped after $10^9$ cycles. The results are in agreement with earlier results showing a flat behaviour at low pulse amplitudes (5 V, d=0.4-0.5 $\mu$m) up to $10^{12}$ cycles and for large amplitudes (10-16 V) a fast decrease in switched polarization in the range $10^8$-$10^{11}$ cycles.[22] It should be noted that the difference between switched and non-switched polarizations exceeds by far the detection limit of 10 fC/$\mu m^2$ (= 1$\mu$C/cm$^2$) for all the results of Fig. 6 and that the flatness of the non-switched polarizations is very useful for one capacitor - one transistor memory cells. In general, it is found that the fatigue can depend on a large number of parameters such as specific film properties (composition, morphology, etc), the electrodes, the test conditions (pulse amplitude and width) and further on the processing of the ferroelectric capacitors, which might e.g. introduce stresses within the layers. The causes for fatigue can be of intrinsic nature, e.g. domain pinning effects, as well as of extrinsic nature related to e.g. degradation of the electrode-ferroelectric film interphase.

$BaTiO_3$ and $SrTiO_3$ thin films which are of more importance for thin film capacitors and high density DRAMs were prepared with an MOD process. For the $SrTiO_3$ films a dielectric constant of approx. 150-160 was determined. Similar data were reported for the sputtered $SrTiO_3$ layers.[2] The $BaTiO_3$ films, which are fine grained exhibit dielectric constants of 500-800 and a low temperature and field dependence.

In addition to a high dielectric permittivity the performance under a DC voltage stress is essential for these memory applications. Therefore the field dependence of the conduc-

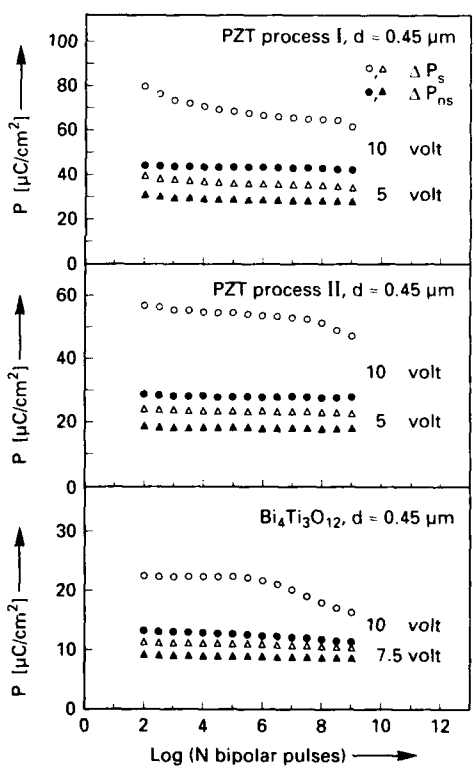


FIGURE 6 Switched and non-switched polarization versus number of bipolar pulses N for PZT(53/47) films prepared by processes I (upper panel) and II (middle panel) and for a $Bi_4Ti_3O_{12}$ film (lower panel).

tivity as well as the resistance degradation have been studied. A varistor-type behaviour for the leakage current was observed and interpreted in a model of an electron emission over a distributed Schottky barrier.[17] The long-term resistance degradation behaviour of the thin films turned out to be superiour compared to conventional ceramics, probably due to the very small grain sizes.[18]

We are indebted to W. Brand, R. Eusemann, G. Kampschöer, U. Mackens and G. Spierings for discussions and technical assistance.

## REFERENCES

1. J.F. Scott and C.A. Araujo, Science, 246, 1400 (1989).
2. T. Sakuma, S. Yamamichi, S. Matsubara, H. Yamaguchi, Y. Miyasaka, Appl. Phys. Lett., 57 (23) 2431-2433 (1990).
3. J.B. Blum and S.R. Gurkowich, J. Mat. Sc., 20, 4459 (1985).
4. K.D. Budd, S.K. Dey, D.A. Payne, Mat. Res. Soc. Symp. Proc., 73, 711 (1986).
5. D. Payne, Proc. MRS Fall Meeting, Boston, Dec. 1991.
6. G. Yi, Z. Wu and M. Sayer, J. Appl. Phys., 64, 2717 (1986).
7. G.A.C.M. Spierings, M.J.E. Ulenaers, G.L.M. Kampschöer, H.A.M. van Hal and P.K. Larsen, J. Appl. Phys., 70, 2290 (1991).
8. M. Klee, R. Eusemann, R. Waser, W. Brand and H. van Hal, submitted to J. Appl. Phys.
9. P.C. Joshi and A. Mansingh, Appl. Phys. Lett., 59 (19), 2389 (1991).
10. J. Fukushima, K. Kodaira and T. Matushita, J. Mat. Sc., 19, 595 (1985).
11. R. Vest and J. Xu, Ferroelectrics, 93, 21 (1989).
12. M. Klee, P. Schnabel, W. Brand and R. Mauczok, 1990 IEEE 7th Int. Symp. Appl. Ferroelectrics, IEEE Catalog nr. 90CH2800-1 (1991), p. 685.
13. G.A.C.M. Spierings, J.B.A. van Zon, M. Klee and P.K. Larsen, unpublished.
14. R.W. Schwarts , Z. Xu, D.A. Payne, T.A. DeTemple and M.A. Bradley, MRS Vol., 200, p. 167 (1990).
15. B. Jaffe, W.R. Cook and H. Jaffe, Piezoelectric Ceramics, Academic Press, London (1971).
16. K. Uchino, E. Sadanaga, T. Hirose, J. Am. Ceram. Soc., 72, 1555 (1989).
17. M. Klee and R. Waser, Proc. ISIF'91, Colorado Springs April 3-5, 1991, Ferroelectrics (in press).
18. D. Hennings, M. Klee and R. Waser, Adv. Mat., 3, 334 (1991).
19. H. Buhay, S. Sinharoy, W.H. Kasner and M.H. Francombe, 1990 IEEE 7th Int. Symp. Appl. Ferroelectrics, IEEE Catalog nr. 90CH2800-1 (1991), p. 139.
20. J.F. Scott, L. Kammerdiner, M. Parris, S. Traynor, V. Ottenbacher, A. Schawabkeh and W.F. Oliver, J. Appl. Phys., 64, 787 (1988).
21. P.K. Larsen, G.L.M. Kampschöer, M.J.E. Ulenaers, G.A.C.M. Spierings and R. Cuppens, Appl. Phys. Lett., 59, 611 (1991).
22. P.K. Larsen, R. Cuppens, G.A.C.M. Spierings, Ferroelectrics, 128 (1992).

*Ferroelectrics*, 1992, Vol. 133, pp. 97–102
Reprints available directly from the publisher
Photocopying permitted by license only

© 1992 Gordon and Breach Science Publishers S.A.
Printed in the United States of America

**Tf115**

# DOMAIN ORIENTATION CHANGE INDUCED BY FERROELECTRIC FATIGUE PROCESS IN LEAD ZIRCONATE TITANATE CERAMICS

Wuyi Pan, Cheng–Feng Yue and Shan Sun
Department of Materials and Metallurgical Engineering
New Mexico Institute of Mining and Technology
Socorro, NM, 87801

Abstract Domain orientation change induced by ferroelectric fatigue process is investigated in lead zirconate titanate type ceramics using X–ray diffraction. For hard lead zirconate titanate ceramics, a conversion of the domains, from the orientations perpendicular to the cycling field to the orientation parallel to it, is verified. For soft lead lanthanum zirconate titanate ceramics near the tetragonal–rhombohedral morphotropic phase boundary, a rhombohedral to tetragonal phase conversion and consequent stabilization of the tetragonal phase is revealed. The results can be well explained by the gradual buildup of a directional pinning force which impedes ferroelectric switching. The reorientation and migration of the defects and/or space charge induced by the cycling electric field are proposed to be responsible for the buildup of the directional pinning force.

## INTRODUCTION

Ferroelectric switching has been considered for many potential applications[1] among which lead zirconate titanate thin film ferroelectric memories have received special attention.[2] All these applications rely upon ferroelectric ceramics and thin films to switch a large spontaneous polarization without degradation. However, ferroelectric fatigue effect—a degradation of ferroelectric properties induced by the repeated polarization reversal—has presented a serious problem for all the potential ferroelectric devices. Since the ferroelectric polarization decreases and coercive field increases during ferroelectric fatigue, some investigators considered a preferential blockage of the applied electric field on the high impedance regions as the mechanism for ferroelectric fatigue.[3–5] For example, it was considered that the microcracks induced by the electromechanical stresses could block the applied electric field, reduce the effective electric field and lead to the observed ferroelectric fatigue.[3,4] The possibility of this nature was virtually eliminated by the directional nature of ferroelectric fatigue observed by Pan et al.[6]

Recently, the pinning of the spontaneous polarization by defects and/or space charge has been proposed by a number of investigators to explain the observed ferroelectric fatigue.[6–8] In the past, the same model was also proposed to be the mechanism of dielectric aging in ferroelectric ceramics.[9] However, in the case of dielectric aging, the pinning of the spontaneous polarization by defects is not

perturbed by an external applied electric field because dielectric aging is performed under the absence of an applied electric field. In this paper, we report the domain orientation change induced by ferroelectric fatigue process to illustrate the buildup of a directional pinning force which impedes ferroelectric switching.

## EXPERIMENTAL PROCEDURES

(1) Sample Preparation

The ceramics samples used for this study were lead zirconate titanate (PZT) and lead lanthanum zirconate titanate (PLZT) ceramics. The PLZT ceramic disks were prepared according to the procedures described in an earlier paper.[10] The PZT ceramics were commercial PZT–8 (hard PZT) ceramic disks purchased from Piezokinetics Inc. The ceramic disks were cut in to rectangular plates (0.6cm x 0.3cm x 0.03cm) using a diamond coated blade. The two major surfaces (0.6cm x 0.3cm) of the plates were ground using 600 grit SiC abrasive. The samples were thermally annealed at 600°C for 24 hours to release the stresses introduced during the grinding.

(2) Electric Poling and Cycling

Silver paste was used as the electrode for applying an electric field to the sample because it was easy to remove after electric poling and cycling for X–ray diffraction study. The poling was carried at room temperature by applying a large d.c. electric field for over five minutes. The cycling was carried out at room temperature by driving the sample with a large sinusoidal electric field to constantly switch the ferroelectric polarization. A modified Diamant–Pepinsky circuit was used to measure the ferroelectric polarization. The change of ferroelectric polarization due to ferroelectric fatigue was evaluated from the dielectric hysteresis loop displayed by a digital oscilloscope. The cycling electric field was released from the sample, within approximately one second, by gradually reducing the amplitude of the applied electric field to zero. Since the frequency of the cycling electric field was 100 Hz, the sample was cycled by the gradually reducing electric field for approximately 100 cycles during the release of the applied electric field. The domain configuration after the release of electric cycling corresponded to an a.c. field depoled domain configuration. It is such a domain configuration that was characterized by X–ray diffraction.

(3) X–ray Diffraction Study

X–ray diffraction was performed on the ceramic samples after electric poling and electric cycling. The electrode (silver paste) on the major surface (0.6cm x 0.3cm) of the ceramic sample was washed out using acetone and the surface was then exposed to the X–ray beam for X–ray diffraction scanning. A Phillip's X–ray diffractometer controlled by an IBM computer was used for the diffraction study. The scan speed was 0.01° per step with a duration of two seconds at each step.

## EXPERIMENTAL RESULTS AND DISCUSSIONS

Figure 1 shows the X-ray diffraction peaks corresponding to the pseudo-cubic index {200} for the hard PZT (PZT-8) ceramic sample sequentially after electric poling, initial cycling and significant ferroelectric fatigue. After poling, the (200) subpeak was high, implying that substantial domains were still oriented parallel to the major surface without being switched. The (200) subpeak decreased relative to the (002) subpeak after the initial cycling and further decreased after ferroelectric fatigue due to the fact that a significant fraction of domains switched from the orientations parallel to the major surface to the orientation perpendicular to it. Since the major surface was perpendicular to the cycling electric field, it further implies that domains were switched from the orientation perpendicular to the electric field to the orientation parallel to it.

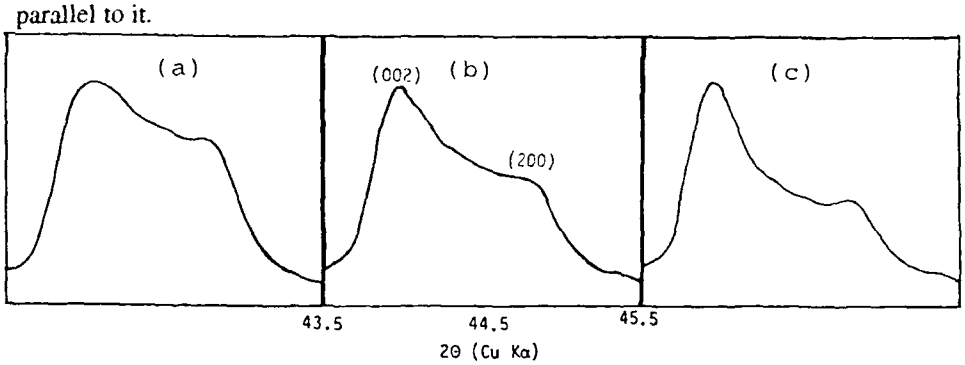


Figure 1: {200} peaks for a hard PZT ceramic sample (a) after poling (45 kV/cm), (b) after initial cycling (3000 cycles) and (c) after ferroelectric fatigue ($8.46 \times 10^5$ cycles). The remanent polarization of the sample was 25.7 $\mu C/cm^2$ initially, 24.2 $\mu C/cm^2$ after initial cycling and 5.3 $\mu C/cm^2$ after ferroelectric fatigue. The amplitude of the cycling electric field was 28.5 kV/cm.

The rotation of domains can be explained well by two processes which took place during the electric cycling : the a.c. field de-aging and the ferroelectric fatigue. The a.c. field de-aging effect is the process in which the domains which have been stabilized by the aging break away from the stabilized directions and participate in ferroelectric switching.[11] The ferroelectric fatigue is the process in which the domains which have already participated in ferroelectric switching lose the ferroelectric nature and get stabilized. During the a.c. field de-aging process, the domains oriented perpendicular to the cycling field were rotated to the direction of the applied electric field to participate in the polarization reversal. During ferroelectric fatigue, the domains were eventually stabilized in the orientation of the electric cycling. The domains stabilized by fatigue could withstand the depoling effect during the electric field release to remain in the orientation of the electric cycling. As a result, a net conversion of domains, from the orientations perpendicular to the cycling electric field to the orientation parallel to it, was observed when the sample changed from the initially cycled state to to the fatigued state. It should be pointed out that the domains excited by the a.c. field de-aging effect can replenish the domains stabilized by fatigue and modify the initial apparent fatigue

rate. We found out that when the ceramic was seriously aged and the applied electric field was insufficiently large, the "replenishing" rate due to the a.c. field de-aging could lead to an initial increase of the observed ferroelectric polarization. This effect was also observed in a sol-gel deposited PZT thin film by Dey et al..[12].

X-ray diffraction was also performed on several soft PLZT ceramic compositions across the tetragonal-rhombohedral morphotropic phase boundary (MPB) sequentially after the electric poling, initial cycling and ferroelectric fatigue. The initial cycling was continued for about 3000 cycles and over 95% of the initial ferroelectric polarization remained after the initial cycling for the compositions. Ferroelectric fatigue was continued after the initial cycling, until approximately one-third of the initial ferroelectric polarization was reached. The X-ray diffraction peaks corresponding to the pseudo-cubic index {200} for a PLZT 7/60/40 ceramic sample are shown in Figure 2. Apparently, the valley separating the (002) subpeak and (200) subpeak was deeper after electric poling and ferroelectric fatigue than after the initial cycling.

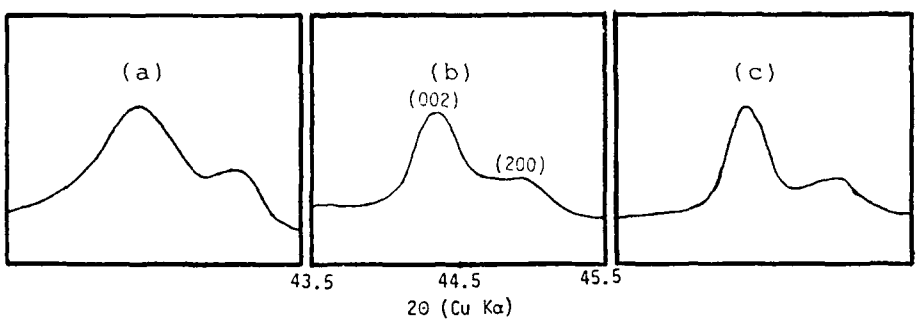


Figure 2 : {200} peaks for a soft PLZT 7/60/40 ceramic sample (a) after poling (40 kV/cm), (b) after initial cycling (3000 cycles) and (c) after ferroelectric fatigue ($5.238 \times 10^6$ cycles). The amplitude of the cycling electric field was 23 kV/cm. The remanent polarization was 20 $\mu C/cm^2$ initially, 19 $\mu C/cm^2$ after initial cycling and 6.2 $\mu C/cm^2$ after ferroelectric fatigue.

For a tetragonal composition near the MPB, the intensity at the valley is raised by the rhombohedral phase which has a {200} d-space in between the (200) d-space and (002) d-space of the tetragonal due to the coexistence of the two phases. For the bulk sample X-ray diffraction, the unit cells which contribute to the intensity of {200} peak are those cells with their {200} d-space parallel to the major surface upon which X-ray incidents. For the tetragonal phase, the contributing cells are the cells with the spontaneous polarization vectors perpendicular or parallel to the major surface. For the rhombohedral phase, the contributing cells are those with the spontaneous polarization vectors inclined to the major surface by approximately either $54.7^o$ or $144.7^o$. The deepening of the valley for the poled state is due to the fact that the rhombohedral cells had been converted into tetragonal cells parallel to the applied electric field via a rhombohedral to tetragonal phase switching. The increase of the intensity at the valley after the initial cycling is due to the fact that the a.c. field depoling effect during the electric field release drove some of the polarization vectors parallel to the cycling electric field back to the orientations inclined to the field via a tetragonal to

rhombohedral phase switching. After ferroelectric fatigue, the polarization vectors converted from the rhombohedral phase were stabilized in the tetragonal form parallel to the field and could withstand the depoling effect during the release of the cycling field.

Figure 3 shows the {200} peaks after the initial electric cycling and after ferroelectric fatigue for four PLZT ceramic compositions near the morphotropic phase boundary. For the tetragonal compositions 7/58/42 and 7/60/40, the deepening effect is quite obvious. For the MPB composition 7/62.5/37.5, and rhombohedral composition 7/65/35, the deepening effect is less obvious. Clearly, as the rhombohedral nature of the composition increases, the rhombohedral phase is more stable, a phase conversion from the rhombohedral to the tetragonal becomes more difficult.

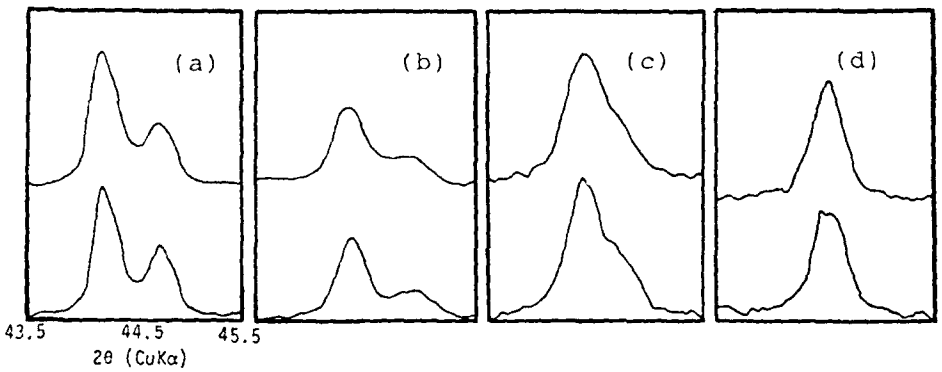


Figure 3: {200} peaks for four PLZT ceramic compositions, (a) 7/58/42), (b) 7/60/60, (c) 7/62.5/37.5 and (d) 7/65/35. The upper peaks: after initially cycling (3000 cycles) and bottom peaks: after ferroelectric fatigue. The amplitude of the cycling electric field was 23 kV/cm.

The results of this investigation are quite consistent with our earlier observed directional nature of ferroelectric fatigue.[6] Both investigations suggest that the pinning force that impedes the ferroelectric switching is effective only in the orientation of the electric cycling. In the earlier investigation, virgin ferroelectric properties were measured perpendicular to the orientation along which the ferroelectric ceramic was cycled and fatigued[6] due to the directional nature of this pinning force. In this investigation, the pinning force built up by the electric cycling maintained spontaneous polarization vectors in the orientation of the electric cycling and prevented them from being randomized when the cycling electric field was released. We think that the reorientation and directional migration of the defects and/or space charge by the applied electric field are responsible for the build-up of the directional pinning force. Although the bipolar sinusoidal electric field averages to zero over a long time, it is polar within a half period during which the reorientation and directional migration of defects and/or space charge can build up a space charge field which counteracts the applied field and cause back-switching when the applied field reaches zero.[13] The polarization vectors switched by the space charge field are coupled with the space charge field, leading to a mutual stabilization of each other and an increased resistance to further switching when

the polarity of the field is changed. In this manner, ferroelectric fatigue cumulates with switching cycles. For the hard PZT ceramic, the defects are initially randomly oriented to stabilize the domains in a random configuration via aging effect. The cycling electric field constantly reorients these defects dipoles to its orientation, the pinning force therefore changes from being isotropic to being one dimensional. The amplitude of the pinning force may be expected to increase when the three dimensional defect distribution is converted to the one dimensional distribution. In the soft PLZT ceramics, the dielectric aging effect was minimal and the spontaneous polarization vectors were not stabilized significantly before the electric cycling. Apparently, a simple orientation of the existing defects cannot amplify the pinning force to the extent to cause fatigue. We believe that the directional migration of the defects by the applied electric field, which leads to a concentration polarization, amplifies the pinning effect of global existing defect to cause ferroelectric fatigue. If the defects are electronic in nature, the charge externally injected during the electric cycling can also amplify the pinning force to cause ferroelectric fatigue.

## ACKNOWLEDGMENTS

The authors would like to thank Dr. Bruce Tuttle for valuable discussions. The financial support for this work was provided by Sandia National Laboratories via University–Sandia Research Proposal Grants. Copy editing was provided by G. Zamora of New Mexico Tech Public Information Office.

## REFERENCES

1 Proc. 7th International Symposium on Applications of Ferroelectrics, June 6–8, 1990, Urbana Champaign, IL.
2 Proc. of 3rd International Symposium on Integrated Ferroelectrics, April 3–5, 1991, Colorado Spring, CO.
3 W.R. Salaneck, Ferroelectrics, **4** pp97–101, (1972).
4 K.Carl, Ferroelectrics, **9** pp23–32, (1975).
5 C.F. Pulvar and J.R. Sprour, IEEE Transaction on Electron Devices, Vol. Ed 1–6, pp532–35, (1969).
6 W.Y. Pan, C.F. Yue and B. A. Tuttle, Submitted to J. Amer. Ceram. Soc., A special issue for Sympoium on Ferroelectric Thin Films, 93rd Annual Meeting of American Ceramic Society, Cincinnati, OH, 1991.
7 C. A. Paz De Araujo, T. Mihara, As Carrico, Proc. 3rd International Symposium on Integrated Ferroelectrics, April 3–5, 1991.
8 J. F. Scott and C.A. Paz de Araujo, Science **246**, pp1400, (1989).
9 H. Neumann and G. Arlt, Ferroelectrics, **76**, pp303–10 (1987).
10 W.Y. Pan, Q.M. Zhang, Q.Y. Jiang and L.E. Cross, Ferroelectrics, **88**, pp1–12, (1989).
11 K. Carl and K. H. Hardtl, Ferroelectrics, **17** pp473, (1978).
12 S.K. Dey and R. Zuleeg, Ferroelectrics, **112** pp309–19, (1990).
13 R. William, J.Phys. Chem. Solids, Pergamon Press **26**, pp399 (1964).

*Ferroelectrics*, 1992, Vol. 133, pp. 103–108
Reprints available directly from the publisher
Photocopying permitted by license only

© 1992 Gordon and Breach Science Publishers S.A.
Printed in the United States of America

# ThI3

## THERMODYNAMIC PHENOMENOLOGY OF SELECTED COMPOSITIONS IN THE LANTHANUM-MODIFIED LEAD ZIRCONATE-TITANATE SOLID SOLUTION SYSTEM

GEORGE A. ROSSETTI, JR.
Materials Research Laboratory, The Pennsylvania State University
University Park, Pennsylvania 16802 USA

Abstract The application of the Landau-Devonshire thermodynamic formalism to selected compositions in the La-modified PZT system is described. For both pure lead titanate and PZT 65/35, experimental data least likely to be influenced by the elastic boundary conditions in polycrystalline specimens are used to investigate the renormalization of the phase transition temperature and higher-order dielectric stiffness coefficients as a function of the extent of lanthanum doping. Implications with regard to the intrinsic elastodielectric properties and phase transition behavior are briefly discussed.

## INTRODUCTION

Perovskite-structured solid solutions in the $(Pb,La)(Zr,Ti)O_3$ (PLZT) system find applications as piezoelectric and optoelectronic materials. From a theoretical as well as practical point of view, an important characteristic feature of these materials is that they exhibit increasingly diffuse and/or relaxor ferroelectric phase transition behavior as the extent of the aliovalent substitution of lanthanum is increased at a fixed Zr/Ti ratio. Due, in part, to the lack of suitable quality single-crystals, the intrinsic properties of technologically important compositions showing this type of behavior are not well understood. In separating the intrinsic, single-domain contributions to properties from extrinsic factors, it proves useful to describe these properties within the context of the Landau-Devonshire thermodynamic formalism, the relevant parameters of which are determined from spontaneous strain and calorimetric measurements made on powder specimens. These data are preferred because they are not likely to be strongly compromised by the effects of elastic boundary conditions, which are uncertain in densely sintered ceramics, and which can significantly alter the phase transition behavior and ferroelectric properties, particularly in the case of PLZT.[1] In addition, although the renormalized transition temperature in impure crystals may be difficult to determine directly due to the presence of defect tails associated with fields conjugate to the order parameter,[2] for second-order transitions, it can be conveniently extrapolated from the low temperature spontaneous strain data based on the expectation of simple Landau-Devonshire behavior.

This approach has been previously used to characterize, on a simple phenomenological basis, the effects of aliovalent La-doping on the renormalization of the phase transition temperature and higher-order dielectric stiffness coefficients for the rhombohedral PZT 65/35 composition.[3] Consistent with other more direct determinations,[4] the extrapolated transition temperature was found to be independent of the La dopant concentration, and to coincide with that of the pure PZT end member. Using typical values for the electrostrictive constants, the root mean squared (RMS) polarization determined from the spontaneous strain data agreed well with the remanent polarization obtained directly from dielectric hysteresis measurements[5] at low temperature, although, as expected, the values derived using the two methods began to differ substantially as the transition temperature was approached. Fitting of the RMS polarization data to the Landau-Devonshire formalism showed that although the sixth-rank dielectric stiffness was not strongly renormalized by the addition of lanthanum, the fourth-rank coefficient increased markedly. This then predicted a sharp decrease in the magnitude of the elastic Gibbs free-energy density with increasing lanthanum doping, and gave rise to near degeneracy of the rhombohedral, orthorhombic, and tetragonal energies over a considerable temperature interval below the onset of the transition. These findings were in agreement with the fact that only modest additions of lanthanum (12-15 mol %) are required to induce cubic symmetry in this composition at room temperature[5], and with X-ray scattering measurements,[6] that showed no well defined rhombohedral distortion until 80 °C below the temperature at which a local polarization could first be detected.

In this paper, some of the main observations from experiments recently conducted on La-modified lead titanate are summarized. This composition is considered representative of the tetragonal side of the PZT phase diagram, and in contrast to the PZT 65/35 composition, was chosen to investigate the effects of lanthanum doping on transitions that are initially strongly first-order. As with the PZT composition, however, these experiments were restricted to low level (< 4 mol %) lanthanum additions. At these dopant levels, substantial smearing of the phase transition does not occur, and so the simply formulated Landau-Devonshire formalism is expected to be valid over an appreciable temperature interval (not too close to the transition). The detailed findings of these studies, along with work currently in progress, will be reported in a future publication.

THERMODYNAMICS

In contracted tensor notation, an appropriate modified form of the Devonshire energy function for lead titanate is:[7]

$$
\begin{aligned}
G_1 = \; & \alpha_1(P_1^2 + P_2^2 + P_3^2) + \alpha_{11}(P_1^4 + P_2^4 + P_3^4) \\
& + \alpha_{12}(P_1^2P_2^2 + P_2^2P_3^2 + P_3^2P_1^2) + \alpha_{111}(P_1^6 + P_2^6 + P_3^6) \\
& + \alpha_{112}[P_1^4(P_2^2 + P_3^2) + P_2^4(P_1^2 + P_3^2) + P_3^4(P_1^2 + P_2^2)] \\
& + \alpha_{123}(P_1^2P_2^2P_3^2) - 1/2s_{11}(X_1^2 + X_2^2 + X_3^2) - s_{12}(X_1X_2 + X_2X_3 + X_3X_1) \\
& - 1/2s_{44}(X_4^2 + X_5^2 + X_6^2) - Q_{11}(X_1P_1^2 + X_2P_2^2 + X_3P_3^2) \\
& - Q_{12}[X_1(P_2^2 + P_3^2) + X_2(P_1^2 + P_3^2) + X_3(P_1^2 + P_2^2)] \\
& - Q_{44}(X_4P_2P_3 + X_5P_1P_3 + X_6P_1P_2) \qquad (1)
\end{aligned}
$$

where $P_i$ and $X_i$ are the polarization and stress, respectively; $\alpha_i$, $\alpha_{ij}$, $\alpha_{ijk}$ are the dielectric stiffness and higher order stiffness coefficients at constant stress; $s_{ij}$ are the elastic compliances at constant polarization; and $Q_{ij}$ are the cubic electrostrictive constants in polarization notation. The function is complete through the sixth-rank terms in polarization, but contains only the first allowed elastic and coupling terms. The dielectric stiffness constant, $\alpha_1$, is given a linear temperature dependence based on the Curie-Weiss law. All other coefficients are taken to be independent of temperature, an assumption that appears to be generally valid for lead-based perovskites exhibiting transitions to only one of the symmetry allowed ferroelectric phases.

In the present instance, Eq. (1) has two relevant solutions corresponding to the prototypic cubic (*Pm3m*, $P_1^2=P_2^2=P_3^2=0$) and ferroelectric tetragonal (*P4mm*, $P_1^2=P_2^2=0$, $P_3^2 \neq 0$) states. The spontaneous polarization ($P_s=P_3$) is determined from the first partial derivative stability condition

$$\delta G_1/\delta P_3 = 0 \qquad (2)$$

and the spontaneous strain matrix from

$$\delta G_1/\delta X_i = -x_i \qquad (3)$$

Equating the energies of the tetragonal and cubic states, and combining with Eq. (2) and (3), one obtains for the higher-order dielectric stiffnesses

$$\alpha_{11} = [-(T_c - \theta)]/\varepsilon_o C P_o^2 \qquad \alpha_{111} = [(T_c - \theta)]/2\varepsilon_o C P_o^4 \qquad (4)$$

and for the spontaneous strains

$$x_1 = \psi Q_{12} P_o^2 \qquad x_3 = \psi Q_{11} P_o^2 \tag{5}$$

with $P_o$ the polarization at the transition and $\psi = (2/3)\{1 + (1 - 3[T - \theta]/4[T_c - \theta])^{1/2}\}$. The spontaneous strains are defined in terms of the tetragonal lattice constants $a_t$, $c_t$ by

$$x_1 = (a_t - a'_c)/a'_c \qquad x_3 = (c_t - a'_c)/a'_c \tag{6}$$

where the extrapolated cubic cell constant $a'_c$ may be expressed using Eq. (3) and (6) as[7]

$$a'_c = [a_t - (c_t)Q_{12}/Q_{11}]/(1 - Q_{12}/Q_{11}) \tag{7}$$

The value of $Q_{12}/Q_{11}$ is determined from Eq. (3) at a temperature close to the transition and is taken to be independent of temperature. The strain, when fitted to Eq. (5), gives the values for $\theta$ and $P_o$. The Curie constant and higher-order dielectric stiffnesses may then be obtained with the aid of the relation

$$\delta G_1/\delta T = \Delta H/T_c = P_o^2/2\varepsilon_o C \tag{8}$$

In order to implement these relations, precise lattice constants have been determined as a function of temperature by refinement from wide angle scans obtained on a diffractometer equipped with an incident beam monochromator and position sensitive detector. Transition temperatures and enthalpies were assessed from differential scanning calorimetry performed at modest scan rates. All measurements were conducted on well crystallized, sol-gel derived powders having the general formula $Pb_{1-\alpha x}La_xTiO_3$ where $\alpha \approx 1.5$.

## SUMMARY OF RESULTS AND DISCUSSION

The calorimetric measurements indicated a linear change in Curie temperature of slightly less than -20 °C/mol % La, the same as that previously adduced from dielectric measurements.[8] For doping levels as low as 0.5 mol %, there was no indication of a plateau effect[2]. At the same time, these low doping levels gave rise to a rather dramatic loss in the first-order character of the transition, as evidenced by rapidly diminishing values of the transition enthalpy, $P_o$, and $T_c - \theta$. The Curie constant, on the other hand, was not strongly dependent on the lanthanum concentration. As with the La-modified PZT 65/35 compositions, these changes in

phase transition behavior manifested themselves in a strong renormalization of the fourth-rank dielectric stiffness with almost no renormalization of the sixth-rank term. Consistent with experimental findings[8], substitution of these values into Eq. (1) predicted an increase with La content in the dielectric susceptibility and piezoelectric charge coefficient along the polar axis. If the ratio $\phi = -\alpha_{12}/\alpha_{11}$ is constrained to a value sufficient to maintain metastability of the orthorhombic phase, an increase in the dielectric anisotropy $\eta_{11}/\eta_{33}$ may also be expected.

In considering the changes in the order of a transition subject to the variation of an external parameter, it is instructive[9] to rewrite the elastic Gibbs energy using the transformation

$$G_1(X,P) = A(x,P) - xX \tag{9}$$

where

$$A(x,P) = A_1(P) + A_2(x) + A_3(x,P) \tag{10}$$

with A(x,P) representing the Helmholtz energy and where X, x, and P are identified with the stress, strain, and polarization, respectively. If $A_1(P)$ has the usual Landau form, it is found that, by calculating the strain from the condition $\delta G_1(X,P)/\delta x = 0$, higher-order terms in $A_2(x)$ and/or $A_3(x,P)$ are required to change the order of the transition.[9] In view of the strong coupling to the strain in lead titanate, at least for illustrative purposes, a reasonable approximation might be to add a biquadratic coupling term.[10] The terms in Eq. (10) are then

$$\begin{aligned} A_1(P) &= \alpha P^2 + \gamma P^4 + \delta P^6 \\ A_2(x) &= cx^2 \\ A_3(x,P) &= gxP^2 + hx^2P^2 \end{aligned} \tag{11}$$

where $\alpha$, $\gamma$, and $\delta$ are the Helmholtz dielectric stiffnesses and c, g, and h are the appropriate elastic and coupling constants. When $X \equiv 0$, the fourth-rank dielectric stiffness coefficient in Eq. (9) takes the form $\gamma - g^2/2c$, while the sixth-rank term becomes $\delta + g^2h/4c^2$. In previous investigations, compositionally driven lowering of the $g^2/2c$ coupling term has been proposed as a possible mechanism for the tricritical behavior in the PZT system.[11,12] This suggestion can be more fully explored by investigating the tensorial nature of this term according to Eq. (1). It is straightforward to show that

$$\begin{aligned} \alpha_{11} &= \gamma_{11} - \{2(Q^2_{11} + 2Q^2_{12})\, c_{11} + 4Q_{12}(2Q_{11} + Q_{12})\, c_{12}\} \\ \alpha_{12} &= \gamma_{12} - \{2Q_{12}(2Q_{11} + Q_{12})\, c_{11} + 2(Q^2_{11} + 3Q^2_{12} + 2Q_{11}Q_{12})\, c_{12} + Q^2_{44}\, c_{44}\} \end{aligned} \tag{12}$$

For lead titanate, the value of $\alpha_{11}$ has been estimated[7] to be $\approx -7 \times 10^7 m^5/C^2F$. From single crystal data,[13] the second term on the right of Eq. (12) is expected to be more than an order of magnitude larger. Consequently, within the quasi-homogeneous approximation dictated by the assumptions implicit in Eq. (1), the strong renormalization of the fourth-rank dielectric stiffness observed on La-doping can conceivably occur owing to rather subtle changes in the elastic and electrostrictive constants, even if $\gamma_{11}$ is unaltered. Alternatively, this same effect may be ascribable to an effective lowering of the coupling term due to localized strain nonuniformity. Given the changes in X-ray line profiles as observed for La-doped PZT 65/35, [3,6] the latter explanation seems the more plausible one and similar X-ray scattering studies on La-doped lead titanate are currently underway.

In summary, the Landau-Devonshire formalism provides useful insight into the phase transition behavior and intrinsic physical properties of La-modified PZT compositions. Within the context of this simple approach, the primary initial effect of lanthanum doping for both lead titanate and PZT 65/35 appears as an increase in the fourth-rank dielectric stiffness. This effect may be interpreted as arising due to an effective lowering of the electrostrictive coupling related terms.

## REFERENCES


1. A. J. Burggraaf and K. Keizer, Mater. Res. Bull., 10, 521 (1975).
2. E. Salje, U. Bismayer, B. Wruck, and J. Hensler, Phase Transitions, 35, 61(1991).
3. G. A. Rossetti, Jr., T. Nishimura, and L. E. Cross, J. Appl. Phys., 70, 1630 (1991).
4. G. Burns and F. Dacol, Phys. Rev., B28, 2527 (1983).
5. G. H. Haertling, J. Am. Ceram. Soc., 54, 303 (1971).
6. C. N. W. Darlington, J. Phys., C21, 3851 (1988).
7. M. J. Haun, E. Furman, S. J. Jang, H. A. McKinstry, and L. E. Cross, J. Appl. Phys., 62, 3331 (1987).
8. K. Keizer and A. J. Burggraaf, Ferroelectrics, 14, 671 (1976).
9. L. Benguigui, Phys. Stat. Sol. (b), 60, 835 (1973).
10. E. Pytte, Phys. Rev., B5, 3758 (1972).
11. K. Roleder and J. Handerek, Phase Transitions, 2, 285 (1982).
12. R. W. Whatmore, R. Clarke, and A. M. Glazer, J. Phys., C11 3089(1978).
13. H. Landolt and B. Bornstein, Ferroelectrics: Oxides, (Springer-Verlag, Berlin, 1981) vol. III/16a.

*Ferroelectrics*, 1992, Vol. 133, pp. 109–114
Reprints available directly from the publisher
Photocopying permitted by license only

© 1992 Gordon and Breach Science Publishers S.A.
Printed in the United States of America

**TrI4**

# THE ROLE OF GRAIN BOUNDARIES IN CONDUCTION AND BREAKDOWN OF PEROVSKITE-TYPE TITANATES

RAINER WASER *
Philips GmbH Forschungslaboratorien, W–5100 Aachen, Germany

Abstract Based on the defect chemistry of acceptor–doped strontium titanate model materials, the role of interfaces in conduction and voltage–induced failure mechanisms is discussed. The impedance behaviour of conventional ceramics and ceramic thin films is compared.

## 1 Introduction

A variety of dielectric components for electronic applications are based on perovskite–type titanates such as barium titanate and lead based perovskites (e. g. lead titanate zirconate, PZT) as well as related materials. Among these components are ceramic multilayer capacitors, ceramic multilayer actuators, as well as ferroelectric random access memories (FRAMs) and other ceramic thin film devices. Although the application conditions differ considerably, most of these components are subjected to high dc electrical fields during varying periods of their life. Especially in combination with high operating temperatures, this may give rise to dc voltage–induced failure mechanisms. Despite the fact that ceramic components today usually exhibit very low failure rates, there is a permanent challenge for an even further improvement of their reliability. An essential contribution towards this aim is the investigation into **residual conductivity** and the conduction mechanism as well as into the underlying mechanism of **material–inherent failure modes**. The importance of this task steadily increases due to the sustaining trend towards further miniaturization of the multilayer devices. For multilayer capacitors, besides enhancing the permittivity of the material, this is primarily achieved by a reduction of the thickness of the dielectric layers. As a consequence, the field stress in the ceramic material increases if the specified voltage rating of the capacitor types is kept constant. Hence, we have to consider the material–inherent dc voltage–induced failure modes which can, in principle, occur in all dielectric materials.

For the studies reported in this paper, acceptor–doped $SrTiO_3$ served as a model material. Single crystals, ceramics, and thin films of the same composition were investigated in order to separate impedance contributions of the bulk, the electrode interfaces, and – in particular – the grain boundaries.

* present address: Institut für Werkstoffe der Elektrotechnik II, RWTH Aachen
Templergraben 55, W–5100 Aachen, Germany

## 2 Defect chemistry of titanates

The types and concentrations of charge carriers in the crystal lattice of barium or strontium titanate are determined by the defect chemistry and are affected by the temperature, the oxygen partial pressure during annealing, $P_{O_2}$, and the concentration of dopants. The defect chemistry of titanates in the high temperature regime (approx. T > 900 K) were the subject of several comprehensive studies. The reader is referred to the contribution of D. M. Smyth [1] and the references cited therein. The high temperature regime is characterized by equilibria with the $P_{O_2}$ of the ambient atmosphere which are established within reasonable times. Since undoped titanates are usually governed by an unknown concentration of acceptor–type dopants, slightly acceptor–doped titanates represent better defined model systems and were used in the present study.

The defect chemistry of acceptor–doped titanates after quenching from high temperature equilibria to temperatures at which the oxygen content is frozen–in (approx. T < 700 K) has been investigated recently by means of the impedance analysis [2]. This temperature regime is relevant for the regular operation of electronic ceramic components. It has been shown that annealing in the regime of conventionally oxidizing to moderately reducing atmospheres leads to a **dominant ionic conductivity** and a certain contribution by a **p–type electronic conductivity**. The mobile ionic species are oxygen ions which move by a vacancy mechanism. The mobility of the oxygen vacancies, $V_O^{\cdot\cdot}$ (notation: see [3]), is thermally activated with an activation energy of 1.0 to 1.1 eV which fits well to high temperature data [4]. Holes (and electrons as well) can be regarded as polarons in the titanate lattice which move by a hopping process.

Donor–doped titanates show a different conduction mechanism due to the very low concentration of $V_O^{\cdot\cdot}$. Single crystal and coarse–grained ceramic are semiconducting due to an electron compensation of the donor centers, while fine–grained ceramic sintered under oxidizing atmospheres is highly insulating at room temperature due to a cation vacancy compensation [5]. While in both cases there is virtually no ionic transport in the lattice due to the low mobility of the cation vacancies, oxygen ions are known to show a certain motion along the grain boundaries under gradients of the oxygen activity or the electrical potential [6].

## 3 Conduction through grain boundaries

In Section 2, the defect chemistry of the bulk crystal lattice of acceptor–doped titanates is sketched. In **ceramic devices**, the grain boundaries (GB) as well as the metal electrode interfaces (EI) contribute to the total impedance of a component as illustrated by the simplified network in Fig. 1. It is well known that ionically conducting ceramics as, for instance, stabilized $ZrO_2$ [9] as well as mixed conducting ceramics such as titanates [10, 11] tend to build highly resistive layers at electrode and GB interfaces. These are commonly interpreted as **depletion space charge layers** similar to Schottky barriers at semiconductor interfaces [12]. Consequently, the conductivities $\sigma_{EI}$ and $\sigma_{GB}$ are usually very small compared to the bulk conductivity $\sigma_b$ because the corresponding layers are strongly depleted by charge carriers. In conventional ceramics, the depletion layer thicknesses $d_{GB}$ and $d_{EI}$

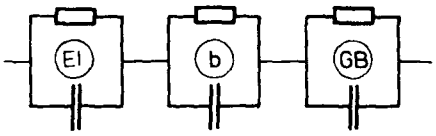


FIGURE 1: Simplified electrical equivalent network of a titanate ceramic illustrating the conduction and polarization contributions. The contributions of both electrode interfaces are merged into the branch 'EI'. The contributions of all grains and all grain boundaries are merged into the branch 'b' and the branch 'GB', respectively.

are approx. 100 nm and, hence, much smaller than the grain size $d_{gr}$ of conventional ceramics:

$$d_{gr} \gg d_{GB}, d_{EI} \quad . \tag{1}$$

Usually, the large number of grain boundaries crossing the current path between the electrodes outweighs the influence of the just two electrode interfaces (EI) on the impedance of a ceramic component. In the present study, the impedance contributions were determined by an impedance analysis technique in the time domain based on recording the time evolution of the current response after applying a dc voltage step [7, 8]. After applying the voltage step, the Maxwell–Wagner polarization causes the current to decay in a manner which is typical for a Debye relaxation:

$$J \propto \exp(-t/\tau_R) \tag{2}$$

where $\tau_R$ is the relaxation time of the space charge polarization at the grain boundaries. Switching off the applied voltage leads to a depolarization current of reversed sign which proceeds until the capacitive elements are discharged. Fig. 2a shows the results of dc voltage step experiments at different field strengths E for Ni acceptor–doped $SrTiO_3$ ceramics. The regimes of the |J/E| curves are formally attributed to components of the schematic equivalent network (Fig. 1). These assignments are confirmed by additional experiments using samples of different grain sizes and different sample thicknesses.

The local conductivity $\sigma_{GB}$ in the GB depletion layer is calculated from the long–term conductivity $\sigma_l$, the geometry of the system in combination with relation (1), and the fact that usually $\sigma_l \ll \sigma_b$ :

$$\sigma_{GB} \approx \frac{d_{GB}}{d_{gr}} \cdot \sigma_l \quad . \tag{3}$$

For the system shown in Fig. 2, $\sigma_{GB}$ turns out to be more than **four** orders of magnitude below the conductivity $\sigma_b$ in the bulk of the grains (Fig. 2b). In combination with the fact that the ionic conductivity in the crystalline bulk of e. g. Ni–doped $SrTiO_3$ is dominating but still in a similar order of magnitude as the electronic conductivity, this means that the GB depletion layers build significant barriers for the cross transport of **both** ionic and electronic charges.

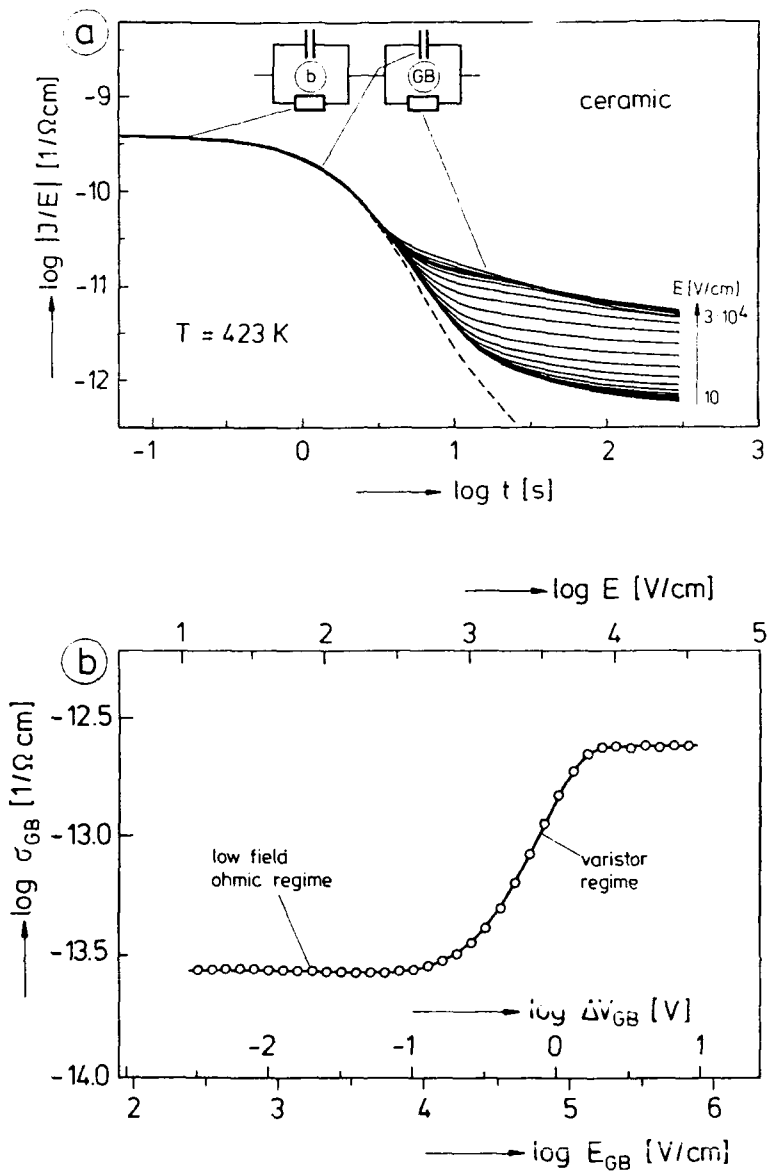


FIGURE 2 (a) Current density – field ratio |J/E| vs. time t for a fine grained, 0.1 at% Ni–doped $SrTiO_3$ ceramic at T = 423 K for different dc voltage steps corresponding to dc fields in the range E = 10 V/cm to $3 \cdot 10^4$ V/cm. The determining components of the equivalent network are sketched on top. The discharging curve (dashed line) is shown for E = 300 V/cm. (b) Field dependence of the conductivity at t = 300 s in diagram (a), interpreted as the conductivity in the GB space charge layer $\sigma_{GB}$ [8]. Abszissa from top to bottom: externally applied field at the sample E = U/d, voltage drop at a grian boundary $\Delta V_{GB}$, and field across a GB depletion layer $E_{GB}$. Thickness of the sample: d = 500 μm. Average grain size: $d_{gr}$ = 2.5 μm. Sample preparation: see [2].

## 4 Ultrafine-grained ceramic thin films

Ni–doped $SrTiO_3$ thin films of 0.3 – 1 μm thickness were prepared using a modified sol/gel spin coating technique which is discussed in the contribution of M. Klee and P. Larsen [13]. The films have been subjected to an impedance analysis in the time domain using the temperature and the electrical field as parameters. Details are reported in Ref. [8].

As in the ceramic, the **polarization** current predominates in the beginning after applying a dc voltage while at long times the current is determined by the **conduction** through the film. The eminent difference between the space charge polarization behaviour of the ceramic and the thin film of the composition is given by the fact that the first shows a Debye relaxation, Eq. (2), while the latter is described by a Curie – von Schweidler law (the so–called "universal law" [7]):

$$J \propto t^{-m} \quad . \tag{4}$$

An exponent m of approx. 0.5 with a slight temperature dependence is observed [8]. The time dependence expressed by Eq. (4) is usually found for disordered systems. Possibly, its occurrence can be attributed to the extremely fine–grained microstructure of the thin films described here. The grain size is below the GB space charge layer width in conventional ceramics. Hence, no region with a bulk conductivity can be expected in the ultrafine–grained thin films due to the overlap of the GB depletion layers. Instead, a distributed spectrum of local conductivities on a level far below the bulk conductivity of the material may be assumed giving rise to a polarization behaviour according to Eq. (4). The average conductivity of the 0.1 at% Ni–doped $SrTiO_3$ thin film was found to be very significantly below the bulk conductivity of the material and close to the residual conductivity in the GB depletion space charge layer. This indicates unequivocally that the complete film is strongly depleted of mobile charge carriers compared to a bulk crystal.

## 5 High–field conduction and breakdown

In Fig. 2b, $\sigma_{GB}$ is shown for Ni–doped ceramic as a function of the externally applied field $E = U/d$. After the Maxwell–Wagner polarization is settled, the grain bulk regions are virtually field–free. Based on this, additional abscissa are included in Fig. 2b showing the actual field across the GB depletion layer, $E_{GB}$, and the voltage drop per grain boundary, $\Delta V_{GB} = E_{GB} \cdot d_{GB}$. At a low voltage drop, $\sigma_{GB}$ exhibits an ohmic behaviour. Above approx. $\Delta V_{GB} = 0.5$ V, $\sigma_{GB}$ starts to enhance strongly with incremented voltages. This varistor–type regime is succeeded at very high fields by another ohmic regime. Adopting the interpretation for grain boundaries in n–type semiconducting ceramics (see Ref. [14] and references cited therein), the ohmic regime at low voltages and the varistor regime of GB depletion space charge layers in the mixed conducting acceptor–doped $SrTiO_3$ ceramics can be described in terms of charge transport over a Schottky barrier [8]. The nature of the subsequent high–field ohmic regime in Fig. 2b may be caused by the specific density of GB state distribution of Ni–doped $SrTiO_3$ ceramic.

The voltage dependence of the conductivity of Ni–doped $SrTiO_3$ thin films is similar to grain boundaries. At low fields, an ohmic regime is observed. Above an onset voltage, the conductivity exhibits an enhancement over many orders of magnitude [8]. The high–

field ohmic plateau which was observed for grain boundaries is much less pronounced for thin films. Although the mechanism is not yet completely elucidated, a working model is suggested by the author which characterizes the behaviour of the titanate thin films as an electron emission over an extended Schottky barrier.

As described, grain boundaries give rise to depletion regions which act as barriers for the cross transport of charge carriers. Hence, for ceramics and fine–grained thin films in comparison with single crystals the residual leakage current is reduced and the onset of the **thermal breakdown** is shifted to higher fields. In contrast to large band–gap materials such as $SiO_2$ [15], however, a thermal breakdown always sets in before purely dielectric breakdown mechanisms are triggered in titanates. This is due to their relatively low band gap and it is supported by the varistor–type behaviour of the charge transport across interfaces.

Even moderate temperatures and dc voltages applied to acceptor–doped titanates lead to a breakdown mechanism which is known as the long–term **resistance degradation** [16]. This effect is caused by a concentration polarization of the oxygen vacancies between the anode and the cathode. Details are reported in Refs. [17]. Grain boundaries show a pronounced impact on the degradation rate. It was observed that the degradation rate strongly decreased with increasing numbers of grain boundaries between the electrodes. This was attributed to the barrier character of the space charge depletion layers at grain boundaries discussed above [18].

## References


1. D. M. Smyth, *Proceedings of the 2nd European Conference on Applications of Polar Dielectrics ECAPD2*, Ferroelectrics (present volume).
2. R. Waser, *J. Am. Ceram. Soc.*, **74**, 1934 (1990).
3. F. A. Kröger and H. J. Vink, *Solid State Physics* **3**; Ed. F. Seitz and D. Turnbull, Academic Press, New York 1956.
4. N.–H. Chan, R. K. Sharma, and D. M. Smyth, *J. Am. Ceram. Soc.*, **64**, 556 (1981).
5. J. Daniels, K. H. Härdtl, D. Hennings, and R. Wernicke, *Philips Res. Rep.*, **31**, 489 (1976).
6. K. Okazaki, *Adv. Ceram.*, **1**, 23 (1979).
7. A. K. Jonscher, Dielectric Relaxation in Solids, Chelsea Dielectrics Press Ltd., London 1983.
8. R. Waser and M. Klee, *Proceedings of the 3rd International Symposium on Integrated Ferroelectrics ISIF'91*, Ferroelectrics, 1992 (in press).
9. T. G. Stratton, D. Reed, and H. L. Tuller, *Adv. Ceram.*, **1**, 114 (1983).
10. H. Neumann and G. Arlt, *Ferroelectrics*, **69**, 179 (1986).
11. H.–Y. Lee, S. S. Villamil, and L. C. Burton, *IEEE Proc. of the 6th ISAF*, Bethlehem, PA, June 8–11, 1986.
12. S. M. Sze, Physics of Semiconductor Devices, John Wiley & Sons, New York 1981.
13. M. Klee and P. K. Larsen, *Proceedings of the 2nd European Conference on Applications of Polar Dielectrics ECAPD2*, Ferroelectrics (present volume).
14. G. E. Pike and C. H. Seager, *Adv. Ceram.*, **1**, 53 (1983).
15. D. R. Wolters and J. J. van der Schoot, J. Appl. Phys., **58**, 831 (1985).
16. K. Lehovec and G. A. Shirn, *J. Apply. Phys.*, **33**, 2036 (1962).
17. R. Waser, T. Baiatu, and K. H. Härdtl, *J. Am. Ceram. Soc.*, **73**, 1645, 1654, 1663 (1990) & T. Baiatu, K. H. Härdtl, and R. Waser, *Brit. Ceram. Proceed.*, **41**, 149 (1989).
18. R. Waser, *Proceedings of the International Summer School on Ferroelectrics*, Ascona, Sep. 2–8, 1991; to be published by Birkenhäuser Verlag.

# SECTION III
# CONTRIBUTED PAPERS

## IIIa. Dielectrics/Domains/Microstructure

*Ferroelectrics*, 1992, Vol. 133, pp. 115–120
Reprints available directly from the publisher
Photocopying permitted by license only

© 1992 Gordon and Breach Science Publishers S.A.
Printed in the United States of America

# DiC7

# AN ORIENTATIONAL GLASS MODEL OF ELECTROSTRICTION IN RELAXOR DIELECTRICS

A.J. BELL, F. CHU AND M. DAGLISH
Laboratoire de Céramique, EPFL, MX-C Ecublens, 1015 Lausanne, Switzerland

Abstract Electrostriction in relaxor dielectrics is discussed in terms of orientational glass behaviour. A phenomenological model is presented for the field-induced polarisation and strain in relaxors which employs parameters from the empirical Vögel-Fulcher relationship. Comparison is made with measured values for different materials and the use of the model as a tool for the optimization of field induced strain in electromechanical devices is discussed.

## INTRODUCTION

Relaxor dielectrics are characterized by a broad maximum in the dielectric permittivity as a function of temperature, together with a dielectric relaxation in the radio frequency range such that the magnitude of the maximum in permittivity decreases and its temperature ($T_m$) increases with increasing frequency of the applied field[1]. In the case of perovskite structure relaxors, there is no change of crystal structure detectable by X-ray diffraction on cooling through $T_m$ and they appear to remain cubic. However at temperatures somewhat lower than $T_m$ the materials are apparently ferroelectric, displaying a square hysteresis loop and a stable spontaneous polarization on poling[2].

Relaxors are of interest for a number of applications. Close to $T_m$ they exhibit large electrostrictive strains which may be utilized in displacement actuators[3]. In their ferroelectric phase they often have useful piezoelectric coefficients which are exploited in a range of sensors and transducers. Large induced pyroelectric coefficients may be observed by the application of applied fields close to $T_m$ and are useful for infra-red detection[4].

In the group of relaxors belonging to the complex perovskites, $Pb(B1_{1-x}B2_x)O_3$ where $x = {}^1/_2$ or ${}^2/_3$, there is considerable scope for the modification of properties to match particular applications by the formation of solid solutions with other perovskite compounds. At present, optimization of compositions for device applications follows an empirical approach, guided by an intuitive understanding of likely effects of modifications to a given material. A deeper understanding of these effects, based upon microscopic models, is being sought, to act as a more accurate guide to materials development. Recently significant progress has been made in identifying the dielectric properties of relaxor dielectrics as being consistent with a spin-glass or orientational-glass model[5]; although the materials appear macroscopically non-polar, the observed properties may be understood in terms of the ordering energies within and between polar clusters.

Of particular current interest is the case of electrostriction in relaxors. Electrostrictive actuators based upon complex perovskite relaxors have shown a number of advantages over conventional piezoelectric actuators; they exhibit a greater useful range of strain, with virtually zero hysteresis and aging. However, they are generally non-linear in their strain-electric field characteristics which can change markedly as a function of temperature. Compositional modifications are presently being explored in order to tailor the strain-field characteristics to particular device applications. An example of the widely

different characteristics that may be obtained from two different relaxor materials at room temperature is given in Figure 1. It would be beneficial to be able to model this behaviour according to the presently held theories of relaxor dielectrics in order to guide the development of specific strain-field characteristics. In the following, a model of the strain and polarization in relaxor dielectrics, based upon an orientational glass interpretation of relaxors, is presented.

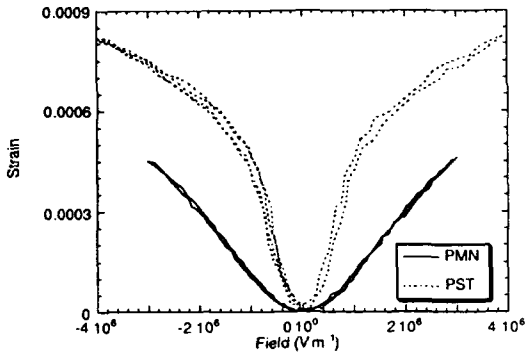


FIGURE 1. Polarization-field and strain-field characteristics for PMN and disordered PST.

## ORIENTATIONAL GLASSES

An interpretation of the properties of relaxor dielectrics analogous to that of spin-glasses has been given by Viehland[8]. A more general survey of orientational glasses, covering dilute or frustrated ferroelectric systems such as Li- or Nb-doped potassium tantalate and rubidium ammonium dihydrogen phosphates, but not those systems known as relaxors, has been presented by Höchli[6]. Viehland showed that the permittivity of $Pb(Mg_{1/3}Nb_{2/3})O_3$-$PbTiO_3$ follows the Vögel-Fulcher relationship, an empirical relationship which describes the frequency dependence of many response functions of glassy systems and hence is taken as a strong evidence for the "glassy nature" of a system. In this case the relationship is of the form:

$$\omega = f_o \exp\left(\frac{-E_a}{k(T_m - T_f)}\right) \tag{1}$$

in which $T_m$ is the temperature of maximum permittivity at frequency $\omega$ and k is Boltzman's constant. $E_a$, $T_f$ and $f_o$ are parameters which may interpreted in terms of the following microscopic model, as presented specifically for the complex perovskites.

In systems such as $Pb(Sc_{1/2}Ta_{1/2})O_3$ [PST] it has been shown that the presence of relaxor-like properties is related to the degree of chemical or crystalline order on the B-site of the lattice[7]. In addition, $Pb(Mg_{1/3}Nb_{2/3})O_3$ [PMN] has been shown to be mainly disordered with small regions (of order 100 Å diameter) of ordered material[8]. However, there may exist small regions, or "clusters", in which the B-site chemistry favours the existence of a local order parameter in the form of a spontaneous polarization. Evidence for the existence of such polarization fluctuations well above the maximum in permittivity in PMN has been presented by Burns[9]. It is therefore appropriate to think in terms of an "incipient" ferroelectric in which, as a consequence of inhomogeneity in the distribution of B-site cations, the long range ferroelectric ordering is frustrated by competition from other types of ordering, or by concentration fluctuations in the B-site species.

In common with other ferroelectric perovskites the local polarization vector may be expected to lie parallel to a number of pseudo-cubic directions, most probably along the <001>, <011> or <111> directions. The energies of these different orientation states may be similar, such that clusters may exhibit polarization in any of the variant directions. However, if the energy difference between the different orientation states is of the order of thermal energies then the polarization direction will fluctuate between the different variants. In the simplest case, to be considered in more detail below, where the energy of, say, the <111> polar variants is significantly lower than in other directions, then the cluster polarization would fluctuate between the eight equivalent <111> directions. The existence of such independent "superparaelectric" clusters would be expected to give rise to a

relationship between the $T_m$ and $\omega$ of the form:

$$\omega = f_o \exp\left(\frac{-E_a}{kT_m}\right) \qquad (2)$$

in which $E_a$ is the activation energy for reorientation of the polarization between variants and $f_o$ is the attempt frequency. However, to fit existing data the equation is modified to the form of Equation (1), in which the temperature $T_f$ is interpreted as a freezing temperature. That is, the clusters are not independent, but are subject to cooperative interactions which favour freezing of the polarization fluctuations about some temperature, $T_f$. The energy $kT_f$ may be considered to be a measure of the variance of the interaction strengths[6]. The activation energy, $E_a$, is proportional to the cluster volume, $V_c$. It may be expected that there is some distribution of cluster sizes, determined by the nature of the chemical inhomogeneity and hence a corresponding distribution of activation energies. It is consistent therefore to interpret the $\omega$ of the Vögel-Fulcher relationship as the mean relaxation frequency of some distribution $F(\omega)$. Further detailed discussions of the orientational glass model as applied to relaxors are given in references 5, 10 and 11.

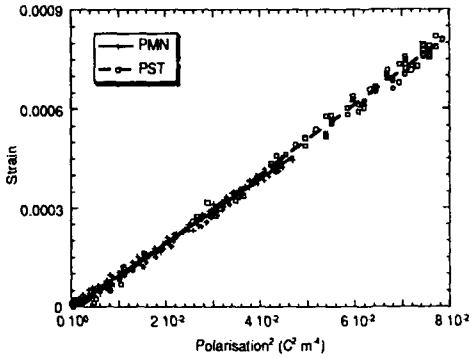


FIGURE 2. Strain as a function of the square of polarization for PMN and PST.

## ELECTROSTRICTION IN ORIENTATIONAL GLASSES

Electrostriction in non-polar solids is normally discussed in the context of the induced polarization, $P_i$, such that:

$$x_{ij} = Q_{ijkl} P_k P_l \qquad (3)$$

where $x_{ij}$ is the strain and $Q_{ijkl}$ is the electrostriction coefficient. In the case of relaxors above the freezing temperature and close to $T_m$, Equation (3) is generally believed to be applicable. In the examples of Figure 1, the polarization and strain were measured simultaneously, parallel to the applied field, using a Sawyer-Tower circuit and capacitance dilatometer. Plotting the strain as a function of the square of the polarization for each, gives the result of Figure 2

The linear regression fits are shown by the solid and dashed lines, with correlation coefficients of > 0.997. The electrostriction coeff-icients for the PMN and PST samples are thus found to be 0.0098 and 0.0105 $m^4 C^{-2}$ respectively, confirming the quadratic relationship between strain and polarization. For the purpose of a phenomenological model one may assume that the strain exhibited by a polar cluster is similarly proportional to the square of the local polarization, with an electrostriction coefficient which is independent of the applied field. At zero applied field, the strain fluctuations macroscopically sum to zero, as do those of the polarization. In modeling the electromechanical properties of a relaxor close to $T_m$, it is therefore sufficient to derive the polarization-field relationship for an orientational glass.

At a temperature T, close to $T_m$ one may consider a population of clusters with a distribution of relaxation frequencies, $F(\omega)$, where the mean relaxation frequency is, from Equation (1):

$$\overline{\omega} = f_o \exp\left(\frac{-\overline{E}_a}{k(T - T_f)}\right). \qquad (4)$$

On the application of a field parallel to one of the polarization variants, the crystalline

anisotropy energy of that variant will be lowered with respect to the other variants by $P_{local}E_{app}$, where $P_{local}$ is the spontaneous polarization of the cluster and $E_{app}$ is the applied field. That is, the activation energy to reorient the polarization of a cluster of volume $V_c$, will be increased by, on average, $P_{local}E_{app}V_c$. The orientation of the polarization parallel to the field will therefore be favoured, effectively reducing the frequency of the polarization fluctuations. The mean relaxation frequency as a function of applied field is therefore given by:

$$\overline{\omega}(E_{app}) = f_o \exp\left(\frac{-(\overline{E}_a + P_{local}E_{app}\overline{V}_c)}{k(T-T_f)}\right). \tag{5}$$

For simplicity, on the application of an alternating field of frequency $\omega_{app}$, three types of polar regions or clusters may be considered: following Zhang et al[12], Type I, are small clusters and have relaxation frequencies greater than the $\omega_{app}$, Type II have relaxation frequencies of the order of $\omega_{app}$, and the largest Type III clusters have frequencies much less than $\omega_{app}$. During one cycle of the applied field, the fluctuation frequency of Type I clusters is reduced with increasing field, the polarization vector favouring orientations parallel to the field. However, as their frequency of fluctuation is still greater than $\omega_{app}$, the contribution to the macroscopic polarization is small. Effectively, Type I clusters contribute a small "induced" polarization. In contrast, the effect of increasing field upon Type II clusters is an orientation and freezing of the polarization parallel to the field. That is, they contribute the full local polarization to the measured value. Type III clusters are effectively already frozen with respect to the applied field frequency. However, they may reorientate with respect to the field. It is possible that such clusters exhibit multidomain states, and thus their reorientation behaviour may be more like that of a ferroelectric. In which case it may be assumed that the minor hysteresis observed in relaxors is due to the Type III clusters, becoming more significant as the temperature approaches $T_f$. Close to $T_m$ the largest contribution comes from the Type II clusters, whilst with increasing field Type I clusters are converted to Type II. It is therefore most relevant to model the freezing behaviour of the Type II clusters.

Assuming no other change in the distribution of frequencies, those clusters for which $\omega(0) < \omega(E_{app}) \leq \omega_{app}$, contribute to the macroscopic polarization, whereas the contribution of those with $\omega(E_{app}) > \omega_{app}$, is assumed to be negligible. Thus the polarization as a function of field is given by:

$$P(E_{app}) = P_{local}\frac{\int_0^{\omega_{app}} F(\omega, E_{app})d\omega - \int_0^{\omega_{app}} F(\omega, 0)d\omega}{\int_{-\infty}^{\infty} F(\omega, E_{app})d\omega}. \tag{6}$$

This assumes that $P_{local}$ is independent of applied field or cluster volume. The second term in the numerator fixes the contribution of the Type III clusters to zero.

## RESULTS

Calculations of $P(E_{app})$ were carried out for PMN and PST using values of $E_a$, $T_f$ and $f_o$ determined by fitting values of $T_m$ and $\omega$, measured on polycrystalline samples, to the Vögel-Fulcher relationship. A log-Gaussian distribution of relaxation frequencies was assumed, as has previously been found useful in models of orientational glasses[6]:

$$F(\omega) = \exp\frac{\left(-\ln\left(\omega/\overline{\omega}\right)\right)^2}{(\ln(\Delta\omega))^2}. \tag{7}$$

Values for the cluster volume, $V_c$, the cluster polarization, $P_{local}$ and the width of the frequency distribution $\Delta\omega$ were found by inspection, fitting to measured data for the polycrystalline PMN and PST. The relevant values of the parameters, at 22°C, are shown in Table 1.

A comparison of the measured and calculated behaviours for PMN and disordered PST at 22°C is shown in Figure 3. The model calculations are for single crystals with the field applied parallel to one of the preferred orientations for polarization. In the case of polycrystalline samples of random orientation a geometric factor should be introduced into Equation (5), with a further integration over all possible orientations. However, this should not introduce any qualitative difference to the model, and it may be assumed that any discrepancies in the fitting to the polycrystalline data appear in the values of $P_{local}$ and $V_c$.

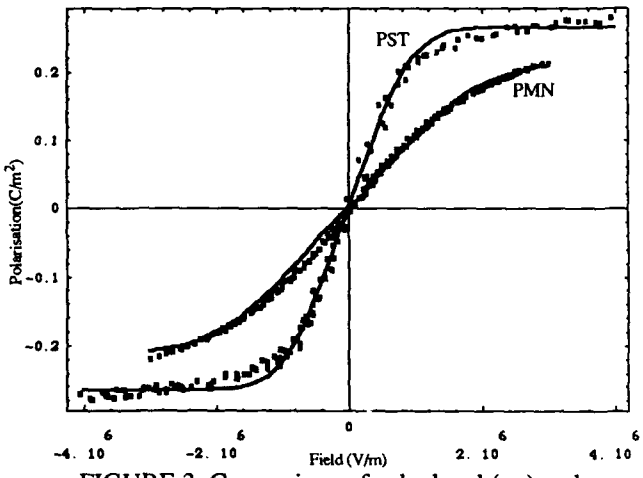


FIGURE 3. Comparison of calculated (—) and measured (■) polarisation as a function of field.

| | PMN | PST |
|---|---|---|
| $E_a/k$ (K) | 1120 | 364 |
| $T_f$ (K) | 215 | 277 |
| $f_0$ ($s^{-1}$) | $6.86 \times 10^{13}$ | $1.16 \times 10^{12}$ |
| $P_{local}$ ($C\ m^{-2}$) | 0.29 | 0.42 |
| $V_c^{1/3}$ (Å) | 41 | 28 |
| $\Delta\omega$ ($s^{-1}$) | $10^{12}$ | $10^{14}$ |

TABLE 1. Parameters used in the model calculations.

## DISCUSSION

Considering that the model parameters were fitted by inspection to the experimental data, the agreement between them is surprisingly good. Further work is intended, using a more rigorous fitting procedure. For PMN the value of $T_f$ used is close to that found for single crystal PMN[11], however the value of $f_0$ is over an order of magnitude greater ($10^{12}$ for single crystal PMN). The cluster size obtained from the fit to the PMN data is in good agreement with experimental evidence for the size of ordered regions, which has been estimated by transmission electron microscopy[8] to be of the order of 50 to 100 Å. The local polarisation estimated from the fitting is 16% greater than that found optically[9]. However, the width of the relaxation frequency distribution is several orders of magnitude greater than that calculated from the imaginary part of the dielectric susceptibility[11]. The calculated behaviour is not particularly sensitive to this parameter, whereas small changes made to the cluster diameter have a profound effect on the shape of the curve. A more accurate fitting could well produce a significant reduction in the estimate of $\Delta\omega$.

In general, increasing the cluster size increases the slope of the polarisation-field curve and reduces the field at which saturation occurs, whist increasing $\Delta\omega$ increases the non-linearity. Somewhat perversely, the fitted values of the distribution width and cluster size for PST appear contrary to this trend, i.e. the P-E curve is steeper than that for PMN, saturating at lower field. However, it is consistent with the higher freezing temperature. That is, the interactions between clusters play a greater role in PST at 22°C than in the PMN example. Field-enforced freezing therefore occurs at lower applied fields.

An indication of the importance of the Type III clusters can be gained by consideration of the ratio of the saturation polarisation to $P_{local}$. In PMN this is approximately 0.76, whilst in the PST calculation it is 0.62. As expected, the "non-

contribution" of Type III clusters is more apparent closer to $T_f$. It is probable that the high value of $P_{local}$ obtained for PST is a consequence of ignoring Type III contributions. Whilst the "induced" contribution of Type I clusters is considered to be negligible, it would be of some benefit to be able to model the true Type III behaviour. Even in the experimental data selected for this work, some hysteresis is apparent. Initial attempts to introduce hysteresis into the present model have shown that $\Delta\omega$ may be reduced and $P_{local}$ reduced to obtain a fit. However, the present procedure introduces parameters which are not physically meaningful and requires further work to be consistent with the basis of the model reported here.

For the sake of materials development the model has some advantages over those presented elsewhere. The purely phenomenological model of von Cieminski[13], based on a Landau-type free energy polynomial for the calculation of strain-field characteristics, is self consistent and fits well to experimental data, but the parameters employed provide little insight into the physical mechanisms in relaxors. That of Viehland[11] based on the dipole interactions of superparaelectric clusters and adapted from work on superparamagnetism provides a more atomistic approach, but does not incorporate a consistent set of easily accessible parameters from other areas of the spin glass treatment.

## CONCLUSIONS

A phenomenological model of polarisation and strain of relaxor dielectrics based upon the empirical Vögel-Fulcher relationship has been shown to fit to experimental data for PMN and disordered PST at 22°C. Using a log-Gaussian distribution of polar cluster sizes only three parameters, two of which are in close agreement with experimental estimates, are required to fit the model to experimental data. Further work is required to confirm the applicability of the present model. It is important that it be tested as a function of temperature and frequency against known materials. It is apparent that the contribution from low relaxation frequency clusters (Type III) should be included, for which further complexity is required.

## ACKNOWLEDMENTS

F. Chu and M. Daglish gratefully acknowledge the financial support of Fonds National Suisse de la Recherche Scientifique.

## REFERENCES

1. G. Smolenskii J. Phys. Soc. Jpn., 28 Suppl, 26 (1970)
2. G. Schmidt, Ferroelectrics, 20 127 (1990)
3. K. Uchino, S. Nomura, L.E. Cross, R.E. Newnham and S.J. Jang, J. Mat. Sci., 16, 569, (1981)
4. M. Daglish, Ph.D. Thesis, University of Leeds (1990)
5. D.Viehland, S.J. Jang, L.E. Cross and M. Wuttig, J. Appl. Phys., 68 2916, (1990)
6. U.T. Höchli, K. Knorr and A. Loidl, Adv. Phys, 39 405 (1990)
7. N. Setter and L.E. Cross, J. Mat. Sci., 15 2478 (1980)
8. A.D. Hilton, D.J. Barber, C.A. Randall and T.R. Shrout, J. Mat. Sci., 25 3461 (1990)
9. G. Burns and F. Dacol, Solid State Commun., 48 853 (1983)
10. D. Viehland, S.J. Jang, L.E. Cross and M. Wuttig, J. Appl. Phys., 69 414 (1991)
11. D. Viehland, Ph.D. Thesis, Pensylvania State University, (1991)
12. Q. Zhang, W. Pan, A. Bhalla and L.E.Cross, J. Am. Ceram. Soc., 72, 599, (1989)
13. J. von Cieminski, Z. Naturforsch, 45a, 1090 (1990)

*Ferroelectrics*, 1992, Vol. 133, pp. 121–125
Reprints available directly from the publisher
Photocopying permitted by license only

© 1992 Gordon and Breach Science Publishers S.A.
Printed in the United States of America

# DiC9

# MODIFICATION OF THE RELAXOR PROPERTIES OF PLZT-1/95/5 BY THERMAL AND ELECTRICAL TREATMENT

G.E.KUGEL, M. HAFID
CLOES - University of Metz and Supelec
2, rue Edouard Belin 57078 Metz Cedex 3 FRANCE
J.HANDEREK, Z.UJMA, D.DMYTROW
Silesian University, ul.Universitecka 4 40007 Katowice POLAND

Abstract : Dielectric, pyroelectric, thermally stimulated current and optical measurements have been performed on PLZT 1/95/5 semitransparent ceramics. The temperature dependence of these properties was studied in the vicinity of the phase transitions between the antiferro- ferro- and paraelectric phases. Some indication of relaxor behaviour of these ceramics was confirmed in wide temperature ranges around these transitions, particularly at the AFE-FE one. It has been shown that the relaxor behaviour can be modified by suitable thermal and electric treatment.

## INTRODUCTION

The $Pb(Zr,Ti)O_3$ (PZT) ceramic materials with specific Zr/Ti ratio lower than 95/5 exhibit the characteristic antiferroelectric (AFE), ferroelectric (FE), paraelectric (PE) phase transition sequence with a big thermal hysteresis at the AFE-FE transition, a strongly diffuse nature in the transitions between particular phases as well as a wide temperature range of the phase coexistence. The main physical properties related to the various phase transitions can be deeply modified by introducing doping elements like $Nb_2O_5$, $La_2O_3$. [1-4]

Relaxor behaviour [5] was found in Nb doped PZT 95/5 ceramics [6]. Similar relaxor properties, namely symptoms of fast response in the ferroelectric microdomains were also seen in PLZT ceramics with Zr/Ti ratio 95/5 and low La concentration [7,8]. Fast polarization reversal in such microdomains leads to a huge electron release and emission. It has been shown that these features can be modified by suitable thermal and electric treatment.[9] More systematic studies on these modifications are the aim of the present paper in which are reported dielectric and pyroelectric studies of PLZT-1/95/5 ceramics together with Raman scattering and thermally stimulated current (TSC) measurements.

## DIELECTRIC MEASUREMENTS

The PLZT ceramic material with Zr/Ti ratio 95/5 and 1% of La was sintered using conventional mixed-oxide method. The final sintering was performed at 1250°C during 3 hours in double crucible under PbO atmosphere. The obtained ceramic was nearly semitransparent due to the La dopant and suitable selection of the sintering conditions. Samples cut with a thickness of 0.6 mm were used in our various measurements.

The temperature dependence of ε and tan (δ), shown in Figure 1a and b respectively, was measured with an electric field of 1 kHz frequency. The temperature dependent spontaneous polarization, reported additionally in Figure 1a, was deduced from hysteresis loop measurements using a field of 50 Hz frequency and 5 kV/cm strength. A transformation from a slim to a square hysteresis loop was observed in the temperature range where a step like increase occurs in the ε (T) curves. The dielectric and polar properties show big thermal hysteresis at the AFE-FE transition as well as strong diffuse character. Deviations from the Curie-Weiss law, specific behaviour of tan (δ) and $P_S(T)$ in the vicinity of the FE-PE transition also confirm the diffuse nature of the transition.

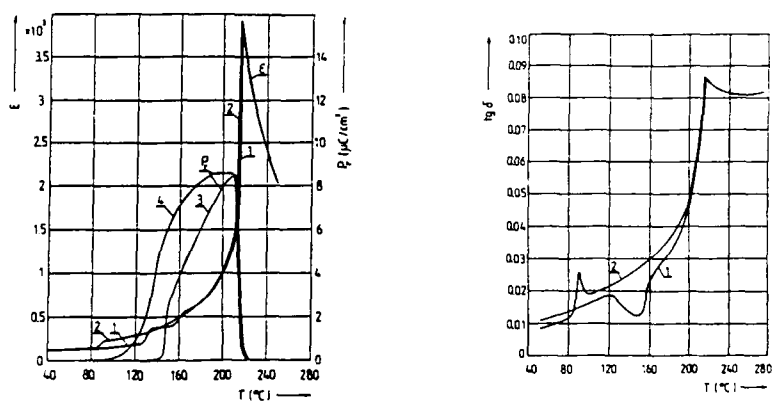


FIGURE 1 : Temperature dependence of a) permittivity and remanent polarization b) dielectric loss tan (δ ) in PLZT 1/95/5 ceramics.

The frequency dependence of the dielectric constant was measured using HP Analysers with fields from 0.1 kHz to 20 MHz (Figure 2a) and from 1 kHz to 1 MHz (Figure 2b). In the low frequency range, it is observed that the ε (T) do not exhibit a frequency dependence in the temperature range from 20°C up to the temperature

where sharp maximum in permittivity occurs. At high temperatures inside the PE phase frequency dispersion takes place. On the contrary, the dielectric loss exhibits a strong frequency dependence also observed in the transient FE phase, with a sharp local maxima corresponding to the FE-PE transition. On the contrary, in the higher frequency range (Fig 2b), clear dispersion behaviour is observed with increase of Tc and fall in dielectric constant with increasing frequency. This indicates relaxor behaviour.

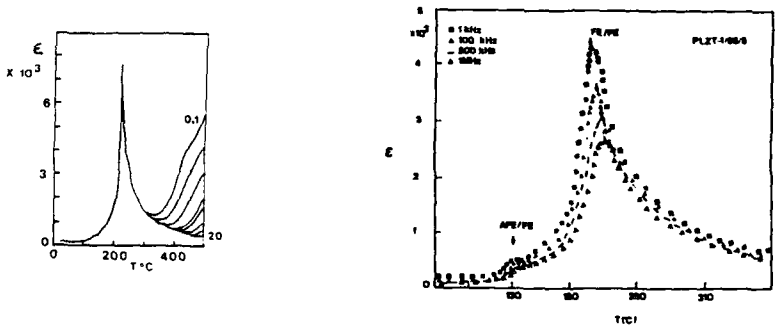


FIGURE 2 : Temperature dependence of the dielectric permittivity measured in the frequency ranges a) 0.1 kHz to 20 kHz (0.1kHz, .0.2 kHz, 0.4 kHz, 0.8 kHz, 1 kHz,2 kHz, 4 kHz, 10 kHz, 20 kHz) b) 1 kHz, 100 kHz, 500 kHz, 1 MHz.

## PYROELECTRIC AND THERMALLY STIMULATED CURRENT MEASUREMENTS

The variations with temperature of the polarization around the AFE-FE and FE-PE phase transition were also obtained using pyroelectric current measurements. The sample, previously polarized in a DC field of 4kV/cm applied inside the transient phase (180°C) during 10mn, was heated through the FE-PE transition with recording the pyroelectric current. The same procedure was applied to measure the pyrocurrents through the FE-AFE transition. The results are reported on Figure 3.

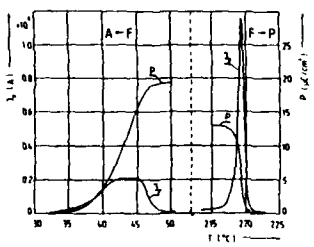


FIGURE 3 : Variation of the pyroelectric current and the spontaneous polarization around FE-AFE and FE-PE phase transitions.

We observed that the intensity of the whole Raman spectra is considerably decreased in the case of a field cooled (FC) state sample. Its typical evolution from FE to AFE type [14-15] is shifted downward in comparison with the annealed and the ZFC states. In the case of the sample which was pre-polarized by the DC field applied on cooling from the FE state or through both phase transitions (FC state), the fact that only weak pyroelectric peaks and slim hysteresis loops were observed on subsequent cooling can be compared to this light scattering behaviour.

On the other, the light transmission of the sample, measured in range of visible light, was considerably lower for the sample in FC and ZFC states. During annealing by thermal treatment at T>500°C, this transmission increases again gradually to the initial value. Here too, there seems to be a clear correlation between the light transmission increasing and the TSC behaviour observed in equivalent temperature range (Figure 4).

## DISCUSSION

The previously reported experimental results indicate symptoms of relaxor properties in the PLZT 1/95/5 ceramics occuring inside the transient FE phase and in wide temperature intervals below and above AFE-FE transitions respectively. This relaxor behaviour is thermally stabilized by two different processes implying mobile ion defects i) screening of the FE domains which remain as clusters in the AFE and PE matrix, ii) forming macroscopic concentration polarization [10] by motion towards the electrodes in the case of prepoled samples. (Figure 5)

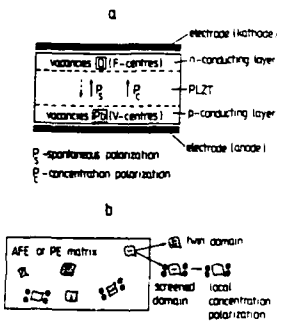


FIGURE 5 : Concentration polarization and local depolarization field of FE domains induced by mobile ion defects.

The vacated sites (vacancies in Pb and O sublattices) enable these ionic motions. The in this way formed concentration polarization of donor and acceptor centers lead to appearence of n- and p- conducting cathodic and anodic surface layers (Figure 5).

At high enough temperatures, release of electrons by thermal generation takes place. These electrons diffuse toward the sample bulk under concentration gradient. The emptyed donor centers (for exemple F centers) are refilled again by electron injected from electrodes. These two processes give rise to the thermally stimulated current observed in the PE phase. Superposition of pyroelectric and TSC occurs inside the transient FE phase and close temperature intervals, where neighbour AFE, FE and PE phases coexist. Even in the case of ZFC state, the local concentration polarization is formed under depolarization field associated with spontaneous polarization $P_s$ of the remaining FE clusters. The strong interactions between the spontaneous polarization and concentration polarization explain the deep changes in the permittivity and the hysteresis loop as above mentioned case of FC and ZFZ states of the sample.

The relation between the number of domains compensated in the two possible ways as shown in Figure 5 decides on the dielectric properties and especially on relaxor behaviour. This relation can be intentionaly changed by suitable thermal-electric treatment.

## REFERENCES


1. M.Troccaz, L.E. Eyraud, V. Fettiveau and P. Gonnard, Acad. Sci. Paris, ser. B 276, 547 (1973)
2. Yu Lin Chang, J. Appl. Phys. 29, 237 (1982)
3. Y.L. Wang, Z.M. Chang, Y.R. Sun and X.H. Dai, Physica B, 150, 168 (1988)
4. X. Dai and J. Wang, Ferroelectrics, 109, 253 (1990)
5. L.E. Cross, Ferroelectrics, 76, 241 (1987)
6. M. Hafid, J. Handerek, G.E. Kugel and Z. Ujma, Ferroelectrics, (paper submitted in 1991)
7. H. Gundel, H. Riege, E.F.N. Wilson, J. Handerek and K. Zioutas, Ferroelectrics, 100, 1 (1989)
8. H. Gundel, H. Riege, E.F.N. Wilson, J. Handerek and K. Zioutas, Ferroelectrics, 109, 137 (1990)
9. H. Gundel, J. Handerek and H. Riege, J. Appl. Phys. 69, 975 (1991)
10. R. Waser, T. Baiatu and K.H. Hardtl, Feroelectrics, 109, 89 (1990)
11. "Thermally Stimulated Relaxation in Solids" Copies in Applied Physics, vol. 37 ed. P. Braunlich Springer Verlag Berlin 1979
12. Z. Ujma and J. Handerek, Acta Phys. Polon., 153, 665 (1978) - Z. Ujma and J. Handerek, Phase Transitions, 1; 363 (1980)
13. J. Handerek, J. Kwapulinski, Z. Ujma and K. Roleder, Ferroelectrics, 81, 253 (1988)
14. C. Carabatos-Nedelec, J.El. Harrad, J. Handerek, F. Brehat and B. Wyncke, Ferroelectrics , 125, 483 (1992)
15. M. Hafid, J. Handerek, G.E. Kugel and M.D. Fontana, Ferroelectrics, 125, 477 (1992)

Ferroelectrics, 1992, Vol. 133, pp. 127–132
Reprints available directly from the publisher
Photocopying permitted by license only
© 1992 Gordon and Breach Science Publishers S.A.
Printed in the United States of America

# DiC12

## MAGNESIUM TITANATE MICROWAVE DIELECTRIC CERAMICS

V.M. FERREIRA*, F. AZOUGH+, J.L. BAPTISTA*, R. FREER+
* Departamento de Engenharia Cerâmica e Vidro,
Universidade de Aveiro, 3800 Aveiro, Portugal.
+ Materials Science Centre,
University of Manchester/UMIST,
Manchester M1 7HS, United Kingdom.

Abstract Magnesium titanate ceramics have been prepared by a chemical route (Pechini method) and by the conventional mixed oxide route. Dielectric properties of sintered samples were measured at 8 GHz by the Hakki and Coleman technique. Microstructures were examined by optical microscopy and scanning electron microscopy. The use of the chemical method enabled the sintering temperature to be lowered and good quality, single phase, dense ceramics were obtained at temperatures down to 1150°C. Dielectric constants were approximately 17.5 and Q values up to 21200 were obtained at 8 GHz.

The effect of powder preparation processes, sintering temperature and cooling rate on the densification, microstructure and microwave dielectric properties are discussed.

## INTRODUCTION

Several dielectric ceramics are used at microwave frequencies as resonators in filters or oscilators in communications systems[1-3]. Their great advantage is to enable the reduction of size of the components. A high dielectric constant ($\varepsilon_r$), a high quality factor (Q) and the least variation possible in the value of the characteristic resonant frequency with temperature are the most important features of these materials.

Magnesium titanate ($MgTiO_3$)-based ceramic compositions are commonly used for microwave applications. When magnesium titanate is prepared by solid state reaction between the oxides of magnesium and titanium, $MgTi_2O_5$ is formed as an intermediate phase which is difficult to eliminate completely from the reaction products[4]. The presence of second phases usually increases the dielectric losses of these materials[1]. Therefore it is important to prepare $MgTiO_3$ powders without any second phase.

It has been shown by Sato et al[5] for $MgTiO_3$ that an increase in the quality factor can be obtained for samples sintered above 1350°C. As no data on densification or grain size was reported it is not possible to ascertain which of

these parameters was responsible for the variation in Q.

In an attempt to gain information about the importance of densification and grain size, and the processing conditions on the microwave dielectric characteristics of $MgTiO_3$, ceramic samples have been prepared by two routes. In one, a conventional mixed oxide reaction route was used, and in the other $MgTiO_3$ was obtained by a chemical route (the Pechini method).

## EXPERIMENTAL

For the Pechini method the starting materials were reagent grade magnesium nitrate, ammonium carbonate, ethylene glycol, tetraethylorthotitanate, citric acid and nitric acid. Deionized water with a very low calcium content was used. Magnesium carbonate was obtained by precipitation from the reaction between magnesium nitrate and ammonium carbonate. The magnesium carbonate was then introduced into a solution of tetraethylorthotitanate and citric acid on ethylene glycol with a small amount of nitric acid. The solution was then dried in several steps up to the maximum temperature of 250°C. This procedure yielded a polyester resin which, by a single calcination process at 600°C, gave single phase $MgTiO_3$ powder. Powders were milled for 16 hours (using nylon vials and agate balls).

Mixed oxide powders were prepared from reagent grade MgO and titania (Tiona AG). These were wet mixed for 12 hours, calcined at 1100°C for 4 hours and mixed for a further 18 hours.

Powders were pressed either uniaxially or isostatically at 1000 or 2000 $Kgf/cm^2$ into rods of 10 mm diameter. These pellets were sintered in air at 1150°C to 1500°C for two or four hours. The heating rate was 5°C/min and the cooling rate was either 5°C/min or a fast quench in air.

Densities of products were determined by an immersion method. X-ray diffraction (XRD) techniques were used to analyse the powders and products. Microstructures of powders and sintered specimens were studied by optical microscopy and scanning electron microscopy (SEM). Microwave dielectric properties were determined at 8 GHz by the Hakki and Coleman method[6].

## RESULTS AND DISCUSSION

X-ray diffraction data for chemically prepared and mixed oxide calcined powders revealed only single phase magnesium titanate. Figure 1 shows that the chemically prepared powder was sub-micron in size, with some agglomerates.

Mixed oxide-derived powders could only be sintered adequately at high temperature, and at 1350°C and 1400°C the products were of ~ 95% theoretical density. The microstructures were characterised by grains of variable size and shape, containing a large amount of intergranular porosity (Figure 2a). In

contrast, the use of chemically prepared powders enabled the sintering temperature to be lowered significantly and good quality dense ceramics (96-97% theoretical density) were obtained at temperatures as low as 1150°C. For these materials the grain size increased with sintering temperature (Table 1) but abnormal grain growth resulting in intergranular porosity was only found in products sintered at ≥ 1450°C, (Figures 2b,2c,2d, Figure 3 and Table 1). In most cases the grain structure was uniform, with porosity at the grain boundaries and triple points, (Figures 2b,2c).

X-ray diffraction analysis of the products confirmed that both mixed oxide and chemically prepared ceramics were single phase $MgTiO_3$.

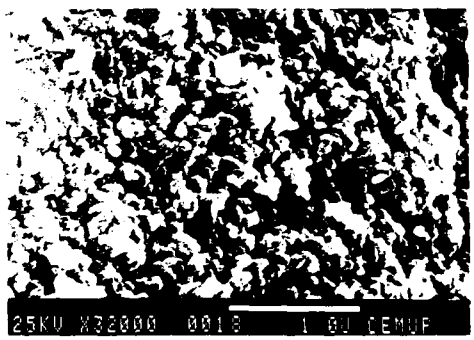


FIGURE 1. SEM micrograph of the chemically prepared magnesium titanate powder.

TABLE 1. Microstructure data for $MgTiO_3$ ceramics prepared via chemical (C) and mixed oxide (MO) routes.

| Powder preparation | Sintering temperature (°C) | Cooling Rate (°C min) | Density % theoretical | Grain size (μm) |
|---|---|---|---|---|
| C | 1150 | 5 | 97.0 | 3.6 |
| C | 1350 | 5 | 96.8 | 9.6 |
| C | 1450 | 5 | 96.5 | 18.3 |
| MO | 1350 | 5 | 95.0 | 15.7 |
| MO | 1400 | 5 | 95.4 | 49.7 |
| C | 1350 | Air quench | 97.3 | 9.5 |
| C | 1450 | Air quench | 97.3 | 21.5 |
| C | 1500 | Air quench | 96.0 | 35.6 |

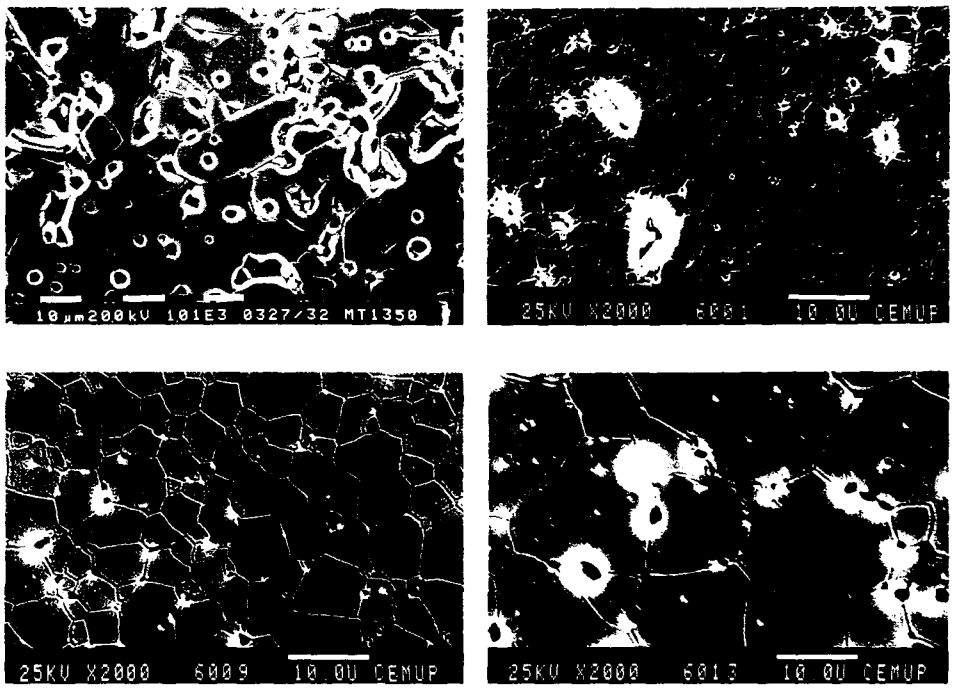


FIGURE 2. SEM micrographs of $MgTiO_3$ ceramics: (a) prepared via oxide route and sintered at 1350°C; prepared via the chemical route and sintered at (b) 1150°C, (c) 1350°C, (d) 1450°C.

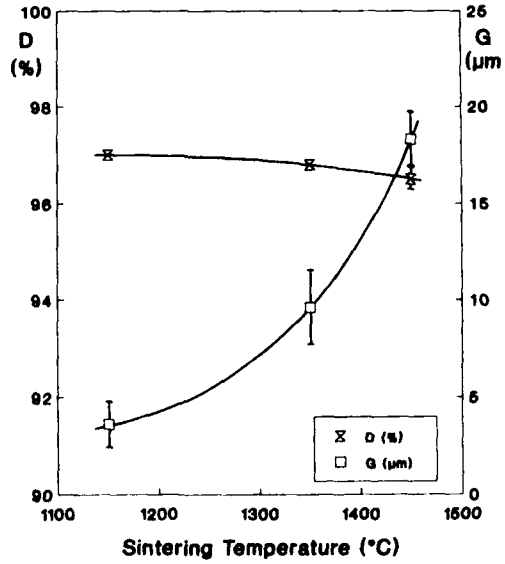


FIGURE 3. Density (D) and grain size (G) of chemically prepared $MgTiO_3$ ceramics as a function of sintering temperature.

The relative permittivity was relatively insensitive to preparation conditions with $\varepsilon_r$ in the range 16.6-17.5. The lowest $\varepsilon_r$ values were obtained with the chemically prepared material sintered at 1150°C (i.e. the lowest density specimens).

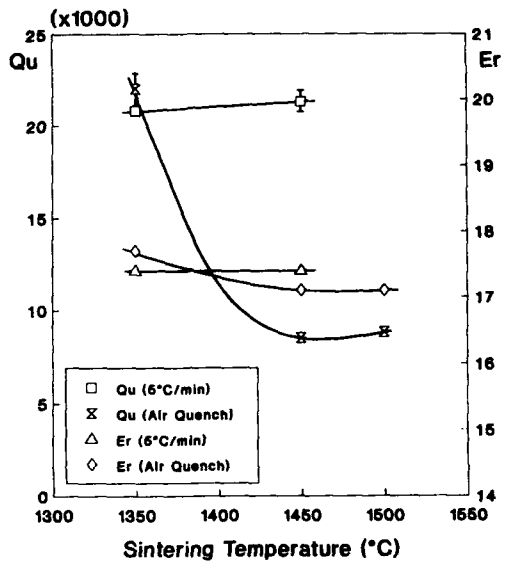


FIGURE 4. Dielectric Q value and relative permittivity of chemically prepared $MgTiO_3$ ceramics as a function of sintering temperature and cooling rate.

Dielectric Q values at 8 GHz varied from 7000 to 22000, being dependent on powder preparation route, and the pressing and sintering conditions. Mixed oxide powders fired at 1350 and 1450°C had the lowest Q values of 7000-9800. These low Q values may be due to the trapped porosity, presence of impurities and marginally lower densities. Uniaxially-pressed, chemically-prepared powders sintered at 1150 and 1350°C had Q values of 9800 and 20800 respectively, whilst isostatically-pressed chemical powders sintered at the same temperatures had uniformly high Q values ~ 20700 when the cooling rate was 5°C/minutes, (Figure 4). Neither grain size nor density (Table 1 and Figure 3) have a significant effect on the Q value. The consistently high Q values in the isostatically-pressed specimens are probably because of the high homogeneity throughout the series of samples. When a fast cooling rate was used (air quench), there was little change in the relative permittivity, but the Q value fell dramatically as the sintering temperature increased from 1350 to 1500°C, (Figure 4). It is tempting to compare this trend with the data for another dielectric resonator composition ($Zr_{0.8}Sn_{0.2}TiO_4$) where it was shown that an order-disorder transition occurred as a function of cooling rate, modifying the cell parameters and changing the Q value[7]. Wechsler et al[8] reported on the air

quenching of $MgTiO_3$ samples from temperatures up to 1400°C and, based on X-ray diffraction data, reached the conclusion that the structure remained crystallographically ordered until 1400°C. temperature. There is, however, as yet no clear evidence of an order-disorder transition in $MgTiO_3$, or the reasons for the effect of cooling rate on the dielectric Q value.

## CONCLUSIONS

High quality $MgTiO_3$ ceramics (with dielectric Q values of ~ 21800 at 8 GHz) were prepared via a chemical route; the powders were pressed isostatically, sintered at temperatures of 1150-1450°C, and cooled slowly. The relative permittivity was insensitive to preparation conditions (with $\varepsilon_r$ 16.6-17.5) but uniaxially pressed powders sintered at low temperatures (~ 1150°C) and mixed oxide prepared powders sintered at temperatures up to 1400°C yielded products with Q values down to 7000. Grain size and specimen density did not have a significant effect on Q values.

## REFERENCES

1. K. Wakino, Ferroelectrics, 91, 66, (1989).

2. R.C. Kell, A.C. Greenham and G.C.E. Olds, J. Amer. Ceram. Soc., 56, 352, (1973).

3. J.K. Plourde and C.L. Ren, IEEE Trans. Microwave Theory and Techniques, 29, 754, (1981).

4. F. Cambier, C. Leblud and M.R. Anseau, Ceramic International, 8, 77, (1982).

5. T. Sato, R. Miyamoto and A. Fukasawa, Japan. J Appl. Phys., 20 (Suppl. 20-4), 151-154, (1981).

6. B.W. Hakki and P.D. Coleman, IRE Trans. Microwave Theory and Tech., 8, 402, (1960).

7. F. Azough and R. Freer, Proceedings 1990 ISAF meeting, (in press).

8. B.A. Wechsler and R.B. Von Dreele, Acta Cryst., B45, 542, (1989).

*Ferroelectrics*, 1992, Vol. 133, pp. 133–138
Reprints available directly from the publisher
Photocopying permitted by license only

© 1992 Gordon and Breach Science Publishers S.A.
Printed in the United States of America

# DiCl4a

## NEW BARIUM TITANATE BASED MATERIAL FOR MLCs WITH Ni ELECTRODE

YUKIO SAKABE, YUKIO HAMAJI, TOSHIKI NISHIYAMA
Murata Manuf. Co., Ltd. Nagaokakyo-shi, Kyoto, Japan

Abstract A new barium titanate based X7R material has been developed for MLCs with Ni electrode. Dielectric properties of the new material are; K=3600, DF=1.6%, insulation resistance=6500MΩ · μF as RC product, when the dielectric layer thickness is 10μm. Performance on an accelerated life test was much superior to conventional base metal MLCs. This new material contains dysprosium oxide and cobalt oxide as main dopants to barium titanate. The performances presented in the above are attributed to this new formulation.

## INTRODUCTION

The use of Ni electrode has been expanded for MLCs recently because of its cheapness compared with novel metals such as Pd and Ag-Pd alloy. To fabricate MLCs, a dielectric material is cofired with an inner electrode. Since Ni metal is easily oxidized with existence of oxygen at elevated temperature, green MLC chips have to be fired in a reduced atmosphere. This condition requires the dielectric material not to be reduced in such an atmosphere. Therefore, degradation of insulation resistance has been always the biggest concern for the MLCs with Ni electrode. Extended work has been done regarding new dielectrics and degradation mechanisms mainly for Y5V/Z5U characteristics.[1-5] However,there are only a few reports on X7R dielectrics[6] other than the patents.[7,8,9] In this paper, the properties of a newly developed X7R dielectric are reported comparing with those of a conventional one.

## EXPERIMENTAL PROCEDURE

### Sample Preparation

High purity barium titanate and industrial grade raw materials; $Dy_2O_3$, $Co_2O_3$, MgO, $MnO_2$ and $BaCO_3$ were batched to a certain formulation with glass frit consisting of $Li_2O$, $Al_2O_3$ and $SiO_2$ as main constituents. This dielectric is designated as "DYCO" in this paper.

Another formulation was prepared as a control with high purity barium titanate, calcium zirconate, calcium titanate, $MnO_2$, $BaCO_3$ and $SiO_2$. This is designated as "CZCT".

The powders were mixed with organic binder to prepare slurries. Ceramic green films were prepared with doctor blade method and then Ni paste was printed on them. After drying, the printed films were stacked and pressed with blank films to build monolithic capacitors(MLCs). To evaluate dielectric properties, chip capacitors were constructed to be 3.2mm×1.6mm in size with an active dielectric thickness of 10$\mu$m for DYCO and 20$\mu$m for CZCT.

The green chips were baked out at 350℃ in air to remove binder and then fired at 1280℃ in a low oxygen atmosphere controlled by nitrogen and hydrogen gasses. The oxygen partial pressure was maintained at $5\times10^{-11}$MPa at the soaking zone. The fired chips were terminated with silver paste, fired and then nickel and tin plated to provide surface mountable MLCs.

### Dielectric Measurements

Capacitance and dissipation factor were measured at 1KHz/1Vrms using YHP4274A LCR meter. Insulation resistance was measured with Keithley 195A Digital Multimeter after applying 16V for DYCO and 25V for CZCT for 2 minutes, then RC products were calculated. Accelerated life test was performed at 150℃ under DC field of 8.5 KV/mm and the Mean Time To Failure (MTTF) was calculated.

### Structural Analyses

Cross sections of the chips were observed using SEM and the existing elements were checked by XMA. X ray diffraction analysis was made to check crystal phases before and after firing. TEM analysis was performed to observe the microstructure, also.

## RESULTS AND DISCUSSION

### Dielectric Properties

Constructions and basic electrical properties of the sample MLCs with DYCO and CZCT materials are shown in Table 1. The electrical properties in this table are the averages of 30 piece samples except for the $C/C_{25}$ and the aging rate. The averages of 5 piece samples are shown for these two measurements.

Calcium zirconate and calcium titanate are known to flatten the temperature dependence of capacitance of barium titanate. Addition

of these calcium compounds are also known to prevent dielectric materials from reduction even when they are fired under low oxygen atmosphere[4]. In this sense, CZCT is one of the typical conventional X7R dielectrics fired in the reduced atmosphere.

TABLE 1 Constructions and electrical properties

| Dielectric | | DYCO | CZCT |
|---|---|---|---|
| Chip size(L×W×T)(mm) | | 3.2×1.6×1.3 | 3.2×1.6×1.0 |
| Dielectric thickness($\mu$m) | | 10 | 20 |
| No. of active layers | | 115 | 32 |
| Capacitance(nF) | | 1050 | 150 |
| Dielectric constant | | 3590 | 3290 |
| Dissipation factor(%) | | 1.6 | 1.3 |
| RC product(M$\Omega \cdot \mu$F) | | 6500 | 1100 |
| $C/C_{25}$ (%) | -55℃ | -0.6 | -8.3 |
| | -25℃ | +2.0 | -5.1 |
| | +85℃ | -9.6 | -7.6 |
| | +125℃ | -12.5 | -8.0 |
| Breakdown voltage(kv/mm) | | 60 | 50 |
| Aging rate of cap.(%/decade) | | -1.9 | -3.2 |

(DYCO: $BaTiO_3$, $Dy_2O_3$, $Co_2O_3$, MgO, $MnO_2$, $BaCO_3$ and glass frit
CZCT: $BaTiO_3$, $CaZrO_3$, $CaTiO_3$, $MnO_2$, $BaCO_3$ and $SiO_2$)

The properties of CZCT are basically acceptable as shown in the table, although the aging rate is a little too high. In comparison with this dielectric, DYCO has higher dielectric constant, insulation resistance and breakdown voltage. The temperature dependence of capacitance meets X7R of EIA specification and the aging rate is equivalent to the one of conventional X7R dielectrics fired in air.

DYCO contains $Dy_2O_3$ and $Co_2O_3$ as main dopants. The effect of these dopants on the temperature dependence of capacitance is shown in Figure 1. With an increase of $Dy_2O_3$, capacitances at high and low temperatures descrease and the curve becomes sharper. On the other hand, an increase of $Co_2O_3$ makes the peak around 125℃ higher. These phenomena suggest that $Dy_2O_3$ tends to diffuse into barium titanate and $Co_2O_3$ works to suppress the diffusion of $Dy_2O_3$. In DYCO, MgO works to improve the temperature dependence at low temperature. $MnO_2$, $BaCO_3$ and the glass frit are to prevent the dielectric from reduction at firing. The glass frit also works as a sintering aid.

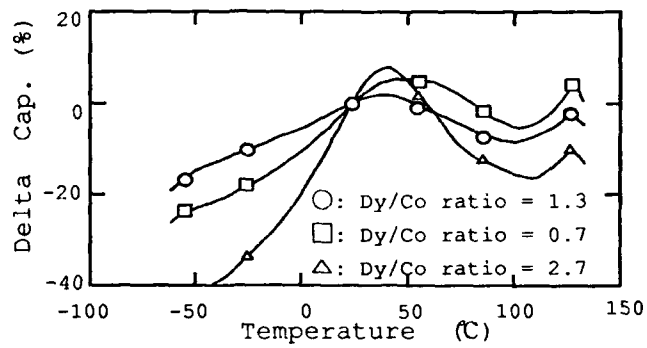


FIGURE 1 Effect of $Dy_2O_3$ and $Co_2O_3$ on the temperature dependence of capacitance. (No MgO is contained)

Accelerated life test was also performed to evaluate the reliability of the two formulations. The results are shown in Figure 2.

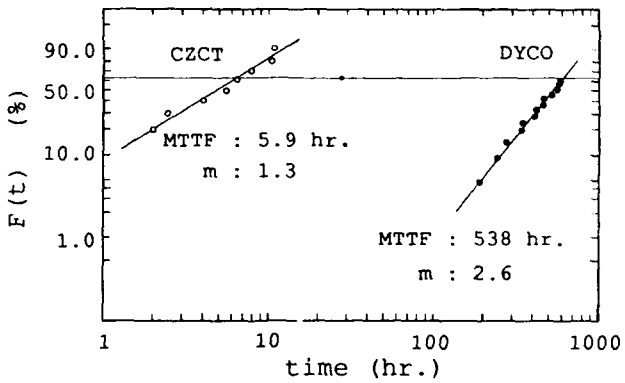


FIGURE 2 Weibull plotts for life times at 150℃ under DC field of 8.5 KV/mm.

MTTF of CZCT is only 5.9 hours and m value is as small as 1.3. On the other hand, MTTF of DYCO is 538 hours which is longer than CZCT's by two orders. M value is larger,also. Due to the trend to miniaturize electronic devices, MLCs have been strongly required to have larger capacitance values in smaller case sizes. In order to satisfy this requirement, the dielectric material has to have sufficient reliability even with very thin dielectric layers. DYCO shows an acceptable performance with such a condition as shown in the figure.

Structural features

SEM photographs of the cross sections are shown in Figure 3 for DYCO and CZCT.

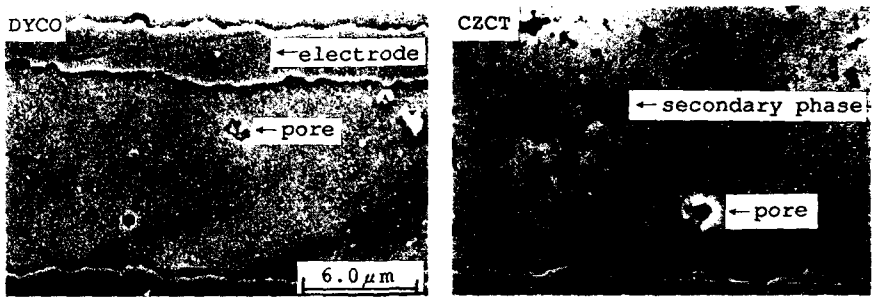


FIGURE 3 SEM photographs of the cross sections.

As can be seen in the photograph, DYCO has a dense and uniform structure. However, in the case of CZCT, the secondary phase exists not only at the triple granular points but also among the main phase as agglomerate. XMA analysis was performed for each phase. Only Ba and Ti were detected in DYCO. The main phase of CZCT had Ca besides Ba and Ti, which is reasonable. On the other hand, a very sharp peak of Ca was observed in the secondary phase of CZCT besides Ba, Ti and Si peaks. X ray diffraction analysis was performed for the two materials, also. In the case of DYCO, peaks of $Dy_2O_3$ and $BaCO_3$ in the sample before firing disappear and only the main peaks exist after firing, indicating the structure is uniform. X ray diffraction patterns of CZCT are shown in Figure 4. As can be seen, peaks of calcium titanate in the sample before firing remain and become even larger after firing. This result suggests that barium titanate reacts with calcium zirconate and additional calcium titanate is generated during firing, resulting in the large amount of secondary phase after firing. The existence of the secondary phase or the agglomerate consisting of the different material from the main phase is not good for reliability, especially when the dielectric layer is thin. The poor reliability of CZCT may be attributed to this secondary phase.

TEM photograph is shown in Figure 5 for DYCO. It is clearly observed that a grain consists of a domain structure and a surrounding area. This is a typical core-shell structure generally observed in the conventional X7R dielectrics fired in air. It was confirmed by the XMA analysis that the core consists of Ba and Ti and the shell consists of Ba, Ti, Dy and Co.

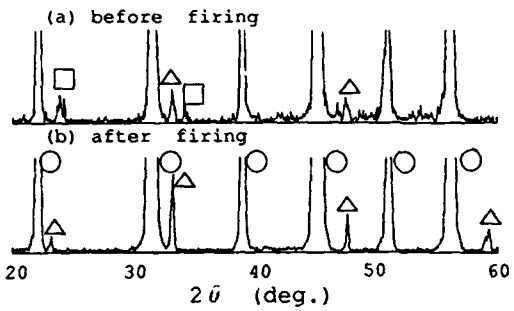


FIGURE 4 X ray diffraction patterns of CZCT; (○$BaTiO_3$, △$CaTiO_3$, □$BaCO_3$).

FIGURE 5 TEM photograph of DYCO dielectric.

## CONCLUSIONS

A new X7R dielectric has been developed for MLCs with Ni electrode. This dielectric has high dielectric constant, insulation resistance and breakdown voltage. The MLCs with this dielectric showed a good performance at an accelerated life test, also.

The structural analysis indicated that this material consisted of a single phase and each grain had a core-shell structure.

It is expected that this new dielectric material is suitable for small and high capacitance MLCs because this material is cofirable with Ni electrode and is highly reliable.

## REFERENCES

1. J. M. Herbert, Trans. Brit. Soc., 62, 645 (1963).
2. I. Burn and G. M. Maher, J. Mat. Sci., 10, 633 (1975).
3. H. J. Hageman and D. Hennings, J. Amer. Ceram. Soc., 64, 590 (1981).
4. Y. Sakabe, K. Minai and K. Wakino, Jpn. J. Appl. Phys. Suppl., 20, 147 (1981).
5. T. Nomura, et al., Amer. Ceram. Soc. 1990 Annual Meeting.
6. H. Kishi, et al., Jpn. J. Appl. Phys. Suppl., 26, 31 (1987).
7. T. Wada, et al., Japan Publication Patent No. Sho61-14607.
8. M. Ikeda, et al., Japan Un-examined Publication Patent No. Sho61-250905.
9. N. Fujikawa, et al., Japan Un-examined Publication Patent No. Sho62-256422.

*Ferroelectrics*, 1992, Vol. 133, pp. 139–144
Reprints available directly from the publisher
Photocopying permitted by license only

© 1992 Gordon and Breach Science Publishers S.A.
Printed in the United States of America

# DiCl5a

## MULTILAYER CAPACITORS WITH COPPER INNER ELECTRODES

KEIGO HIRAKATA, SHIN-ICHI SATO, FUMIO UCHIKOBA, YOSHIO KOSAKA and KENTARO SAWAMURA
Materials Research Center, TDK Corp., Chiba, Japan

Abstract A new Multilayer Capacitor(MLC), made from **relaxor** material and copper inner electrodes was fabricated by using atmosphere controlled heat treatments. $Pb(Mg_{1/3}Nb_{2/3})O_3$-$PbTiO_3$ modified material was used as a dielectric material. MgO and CaO additives were used to keep its IR in a low $Po_2$ sintering state. The organic binder burnout section needs accurate atmosphere control. The carbon residue causes lead oxide to be reduced to metal, and other serious influences. On the other hand, treatment in higher $Po_2$ induces copper oxidation. In this study, as a new technique, an $H_2$-$H_2O$-$N_2$ gas mixture was used for the binder burnout section. The obtained MLC has a high capacitance, low DC bias dependence.

## INTRODUCTION

Conventional multilayer ceramic capacitors are made from barium titanate or **relaxor** related materials for ferroelectrics, and inner electrodes are made from platinum, palladium, or a silver-palladium alloy. These electrodes are made from precious metals, so the total cost is high. Recently several papers have been published about MLC that used base metals as inner electrodes [1,2] In this study, lead contained relaxer and copper combinations are presented.

## DIELECTRIC MATERIAL

The $Pb(Mg_{1/3}Nb_{2/3})O_3$-$PbTiO_3$ based dielectric material[3] was designed for copper inner electrodes. This material has a high dielectric constant, K = 24000 in room temperature, and

a low DC bias dependence of its dielectric constant. To make MLC's with copper as inner electrodes, the firing atmosphere should be controlled in low oxygen partial pressure ($Po_2$). The relaxor loses oxygen when fired in low $Po_2$, and its insulating resistance (IR) becomes low. This effect happens even in the PbO stable condition. Figure 1 shows the $Po_2$ dependence of conductivity in high temperature[4]. The MgO excess sample has a curve shifted to lower $Po_2$ region. This shift means that additional $Mg^{2+}$ ion has an effect of acceptor type dopant.

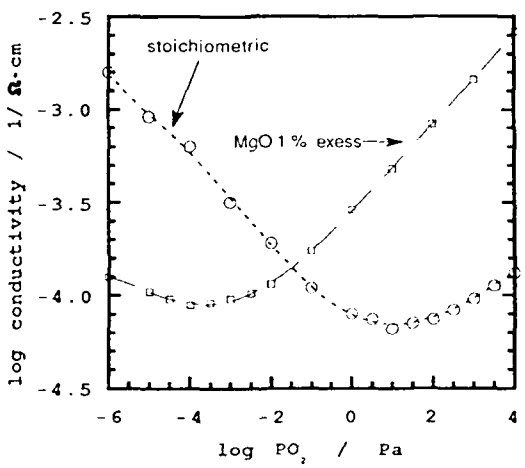


FIGURE 1 Electrical conductivity of PMN measured at 800 °C. Sample was sintered at 1200 °C in Air.

FABRICATIONS

A green chip sample was manufactured using the conventional sheet stacking method. We decided to use copper metal as the starting material for making inner electrodes. Copper oxide can also be used as the starting material[2]. In this case, binder burnout can be performed in air before doing the reduction process of copper oxide. That reduction of copper causes volume change. When that volume change occures, it is

difficult to make MLC's without structural defects. For this reason, we chose to use copper metal as the starting material. When using copper metal, all heat treatments should be performed under low $Po_2$ atmosphere so that copper maintains it's metal state, therefor the binder burnout process becomes difficult. If carbon residue exists, PMN's reduction occurs unavoidably during the sintering process, and the characteristic of the MLC's is seriously influenced. A new technique, $H_2$-$H_2O$-$N_2$ gas mixture atmosphere burnout could produce good result to reduce carbon. The main reaction is explained as

$$C + 2H_2O \rightarrow CO_2 + 2H_2$$

$H_2$ gas is added to keep $Po_2$ low so that the copper does not oxidize. The temperature pattern for the binder burnout section with which we obtained best result is illustrated in Figure 2.

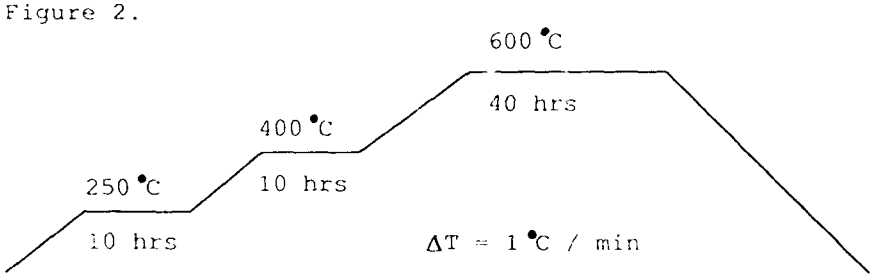


FIGURE 2 Temperature pattern for binder burnout

Table 1 shows the influence of the atmosphere upon the amount of carbon residue. The amount of carbon residue can be reduced to less than 100 ppm with the addition of $H_2O$.

TABLE 1 The amount of carbon residue after burnout

| atmosphere | carbon / ppm |
|---|---|
| $N_2$ | 800 |
| $N_2$+$H_2$ (8 ppm) | 820 |
| $N_2$+$H_2$(8 ppm)+$H_2O$(wetter) | 60 |

The sintering process was also done in the low $P_{O_2}$ atmosphere, controlled by an $H_2$-$H_2O$ gas mixture. In Figure 3, the $P_{O_2}$ must be controlled so that Cu oxidizing nor PbO reducing occurs. We can make MLC's with copper inner electrodes by sintering at 950 degree Celsius within that $P_{O_2}$ region. A SEM photograph of that internal structure is showed in Figure 4.

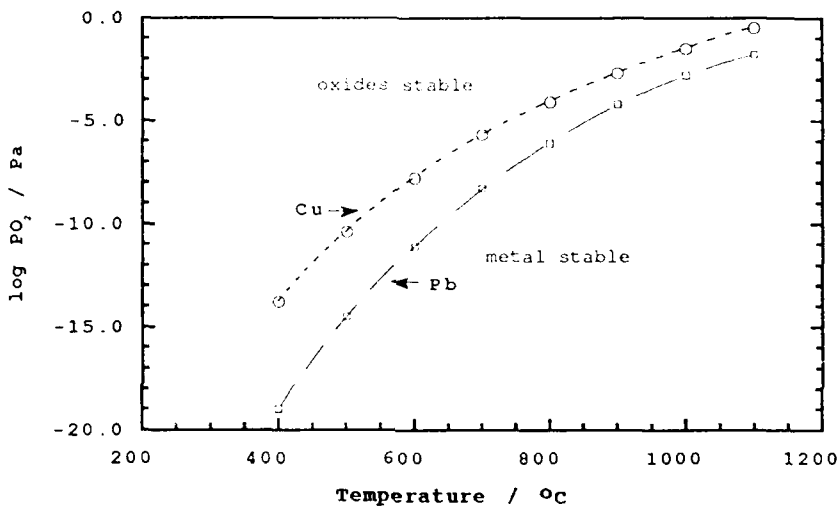


FICURE 3 Stable oxidation states of Cu and Pb

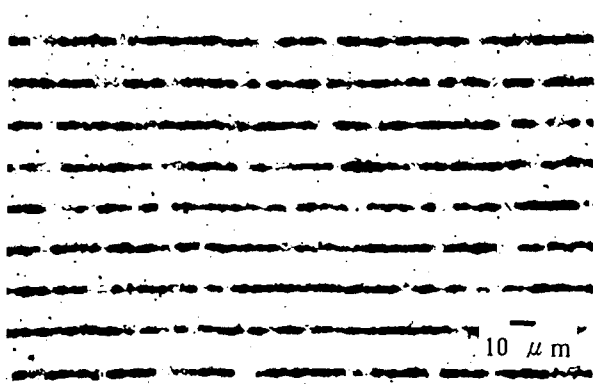


FIGURE 4 SEM of internal structure

## CHARACTERISTICS

The properties of this MLC are listed in table 2. Figure 5 shows capacitance and dielectric loss vs. temperature. This meets EIA characteristic Y5V specifications. The dielectric constant at curie temperature is about 23,000 calculated from dielectric layer thickness and the electrode's area. Figure 6 shows the DC bias dependence of capacitance. In a comparison with $BaTiO_3$, the relaxer is less effected by DC bias voltage.

TABLE 2 Properties of MLC with copper inner electrodes

| size / mm | capacitance at R.T. / μF | tan δ | IR /Ω·cm | VB* / $V \cdot \mu m^{-1}$ |
|---|---|---|---|---|
| 1.2×1.6×1 | 1.3 | .02 | $1 \times 10^{10}$ | 43 |

Layer thickness 14 μm 48 layers
* brake down voltage

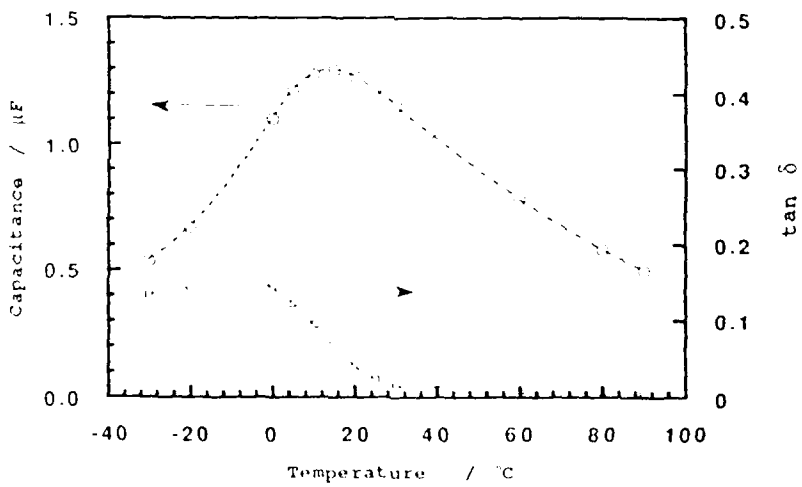


FIGURE 5 Capacitance and dielectric loss vs. temperature

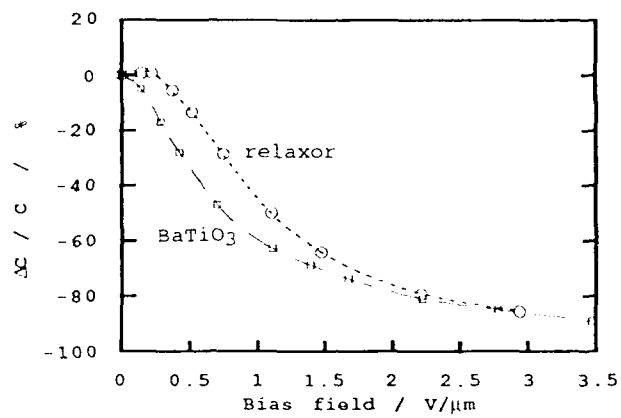


FIGURE 6 Capacitance change vs. bias field

## CONCLUSION

A new MLC with copper inner electrodes was fabricated by using MgO excess PMN-PT. During the binder burnout section, an $H_2$-$H_2O$-$N_2$ gas mixture atmosphere was effective to decrease carbon residue. The resulting MLC has excellent properties, large capacitance and low DC bias dependence.

## References

1. Y. Sakabe, Am. Ceram. Soc. Bull., 66, 9, 1338-41 (1987).
2. J. Kato, Y. Yokotani, H. Kagata and H. Niwa, Jap. J. Appl. Phys., 26, suppl. 26-2, p.90-92, (1987)
3. S. Fujiwara, K. Furukawa and N. Kikuchi, Jap. Pat., 55-51758 (1980)
4. F. Uchikoba and K. Sawamura, Ferroelectrics, 93, 387-388, (1989)

*Ferroelectrics*, 1992, Vol. 133, pp. 145–149
Reprints available directly from the publisher
Photocopying permitted by license only

© 1992 Gordon and Breach Science Publishers S.A.
Printed in the United States of America

# DiC16a

## PLASMA POLYMERISED THIN INSULATING FILMS

ADIANTO AND CYRIL W SMITH
Department of Electronic and Electrical Engineering, University of Salford, Salford M5 4WT

Abstract Volatile organic materials, in argon as a carrier gas, can be deposited as thin insulating films after polymerisation in an r.f. plasma discharge. When deposited on n-type silicon with evaporated gold electrodes, diodes of the Metal - Insulator - Semiconductor type can be produced. Using toluene as the monomer, these can be made with high reverse bias breakdown fields in the thin-film insulator (50-2500 V/$\mu$m). The conduction appears to be determined by charge injection processes. The thin film capacitance is voltage dependent and the reverse bias characteristic is photosensitive.

Thin films of polymerised toluene between metal electrodes have shown well defined hysteresis loops (1) at frequencies below 10 Hz. The polarisation changes giving rise to the hysteresis loops following the application of a step voltage have been investigated. The results did not show a true ferroelectric coercivity for thin films of polymerised toluene.

This technique does give thin insulating films in which very high electrical fields can be maintained and could be used to prepare thin polymeric films of more highly polar volatile materials.

## INTRODUCTION

This paper considers polymerisation process in relation to its application for thin dielectric film preparation. Electrical properties of plasma polymerised thin organic films have been investigated by Gazicky and Yasuda (2) and the possibility of making useful electronic devices incorporating thin organic films has been demonstrated by Forrest and co-workers (3,4,5) amongst others.

The work described in this paper was undertaken to extend preliminary work by Al-Nuaemi (1) Al-Mohamad (6) and Al-Hashmi (7), subsequently published on the results from fabricated of Metal - Organic films - Silicon diodes where the organic film used was toluene ($C_6H_5CH_3$).

## EXPERIMENTAL TECHNIQUE

The Plasma Deposition System used in this experiment is similar to the apparatus used previously (6) with slight modification. The vacuum pump on this system evacuated down to 1.3 mPa and a mixture of argon and the volatile organic material was flowed into the plasma chamber where a 5 MHz r.f. field ionised the mixture. The positive ions were extracted from the plasma chamber by a negative electrode and focused on to the subtrate holder by an Einzel lens.

The uniformity of the films can be better than 10% by correct choice of applied voltages +200 V for the positive electrode, -400 V for the Einzel lens, and an r.f. power of 250 W. The flow rate of the volatile organic material vapour is within the range of 100 ml/min - 140 ml/min. The distance between Einzel lens and substrate holder is about 2.3 cm. The ion current density was of the order 400 $\mu A/cm^2$.

## SAMPLE PREPARATION

For the investigations presented in this paper, two device configurations were made. A metal - Insulator - Metal configuration was made to investigate the properties of plasma polymerised toluene films, and a Metal - Insulator - Semiconductor configuration was used to investigate other electrical properties of the M-I-S diode.

Having etched a silicon water in HF, the wafer was dried and immediately placed on to the sample holder. The films were deposited on n-type silicon of 250-500 Ωcm resistivity and ⟨100⟩ orientation at a thickness of 380 +/- 15 $\mu m$ thickness. These techniques were able to produce organic films with a range of thickness from 150 nm to 300 nm. The metal electrode of gold was thermally evaporated to provide electrical contact on the insulator side and sputtered nickel provided an ohmic contact on the silicon side.

To fabricate a Metal - Insulator - Metal capacitor, a glass microscope slide with pre-deposited gold metal contacts was used as a substrate on which to deposit the film. The capacitor structure was completed by the evaporation of a top electrode also of gold.

## EXPERIMENTAL RESULTS

The M-I-S diodes fabricated have given reverse breakdown voltages of more than 500 V across polymerised toluene films of 200 nm thickness and with forward turn-on voltages between 0.8 - 1.0 V according to the thickness of polymer films. This is shown in Figure 1. Under reverse bias the diode was photosensitive. The capacitance C was measured as function of the applied bias voltage V. Under dark conditions, the points fitted a $1/C^2$ vs V curve (Figure 2). But with illumination, the non-linear results shown in Figure 3 were obtained. The points are the average of 5-10 measurements.

For the M-I-S diode, the photoresponse of the reverse bias characteristic was high and had a spectral dependence as shown in Figure 4.

When M-I-M capacitors were measured in the range 0.01-5 Hz, the voltage/current characteristics were found to be in the form of hysteresis loops such as shown in Figure 5, which is taken from Ref (1).

## CONCLUSION

These results confirm the possibility of using organic polymers as insulating thin films which give photosensitivity on the reverse bias characteristics and very high reverse breakdown voltages under dark condition (7). Below 1 Hz these films give very broad hysteresis loops but no coercivity. Thus it is concluded that true ferroelectricity was not present, and the effect was due to charge injection phenomena.

## REFERENCES


1. I.H. A-J. Al-Nuaemi, "Fundamental and applied study of plasma polymerised thin films and their incorporation in gas sensors and solar cells". **Ph.D. Thesis**, Salford University 1988.
2. M. Gazicky and H Yasuda, **Plasma Chemistry and Plasma Processing**, Vol 3, (3) (1983).
3. S.R. Forrest, M.L. Kaplan, P.H. Schmidt, W.L. Feldmann, and E. Yanowski, **Applied Physics Lett.**, 41, 90 (1982)
4. S.R. Forrest, M.L. Kaplan, and P.H. Schmidt, **Applied Physics**, 55 1492 (1984).
5. S.R. Forrest, and P.H. Schmidt, **Applied Physics**, 59, 513 (1986)
6. A. Al-Mohamad, C.W. Smith, I.S. Al-Saffar, and M.A. Slifkin, **Thin Solid Films**, 189, 175-181 (1990).
7. S.A.R. Al-Hashmi, and C.W. Smith, **Vacuum**, 38, (8-10), 861-64 (1988)


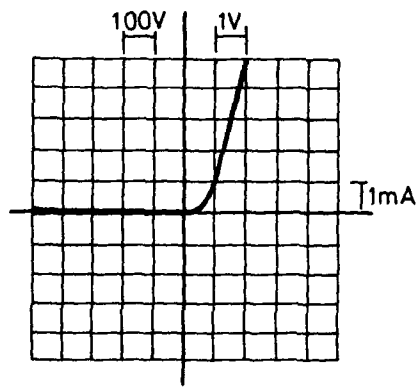


Figure 1. I-V Characteristics of the M-I-S diode. At 500 V (Max. reverse voltage of the Oscilloscope) no reverse breakdown indicated.

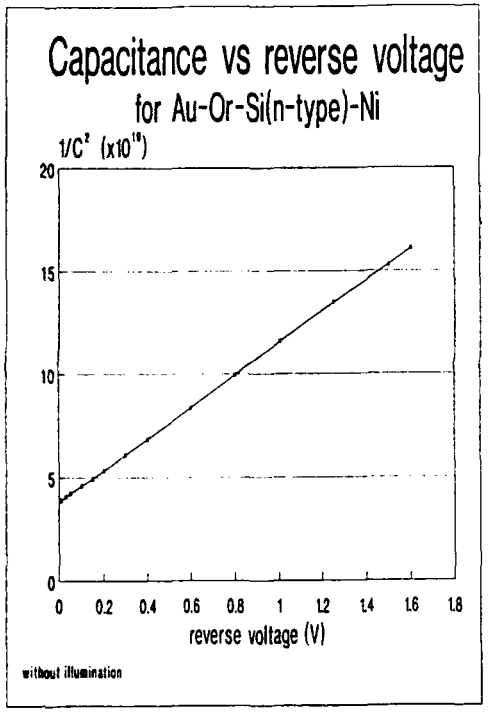


Figure 2. $1/C^2$ vs V under dark conditions.

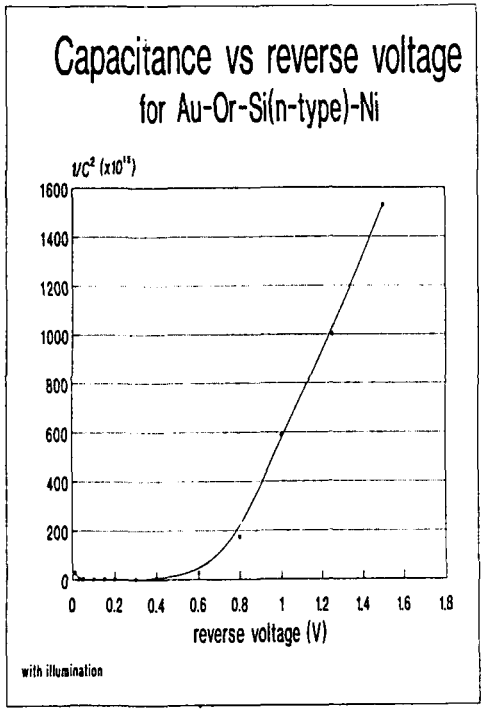


Figure 3. $1/C^2$ vs V under illumination

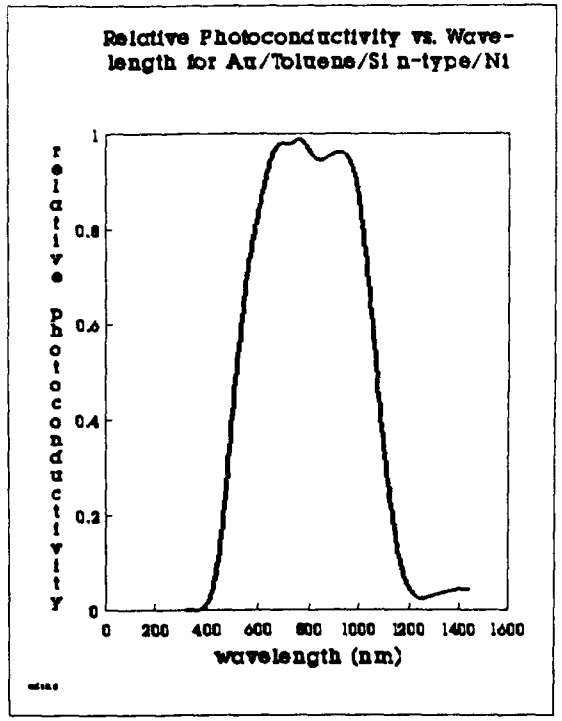


Figure 4. Relative Photoconductivity of the M-I-S diode.

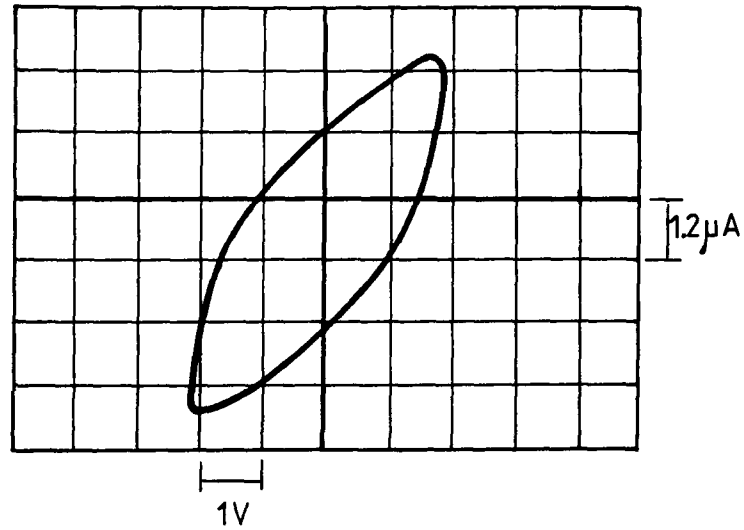


Figure 5. The Hysteresis loop of the M-I-M capacitor.

*Ferroelectrics*, 1992, Vol. 133, pp. 151–158
Reprints available directly from the publisher
Photocopying permitted by license only
© 1992 Gordon and Breach Science Publishers S.A.
Printed in the United States of America

**DiC16b**

# DIELECTRIC RELAXATION SPECTROSCOPY OF A MODEL ANAEROBIC ADHESIVE

**B.P. McGettrick and J.K. Vij**
**Department of Microelectronics and Electrical Engineering, University of Dublin, Trinity College, Dublin 2, Ireland**

## Abstract

The cure behaviour of a model anaerobic adhesive designed to exhibit poor cure through volume (CTV) was investigated using Dielectric Relaxation Spectroscopy. Preliminary results and analysis are presented in this paper. Three different stages in the cure process have been identified. The effects of sample thickness and copper priming of substrates are discussed.

## 1.0 Introduction

In the application of thermosetting resins the end properties depend greatly on the completeness of the crosslinking reaction or the degree of cure. Undercure results in poor physical characteristics. With a view towards monitoring the cure behaviour of thermosets many physical techniques have been used. These include Differential Scanning Calorimetry (DSC) (1,2,3,4), Dynamic Mechanical Thermal Analysis DMTA (5,6), Ultrasonic pulse propagation (7), Nuclear Magnetic Resonance Spectroscopy NMR (8) and Dielectric Spectroscopy (9,10,11,12,13,14,15,16,17).

Dielectric spectroscopy has been used to monitor chemical reactions in organic materials for over 50 years. A comprehensive preview of dielectric analysis of thermoset cure has been published by Senturia et al (18). A vast amount of published literature relates to the studies of epoxy-amine systems. Curing reaction in adhesives have been investigated by Senturia et al (14,18). They report the use of a new microelectronic technique known as microdielectrometry. This involves the implantation of a microdielectrometer chip into a specimen and employs an off-chip electronic feed-back system to monitor changes in dielectric properties of the specimen.

Many dielectric studies of thermosets are influenced by the onset of electrode polarisation effects at short times and the inherent large d.c. conductivity of

thermosets in their fluid state. These factors complicate interpretation of dielectric data. Mangion and Johari (13) have addressed this problem by using model epoxy systems of controlled purity which are relatively free from space charge effects.

We report the use of dielectric relaxation spectroscopy to monitor the process of heterogenous cure in surface initiated bulk polymerisation of a model anaerobic adhesive designed to exhibit poor cure through volume (CTV) at room temperature. "Anaerobics" are a member of the large acrylic adhesive family (19). As the term implies these adhesives require a relatively oxygen-free environment for proper cure such as is found between closely mating assemblies. Cure proceeds by redox initiated free radical polymerisation and is initiated by metallic species inherent on the substrates. Most metallic substrates are sufficiently active to initiate the redox chemistry required for cure. Cure speed can be increased by treating one or both substrates with a suitable accelerating primer. Such primers normally comprise of transition metal salts in a volatile organic solvent. Since cure initiation is surface catalysed and thin bondlines reduce the diffusion rate of reaction inhibiting oxygen, cure homogeneity is favoured by a small gap between substrates (of the order of 10μm). A model has been developed recently by McArdle et al (20) which uses dielectric data to estimate the depth of complete or homogenous cure in thick gap situations (of the order of 300μm).

## 2.0 Experimental

Measurements of the dielectric permittivity, $\varepsilon'$ and the dielectric loss, $\varepsilon''$ in the frequency range 100Hz - 10MHz as a function of cure time up to 100 hours were made on a model anaerobic adhesive formulation FCH. FCH has been designed to exhibit poor cure through volume (CTV) performance. To investigate CTV two adhesive layer thickness of 56μm and 250μm were examined. The electrodes were made of 99.5% pure iron (Goodfellow Metals, Cambridge, UK; FE 000405/11) with (1) no primer and (2) copper primer applied. Copper primer accelerates cure in this formulation. Results are shown in Figures 1(a), 1(b), 1(c), 1(d), 2(a), 2(b), 2(c) and 2(d).

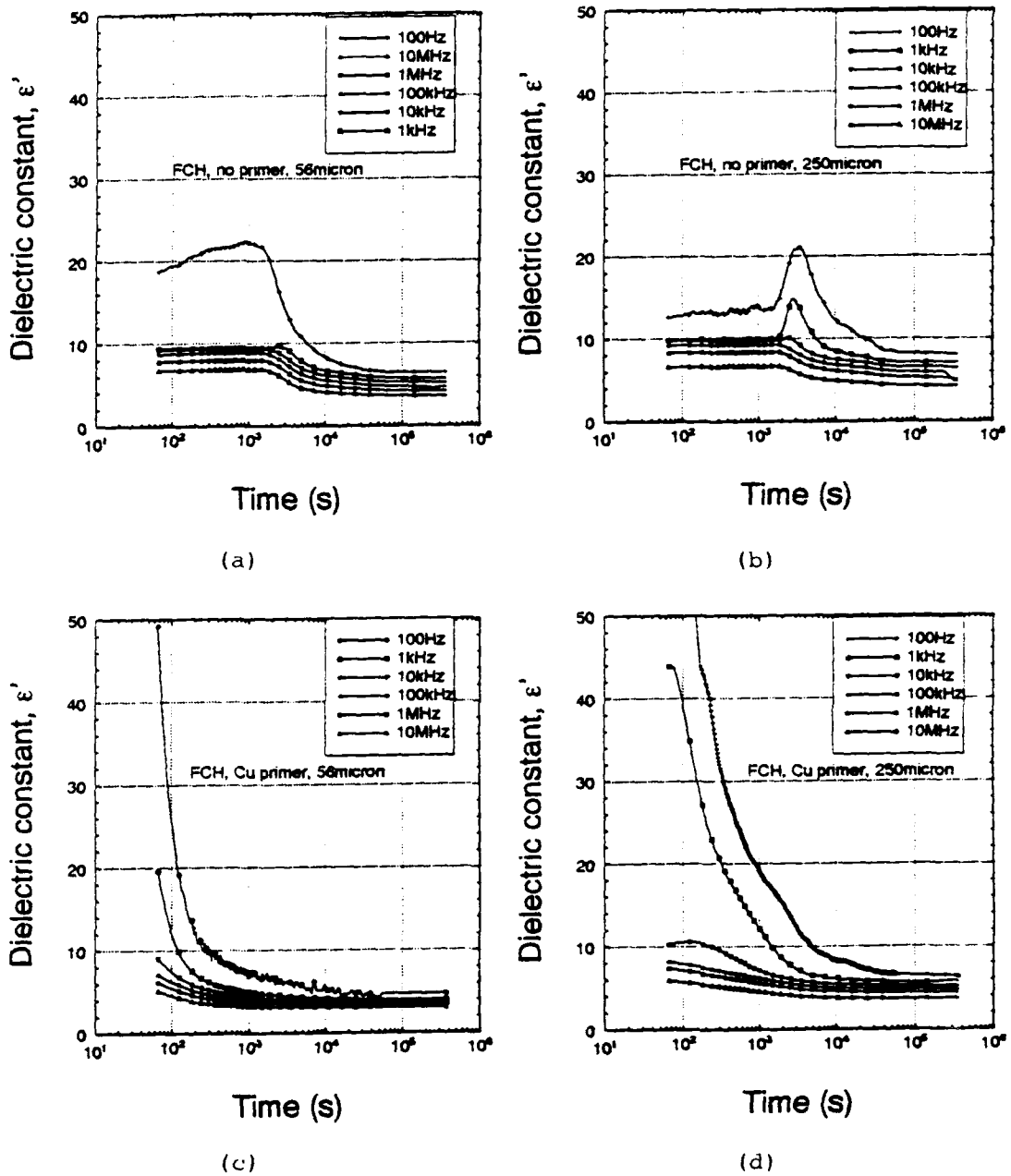


Figure 1. ε' vs time for:
(a) FCH formulation, no primer, 56μm.
(b) FCH formulation, no primer, 250μm.
(c) FCH formulation, Cu primer, 56μm.
(d) FCH forumlation, Cu primer, 250μm.

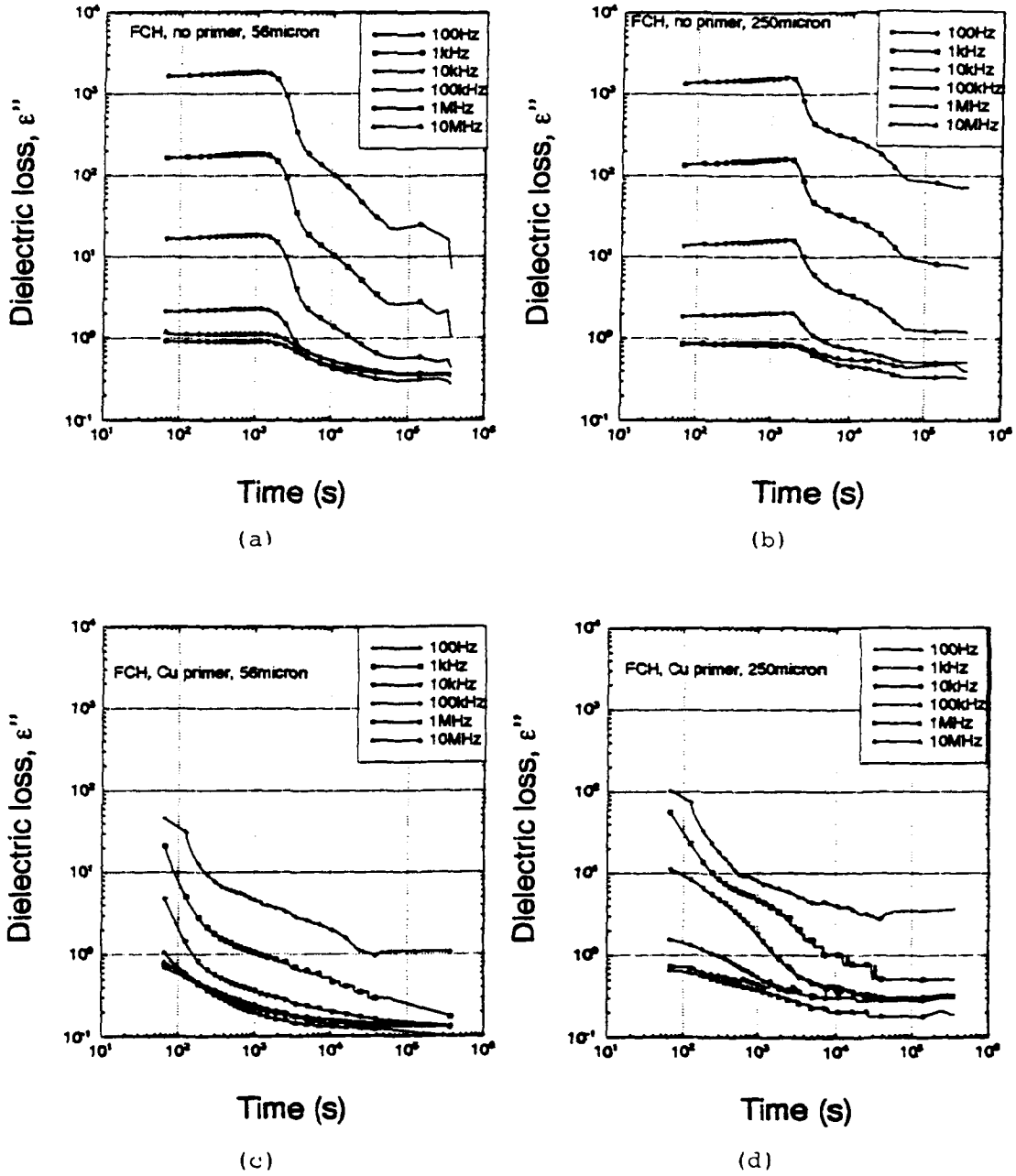


Figure 2. ε'' vs time for:
(a) FCH formulation, no primer, 56μm.
(b) FCH formulation, no primer, 250μm.
(c) FCH formulation, Cu primer, 56μm.
(d) FCH formulation, Cu primer, 250μm.

## 3.0 Discussion

The complex permittivity, $\varepsilon^*$, of a curing system as a function of the cure time can be written as

$$\varepsilon^*(t) = \varepsilon'(t) - i\left[\sigma_0(t) + \sigma_{dip}(t)\right]/\omega\varepsilon_0 \qquad (1)$$

where $\sigma_0$ is the d.c. or ionic conductivity, $\sigma_{dip}$ is the a.c. or dipolar conductivity, $\omega$ is the angular frequency of measurement and $\varepsilon_0$ is the permittivity of free space ($8.854 \times 10^{-12}$ pFm$^{-1}$). As curing proceeds the decrease in $\sigma_0$ relative to the decrease in $\sigma_{dip}$ is relatively greater before gelation. Thereafter the increase in $\sigma_{dip}$ should become more dominant.

### 3.1 Dielectric Permittivity, $\varepsilon'$

Figures 1(a) to 1(d) illustrate the change in $\varepsilon'$ as cure progresses. Three stages in the cure process are evident. For ease of discussion these have been given the following names:

(1) The induction stage.

(2) The activation stage.

(3) The end reaction stage.

The induction stage is the initial time period during which there is no change in $\varepsilon'$ with time. This indicates that during this stage no significant change in the physical properties of the sample is discernible and crosslinking has not commenced. The induction stage may arise due to the time dependent depletion of reaction inhibiting oxygen from the sample. Alternatively it may result from the redox decomposition of the initiator since a finite time is necessary for the formation of the critical free radical concentration required to commence cure. The induction stage is not visible in copper (Cu) primed specimens, implying it is less than 65 seconds (the time taken to assemble the cell and commence measurement). This result illustrates the accelerating effect of a copper primer.

The induction stage is similar for both 56 and 250μm samples. We would expect a shorter induction stage in a thinner sample since cure in surface initiated. We attribute this similarity in induction times to the poor cure through volume (CTV) performance of this material, i.e. CTV is still poor at 56μm. We would expect the induction time to be much less in the 56μm case.

The activation stage describes a period during which $\varepsilon'$ changes with time. Typical results from the literature show a decrease in $\varepsilon'$ during this stage. We

report a significant rise in $\varepsilon'$ to a peak and a subsequent decrease. The peak is greater in the thicker 250μm sample indicating that it may be linked to poor CTV performance. We propose that this phenomenon is due to the gradual build-up and subsequent decay of a mobile layer of charged species in the curing material. These charges are created by the chemical reaction which seems to accelerate after the induction stage. A quantitative analysis of this theory is being carried out by the authors at present.

The third and final stage involves a slow decrease in $\varepsilon'$ with time which eventually flattens off. At this stage the viscosity of the material is increasing as gelation proceeds and $\varepsilon'$ falls because of the gradual immobilisation of polar groups. After 100 hours it is assumed that the material will not cure any further under these conditions. (This assumption was verified by taking spot measurements after the 100 hour period).

## 3.2 The Dielectric Loss, $\varepsilon''$

Figures 2(a) to 2(d) illustrate the change in $\varepsilon''$ with cure time. The three stages discussed in Section 3.1 are identifiable and correspond to the same time periods as those seen in $\varepsilon'$. During the induction stage there is a slight increase in $\varepsilon''$. We attribute this to a build-up of ions arising from the cure initiator activity. $\varepsilon''$ drops at a fast rate during the activation stage. This occurs due to the impeding effect of increasing viscosity on ionic mobility in the material. $\varepsilon''$ is given by the imaginary part of equation (1). If there are N ions per unit volume each carrying a charge magnitude of q and a mobility $\mu$, the ionic conductivity can be expressed by:

$$\sigma_o = Nq\mu \tag{2}$$

$\mu$ is related to the viscosity of a resin by the following equation which is derived from Stoke's law:

$$\mu = \frac{q}{6\pi\eta R} \tag{3}$$

where $\eta$ is the dynamic viscosity of the medium and R is the radius of the ion. The ion mobility in a resin depends primarily on the mobilities of the polymer segments. As cure proceeds polymer segment mobility is impeded due to the formation of a three dimensional macroscopic molecular network. Ion mobility is thus impeded.

The end reaction stage exhibits a slow fall in $\varepsilon''$ with time which eventually levels off as shown in the figures.

## 4.0 Conclusions

Dielectric Spectroscopy was used to study cure in a model anaerobic adhesive designed to exhibit poor CTV. Three stages in the cure process were identified and given the following names:

(1) The induction stage

(2) The activation stage

(3) The end reaction stage.

The induction stage was not visible in copper primed samples illustrating the accelerating effect of copper. Both thick and thin samples exhibited similar induction times as a consequence of the specific formulation used.

Unprimed samples exhibited an increase in $\varepsilon'$ during the activation stage. We propose that this arises from a gradual build-up followed by a collapse of a mobile charged layer during cure. A quantitative analysis of this theory is currently under way. All samples exhibited a large drop in $\varepsilon''$ during the activation stage. This is due to hindered migration of ions through the bulk as viscosity increases.

Dielectric spectroscopy has been shown to be a powerful technique for the analysis of thermoset cure.

## 5.0 References

1. S. Souror and M.R. Kamal, Thermochemica Acta, 14, (1976), 41.
2. A.A. Van Dooren and B.W. Muller, Thermochemica Acta, 65, 1983, 269.
3. A.A. Van Dooren and B.W. Muller, Thermochemica Acta, 65, (1983), 257.
4. J.N. Leckenby, The British Polymer Journal, 15, (1983), 45.
5. W.A. Lee and M.J. Oliver, The British Polymer Journal, 15, (1983), 41.
6. R. Jenkins and L. Karre, J. Appl. Poly. Sci., 10, (1966), 303.
7. G.A. Sofer, A.G.H. Dietz and E.A. Hauser, Ind. Eng. Chem., 45, (1953), 2743.
8. N.M. Grad and I.M. Al'shits, Vysokomol. Sci., A9, No. 4, (1967), 832.
9. M.B.M. Mangion and G.P. Johari, Polymer, 32, No. 15, (1991), 2747.
10. M.B.M. Mangion and G.P. Johari, J. Poly. Sci., Part B, 29, (1991), 437.
11. M.B.M. Mangion and G.P. Johari, J. Poly. Sci., Part B, 29 (1991), 1117.
12. M.B.M. Mangion and G.P. Johari, J. Poly. Sci., Part B, 29 (1991), 1127.

13. M.B.M. Mangion and G.P. Johari, J. Poly. Sci., Part B, 28 (1990), 1621.
14. D.R. Day, T.J. Lewis, H.L. Lee and S.D. Senturia, J. Adhesion, 18, (1985), 73.
15. J.W. Lane, J.C. Seferis and M.A. Bachmann, Poly. Eng. Sci., 26, (1986), 346.
16. G.W. Lawless, Poly. Eng. Sci., 20, (1980), 546.
17. D. Kranbuehl, S. Delos, E. Yi, J. Mayer, T. Hou and W. Winfree, 30th National Sampe Symposium, (1985).
18. S.D. Senturia and N.F. Sheppard, Jr., Adv. Poly. Sci., 80, 1986.
19. C.W. Boeder, Structural Adhesives - Chemistry and Technology, Chap. 5, (1986), 273.
20. C.B. McArdle, J. Burke and B.P. McGettrick, Plastics, Rubber and Composites Processing and Applications, (1991), 16, No. 4, 245.

**Acknowledgements**

The authors are grateful to Loctite Corp. for permission to publish the results outlined above and to Dr. C.B. McArdle of Loctite (Ireland) Ltd. for useful discussions.

*Ferroelectrics*, 1992, Vol. 133, pp. 159-161
Reprints available directly from the publisher
Photocopying permitted by license only

© 1992 Gordon and Breach Science Publishers S.A.
Printed in the United States of America

# DiC17

## HIGH DIELECTRIC CONSTANT CERAMICS IN THE $PbSc_{0.5}Ta_{0.5}O_3$ - $PbZrO_3$ SYSTEM

P. C. OSBOND and R W WHATMORE
GEC-Marconi Materials Technology Ltd., Allen Clark Research Centre, Caswell, Towcester, Northants, United Kingdom. NN12 8EQ

ABSTRACT

Lead scandium tantalate (PST) ceramic has been shown [1,2] to be a ferroelectric material with the perovskite $Pb(B_1B_2)O_3$ structure, and showing a first order phase transition at 25-30°C. The material has a reversible pyroelectric effect under bias, and it has been fully assessed for thermal detector applications [3]. More recently, the properties of a solid solution of (1-x)PST - (x)$PbTiO_3$ have been reported [4,5]; for an x value of 0.4, the Curie temperature was increased to 182°C and the maximum dielectric constant was $>30x10^3$. This paper presents results of a study into the solid solution (1-x)PST - (x)$PbZrO_3$, ($0.075<x<0.20$), and in particular discusses the optimum ceramic process route for obtaining a dielectric exhibiting a sharp phase transition, a high maximum dielectric constant and a low dielectric loss.

Three process routes were investigated for the preparation of (1-x)PST - (x)PZ ceramics using metal oxide powder precursors. The starting materials were PbO, $Sc_2O_3$, $Ta_2O_5$ and $ZrO_2$, all with purities greater than 99.9%. The first method (Method A) involved the ball-milling and single calcination at 900°C of the above oxides. This was then followed by hot-pressing the powder at 40 MPa and 1200°C for 6 hours. The second method (Method B) involved the initial formation of single phase $ScTaO_4$ via the high temperature wolframite prereaction stage, and then the separate preparation of PST and PZ powders using standard ball-milling and calcination conditions. The PST and PZ powders were milled together and calcined at 900°C. The powder was hot-pressed as above, and the ceramic was annealed at temperatures between 1200°C and 1400°C for 4 hours in an alumina crucible. The cooling rate after annealing was 100°C per hour. A PZ spacer powder was used in the crucible in order to maintain a partial pressure of PbO. The third

method (Method C) involved the prereaction of $Sc_2O_3$, $Ta_2O_5$ and $ZrO_2$ to form a $ZrO_2$ 'modified' $ScTaO_4$ phase. This was then calcined with PbO at 900°C and hot-pressed at temperatures between 1100°C and 1200°C. Ceramics prepared via this route were left unannealed.

The X-ray data for the ceramic produced via Method A indicated about 20 wt% of the undesirable pyrochlore phase together with 80 wt% of the perovskite phase. The diffraction lines corresponding to ordering were weak and almost below the limits of detection (1-2 wt%). The phase transition was seen to be very diffuse with a maximum dielectric constant ($\varepsilon_r$) of below 9000 occurring at about 70°C. This poor value was attributed to the relatively large concentration of the the low permittivity pyrochlore phase.

Hot-pressed ceramics (for $0.075<x<0.2$) prepared using Method B, exhibited two peaks in dielectric constant and loss (D) over the temperature range 0°C to 120°C. For all samples, the lower transition temperature ($T_l$) occurred at approximately 35°C, whereas the higher transition temperature ($T_h$) was dependent on the ratio of PZ to PST. It was also found that the relative heights of the two peaks were dependent on the PST - PZ ratio. After annealing at 1400°C, the above ceramics were found to have single, sharper peaks in dielectric constant ($\varepsilon_r$=30 000 at 60°C for x=0.125) and loss. The $T_h$ values, for each composition, were reduced in value after annealing; Eg. for x=0.125, $T_h$=82°C (hot-pressed) and 60°C (annealed).

X-ray diffraction patterns for the calcined powders, hot-pressed ceramics and annealed ceramics prepared via Method B, were compared with undoped PST ceramic. Whereas at least two distinct phases were observed from the PST - PZ powder and the hot-pressed ceramic, the annealed ceramic had a single phase perovskite crystal structure similar to the undoped material. These results, together with the dielectric data, therefore indicated that the calcination of PST+PZ at 900°C, does not form a complete PST - PZ solid solution. Likewise, a mixture of the two phases still exists after hot-pressing. It is only after high temperature annealing, that the single phase (1-x)PST - (x)PZ solid solution is formed.

It was noticeable from the dielectric data for samples prepared via Method C, that a very high dielectric constant (36 000 at 64°C for x=0.125) and sharp dielectric peak were obtained without high temperature annealing. A coarse grain microstructure for this material was observed (15 μm) and it was seen that there was an absence of porosity within individual grains. X-ray data from the calcined powder and the ceramic showed that

there was little or no ordering in the lattice. Since these results indicated that a solid solution had probably been formed during the calcination stage at 900°C, this material was also hot-pressed at 1100°C and 1150°C. Material processed under these conditions exhibited maximum dielectric constants of 24 000 and 27 500 respectively, and average grain sizes of 2 and 4 μm respectively. Unlike the samples produced via Method B, samples with a fine grain size exhibited very high permittivities. Also, the phase transition temperature ($T_h$) decreased with increase in hot-pressing temperature ($T_h$=75, 70 and 64°C for 1100, 1150 and 1200°C respectively). It was interesting to note that the density values were all approximately 100% of the single crystal value calculated from X-ray data (8.900 $gcm^3$); this would explain the high transparency (65-70%) that these sample exhibited over the visible spectrum, and out to a wavelength of almost 6 μm (1670 $cm^{-1}$).

From the above studies, it was seen that the PST - PZ composition which exhibited the highest dielectric constant had an x value of 0.125. The optimum preparation route for this composition was found to be Method C; this gave hot-pressed material with a dielectric constant and loss of 24 000 and 0.1% respectively when the average grain size was 2 μm, and values of 36 000 and 0.075% respectively for a grain size of 15 μm. The microstructure and dielectric properties of PST - PZ samples prepared using method B were found to be highly dependent on the annealing temperature. X-ray and dielectric measurements for these samples indicated that the PST - PZ solution was only achieved when the annealing temperature was >1300°C.

## REFERENCES


1. C.G.F. Stenger and A.J. Burggraaf, Phys. Stat. Sol. (a), **61** (1980) 275
2. C. Zhili, Y. Xi and L.E. Cross, Ferroelectrics, **49** (1983) 213
3. N.M. Shorrocks, R.W. Whatmore and P.C. Osbond, Ferroelectrics, **106** (1990) 1223
4. J.R. Giniewicz, A.S. Bhalla, and L.E. Cross, Ferroelectrics Letters, **12** (1990) 355
5. J.R. Giniewicz, A.S. Bhalla, and L.E. Cross, Ferroelectrics, **118** (1991) 157


## ACKNOWLEDGEMENTS

This work has been carried out with the support of the Procurement Executive, Ministry of Defence. The Authors would also like to thank R. Watton (DRA Malvern), N.M. Shorrocks and J.M. Herbert for useful discussions, and M.J. Latimer for assistance with the production of ceramic samples.

*Ferroelectrics*, 1992, Vol. 133, pp. 163–168
Reprints available directly from the publisher
Photocopying permitted by license only

© 1992 Gordon and Breach Science Publishers S.A.
Printed in the United States of America

# DiP219

## LINEARIZATION OF DIELECTRIC NONLINEARITY BY INTERNAL BIAS FIELDS

U. ROBELS, CH. ZADON AND G.ARLT
Institut für Werkstoffe der Elektrotechnik, Aachen University of Technology, W-5100 Aachen, Germany

Abstract The dielectric response of $BaTiO_3$ and PZT ceramics to an applied ac field is found to be nonlinear even at weak signals. The nonlinearity shows a substantial dependence on acceptor doping and a pronounced aging behaviour. The nonlinear dielectric behaviour $\varepsilon(\hat{E})$ can be described by a polynomial fit using only even powers up to the fourth. The polynomial coefficients decrease with time. The aging of the dielectric nonlinearity is correlated to the buildup of the internal bias.

## INTRODUCTION

The aging behaviour of the dielectric, piezoelectric and elastic material properties of ferroelectric ceramics is well known and attributed to domain wall motion by many authors (e.g. [1, 2, 3]). In this paper we describe the aging of the nonlinear dielectric response, which is another aspect of aging [4, 5, 6] and becomes important for thin film applications. The observed aging of the dielectric nonlinearity is correlated to the buildup of internal bias fields and attributed to domain wall motions too.

During the aging of the specimen the weak signal dielectric response versus the applied ac field is measured. The measurements were performed on undoped and on acceptor doped barium titanate (BT) and PZT ceramics having the following compositions:

| | | |
|---|---|---|
| PZT-Fe-y | $Pb(Zr_{0.58}Ti_{0.42})_{1-y}Fe_yO_3$ | |
| BT-X-y | $Ba(Ti_{1-y}X_y)O_3$ | with X = Al, Cr, Ni |

All samples were prepared by the mixed oxide method and conventional sintering techniques. Before the beginning of the aging measurement the ceramic samples were thermally deaged at $T > T_C$ and poled after cooling to the appropriate aging temperature. All of the measurements discussed here were performed on fully poled ceramics.

For the measurement of the dielectric nonlinearity a modified Schering bridge and a two phase lock-in amplifier for zero adjustment were used. From the measured capacitance and $\tan\delta$ values of the specimen the effective dielectric constant $\underline{\varepsilon} = \varepsilon' - j\cdot\varepsilon''$ at the fundamental mode of the applied ac field is determined. The largest ac field applied to the ceramics was small enough to avoid irreversible effects in the small signal dielectric constant.

## EXPERIMENTAL RESULTS

### Dependence on dopand type

The dielectric nonlinearity of BT and PZT ceramics depends strongly on the presence and the kind of dopands. In Fig. 1 the measurements for some of the observed acceptor doped ceramics in their aged state are shown. In order to compare the nonlinear dielectric behaviour of different types of ceramics the relative deviation $\frac{\varepsilon'(E) - \varepsilon'(0)}{\varepsilon'(0)}$ is plotted.

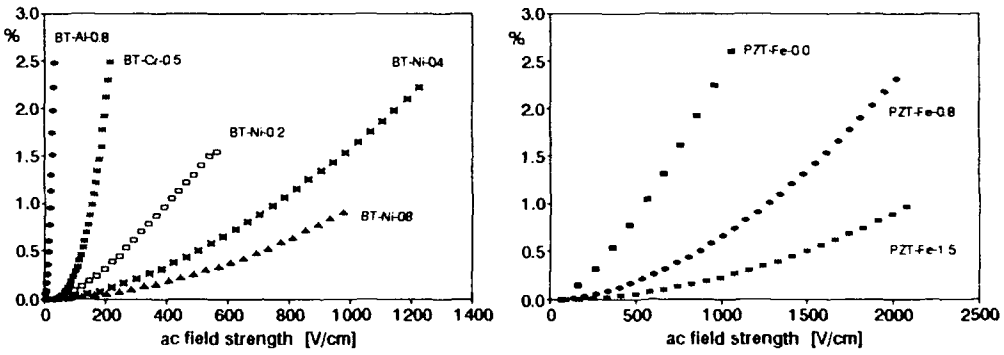


FIGURE 1: Relative increase of $\varepsilon'$ of various acceptor doped BT and PZT ceramics. All samples were aged 72 hours at 80°C prior to measurement. (f = 222 Hz)

As it is clear from the figure by doping the dielectric nonlinearity can be decreased drastically. At the beginning of aging the differences in the nonlinear behaviour are more pronounced. In BT ceramics double charged acceptors ($Ni^{2+}$) cause less nonlinearities than single charged acceptor ions ($Al^{3+}$, $Cr^{3+}$).

### Phenomenological treatment of the dielectric nonlinearity

In Fig. 2 the complex dielectric constant $\underline{\varepsilon}$ versus the applied ac field strength $\hat{E}$ is shown for various aging times. The measurement was performed on a Fe doped PZT ceramic. In the figure two different aging phenomena are clearly visible: The decrease of $\underline{\varepsilon}(E = 0)$

with time is well known and has been observed in other papers [2, 3]. In addition with increasing aging time the nonlinear dielectric behaviour $\underline{\varepsilon}(E)$ decreases too. The observed linearization is similar for both, the real and the imaginary part of the dielectric constant and has been found in all of the observed acceptor doped ceramics.

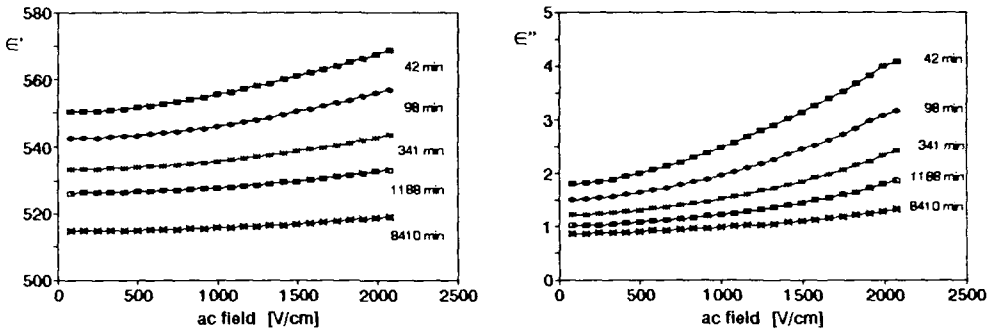


FIGURE 2: $\varepsilon'(E)$ and $\varepsilon''(E)$ at different aging times for a PZT-Fe-1.5 ceramic. (T = 80°C, f = 222 Hz)

In order to get a useful description for the dielectric nonlinearity the measured dielectric constant is approximated by a polynomial

$$\underline{\varepsilon}(\hat{E}) = \underline{\varepsilon}(0) + \underline{a} \cdot \hat{E}^2 - \underline{b} \cdot \hat{E}^4 \qquad a', a'', b', b'' > 0$$

For all of the observed ceramics only even potencies of $\hat{E}$ up to the power of 4 are sufficient. The two polynomial terms are opposite in sign. The first term softens the dielectric behaviour, the second term hardens it. The polynomial coefficients decrease with time describing the linearization of $\underline{\varepsilon}(\hat{E})$ during the aging (fig 3). The second coefficient $\underline{b}$ decreases more rapidly than the first one $\underline{a}$. Both time dependencies can not be described with simple logarithmic time laws.

The linearization of the nonlinear dielectric constant is thermally activated according to an Arrhenius law. As it is shown in fig 4 with increasing temperature the decrease of the polynomial coefficients proceeds faster. At higher temperature the extent of aging decreases and the saturation of the aging behaviour is observed in less time. For lower temperatures (40°C) within the time of measurement no saturation is observed.

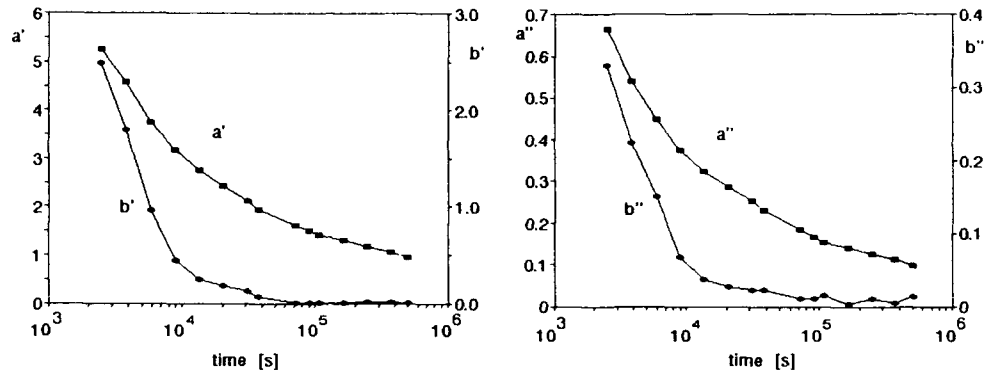


FIGURE 3: The polynomial coefficient $\underline{a}$ and $\underline{b}$ (left: real parts, right: imaginary parts) for a PZT-Fe-1.5 ceramic. The coefficients are plotted in arbitrary units. (T = 80°C, f = 222 Hz)

Sometimes the dielectric nonlinearity is described by a single parameter $E_{cr}$, defined as the ac field strength applied to the specimen in order to increase $\varepsilon'$ by a certain percentage $\Delta\varepsilon'$ (here: $\Delta\varepsilon' = 1\%$) [4, 6]. Between the polynomial coefficients $a'$, $b'$ and the critical field $E_{cr}$ a fixed relation exist by the root of $\varepsilon'(0) \cdot \Delta\varepsilon' = a' \cdot E_{cr}^2 - b' \cdot E_{cr}^4$. The critical field increases in time almost logarithmically until saturation occurs (Fig. 5, 6). For the imaginary part we get a similar behaviour, however, the difference $\Delta\varepsilon''$ must be greater.

With increasing temperature the dielectric nonlinearity decreases leading to an increase of $E_{cr}$ (Fig. 5). This behaviour is contrary to that found in [6]. The critical field is almost proportional to the amount of acceptor doping as can be seen for Ni doped BT ceramics in Fig. 6 and observed also for Fe doping [4].

Linearization and internal bias

In acceptor doped ceramics a distinct relation between the decrease of the weak signal dielectric constant during aging and the buildup of internal bias fields is observed [7, 8].

A similar relation of the internal bias $E_i(t)$ to the critical field $E_{cr}(t)$, which describes the nonlinear dielectric behaviour, is observed. The increase of both properties with time proceeds with similar time laws. This can be seen in Fig. 7, where the $E_{cr}(t)$ values are plotted versus $E_i(t)$ with the time of aging as a parameter. This linear relation between $E_{cr}$ and $E_i$ in well aged ceramics (saturated values) has been observed already for acceptor doped ceramics [4]. The temperature dependence of both properties, however, are contrary: whereas $E_i$ decreases at higher temperatures [9] $E_{cr}$ increases.

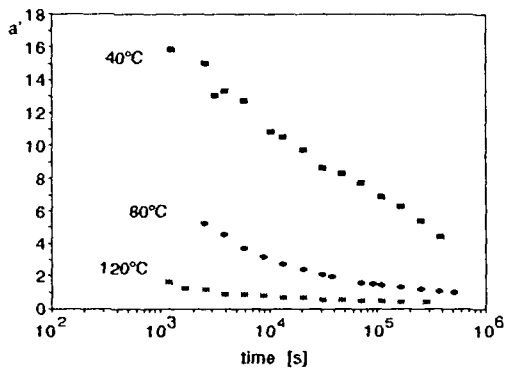


FIGURE 4: $a'(t)$ for PZT-Fe-1.5 at different temperatures (arbitrary units, f = 222 Hz)

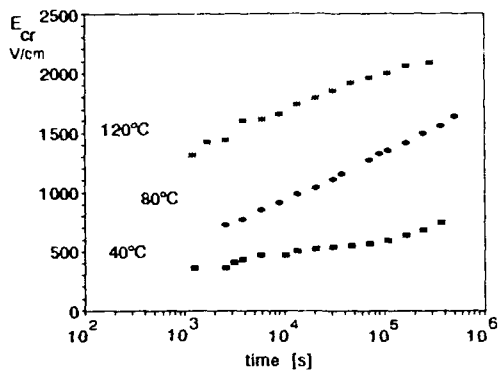


FIGURE 5: $E_{cr}(t)$ for PZT-Fe-1.5 at different temperatures

If the measurements shown in Fig. 7 are approximated by straight lines the critical fields for the not aged ceramics ($E_i \rightarrow 0$) can be calculated. These values should be positive. For some of the observed ceramics the extrapolated $E_{cr}$ values are negative (e.g. PZT-Fe-1.5), indicating other aging processes not correlated to internal bias fields at the initial time of linearization.

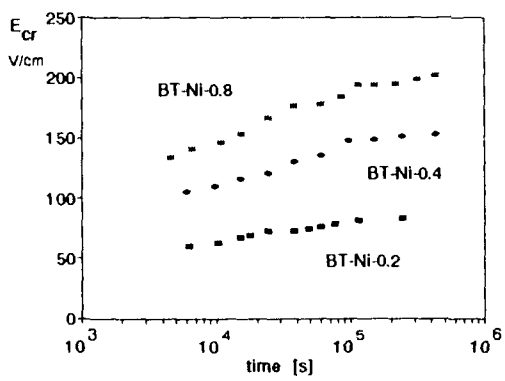


FIGURE 6: $E_{cr}(t)$ for Ni doped BT ceramics at T = 70°C

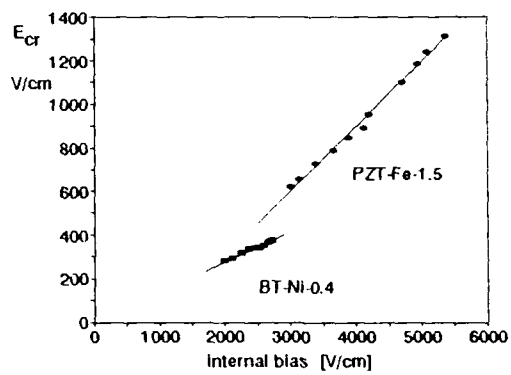


FIGURE 7: $E_{cr}(t)$ vs. $E_i(t)$ for PZT-Fe-1.5 (80°C) and BT-Ni-0.4 (70°C) ceramics

## CONCLUSION

The performed aging measurements reveal a linearization of the dielectric behaviour in time for acceptor doped BT and PZT ceramics. This aging depends strongly on the kind and on the amount of acceptor doping. Thus it is closely related to the buildup of internal

bias fields, which are also caused by acceptor doping [9].

The nonlinear dielectric behaviour discussed above is attributed to the domain wall movement mainly [6, 10]. Intrinsic contributions to the dielectric nonlinearity are expected to occur only at much higher ac fields than the applied fields. By the clamping model discussed in [8] the linearization can be understood qualitatively: As a result of the increasing internal bias (i.e. the alignment of defect dipoles) the domain walls are clamped by additional clamping forces, leading to lower domain wall contributions to the material properties. According to the reduced domain wall movement the dielectric nonlinearity decreases too.

The opposite temperature dependence, however, of the internal bias and the strength of the nonlinearity indicates additional effects causing the observed linearization. The physical origin for the observed nonlinearities is not clear yet. They are possibly caused by bending effects in domain wall displacement [11].

## References

[1] K.W. Plessner, Proc. Phys. Soc., B 69, 1261 (1956)
[2] K. Carl and K.H. Härdtl, Ferroelectrics, 17, 473 (1978)
[3] R. Herbiet, H. Tenbrock and G. Arlt, Ferroelectrics, 76, 319 (1987)
[4] H-J. Hagemann, J. Phys. C: Solid State, 11, 3333 (1978)
[5] U. Robels and G. Arlt, 19th Spring Conference on Ferroelectricity, Halle (1991)
[6] Shaoping Li, Wenwu Cao and L.E. Cross, J. Appl. Phys., 69, 7219 (1991)
[7] U. Robels, R. Lohkämper and G.Arlt, ISAF 90, Urbana/Champaign (1990)
[8] U. Robels, L. Schneider-Störmann and G. Arlt, ECAPD 2, London (1992)
[9] G. Arlt and H. Neumann, Ferroelectrics, 76, 451 (1987)
[10] Q.M. Zhang, W.Y. Pan, S.J. Jang and L.E. Cross, J. Appl. Phys., 64, 6445 (1988)
[11] G. Arlt and N.A. Pertsev, J. Appl. Phys., 70, 2283 (1991)

*Ferroelectrics*, 1992, Vol. 133, pp. 169–174
Reprints available directly from the publisher
Photocopying permitted by license only
© 1992 Gordon and Breach Science Publishers S.A.
Printed in the United States of America

**DiP222**

# MACROSCOPIC BEHAVIOUR OF THE DIFFUSE PHASE TRANSITIONS IN FERROELECTRIC RELAXORS

R.P.S.M. LOBO and R.L. MOREIRA
Depto. de Fisica, ICEx, UFMG, C.P. 702, CEP 30161, Belo Horizonte MG, Brazil.
E-mail: OPTIKA@BRUFMG.BITNET

and N.D.S. MOHALLEM
Fundaçao Centro Tecnologico de Minas Gerais, Materiais Opticos e Eletronicos, C.P. 2306, CEP 31170, Belo Horizonte MG, Brazil.

Abstract In this work we have explained the diffuse phase transitions (PT) of sol-gel grown Barium Titanate samples through a model where weighted sums of "normal" PT from micro-regions of the material are performed. Using Landau-Devonshire's expressions for ferroelectric transitions, we obtain the smeared macroscopic behaviour of the PT. The results are used to show why deviations from Curie-Weiss, and also Smolensky-Isupov, behaviours of the dielectric permittivity are very often found in ferroelectric relaxors.

## INTRODUCTION

Diffuse phase transition is a very common occurrence in solid solutions and other disordered structures.[1-8] The ferroelectric-paraelectric transition, in these systems, is characterized by a smoothness of the physical anomalies in the critical region (due to the coexistence of the two phases in a large temperature interval). In ferroelectric relaxors this kind of transition is present, and even, is at the origin of their characteristic properties.[9]

In the systems presenting diffuse PT, the macroscopic properties can be described by a weighted sum of contributions from a large number of micro-regions undergoing normal PT at different critical temperatures.[2,3,5,10] When investigating the dielectric

properties, this approach leads, in a crude calculation, to the Smolensky-Isupov law, i.e., the reciprocal dielectric susceptibility ($\chi^{-1}$) in these systems has a quadratic temperature dependence, instead of a linear one as in normal ferroelectrics. In fact, many authors have used an empirical law - $\chi^{-1} \propto (T-T_{peak})^{\gamma}$ - with a constant $\gamma$ exponent between 1 and 2, for the temperature dependence of $\chi^{-1}$.[4,11]

The purpose of the present work is to report our investigations on the dielectric properties of ferroelectric materials presenting diffuse PT. Barium Titanate samples have been used to exemplify both, the use of the above mentioned model (the macroscopic properties viewed as an envelope of a great number of contributions) and the general thermal behaviour of $\chi^{-1}$ after the peak maximum.

## EXPERIMENTAL

Barium Titanate samples have been prepared by sol-gel techniques.[12] The diffuse nature of their transitions is linked to the small size of their grains: the smaller the grains, the greater the diffuse character.[13] The grain sizes have been determined by Scanning Electron Microscopy.

Dielectric measurements were realized at 10 KHz using a General Radio 1615-A capacitance bridge, after deposition of gold electrodes on the surfaces.

## RESULTS AND DISCUSSION

In a sample undergoing diffuse PT, the ferroelectric and paraelectric phases coexist in a large temperature interval. So, in order to describe its macroscopic properties, one can consider the sample as divided up into a very large number of micro-regions, each one with a specific critical temperature. The overall macroscopic properties would be the sum of the individual

contributions. Thus, if we are looking for dielectric response, we will have[2]

$$\varepsilon(T) = \int_0^{\infty} \varepsilon'(T,T_c)\ f(T_c)\ dT_c\ ; \qquad (1)$$

where $\varepsilon'(T,T_c)$ is a classical expression for the temperature dependence of the dielectric constant for a material undergoing normal PT at $T_c$,[10,14] and $f(T_c)$ a particular critical temperature distribution function.

Now, this approach is applied to study the diffuse PT of Barium Titanate samples. In order to fit the experimental data, a gaussian form has been used in Eq.(1), following the suggestion of Diamond.[2] The results are presented in Figure 1, where a, b and c represent the samples in increasing order of grain sizes (the converse holds for the diffuse character of the PT). The grain sizes (L) and the adjust parameters are presented in Table I, where C is the Curie constant, $\Delta T = T_c - T_o$ ($T_o$ is the Curie-Weiss temperature) and $\nu$ and $T_m$ characterize a Gaussian distribution function ~ $f \propto \exp\ [-(T_m-T_c)^2/\nu^2]$. The poor adjust for the lower temperature region can be understood in terms of the increasing of the dielectric constant by domain wall effects, what has been neglected in this treatment.[15]

TABLE I Adjust parameters for Barium Titanate samples.

| Sample | L(μm) | $\nu$(°C) | $T_m$(°C) | C(°C) | ΔT(°C) |
|---|---|---|---|---|---|
| a | 0.8±0.2 | 13 | 121.0 | $1.60\times10^5$ | 14 |
| b | 3.5±1.5 | 5 | 126.5 | $1.05\times10^5$ | 19 |
| c | 5±1 | 1.7 | 128.0 | $1.65\times10^5$ | 15 |

We remark that this approach contains several important implicit consequences. First, it assumes that all micro-regions have the same Landau expansion parameters, the only difference being the transition temperature $T_c$. So, the entropy change (per unity volume) and the polarization jump

at $T_c$ are assumed to be the same for all micro-regions. Further, the peak temperature occurs into the transition range interval, when around one nineth of the material still remains ferroelectric. Finally, the most important consequence is the fact that the observed deviations of the Curie-Weiss law in the diffuse PT can be easily understood, as we discuss in the following.

In a recent work,[16] we have proposed that the assumption of the Landau-Devonshire's theory for micro-regions of a material undergoing diffuse PT leads to a crossover region between a Smolensky-Isupov behaviour and a Curie-Weiss one. Let us now use the dielectric data of Figure 1 in order to investigate their behaviours after the peak maximum. Figure 2 shows both, theoretical and experimental data, in a log-log plot of $\chi^{-1}(T)-\chi^{-1}(T_{peak})$. The two straight lines drawn represent the Curie-Weiss ($\gamma$=1) and Smolensky-Isupov ($\gamma$=2) behaviours. This figure shows that the $\gamma$ exponent of the generally used empirical expression is actually temperature dependent and goes from 2, near the transition, to 1, far from it. In fact, the two laws above mentioned are two limits for the $\gamma$ coefficient in the diffuse PT.

## SUMMARY

The diffuse PT of sol-gel grown $BaTiO_3$ ceramics have been investigated by dielectric techniques. The diffuse character of the transition is shown to increase for decreasing grain sizes. The experimental data could be adjusted as an envelope of individual (normal) responses, and then, the Curie constant could be determined for each sample. It has been shown that the reciprocal dielectric susceptibility presents a crossover region between the Smolensky-Isupov and Curie-Weiss behaviours.

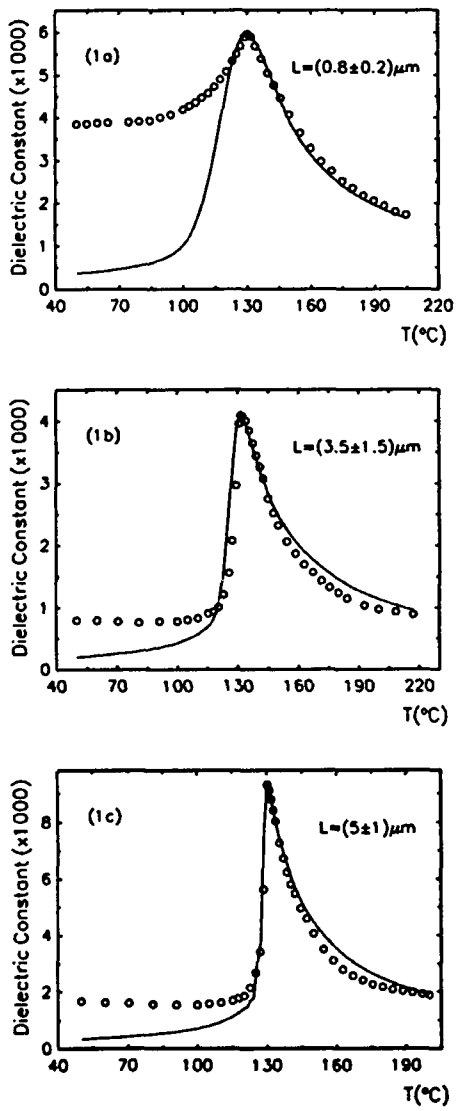


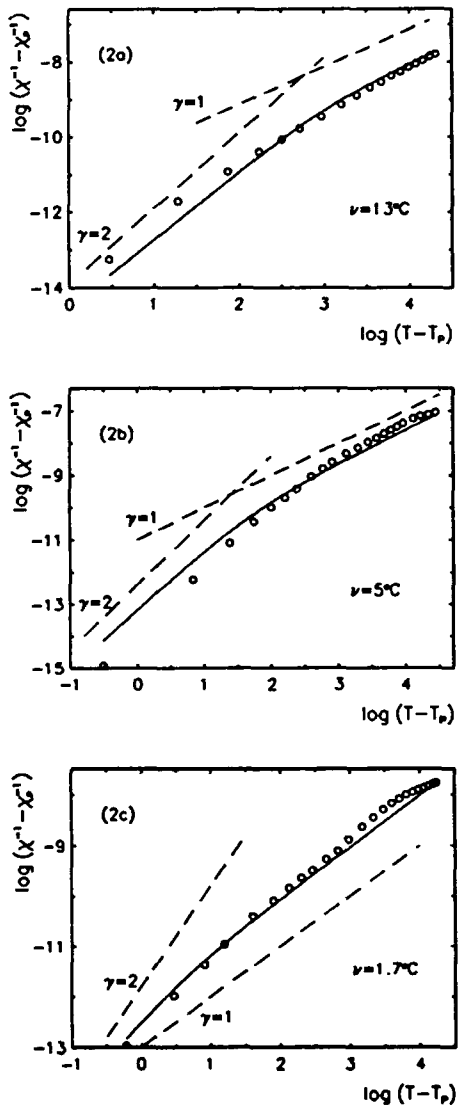


FIGURE 1 Experimental (circles) and theoretical (continuous line) thermal behaviours of the dielectric constant of Barium Titanate samples with increasing grain sizes from a to c.

FIGURE 2 Log - log plot of $\chi^{-1} - \chi^{-1}_{peak}$ vs. $T-T_{peak}$ for the corresponding data of Figure 1, showing the crossover between Smolensky-Isupov ($\gamma=2$) and Curie-Weiss ($\gamma=1$) regions. Log is taken for natural logarithm.

ACKNOWLEDGEMENTS

We would like to thank the Brazilian agencies CNPq, RHAE and FAPEMIG for financial support towards this work.

REFERENCES

1. G. A. Smolensky and V. A. Isupov, Soviet Journ. Techn. Phys., 24, 1375 (1954).
2. H. Diamond, J. Appl. Phys., 32, 909 (1961).
3. V. V. Kirillov and V. A. Isupov, Ferroelectrics, 8, 3 (1973).
4. R. Clarke and J. C. Burfoot, Ferroelectrics, 8, 505 (1974).
5. J. Kuwata, K. Uchino and S. Nomura, Ferroelectrics, 22, 863 (1979).
6. N. Setter and L. E. Cross, J. Appl. Phys., 51, 4356 (1980).
7. V. A. Isupov, Ferroelectrics, 90, 113 (1989).
8. M. Kuwabara, K. Goda and K. Oshima, Phys. Rev. B, 42, 10012 (1990).
9. L. E. Cross, Ferroelectrics, 76, 241 (1987).
10. R. P. S. M. Lobo, R. L. Moreira, N. D. S. Mohallem and B. V. Costa, submitted to Ferroelectrics.
11. C. Alemany, J. Garcia-Gallo, B. Jimenez, E. Maurer and J. Mendiola, Ferroelectrics, 54, 137 (1984).
12. N. D. S. Mohallem, PhD Thesis (University of Sao Paulo, 1990).
13. R. P. S. M. Lobo, N. D. S. Mohallem, R. L. Moreira and B. V. Costa, in preparation.
14. J. Grindlay, An Introduction to the Phenomenological Theory of Ferroelectricity (Pergamon Press, Oxford, 1970), pp. 198-202.
15. G. Arlt, Ferroelectrics, 104, 217 (1990).
16. R. L. Moreira and R. P. S. M. Lobo, to appear in J. Phys. Soc. Japan, 61 (6) (1992).

*Ferroelectrics*, 1992, Vol. 133, pp. 175–180
Reprints available directly from the publisher
Photocopying permitted by license only
© 1992 Gordon and Breach Science Publishers S.A.
Printed in the United States of America

# DiP223

## STRONGLY TEMPERATURE DEPENDENT ELECTRO-OPTIC COEFFICIENTS IN $BaTiO_3$

F. ABDI, M.D. FONTANA, M. AILLERIE
Groupe Matériaux Optiques à Propriétés Spécifiques-C.L.O.E.S., Université de Metz et Supelec, 2 rue E. Belin, 57078 Metz Cedex 3, France
G. GODEFROY
Laboratoire de Physique des Solides-UA CNRS 785, Université de Bourgogne, B.P. 138, 21004 Dijon Cedex, France

Abstract : By means of a Sénarmont set up and a very sensitive method, electro-optic coefficients in $BaTiO_3$ are accurately determined from the phase measurement of the retardation $\Gamma$ due to the electric field induced birefringence of the crystal. Electro-optic properties are investigated as a function of temperature around room temperature. A very large value of the coefficient $r_{42}$ is found, in agreement with previous investigations. In addition, this coefficient is shown to be very sensitive to the temperature even for a very small change. The importance of both the thermo-optic effect and the thermal variation of electro-optic properties is pointed out for device applications of $BaTiO_3$.

## INTRODUCTION

Perovskite oxide crystals are well known materials with large non-linear optical and electro-optical (EO) coefficients[1]. Among this family, $BaTiO_3$ exhibits the largest EO coefficient which was up to now detected[1]. It leads this compound to be promising for various optical applications. In particular, it can be favourably used for photorefractive applications such as light diffraction, two- of four- wave mixing, phase conjugating mirror[2], or for EO applications, such as bulk or waveguide modulator or switcher[3,4].

EO properties are known to be strongly affected by impurities specially iron doping[4,5] or oxygen vacancies[6]. The accurate determination of the EO coefficients is needed for the various reasons as follows i) the knowledge of the figures of merit and switching voltage[4] ii) the relative contribution of electrons and holes in the photorefractive properties[7] iii) the influence of the nature and concentration of defects[7]. We have recently shown that the thermal variation of the refractive index via the thermo-optic effect has to be accounted for in order to obtain correct values of the EO coefficients[8]. Therefore the results previously reported[9,10] in $BaTiO_3$ may

be questionable. Further the potential applications of $BaTiO_3$ requires that the coefficients have to be independent of temperature.

Our study therefore concerns the accurate determination of the EO coefficients in $BaTiO_3$ and their temperature dependence with a new and very sensitive method.

## ELECTRO-OPTICAL EFFECT IN $BaTiO_3$

Electro-optic properties in $BaTiO_3$ ($C_{4v}$ point group) can be described by the three components $r_{13}$, $r_{33}$ and $r_{42}$ of the EO tensor.

With the applied electric field $E=(E_1,E_2,E_3)$ the optical indicatrix is given in the principal axis system of the crystal without field by :

$$\left(\frac{1}{n_o^2} + r_{13}E_3\right)x^2 + \left(\frac{1}{n_o^2} + r_{13}E_3\right)y^2 + \left(\frac{1}{n_e^2} + r_{33}E_3\right)z^2 + 2r_{42}xzE_1 + 2r_{42}yzE_2 = 1 \tag{1}$$

where $n_o$ and $n_e$ are respectively the ordinary and extraordinary refractive indices.

The EO $r_{42}$ coefficient is determined in the transverse configuration when the electric field is along the x axis and the light propagation along the y axis.

With E=(E,O,O), eq 1 becomes :

$$\frac{x^2}{n_o^2} + \frac{y^2}{n_o^2} + \frac{z^2}{n_e^2} + 2r_{42}xzE = 1 \tag{2}$$

The indicatrix can be expressed in a new axis system (primed axes) by a rotation through an angle $\theta$ around the y axis :

$$X'^2\left(\cos^2(\theta)/n_o^2 + \sin^2(\theta)/n_e^2 + 2r_{42}E\cos(\theta)\sin(\theta)\right) + Y'^2/n_o^2 + Z'^2\left(\sin^2(\theta)/n_o^2 + \cos^2(\theta)/n_e^2 - 2r_{42}E\cos(\theta)\sin(\theta)\right) + 2X'Z'\left(\cos(\theta)\sin(\theta)\left(1/n_e^2 - 1/n_o^2\right) + r_{42}E\left(\cos^2(\theta) - \sin^2(\theta)\right)\right) = 1 \tag{3}$$

where the axis X',Y' and Z' are the principal axes of the indicatrix if the last term of the right member of equation 3 is equal to zero, or if :

$$tg(2\theta) = \frac{2r_{42}E}{\frac{1}{n_e^2} - \frac{1}{n_o^2}} \tag{4}$$

Introducing the condition eq 4 into eq 3, we obtain :

$$\left[\frac{1}{n_o^2} + r_{42}E\,tg(\theta)\right]X'^2 + \frac{Y'^2}{n_o^2} + \left[\frac{1}{n_e^2} - r_{42}E\,tg(\theta)\right]Z'^2 = 1 \qquad (5)$$

Since the rotation angle is necessarily very small, the change in the refractive indices can be therefore written :

$$\delta n_x(E) = -\frac{n_o^3 r_{42}^2 E^2}{2\left(\frac{1}{n_o^2} - \frac{1}{n_e^2}\right)} \quad , \quad \delta n_y(E) = 0 \quad , \quad \delta n_z(E) = \frac{n_e^3 r_{42}^2 E^2}{2\left(\frac{1}{n_o^2} - \frac{1}{n_e^2}\right)} \qquad (6)$$

Consequently, the phase shift between the x and z light polarization components is :

$$\Gamma_{zx}(E) = \frac{2\pi L_y}{\lambda}\Delta n_{zx}(E) = \frac{\pi L_y}{\lambda}\frac{n_e^3 + n_o^3}{\left(\frac{1}{n_o^2} - \frac{1}{n_e^2}\right)} r_{42}^2 E^2 \qquad (7)$$

where $L_y$ is the crystal length along the laser propagation direction and $\lambda$ is the laser wavelength. The phase shift induced by the external electric field is thus a function which is quadratic on the field magnitude. The $r_{42}$ coefficient is determined from the measurement of $\Gamma_{zx}$ (E) as funtion of DC applied voltage. V=Ed, where d is the electrode spacing.

## EXPERIMENTAL

The $BaTiO_3$ crystals used for this study were grown by the Czochralski method. A particular attention was paid in order to obtain single domain crystals with a good optical quality by the application of appropriate electric field and thermal gradient during the cooling process through the cubic tetragonal phase transition. A nominally pure sample of 4.15x2.96x2.07mm$^3$ size and a 0.135% iron-doped sample of 4.87x3.92x2.85mm$^3$ size were used. They were cut normal to the principal axes, polished and electroded with evaporated gold.

EO coefficients were determined with a new method described elsewhere[11] which is based upon the Sénarmont compensating set-up. The optical transmission of such a system follows the general law : $I = I_0 \sin^2(\Gamma/2-\beta+\pi/4)$ if the optical absorption is neglected. In this equation $I_0$ and I are respectively the input and output laser intensity and $\Gamma$ the phase shift introduced by the sample. $\Gamma$ can be caused to the natural birefringence and/or by its variation due to a change of the temperature, electric field or strain applied to the sample. The method consists to add an AC

voltage with a frequency f to the DC voltage and to measure the angle $\beta_{2f}$ of the analyser corresponding to the detection of the output signal with the frequency 2f.

## RESULTS

The EO $r_c$ and $r_{42}$ coefficients are determined in the "pure" and the iron-doped samples for various modulation frequencies. Complete results are presented and discussed elsewhere. Here we focus our attention on the $r_{42}$ coefficient obtained in the "pure" crystal as a function of temperature for a modulation frequency f=1kHz and a laser wavelength $\lambda$=633nm.

Figure 1 exhibits the value of the angle $\beta_{2f}(E)=\Gamma(E)/2$ as function of the DC voltage amplitude V=Ed. Data obtained for increasing and decreasing V are similar, which is indicative that no memory effect or optical damage is induced by the field. Fit of the data to eq 7 yields the value of the $r_{42}$ coefficient for a given temperature. The values of the indices $n_e$ and $n_o$ are taken in Ref. 12. At 19.1°C, we find the value $r_{42}$= 1776 $pmV^{-1}$.

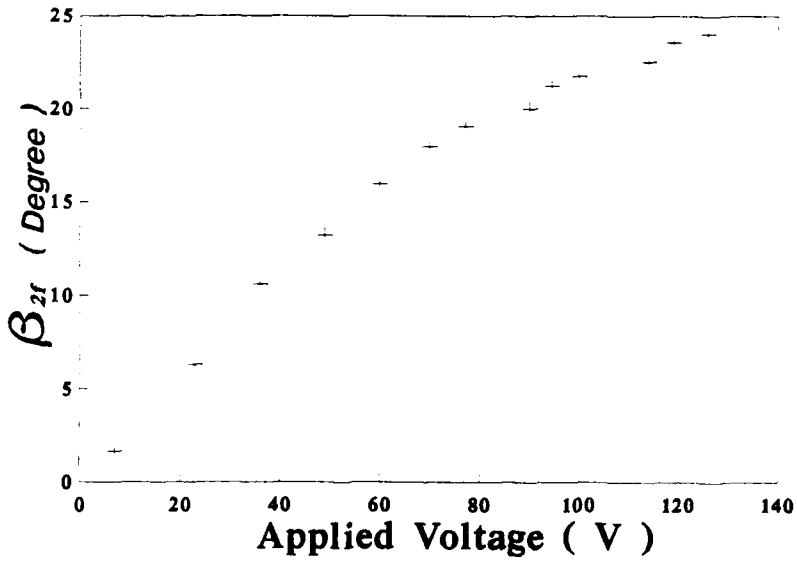


FIGURE 1 Variation of the retardation angle $\beta_{2f}$ due to the applied DC voltage

To obtain the temperature dependence of the $r_{42}$ coefficient, we repeat the same measurements around room temperature. This requires a perfect stabilization of the temperature for each data. Indeed the measured phase shift $\Gamma$ includes the value $\Gamma(O)$ wich is due to the natural birefringence together with the value $\Gamma(E)$ which is induced by the field via the EO effect. It is necessary to discriminate between these

both contributions during the measurements of $\Gamma = 2\beta_{2f}$, particularly if each one depends on the temperature. For the first contribution we find $\delta\beta_{2f}(0)/\delta T=167$ degrees°$C^{-1}$, which corresponds to a thermal dependence of the natural birefringence of $\delta\Delta n_{zx}(0)/\delta T=1.42\ 10^{-4}$°$C^{-1}$. This very large dependence determined from our modulation technique is in good agreement with the results previously measured by other techniques[13]. This shows that the determination of the $r_{42}$ coefficient versus T requires, for each temperature, the measurement of the difference between $\delta\beta_{2f}$ and$\delta\beta_{2f}(0)$., or the measurement of $\beta_{2f}(E)$ after a perfect temperature stabilization. In our data, the temperature is assumed to be constant within a 0.01°C shift. The temperature dependence of the $r_{42}$ coefficient is illustrated in the figure 2. A very large variation of the value of $r_{42}$ is pointed out, even for a very small temperature shift. A change of 1°C can thus lead to multiply by a factor two the value of $r_{42}$. A smaller dependence was reported in Refs 14 and 15, when a wide temperature range is considered. The understanding of such dicrepancies is actually in progress and involves various elasto-optic, thermo-optic ... effects.

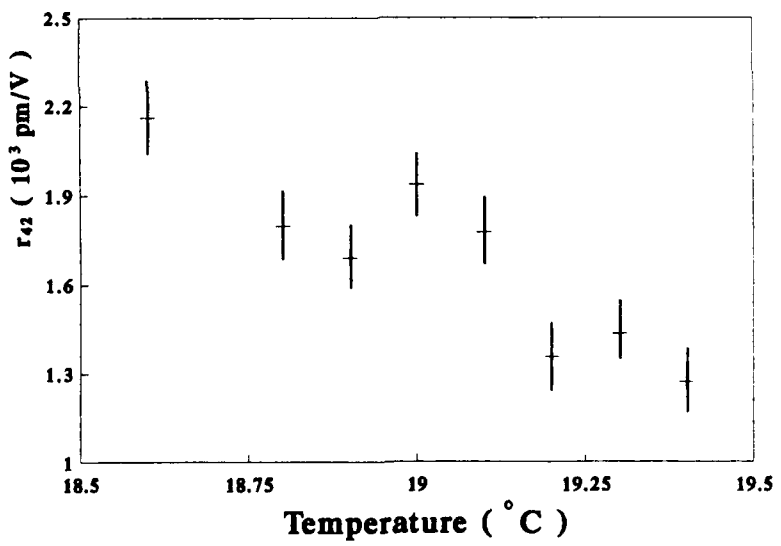


FIGURE 2 Temperature dependence of the $r_{42}$ EO coefficient of pure $BaTiO_3$

## DISCUSSION

The extremely large dependence on the temperature of both the natural birefringence $\Delta n_{zx}(0)$ and the electric-field induced birefringence $\Delta n_{zx}(E)$ constitutes the main results pointed out in our investigations. The first consequence concerns the necessity to insure a perfect temperature stabilization for a determination of EO coefficients as

well as for the use of $BaTiO_3$ in optical devices. Concerning the thermo-optic effect, it could be compensated by associating with a first crystal of $BaTiO_3$ a second one with the same dimensions but the axes crossed as regards to the axes of the first crystal[16]. In fact, this possibility is doubtful from a practical point of view since a temperature shift of 0.1°C between both crystals should be sufficient to lead a change in the birefringence of 1.4 $10^{-5}$ while the same variation in $\Delta n$ can be caused by an applied electric field of 47.2 kV/m. The variation of temperature can be due by the laser beam itself. This needs to wait a sufficient time to obtain a temperature stabilization after application of the laser. This was previously mentioned for 2 or 4 wave mixing experiments[17], where only the thermo-optic effect was considered. In fact, we have shown that the thermal dependence of the electro-optical effect causes an additional problem. The determination of precise values of figures of merit of $BaTiO_3$, for instance the driving voltage required in switcher or modulator is very delicate. This limits the use of $BaTiO_3$ crystals for various applications in optical devices.

## REFERENCES


1- P.Günter , Ferroelectrics 24, 35 (1980).
2- M.B.Klein and R.N.Schwartz, J.Opt Soc. Am B,3 , 293(1986).
3- I.P.Kaminow, Appl. Phys Lett 7, 123 (1965).
4- M.B.Klein and G.C.Valley, SPIE Proceedings 567,116(1985).
5- G.Godefroy, G.Ormancey, P.Jullien, W.Ousi Benomar and Y.Semanou. Proc of 6th conf IEEE, 12. (1986).
6- S.Ducharme and J.Feinberg, J.Opt Soc. Am B,3 (2), 283(1986).
7- M.B.Klein , in " Electrooptic and Photorefractive Materials ". Ed by P.Günter,Springer, Berlin, p266 (1986).
8- M.Aillerie, M.D.Fontana. F.Abdi, C.Carrabatos-Nedelec, N.Theophanous and G.Alexakis, J.Appl.Phys. 65, 2406(1989).
9- S.Ducharme, J.Feinberg and R.R.Neurgaonkar,.IEEE J Quant Elect, QE 23; 12, 2116(1987).
10- P.Jullien,A.Maillard,G.Ormancey and A.Lahlafi, Ferroelectrics 94 ,81(1989).
11- M.Aillerie, M.D.Fontana. F.Abdi, C.Carabatos-Nedelec and N.Theophanous,SPIE, 1018,94(1988).
12- S.H.Wemple, M.Didomenico and I.Camlibel, J.Phys Chem Solids, 29, 1797(1968).
13- N.N.Kristoffel and A.V.Gulbis, Opt Spectrosc , 49, 175.(1980).
14- A.R.Johnston and J.M.Weingart, J.Opt.Soc.Am, 55(7), 828(1965).
15- P.Jullien, Y.Abid and G.Godefroy, Private Communication.
16- P.Günter, in "Electrooptic and Photorefractive Materials". ref.7, p2 (1986).
17- D.W.Rush, B.M.Dugan, and G.L.Burdge, CLEO, Baltimore 1991.

*Ferroelectrics*, 1992, Vol. 133, pp. 181–186
Reprints available directly from the publisher
Photocopying permitted by license only
© 1992 Gordon and Breach Science Publishers S.A.
Printed in the United States of America

**DiP224**

# NEODYMIUM TITANATE ($Nd_2Ti_2O_7$)CERAMICS

G. WINFIELD, F. AZOUGH AND R. FREER
Materials Science Centre
University of Manchester/ UMIST,
Grosvenor Street,
Manchester, M1 7HS, United Kingdom.

Abstract Neodymium titanate ceramics have been prepared by the mixed oxide route. Specimens were sintered in air at temperatures in the range 1300 to 1500°C. Fired densities were sensitive to sintering temperature with the highest densities for undoped specimens (~ 95% theoretical) being achieved at 1375 to 1400°C. The microstructures of such specimens exhibited abnormal grain growth; tabular to lath-shaped grains up to 100$\mu$m in size. Doping with $Nb_2O_5$ controlled grain growth, but at dopant levels greater than 1 mole % an increasing amount of second phase was formed.

Undoped $Nd_2Ti_2O_7$ ceramic has a relative permittivity of ~ 35 and a positive temperature coefficient of capacitance of 270 ppm /°C (for the range 25 to 150°C). TEM studies revealed the presence of fine domain structures which are twinned, confirming the ferroelectric nature of $Nd_2Ti_2O_7$.

## INTRODUCTION

Neodymium titanate ($Nd_2Ti_2O_7$)is a member of a family of ferroelectric materials characterised by a perovskite-type layered structure[1]. Other members of the family include[2-4] $La_2Ti_2O_7$, $Sr_2Nb_2O_7$ and $Ca_2Nb_2O_7$. Kimura et al[1] demonstrated that single crystals of $Nd_2Ti_2O_7$ exhibited piezoelectric and electro-optic properties and had a Curie temperature in excess of 1500°C. Such behaviour makes neodymium titanate and other members of the same structural family, eg $La_2Ti_2O_7$, attractive as high temperature ferroelectrics for use in high temperature piezoelectric devices, as well as being potentialy useful for dielectrics and resonators at ambient temperatures[5].

Whilst the isostructural lanthanum titanate has been investigated in both single crystal and ceramic form[2,5,6,7], neodymium titanate has received comparatively little attention. Marzullo and Bunting[8] studied a number of ceramics based on rare earth titanates. They found that $Nd_2Ti_2O_7$ had a relative permittivity of ~37, a high dielectric Q value and a high positive temperature coefficient of capacitance of ~ 190ppm/°C.

The present study is concerned with the preparation of $Nd_2Ti_2O_7$ by the mixed oxide route from high purity starting powders. The products have been examined by optical, scanning and transmission electron microscopy. Dielectric properties were studied at 10kHz-1MHz. The relationship between processing conditions and properties is examined.

## EXPERIMENTAL

High purity (>99.9%) powders of $Nd_2O_3$ and $TiO_2$ (obtained from Fluka Chemicals, UK) in the molar ratio 1:2 were wet mixed for 8 hours with zirconia balls, calcined at 1100°C for 4 hours and wet mixed again for 12 hours. The resulting slurry was dried and uniaxially pressed into pellets of 15mm diameter. No binder was employed. Pellets were sintered in air for 4 hours at temperatures in the range 1375 to 1400°C. Heating and cooling rates were usually 360°C/hour. Additional specimens doped with $Nb_2O_5$ (1-6 mole %) were fired at temperatures of 1400-1500°C.

Particle size and size distribution of starting and calcined powders was determined by a sedimentation method. X-ray diffraction anlaysis, using CuK$\alpha$ radiation and a Philips diffractometer with horizontal goniometer was used to examine calcined powders and sintered specimens. Densities were determined by an immersion method. Product morphologies were examined by optical microscopy and scanning electron microscopy (Philips 305 and 525 instruments) on polished and etched surfaces.

Selected samples were examined by transmission electron microscopy (TEM). Discs of ceramic were thinned mechanically and by ion beam thinner to yield TEM specimens of 3mm diameter. Philips 400 and EM430 transmission eletron microscopes were used for lattice image and electron diffraction studies.

Electrical studied were performed at 1kHz - 1MHz over the temperature range 25-150°C using a Hewlett Packard HP4284A Precision LCR meter.

## RESULTS AND DISCUSSION

The colour of the mixed starting powders was pale blue, but this changed to pale violet after calcining. The average size of the calcined powder was estimated by particle size analysis to be ~ 3 $\mu$m, but this reflected agglomeration of the smaller crystallites. X-ray diffraction analysis confirmed that the calcined powder was single phase $Nd_2Ti_2O_7$. There was no evidence of unreacted starting materials or second phase. Sintered products were dark violet in colour and typically 93-95% theoretical density, with values inreasing with sintering temperature. Niobium doped specimens were of 94-97% theoretical density. X-ray diffraction patterns for fired specimens were in excellent agreement with reference data in JCPDS files and confirm a single phase product.

Optical micrographs of polished and etched specimens are shown in

Figure 1. The microstructures are characterised by anisotropic plate-like grains of variable size and shape. The grain size of undoped specimens increased with sintering temperature, but was predominantly in the range 50-100$\mu$m, with the

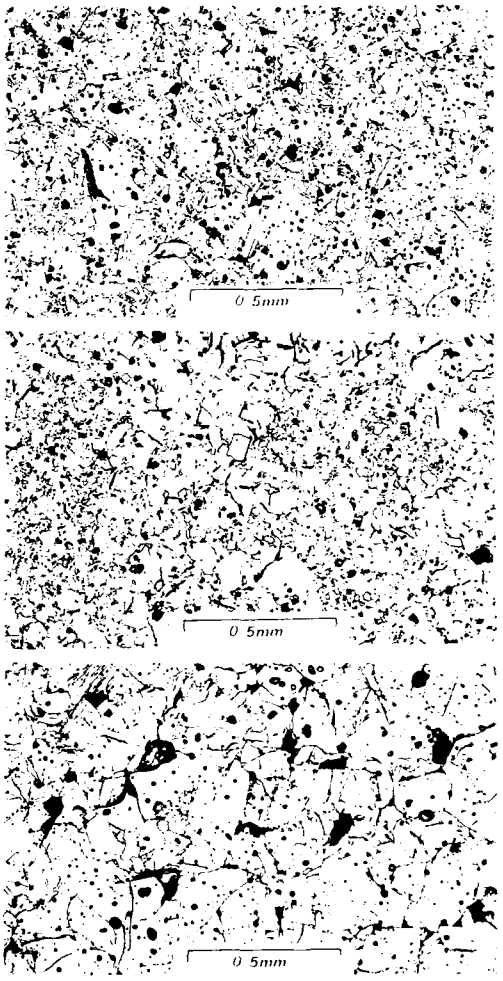


FIGURE 1 Optical micrographs of neodymium titanate ceramics sintered at (a) 1400°C, (b) 1450°C (doped with 2 mole % niobia) and (c) 1475°C (doped with 5 mole % niobia).

interstices filled with randomly oriented grains less than 10$\mu$m in size. Intergranular porosity is present in all the products (Figure 1a). Specimens heated and cooled at the faster rate of 720°C/hour exhibited less anisotropic grain growth, slightly smaller grain size and marginally lower density. In general the microstructures resemble those of $La_2Ti_2O_7$ prepared by the mixed oxide route[5].

The addition of small amounts of $Nb_2O_5$ (1-2 mole %) reduced grain growth and in specimens sintered at 1450°C the grain size distribution was strongly bimodal, 10-50$\mu$m in range, but the shape more uniform (Figure 1b).

However, increasing the firing temperature and niobium content leads to massive grain growth, with grain sizes typically 75-150$\mu$m (Figure 1c). TEM studies of $Nd_2Ti_2O_7$ ceramics revelaed characteristic domain structures in which a fine scale domain pattern was parallel to a single axis within each grain. Figure 2 shows a TEM micrograph of a niobium doped ceramic sincered at 1450°C. This particular specimen exhibits curved boundaries to the domains, but all specimens showed the same internal structure. Electron diffraction patterns of neodymium titanate ceramics[9] exhibit continuous streaking in the b-direction, possibly due to the twinned nature of the ferroelectic domains. The presence of a twinned domain structure has been reported for lanthanum titanate[10] which is isostructural with $Nd_2Ti_2O_7$.

FIGURE 2 TEM micrograph showing the domain structure in a single grain of $Nd_2Ti_2O_7$ sintered at 1450°C (doped with 3 mole % $Nb_2O_5$).

Electrical properties (relative permittivity and loss factor) for the samples were determined as a function of frequency and temperature. For the undoped neodymium titanate the relative permittivity ($\epsilon_r$) was approximately 35, in agreement with published values[1,8]. However, at room temperature $\epsilon_r$ varies with sintering temperature and heating rate; for specimens sintered at 1375°C, $\epsilon_r \sim 33$; and this increased to 35 for specimens sintered at 1400°C, largely reflecting density differences (Figure 3). Values of $\epsilon_r$ for the doped specimens were uniformly higher at $\sim 36$. There was little or no change in relative permittivity with frequency (1kHz - 1MHz), but all specimens exhibited a strong positive temperature coefficient of capacitance (TCC) $\sim$ 270 ppm/°C for the undoped ceramics. TCC values (based on the range 25-150°C) are independent of frequency and sintering temperature. Even higher TCC values $\sim 400$ were

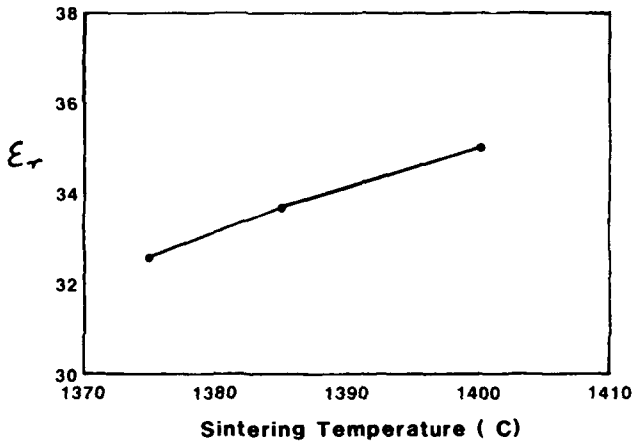


FIGURE 3 Relative permittivity of $Nd_2Ti_2O_7$ (at 10kHz) as a function of sintering temperature.

reached in the highly doped samples. Dielectric Q values were generally independent of temperature (25-150°C), but varied slightly with frequency (10kHz-1MHz) yielding values in the range 4000-10000. These are comparable with results obtained in an early study of neodymium titanate[8].

The addition of small amounts of niobium oxide therefore improved densification, controlled gain growth, increased the relative permitivity without seriously degrading the dielectric Q value. In contrast the TCC for $La_2Ti_2O_7$ is much lower ~ 50 ppm/°C, but varies with frequency, sintering temperature and cooling rate[9].

## CONCLUSIONS

Good quality single phase $Nd_2Ti_2O_7$ ceramics can be prepared by the mixed oxide route using sintering temperatures in the range 1375-1500°C. Product densities were 93-97%. All undoped specimens exhibited abnormal grain growth, with a bimodal grain size distribution; grains were predominantly large 50-100$\mu$m, but a significant fraction were less than 10$\mu$m. Niobium doping controlled grain growth. Relative permittivities were in the range 33-36, and the temperature coefficient of capacitance was ~ + 270 ppm/°C. Individual grains exhibited a fine scale domain structure.

## REFERENCES

1. M. Kimura, S. Nanamatsu, T. Kawamura and S. Matsushita, Japan J. Appl. Phys., 13, 1473 (1974)
2. M. Kimura, S. Nanamatsu, K. Doi, S. Matsushita and M. Takahashi, Japan J. Appl. Phys., 11, 904, (1972)

3. S. Nanamatsu M. Kimura, K. Doi and M. Takahashi, J. Phys. Soc. Japan, 30, 300, (1971)
4. N. Ishizawa, F. Marumo, T. Kawamura and M. Kimura, Acta Cryst., B31, 1912, (1975)
5. P.A. Fuierer and R.E. Newnham, J. Amer. Ceram. Soc., 74, 2876, (1991)
6. J.B. MacChesney and H.A. Sauer, J. Amer. Ceram. Soc., 45, 416 (1962)
7. J. Takahashi and K. Kageyama, Ceramic Dielectrics, Ceramic Transactions Volume 8 American Ceramic Society, Ohio, (1990), p333
8. S. Marzullo and E.N. Bunting, J. Amer. Ceram. Soc., 41, 40, (1958)
9. G.M. Winfield, M.Sc. Dissertation, University of Manchester (1992)
10. M. Tanaka, H. Sekii and K. Ohi, Japan J. Appl. Phys., 24, 814 (1985).

*Ferroelectrics*, 1992, Vol. 133, pp. 187–192
Reprints available directly from the publisher
Photocopying permitted by license only

© 1992 Gordon and Breach Science Publishers S.A.
Printed in the United States of America

# DiP227

## MICROWAVE DIELECTRIC PROPERTIES OF COMPLEX PEROVSKITE $Ba(Mg_{1/3}Ta_{2/3})O_3$

EUNG SOO KIM* AND KI HYUN YOON
Department of Ceramic Engineering, Yonsei University, Seoul, Korea

**Abstract** The microwave dielectric properties of complex perovskite $Ba(Mg_{1/3}Ta_{2/3})O_3$ have been investigated in the temperature range from 20°C to 110°C and the frequency range from 10.5 GHz to 14.5 GHz as a function of annealing time. The ordering of Mg and Ta in $Ba(Mg_{1/3}Ta_{2/3})O_3$ increases with increasing annealing time, and there is no drastic change in the ordering of Mg and Ta when the annealing time was over 20 hr at 1500°C. Unloaded Q which depends on the ordering of Mg and Ta shows maximum value when the specimens are annealed at 1500°C for 20 hr. With increasing annealing time, the dielectric constant, the temperature dependence of dielectric constant and the temperature coefficient of resonant frequency increase, while the temperature dependence of unloaded Q decreases. These results are due to the increase of lattice distortion with increasing annealing time.

## INTRODUCTION

The requirement of broadcasting by satellite and the increase in the amount of communications information have lead to a rapid development of microwave communication systems. The advancement of microwave integrated circuits has required dielectric materials with a low dielectric loss, a suitable dielectric constant and temperature stability of resonant frequency. To satisfy this requirement, a number of materials have been investigated as microwave dielectrics up to now[1-4].

Recently, many studies have been made of the complex perovskite compounds[5-7] and their solid solutions[8-10] which make good dielectric materials for microwave resonators. The complex perovskite compounds of the general formula $Ba(B_{1/3}Ta_{2/3})O_3$ (B=Zn, Mg) have shown very interesting results on microwave loss quality Q. For the composition with Zn, Kawashima et al.[5] explained the increased Q in terms of ordering of Zn and Ta ions in B site of the perovskite lattice, while Desu et al.[7] reported that there was Q improvement due to Zn loss and lattice distortion even after such ordering was completed. For the composition with Mg which is not volatile, the Q values strongly rely on the ordering of B site ions and the density of the specimens. In general, the dielectric constant and temperature coefficient of resonant frequency depend on composition, but the loss quality depends on process variables such as time, temperature and atmosphere. The extensive study of the relation between the loss quality and the process variables is still needed to prepare good microwave dielectric materials. This study describes the effect of ordering and lattice distortion of B site ions on the microwave dielectric properties of $Ba(Mg_{1/3}Ta_{2/3})O_3$ as a function of annealing time.

## EXPERIMENTAL

The starting materials composed of $BaCO_3$, MgO, and $Ta_2O_5$ powders with purity of 99.9 % were

---

* Permanent Address :
Department of Materials Engineering, Kyonggi University, Suwon, Korea

weighed and ball milled together in polyethylene jar with $ZrO_2$ media. Mixing was carried out for 24 hr in ethanol. The mixed raw materials were dried and calcined at 1200°C for 10 hr in air. After calcination the powders were remilled the same as the one for raw material milling, and finally screened through 80 mesh. The screened powder was isostatically pressed into disks under pressure of 1500Kg/cm$^2$ and then sintered at 1650°C for 2 hr in air. The sintered specimens were also annealed at 1500°C in air for various time.

The sintered and the annealed specimens were examined by X-ray diffraction analysis with CuKα radiation. A least mean square method of analysis was used to calculate lattice parameters.[11] The density of the sintered and the annealed specimens was measured by immersion technique. The specimens were polished and thermally etched at 1300°C for 1 hr to observe the microstructure using scanning electron microscopy(Jeol, JSM 820, Japan) and energy dispersive X-ray spectrometry (Link, AN-10000, England). The microwave dielectric properties of the specimens were measured by Hakki and Coleman's dielectric resonator method[12] on the $TE_{011}$ mode. The dielectric constant and unloaded Q were measured at 20°C with the frequency range from 10.5GHz to 14.5GHz, while the temperature coefficient of resonant frequency was measured at 10.5GHz in the temperature range from 20°C to 110°C.

## RESULTS AND DISCUSSION

Figure 1 shows dependence of lattice parameter ratio, c/a on annealing time at 1500°C. Galasso et al.[13] reported that $Ba(Mg_{1/3}Ta_{2/3})O_3$ has a hexagonal perovskite structure with Mg and Ta showing 1:2 order. The order of Mg and Ta expands the original perovskite unit cell along the <111> so that c/a has a value greater than 3/2 (=1.2247). As shown, the ordering of Mg and Ta in $Ba(Mg_{1/3}Ta_{2/3})O_3$ increases with increasing annealing time, and there is no drastic change in the ordering of Mg and Ta when the annealing time is over 20 hr at 1500°C. The lattice distortion due to Mg and Ta ordering produces the split of the (422) and (226) reflections in the XRD pattern. The

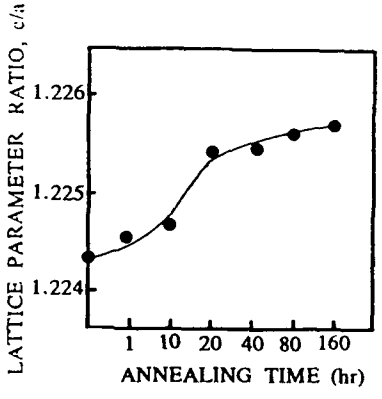


FIGURE 1 Dependence of lattice parameter ratio, c/a on annealing time at 1500°C for $Ba(Mg_{1/3}Ta_{2/3})O_3$.

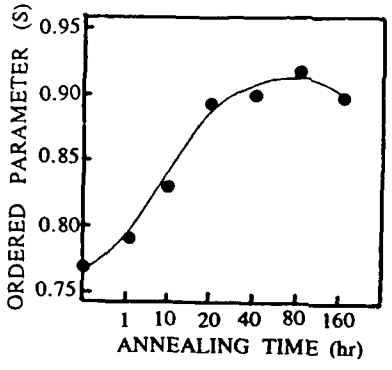


FIGURE 3 Dependence of ordered parameter on annealing time at 1500°C for $Ba(Mg_{1/3}Ta_{2/3})O_3$.

splitting of (422) and (226) reflections with annealing time is shown in figure 2. The specimen sintered at 1650°C for 2 hr shows no lattice distortion. The lattice distortion was observed for the specimens which the annealing time was over 20 h at 1500°C.

Figure 3 shows the results of the ordered parameter S[14] which can be quantitatively evaluated the degree of ordering as a function of annealing time. The degree of ordering increases with increasing annealing time. When the annealing time is over 20 hr, the ordered parameter S shows about 0.9. These results consistent with the report[5,9] that the ordering of B site ions increased with increasing the heat treatment time. Figure 4 shows the apparent density of the specimens annealed at 1500°C for various time. The density of the specimens increased with increasing the annealing time. This results is due to the increase in the grain size with annealing time as shown in figure 5.

The microstructure of the specimens shows that the needle shaped grains appear in grain boundary when the annealing time is over 40 hr and the needle shaped grains are grown with increasing annealing time. The EDS spectra taken from the grain (in figure 5 (d)-A) and the needle shaped grains in grain boundary (in figure 5 (d)-B) of the specimens annealed at 1500°C for 160 hr are shown in figure 6. It can be seen from figure 6 that the needle shaped grains in grain boundaries are deficient in Ba, Mg

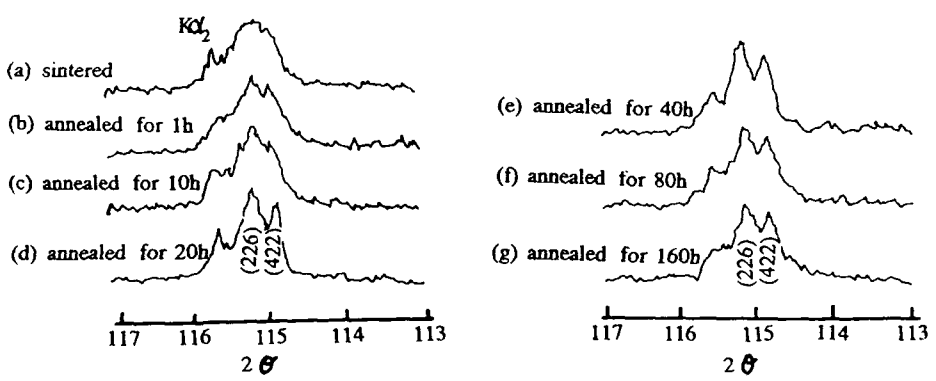


FIGURE 2 Profiles of (226) and (422) reflections of the specimens annealed at 1500°C for various time.

and enriched in Ta concentration as compared with grain. As the phase diagram of BaO-MgO-$Ta_2O_5$ ternary system have not been reported yet, we used the binary phase diagram of BaO-MgO system[15], MgO-$Ta_2O_5$ system[16] and $Ta_2O_5$- $MgTa_2O_6$ system[17] in which the liquid phase formation temperature is 1500°C, 1600°C and 1750°C, respectively. Thus, the needle shaped grains in grain boundary is due to the liquid phase formation of BaO-MgO system and the small amount of BaO, MgO loss when the annealing time is over 40 hr.

Figure 7 shows the microwave loss quality Q and dielectric constant measured at 10.5GHz and 20°C. The increase of dielectric constant with annealing time is due to the increase of density and grain size as shown in figure 4 and figure 5. This result is in accord with the report of Jonker[18] in which the dielectric constant increased with increasing the grain size and the report of Takata et al.[19] in which

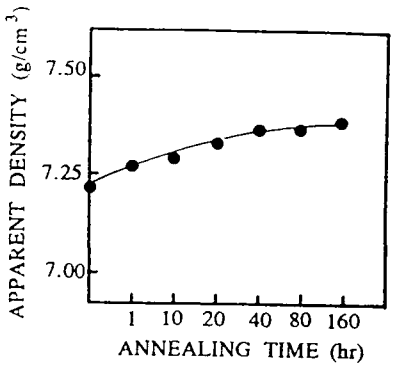


FIGURE 4 Apparent density of the specimens annealed at 1500°C for various times.

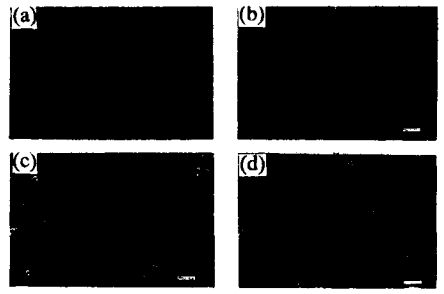


FIGURE 5 SEM photographs of the specimens annealed at 1500°C for various time. (bar = 1.25μ)
(a) sintered at 1650°C for 2hr
(b) annealed at 1500°C for 10hr
(c) annealed at 1500°C for 40hr
(d) annealed at 1500°C for 160hr

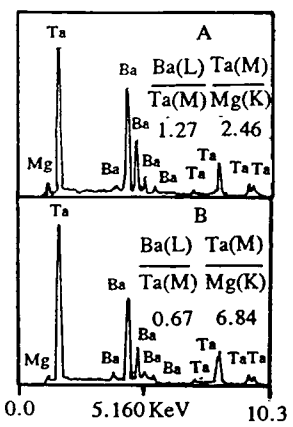


FIGURE 6 EDS spectrums taken from surface of $Ba(Mg_{1/3}Ta_{2/3})O_3$ annealed at 1500°C for 160 hr.

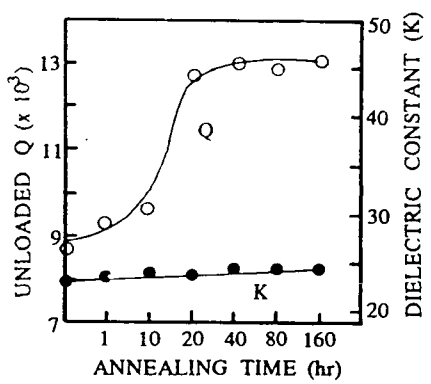


FIGURE 7 Unloaded Q and dielectric constant of the specimens annealed at 1500°C for various times.

the increase of dielectric constant with density. The microwave loss quality Q drastically increased with increasing annealing time. This result is due to increase of Mg-Ta ordering with increasing annealing time. When the annealing time is over 20 hr, there is no drastic change of Q, because the Mg-Ta ordering is slightly changed and the needle shaped grains are formed in grain boundary.

The temperature dependence of dielectric constant, loss quality, and resonant frequency at 10.5GHz are shown in figures 8, 9,and 10, respectively. The temperature coefficient of dielectric constant (TCK) for the specimens is the slope of the line in figure 8. Both the sintered and the annealed specimens shows the negative value of TCK. These results are in agreement with the report[20] in which TCK of paraelectrics shows negative value. Kell et al.[21] and Megaw[22] reported that perovskite materials with tilted oxygen octahedra enhance temperature coefficient of expansion because tilt changed with temperature. As seen in figure 8, TCK increased with increasing the annealing time

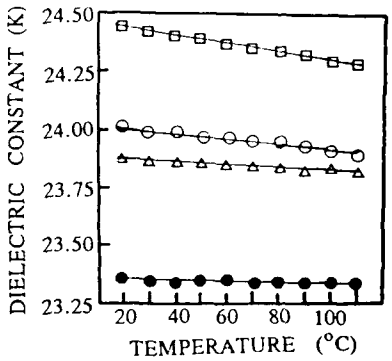


FIGURE 8 Temperature dependence of dielectric constant for $Ba(Mg_{1/3}Ta_{2/3})O_3$.
● sintered at 1650°C for 2hr
△ annealed at 1500°C for 10hr
○ annealed at 1500°C for 40hr
□ annealed at 1500°C for 160hr

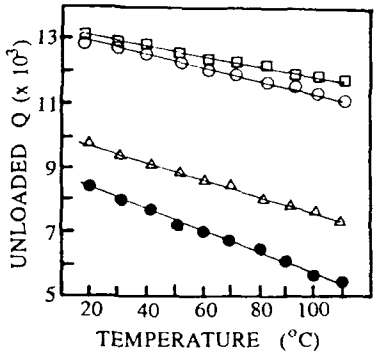


FIGURE 9 Temperature dpendence of unloaded Q for $Ba(Mg_{1/3}Ta_{2/3})O_3$.
● sintered at 1650°C for 2hr
△ annealed at 1500°C for 10hr
○ annealed at 1500°C for 40hr
□ annealed at 1500°C for 160hr

because of the lattice distortion. Rupprecht et al.[23] and Silverman[24] reported that the temperature dependence of dielectric loss can be expressed by the sum of constant term which is inversely proportional to grain size and anharmonicity term of lattice vibration, and dielectric loss is generally increased with increasing temperature because of anharmonicity term. As seen in figure 9, the loss quality Q which is inversely proportional to dielectric loss decreases with increasing temperature for both sintered and annealed specimens. The annealed specimens show smaller value of slope than that of the sintered specimens. This result is due to the effect of grain size and needle-shaped grains in grain boundary. The temperature coefficient of resonant frequency increases with increasing annealing time because of the lattice distortion and increase of TCK. Figure 11 shows the frequency dependence

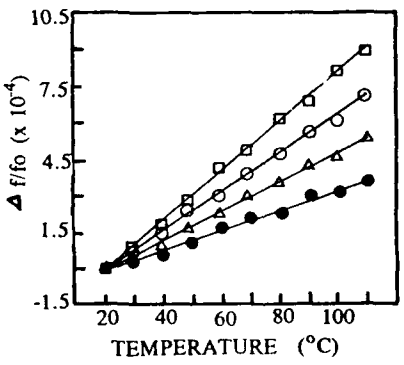


FIGURE 10 Temperature dependence of resonant frequency for $Ba(Mg_{1/3}Ta_{2/3})O_3$.
● sintered at 1650°C for 2hr
△ annealed at 1500°C for 10hr
○ annealed at 1500°C for 40hr
□ annealed at 1500°C for 160hr

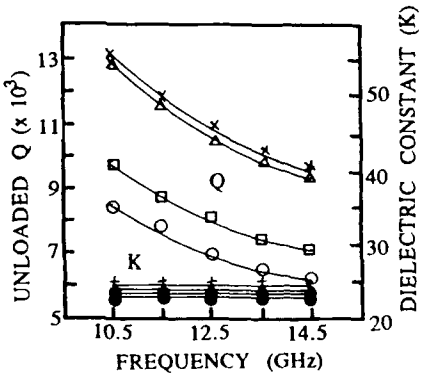


FIGURE 11 Frequency dependence of unloaded Q and dielectric constant for $Ba(Mg_{1/3}Ta_{2/3})O_3$.
●○ sintered at 1650°C for 2hr
■□ annealed at 1500°C for 10hr
▲△ annealed at 1500°C for 40hr
+ X annealed at 1500°C for 160hr

of loss quality Q and dielectric constant at frequency range from 10.5GHz to 14.5GHz and 20°C. With increasing the frequency, the dielectric constant shows constant value, but loss quality is drastically decreased. These results are attributed to ionic polarization with the variation of frequency.

## CONCLUSIONS

(1) The ordering of Mg and Ta in $Ba(Mg_{1/3}Ta_{2/3})O_3$ increased with increasing annealing time, and there was no drastic change in the ordering of Mg and Ta when the annealing time was over 20 hr at 1500°C. The density and grain size increases with increasing annealing time and the needle-shaped grains which were Mg-Ta rich phases were observed in grain boundaries when the annealing time was over 40 hr at 1500°C.

(2) Unloaded Q which depended on the ordering of Mg and Ta showed the maximum value when the specimens were annealed at 1500°C for 20 hr. With increasing the annealing time, the dielectric constant, the temperature dependence of dielectric constant and the temperature coefficient of resonant frequency increased, while the temperature dependence of unloaded Q decreased. These results are due to the increase of lattice distortion with increasing annealing time. The unloaded Q was drastically decreased with increasing frequency because of the ionic polarization.

## ACKNOWLEDGEMENT

This work was supported by the Korea Science and Engineering Foundation.

## REFERENCES

1. H.M.O'Bryan, J.Thomson and J.K.Plourde, J.Am.Ceram.Soc., 57, 450 (1974).
2. K.Wakino and H.Tamura, Yogyo-kyokai-Shi, 88, 475 (1980).
3. A.E.Paladino, J.Am.Ceram.Soc., 54, 168(1971).
4. T.Yamaguchi, Y.Komatsu, T.Otobe and Y.Murakami, Ferroelectrics, 27, 273 (1980).
5. S.Kawashima, M.Nishida, I.Ueda and H.Ouchi, J.Am.Ceram.Soc., 66, 421 (1983).
6. S.Nomura and K.Kaneta. Jpn.J.Appl.Phys., 23, 507 (1984).
7. S.B.Desu and H.M.O'Bryan, J.Am.Ceram.Soc., 68, 546 (1985).
8. M.Onoda, J.Kuwata, K.Kaneda, K.Toyama and S.Nomura, Jpn.J.Appl.Phys., 21, 1707 (1982).
9. K.Endo, K.Fujimoto and K.Murakawa, J.Am.Ceram.Soc., 70, c215 (1987).
10. K.H.Yoon, B.J.Jung and E.S.Kim, J.Mat.Sci.Lett., 8, 819 (1989).
11. M.U.Cohen, Rev.Sci.Instrum., 6, 68 (1963).
12. B.W.King, P.D.Coleman, IRE Trans. Microwave Theory Tech., 8, 402 (1960).
13. F.Galasso and J.Pyle, Inorg.Chem., 2, 482 (1963).
14. K.Matsumoto, T.Hiuga, K. Takada and H.Ichimura, Proc. 6th IEEE Inter. Sympo. on Appl. of Ferro., 118 (1986).
15. H.Von Wartenberg and E.Prophet, in Phase Diagram for Ceramist 1975 Supplement, edited by E.M.Levin, C.R.Robbins, H.F.McMurdie and M.K.Reser(The American Ceramic Society, Ohio, 1964), Fig.274, p113.
16. B.W.King, J.Schultz, E.A.Durbin and U.S.Duckworth, ibid, Fig.273, p113.
17. J.J.Landre, ibid, Fig.205, p96.
18. G.Jonker, Science of Ceramic, 1, 262 (1962).
19. M.Takata and K.Kageyama, J.Am.Ceram.Soc., 72, 1955 (1989).
20. P.J.Harrop, J.Mat.Sci., 4, 370 (1969).
21. R.C.Kell, A.C.Greenham and G.C.E.Olds, J.Am.Ceram.Soc., 56, 352 (1973).
22. H.D.Megaw, Acta Crystallogr., Sect.A, 24, 589 (1968).
23. G.Rupprecht and R.O.Bell, Phys.Rev., 125, 1915 (1962).
24. B.D.Silverman, Phys.Rev., 125, 1921 (1962).

*Ferroelectrics*, 1992, Vol. 133, pp. 193–198
Reprints available directly from the publisher
Photocopying permitted by license only
© 1992 Gordon and Breach Science Publishers S.A.
Printed in the United States of America

# DiP228

## TIME DEPENDENCES OF DIELECTRIC CONSTANT IN $Ba(Ti_{0.95}Sn_{0.05})O_3$

CZESLAW KAJTOCH
Pedagogical University, Cracow, Poland
ul.Podchorążych 2

Abstract: The time measurements of dielectric constant in polycrystalline $Ba(Ti_{0.95}Sn_{0.05})O_3$ sample have been performed in the temperature range from 358 K to 378 K. The relaxation times $\Theta_i$ have been determined. The minimum value of $\Theta_2$ (15 - 30 min) and the maximum value of $\Theta_3$ (60 - 200 min) have been observed in the same temperature of 367.3 K. The obtained results seem to be connected with the existence of glasslike phase as well as with the stabilization of paraelectric phase.

## INTRODUCTION

In the last few years a great deal of high-temperature roentgenographic[1,2], neutronographic[3] and dilatometric[4,5] researches in polycrystalline $BaTiO_3$(BT) and $Ba(Ti_{1-x},Sn_x)O_3$ (BTS-x) have been carried out. On the base of these researches the existence of polar areas of dynamic character in paraelectric phase has been predicated. The confirmation of the existence of polar areas allows to consider the para - -ferroelectric phase transition in BT and BTS-0.05 as an order-disorder transition (OD) with some displacive-type contribution[5]. Dilatometric investigations performed on polycrystalline BTS-x have revealed, in the temperature equal to 600 K, the abnormality which is similar to the abnormality usually observed for glasslike transition (Figure 1). The character of this abnormality does not dependent on the Sn content - x. Our measurements have revealed slight changes in the coefficient of linear expansion $\alpha$ observed in BT below $T_c$ as well as

the diffuseness of the phase transition in BTS-0.05. These results can be the evidence of the existence of glasslike phase, both in BT and BTS-0.05 not only in high temperatures, in which the samples are synthesized[6], but also in the temperatures near to the temperature of the para-ferroelectric phase transition.

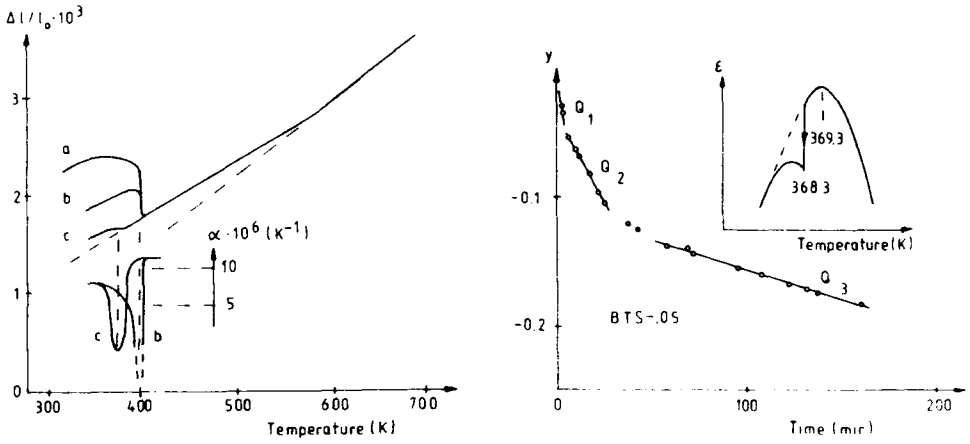


FIGURE 1 Temperature dependences of linear expansion $\Delta l/l_0$ and coefficient $\alpha$ for: monocrystalline BT (a) polycrystalline BT (b), polycrystalline BTS-0.05.

FIGURE 2 The plot of y(t) at 368.3 K and temperature dependence of dielectric constant $\varepsilon$ for BTS-0.05.

The calorimetric and dilatometric researches have revealed a strong influence of Sn-substitution on the character of para-ferroelectric phase transition in BTS-x. When the Sn content is small, the linear increase of parameters characterising the degree of the diffuseness of the phase transition (for example peak width of coefficient of thermal expansion and peak width of DSC-signal) is observed with the increase of Sn-content. At the Sn content $x \geq 10\%$ the change of the character of phase transition to a glasslike one can be registered.

The above mentioned facts as well as the previous results for other materials with perovskite structure[7] suggest the hypothesis that the stabilization of paraelectric phase can be connected with the

strenghtening of glasslike phase. Our hypothesis may be treated as an extention of the previous conclusion by Schmidt[8] that the stabilization of paraelectric phase is accompanied by increase of the degree of the diffuseness of the phase transition. In order to verify the present hypothesis the time-research of dielectric constant has been carried out for BT and BTS-0.05 in the temperatures from the region of para-ferroelectric phase transition.

## EXPERIMENTAL

The polycrystalline BT and BTS-0.05 samples have been obtained in Ceramic Works in Hermsdorf (BRD). Silver electrodes have been deposited on the samples. Before each measurement the samples have been annealed for 0.5 hours in the temperature higher than the temperature of displacive-order-disorder crossover[5,9].
After annealing the samples have been quickly cooled to the required temperature of time-measurements. This temperature has been stabilized within 0.03 K.
The obtained results have been analyzed according to the formula:

$$y(t) = \ln\left(\frac{\varepsilon_t \quad \varepsilon_n}{\varepsilon_0 \quad \varepsilon_t}\right) = -\frac{1}{\Theta}\, t,$$

where $\varepsilon_0$ - dielectric constant for t=0
$\varepsilon_t$ - dielectric constant after time t
$\varepsilon_n$ - dielectric constant equal to $\varepsilon_{min}$ at cooling
$\Theta$ - relaxation time.

## RESULTS.

For the investigated samples the linear dependence of y(t) - in two time intervals for parelectric phase, and in three time intervals for ferroelectric phase - has been obtained (Figure 2). The respective values of time constants $\Theta_i$ increase with time. The obtained values of $\Theta_i$ for BTS-0.05 as a function of temperature are presented in Figures 3,4.

The temperature $T_{mc}$ = 369.3 K corresponds to $\varepsilon_{max}$ at cooling at the rate of 10K/min. The first value of $\Theta_i$ has been neglected because we have supposed that it is connected with temperature gradient in the sample.

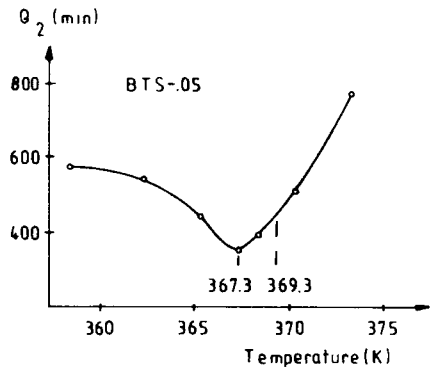


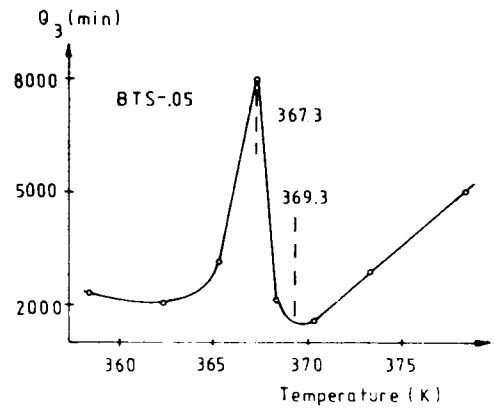


FIGURE 3 The time dependence of relaxation time $\Theta_2$ for polycrystalline BTS-0.05.

FIGURE 4 Temperature dependence of relaxation time $\Theta_3$ for polycrystalline BTS-0.05.

The plot of relaxation time versus temperature has revealed a minimum of $\Theta_2$ and a sharp local maximum of $\Theta_3$ ,both at the same temperature of 367.3 K. This temperature is 2 K smaller than $T_{mc}$. At the temperature of 367.3 K the minimum of $\varepsilon_{max}$ for the whole cooling process has been observed. The dependence $\Theta_3(T)$ shows the linear increase of $\Theta_3$ value with temperature in paraelectric phase (T>370 K).

The variety of relaxation time $\Theta_i$, which has been observed in both materials, is the evidence that several mechanisms are responsible for time changes of $\varepsilon$. According to literature these mechanisms are connected with appearance and movement of domain walls and with their ordering[10]. The glasslike properties in materials with diffuse phase transition are connected with the existence of polar areas. These materials can be characterized by great variety of the values of relaxation time[11].

The obtained results suggest, that in polycrystalline BT and BTS-0.05

polar areas stabilized by glasslike phase can occur. These areas appear in paraelectric phase and preserve the initial structure of high temperature phase even below $T_C$ although in a narrow temperature range. Below $T_C$ the ferroelectric phase appears round the overcooled areas which, with further drops in the temperature, can strongly influence the induction of ferroelectric phase from polar areas. This may be treated as a continuation OD-type phase transition with some displacive-type contribution.

This shift increases rapidly, even when the Sn-substitution is equal to 5%, which proves strong influence of nonferroelectric substitution and the glasslike behaviour on the observed relaxation effects.

The minimum of $\Theta_2$ (the fastest changes of $\varepsilon$) obsereved in BTS-0.05 for the temperature of 367.3 K can be an evidence that in the time interval which corresponds to $\Theta_2$ (15 -30 min) the diffuse process of the ordering dominates in the system. This process leads quickly to the ordered low-temperature ferroelectric state. It could be connected with the induction of ferroelectric phase in overcooled paraelectric areas. The local maximum of $\Theta_3$ in the same temperature (related to the longest interval of time - 60 - 200 min) suggests that the contribution of the above mentioned process to the increase of $\varepsilon$ vanishes. In this interval of time, the glasslike processes are strongly marked and they cause that only slow changes of $\varepsilon$ in the sample are possible. These processes are likely to play the great role in paraelectric phase, where the increase of $\Theta_3$ with the temperature is linear. The time changes of $\varepsilon$ in the temperature of 368.3 K and the changes of $\varepsilon$ at cooling the sample (a second time) are presented in Figure 2. From these plots the existence of two opposing processes can be deduced. The first one - of ordering type - manifests itself as the increase of ferroelectric order and the decrease of $\varepsilon$ with time. The second one - destructive - is connected with unsettling of thermal balance and it leads to increase of $\varepsilon$ (in comparison with $\varepsilon_{t\to\infty}(T)$), when the temperature changes.

Summing up, we can state that even 5% Sn-substitution (for Ti) in BT can lead to significant increase of the contribution of glasslike behaviour in phase transition in BTS. It results in significant increase of relaxation effects revealed in dielectric research for BTS-0.05.

REFERENCES

1. R. Comes, M. Lambert, A. Guinier, Acta Crystall.,A26 244 (1970)
2. K. Itoh, L.Z. Zeng, E. Nakamura, N.Mishima, Ferroelectrics, 63, 29 (1985)
3. J. Harada, J. D. Axe, G. Shirane, Phys. Rev. B4, 155 (1977)
4. C. Kajtoch, H.Arndt, IMF7, Saarbrücken (1989)
5. C. Kajtoch, doctor's thesis, MLU Halle-Wittenberg (1990)
6. U. Jaroch, V. Hilarius, B. Krause, KTB Ferroelektrizität 88, 80 (1989)
7. G. Burns, F. H. Dacol, Ferroelectrics, 104, 25 (1990)
8. G. Schmidt, Ferroelectrics, 78, 199 (1988)
9. F. Gervais, Ferroelectrics, 53, 91 (1984)
10. A. Jaśkiewicz, W. Daszyńska, K. Dąbrowska, Acta Phys. Polon. A51, 817 (1977)
11. P. Roth, E. Hegenbarth, KTB Ferroelektrizitat'88, 146 (1989)

*Ferroelectrics*, 1992, Vol. 133, pp. 199–203
Reprints available directly from the publisher
Photocopying permitted by license only

© 1992 Gordon and Breach Science Publishers S.A.
Printed in the United States of America

**DiP229**

# MICROWAVE AND MILLIMETRE WAVE DIELECTRIC SPECTROSCOPY OF FUNDAMENTAL DIELECTRIC DISPERSION IN FERROELECTRICS

JONAS GRIGAS, JURAS BANYS
and RICHARDAS SOBIESTIANSKAS
Faculty of Physics, Vilnius University, 2054 Vilnius, LITHUANIA

Abstract The paper presents the results which shows that the fundamental dielectric dispersion in ferroelectrics of both displacive and order-disorder type occurs in the microwave and millimetre wave region.

## INTRODUCTION

With the appearance of new means of communication using microwaves, ferroelectrics have become increasingly important for microwave and millimetre wave techniques. A number of passive and active devices can be realised by using the high dielectric permittivity, high ionic non-linearity and small dielectric loss of ferroelectrics. In some ferroelectrics the medium response time is instantaneous up to ≈1000 GHz and electro-optic devices can function up to these frequencies. Thus there is a need for reliable methods to control the dynamical dielectric properties of these materials in the wide microwave and millimetre wave region. Dynamic dielectric properties of ferroelectrics are mainly determined by the value and temperature dependence of the soft mode. Generally the soft mode can be defined as the pole of the order-parameter susceptibility which moves to the origin in the complex-frequency $\nu^* = \nu' - i\,\nu''$ plane when the temperature approaches the Curie temperature, $T_C$. When $\nu' > \nu''_S$ the mode is underdamped and lies on the real $\nu^*_S$ axis, and when $\nu' < \nu''_S$ the mode is relaxational and lies on the imaginary $\nu^*_S$ axis.

The soft mode contributes to both dielectric permittivity and loss. Soft mode loss, which dominates in dielectric dispersion region, limits the application of ferroelectrics except for use as wide-band absorbers of redundant microwave radiation.

The recent progress in microwave and millimetre wave dielectric spectroscopy[1,2] jointly with the submillimetre and IR spectroscopy[3] makes it possible to investigate the dielectric spectra of ferroelectrics in all frequency region of

the interaction of electromagnetic waves with phonons and dipoles. Dielectric spectroscopy enables the simultaneous measurement of both the real and imaginary parts of the complex dielectric permittivity. Applying dielectric spectroscopy, it was found that in displacive ferroelectrics the soft mode on approaching $T_c$ becomes strongly overdamped and softens up to the millimetre wave range, whilst in some order-disorder ferroelectrics the fundamental ferroelectric dispersion far from $T_c$ ranges to $10^{12}$ Hz.

In this communication we present some results of our latest investigations, showing that the fundamental ferroelectric dispersion and the frequency of the soft mode lie in the microwave and millimetre wave region.

## RESULTS AND DISCUSSION

Fig.1 shows the frequency dependence of the dynamic dielectric permittivity of the representatives of three families of ferroelectrics treated as the displacive type, namely SbSJ, $Sn_2P_2S_6$ and $TlGaSe_2$. Dielectric dispersion in SbSJ and its solid solutions were intensively investigated in the seventies and eighties, and it was supposed that the microwave and IR dispersion were caused by different excitations. New measurements show that there is only one peak of loss, and ferroelectric dispersion in the frequency range $10^9$ to $10^{12}$ Hz can be explained by the soft $B_{1u}$ mode, which on approaching $T_c$ becomes strongly overdamped, its frequency softens up to the millimetre wave range and makes the dielectric contribution $\Delta\varepsilon_s \approx \varepsilon(0)$ which fits the Curie-Weiss law.

Another family of ferroelectric crystals with an extremely low-frequency soft $B_u$ mode are $Sn_2P_2S_6$ type crystals[2]. At $T_c$ = 339 K $Sn_2P_2S_6$ undergoes the second order ferroelectric phase transition (PT). The dielectric spectroscopy of these crystals showed that the soft mode in $Sn_2P_2S_6$ changes with temperature according to $\nu_s = 35(T-339)^{1/2}$ GHz[4]. Near $T_c$ it becomes strongly overdamped and is again alone responsible for the value and temperature dependence of the static dielectric permittivity which at $T_c$ reaches $\varepsilon(0) = 7\cdot10^4$.

$TlGaSe_2$ and $TlInS_2$ crystals are an example of the third family of displacive type ferroelectrics with incommensurate phase, in which the frequency of the soft mode is extremely low in the vicinity of $T_i$ and $T_c$[5,6]. The soft mode is also strongly overdamped. At $T_i$ the soft mode splits into a phason and an amplitudon. The phason in real crystals is pinned and strongly overdamped. It reveals itself as a relaxor. The frequency of the phason is about $10^7$ Hz[7]. Crystal imperfections result in the pinning

of the phason and increase the gap in the phason spectrum, i.e. increase the frequency of the phason to $10^9$ Hz.

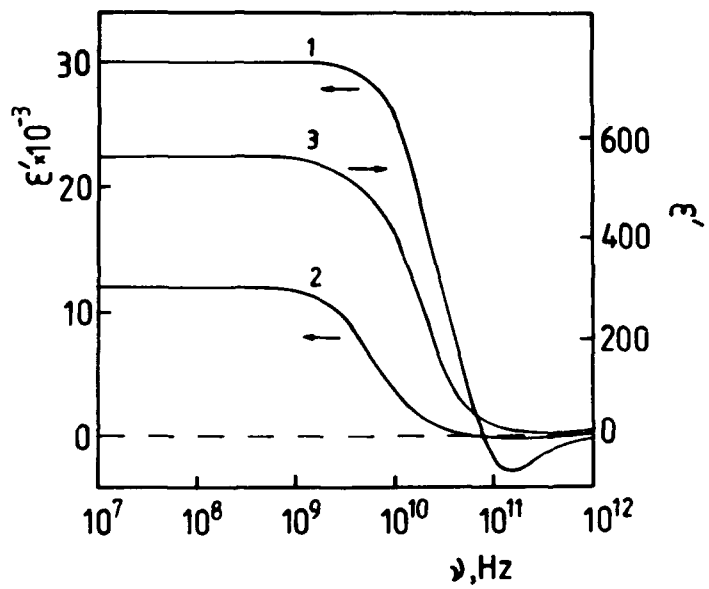


FIGURE 1 Frequency dependence of the dielectric permittivity of: 1-SbSJ at 296 K; 2-$Sn_2P_2S_6$ at 344 K; 3-$TlGaSe_2$ at 113 K. (All measurements at $\nu > 10^{11}$ were performed elsewhere)

In all of these nonlinear crystals the paraelectric soft mode on approaching $T_c$ softens to the millimetre wave range (Fig.2) and lies below the limits of IR and neutron spectroscopies. It shows a change from a displacive to an order-disorder like regime on approaching the Curie point.

Generally, the soft relaxational (diffuse) mode in order-disorder ferroelectric is pseudospin relaxator. The relaxational mode is $\nu_s = 1/(2\pi\tau)$, where $\tau$ is the relaxation time. Fig.2 shows also the temperature dependence of the relaxational modes of some of the order-disorder type ferroelectrics. In the H-bonded CDP-type ferroelectrics[8,9] the loss spectrum caused by monodispersive relaxation lies in the frequency range $10^6$ to $10^{12}$ Hz. The relaxation frequency of all these compounds is similar to that of $CsH_2PO_4$.

*Diglycine nitrate* is a less studied H-bonded ferroelectric of the TGS family, which at $T_c$ = 206 K undergoes the second-order proper PT. The relaxational mode

is associated with the flipping motion of protons in the H-bonds linking two glicyne ions[10].

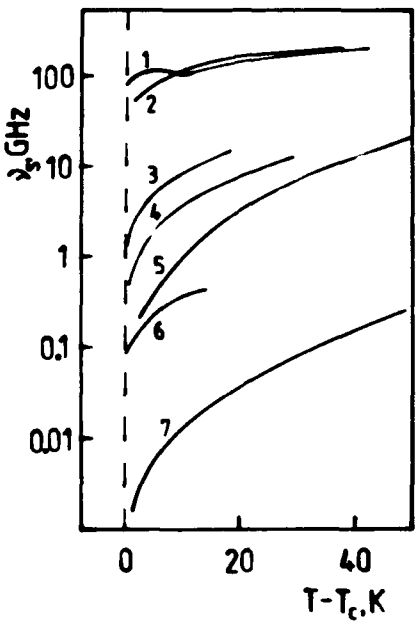


FIGURE 2 Temperature dependence of the soft modes in different ferroelectrics: 1-$TlGaSe_2$; 2-$Sn_2P_2S_6$; 3-TAAP; 4-DGN; 5-$CsH_2PO_4$; 6- TMACA; 7-DMAAS.

H-bonded *telluric acid ammonium phosphate* (TAAP) at $T_C$ = 317.3 K undergoes a second order ferroelectric PT. The relaxational mode of the correlated flipping motion of protons on approaching $T_C$ drops to 1.75 GHz[11]. In all these crystals the large dielectric contribution of the relaxational mode accounts for all the value of the static dielectric permittivity which follows the Curie-Weiss law.

The lower part of Fig.2 shows that the relaxational modes behaviour of the two new ferroelectrics, in which ferroelectric dynamics are related with heavy dipoles. At $T_C$ = 363 K, the $[(CH_3)_3NH]_3Sb_2Cl_9$ (TMACA) crystal undergoes a first order ferroelectric PT. The Curie-Weiss law follows from the critical slowing down of the relaxational frequency $\nu_S$, which varies according to $\nu_S$ = 32(T-360.5) MHz in the paraelectric phase and reaches 80 MHz at $T_C$.

*Dimethylammoniumaluminium sulphate* (DMAAS) undergoes a nearly critical PT[12] at $T_c$ = 152.5 K. The dielectric relaxation is caused by dimethylammonium cations dynamics and in all paraelectric phases shows monodispersive nature. The relaxation frequency is extremely low.

Thus the soft mode frequency gap in the discussed above type of ferroelectrics is not large. This frequency in most ferroelectrics lies at microwaves and causes high dielectric loss which hinder applications of ferroelectrics at these frequencies in components and subsystems.

## REFERENCES

1. A.Brilingas, R.L.Davidovich, J.Grigas, S.Lapinskas, M.A.Medkov, V.Samulionis and V.Skritskii, Phys.Stat.Sol. (a), 96, 102(1986).
2. J.Grigas, A.Brilingas and V.Kalesinskas, Ferroelectrics, 107, 61(1990).
3. J.Petzelt, S.Pacesova, J.Fousek, S.Kamba, V.Zelezny, V.Koukal, J.Shhwarzbach, B.P.Gorshunov, G.V.Kozlov and V.V.Volkov, Ferroelectrics, 93, 77(1989).
4. J.Grigas, Kalesinskas, S.Lapinskas and I.M.Gurzan, Phase Transitions, 12, 263(1988).
5. J.Banys, A.Brilingas, J.Grigas and G.Guseinov, Sov.Phys.Solid State, 29, 1906(1987).
6. J.Banys, J.Grigas and G.Guseinov, Ferroelectrics, 83, 3(1988).
7. J.Banys, A.Brilingas and J.Grigas, Phase Transitions, 20, 211(1990).
8. R.Mizeris, J.Grigas, R.R.Levitsky, I.R.Zachek and S.I.Sorokov, Ferroelectrics, 108, 261(1990).
9. J.Grigas, R.Mizeris and R.Sobiestianskas, Proc.Radio and Microwave Spectroscopy, Poznan, 1991, p.177.
10. R.Sobietianskas, J.Grigas, and Z.Czapla, Ferroelectrics, 100, 187(1989).
11. R.Sobiestianskas, J.Grigas and Z.Czapla, Phase Transitions, (1991).
12. R.Sobiestianskas, J.Grigas, V.Samulionis and E.F.Andreyev, Phase Transitions, 29, 167(1991).

*Ferroelectrics*, 1992, Vol. 133, pp. 205–210
Reprints available directly from the publisher
Photocopying permitted by license only
© 1992 Gordon and Breach Science Publishers S.A.
Printed in the United States of America

**DiP230**

# DIELECTRIC SPECTROSCOPY OF SOME $Ba(B'_{1/2}B''_{1/2})O_3$ COMPLEX PEROVSKITES IN THE $10^{11}$ - $10^{14}$ Hz RANGE

J. Petzelt†, R. Zurmühlen+, A. Bell+, S. Kamba†, G.V. Kozlov≠, A.A. Volkov≠, N. Setter+

† Inst. Phys., Czech. Acad. Sci, Na Slovance 2, 18040 Praha 8, CSFR
+ Lab. de céramique, EPFL, MX-D Ecublens, 1015 Lausanne, Switzerland
≠ Inst. General Physics, Vavilov St. 38, 117942 Moscow, Russia

Abstract

Five $Ba(B'_{1/2}B_{1/2}'')O_3$ ceramic compounds ($B' = Y^{3+}, Gd^{3+}, Nd^{3+}, In^{3+}$; $B'' = Ta$ and $B' = Mg^{2+}$; $B'' = W^{6+}$) have been prepared to investigate the origin of microwave losses. Infrared reflectivity and submillimetre transmission measurements as well as low-frequency dielectric measurements were performed and evaluated. An attempt was undertaken to divide the submillimetre losses into intrinsic lattice losses (multiphonon absorption) proportional to temperature and extrinsic temperature independent loss contributions.

## INTRODUCTION AND SYMMETRY CONSIDERATIONS

Recently, it was shown[1-4] that infrared (IR) spectroscopy may help to characterize the microwave (MW) properties of materials. It is generally accepted[3,5] that intrinsic MW losses are determined by anharmonic phonon decay processes in the pure crystal lattice which represent the lower loss limit achievable by material processing. The basic question is whether we can estimate these intrinsic losses solely from IR data.

From the viewpoint of IR spectroscopy and lattice vibrations, the materials so far investigated are too complex. For instance, in ordered $Ba(B'_{1/3}B''_{2/3})O_3$ perovskites which seem to be promising for low MW losses the structure is trigonal (space group $P\bar{3}m1$, Z=3)[6] and the factor group analysis gives 16 polar optic modes. In addition, one has to take into account that the anisotropy of the IR reflectivity is averaged out in ceramic samples which may lead to effective broadening of modes.

In order to simplify the IR spectra and stay in complex perovskite systems which so far offer the greatest application possibilities, we decided to investigate some of the $Ba(B'_{1/2}B''_{1/2})O_3$ compounds. Structural analysis[6] shows that these compounds mostly exhibit cubic superstructure (space group $Fm\bar{3}m$, Z=2) with the following site-symmetry of atoms: $A(\bar{4}3m)$, $B',B''(m\bar{3}m)$ and O(4mm). This leads to the following decomposition of the vibrational representation: $A_{1g} + E_g + F_{1g} + 5F_{1u} + 2F_{2g} + F_{2u}$, and predicts only 4 triply degenerate IR active modes - 3 of the simple cubic perovskite structure plus one where the neighboring B' and B" atoms vibrate against each other.

## EXPERIMENTAL

Materials were produced following a standard mixed oxide route. Final sintering was in air (4h, 1650 °C). For $Ba(Gd_{1/2}Ta_{1/2})O_3$ (BGT), $Ba(Nd_{1/2}Ta_{1/2})O_3$ (BNT) $Ba(Y_{1/2}Ta_{1/2})O_3$ (BYT) and $Ba(In_{1/2}Ta_{1/2})O_3$ (BIT) no second phase could be detected. In $Ba(Mg_{1/2}W_{1/2})O_3$ (BMW) the amount of second phase ($BaWO_4$, MgO) was around 5%. TEM of the samples (density > 97%) confirmed the single phase character of BGT, BNT BYT and BIT. In addition, BGT and BNT samples showed domains (~ 200 nm wide) which are assumed to be ferroelastic, implying structural distortion. All samples seem to be well ordered concerning the B' and B" ion distribution.

Dielectric measurements have been carried out from $10^2$ - $10^6$ Hz ([-30 °C] - [+70 °C]) using a HP-LC 4284 bridge. IR measurements were performed with a Fourier transform interferometer Bruker IFS 113v. Normal bulk reflectivity at room temperature was measured in the 30 - 3000 $cm^{-1}$ range. Transmission measurements have been carried out using tunable backward wave oscillators (BWO) as monochromatic sources in the 6 - 30 $cm^{-1}$ range[7,8].

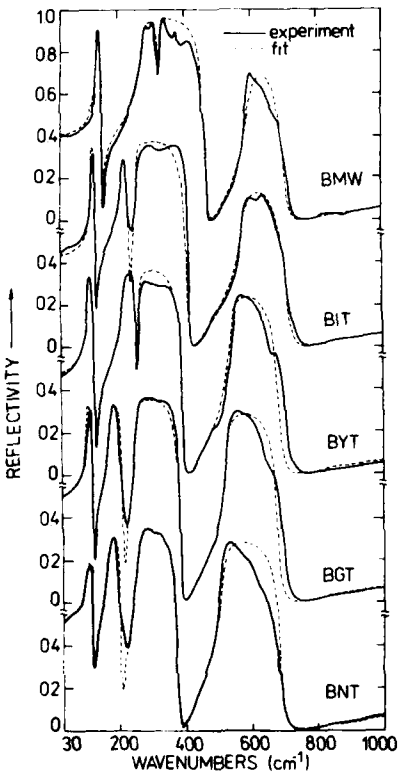


Fig. 1 Measured IR reflectivities (full lines) compared with classical oscillator fit (dashed).

## RESULTS

In Fig. 1 the measured reflectivity is compared with the results of a four classical oscillator fit using the formula[9]:

$$\varepsilon(\upsilon) = \sum_{i=1}^{4} \frac{\Delta\varepsilon_i \upsilon_i^2}{\upsilon_i^2 - \upsilon^2 + i\upsilon\gamma_i} + \varepsilon_\infty \quad (1)$$

for all five compounds.

The parameters of the fit are listed in Table 1. The calculated values of the static permittivity $\varepsilon_o = \Sigma\Delta\varepsilon_i + \varepsilon_\infty$ compare well with the permittivity values from transmission measurements in the millimetre range (Table 2) and from dielectric measurements in the $10^2$ - $10^6$ Hz range. The negligible dispersion in the $10^2$-$10^{11}$ Hz spectrum is also supported by unmeasurable losses (tan $\delta < 10^{-3}$) in the low-frequency range over the whole investigated temperature interval.

| Mode Parameters | BNT | | BGT | | BYT | | BIT | | BMW | |
|---|---|---|---|---|---|---|---|---|---|---|
| | KK | Fit | KK | Fit | KK | Fit | KK | Fit | KK | Fit |
| $\nu_1$ ($cm^{-1}$) | 104 | 104 | 105 | 106 | 110 | 110 | 124 | 124 | 142 | 42 |
| $\gamma_1$ ($cm^{-1}$) | 4 | 10 | 4 | 2.5 | 2 | 2.5 | 2 | 1.2 | 2 | 1.6 |
| $\Delta\varepsilon_1$ | 15.9 | 13.3 | 13.3 | 11.5 | 14.8 | 10.7 | .6 | 4.7 | 5.3 | 4.4 |
| $\Delta\varepsilon''_1/\nu_1$ ($10^{-3}$ cm) | 5.9 | 12.3 | 4.8 | 2.6 | 2.4 | 2.2 | 0.6 | 0.4 | 0.5 | 0.3 |
| $\nu_2$ ($cm^{-1}$) | 66 | 166 | 172 | 172 | 217 | 218 | 213 | 214 | 280 | 281 |
| $\gamma_2$ ($cm^{-1}$) | 8 | 6.8 | 7 | 5.5 | 7 | 6 | 7 | 6.2 | 10 | 8 |
| $\Delta\varepsilon_2$ | 12.4 | 0.5 | 14.6 | 11.4 | 13.5 | 11.8 | 8.9 | 9 | 12.5 | 10.0 |
| $\Delta\varepsilon''_2/\nu_2$ ($10^{-3}$ cm) | 3.6 | 2.6 | 3.4 | 2.1 | 2.0 | 1.5 | 1.4 | 1.1 | 1.6 | 1.0 |
| $\nu_3$ ($cm^{-1}$) | 250 | 251 | 248 | 249 | 264 | 264 | 261 | 262 | 327 | 328 |
| $\gamma_3$ ($cm^{-1}$) | 9 | 8 | 8 | 7 | 7 | 6 | 6 | 4 | 5 | 5.2 |
| $\Delta\varepsilon_3$ | 6.7 | 5.9 | 6.0 | 5.2 | 1.7 | 1.5 | 7.4 | 5.2 | 0.5 | 0.45 |
| $\Delta\varepsilon''_3/\nu_3$ ($10^{-3}$ cm) | 1.0 | 0.8 | 0.8 | 0.6 | 0.2 | 0.1 | 0.7 | 0.3 | 0.0 | 0.0 |
| $\nu_4$ ($cm^{-1}$) | 508 | 510 | 525 | 526 | 538 | 540 | 578 | 580 | 592 | 594 |
| $\gamma_4$ ($cm^{-1}$) | 6 | 16 | 15 | 14 | 20 | 19 | 32 | 31 | 32 | 31 |
| $\Delta\varepsilon_4$ | 0.9 | 1.9 | 1.7 | 1.6 | 1.5 | 1.4 | 1.3 | 1.3 | 0.9 | 0.86 |
| $\Delta\varepsilon''_4/\nu_4$ ($10^{-3}$ cm) | 0.12 | 0.12 | 0.09 | 0.08 | 0.10 | 0.09 | 0.13 | 0.12 | 0.08 | 0.08 |
| $\Sigma\,\Delta\varepsilon_i + \varepsilon_\infty$ | 41.1 | 35.8 | 39.5 | 33.9 | 35.7 | 29.6 | 26.4 | 23.3 | 23.4 | 19.9 |
| $Q*\nu$ Total ($10^{12}$Hz) | 94 | 63 | 110 | 186 | 213 | 257 | 353 | 521 | 459 | 725 |

Table I: Mode parameters from the fit.

In Fig.2 we compare the extrapolated losses from the reflectivity fit with the directly measured transmission data in the 200-1000 GHz range. The estimated accuracy of extrapolated losses is +/-30 % whereas the accuracy of transmission measurements is much higher (+/-5%). We also measured temperature dependencies of the submillimetre transmission. The resulting dependencies for a fixed frequency around 25cm$^{-1}$ are shown in Fig. 3. In Fig. 4 we compare the spectral dependencies at low and high temperatures.

## DISCUSSION

The most detailed microscopic discussion of microwave and submillimetre losses ($\upsilon << \upsilon_{Ti}$) in crystals was carried out by Gurevich and Tagantsev[10,11]. In the high temperature approximation $T \geq \Theta$ ($\Theta$ = Debye temperature, here: ~400 K) the two-phonon difference absorption processes dominate. They should approximately obey the proportionality $\varepsilon'' \propto T^2\upsilon$ within the low-frequency range ($\upsilon << 1/2\pi\tau \approx 20$ cm$^{-1}$, $\tau$ = mean thermal phonon lifetime), whereas $\varepsilon'' \alpha T\upsilon^2$ in the higher frequency range ($\upsilon_i >> \upsilon >> 1/2\pi\tau$).

Extrapolating Fig. 3 to T = 0 shows that part of the losses (except BMW) result from an absorption background $\varepsilon''_b$. As seen from $\varepsilon''(\upsilon)$ dependencies in Fig. 2, $\varepsilon''_b(\upsilon) \propto \upsilon$, at least for $\upsilon > 15$ cm$^{-1}$, because the total losses obey this proportionality, too. Such a behavior is characteristic for charged point defects or two-dimensional defects coupled to strain[11]. The latter may be the case for dense ferroelastic domain structure observed in BGT and BNT. If these mechanisms were operative one would expect $\varepsilon''_b$ to be temperature independent[11].

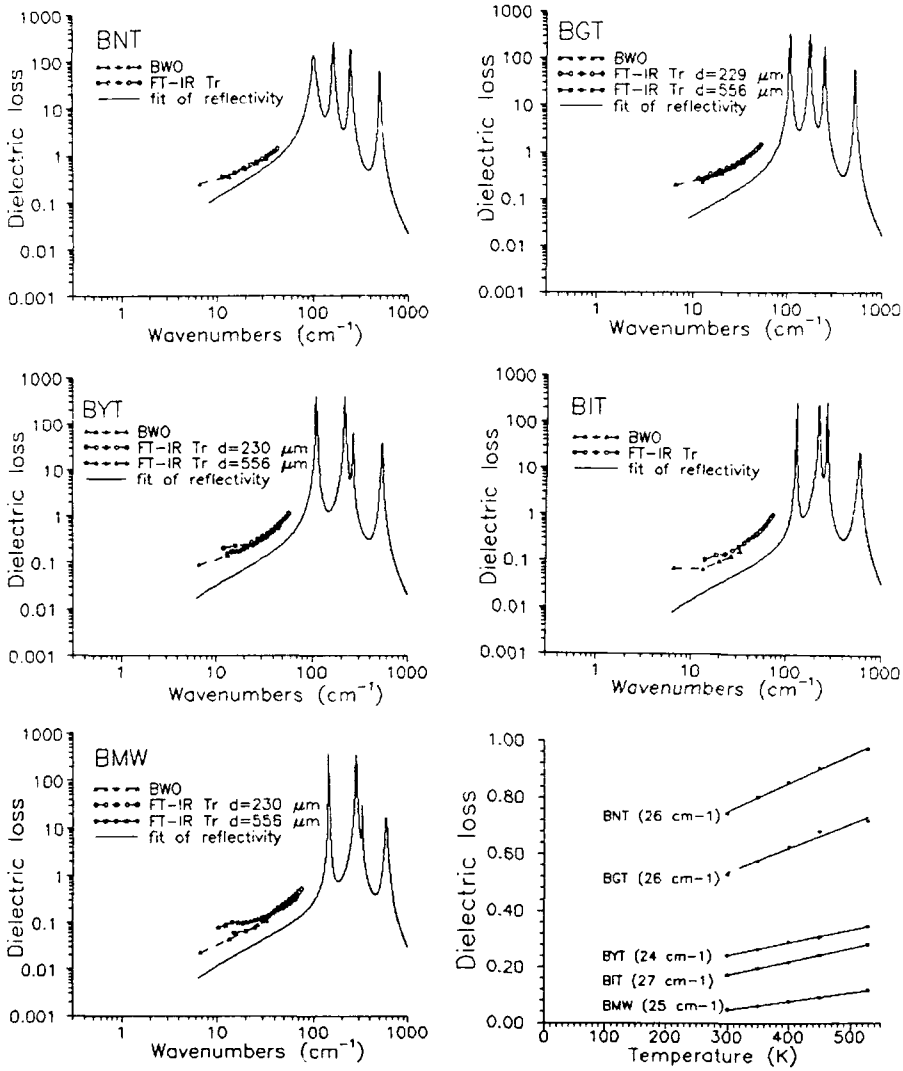


Fig. 2 Calculated losses from reflectivity fit (lines) compared with losses from transmission measurement.




Fig. 3 Temperature dependences of ε" near 25 cm$^{-1}$.

Assuming this independence and concerning the intrinsic part of the losses, Figs. 2 and 4 indicate that at high temperatures and for $\upsilon \geq 12$ cm$^{-1}$, a proportionality $\varepsilon'' \propto T\upsilon^a$ with $a > 1$ is obeyed for BGT, BNT and BYT. The theoretically predicted $\varepsilon'' \propto T\upsilon^2$ behaviour could be seen only in a limited frequency range. At lower frequencies at room temperature a cross-over behavior $\varepsilon'' \propto T\upsilon$ is observed. The observation of the low-frequency regime $\varepsilon'' \propto T^2\upsilon$ is apparently obscured by the extrinsic temperature independent part of the losses.

| | BNT | | BGT | | BYT | | BIT | | BMW | |
|---|---|---|---|---|---|---|---|---|---|---|
| $\varepsilon_0$ | 34.5 | | 33.0 | | 30.7 | | 22.5 | | 18.9 | |
| Q*ν ($10^{12}$ Hz | KK | fit | KK | fit | KK | fit | KK | fit | KK | fit |
| extrapol.) | 94 | 63 | 110 | 168 | 213 | 257 | 353 | 521 | 459 | 725 |
| Q*ν ($10^{12}$ Hz transmission) | 36 | | 56 | | 89 | | 137 | | 197 | |
| Q*ν ($10^{12}$ Hz ("intrinsic" trans) | 90 | | 92 | | 189 | | 246 | | 184 | |
| R (B') (A) | 1.123 | | 1.078 | | 1.04 | | 0.94 | | 0.86 | |
| R (B") (A) | 0.78 | | 0.78 | | 0.78 | | 0.78 | | 0.74 | |
| M (B') (amu) | 144.2 | | 157.2 | | 88.9 | | 114.8 | | 24.3 | |
| 1-t | .035 | | .025 | | .016 | | -0.008 | | -0.038 | |

Table 2: $Q^*\upsilon$ "instrincic" trans. is calculated by the substraction of $\varepsilon''_b$ (T=0) from $\varepsilon''$ (T=300K). Parameters characterizing the intrinsic sample quality: $Q\upsilon$ is the quality product, $\varepsilon_0$ = static permittivity (200 GHz), M(B') = B'-ion mass, R(B'). R(B") = B',B"-ion radii, t = tolerance factor of ionic sizes for the perovskite structure.

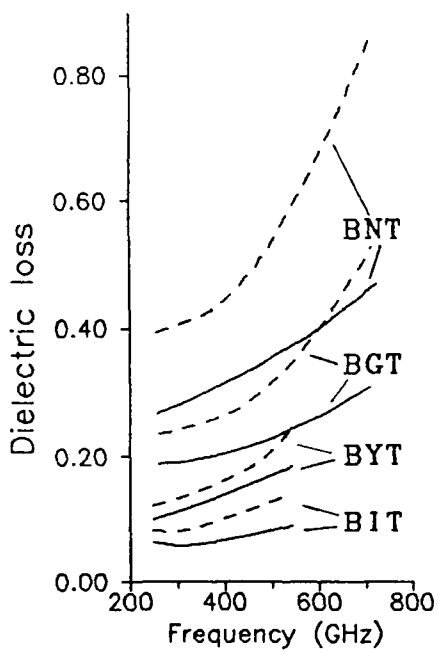


Fig. 4 Spectral dependence of ε" in BNT, BGT, BYT and BIT at 20 (full lines) and 350 °C (dashed lines).

Let us now discuss the question of extrapolating intrinsic microwave losses from the high frequency one-phonon absorption region (Fig. 2). As stated previously[3] and demonstrated here, such an extrapolation using a damped harmonic oscillator model works surprisingly well in many cases. Also here it seems that it estimates well the

intrinsic millimetre and microwave losses. However, one has to consider that the microscopic theory[10,11] does not justify such a simple empirical extrapolation law.

Finally, we would like to discuss how various structural parameters like B'-ion mass, radius, and valence influence the loss and permittivity values. In Table 2 we compare all the relevant parameters listed according to the increasing quality product $Q\upsilon$ where Q is the quality factor $\varepsilon'/\varepsilon''$ at 20 $cm^{-1}$ and 300 K. As known from other systems[1-3], there is a clear correlation between $Q\upsilon$ and $\varepsilon_o$. Another correlation can be seen between $\varepsilon_o$, $\upsilon_i$ and R(B'): the lower R(B'), the higher the mode frequencies $\upsilon_i$ and the lower $\varepsilon_o$. The most interesting feature seems to be the correlation between the tolerance factor and lattice anharmonicity characterized by the mode dampings and the quality product. The underlying physical idea is simple: the more ideal space filling, the less space for vibrations and therefore the smaller the anharmonicity. Weaker anharmonicity results finally in lower microwave losses. However, the tolerance factor averages the B' and B"-ion radius. If we include BMW (oxidation state: $2^+$,$6^+$) showing the lowest loss but tolerance factor most different from one, one could conclude only that the above considerations should be taken with precaution and not be generalized to compounds of different B" ions such as $W^{+6}$ or $Nb^{+5}$.

To understand quantitatively how the mass and valence influences the microwave properties requires an accurate knowledge of polar mode eigenvectors in these compounds which is possible only on the basis of microscopic model calculations. This goes beyond the scope of this work.

Acknowledgement

The research is in part supported by the Swiss Science Foundation for the Scientific Research.

References

1. K. Wakino, M. Murata and H. Tamura, J. Am.Ceram.Soc., 69, 34 (1986).
2. H. Tamura, D.A. Sagala and K. Wakino, Jap. J. Appl. Phys., 25, 787 (1986).
3. J.Petzelt, S.Pacesova, J.Fousek, S.Kamba, V.Zelezny, V.Koukal, J. Schwarzbach, B.P.Gorshunov, G.V.Kozlov and A.A.Volkov, Ferroelectric 93, 77 (1989).
4. A. Sawada and T. Kuwabara, Ferroelectric, 95, 205 (1989).
5. W. Wersing, in Electronic Ceramics, edited by B.C.H. Steele (Elsevier Appl. Sci., London, 1991), pp. 67-119.
6. F.S. Galasso, Structure, Properties and Preparation of the Perovskite-Type Compounds (Pergamon Press, 1969), p. 15.
7. A.A. Volkov, Yu.G. Goncharov, G.V. Kozlov, S.P. Lebedev and A.M. Prokhorov, Infrared Physics, 25, 369 (1985).
8. A.A.Volkov, G.V.Kozlov and A.M. Prokhorov, Infrared Physics, 29, 747 (1989).
9. P. Brüesch, Phonons: Theory and Experiment II, Springer Ser. in Solid State Sciences 65, Berlin (1986).
10. V.L. Gurevich and A.K. Tagantsev, ZhETF, 97, 1335 (1990).
11. V.L. Gurevich and A.K. Tagantsev, Adv. Phys., 40, 719 (1991).
12. R.D. Shannon, C.T. Prewitt, J. Inorg. Nucl. Chem., 30, 1389 (1968).

*Ferroelectrics*, 1992, Vol. 133, pp. 211–215
Reprints available directly from the publisher
Photocopying permitted by license only

© 1992 Gordon and Breach Science Publishers S.A.
Printed in the United States of America

**DiP233**

# DIELECTRIC LOSS OF FERROELECTRIC LITHIUM TRIHYDROGEN SELENITE UNDER HYDROSTATIC PRESSURE

SANJI FUJIMOTO AND KEN KANAI
Fukui Institute of Technology, Fukui 910, Japan

Abstract. This paper is concerned with the dependence of the dielectric loss on the hydrostatic pressure and the electric field for LHS in the ferroelectric phase. The dielectric loss tangent increases with increasing pressure and rapidly near the transition pressure, and decreases with increasing dc electric field. These experimental results are explained by means of a phenomenological theory.

## INTRODUCTION

Lithium trihydrogen selenite $LiH_3(SeO_3)_2$ (abbreviated to LHS) is one of the hydrogen bonded ferroelectrics, and has a large spontaneous polarisation at room temperature[1]. The permittivity and the spontaneous polarisation of LHS have been measured in the ferroelectric phase[1,2]. LHS remains ferroelectric up to its melting point of 110°C. A ferroelectric to paraelectric transition is made possible by simultaneously raising the melting point and lowering the Curie point by the application of hydrostatic pressure[3]. Extrapolating the pressure versus Curie temperature curve back to zero pressure showed that LHS would have a Curie point of 147°C at atmospheric pressure were it not for its melting before reaching 147°C[4].

According to an X-ray study of LHS, the crystal structure is centrosymmetric and is most likely to belong to the monoclinic space group $P2_1/n$ in the paraelectric phase, and Pn in the ferroelectric phase[5].

In this paper, the effect of the hydrostatic pressure and dc electric field on the dielectric loss tangent for the LHS crystal in the ferroelectric phase is reported and explained in terms of a phenomenological theory.

## SPECIMEN AND EXPERIMENTAL METHOD

A specimen was a c-plate cut out with a beryllium-wire cutter froma single crystal which was grown at a constant temperature by evaporation from saturated $H_2O$ solution, and had typically 6.0 x 6.5mm$^2$ area and 0.4mm thickness. The polished specimen was electroded with silver paste. The electrical capacitance and the dielectric loss tangent of the specimen were measured at 10kHz with a field weaker than 5Vcm$^{-1}$ using an impedance analyser

with an accuracy of ±0.3%. The high-pressure apparatus applying hydrostatic pressure to the specimen was an anvil type 700-ton hexahedral press employing pyrophillite as a pressure transmitting medium. The pressure was measured with maganin gauges to an accuracy of ±1.5%. The hysteresis loop was observed with a Sawyer-Tower circuit[6]. The dc electric field superposed was applied along the c-axis (approximately polar direction).

## EXPERIMENTAL RESULTS AND DISCUSSION

When the complex relative permittivity is expressed by the relation $\varepsilon_r^* = \varepsilon_r - i\varepsilon_r'$, the dielectric loss tangent is defined as $\tan\delta = \varepsilon_r'/\varepsilon_r$. Plots of the reciprocal of relative permittivity $1/\varepsilon_r$ and dielectric loss tangent $\tan\delta$ against the hydrostatic pressure p under no dc electric field (E=0) at 21°C are shown by open circles in Figure 1. The $1/\varepsilon_r$ versus p curve shown in Figure 1 (a) is very similar to the experimental results reported by Samara[4]. The reciprocal of relative permittivity has an anomaly, ie, approaching zero at the transition pressure $p_c$ (=20.9kbar). The value of $1/\varepsilon_r$ decreases with increasing pressure in the ferroelectric phase at pressures below $p_c$, and increases in the paraelectric phase at pressures above $p_c$. In view of the above fact, the phase transition of LHS should be second order. As shown in Figure 1 (b), the dielectric loss tangent increases rapidly near the transition pressure $p_c$ because of the large increase in specimen conductivity. The plots of $\varepsilon_r$ and $\tan\delta$ against the dc electric field E at 16kbar and at 21°C are shown by open circles in Figure 2. The values of $\varepsilon_r$ and $\tan\delta$ in the ferroelectric phase decrease with increasing electric field.

According to a phenomenological theory on a second order ferroelectric transition, (a) the dependence of $1/\varepsilon_r$ on the pressure in the paraelectric phase under no dc electric field (E=0) is expressed as follows[7]:

$$1/\varepsilon_0\varepsilon_r = u + gp = g(p - p_c) \qquad (1)$$

(b) the dependence of $1/\varepsilon_r$ and $\tan\delta$ on the pressure in the ferroelectric phase under E=0 are expressed as follows[7]:

$$1/\varepsilon_0\varepsilon_r = -2(u + gp) = 2g(p_c - p) \qquad (2)$$

$$\tan\delta = \sqrt{[1-9\varepsilon P_0^2/2(u + gp)\sin^2\delta' x \tan\delta']} \qquad (3)$$

(c) the dependence of $\varepsilon_r$ and tanδ' on the dc electric field E in the ferroelectric phase under constant pressure are given by the following relations[8]:

$$E = (1/\varepsilon_0\varepsilon_r + 2u + 2gp)\sqrt{[(1/\varepsilon_0\varepsilon_r - u - gp)/3\xi]}/3 \quad (4)$$

$$E = (u + gp + \xi P_a^2)P_a \quad (5)$$

$$P_a = 3P_0/\sqrt{2}(\tan^2\delta - \tan^2\delta') \quad (6)$$

where $e_0$ is the vacuum permittivity, u, g, ξ are phenomenological constants, $P_0$ is the polarisation induced by the ac electric field and tanδ', is a value of tanδ measured in the paraelectric phase. The transition pressure $p_c$ is given by the following relation[7]:

$$p_c = -u/g \quad (7)$$

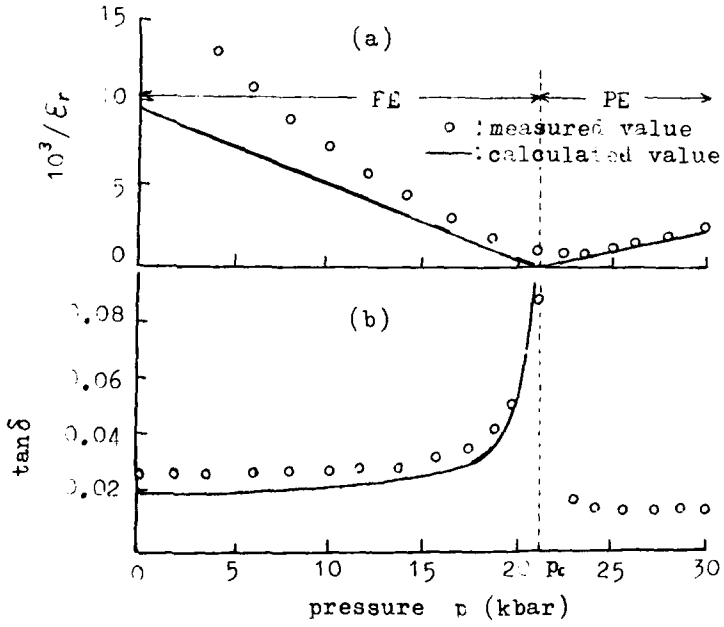


FIGURE 1. Plots of (a) the reciprocal of relative permittivity, and (b) the dielectric loss tangent against the hydrostatic pressure up to 30kbar under no dc electric field at 21°C.

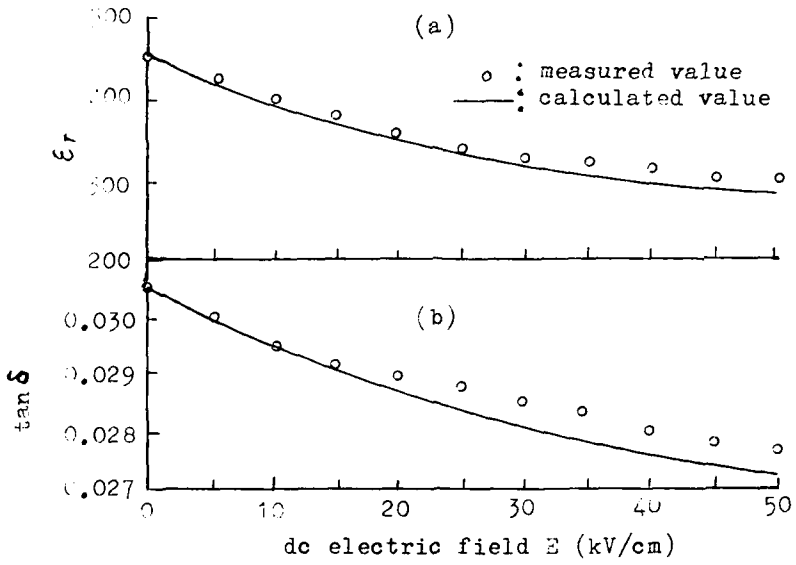


FIGURE 2. Plots of (a) the relative permittivity, and (b) the dielectric loss tangent against the dc electric field of LHS in the ferroelectric phase at 16kbar and at 21°C.

Equation (2) is also obtained by putting E=0 into equation (4). The constants u, g, $\xi$ and the transition pressure $p_c$ at 21°C are determined from the plots in Figure 1(a) and Figure 2(a) as follows:

$$u = -5.45 \times 10^8 \text{m/F},\ g = 2.61 \times 10^7 \text{m/Fkbar},\ \xi = 1.67 \times 10^{10} \text{m}^5/\text{FC}^2, \qquad (8)$$
$$p_c = 20.9\text{kbar}$$

The values of tan$\delta$ measured over the range 22 to 30kbar in the paraelectric phase and at 16kbar in the ferroelectric phase under 21°C and 0.015 (=tan$\delta'$) and 0.0305, respectively. By putting the values obtained above into equation (3), $P_0 = 1.1 \times 10^{-3}\text{C/m}^2$.

The full curves shown in Figure 1 and Figure 2 are calculated values which are obtained by putting the above values into equations (1)-(3) and equations (4)-(6), respectively.

The experimental results agree fairly with the calcuated values. Thus, the dependence of the dielectric loss on the pressure and the electric field was explained by means of a phenomenological theory.

## REFERENCES

1. R. Pepinsky and K. Vedam, Phys. Rev. 114, 1217 (1959).
2. D. Berlincourt, W.R. Cook Jr. and M.E. Rander, Acta. Cryst. 16, 163 (1963).
3. G.A. Samara and D.H. Anderson, Solid State Commun. 4, 653 (1966).
4. G.A. Samara, Phys. Rev. 173, 605 (1968).
5. K. Vedam, Y. Okaya and R. Pepinsky, Phys. Rev. 119, 1252 (1960).
6. C.B. Sawyer and C.H. Tower, Phys. Rev. 35, 267 (1930).
7. S. Fujimoto and N. Yasuda, Trans. IEE. Japan 93-A, 361 (1973).
8. S. Fujimoto and N. Yasuda, Trans. IEE. Japan 94-A, 361 (1974).

*Ferroelectrics*, 1992, Vol. 133, pp. 217–222
Reprints available directly from the publisher
Photocopying permitted by license only

© 1992 Gordon and Breach Science Publishers S.A.
Printed in the United States of America

# DiP256

## THE TEMPERATURE COEFFICIENT OF THE RELATIVE PERMITTIVITY OF COMPLEX PEROVSKITES AND ITS RELATION TO STRUCTURAL TRANSFORMATIONS

E.L.Colla, I.M. Reaney and N. Setter
Laboratoire de Céramique, EPFL, MX-D Ecublens, 1015-Lausanne, Switzerland.

Abstract
The dielectric behaviour and structure of the $Ba_xSr_{1-x}(Zn_{1/3}Nb_{2/3})O_3$ (BSZN) solid solution have been investigated with the intention of understanding an anomaly which exists in the temperature coefficient of the dielectric constant ($\tau_\varepsilon$) at $x \approx 0.5$. A correlation between $\tau_\varepsilon$ and the occurrence of O-octahedra tilts has been established.

## INTRODUCTION

Complex perovskites with high permittivity and low dielectric loss are used as dielectric resonators at microwave frequencies. One of the most selective characteristic for this type of dielectric material is the temperature coefficient of the resonant frequency ($\tau_f$), which is given by, $\tau_f = -(\alpha + \tau_\varepsilon/2)$
where, $\alpha$ = linear thermal expansion coefficient. Although the value of $\tau_f$ is mainly dependent on intrinsic, structural parameters, there have been few studies which have attempted to predict values of $\tau_f$ except by simple empirical methods.

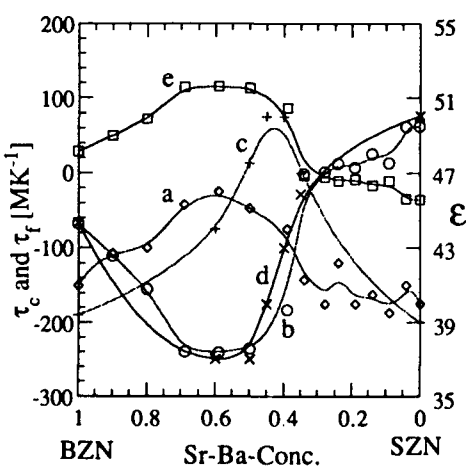


Figure 1 $\tau_c$ (o), $\tau_f$ (□), $\varepsilon$ (◊) (after Onoda et al[1]), $\tau_c$ (×) and $\varepsilon$ (+) as a function of Ba-Sr-concentration.

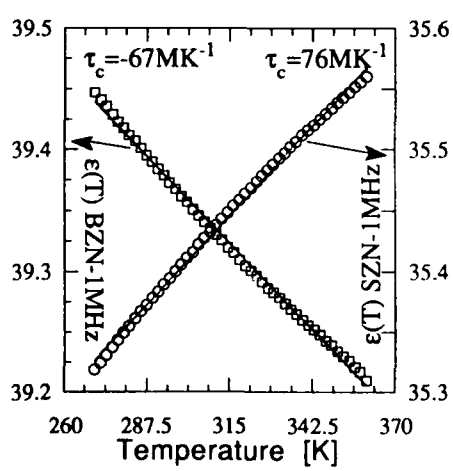


Figure 2 Dielectric constant of BZN (□) and SZN(o) as a function of temperature.

Barium and strontium based complex perovskites show positive and negative $\tau_f$, respectively. Onoda et al[1], in their study of the dielectric properties of BSZN, showed that by substituting Sr for Ba the change of $\tau_f$ was not monotonous and that an anomaly existed at x = 0.5, as shown in Figure 1e. These authors suggested that the anomaly was related to an increase in the degree of order between the $Zn^{2+}$ and $Nb^{5+}$-cations with increasing Sr-concentration. However, a general comparison of the structures of Sr-based

perovskites with those of the equivalent Ba-based compound suggests that an increase in Sr-concentration could also alter the oxygen octahedra framework (tilts of the octahedra). A full description of simple tilt combinations within perovskite-structured compounds has been given by Glazer[2].

The objective of the present study is to relate structural changes, as determined by neutron scattering and TEM, to the dielectric properties. A detailed structural analysis of the BSZN solid solution system is beyond the scope of this paper and will be dealt with elsewhere.

## EXPERIMENTAL METHODS

Pellets of BSZN at compositions x=1.0, 0.6, 0.5, 0.45, 0.4, 0.35, 0.0 were prepared by the 'columbite' route. Particular attention was paid to avoid excessive zinc loss during sintering and all ceramics had densities >97% of the theoretical value.

Dielectric measurements: Standard dielectric measurements were performed on thin ceramic discs (the average capacitance of the pellets was determined to be approximately 50 pF) within a temperature range of 180-400 K and at frequencies varying from 100 Hz up to 1MHz using a temperature controlled chamber and a computer controlled LCR-meter. The temperature coefficient of capacitance ($\tau_c$) was calculated as $1/c(\partial c/\partial T)$. $\tau_c$ is related to $\tau_\varepsilon$ by $\tau_\varepsilon = \tau_c - \alpha$,
where the magnitude of $\alpha$ is considered, for simplicity, to lie between , 9.0-12.0MK$^{-1}$.

Transmission electron microscopy (TEM): Thin foils were prepared by standard techniques using a Gatan ion beam thinner operated under conventional conditions. The foils were investigated using a Philips EM430 and a Philips CM20 TEMs. A Gatan 'hot stage' and a Gatan 'cold stage' were used to examine phase transitions, in situ.

Neutron scattering: Neutron-diffraction measurements on ceramic pellets, x=0.6, 0.5, 0.4 and 0.0, (D=8mm, L=20mm) were performed using the multidetector powder diffractometer DMC at the Saphir reactor (PSI). Spectra were obtained at temperatures 20, 200, 300 and 380 K.

## RESULTS

Figure 2 shows plots of capacitance vs. temperature for BZN and SZN. Figure 1 (curves c+d) shows the dielectric data obtained at room temperature from several compositions of the $Ba_xSr_{1-x}(Zn_{1/3}Nb_{2/3})O_3$ solid solution. Both sets of data correlate well with the work

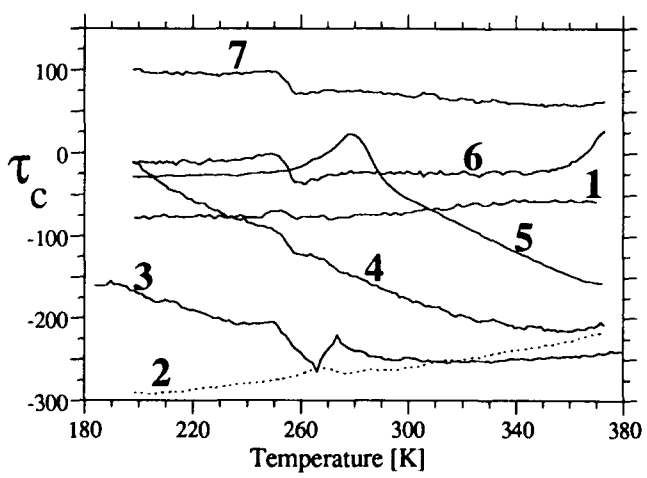


Figure 3 Plots of $\tau_c(T)$ for different Sr-concentrations. Plot (1) corresponds to x=1.0, (2) to x=.60, (3) x=.50, (4) x=.45, (5) x=.40, (6) x=.35 and (7) x=0.0.

previously reported by Onoda et al[1], Figure 1 (curves a+b). However, the flat, almost horizontal, curve which is normally expected for $\tau_c(T)$ does not occur over the temperature range, 180 -

380K, for all samples and, consequently, a simple average value of $\tau_c$ at room temperature can not be used. Figures 3 and 10 are plots of $\tau_c(T)$ and $\tau_c(x,T)$, respectively. At x=0.4 and T≈280K an anomaly was observed in $\tau_c$. Other anomalies and changes of gradient which are less prominent can also be observed.

Figures 4a-d are electron diffraction patterns from grains in BSZN ceramics, x=1.0,0.6,0.4 and 1.0, which have been obtained with the electron beam parallel to a <110> direction of the aristotype perovskite lattice. The most intense maxima can be indexed according to the perovskite-structure, 0.40nm. However, there are two types of superlattices present in all the patterns which can not be indexed using this structure, i.e.: reflections which lie at the {h+1/2,k+1/2,l+1/2}, {h+1/3,k+1/3,l+1/3}*. The {h+1/3,k+1/3,l+1/3} reflections can be explained as arising from the stoichiometric (2:1) ordering between the $Nb^{5+}$ and $Zn^{2+}$-cations.

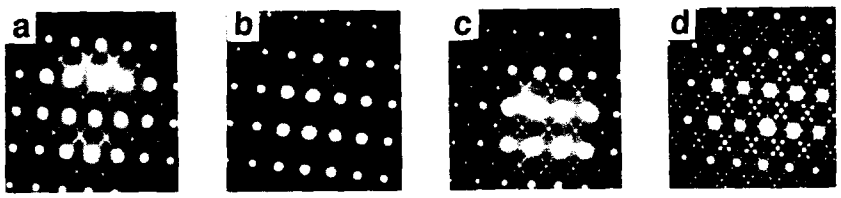


Figures 4a-d Electron diffraction patterns with the beam parallel to a <110>. The patterns are recorded at different compositions: (a) x=1.0, (b) x=0.6, (c) x=0.4 and (d) x=0.0.

This gives rise to a hexagonal structure whose c-axis lies along the <111> directions. In BZN (x=1, Figure 4a) the {h+1/3,k+1/3,l+1/3} reflections are weak and diffuse but they increase in intensity and become more discrete as the Sr-concentration is increased. This can be interpreted as an increase in the degree of B-site order, Figures 4b-d. The {h+1/2,k+1/2,l+1/2} reflections are more difficult to explain because these maxima lie in the positions associated with either anti-phase tilts (Glazer[2]) or non-stoichiometric (1:1) order (Hilton[3]).

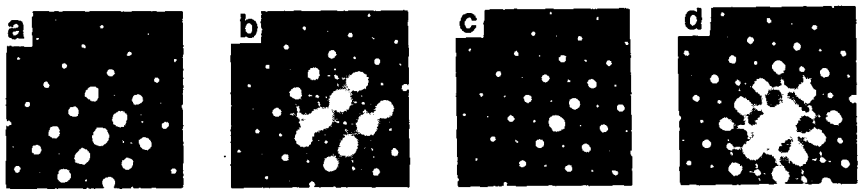


Figures 5a-d Electron diffraction patterns with the beam parallel to a <110> recorded at (a) 350K, (b) 270K, (c) 240K and (d) 90K.

At x=0.4, Figure 4c, the {h+1/3,k+1/3,l+1/3} and {h+1/2,k+1/2,l+1/2} reflections become more discrete and intense. Cooling the specimen from 330K to 93K using a liquid nitrogen cold-stage showed a dramatic increase in the intensities of the {h+1/2,k+1/2,l+1/2} compared to the {h+1/3,k+1/3,l+1/3} reflections, as shown in Figures 5a-d, which suggests that these reflections have arisen from the anti-phase tilting of oxygen octahedra. In SZN (x=0.0, Figure 4d), the {h+1/3,k+1/3,l+1/3} and {h+1/2,k+1/2,l+1/2} reflections have become even more intense and further weaker

* {h+1/3,k+1/3,l+1/3} are used to denote the ordered reflections. However, the ordered reflections are also of the type: {h+1/3,l+1/3,k+2/3}, {h+1/3,k+2/3,l+2/3} and {h+2/3,k+2/3,l+2/3}. This principle equally applies to doubly diffracted reflections. Unless stated otherwise the reflections are indexed with respect to the aristotype perovskite-structured lattice.

superlattice reflections can be observed at {h+1/6,k+1/6,l+1/6}, {h+1/3,k+1/3,0} and {h+1/3,0,0} positions. It seems likely that these reflections can be attributed to double diffraction because simple additive routes exist, e.g.: {h+1/2,k+1/2,l+1/2} - {h+1/3,k+1/3,l+1/3} = {h+1/6,k+1/6,l+1/6} and {h+2/3,k+2/3,l+1/3} - {h+1/3,k+1/3,l+1/3} = {h+1/3,k+1/3,0}.

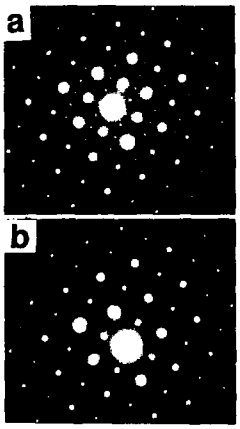


Figures 6 a and b Electron diffraction patterns obtained with the electron beam parallel to a <001> direction and recorded at (a) 450K and (b) 490K.

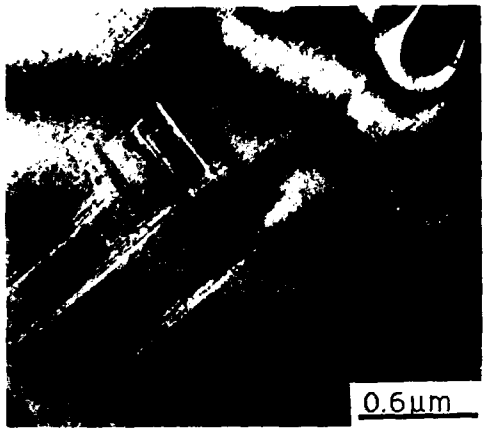


Figure 7 Dark field image obtained using a {hk0} reflection which shows domains that have formed at 280K.

Figures 6a and b are electron diffraction patterns obtained from a grain in a SZN ceramic and which were recorded at (a) 450K and (b) 490K using a hot stage. In each case, the electron beam is parallel to the same <001> direction and the most intense spots can be indexed according to the perovskite-structure, a = 0.40nm.

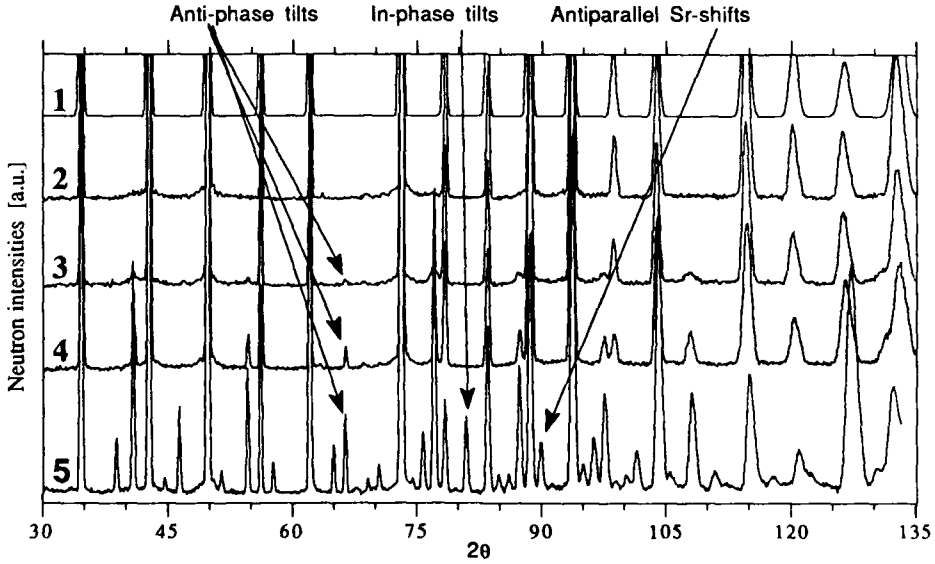


Figure 8 Neutron scattering intensities for BZN (1), SZN (5) and x=0.6, 0.5 and 0.4 plots (2), (3) and (4) respectively (with normalized 2θ-values).

However, in Figure 6a, strong superlattice reflections are present at the {h+1/2,k+1/2,0} positions and weak spots at the {h+1/2,0,0} whereas they are not present in Figure 6b. The disappearance of these reflections was found to occur simultaneously at approximately 470K.

Figure 7 is a dark field TEM image of a BSZN ceramic (x=0.4) obtained using a {hk0} reflection and which was recorded at approximately 90K. The figure shows distinct domains which formed rapidly over a narrow temperature interval at approximately 280K. The phase transition was not associated with any discernible unit cell doubling unlike other transitions observed within this solid solution. Similar domains can be observed in SZN at room temperature but these were not observed to disappear even at 750K.

Figure 8 shows the neutron scans at 20K for x=1.0,.6,.5,.4 and 0.0 (SZN). The scan for BZN is a neutron scattering simulation using the aristotype perovskite-structured lattice. It can be seen that by increasing Sr-concentration several superlattice peaks appear. By following the basic rules of diffraction and taking advantage of the work of Glazer[2], three types of peaks can be recognized which correspond to: "in-phase" tilting of the anion octahedra around <001> axes, "anti-phase" tilting of the same and "anti-parallel" cationic (Sr) displacements along the <110> directions, doubling the d-spacing along the [001] directions. The superlattice peaks given by the chemical order are clearly not present in these scans since neutrons can not distinguish easily the difference in scattering factor between Zn and Nb-cations.

## DISCUSSION

Using the information described in the results section, an approximate structural phase diagram of the BSZN system can be produced, Figure 9. The phase diagram can be separated into three main regions:

1) Ba-rich ceramics (x>0.6), which have the aristotype perovskite structure (disordered and no tilts).

2) The central region (0.2<x<0.6), where at high temperatures the aristotype structure exists (or hexagonal, if ordered) and where at lower temperatures the anion octahedra are tilted in anti-phase

3) Sr-rich ceramics (x<0.2) which at very high temperature (possibly above 1100K) should have the aristotype structure (or hexagonal, if ordered), at lower temperatures have

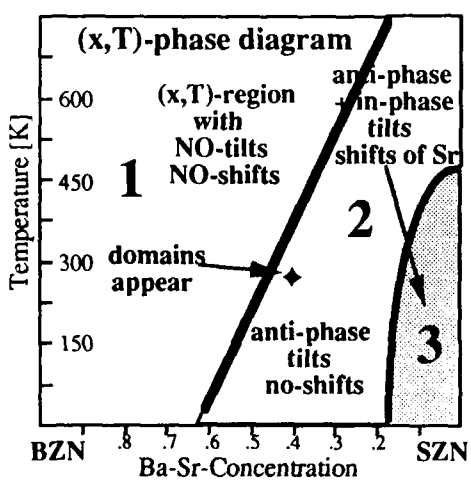


Figure 9 Phase diagram of the $Ba_xSr_{1-x}(Zn_{1/3}Nb_{2/3})O_3$ system.

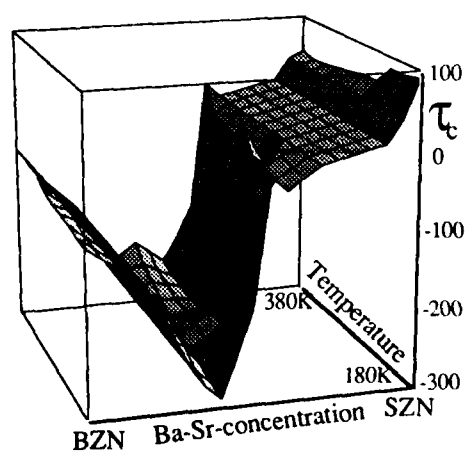


Figure 10 $\tau_c$ as a function of Sr-concentration and temperature.

first an anti-phase tilt that 'freezes-in' and at approximately 470K (depending on the exact Ba-concentration) have an in-phase tilt coupled with an anti-parallel Sr-displacement.

Since the degree of order seems to have an insignificant effect on the magnitude of $\tau_c$ it can be suggested that the tilts of the O-octahedra framework dominate. A comparison of Figure 10 with the phase diagram, Figure 9, should give a reasonable explanation of the changes in $\tau_c$ in terms of the structural changes. The most obvious correlation between the two diagrams within the common temperature interval, is the existence of a strongly negative $\tau_c$ in the untitled region of the phase diagram (region 1) and the presence of a positive $\tau_c$ in the tilted region (regions 2+3). The previously reported anomaly in $\tau_c$, that has been confirmed in this study, takes place in the region where the first anti-phase tilt begins to appear (x=0.6). The increase in $\tau_c$ (from -250ppm to nearly 0ppm) is dramatic but the change in composition is small ($\Delta x$=0.1) and it reverses the obvious trend of decreasing $\tau_c$ with increasing Sr-concentration (region 1).

In Figure 3 the plots of $\tau_c$ for x=0.40 and 0.45 show the most pronounced gradients which belong to the region where the regime changes from the untitled (high temperature) to the tilted (low temperature) structure. However, the strongest anomaly observed at T=280K for x=0.40 (Figure 3) can not be simply related to occurrence of the tilts. In this compound, the transition to the tilted structure was detected at approximately 350K which is far above the temperature of the anomaly. The onset of the tilt is associated with only a gentle rise in $\tau_c$. Nevertheless, as explained previously, in situ experiments in the TEM have discovered the formation of domains at 280K, Figure 7, which could account for the further change in $\tau_c$. More experimental data are needed if the domains and their relationship to $\tau_c$ and to the tilted O-octahedra framework are to be fully explained.

## CONCLUSIONS

The investigation of the dielectric properties and of the structural changes in the BZN-SZN system has shown a correlation between the magnitude of $\tau_c$ and the structure of the oxygen network (tilted-untilted). In order to fully explain the results, more precise information about the type of octahedra tilts and the structure is needed.

## ACKNOWLEDGMENTS

This work was supported by the Swiss National Foundation for Research. The authors would like to thank Dr. P. Fischer, Laboratory for neutron scattering, ETH-Zürich (CH) for his valuable help in the neutron scattering experiments.

## REFERENCES

1. M.Onoda, J.Kuwata, K.Kaneta, K.Toyama and S.Nomura, J.J.A.P. 21, 1707 (1982).
2. A.M.Glazer, Acta Cryst. A31, 756 (1975).
3. A.D.Hilton, Ph.D. Thesis, University of Essex, (1990).

*Ferroelectrics*, 1992, Vol. 133, pp. 223–228
Reprints available directly from the publisher
Photocopying permitted by license only

© 1992 Gordon and Breach Science Publishers S.A.
Printed in the United States of America

# DoP234

## DOMAIN WALL TRAPPING AS A RESULT OF INTERNAL BIAS FIELDS

U. ROBELS, L. SCHNEIDER-STÖRMANN AND G.ARLT
Institut für Werkstoffe der Elektrotechnik, Aachen University of Technology, W-5100 Aachen, Germany

Abstract A model is proposed, which explains quantitatively the aging of material properties as domain wall clamping by orienting defects. The model is examined by aging measurements.

## INTRODUCTION

In acceptor doped $BaTiO_3$ (BT) and PZT ceramics simultaneous with the aging of the small signal material properties an increasing shift of the hysteresis loop on the field axis occurs. The shift of the hysteresis, called internal bias field $E_i$, is caused by the relaxation of defect dipoles consisting of acceptor ions and oxygen vacancies [1]. The relaxation toward equilibrium needs in most cases days, weeks or even longer. Both the aging of small signal material properties and the buildup of the internal bias field are closely related [2].

The aging behaviour of the material properties is attributed to domain wall (DW) effects by many authors [3, 4]. A theory, however, about the physics of aging mechanism is still missing. In this paper we discuss a quantitative model that explains the decrease of DW contributions to the material properties as a result of DW trapping. The trapping is caused by the orientation of defect dipoles.

## MEASUREMENTS

The aging measurements were performed on acceptor doped BT and PZT ceramics with the following compositions:

| | |
|---|---|
| P(Ca)ZT-y | $Pb_{0.92}Ca_{0.08}(Zr_yTi_{1-y})_{0.985}Fe_{0.015}O_3$ |
| BT-X-y | $Ba(Ti_{1-y}X_y)O_3$ with X = Al, Cr, Ni |

The ceramics were prepared by the mixed oxide method and conventional sintering technics. Before the aging measurement has been started the specimen were thermally deaged at a temperature above their curie temperature and poled after cooling down to the appropriate aging temperature. The complex dielectric constant $\underline{\varepsilon}$ is measured with a impedance analyzer and the internal bias $E_i$ is determined from the current loop obtained by applying a triangular ac field to the sample.

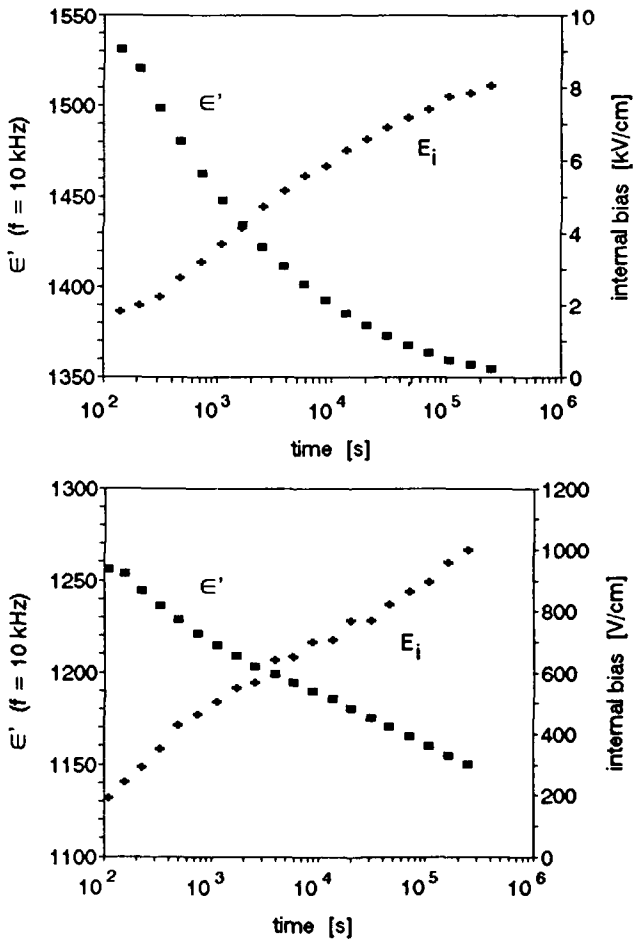


FIGURE 1: Simultaneous measurement of $\varepsilon'(t)$ and $E_i(t)$ of P(Ca)ZT-54 at 80°C (top) and of BT-Al-0.8 at 50°C (bottom)

In Fig. 1 representative measurement results of $E_i(t)$ and $\varepsilon'(t)$ for Fe doped PZT and Al doped BT ceramics are shown. Whereas for Fe doped PZT both the properties show a saturation of their aging behaviour in the final time of measurement, for Al doped BT the

internal bias and the decrease of $\varepsilon'$ do not saturate within the corresponding time period. For many – not for all – of the ceramics investigated the aging of both properties proceeds with similar logarithmic time laws. For the imaginary part $\varepsilon''(t)$ the same relation to the internal bias during aging is observed.

## CLAMPING MODEL

During aging many defect dipoles will align parallel to the spontaneous polarization $\vec{P_0}$ inside the domains (Fig. 2). The alignment takes place by diffusion of the oxygen vacancies within the lattice cell [1].

Due to the alignment the free energy of the domains is lowered by $\Delta W$ per oriented dipole. An internal bias field

$$E_{i0} = \Delta n \cdot \frac{\Delta W}{P_0}$$

is built up by this alignment if $\Delta n$ dipoles are oriented. In the following equations the observable internal bias field is used instead of the oriented defects $\Delta n$, which can not be measured directly.

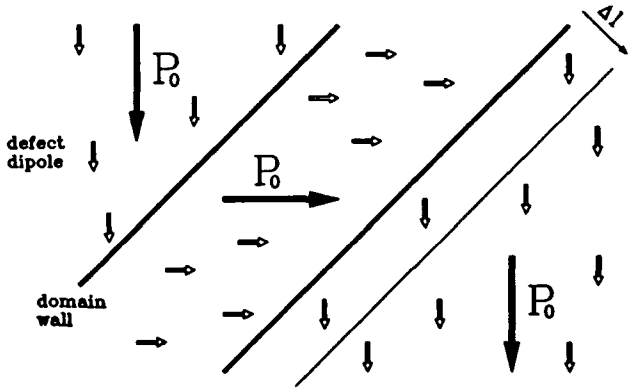


Figure 2: Model of the clamped DW

When a 90° DW is displaced by the length $\Delta l$ in the volume $\Delta V = A \cdot \Delta l$ ($A$ is the domain wall area) the energy of all defects which were oriented by the former polarization is increased until the defects slowly reorient. The increase of the free energy by the displacement of the domain wall thus is $\Delta G = P_0 \cdot E_{i0} \cdot \Delta V$.

The domain wall thus is trapped in a potential discontinuity $P_0 \cdot A \cdot E_{i0} \cdot |\Delta l|$. Therefore in addition to the normal spring force $k \cdot \Delta l$ acting on the elongated DW a clamping force

from both sides

$$F_{cl} = -\frac{\partial \Delta W}{\partial \Delta l} = \begin{cases} -\frac{P_0 \cdot A}{p_r} \cdot E_i & : \quad \Delta l \geq 0 \\ \frac{P_0 \cdot A}{p_r} \cdot E_i & : \quad \Delta l < 0 \end{cases}$$

is effective on the wall in order to restore its aged position. Here $E_i = E_{i0} \cdot p_r$ is the macroscopic internal bias field. The poling parameter $p_r = P_r / P_0$ depends on the remanent polarization $P_r$ of the ceramic [5].

In this model the clamping force $F$ changes its orientation abruptly at $\Delta l = 0$. The DW, however, has a finite width. Therefore we suppose a linear transition (Fig. 3) of the clamping force within the width $a$ of the wall (i.e. a parabolic trap for the wall):

$$\frac{F(t)}{A} = -\frac{2 \cdot P_0 \cdot E_i(t)}{a \cdot p_r} \cdot \Delta l = k_{cl}(t) \cdot \Delta l \qquad \text{for} \quad |\Delta l| \leq \frac{a}{2}$$

By introducing this transition we get an additional force constant $k_{cl}(t)$ by the clamping of the oriented dipoles. The DW contributions to the dielectric constant without an internal bias is derived in other papers [5, 6, 8]:

$$\varepsilon_D = \frac{P_0^2 \cdot f_\epsilon}{\varepsilon_0 \cdot kd}$$

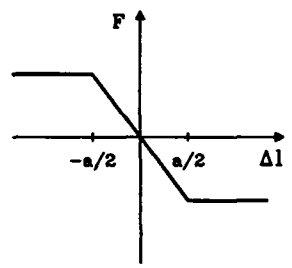


Figure 3: Force profile at the DW

Here $d$ is the domain width and the coefficient $f_\epsilon$ is dependent on the poling parameter $p_r$ [5].

As mentioned above the restoring force $F/A = k \cdot \Delta l$ is increased by the clamping force during aging, leading to

$$\varepsilon_D = \frac{P_0^2 \cdot f_\epsilon}{\varepsilon_0 \cdot d \cdot (k + \frac{2 \cdot P_0 \cdot E_i}{p_r \cdot a})} \qquad (1)$$

With increasing internal bias $E_i(t)$ the effective force constant increases too, leading to a decrease of the DW contributions to the material properties.

## EXAMINATION OF THE MODEL

If the DW contribution $\varepsilon_D$ and the internal bias $E_i$ are known from measurement, the clamping model can be examined by plotting $\frac{1}{\varepsilon_D}$ versus $E_i$. From (1) it is obvious that a straight line should be obtained. The DW mobility $\gamma = \frac{1}{kd}$ of the DWs before trapping

and the DW width $a$ can be calculated from the intersection point and the slope of that line.

The dielectric constant obtained from the aging measurements, however, consist of both the DW contribution and the intrinsic contributions: $\varepsilon_D = \varepsilon_{int} + \varepsilon_D$. From aging measurements [7, 9] and from calculations [6] we estimated the DW contributions $\varepsilon_D$ shown in table I.

In Fig. 4 the $\frac{1}{\varepsilon_D}$ versus $E_i$ plots for Al doped BT and Fe doped tetragonal PZT ceramics are shown. The experimental data can be described by a straight line in a good approximation. In table I the DW mobility $\gamma$ before aging and the DW width $a$ obtained from the lines in Fig. 4 are shown. The $\gamma$ values as expected agree with model calculations [6]. The DW width is expected to be some 10 lattice constants which is confirmed by the results.

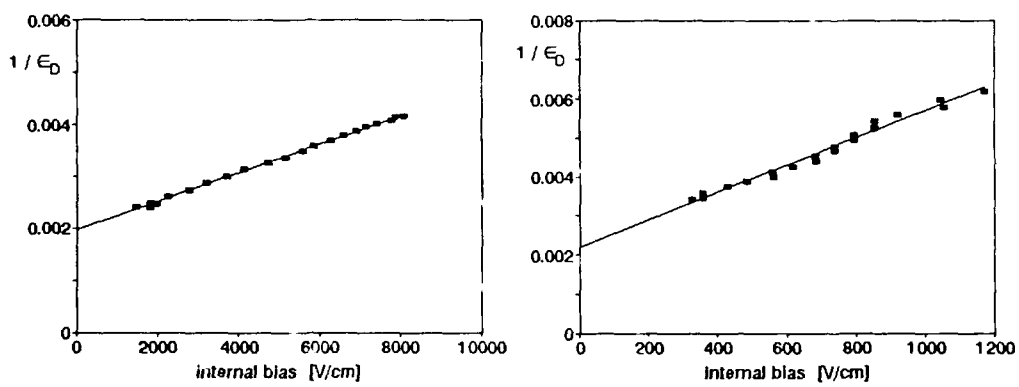


FIGURE 4: $\frac{1}{\varepsilon_D}$ versus $E_i$ measured on P(Ca)ZT-54 at 80°C (left) and on BT-Al-0.8 at 70°C (right) at f = 10 kHz

TABLE I Experimental data for some ceramics

| sample | T (°C) | $\varepsilon_{int}$ | $\varepsilon_D$ ($t = 0$) | $\gamma$ ($10^{-8}\frac{m^2}{N}$) | $a$ (Å) | $d$ ($\mu m$) |
|---|---|---|---|---|---|---|
| P(Ca)ZT-54 | 80 | 1080 | 470 | 2.1 | 121 | 0.2 |
| BT-Al-0.8 | 70 | 930 | 300 | 10.0 | 59 | 0.7 |

## DISCUSSION

In acceptor doped BT and PZT ceramics the observed aging of the dielectric constant are caused mainly by DW trapping due to the orientation of defects in time.

The proposed trapping model predicts that the reciprocal domain wall contribution $\frac{1}{\varepsilon_D}$ is proportional to the internal bias $E_i$, which is confirmed for all ceramics investigated. The model allows to determine the DW width $a$ by measurements of internal bias and aging. The obtained $a$ values confirms the model.

The trapping model describes only one aging process which is predominate in acceptor doped ceramics. The aging measurement pointed out that there are still other aging phenomena particular in the initial time of aging.

## References

[1] G. Arlt and H. Neumann, Ferroelectrics, 76, 451 (1987)
[2] U. Robels, R. Lohkämper and G.Arlt, ISAF 90, Urbana / Champaign (1990)
[3] K.W. Plessner, Proc. Phys. Soc., B 69, 1261 (1956)
[4] S. Ikagami and I. Veda, J. Phys. Soc. Jap., 22, 725 (1967)
[5] G. Arlt, H. Dederichs and R. Herbiet, Ferrolectrics, 74, 37 (1987)
[6] G. Arlt and N.A. Pertsev, J. Appl. Phys., 70, 2283 (1991)
[7] H. Dederichs and G. Arlt, Ferroelectrics, 68, 281 (1986)
[8] V.I. Aleshin, Sov. Phys. Tech. Phys., 35, 107 (1990)
[9] W.Y. Pan, Q.Y. Jiang and L.E. Cross, Ferroelectrics, 82, 111 (1988)

*Ferroelectrics*, 1992, Vol. 133, pp. 229–234
Reprints available directly from the publisher
Photocopying permitted by license only
© 1992 Gordon and Breach Science Publishers S.A.
Printed in the United States of America

# MsP145

## ANOMALOUS TWIN STRUCTURES IN FERROIC CRYSTALS

IVAN SHMYT'KO, IGOR BDIKIN, NATASHA AFONIKOVA
Solid State Physics Institute, 142432, Chernogolovka, Moscow district, RUSSIA

Abstract Anomalous twin characteristics in ferroelectrics $BaTiO_3$ and $KH_2PO_4$, ferroelastics $ReBa_2Cu_3O_{7-x}$ and $Bi_2Sr_2CaCu_2O_{8+x}$ crystal are observed.

## INTRODUCTION

Ferroic crystals below the phase transition to structure of lower symmetry are as a rule divided into twins. In accordance with the Curie Law the twins are interconnected maintaining the macrosymmetry of the sample. If the planes of symmetry perish after such transition, the twins are connected along the planes, which are the mirror planes to the neighboring twins. It is believed that no distortion of the contacting cells occurs in this case. However, it is easy to show that in this case very often in real structures individual atoms can collide with some other near to the twin plane. It has to give rise to anomalous twin boundaries.

We have investigated this problem for classical ferroelectrics $BaTiO_3$ [1] and $KH_2PO_4$ [2] and pure ferroelastics $ReBa_2Cu_3O_7$ [3] and have shown that the twin boundaries in these crystals can realize as a intermediate regions along which the crystallographic parameters of one twin orientation continuously and smoothly transfer to the parameters of the other twin orientation. To confirm this statement we show the rocking curve for X-ray diffraction from (100) planes paralleled to twin boundaries of $KH_2PO_4$, see Figure 1, and selected part of electron microdiffraction pattern with (hk0) spots (twin planes are

parallel to (110)) for $GdBa_2Cu_3O_7$ crystals, see Figure 2.

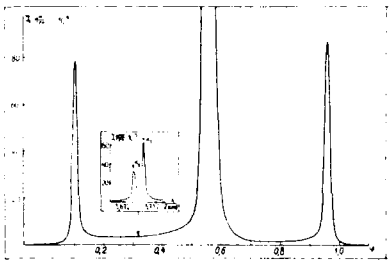

FIGURE 1

FIGURE 2

On the first figure the twin boundaries look as continuous orientations (high level continuous background ) connecting the separate twin orientations. The twin boundaries on Figure 2 are represented as diffuse lines connecting the separate twinned spots.

There are also some other anomalous exhibitions of the twin structures in the real crystals which have rather methodical character rather than physical one. In particular, if the angles of the miss-orientations of the twins are very small then we can't resolve the twinned picks in the diffraction curve and hence assume that the crystal is twin-free. In this case there is a problem of determination of correct structure, too. The same problems emerge for the polar structures if the polarity effect is not pronounced. We show the examples of such cases on the $Bi_2Sr_2CaCu_2O_{8+x}$ and $EuBa_2Cu_3O_{6+x}$ crystals in what follows.

## TWINS IN $Bi_2Sr_2CaCu_2O_{8+x}$ CRYSTALS

Up to now it has been believed that the 2212-Bi crystals have the orthorhombic cell ("a"≈"b"≈5,4 Å, "c"=30.76 Å) and no twins. However, our precision investigations below show that these crystals are in fact divided into twins but they are invisible in the main lattice because of very small twinning angles. They are visible in the superreflection

lattice only.

Indeed, in accordance with the modern representations[4] the $Bi_2Sr_2CaCu_2O_{8+x}$ crystals have the incommensurate modulated state with the wave vector $\underline{k}=\underline{c}^*+0.217\underline{b}^*$. Such modulations produce the additional reflections in reciprocal lattice which are placed in $\underline{c}^*$-$\underline{b}^*$ planes. Figure 3a shows the

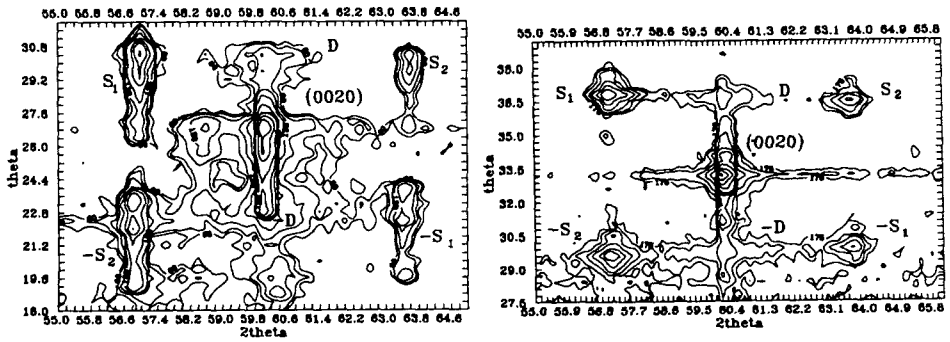


FIGURE 3

distribution of the diffracted X-rays around (0020) reflection and the satellite reflections for upper mentioned modulation ($S_1$) of one of the samples (№1). The positions of the reflections are tabulated.

TABLE I Characteristics of the reflections

| sample (№) | reflections (hkl) | halfwidth (grad.) | $(2\theta_{S_1}-2\theta_{-S_2})$ |
|---|---|---|---|
| 1 | (0020) | $0.32^o$ | |
| | $S_1$ | $0.32^o$ | $0.2^o$ |
| | $-S_2$ | $0.33^o$ | |
| 2 | (0020) | $0.32^o$ | |
| | $S_1$ | $0.54^o$ | $0.05^o$ |
| | $-S_2$ | $0.52^o$ | |

The lengths of the vectors of modulations in $S_1(-S_1)$ and $S_2(-S_2)$ directions are seen to be different. But it is impossible for the orthorhombic cell because of two mirror planes which coincide with a-c, b-c and a-b planes of the direct lattice. Hence, we can conclude that 2212-Bi crystals are not orthorhombic. We can propose that they are monoclinic at least. If this is the case, we can expect to see twins in these crystals. In the structure experiments they have to show up in splitting of the satellite reflections to a few components or in their broadening if the distances between components are less than the halfwidth of the satellites. In this case the lengths of the wave vectors $S_i$ with respect to Bragg reflection have to be equal. Such situation is more common, see Figure 3b and the table (sample №2). It is interesting that the halfwidths of the (0020) reflection for both samples are equal and are smaller than for satellites of the second sample. No anomalous behavior was seen on the other Bragg reflections, either. It means that this is case of the twinned crystal with very small twinning angle and only the structure modulations are sensitive to distortion of the orthorhombic symmetry.

## ANTIPHASE TWINS IN $EuBa_2Cu_3O_{7-x}$ CRYSTALS

The second example of anomalous delay of the twins in the real crystals is the case of antiphase twins in the polar structures. Really, in accordance with the X-ray scattering theory the structure factor F(hkl)=F(-h-k-l) if the wave length ($\lambda_{K_\alpha}$) of the radiation used is far from resonance frequency ($\nu_R$) of the constituting atoms of the sample. In the case when they are close to each other F(hkl) ≠ F(-h-k-l) for polar structures and hence I(hkl)≠I(-h-k-l) if the crystal is not divided into small antiphase domains. In the opposite case I=(I(hkl)+I(-h-k-l))/2 and hence the polar properties will be invisible, too. The same picture will be observed if the polarity of the structure is weakly

expressed. In general case the determination of the polarity and observation of the antiphase domains is a very difficult task. Below we give the results of an investigation of the polar properties in 1-2-3-$O_x$ compounds which are believed to be centrosymmetric.

For the investigation we have used the anomalous transmission X-ray method (Borrmann effect). The investigated $EuBa_2Cu_3O_{7-x}$ crystals had the thickness of about 100 $\mu$m ($\mu t \sim 10$). The X-ray pattern of the sample in the primary beams is shown in Figure 4. The bright field is the image of the

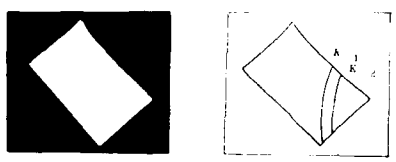

FIGURE 4

sample after absorption of the X-rays ($I=I_o\exp(-\mu t)\approx 2.7^{-10}$). The double curved lines are the image of zero diffracted beams of $K_{\alpha_1}$ and $K_{\alpha_2}$ radiation (anomalously transmitted beams).

The polarity of the structure and antiphase domains are shown in the X-ray topogramms in Figure 5a,b. The topogramms were obtained in the diffracted beams in Laue geometry. Figure 5a shows the case of (110) reflection. Figure 5b shows

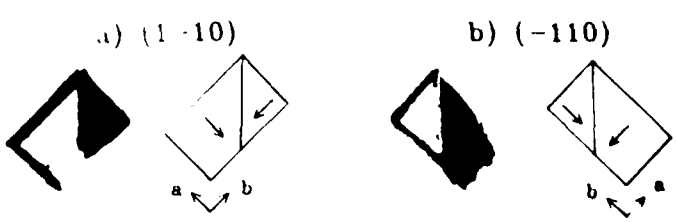


FIGURE 5

the case of (-1-10) reflection which differs from the first case only in the sample rotation by $180^{o}$ as is shown in the neighboring schemes. It is seen that the images consist of two complementary parts: black and white. It is also seen that these parts transfer to each other after the sample rotation (the black lines at the left side of the topogramms are the images of the ends of the sample which are in the Bragg geometry). The change of the contrast of the same sample area with the change of the diffracted planes from (110) to (-1-10) means that $F(hkl) \neq F(-h-k-l)$ and hence the crystal has the polar structure. The division of the images into two parts of the reversible contrast means that the sample consists of two antiphase domains in which the polarity axes have different directions. The direction of the polarity axes was defined from the change of the image contrast of the (hh0), (h00) and (001) reflections and to be along [100] The domain boundary is parallel to (110) planes.

It is obvious that the observation of the polar property of the $1\text{-}2\text{-}3\text{-}O_{7-x}$ structure became possible due to sensitivity of the anomalous transmission of the X-ray to noncentrosymmetricity of the structure.

## REFERENCES

1. N.Afonikova, V.Shekhtman, I.Shmytko, Sov.Phys.Solid State, 27, 3201 (1985)
2. N.Afonikova, V.Borovikov, I.Shmyt'ko, Sov.Phys.Solid State, 29, 813 (1987)
3. I.Shmyt'ko, V.Shekhtman, Yu.Ossipyan, and N.Afonikova: Ferroelectrics, 97, 151 (1989)
4. J.Q.Li,C.Chen et al Z.Phys. B-Condensed Matter 74, 165 (1989)

# SECTION III
# CONTRIBUTED PAPERS
## IIIb. Transport Phenomena/Switching

*Ferroelectrics*, 1992, Vol. 133, pp. 235–240
Reprints available directly from the publisher
Photocopying permitted by license only

© 1992 Gordon and Breach Science Publishers S.A.
Printed in the United States of America

# TrC10

## ELECTRON EMISSION FROM FERROELECTRICS AND ITS APPLICATIONS

G. ROSENMAN
Department of Electrical Engineering - Physical Electronics,
Faculty of Engineering, Tel-Aviv University, Ramat-Aviv, 69978, Israel.

Abstract Electron emission (FEE) is observed from ferroelectric crystals under diverse external perturbations, such as the pyroelectric and piezoelectric effects, polar axis switching, etc. Observation of FEE due to a small variation of temperature or reversal of the polar axis shows that FEE occurs due to the changes in the dipole moment of the crystal lattice. FEE represents a screening current that flows into the vacuum. It makes it possible to use this effect for novel devices such as IR position sensitive detector, neutron flux imaging as well as ferroelectric cold cathodes with high emission current density.

## INTRODUCTION

The fundamental property of the ferroelectric crystals is that their dipole moment changes under the action of any external perturbation. For monodomain crystals possessing macroscopic polarization such disturbance of the initial charge balance results in generation of uncompensated charge and an electric field. This electrostatic field causes some screening currents. One of these is the internal screening current, which occurs due to the finite conductivity of the ferroelectric-semiconductor[1]. Another one is the conventionally measured pyroelectric or piezoelectric current in an external short-circuit connecting the electrodes applied to the polar surfaces. At a free surface of the polar crystal the third type of the relaxation of depolarizing field has been observed. This is an electron emission current from free ferroelectric crystal surface which represents a screening current into the vacuum[2].

At first, electron emission from ferroelectrics (FEE) was measured in $LiNbO_3$ under the pyroelectric effect[3]. Subsequently it has been studied in detail for a wide range of the pyroactive-crystals both ferroelectrics[4-7] and linear pyroelectrics[8]. FEE has been observed also during piezoelectric[9] and bulk photovoltaic effects[10] as well as under polar axis reversal[11,12].

FEE observation due to a small variation of temperature ($\Delta T \sim 1K$) or under polar axis reversal shows that the electrons can not escape from the crystal surface due to the direct absorption of such insignificant external energy. FEE occurs as a result of changes in the lattice dipole moment under heating (pyroelectric effect), mechanical stress (piezoelectric effect), etc. So far the FEE parameters (current density, energy) and kin-

etic properties are determined by the properties of the polar crystal lattice. This is the main distinguishing feature of the FEE from classical types of electron emission of solids. It opens avenues for designing non-traditional electron emission cathodes and devices.

In the present paper some applications of this physical phenomenon for fundamental and applied purposes comprising direct conversion of IR radiation to the visible for imaging and neutron position sensitive detectors as well as ferroelectric cold cathodes with high current density are presented.

## FERROELECTRIC ELECTRON EMISSION AND METHODS OF ITS OBSERVATION

Detailed investigations[2-12] have made it possible to define the basic features of FEE. It is a field emission effect. The source of this field is the electrostatic charge arising at the polar crystal surface under the various external perturbations. For FEE generation from real crystals with finite conductivity-$\sigma$ the rate of charge generation $dP_s/dt$ must be higher than the screening rate. The field emission effect occurs at a field intensity of $E \geq 10^6$ $V \cdot cm^{-1}$. The corresponding uncompensated charge density $\Delta P_s$ for a charged plate is $\Delta P_s \geq 10^{-7}$ $C \cdot cm^{-2}$. Ferroelectric crystals are relaxation semiconductors and the screening rate is determined by the Maxwell relaxation time $\tau_m = \epsilon\epsilon_0/\sigma$. Then the main condition for FEE generation may be written as follows:

$$\frac{dP_s}{dt} \geq 10^{-7}\, \tau_m^{-1} \tag{1}$$

This simple equation makes it possible to choose a suitable ferroelectric material and to determine the necessary rate of crystal heating or polar axis switching.

Two kinds of FEE measurements are known. One method is to measure the emission current density by using a secondary electron multiplier[5-8] or by a Faraday cup[12,13]. Another one has been developed in[3,11,14] for obtaining a ferroelectric surface electron image. This system represents ordinary electronoptical convertor. It consists of one or two microchannel plates and a luminescent screen. An optical image may be registered by a TV camera.

## FEE IMAGING OF IR RADIATION

The FEE imaging method has been successfully used for studying of the static domain structure in TGS crystals[15]. The 180°-domains have been distinguished for artificially formed bidomain structure due to the pyroelectric effect. For monodomain crystals uniform heating (or cooling) led to homogeneous FEE imaging. So far FEE read-out techniques allows to watch a visible image of the surface pyroelectric charge distribution which can be used for IR radiation observation.

There are several requirements for the suitable material for a FEE target. In Ref.4 the following expression for the electrostatic field E causing the FEE current has been obtained:

$$E = \frac{\gamma \Delta T}{\epsilon_0} \frac{1}{\epsilon \frac{a}{d} + 1} . \tag{2}$$

In Eq.2 $\gamma$ is the pyroelectric coefficient, $\Delta T$ is the temperature variation, $\epsilon$ is the dielectric permittivity, a is the gap between the target and the microchannel plate, d is the crystal thickness along the polar axis. Then FEE current must be determined by the ratio $\gamma/\epsilon$ and this parameter may be considered as a figure of merit. It should be noted that the voltage responsivity of pyroelectric detectors and targets for pyroelectric vidicon tubes are also proportional to the ratio $\gamma/\epsilon$ and the best performances have been obtained for TGS and $LiTaO_3$ crystals[16]. The second figure of merit may be obtained from Eq.1, which obviously shows the necessity of maximum value of the Maxwell relaxation time $\tau_m$. For TGS and $LiTaO_3$ crystals this parameter is three orders of magnitude more than for such well known pyroactive crystals as $BaTiO_3$ and $Pb_5Ge_3O_{11}$.

An experimental setup consists of a thin ferroelectric target which is mounted closely to the input microchannel plate of the FEE imaging transformer. The IR irradiated front surface of the wafer is covered with an IR absorbing thin film. The rear polar surface is free. Heating the target front surface by an IR beam results in the appearance of a pyroelectric charge pattern on the rear surface and an electron emission into the small gap between the ferroelectric target and the first, input microchannel plate. The electron flux distribution and subsequently a visible image displayed on the luminescent screen reproduces the infrared one.

In our experiments a monodomain target of $LiTaO_3$ crystal (thickness=50 $\mu$m) was irradiated by a $CO_2$ laser beam through a germanium window in a vacuum chamber. Fig.1a,b,c shows three photographs of the emission image which were registered in every 120 msec. After the $CO_2$ laser was switched on (the power density was about 10 $mW \cdot cm^{-2}$) some bright emission spots appeared (Fig.1a) In some tens of milliseconds almost the whole crystal surface was emitting electrons (Fig.1b). Fig.1c illustrates an emission image after switching off the IR beam. The photographs demonstrate temperature changes of the pyroactive crystal surface, namely: Fig.1a shows the profile of IR beam, Fig.1b corresponds to heating of all the crystal plate and Fig.1c illustrates the cooling of the previously irradiated region.

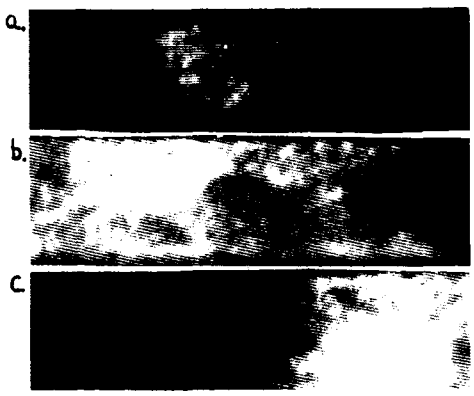


FIGURE 1 FEE imaging of IR radiation ($CO_2$ laser P=10 mW·cm$^{-2}$)

The FEE current responsitivity may be improved by applying of external voltage (of some hundreds of volts) between the front surface and input microchannel plate. As a result a detectivity of 0.1 mW·cm$^{-2}$ was achieved.

## FEE IMAGING OF A NEUTRON BEAM

FEE due to polar axis reversal has been used for studying of the switching process in TGS and $Pb_5Ge_3O_{11}$ crystal[11]. Nucleation of domains and lateral movement of the domain boundaries have been observed in lead germanate. It has been noted that at free TGS surfaces only the nucleation stage occurs. High dielectric viscosity eliminates the domain growth by lateral movement. As a result a homogeneous FEE image during 50 Hz sinusoidal switching of an undoped TGS crystal has been registered. A uniform FEE current from the entire switching surface is also an evidence for the uniform switching field.

At the same time a switching threshold of the domains may be drastically changed by point defects introduced into the ferroelectric crystal matrix. One of the methods of defects formation is the particle irradiation especially by neutrons. An irradiation of ferroelectric crystals leads to the creation of the point defects field. The space distribution of it have to correspond to the density of neutron flux and subsequently may be read out by the FEE techniques. The most attractive medium for such experiments is TGS crystals. On one hand they possess slightly damaged hydrogen bonds[16]. On the other hand TGS crystals are switched by comparatively low voltage and their FEE current may be

registered by the above described method[14,15].

The experimental arrangement comprised of two separate stages recording and read out. The first stage was neutron irradiation. A TGS crystal (area about 10x10 mm) was mounted in a box confining a Cf neutron source. This isotope has a complicated spectrum of the radioactive decay including $\gamma$, slow and fast neutrons. A special screen protecting the TGS crystal from $\gamma$ and slow neutrons were produced. A polar surface has been irradiated by fast neutron flux with a circular spot. The exposure was about $1.1 \cdot 10^{10}$ $n \cdot cm^{-2}$. At the second stage this sample was investigated by the FEE method. The electron emission image of the sample is presented in Fig.2. A dark spot corresponding to the irradiated region is distinctly observed. Apparently the damaged part of the crystal has a damped domain structure which can not be reoriented by applying voltage. The space resolution of the suggested FEE method of neutron imaging is limited by the microchannel plate resolution which is about 40 lines $mm^{-1}$. Fast polar axis reversal producing high FEE current density[12,13] may make it possible to image FEE directly on a luminescent screen. In this case the resolution will be determined only by the domains size of TGS crystal which can be as small as 1 $\mu$m.

FIGURE 2 FEE imaging of a fast neutron beam.

## FEE COLD CATHODES

FEE due to polar axis reversal is the most attractive technique for obtaining high emission current density. The uncompensated charge during switching is $\Delta P_s = 2P_s$ and the emission current density is $10^{-9}$ $A \cdot cm^{-2}$ ($Pb_5Ge_3O_{11}$ crystal[11]) and $10^{-7}$ $A \cdot cm^{-2}$ (TGS crystal[14]) This has been observed under periodical 5OHz switching.

An emission charge was about $10^{-7}$ C·cm$^{-2}$.[14] It has been noted[2] that the total screening charge consists of some components including electron emission charge. In the case of limitation of the other components such as an internal conductive current the emission charge may be dominating. This circumstance has been successfully used first time in[12] and an emission current as large as $10^5$ A·cm$^{-2}$ has been observed under super-fast switching of PLZT ceramic in the subnanosecond range. Consequently this phenomenon has been studied for different compositions of PLZT and PZT in detail[12,13,17-19] and total emission charge about $10^{-5}$ C has been obtained. A very high repetition rate of 2 MHz makes it possible to use FEE cathodes for some important applications.

## CONCLUSIONS

FEE effect possesses some distinguished features which allow to present it as a novel type of electron emission from solids. It makes it possible to develop new devices for imaging of IR beam, corpuscular fluxes as well as cold cathodes.

## ACKNOWLEDGMENT

The author is very grateful to Prof. Y. Shapira for his helpful discussions.
This work was supported by the Israel Ministry of Science & Technology.

## REFERENCES

1. V. Fridkin, Photoferroelectrics, Springer-Verlag, 1979
2. G. Rosenman, Ferroelectrics, **118**, 451 (1991).
3. B. Rosenblum, P. Braunlich, J. Carrico, Appl. Phys. Lett., **25**, 17 (1974).
4. G. Rosenman, M. Tsedrik, I.S. Rez, S. Vasilevsky, Yu. Chepelev, Ferroelectrics, **110**, 113 (1990).
5. K. Biedrzycki, Phys. St. Sol. (a), **117**, 313 (1990).
6. G. Rosenman, V. Pechorskii, Yu. Chepelev, E. Boikova, Phys. St. Sol. (b), **120**, 667 (1983).
7. K. Bredrzycki, R. Poprawski, Solid St. Communication, **73**, 455 (1990).
8. G. Rosenman, Yu. Chepelev, N. Gavrilova, V. Novik, B. Chaianov, Sov. Phys. - Proc. USSR High Education Establishment, Physics, **4**, 114 (1984).
9. G. Rosenman, V. Pechovskii, Sov. Phys.-JTP's Lett., **6**, 1531 (1980).
10. G. Rosenman, Yu. Chepelev, E. Boikova, Ferroelectrics, **100**, 17 (1989).
11. G. Rosenman, V. Okhapkin, Yu. Chepelev, V. Shur, Sov. Phys.-JETP's Lett., **39**, 397 (1984).
12. H. Riege, M. Gundel, E. Wilson, J. Handerek, K. Ziotas, BAPS, **34**, 193 (1989).
13. H. Gundel, J. Handerek, H. Riege, J. Appl. Phys., **69**, 975 (1991).
14. G. Rosenman, O. Malyshkina, Yu. Chepelev, Ferroelectrics, **110**, 99 (1990).
15. G. Rosenman, O. Malyshkina, Yu. Chepelev, Ferroelectrics Lett., **10**, 141 (1989).
16. M. Lines, A. Glass, Principles and Applications of Ferroelectrics and Related Materials, (Clarendon Press, 1977).
17. H. Gundel, J. Handerek, H. Riege, E. Wilson, Ferroelectrics, **110**, 183 (1990).
18. H. Gundel, H. Riege, Appl. Phys. Lett., **56**, 1532 (1990).
19. A. Airapetov, I. Ivanchik, A. Lebedev, N. Tikhonurova Sov. Phys. - Dokl., **35**, 267 (1990).

*Ferroelectrics*, 1992, Vol. 133, pp. 241–246
Reprints available directly from the publisher
Photocopying permitted by license only

© 1992 Gordon and Breach Science Publishers S.A.
Printed in the United States of America

# TrP140

## POLARONIC TRANSPORT IN $LiNbO_3$ AT ELEVATED TEMPERATURES

WOJCIECH BĄK, KRZYSZTOF KRZYWANEK, CZESŁAW KUŚ, WIESŁAW S.PTAK*

Solid State Physics Division, Institute of Physics,
Pedagogical University, Kraków, ul.Podchorążych 2, Poland.

*University for Mining and Metallurgy, Faculty of Materials
Science and Ceramics, Kraków, Al.Mickiewicza 30, Poland.

Abstract The ac electrical response of cleaved undoped $LiNbO_3$ single crystal in very low frequency range (0.001Hz ÷ 0.8Hz) has been analyzed as a function of temperature (300K ÷ 950K) using complex plane analysis techniques. The complex admittance has been used to identify relaxation processes within the crystal. Measurements of the thermoelectric power and dc conductivity have been carried out in the temperature range from 430K to 950K. Obtained results allowed to determine the order of magnitude of charge carrier mobility and their concentration as well as the type and mechanism of electric conduction. Arguments are presented which indicate polaronic transport in $LiNbO_3$ up to about 600K.

## INTRODUCTION

The intrinsic defect structure of lithium niobate[1-3] determines its electric and electro-optic properties, particulary the charge transport at elevated temperatures. In our earlier work[4] we have defined relaxation processes in $LiNbO_3$ with relaxation time of order $10^2$s and we have indicated the role of hopping mechanism in the charge transport.[6-8] The purpose of this paper is to elucidate the transport mechanism phenomena in $LiNbO_3$ utilizing the immitance spectroscopy method together with thermoelectric power measurements.

## EXPERIMENTAL

The investigation was carried out on undoped $LiNbO_3$ single crystal (1.25mm thickness, $51mm^2$ area) with Pt electrodes covered on the cleavage plane[9]. The experiment was made under normal atmospheric conditions at temperature of 300K to 950K. After heating up to 950K the sample was slowly cooled to fixed temperatures of measurement and then held at this temperature for 2h. The temperature of the sample was measured by means of a chromel-alumel thermocouple with 0.1K accuracy. The measurements of immitance with the electric field amplitude 5V/cm and 50V/cm (for temperatures below 500K) in the frequency range 0.001Hz ÷ 0.8Hz were carried out using the equipment described elsewhere.[10] Thermoelectric power measurements have been made using conventional automatic devices.[7]

## RESULTS AND DISCUSSION

As discussed earlier,[4] the impedance response of the sample for temperatures below 550K indicate the presence of relaxation processes and their thermally activated character. The ac electrical response in the admittance plane is shown in the Figure 1a. The shape of the plots in this temperature range (300K ÷ 550K) confirms existence of the strong conductance dispersion. It has been found that the time constant of the equivalent circuit corresponding to these plots, is of order $10^2$s which may be attributed to the presence of low-mobility charge carriers. The plot in Figure 1d reveals likewise the conductance dispersion for temperatures above 830K which may be interpreted as the effect of the ionic mechanism of charge transport. The relaxation time estimated from B(G) plot is of order $10^3$s - $10^4$s and correspondes to ionic space charge polarization. Figure 1b,c shows the admittance plots in the middle temperature range (550K ÷ 770K). These plots show negligible conductance dispersion which indicates another mechanism of the transport in this range. The temperature dependence of Seebeck coefficient shows the three characteristic ranges consistent with character of admittance plot (Figure 2). The course of coth (1/T) (dotted line) in

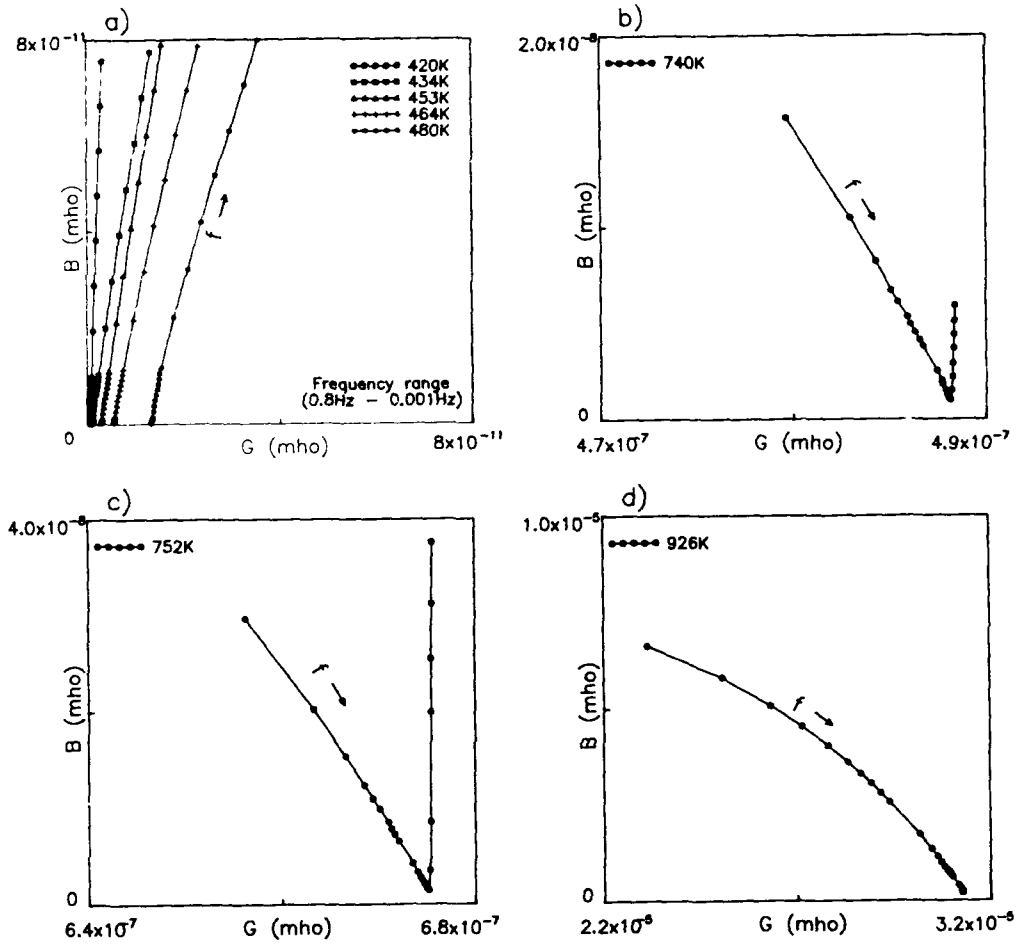


FIGURE 1a,b The complex admittance plots for different temperatures. Arrows in the plots represent the direction of increasing frequency (f).

the lower temperature region (430K ÷ 590K) is in very good agreement with the experimental points. On the basis of the fit of experimental data $\alpha(T)$ to the Eq.(1)[5] the parameters $\gamma$ (electron - phonon coupling constant) and $\hbar\omega_0$ as well as activation energy $E_n$ have been obtained (see Table I).

$$\alpha = \frac{3}{2}\frac{k}{e}\gamma\left(\coth\left(\frac{1}{2}\beta\hbar\omega_0\right) - 1\right) \qquad (1)$$

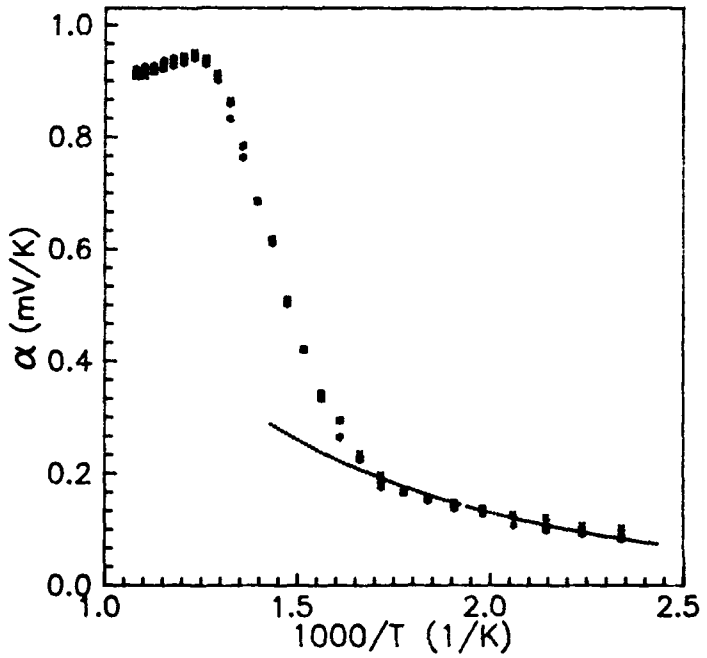


FIGURE 2 Arrhenius plot of the Seebeck coefficient.

TABLE I Carrier mobility $\mu$ and carrier concentration n, calculated from experimental data of Seebeck coefficient $\alpha$ and elctrical conductivity $\sigma$ for two choosen temperatures. ( $\gamma$ = 5.01, $h\nu_0$ = 0.102 eV at T = 570 K )

| T<br>K | $\alpha$<br>mV/K | n<br>$cm^{-3}$ | $\sigma$<br>S/m | $\mu$<br>$cm^2/Vs$ | $E_n$<br>eV | $E_\sigma$<br>eV |
|---|---|---|---|---|---|---|
| 570 | 0.17 | $3.81 \times 10^{12}$ | $5.01 \times 10^{-8}$ | $3.71 \times 10^{-2}$ | 0.81 | 1.24 |
| 670 | 0.93 | $1.62 \times 10^{17}$ | $4.87 \times 10^{-5}$ | $1.87 \times 10^{-1}$ | 1.83 | 1.24 |

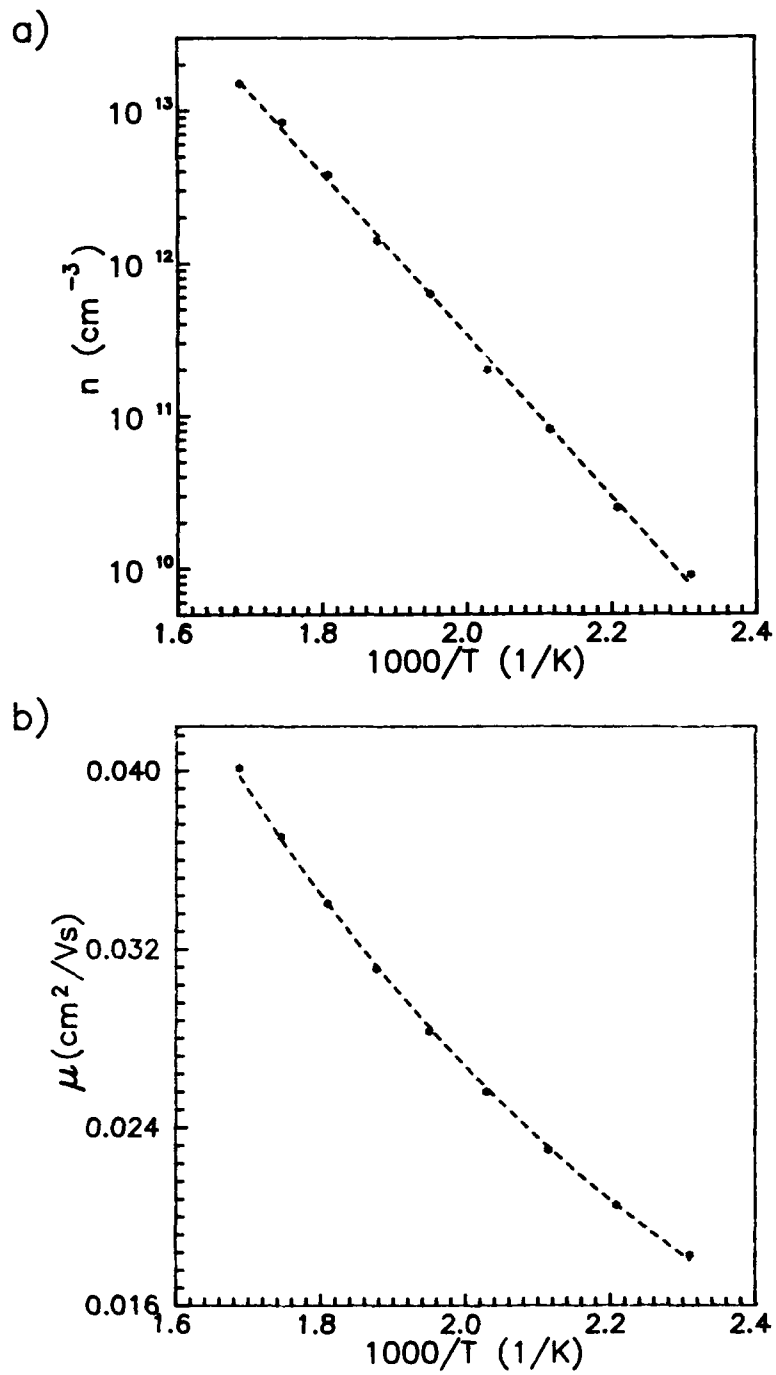


FIGURE 3a,b Carrier concentration (a) and their mobility (b).

The temperature dependence of charge carrier concentration is shown in the Figure 3a. It is necessary to note that this relationship has an activation character with $E_n = 0.81$eV (dashed line mean the best fit to $\exp(-E_n/kT)$ ). Moreover, the activation energy $E_n$ (i.e. the energy required for production of conduction electrons) smaller than $E_\sigma$ (activation energy obtained from the temperature dependence of conductivity) prove the large electron - phonon coupling. The small value of mobility $\mu \approx 10^{-2}$ $cm^2/Vs$ as well as the activation character of the temperature dependence of mobility (Figure 3b) together with earlier mentioned facts allows to explain the electric transport mechanism below about 590K by the polaronic transport mechanism. At the highest temperature range (above 830K), the mentioned conductance dispersion correspondes the flatted part of the Arrhenius plot $\alpha(1/T)$ for which the observed value of mobillity is typical for ionic conductivity ($\mu > 1$ $cm^2/Vs$). The middle temperature range (600K ÷ 770K) may be attributed to the band transport mechanism.

## REFERENCES


1. H.Donnerberg, S.M.Tomlinson, C.R.A.Catlow, O.F.Schirmer, Physical Review B, 40, 11909 (1989)
2. W.Bollmann, M.Gernand, Phys. Stat. Sol. (a), 9, 301 (1972)
3. W.Bollmann, Phys. Stat. Sol. (a), 40, 83 (1977)
4. W.Bąk, C.Kuś, W.S.Ptak, W.Śmiga, Ferroelectrics, 126, 179 (1992)
5. K.Krzywanek, C.Kuś, W.S.Ptak, W.Śmiga, Ferroelectrics, 126, 173 (1992)
6. H.Bötger and V.Bryksin, Hopping Conduction in Solids, (Akademie Verlag, Berlin, 1985)
7. C.Kuś, W.Śmiga, K.Krzywanek, Ferroelektrizitat, Halle (1988)
8. T.Holstein, Annales of Physics, 18, 42 (1959)
9. I.P.Kaminow, E.H.Turner, R.L.Barns, J.L.Bernstein, J. Appl. Phys., 51 (8), 4379 (1980)
10. W.Bąk, C.Kuś, W.S.Ptak, Ferroelectrics, 115, 105 (1991)

*Ferroelectrics*, 1992, Vol. 133, pp. 247–252
Reprints available directly from the publisher
Photocopying permitted by license only
© 1992 Gordon and Breach Science Publishers S.A.
Printed in the United States of America

# TrP141

## PECULIARITIES OF POLARON ELECTRONICS OF COMPLEX OXIDES

ANNA MYASNIKOVA
Rostov University, Rostov-on-Don, Russia

Abstract The theory of polarons in the complex oxides is developed. Different charge carrier states have been found in them and their properties are described.

## INTRODUCTION

Pecar's polaron theory[1] was constructed for the alkali-halide crystals, having only one branch of interacting with the charge carrier phonons. In the complex oxides among many phonon branches there are several branches, satisfying the adiabatic condition of the polaron theory[1]. The present article is an attempt to study the effect of this circumstance on charge carrier states in the complex oxides. Consideration of the spatial dispersion of dielectric permittivity (DP) due to the finite effective mass of phonons [2,3]* makes it possible to investigate effects of different dispersion of phonon branches.

## THE "TWO-COATS" POLARON MODEL

Let us consider, using the mathematical formalism of Ref. 3, the carrier autolocalized state (AS) in the medium with two branches of longitudinal phonons, having the dispersion law $\Omega_i^2(k)=\Omega_i^2+u_i^2k^2$, $i=1,2$, where $u_i$ are the minimum phase velocities of i-branch phonons. The Hamilton's function for the such system has the form

$$H = \int d^3\underline{r}\Big\{\psi^*(E_o-\frac{h^2}{2m^*}\nabla_{\underline{r}}^2)\psi + \sum_{i=1,2}\Big(\frac{2\pi}{c_i\Omega_i^2}\Big(\Omega_i^2\underline{P}_i^2+\Big[\frac{\partial\underline{P}_i}{\partial t}\Big]^2 - u_i^2\underline{P}_i\nabla_{\underline{r}}^2\underline{P}_i\Big) + e\underline{P}_i\nabla_{\underline{r}}\int|\psi(\underline{r}',t)|^2/|\underline{r}-\underline{r}'|\,d^3\underline{r}'\Big)\Big\}, \qquad (1)$$

where $c_1=\varepsilon_1^{-1}-\varepsilon_o^{-1}$, $c_2=\varepsilon_\infty^{-1}-\varepsilon_1^{-1}$; $\varepsilon_o$ and $\varepsilon_\infty$ are static and

* The polaron velocity has been shown there to be limited by the minimum phase velocity of phonons

high-frequency DP's, $\varepsilon_{\mathrm{I}}$ - intermediate DP: $\varepsilon_{\mathrm{I}} = \varepsilon_{\infty}(\Omega_2/\Omega_{to2})^2$, if $\Omega_2 > \Omega_{\mathrm{I}}$; $m^*$ and $E_o$ are the effective mass and minimum energy of the free carrier; $\underline{P}_{\mathrm{I}}, \underline{P}_2$ are the dipole moments due to the i branch. The term $\underline{P}_i \underline{P}_j$ is absent in H because of independence of different branch vibrations in harmonic approximation. Eq. (I) yields the following equations for the carrier wave function $\psi(\underline{r},t)$ in stationary state and polarization charge distributions $\rho_i = -\mathrm{div}\underline{P}_i$, $i=\mathrm{I},2$

$$\left[i\hbar\partial/\partial t - E_o + h^2/(2m^*)\nabla_{\underline{r}}^2 - e\int(\rho_{\mathrm{I}}(\underline{r}',t)+\rho_2(\underline{r}',t))/|\underline{r}-\underline{r}'|d^3\underline{r}'\right]\psi = 0,$$

$$(\partial^2/\partial t^2 + \Omega_i^2 - u_i^2\nabla_{\underline{r}}^2)\rho_i(\underline{r},t) = -c_i\Omega_i^2|\psi(\underline{r},t)|^2 \quad \begin{matrix} i=\mathrm{I} \ (3), \\ i=2 \ (4). \end{matrix}$$

All effects in such model can be easily revealed in the particular case $c_{\mathrm{I}} \gg c_2$. It allowes to consider the polarization $\underline{P}_{\mathrm{I}}$ as a small perturbation and to solve the system of Eqs. (2-4) by the consequence approaches method. For a zero approximation $\rho_{\mathrm{I}}^{(0)} = 0$, $\psi^{(0)}$ and $\rho_2^{(0)}$ are found from Eqs. (2,4) as in Ref. 3. In a first approximation $\rho_{\mathrm{I}}^{(1)}(\underline{r},t)$ is obtained, substituting $\psi^{(0)}$ to Eq. (3), and the wave function $\psi^{(1)}$ is the function, minimizing the functional

$$J = -\int d^3\underline{r}\psi^{(1)}(\underline{r})\Big\{h^2/(2m^*)\nabla_{\underline{r}}^2 + e^2/2\int(G_1(\underline{r}_{\mathrm{I}}-\underline{r}_2)|\psi^{(0)}(\underline{r}_2)|^2 c_{\mathrm{I}}\Omega_{\mathrm{I}}^2 + G_2(\underline{r}_{\mathrm{I}}-\underline{r}_2)|\psi^{(1)}(\underline{r}_2)|^2 c_2\Omega_2^2)/(\underline{r}-\underline{r}_{\mathrm{I}})d^3\underline{r}_{\mathrm{I}}d^3\underline{r}_2\Big\}\psi^{(1)}(\underline{r}), \quad (5)$$

where $\rho_i$ are expressed, using the Green's function to Eqs. (3,4)

$$\rho_i(\underline{r},t) = -ec_i\Omega_i^2\int G_i(\underline{r}-\underline{r}',t)|\psi(\underline{r}',t)|^2 d^3\underline{r}', \quad (6)$$

$$G_i(r,t) = \begin{cases} \dfrac{\exp(-\Omega_i\sqrt{(z-vt)^2/\beta_{1i}^2 + r^2}/u_i)}{4\pi u_i^2\beta_{1i}((z-vt)^2/\beta_{1i}^2 + r^2)^{1/2}}, & v \le u_i, \ \beta_{1i} = \sqrt{1-\dfrac{v^2}{u_i^2}} \\ \dfrac{\cos(\Omega_i\sqrt{(z-vt)^2/\beta_{2i}^2 - r^2}/u_i)}{2\pi u_i^2\beta_{2i}((z-vt)^2/\beta_{2i}^2 + r^2)^{1/2}}, & v > u_i, \ \begin{matrix} z-vt<0 \\ r \le \dfrac{|z-vt|}{\beta_{2i}} \end{matrix} \\ 0, \ v > u_i, \ r > \dfrac{|z-vt|}{\beta_{2i}}, \ z-vt > 0, & \beta_{2i} = (v^2/u_i^2 - 1)^{1/2} \end{cases} \quad (7)$$

$i=\mathrm{I},2$

from Refs. 2,3 in the cylindrical coordinate system with z axis directed along the polaron velocity $\underline{v}$. It is clear from Eqs. (6,7) that $v=u_i$ is the critical velocity for i

polarization"coat"of the carrier: in the vicinity of $v=u_i$ $G_i(\underline{r},t)$ and, hence, $\rho_i(\underline{r},t)$ changes dramatically. Therefore there must be three plots of the velocity axis: $v<u_1$, $u_1<v<u_2$, $v>u_2$ (in case of $u_1<u_2$), corresponding to different states of the carrier.

## THE CARRIER STATES IN THE "TWO-COATS" MODEL

When $v<u_1$, AS, obtained as the Eqs. (2-4) solution in a first approximation, has less radius and more binding energy and effective mass than zero approximation does, because the latter is AS with only one polarization"coat" of branch 2 (i=2) phonons whereas for the former the extra polarization caused by branch 1 appears. It can be verified by the complete polaron charge calculation: it appears to be equal $e/\varepsilon_o$. The binding energy and radius of such heavy polaron (HP) can be evaluated, using the polaron theory formulae with the inversed effective DP $c=\varepsilon_\infty^{-1}-\varepsilon_o^{-1}=c_1+c_2$.

When $v \gtrsim u_1$, $G_1(\underline{r},t)$ oscillates with the period $u_1\beta_{21}/\Omega_1$ along z axis, that is much less than the radius of the carrier localization region, so that Eq. (6) yields $\rho_1 \approx 0$. Therefore the first-order solution of Eqs. (2-4) does not differ from the zero approximation. Hence in the polaron, moving with $v>u_1$, the carrier localization is kept up by only second phonon branch. Such polaron has less binding energy and effective mass than HP does, we shall call it light polaron (LP). Its characteristics are determined by the usual polaron theory[1,3] with one phonon branch 2.

When $v>u_2$, $G_2(\underline{r},t)$ becomes oscillating and Eq.(6) does not yield the polarization charge distribution, needed to keep the carrier in AS. Therefore the upper limit of the polaron velocity in considered model is $v=u_2$.

## THE DISPERSION OF FREE AND LOCALISED CARRIER IN THE MODEL

Different ASs of the carrier have been shown above to exist in medium of complex-oxide type in different intervals of the polaron velocity. To classify these states, using the characteristics of the carrier itself is useful too. Since the polaron velocity is equal to the average carrier velocity

in AS, the united curve of dispersion versus the carrier impulse, averaged over the state, can be drawn. This impulse characterizes the carrier with uncertainty which, being connected with uncertainty of the carrier coordinate, is much for HP than for LP and is equal to zero for the free carrier. Figure I presents the example of such dispersion. It demonstrates segmentized carrier zone, consisting of three segments, corresponding to HP, LP and free

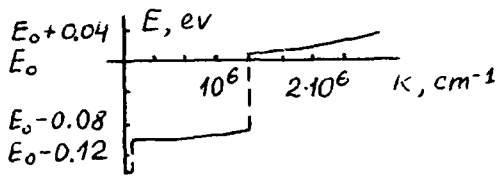


FIGURE I The carrier dispersion.

carrier. The boundary impulses are determined by the phonon minimum phase velocities: $p_I=m^*u_I$, $p_2=m^* u_2$. In classic polaron theory the carrier zone is segmentized into two parts - of localized and free carriers, that is why it is not correctly to consider in such model the AS motion with velocities $v > u$.

LP BRAKING BY THE COHERENT RADIATION

The form of $\rho_I(\underline{r},t)$ at $v > u_I$, which is oscillating (and quasiharmonic when $v \gg u_I$), leads to the conclusion,[2] that LP, moving with the velocity exceeded the minimum phase velocity of one branch, excites not virtual but real phonons of this branch as a result of effect similar to Cherenkov's one. If $v \gg u_I$ the radiation of different parts of the electron density distribution is coherent , and the wave of real coherent phonons is formed in the acoustic cone $r \leq |z-vt| / \beta_{2I}$ behind LP. Hence, the mechanism of braking by coherent radiation is actual for LP at velocities $u_I \ll v < u_2$. Using Eqs. (6,7), it is easily to derive the expression for the equilibrium velocity of LP in electric field E:

$$v(E) = (c_I \Omega_I^2 e/E)^{I/2}. \qquad (8)$$

This expression corresponds to the high-velocity limit of v(E) curve proposed in Ref. 4. But there it was derived from an inwardly contradictionary model, because the polaron motion with $v > u$ was considered in medium with one phonon branch. Present analysis shows that results, obtained in such conditions, will be correct in the region $u_I < v < u_2$, if the second phonon branch with dispersion $u_2$ exists in medium.

Figure 2 represents the equilibrium average velocity of carrier versus the electric field in every of three segments of the carrier zone, taking into account the ohmic relaxation with the relaxation time $\tau = 10^{-9}$c (dashed line) and $\tau = 2 \cdot 10^{-9}$c (dash-dotted line). By this lines unification, assuming that in two-solutions regions the solution with less v realizes, the complete v(E) function for our model is obtained. It (solid line) reflects the

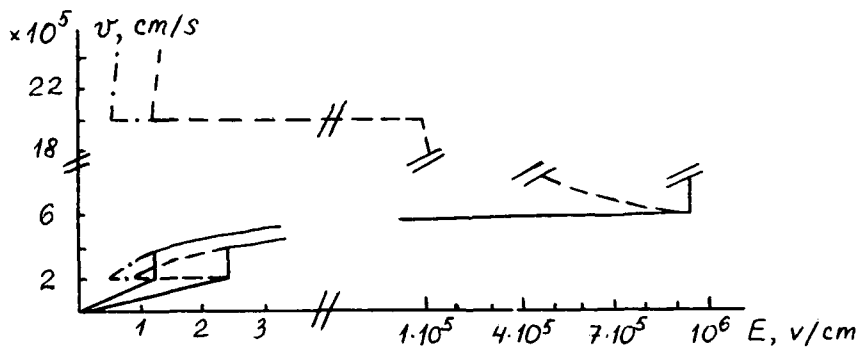


FIGURE 2 The equilibrium average velocity of carriers versus the electric field strength E.

effects of one polarization "coat" break off and LP braking by coherent radiation. It is clear from the Figure 2, that giant losses due to the radiation make it impossible to overcome the threshold of coherent radiation "tail" forming in usual crystals.

The main conductivity characteristic - the mobility of carriers $\mu$ is strictly connected with the equilibrium velocity: $\mu(E) = v(E)/E$. Therefore the constant mobility corresponds to the interval of v(E) increase before the first polarization "coat" break off, then it spasmodically rises,

and, in the region of constant $v(E)$, $\mu(E)$ decreases rapidly. An experimental observation of this demands low temperatures and crystals with high dispersion.

## CONCLUSION

Thus, because the polarization cannot follow the carrier translation with the velocity exceeding the minimum phase velocity of the appropriate phonons, two types of polarons exist in fitting complex oxides medium with two phonon branches capable to participate in the carrier localization and having different dispersions. HP has two "coats" of phonons of the both branches. When HP velocity exceeds $u_I$ it loses one, "slow", coat, transforming into LP. LP moving with $u_I \ll v < u_2$ excites real coherent phonons of the low-velocity branch and is braked by the coherent radiation. These effects must manifest itself, in particular, in the behaviour of low-temperature carrier mobility.

It should be noted that two LP can form a bipolaron due to their interaction with real phonons under the resonance condition,[5] with Bose-condensation of such bipolarons being possible at typical for the high-$T_c$ superconductors temperatures and carrier concentrations. Detailed consideration of this will be publeshed slsewhere.

## REFERENCES


I. S.I. Pecar, Studies in Electronic Theory of Crystals (Gostekhizdat, Moscow, I95I), Chap.2, pp 38-57.

2. E.N. Myasnikov and A.P. Popov, Doklady Akad. Nauk Ukr SSR. Ser.A, 5, N6, 73 (I980).

3. A.S. Davydov and V.Z. Enolskii, Phys. Stat. Sol. (b), I43, I67 (I987).

4. V.V. Bryksin, V.V. Onuchin, A.V. Prokasnikov and G.U. Yashin, Fiz. Tverdogo Tela, 30, 462 (I988).

5. E.N. Myasnikov and A.L. Martunyuk, Izv. Vuzov. Fizika, N II, 7 (I986).

*Ferroelectrics*, 1992, Vol. 133, pp. 253–258
Reprints available directly from the publisher
Photocopying permitted by license only

© 1992 Gordon and Breach Science Publishers S.A
Printed in the United States of America

# TrP142

## ELECTRON EMISSION AND SPONTANEOUS POLARIZATION DISTRIBUTION OF PROTON-EXCHANGED $LiNbO_3$

SIDNEY B. LANG
Department of Chemical Engineering, Ben-Gurion University of the Negev, Beer Sheva 84105, Israel

G. ROSENMAN, S. RUSHIN, V. KUGEL and D. NIR
Faculty of Engineering, Tel-Aviv University, Ramat-Aviv 69978, Israel

Abstract The spatial distribution of the spontaneous polarization in $LiNbO_3$ may be changed by proton-exchange. The treatment of this crystal in benzoic acid causes the appearance of a layer of reversed-direction spontaneous polarization near the $z^+$-surface. We have investigated proton-exchanged $LiNbO_3$ utilizing both ferroelectric electron emission (FEE) and the Surface Laser Intensity Modulation Method (SLIMM) to measure the spatial distribution of spontaneous polarization. The FEE diminished sharply in benzoic acid-treated samples. SLIMM showed that the proton-exchange treatment caused reversal of the direction of spontaneous polarization in a layer about 1.2 $\mu$m thick on the $z^+$-surface. No reversal occurred on the $z^-$-surface.

## INTRODUCTION

Light modulators, frequency doublers and optical switches are widely used in modern optical communication systems. The most attractive implementation of these optical devices is the optical waveguide which can be incorporated into an electronic integrated solid-state circuit. Dielectric waveguides for the visible and near infrared spectrum are usually fabricated from ferroelectric crystals such as $LiNbO_3$, $LiTaO_3$, $KNbO_3$ and KTP. For light beam propagation inside the waveguide structure, the refractive index of the guide region must be greater than that of the surroundings.[1] A suitable refractive index in $LiNbO_3$ and $LiTaO_3$ can be achieved by $Li_2O$-outdiffusion, Ti-indiffusion and proton exchange.[2]

The unusual effect of ferroelectric domain reversal in the diffused zone has been observed.[3-5] This process is asymmetric in that it only occurs at the $z^+$-surface of $LiNbO_3$ and at the $z^-$-surface of $LiTaO_3$ crystals[3-4]. Some attempts have been made to explain the domain inversion process by a mechanism based on creation of an internal electric field opposite in direction to the spontaneous polarization.[3,6-7] Optical micrography of etched surfaces has been the principal method employed for observation of domain reversal in $LiNbO_3$ and $LiTaO_3$ crystals.[3-7] However, this method is not applicable for KTP.[8] In this paper, we have studied domain reversal by means of ferroelectric electron emission (FEE) and the Surface Laser Intensity Modulation Method (SLIMM).

FEE AND SLIMM TECHNIQUES

Electron emission from ferroelectric crystals (FEE) is due to the creation of uncompensated negative charge on the polar surface. It has been observed as a consequence of pyroelectric, piezoelectric and anomalous photovoltaic effects as well as during switching of the polar axis.[9-11] The FEE current is determined both by the intensity of the unscreened depolarizing field[12] and by the potential threshold of electrons at the crystal-vacuum boundary.[13] A detailed description of the experimental technique has been reported elsewhere.[12]

SLIMM[17] is a modification of the Laser Intensity Modulation Method (LIMM)[18-19] which has been used for the study of polarization in the bulk of single crystals, ceramics and polymers. In LIMM, each surface of the sample is exposed in turn to a laser beam which is intensity-modulated sinusoidally at approximately 100 different frequencies. The energy of the laser beam is absorbed and a spatially non-uniform time-varying temperature distribution is established in the sample. The interaction of the temperature distribution and the unknown polarization distribution produces a pyroelectric current. Numerical techniques have been developed for computing the polarization distributions from the measurements. The major changes introduced in SLIMM are the use of a much higher range of modulation frequencies and analysis of data from only one side of the sample. Because of the higher frequencies, the sample behaves thermally as a semi-infinite solid rather than as a bounded solid. The heat conduction differential equation and boundary conditions are

$$\frac{\partial T}{\partial t} = K\frac{\partial^2 T}{\partial x^2} \quad \textit{where} \quad -k\frac{\partial T(0,t)}{\partial x} = q_0 \eta e^{i\omega t} \quad \textit{and} \quad T(\infty,0) = 0 \qquad (1)$$

Here T = temperature, t = time, k = thermal conductivity, K = thermal diffusivity, $q_0$ = laser beam flux, $\eta$ = surface emissivity, i = imaginary operator and $\omega$ = radial frequency of modulation. The solution to Eq. (1) is inserted into the fundamental equation of LIMM which describes the relationship between the pyroelectric current and the temporal and spatial temperature distribution in the sample.[19] The result is the SLIMM equation:

$$\frac{I}{pA\left(\frac{d\langle T\rangle}{dt}\right)} = 1 + \int_0^{\infty}\left(\frac{P^*}{P_0}\right) D\,(1+i)\,\exp[-(1+i)Dx]\,dx \qquad (2)$$

The polarization distribution is $P(x)=P_0+P^*(x)$, where $P_0$ = spontaneous polarization. The other parameters are I = pyroelectric current, p = pyroelectric coefficient, A = laser beam cross-sectional area, $d\langle T\rangle/dt$ = average rate of temperature change in sample and

$D = (2\,\omega/K)^{1/2}$. We assume that a proton-exchanged crystal has a uniform spontaneous polarization $P_0$ everywhere in its thickness L with the exception of a layer of thickness $\delta$ of reversed polarization ($-P_0$) adjacent to one surface. The pyroelectric current is found by integration of Eq. (2) to give

$$\frac{I}{pA\left(\frac{d(T)}{dt}\right)} = 1 - \frac{2(L-\delta)}{L-2\delta} + \frac{2L}{L-2\delta}\exp[-(1+I)D\delta] \qquad (3)$$

The real and imaginary components of Eq. (3) correspond to the amplitude of the pyroelectric current in phase with the laser beam modulation and in quadrature, respectively.

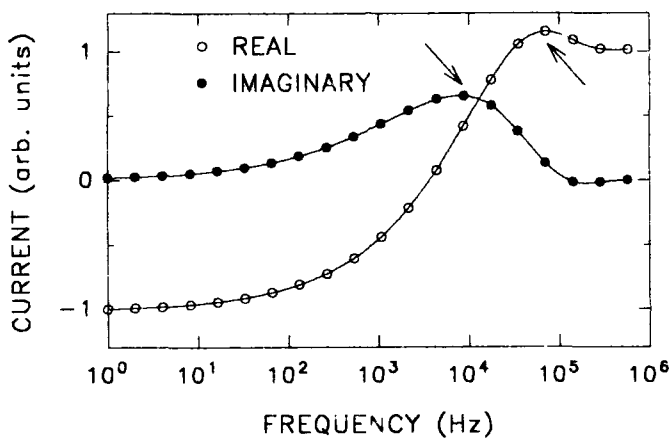


FIGURE 1 Calculated pyroelectric currents for a 0.5 mm-thick $LiNbO_3$ plate with a 5 $\mu m$ inverted region at surface.

Figure 1 illustrates the calculated real and imaginary pyroelectric currents which would be measured on the $z^+$-surface of a 0.5 mm thick $LiNbO_3$ plate with polarization reversal to a depth of 5 $\mu m$. At very low frequencies, the laser heats the bulk of the sample. The real component becomes asymptotically constant and the imaginary component tends to zero. At very high frequencies, only the reversed layer is heated and the real component has a sign opposite to that at low frequencies. The behavior at intermediate frequencies uniquely characterizes a material with regions of opposed polarization.

EXPERIMENTAL TECHNIQUES

A poled z-cut plate of $LiNbO_3$ measuring about 25 by 12 mm in cross-section and 0.54 mm in thickness was used. The sample was coated with an alternating pattern of Al film so that only the exposed areas would be proton-exchanged. The plate was then immersed in pure molten benzoic acid at 230°C for 30 minutes after which the Al mask was etched away. This

was followed by annealing for 4 hours in air at 400°C. Aluminum electrodes were applied by sputtering. FEE measurement were made in vacuum ($10^{-6}$ torr) by varying the sample temperature at a constant rate of $6.6 \times 10^{-2}$ K $s^{-1}$. In the SLIMM measurements, the laser beam was allowed to impinge on various points on both surfaces of the sample. Modulation frequencies were varied from 100 Hz to 100 kHz. All measurements were made at ambient temperature. The thermal diffusivity was measured by a technique developed by Lang.[20] Its value was $0.986 \times 10^{-2}$ $cm^2$ $sec^{-1}$.

## EXPERIMENTAL RESULTS

The temperature dependencies of the FEE current measured on the $z^+$-surface are illustrated in Figure 2 for both a virgin and a proton-exchanged $LiNbO_3$ crystal. The virgin crystal exhibited the usual temperature behavior of electron emission currents.[14] The emission current was constant over a temperature interval from 320 to 450 K and had a maximum value of about $1.3 \times 10^{-14}$ A $cm^{-2}$. The proton-exchange treatment changed the FEE current drastically. A narrow peak with a width of about 12 K was observed. The electron current decreased sharply to a maximum of about $6.4 \times 10^{-17}$ A $cm^{-2}$, about three orders of magnitude less than for the virgin crystal.

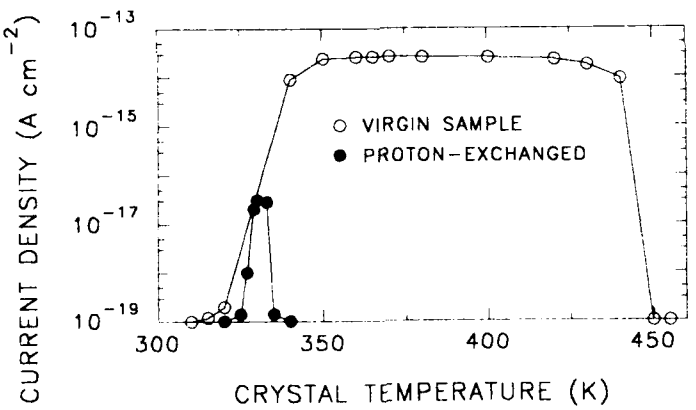


FIGURE 2 Temperature dependence of FEE current density for virgin and proton-exchanged $LiNbO_3$ crystals.

SLIMM measurements on a proton-exchanged $z^+$-surface are shown in Figure 3. This surface underwent proton-exchange as indicated by the distinct increase in pyroelectric current at high frequencies, observed in both the real and imaginary components. The depth of proton-exchange was found by a nonlinear least-squares fit of the Eq. (2) to the data in Figure 3 (shown as solid lines). The thickness of the reversed region was 1.2 $\mu$m. The experimental data do not show the peaks that appear in Figure 1 (marked with arrows). This is due to the very shallow depth of proton-exchange. The peak in the imaginary current would have appeared at about 135 kHz and the peak in the real component at about 1.2

MHz, but these frequencies are far above the 100 kHz limit of the lock-in amplifier used in the experiments. The pyroelectric current was also measured on a $z^-$-surface which had been treated with benzoic acid. As mentioned in the introduction, no reversal should occur on $z^-$-surfaces of $LiNbO_3$. The SLIMM results showed a constant real component of the pyroelectric current and a zero imaginary component indicating that the sample had a completely uniform spontaneous polarization, with no reversal near the $z^-$ surface.

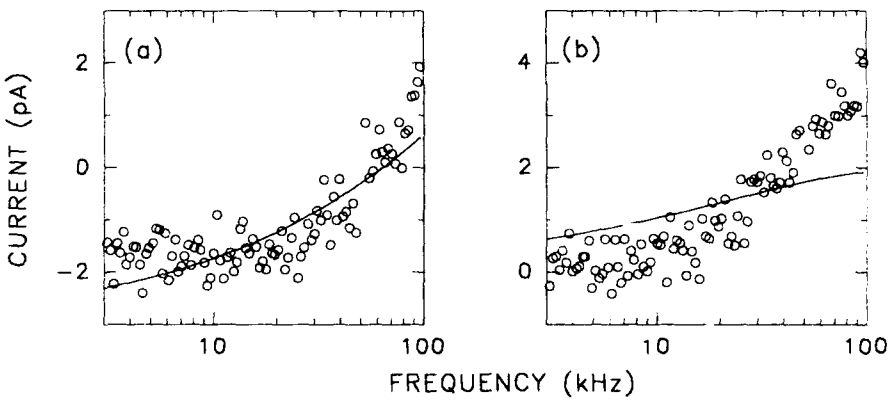


FIGURE 3 SLIMM measurements on a proton-exchanged $z^-$-surface. Solid line is nonlinear least-squares fit of Eq. (3) to data. (a) Real component of current. (b) Imaginary component of current.

## DISCUSSION

The major experimental results are the direct observation of the spontaneous polarization distribution by means of SLIMM and the definite changes of the FEE parameters after proton-exchange. The SLIMM results showed that proton-exchange can only occur on $z^+$-surfaces in $LiNbO_3$ and they gave a quantitative and non-destructive measurement of the thickness of the reversed zone.

The electron emission was studied while the sample was heated; consequently, the emission current was due to a pyroelectric effect. The FEE phenomenon has been shown to be a field tunneling effect.[9-14] The probability of an electron escaping into vacuum depends on the field intensity and the work function. In the virgin sample measurements, a pyroelectric unscreened field at the free $z^+$-surface caused electron emission. In the proton-exchanged sample, the presence of the zone of reversed polarization caused a reduction in the electrostatic pyroelectric field. This then decreased the FEE current which has an exponential dependence upon the field intensity.[13] An additional reason is due to a change in the electron work function. It is known that a stable monodomain state of a

ferroelectric crystal is achieved by internal screening, i.e. by electrons and holes of a ferroelectric semiconductor.[15] Consequently, band bending with opposite signs occurs at the opposing polar surfaces. The screening effect causes the reduction of the work function near the $z^+$-surface and induces it near the $z^-$-surface.[16] The theoretical difference of the band bending ($\Delta\phi$) for the $z^+$ and $z^-$ cuts is equal to the energy gap.[15] Photoemission measurements indicate that $\Delta\phi = 0.4$ eV, instead of the theoretical value of 3.9 eV.[16] Calculations show that there is a contribution to $\Delta\phi$ of 0.25 eV from the $z^+$-surface and 0.15 eV from the $z^-$-surface. In the FEE measurements on the proton-exchanged sample, a reverse of the band bending also took place. This increased the work function significantly to the value of 0.4 eV. The value of the electron affinity without band bendng would have been about 0.5 eV. Thus, the domain inversion doubles the work function leading to a significant decrease in the FEE current, as observed.

ACKNOWLEDGEMENTS

This research was supported in part by the Basic Research Foundation administered by the Israel Academy of Sciences and Humanities (SBL) and in part by the Ministry of Science and Technology of Israel (GR).

REFERENCES

1. A. Yariv, *Optical Electronics* (Saunders College Publishing, Philadelphia, 1991).
2. A. Donaldson, *J. Phys. D: Appl. Phys.* **24**, 785 (1991).
3. S. Miyazawa, *J. Appl Phys.* **50**, 4599 (1979).
4. S. Thaniyavarn, T. Findakly, D. Booher and J. Moen, *Appl. Phys. Lett.* **46**, 933 (1985).
5. K. Nakamura and H. Shimizu, *Appl. Phys. Lett.* **56**, 1535 (1990).
6. M. Yamada and K. Kishima, *Electronics Lett.* **27**, 828 (1991).
7. W.-Y. Hsu and M.C. Gupta, *Appl. Phys. Lett.* **60**, 1 (1992).
8. J. Bierlein and F. Ahmed, *Appl. Phys. Lett.* **51**, 1322 (1987).
9. B. Rosenblum, P. Braulich and J. Cerrico, *Appl. Phys. Lett.* **25**, 17 (1974).
10. G. Rosenman, *Ferroelectrics* **118**, 451 (1991).
11. K. Biedrzyeki and R. Poprawski, *Solid State Commun.* **73**, 455 (1990).
12. G. Rosenman, O.V. Malyshkina and Yu.L. Chepelev, *Ferroelectrics* **110**, 99 (1990).
13. G. Rosenman, V. Pechorskii, Yu.L. Chepelev, E.I. Boikova and L.E. Issakova, *Phys. Stat. Solidi B* **120**, 667 (1983).
14. G. Rosenman and E.I. Boikova, *Phys. Stat. Solidi A* **58**, 379 (1980).
15. V. Fridkin, *Photoferroelectrics* (Springer-Verlag, Berlin, 1979).
16. G. Rosenman, Yu.L. Chepelev and E. Boikova, *Ferroelectrics* **100**, 17 (1989).
17. S.B. Lang, Q.-Y. Jiang and S.B. Krupanidhi, 7th European Meeting on Ferroelectricity, Dijon, France (1991).
18. S.B. Lang and D.K. Das-Gupta, *J. Appl. Phys.* **59**, 2151 (1986).
19. S.B. Lang, *Ferroelectrics* **118**, 343 (1991).
20. S.B. Lang, *Ferroelectrics* **93**, 87 (1989).

*Ferroelectrics*, 1992, Vol. 133, pp. 259–264
Reprints available directly from the publisher
Photocopying permitted by license only
© 1992 Gordon and Breach Science Publishers S.A.
Printed in the United States of America

# SwP218

## ON THE POSSIBILITY OF AMPLITUDE AND DURATION OF ELECTRIC PULSE REGISTRATION BY MEANS OF FERROELECTRICS

I.G.Tolstikov and E.Z.Novitskii
All-Union Scientific Research Institute
of Experimental Phisics
607200, Arzamas, Nizhni Novgorod Region, Russia

The use of conventional techniques for registration electric pulses, including oscillographic means, may be difficult or inadequate in some experiments because of restricted number of measurement channels, measuring line crosstalking,or it may be rather expensive.In these cases energy-independent measurement techniques could be useful, which require neither power supplies nor sophisticated electronic devices to record or store information on the parameters of pulses . These techniques can have the information detected , or recorded, and stored using passive sensing elements (SE) which physical state would change by electric pulse, to be retained for rather a long time. The parameters of the test pulse are then estimated by these changes in SE initial state , such as wire blow - out , dielectric or semiconductor breakdowns , changes in magnetic retentivity etc. Generally, with the energy-independent techniques these measurements can be run by making use of permanently operable detectors placed in close vicinity to the load to which the test pulse is to be applied.

However, the currently available techniques have insufficient information capabilities for they do not enable measurement of both pulse amplitude and duration and, moreover, may cause substantial distortion of the test pulse in a low-resistance load.

The authors suggest, that the above short-comings could be overcome if ferroelectric memory elements (FE) were chosen for use as SEs.The use of these FEs is based on the ferroelectric's capability to conservate their partially or fully polarized state long after the pulse input. This property has found applications in computer technology, where the so-called energy-independent memory devices are used to write-in and store logical information [1].

The present paper addresses the problem of how to find the unknown parameters(i.e. amplitude and duration)

of electric pulse using the polarization values ($P_j$) of the ferroelectric in a number of FEs (j=1,2...N) known before and measured after the pulse input. This problem, as it will be shown further, can be solved if ferroelectric materials are used, which are carrying the affine switching current [1],they being further referred to as "affine" ferroelectrics.

Let at the time t=0 a rectangular electric pulse of amplitude V and duration T is applied to a FE, which creates the electric field E in the ferroelectric directed opposite to spontaneous (remanent) polarization vector $\vec{P}_o$, i.e. here the experimentation version by Merz [2] is observed. This causes the polarization current (or switching current)to flow through the FE,its density i(t,E) being determined by derivative dP/dt (with actual E value included into i(t,E) function as a parameter). The curve i(t,E)is represented by the occurrence of peak $i_m(E)$ and the time $\tau$ (E) of full ferroelectric switching (see fig.1).

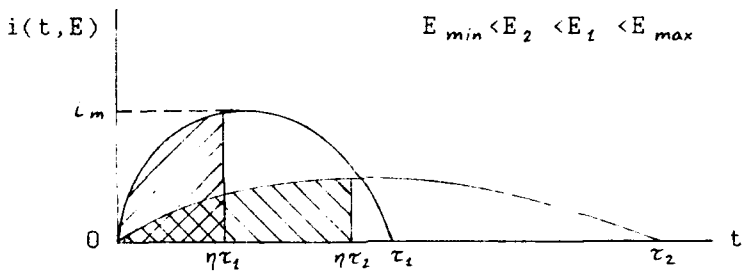


FIGURE 1 FE switching current density i(t,E) as a function of time, for various applied field values $E_1$ and $E_2$ ($E_1 > E_2$).

For the most of ferroelectrics the observed experimental relationships $i_m(E)$ and $\tau$ (E) for a wide range of field are exponential [1,2]

$$\tau = \tau_\infty * \exp(\alpha * E)$$
$$i_m = i_\infty * \exp(-\alpha * E) \qquad (1)$$

where $\tau_\infty$, $i_\infty$, $\alpha$ are the constants, $\alpha$ -the activation field.

As an example, fig.2 show $\tau$ (E) relationships for crystal barium titanate (line 1) and bismuth titanate (line 2) taken from ref.[1], which in the coordinate plane($\lg \tau^{-1}$;$E^{-1}$)may be approximated by straight lines as

$$\lg \tau^{-1} = A * E^{-1} + B \qquad (2)$$

where A and B are the constant coefficients.

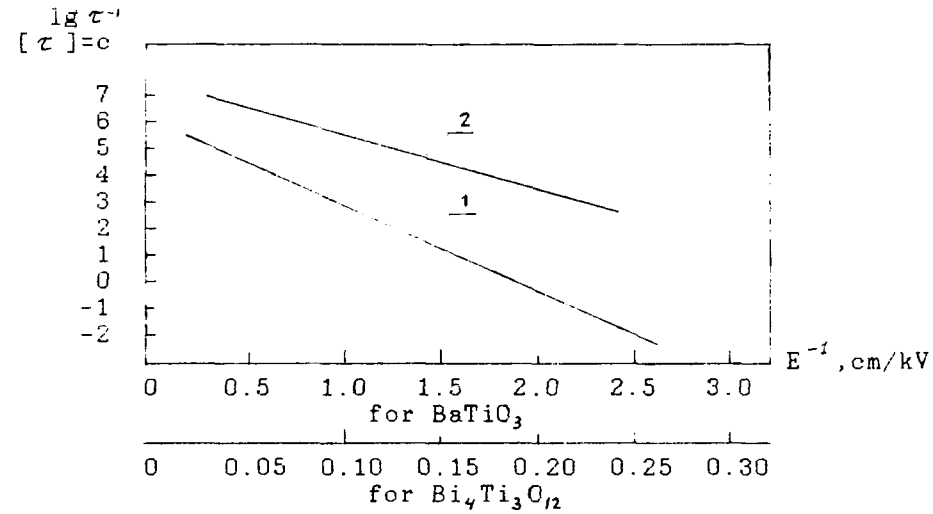


FIGURE 2 Logarithm of full-switching inverse time as a function of inverse field, $\lg \tau^{-1}(E^{-1})$, for the crystal BaTiO (line 1) and Bi Ti O (line 2) from ref.[1].

During the switching, the ferroelectric polarization is changed according to the relation:

$$\Delta P(t,E)= \int_0^t i(t,E)\, dt \ ,$$

i.e. $\Delta P(t,E)$ value is equal to the area below $i(t,E)$ line. Here, if the applied pulse is of duration $t=T \geqslant \tau$, then there would be full switching $\Delta P(t \geqslant \tau)=2P_o$ and if $t=T < \tau$, the switching would be partial, or $\Delta P(t < \tau) < 2P_o$.

$\Delta P$ represents an integrated characteristic of the switching process and depends, generally , on both the field (E) and time (t) contributions, as it's a function of two variables, $\Delta P= \Delta P(t,E)$. Note, that for "affine" ferroelectric case $\Delta P$ can be reduced to a one-valued function of one variable $\eta$ ,i.e. $\Delta P= \Delta P(\eta)$, where $\eta = t/\tau < 1$, $\tau = \tau(E)$.

According to ref.[1], for "affine" ferroelectrics the pulse shape $i(t,E)$ is identical for E varying in some reasonably wide range of fields ($E_{min}$ ,$E_{max}$ ), where $i_m(E)*\tau(E)=$ const, i.e. when E increases, there are the decrease in $\tau$ and the corresponding increase in $i_m$ in the same proportion.

It follows from the shape retention condition, that simple affine transformation such as the reduction of the plane by $i_m$ times in X-axis and by $\tau$ times in Y-axis can be used to reduce all the curves $i(t,E)$ obtained for various $E \in (E_{min}, E_{max})$ to a single form (image), as shown in fig.3.

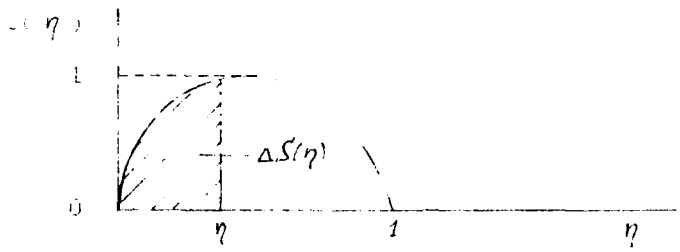


FIGURE 3 Reduced switching current density I as a function of reduced time $\eta$ ,I( $\eta$ ), resulting from affine reduction of function i(t,E).

Analitically, the following relationship describes the form of these curves (image) upon their transformation:

$$I(\eta) = \frac{1}{i_m(E)} * i(\tau * \eta, E) .$$

The area $\Delta S(\eta)$ of the shaded pattern of fig.3 (which is corresponded by those in fig.1) is

$$\Delta S(\eta) = \int_0^{\eta} I(\eta)\, d\eta = \int_0^{\eta} \frac{1}{i_m(E)} \cdot i(\tau \cdot \eta, E)\, d\eta =$$

$$= \frac{1}{i_m(E) \cdot \tau(E)} \cdot \int_0^{\eta} i(\tau \cdot \eta, E)\, d(\tau \cdot \eta) = \frac{\Delta P(\tau \cdot \eta, E)}{i_m(E) \cdot \tau(E)} .$$

For "affine" ferroelectrics $i_m(E) * \tau(E) = q_o$ =const, therefore the resulting relationship may be reduced to

$$\Delta P(\tau \cdot \eta, E) = q_o * \Delta S(\eta) \equiv \Delta P(\eta) \qquad (3)$$

Note, that for $\eta$ =1 the nondimensional (total) area $\Delta S$ (1) below I( $\eta$ ) line represents essentially the coefficient f introduced by Fatuzzo and Merz in [3],i.e. $\Delta S$ (1) = f. Therefore, considering $q_o * \Delta S(1) = 2*P_o$ , the following expression can be written for $\Delta P(\eta)$:

$$\Delta P(\eta) = \Delta S(\eta) * \frac{2*P_o}{f}$$

Clearly, for $\eta < 1$, the relation $\Delta P(\eta)$, as well as $\Delta S(\eta)$, is a one -valued function of the argument. From (3), if the field $E = E_j$ ($E_{min}$ ,$E_{max}$ ) is applied to an "affine" ferroelectric, the polarization change $\Delta P$ by the time $t = T < \tau(E_j)$ would be unambiquously determined by $\eta_j = T * \tau^{-1}(E_j)$. With $\eta_j$ known, find $\Delta P$ from the relation $\Delta P(\eta)$ which can be readily plotted earlier by integrating in time the particular experimental curve $i(t,E_k)$ and taking $\tau(E_k)$ as a measure in X-axis, see fig.4.

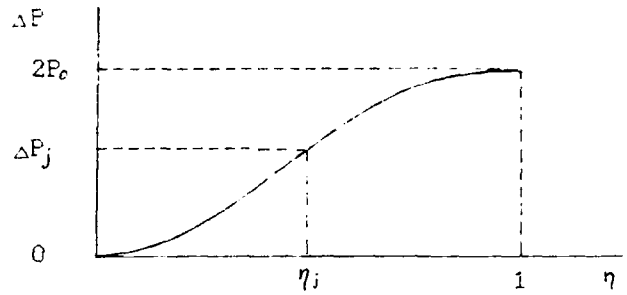


FIGURE 4 "Affine" ferroelectric polarization variation $\Delta P$ as a function of reduced time $\eta$, $\Delta P(\eta)$, $\eta = t/\tau$ .

And otherwise, when after the pulse input the $\Delta P_j$ value results(as measured following the experiment using known techniques such as measurement of hysteresis loop ), then the applied pulse parameters are related to each others as follows :

$$\eta_j = T * \tau^{-1}(E) \qquad (4)$$

where $\eta_j$ has been in its turn estimated from the relationship $\Delta P(\eta)$.

It is assumed here, that since the time the pulse of T duration was applied $\Delta P(T,E)$ has been retained long enough to make measurements.

If the test pulse is used to affect two or more ($N \geq 2$) FEs (see fig.5) thus causing their partial ($\eta < 1$)

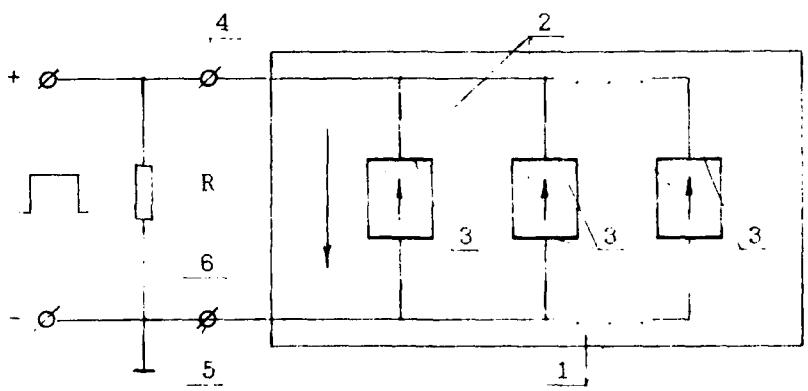


FIGURE 5 Ferroelectric detector connection to the load. 1 -ferroelectric detector; 2-ferroelectric elements; 3 -electrodes; 4,5 -detector terminals; 6 -load. Small arrows indicate ferroelectric polarization vectors in FE with '+' and '-' signed test pulse polarity,large arrow shows the electric field direction in ferroelectric.

switching for various values of $E_j = V * \mu_j$ ( $\mu_j$ is the known coefficient depending on the circuit connection and FE thickness), then V and T parameters can be calculated using (4) . For example, in the exponential case of $\tau$ (E) function , see eq.(1) , relation (4) is reduced to

$$T = \tau_\infty * \eta_j * \exp( \alpha * \mu_j * V^{-1}).$$

Next, by substituting to this equation $\eta_j$ and $\mu_j$ values for two different FEs , a set of two equation can be obtained and solved for V and T. With simple transformations we have (for j = k, l) :

$$V = \frac{( \mu_k - \mu_e )}{\ln( \eta_e / \eta_k )} ,$$

$$T = \tau_\infty * \eta_k * \exp( \frac{\mu_k * \ln( \eta_e / \eta_k )}{\mu_k - \mu_e} )$$

There may be more ways to solve the problem, such as graphically. Using the known values of $\eta_j$ and $\mu_j$ ,lg $\eta$ versus $\mu$ can be plotted in the coordinate plane (lg $\eta$ , $\mu$ ), then approximated by straight line as lg $\eta$ = a * $\mu$ + b ; thereby, a and b coefficients can be found. Then, by substituting the expressions for and into the resultant line equation, we reduce it to(2),i.e.

$$\lg \tau^{-1} =(a * V ) * E +(b - \lg T ) \qquad (5)$$

Hence, by comparing (2) and (5) find V = A / a and lg T = b - B.

Thus, the method considered is quite useful for measuring both amplitude and duration of the test rectangular pulse. The estimated measurement range provided by this technique is from about $10^{-7}$ to $10^{2}$ s in pulse duration (see fig.2) and from about $10^{1}$ to $10^{4}$ V by amplitude.

## References

1. J.C. Burfoot and G.W. Taylor, Polar Dielectrics and Their Applications (in Russian), ed. by L.A.Shuvalov, Moskow, Mir, 1981, 526p.

2. W.J.Merz. J.Appl. Phys., 27, 938 (1956).

3. E.Fatuzzo and W.J.Merz. Rhys.Rew., 116, 61 (1959).

# SECTION III
# CONTRIBUTED PAPERS

## IIIc. Sintering

*Ferroelectrics*, 1992, Vol. 133, pp. 265–270
Reprints available directly from the publisher
Photocopying permitted by license only
© 1992 Gordon and Breach Science Publishers S.A.
Printed in the United States of America

**ThP152**

# COMPUTER SIMULATION OF SINTERING AND FRACTURE OF THE FERROELECTRIC MATERIALS

DMITRY KARPINSKY, IVAN PARINOV and LIDIYA PARINOVA
Mechanics & Applied Mathematics Research Institute,
Rostov-on-Don University, Rostov-on-Don 344104, RUSSIA

Abstract Computer simulation is applied to microstructure and strength property researches of the PZT ceramics. The processes occuring in the ceramic under fracture are studied. Influence of the presspowder initial porosity on different parameters is evaluated.

## INTRODUCTION

Traditional analytical and numerical methods define basic tendencies of the physical and mechanical properties but they neglect by the some connected factors. On the other hand computer simulations allow to represent structure peculiarities of the material in computer form and to describe the processes which typical to given object.

It's known that microstructure of the real ferroelectric ceramic (FC) consists of the chaotic oriented grains, voids and thin glassy film between grains, partitially subjected to microcracking. The occurence of microcracks is associated with the residual stresses typically arising in FC at the Curie temperature due to the deformation phase mismatches.[1] Influence of defects on the strength parameters has discrepant nature.[2,3]

The aim of this article consists in investigation of the microstructure and different properties of the PZT ceramics on the basis computer simulations. We considered FC sintering, cooling and fracture by a macrocrack propagation.

## SINTERING AND COOLING

We used the physical model of gradient sintering for PZT compacts[4] and considered a connected problem of the heat conductivity and structure formation. It was supposed that sintering front with unit thickness was performed as a two-dimensional lattice containing 1000 cells arranged in square pattern. Temperature distribution in the furnace T depended on one coordinate X and consisted of a constant and linear temperature curve. Computer model contained next steps: 1) consideration the first basic problem for quasilinear equation of heat conductivity, 2) presspowder recrystallization in the sintering field, 3) shrinkage FC compact[4,5].

Then we simulated the sample cooling causing a microcracking the intergranular boundaries. We proposed that the microcracks propagate along the grain facets after them nucleation at triple junctions (see Figure 1). The microcracks were arrested at the neighbouring junctions because the adjacent boundary facets are generally subjected to compression.[6] Above the Curie point the thermal gradients may to cause a microcracking[5]. Below the Curie point the deformation mismatches between adjacent grains and thermal expansion anisotropy appear due to phase transition.[1] First is a main reason of the microcracking. Residual stresses decrease due to the reorientation of the 90° domain walls. Other unloading causes are the void existence and arising the arranged orientations of domain polar axises in the adjacent crystals.

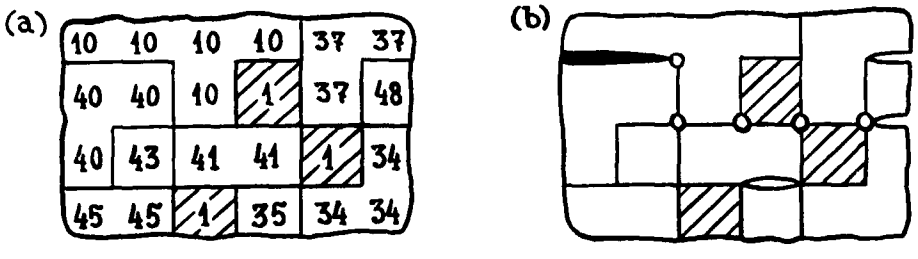


FIGURE 1 Macrocrack in the FC sample (a) FC structure fragment in computer form, (b) a macrocrack propagation in the FC specimen (circles), spontaneous crack (black) and microcracks in the process zone (white) are shown on the boundaries, porosity is shaded.

Spontaneous deformations establish local fluctuations of the residual stresses while middle stresses in the sample volume are equal to zero. Eshelby method and study of the domain structure influence allowed to find critical grain facet size by spontaneous fracture $l_c^s$. It was coincided with experimental values very well.[6,7] It was supposed that the cell side $\delta = l_c^s$. Criterion for the boundary microcrack l was caused by the misorientation of the grains:[6]
$l/l_c^s \geq 2/(1+\cos(2\Theta_1 - 2\Theta_2))$, where $\Theta_i (i=1,2)$ is the angle between the axis of maximum contraction in grain i and its boundary plane. For the calculation we used Monte-Carlo method.[4]

## MACROCRACK IN THE CERAMIC

Computer simulation of a macrocrack in the FC took into account an existence of the microcrack process zone near the crack tip. This zone had provided a crack shielding and transformation of the fracture toughness.[2,3,8,9] Both phenomenas were defined by microcracking peculiarities. Microcracks caused a maximal toughening when they normal to the maximum tensile direction and oriented parallely other to other and to crack plane. The toughening is increased together with the microcrack density $\beta_m$ and it can have significant effects on the observed fracture toughness and crack shielding. However, a microcrack coalescence is formed at the critical value of the density and causes a toughening decrease. As rule the critical microcrack density took by equal to 0.5.[2,3] We defined a process zone width as $2h_m$ by form[8] $h_m = A_m I_m^2$, where $I_m^2 = \beta_m E_m/(E-E_m)$ is the elastic crack interaction parameter and $E_m$. E is Young's modulus of the microcracked and uncracked material, $\beta_m = N_m A_m^3/V_m$, $N_m$ is the microcrack quantity in considered volume $V_m$. We used evaluations of elastic constants of the porous FC. They were found from modified cube model[11]

$$E = E_o(1-P^{2/3}) \quad ; \quad \nu = \nu_o(1-P^{2/3}) \qquad (1)$$

where P is the volume fraction of closed porosity; $E_o$, $\nu_o$ is Young's modulus and Poisson's ratio of FC without pores, respectively. For randomly oriented microcracks we had[10]

$$\frac{E_m}{E} = 1/(1+\frac{16(1-\nu^2)(10-3\nu)}{45(2-\nu)}\beta_m) \quad (2)$$

$$\frac{\nu_m}{\nu} = \frac{1+((16/45)(1-\nu^2)/(2-\nu))\beta_m}{1+((16/45)(1-\nu^2)(10-3\nu)/(2-\nu))\beta_m} \quad (3)$$

where $\nu$, $\nu_m$ are Poisson's ratios of sintered ceramic and material in the microcrack zone. We used Viterbi's algorithm and graph theory[12] for definition of the crack way. At the transition from one cadre to other process zone width and all triple junctions into zone were determined. Then we simulated the facet microcracks with length l. It was defined a critical facet size[2]: $l_c=0.4l_c^s$ and l modelling procedure repeated the algorithm used by the spontaneous cracking. We caused that the microcracks didn't cross a macrocrack and an absence of microcrack coalescence. The graph arcs $C_{ij}$ were given by[12]

$$C_{ij}=\begin{cases} 0, & i=j \text{ or at the favourably oriented microcrack,} \\ 2d, & i,j \text{ are adjacent points on the grain boundary,} \\ L_p, & i,j \text{ belong to one pore,} \\ L_m, & \text{at the unfavourably oriented microcrack,} \\ \infty & \text{in the other cases} \end{cases} \quad (4)$$

here $C_{ij}\neq C_{ji}$, $L_p$ is the pore boundary length, $L_m$ is the microcrack boundary length. An invariance of the J-integral allowed to estimate a ceramic fracture toughness[2]

$$\frac{K_{Ic}^{\infty}}{K_{Ic}^{o}} = (1-f_m)\sqrt{\frac{1-((16/45)(1-\nu^2)(10-3\nu)/(2-\nu))f_{\infty}}{1-((16/45)(1-\nu^2)(10-3\nu)/(2-\nu))f_m}} \quad (5)$$

where $K_{Ic}^{\infty}$, $K_{Ic}^{o}$ is the FC fracture toughness with and without microcracking, respectively, $f_{\infty}$ is the fraction of spontaneous microcracking, $f_m$ is the fraction of microcracked facets in the process zone. Besides, the first factor in the right part defined a local toughening $K_{Ic}^{1}/K_{Ic}^{o}$. Cracked facet fractions for two dimensional microcrack distribution had forms

$$f_m = \frac{N_m S}{2h_m L N_g} \quad ; \quad f_{\infty} = \frac{N_{\infty}}{N_g} \quad (6)$$

where $N_{\infty}$, $N_g$ is the microcrack number caused by the spontaneous fracture and intergranular boundary quantity at the san-

ple square S, respectively, L is the macrocrack way length.

Crack shielding was estimated on the basis macrocrack propagation under monotonically increasing load:[9]

$$\frac{K_I^o}{K_I^\infty} = \left[\frac{(1-\nu^2)E_m}{(1-\nu_m^2)E}\right]^{1/2} \qquad (7)$$

where $K_I^o$ is the plane strain stress intensity factor at the crack tip, $K_I^\infty$ the apparent stress intensity factor. A necessary number of the computer realizations was established on the basis of the stereology method.[13]

## DISCUSSION AND CONCLUSIONS

Results of computer simulation the properties of gradient sintered PZT (E=70GPa, $\nu$=0.25[1]) in dependence from initial porosity $C_p^o$ were received. They are shown in the Table I.

TABLE I Computer simulation results

| Properties | $C_p^o$= 0% | $C_p^o$=10% | $C_p^o$=20% | $C_p^o$=30% | $C_p^o$=40% | $C_p^o$=50% | $C_p^o$=60% |
|---|---|---|---|---|---|---|---|
| $k_\Delta$ | 0.00 | 0.02 | 0.04 | 0.14 | 0.28 | 0.43 | 0.54 |
| $R_c/R_c^o$ | 1.00 | 0.94 | 0.90 | 0.84 | 0.83 | 0.79 | 0.74 |
| $f_\infty$ | 0.12 | 0.11 | 0.10 | 0.10 | 0.10 | 0.09 | 0.08 |
| $f_m$ | 0.11 | 0.17<br>0.16 | 0.19<br>0.19 | 0.21<br>0.21 | 0.24<br>0.23 | 0.17<br>0.16 | 0.17<br>0.16 |
| $K_{Ic}^1/K_{Ic}^o$ | 0.89 | 0.83<br>0.84 | 0.81<br>0.81 | 0.79<br>0.79 | 0.76<br>0.77 | 0.83<br>0.84 | 0.83<br>0.84 |
| $K_{Ic}^\infty/K_{Ic}^o$ | 0.88 | 0.90<br>0.89 | 0.91<br>0.90 | 0.91<br>0.91 | 0.92<br>0.91 | 0.92<br>0.91 | 0.93<br>0.92 |
| $K_I^o/K_I$ | 0.91 | 0.86<br>0.87 | 0.85<br>0.86 | 0.83<br>0.84 | 0.82<br>0.83 | 0.86<br>0.87 | 0.86<br>0.87 |

At upper lines the data for elastic constants don't depending from closed porosity are represented. Lower lines correspond to modified constants (see formulae (1)), where $E_o$=70GPa, $\nu_o$=0.25 and $P=n_{cp}/(n_{cp}+n_{cr})$. Shrinkage koefficient $k_\Delta=n_{op}/(n_{op}+n_{cp}+n_{cr})$ grows with $C_p^o$. Here $n_{op}$, $n_{cp}$, $n_{cr}$ is the cell number of the open, closed porosity and grain phase, respectively. However, decrease of the grain size $R_c$ to compensates $k_\Delta$ increase. This result to causes the close values

of the P for all considered cases of the porous FC. Grain size decrease establishes a spontaneous cracking decrease $f_\infty$ but behaviour of the microcrack process zone demonstrates a discrepant nature. It was reached maximum at the $C_p^o$=40%. Local toughening $K_{Ic}^1/K_{Ic}^o$ and crack shielding $K_I^o/K_I^\infty$ had not monotonical dependences on $C_p^o$, too. Analogous behaviour had been known for fracture energy.[1] Stress intensity decrease at the macrocrack tip coincide with observed tendency[10] and it's caused by the microcrack process zone. Joint influence $f_\infty$ and $f_m$ on the fracture toughness $K_{Ic}^\infty/K_{Ic}^o$ to level marked behaviour and to increase the fracture toughness with $C_p^o$. Received fracture toughness is close to ≃0.9. It's coincided with value for $Al_2O_3$.[3] It's noted that the strength parameters depend on the $C_p^o$ weakly. Thus closed porosity P is a more important for toughness in comparison to the $C_p^o$ and $R_c$.

## REFERENCES


1. G.G. Pisarenko, Prochnost Piezokeramiki (Naukova Dumka, Kiev, 1987), pp. 38, 175 (in Russian).
2. Y. Fu and A.G. Evans, Acta Metallugica, 30, 1619 (1982).
3. A.G. Evans and Y. Fu, Acta Metallurgica, 33, 1525 (1985).
4. A.V. Belyaev, D.N. Karpinsky, S.O. Kramarov and I.A. Parinov, Rep. North-Caucasus Sci. Centre High School. Nature Sciences (USSR), N 4, 66 (1989) (in Russian).
5. D.N. Karpinsky and I.A. Parinov, Izv. AN USSR. J. Priklad. Mech. Techn. Phiz., to be published (in Russian).
6. Y. Fu and A.G. Evans, Acta Metallurgica, 33, 1515 (1985).
7. E.I. Bondarenko, V.D. Komarov, L.A. Reznichenko and V.A. Chernishkov, Izv. AN USSR. J. Techn. Phiz., 58, 1771 (1988) (in Russian).
8. F.E. Buresh, Proc. Int. Conf. on Residual Stress. Sci. and Techn., Garmish-Partenkirchen, 1986, 1, Oberursel, 1987, pp. 539-543.
9. N. Laws and J.R. Brockenbrough, Trans. ASME: J. Eng. Mater. Technol., 110, 101 (1988).
10. N.B. Romalis and V.P. Tamuzh, Razrushenie Strukturno-Neodnorodnih Tel (Zinatne,Riga,1989), p.59 (in Russian).
11. Hisao Banno, Am. Ceram. Soc. Bull., 66, 1332 (1987).
12. D.N. Karpinsky and I.A. Parinov, Izv. AN UkrSSR. Problemi Prochnosti, N 7, 34 (1991) (in Russian).
13. K.S. Chernyavsky, Stereologiya v Metallovedenii (Metallurgiya, Moskva, 1977), pp. 36-37 (in Russian).

*Ferroelectrics*, 1992, Vol. 133, pp. 271–276
Reprints available directly from the publisher
Photocopying permitted by license only

© 1992 Gordon and Breach Science Publishers S.A.
Printed in the United States of America

**SmC5**

# HYDROTHERMALLY PROCESSED PIEZOELECTRIC AND ELECTROSTRICTIVE CERAMICS

C. E. MILLAR, L. PEDERSEN and W. W. WOLNY.
Ferroperm A/S, Hejreskovvej 6, 3490 Kvistgård, Denmark.

Abstract Lead titanate and lead magnesium niobate ceramics are fabricated from powders prepared by hydrothermal synthesis. The results of powder and ceramic characterisation are presented and compared with similar data obtained for ceramics fabrication by conventional mixed oxides.

## INTRODUCTION.

In recent years considerable effort has been concentrated into the preparation of fine powders. Of the techniques studied, hydrothermal synthesis (H.S) has shown promise as a method of obtaining high quality, submicron powders at a relatively low cost. Furthermore, for lead containing materials, the elimination of the calcination step and lowering of the sintering temperature reduces lead loss thus giving improved compositional control.

The object of this study was to develop a simple powder preparation route and to fabricate fine grained electroceramics. Two types of material have been studied: a modified lead titanate composition, for piezoelectric applications, and compositions in the lead magnesium niobate-lead titanate (PMN - PT) system suitable for electrostrictive applications.

## EXPERIMENTAL.

### Lead Titanate Powders

Two compositions of lead titanate were prepared, namely: $PbTiO_3$ and $(Pb_{0.88}, Sm_{0.08})(Ti_{0.98}, Mn_{0.02})O_3$, hereafter PT(Sm).

The $PbTiO_3$ suspensions, with concentration 0.5 M, were

prepared by adding a $Pb(NO_3)_2$ solution to a stirred suspension of fine $TiO_2$ powder in de-ionised water, Figure 1(a). The pH was then adjusted to 10 using NaOH solution. For the PT(Sm) composition, samarium and manganese nitrates were dissolved in water and mixed with the lead nitrate solution before addition to the $TiO_2$ suspension.

(1-x)PMN-xPT Powders

Powders were prepared with compositions: x = 0, 0.1, 0.2, 0.3 and 0.4 by a procedure similar to that described for $PbTiO_3$. The $Pb(NO_3)_2$ solution was added to a suspension of either $Nb_2O_5$ for PMN (x = 0), Figure 1(b), or to a mixture of $Nb_2O_5$ and $TiO_2$ for PMN-PT (x = 0.1-0.4). Again NaOH was added to achieve a pH of 10.

In addition, following the method used for mixed oxide powders[1], the $Pb(NO_3)_2$ solution was added to a columbite ($MgNb_2O_6$) powder, which had previously been prepared by a mixed oxides route.

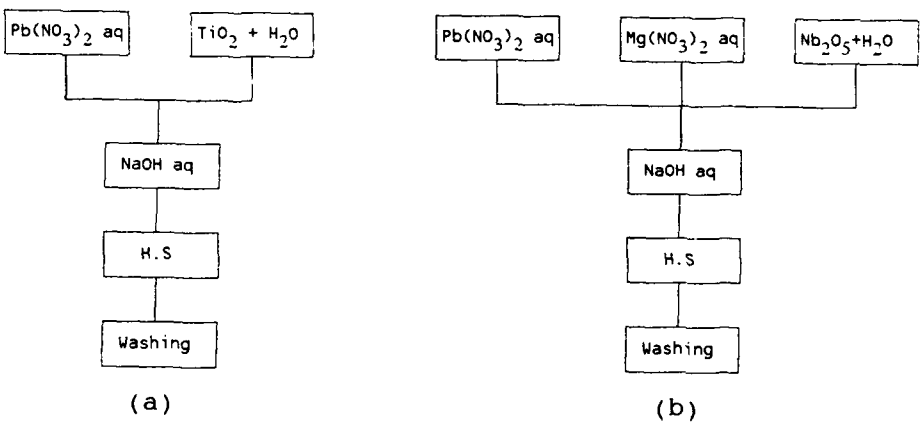


FIGURE 1 Process diagrams for hydrothermal synthesis of (a) $PbTiO_3$ and (b) PMN powders.

Hydrothermal Synthesis

The 0.5 M suspensions were then placed into a 4 litre autoclave. Hydrothermal synthesis were carried out for 10 hours at temperatures between 200-300 °C (P = 2-8 MPa). The resulting powders were washed repeatedly to remove the nitrates and sodium ions, and then dried for 24 hours.

X-ray diffraction was used to determine the crystal structure, and Scanning electron microscopy, SEM was used to examine particle size and morphology.

Fabrication of ceramics

The lead titanate powders were dry pressed into discs, which were sintered at temperatures between 1100 and 1200 °C for 1 or 2 hours. The discs were poled at 130 °C for 10 minutes with an electric field of 8 kV/mm. After ageing for 24 hours, the dielectric properties and piezoelectric coupling coefficient were measured.

For the purposes of comparison a powder with composition PT(Sm) was prepared by a conventional mixed oxide route (M.O) and discs pressed from the calcined powder were sintered at 1240 °C for 1 hour.

The hydrothermal PMN and PMN-PT powders were heat treated at 800 °C for 4 hours in order to increase the perovskite content of the powders. After heat treatment they were milled for 8 hours before binder addition. Sintering of pressed discs was carried out at 1000 - 1150 °C for 1 hour.

RESULTS AND DISCUSSION.

Lead titanate.

For the hydrothermal conditions used, the reaction temperature required to produce the perovskite phase was 270 °C for $PbTiO_3$. This was increased to 300 °C for the modified lead titanate, PT(Sm). Lower reaction temperatures than these resulted in a mixture of the PY ($Pb_2Ti_2O_6$) and PX the phase reported by Suzuki et al[2].

The perovskite powders of $PbTiO_3$ and PT(Sm) were submicron, with particle size 0.1 - 0.2 μm, as shown in Figure 2(a).

The highest density, 98 % of theoretical density, was obtained for PT(Sm) sintered at 1150 °C for 2h. An SEM micrograph of the ceramic is shown in Figure 2(b). The grain size, G, is approximately 1 μm. The sintering

temperature was 90 °C lower than that required for the same composition prepared by the conventional mixed oxide route.

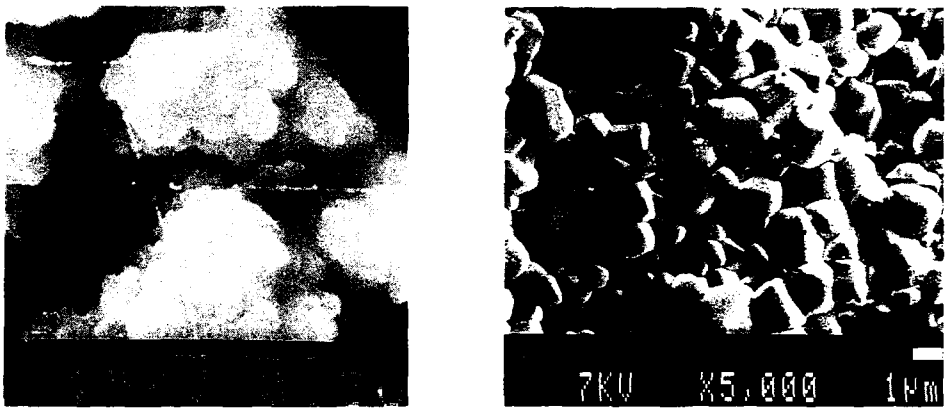


FIGURE 2 (a) PT(Sm) powder prepared by hydrothermal synthesis. (b) Ceramic fabricated from PT(Sm) powder, sintered at 1150 °C.

Similar dielectric and piezoelectric values were obtained for PT(Sm) sintered at 1150 °C and the ceramic prepared from mixed oxide powder as shown in Table 1. The advantages of the ceramics prepared from hydrothermal powders lie in their reduced dielectric loss, probably owing to improved distribution of the manganese, lower sintering temperature and finer grain size.

Table 1. Comparison between PT(Sm) prepared by hydrothermal synthesis and by conventional mixed oxides.

| | $\varepsilon_r$ | tanδ | $k_t$ | G/μm |
|---|---|---|---|---|
| PT(Sm)-H.S | 187 | 0.009 | 42 | <1 |
| PT(SM)-M.O | 200 | 0.019 | 40 | 0.5-2 |

* $k_p$ of both materials was < 3.

(1-x)PMN-xPT

Hydrothermal synthesis of the PMN and PMN-PT compositions was carried out at 300 °C for 10 hours. These conditions were based on results obtained by Krarup[3].

To produce high permittivity PMN ceramics, it is necessary to minimise the pyrochlore content. Unfortunately, all reported attempts to produce PMN by hydrothermal synthesis have resulted in obtaining 100 % pyrochlore[3,4]. The results obtained here were consistent with this for pure PMN. However, powders containing PT (x = 0.1-0.4) comprised a mixture of perovskite and pyrochlore phases, as shown in Figure 3. The powder with composition 0.7PMN-0.3PT had the highest perovskite content of 55 %.

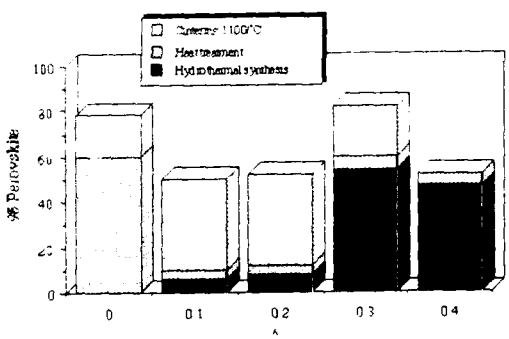


Figure 3 Perovskite content of PMN-PT.

Figure 4 SEM micrograph of 0.7PMN-0.3PT powder.

SEM examination of the powders showed that the pyrochlore phase was present as large plates, up to 10 μm in size, and the perovskite as fine particles, < 1 μm, situated on the plates. The SEM micrograph of the 0.7PMN-0.3PT powder presented in Figure 4 shows the morphology of the 2 phases.

The increase in perovskite content of powders after the heat treatment of 800 °C for 4 h is also presented in Figure 3. It was interesting to note that the perovskite

content of PMN powders prepared from the columbite precursor increased to 60 %, whereas PMN powders prepared using a mixture of $Nb_2O_5$ powder and $Mg(NO_3)_2$ increased to only 30 % (not shown in Figure 3). This result is consistent with that obtained by Yamamoto[4]. The heat treatment had little effect on the powders containing PT.

At present it has not been possible to sinter dense ceramics from these powders due to their high pyrochlore content. On sintering the perovskite content of the ceramics was further increased as shown in Figure 3.

## CONCLUSIONS

1) A simple route, based on $TiO_2$, has been developed for the hydrothermal synthesis of lead titanate powders. The resulting powders have a particle size of approximately 0.1 μm.

2) High density, fine grained ceramics were obtained at a low sintering temperature from the PT(Sm). These ceramics had a high $k_t/K_p$ ratio and very low dielectric loss.

3) Hydrothermal synthesis shows less promise as a method of producing PMN powders due to the formation of the pyrochlore phase. However using columbite powder as a starting material together with a heat treatment, the perovskite content of the powder was increased considerably. Alternatively, additions of PT promoted the formation of the perovskite phase during synthesis.

## REFERENCES

1. S. L. Swartz and T. R. Shrout. Mat. Res. Bull, vol 17 1245 (1982).
2. M. Suzuki, S. Uedaira, h. Masuya and H. Tamura. Ceram. Trans: Ceramic Powder Science II vol I 163 (1988).
3. H Krarup. Private Communications.
4. T. Yamamoto, Y Shimizu andf M. Watanabe ISAF 4 (1990)

## ACKNOWLEDGEMENTS

This work was funded by Brite/Euram project, contract number 0504 and the Danish Centre for Advanced Technical Ceramics.

*Ferroelectrics*, 1992, Vol. 133, pp. 277–282
Reprints available directly from the publisher
Photocopying permitted by license only

© 1992 Gordon and Breach Science Publishers S.A.
Printed in the United States of America

# SmC11

## EFFECT OF $V_2O_5$ ON DIELECTRIC PROPERTIES OF $Pb(Mg_{1/3}Nb_{2/3})O_3$ - $PbTiO_3$ CERAMICS

KI HYUN YOON, JAE HYUK CHUNG and DONG HEON KANG*
*Department of Ceramic Engineering, Yonsei University, Seoul, Korea*
**Department of Electronic Materials Engineering, Suwon University, Suwon, Korea*

Abstract Dielectric properties and sinterability of $Pb(Mg_{1/3}Nb_{2/3})O_3$ - $PbTiO_3$ ceramics prepared by KCl-NaCl molten salt synthesis have been investigated as a function of the amount of $V_2O_5$. Even though the calcination temperature was around 750°C, the perovskite phase was synthesized about 97%.As the amount of $V_2O_5$ increased up to 0.25 wt%, the density approaching 97% of the theoretical value was achieved at 1100°C, with maximum dielectric constant of 22000. However, the further addition of $V_2O_5$ decreased sinterability and dielectric properties. These results can be explained by the analysis of phase present and microstructure.

## INTRODUCTION

Complex perovskite compounds based on $Pb(Mg_{1/3}Nb_{2/3})O_3$ - $PbTiO_3$ (PMN-PT) systems are current interest for electrostrictors and capacitors due to the large field induced strain and high dielectric constant(K).[1-4] Previous studies[5,6] in the system have been concerned with processing characteristics and dielectric properties.

Various methods such as the conventional mixed oxide method including precalcination of columbite[2] and the wet chemical process[7] have been applied in order to avoid the formation of pyrochlore phase and prepare the reactive powder at lower temperatures. Also, the effect of liquid phase sintering on the microstructure and dielectric properties of PMN-PT ceramics has been studied by adding $Bi_2O_3/Li_2O$[8] and excess PbO[9,10] as sintering aid.

This study introduces the molten salt synthesis method using the eutectic salt mixture of 0.5KCl-0.5NaCl in preparing 0.9PMN-0.1PT powders. And then the dielectric properties and sinterability of PMN-PT ceramics have been investigated as a function of the amount of $V_2O_5$ .

## EXPERIMENTAL PROCEDURE

For preparing 0.9PMN-0.1PT powders with $V_2O_5$ in the range of 0 to 1.0 wt%, reagent grade PbO, MgO, $Nb_2O_5$, $TiO_2$ and $V_2O_5$ were mixed with 0.5KCl-0.5NaCl in the ratio of 0.5 (wt.of salts/wt.of raw materials) and then ball milled for 20h in ethanol.

The oxides-salt mixtures were calcined at 650-850°C for a soaking time of 1h with a heating rate of 300°C/h. The salt was washed with deionized water until no free $Cl^-$ ions were detected using $AgNO_3$ solution. The powders calcined at 750°C were mixed with PVA binder and pressed into the form of disks of 12 mm diameter, under 1500kg/cm$^2$, using a uniaxial press. Following binder burnout at 500°C, the disks were sintered at temperatures ranging from 950 to 1200°C for 4h. The disks were buried in calcined powder to minimize PbO weight loss. The determinations of pyrochlore phase and lattice parameter by X-ray analysis can be found in References 11 and 12. The microstructure was observed by SEM equipped with an EDS analyzer.

Dielectric properties were measured from the sintered pellets with Ag electrodes fired at 470°C and obtained from a LCR meter and temperature controller.

## RESULTS AND DISCUSSION

Fig.1 shows the variation of the perovskite phase in PMN-PT powders prepared by molten salt synthesis method as a function of calcination temperature. The percentage

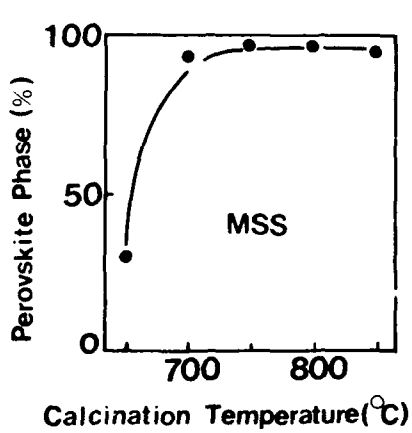


FIGURE 1 Percentage of perovskite phase vs. calcination temperature for 0.9PMN-0.1PT powders prepared by molten salt synthesis method.

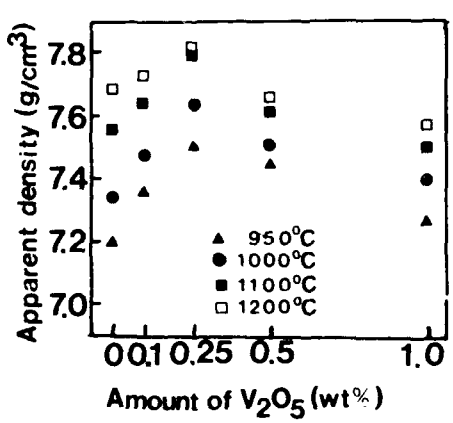


FIGURE 2 Apparent density vs. amount of $V_2O_5$ for 0.9PMN-0.1PT specimens sintered at various temperatures.

of the perovskite phase formed was about 20% at 650°C. Only 3% of the pyrochlore phase exists at the calcination temperature of 750°C despite a shorter soaking time, 1h. And[illegible] et al.[7] reported that in case of 0.9PMN-0.1PT powders with 5 mol% excess MgO prepared by oxalate process, the perovskite phase began to form at about 660°C and became nearly 50% at 750°C. A lower amount (20-30%) of the perovskite phase was formed by the simple mixed oxide process for the PMN-PT ceramics. Thus, these results can be explained by the higher diffusivities and reactivities of the oxide powders in KCl-NaCl molten salts as reported earlier on PMN prepared by KCl salt[12]. As the content of $V_2O_5$ increased, the perovskite phase was kept constant at about 97%. However, the pyrochlore phase was slightly increased when $V_2O_5$ exceeded 0.5 wt%.

In Fig.2, the densities of the PMN-PT specimens sintered at various temperatures are plotted as a function of $V_2O_5$ content. It shows that the addition of $V_2O_5$ up to 0.25 wt% improves densification at all sintering temperatures, but further addition of $V_2O_5$ decreases it. A relative density around 97% of the theoretical value was obtained at 1100°C with the addition of 0.25 wt% $V_2O_5$, which is comparable to that of specimens sintered at 1200°C as shown in Fig.2.

Typical SEM photographs of the specimens sintered at 1100°C with different amounts of $V_2O_5$ are shown in Fig.3. It is clear that the grain size increased greatly

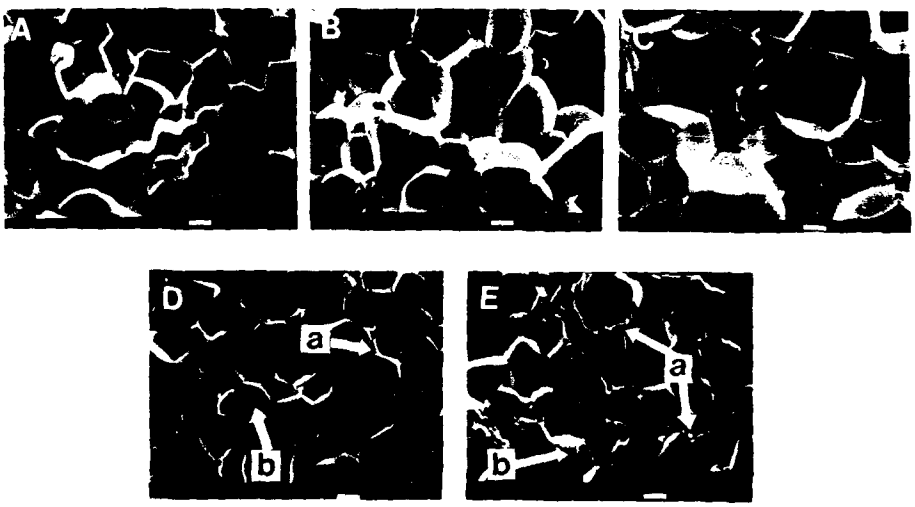


FIGURE 3 SEM photographs of 0.9PMN-0.1PT specimens sintered at 1100°C for 4h as a function of the amount of $V_2O_5$. A) pure, B) 0.1 wt%, C) 0.25 wt%, D) 0.5 wt% and E) 1.0 wt% (bar=2μm)

with the addition of $V_2O_5$ up to 0.25 wt% and that good densification is achieved as confirmed by the microstructure. Above 0.5 wt% $V_2O_5$, the grain growth was inhibited , and the precipitated second phase in grain boundary region was evident as shown in Fig.3-(D,E). From EDS analysis in Fig.4, it was found that the second phase(Fig.4-(a)) is enriched with vanadium, other than the grain region in Fig.4-(b). According to these results, the liquid phase formed by lower-melting $V_2O_5$ during sintering process improved densification and grain growth. However, the formation of a lower-density second phase, namely the excess liquid phase, resulted in the grain growth inhibitation and the decrease in density as shown in Figs.2,3 and 4. Also, the microstructures of specimens sintered at other temperatures showed similar tendencies. Wittmer *et al.*[13] reported that the addition of $V_2O_5$ made it possible to sinter the PZT ceramics at 950-1000°C, and with higher than 0.5 wt% $V_2O_5$ to stoichiometric PZT, the density decreased due to the formation of second phase. Chen *et al.*[14] studied the liquid phase sintering of $SrTiO_3$ at 1250°C with the use of 2-4 wt% $V_2O_5$.

Fig.5 shows the temperature dependence of the dielectric constant for the specimens sintered at 1100°C as a function of the amount of $V_2O_5$ . As shown in Fig.5, the diffuse character of the transition was enhanced by the addition of $V_2O_5$ . The calculated diffuseness coefficient, $\delta$, based on the compositional fluctuation model of Kirillov *et al.*[15], increased from ~50 to ~82 with increasing amount of $V_2O_5$ . A large increase in the dielectric constant was achieved by adding 0.25 wt% $V_2O_5$ , but the dielectric constant decreased with further addition of $V_2O_5$. The increase in the dielectric constant is likely due to the increase of density and grain size as shown in Figs. 2 and 3. The similar effect of density and grain size on the dielectric properties of Pb-based

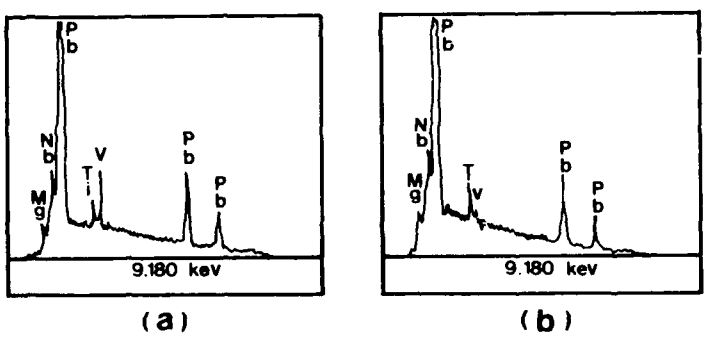


FIGURE 4 EDS analysis for 0.9PMN-0.1PT specimens added with 0.5 wt% and 1.0 wt% $V_2O_5$
a) grain boundary, b) grain region

ferroelectrics has been reported by many investigators.[2,10,11] The decrease in the dielectric constant with increasing $V_2O_5$ above 0.5 wt% is ascribed to the grain growth inhibitation and the density reduction, resulting from the precipitation of vanadium rich second phase. Additionally, the increase of the pyrochlore phase degraded the dielectric properties. The tanδ for PMN-PT specimens with various $V_2O_5$ content was stable at 0.01-0.015 above the Curie temperature.

Fig. 6 shows the variation of the Curie temperature and lattice constant as a function of the amount of $V_2O_5$ at various sintering temperatures. The Curie temperature decreased exponentially by the addition of $V_2O_5$. When the amount of $V_2O_5$ exceeded 0.5 wt%, the shift of the Curie temperature ceased. Besides, The Curie temperature also shifted downward under higher sintering temperatures as shown in Fig.6. The reduction of the Curie temperature is probably due to the cell contraction of PMN-PT ceramics, which results from the substitution of B site ions in PMN-PT lattices by vanadium ion (0.54 Å). Above 0.5 wt%, the Curie temperature hardly varied with the $V_2O_5$ content, likely due to the saturation of vanadium ion in lattice as confirmed by the variation of lattice constant in Fig.6.[16,17]

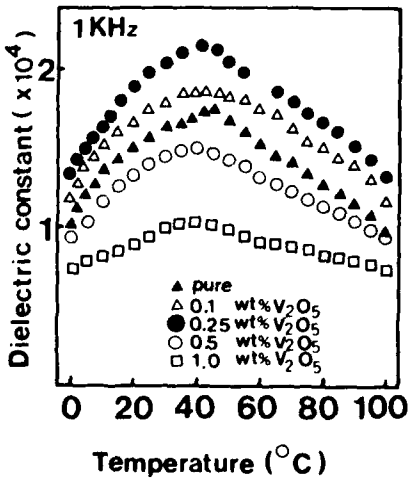


FIGURE 5 Dielectric constant vs. temperature for 0.9PMN-0.1PT specimens sintered at 1100°C for 4h as a function of the amount of $V_2O_5$.

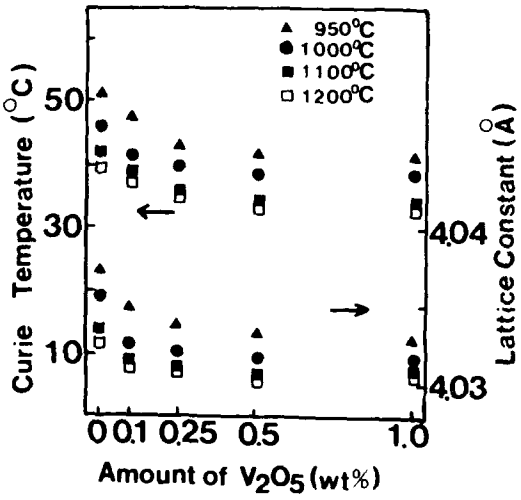


FIGURE 6 Curie temperature and lattice constant vs. amount of $V_2O_5$ for the specimens sintered at various temperatures.

## CONCLUSIONS

1) In the case of the 0.9PMN-0.1PT powders prepared by KCl-NaCl molten salt synthesis, the perovskite phase formed at a low calcining temperature of 750°C for 1 h was about 97%.

2) With increasing amount of $V_2O_5$ , both the density and dielectric constant increased sharply and reached the maximum values at 0.25 wt%. The further addition of $V_2O_5$ decreased the sintering and dielectric properties, in association with changes in grain size, perovskite phase, and the precipitated second phase.

ACKNOWLEDGEMENT

This work was supported by the Ministry of Education Research Fund for Advanced Materials in 1991

## REFERENCES

1. T. R. Shrout and A. Halliyal, *Am. Ceram. Soc. Bull.*, 66 (4) 704 (1987).
2. S. L. Swartz, T. R. Shrout, W. A. Schulze and L. E. Cross, *J. Am. Ceram. Soc.*, 67 (5) 311 (1984).
3. K. Furukawa, S. Fujiwara and T. Ogasawara, p.T-4 in Proceedings of Japan-US Study Seminar on Dielectric and Piezoelectric Ceramics (1982).
4. K. Uchino, *Am. Ceram. Soc. Bull.*, 65 (4) 647 (1986).
5. M. Lejeune and J. P. Boilot, *Mater. Res. Bull.*, 20, 493 (1985).
6. D. J. Voss, S. L. Swartz and T. R. Shrout, *Ferroelectrics*, 50, 203 (1983).
7. T. Ando, R. Suyama and K. Tanemoto, *Jpn. J. Appl. Phys.*, 30 (4) 775 (1991).
8. G. F. Chen and S. L. Fu, *J. Mater. Sci.*, 25, 424 (1990).
9. J. P. Guha, D. J. Hong and H. U. Anderson, *J. Am. Ceram. Soc.*, 71 (3) C-152 (1988).
10. D. H. Kang and K. H. Yoon, *J. Mater. Sci.*, 26, 56 (1991).
11. D. H. Kang and K. H. Yoon, *Ferroelectrics*, 87, 255 (1988).
12. K. H. Yoon, C. K. Kwak and D. H. Kang, *Ferroelectrics*, 116, 231 (1991).
13. D. E. Wittmer and R. C. Buchanan, *J. Am. Ceram. Soc.*, 64 (8) 485 (1981).
14. J. S. Chen, R. J. Young and T. B. Wu, *J. Am. Ceram. Soc.*,70 (10) C-260(1987).
15. V. V. Kirillov and V. A.Isupov, *Ferroelectrics*, 5, 3 (1973).
16. M. Halmi, G. Desgardin and B. Raveau, *Adv. Ceram. Mater.*, 3 (1) 32 (1988).
17. S. L. Fu and G. F. Chen, *Am. Ceram. Soc. Bull.*, 66 (9) 1397 (1987).

*Ferroelectrics*, 1992, Vol. 133, pp. 283–288
Reprints available directly from the publisher
Photocopying permitted by license only
© 1992 Gordon and Breach Science Publishers S.A.
Printed in the United States of America

## SmP104

# EFFECT OF THE INITIAL PARTICLE SIZE ON THE DIELECTRIC PROPERTIES OF $Pb(Fe_{1/2}Nb_{1/2})O_3$ CERAMICS

KYUNG BONG PARK* AND KI HYUN YOON
Department of Ceramic Engineering, Yonsei University, Seoul, Korea

**Abstract** Effect of the initial particle size on the sintering and dielectric properties of $Pb(Fe_{1/2}Nb_{1/2})O_3$ prepared by the molten salt synthesis method using an equimolar mixture of NaCl-KCl flux has been investigated. As the weight ratio of the NaCl-KCl flux to the raw materials increases, the average particle size decreases and the particle size distribution tends to narrow due to the uniform reaction. The density and dielectric constant increase with decreasing the initial particle size. This result can be explained by the variation of microstructure during the sintering of $Pb(Fe_{1/2}Nb_{1/2})O_3$ ceramics.

## INTRODUCTION

It is reported that the powder characteristics such as an initial particle size, particle size distribution and particle morphology play an important role in the densification of powder during the sintering of ceramics.[1] The variation of free energy resulting in the densification of particle is caused by the reduction of the surface area and surface energy due to the removal of the solid-vapor interfaces.[2] Therefore, the smaller the particle sizes are, the more the surface energy is, which improves the densification. However, the submicron sized powders are very agglomerated by the attraction forces between the particles, which have reverse effects on the sintered density.[3] Accordingly, it is very important that the fine particle powder with less agglomerates is prepared using relatively simple method. The molten salt synthesis (MSS) method is based on the molten salt to act as the medium of reaction between the constituents, and therefore, it requires the accompanying salt-washing procedure in comparison with the conventional calcining of mixed oxide (CMO) method.[4] Because of the small diffusion distance between constituent oxides, the reaction can be proceeded effectively a very short time.

*Present address : Department of Materials Engineering,
Andong National University, Andong, Korea

It can also have great merits in the control of particle size and powder morphology and the low temperature synthesis, as reported by Kimura et al.[5] In the laboratory, $BaTiO_3$[6] and $Pb(Mg_{1/3}Nb_{2/3})O_3$(PMN)[7] were prepared by the MSS method using KCl flux.

Therefore, in this report, the $Pb(Fe_{1/2}Nb_{1/2})O_3$(hereafter designated PFN) powders with different particle sizes and particle size distributions are prepared using the MSS method with the different weight ratios of flux to raw materials. The sintering and dielectric properties of PFN ceramics prepared with different powder properties have also been investigated.

## EXPERIMENTAL

The raw materials used were PbO, $Fe_2O_3$ and $Nb_2O_5$ with purities of above 99.9%. An equimolar mixture of NaCl-KCl was used as a source of flux, and the weight ratio of flux to the raw materials(defined as W) was varied from 0.1 to 1.0. In order to reduce the dielectric loss, 0.25wt% $MnO_2$ was added to all compositions. The mixtures were calcined at 800°C for 1h. The calcined powders were washed with hot deionized water until no $Cl^-$ ions were detected using $AgNO_3$ solution. The washed powders were pressed into pellets isostatically at 20,000 psi. The pressed pellets were sintered at temperature ranging from 900°C to 1050°C for 4hrs. In order to minimize PbO loss, the pellets were covered with the powders of the same composition. Samples for dielectric measurements were ground parallel and electrodes were applied by firing on silver electrode at 590°C.

The average particle size and distribution were examined using the laser diffraction method. The density of sintered specimens was measured using the water-immersion method.[8] The powder morphology and the polished surface of sintered specimens were examined by scanning electron microscopy(SEM). Dielectric properties were measured by an LCR meter at 1kHz with a temperature controller.

## RESULTS AND DISCUSSION

Figure 1 shows the SEM micrographs and particle size distributions of PFN powders prepared at 800°C for 1h with various amounts of flux. As shown in Fig.1, the MSS powders have less agglomerates and the morphology of the cubic-like

phase. As the flux weight ratio increases, the particle size distribution with bimodal form tends to narrow, and the average particle size decreases. When the flux weight ratio is very small(W=0.1), the particle grows abnormally resulting from the maldistribution of salt. The reaction occurs uniformly with increasing the flux weight ratio, and the particle shows the small size with narrower distributions. Yoon et al. reported [6] that as the flux weight ratio increased, the particle size was small and the particle size distribution tended to narrow, in the preparation of $BaTiO_3$ powders by the MSS method, which was similar to this result. In the preparation of ferrite and $PbNb_2O_6$ by the MSS method, Kimura et al.[9] reported that the angular particles could be produced rather than the spherical particles. In this experiment, the particles also have the cubic-like morphology by the effect of chloride salt. The variation of the flux weight ratio has little effect on the ability to form the perovskite PFN phase.

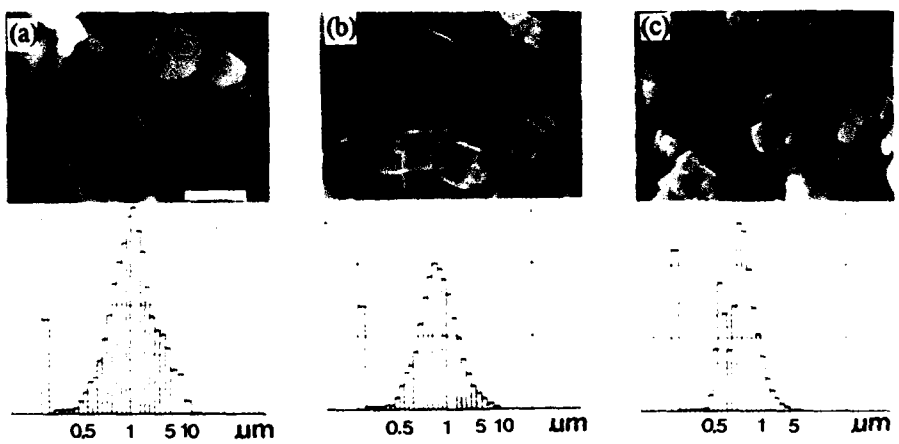


FIGURE 1 SEM photographs and particle size distribution of PFN powders prepared by the MSS method ;(a)W=0.1, (b)W=0.5 and (c)W=1.0 (bar=1μm).

On the other hand, the results of the atomic absorption spectroscopy about the CMO powder and MSS powder prepared by W=1.0 show that the major impurities were $Na^+$ and $K^+$ ions and the concentration of the impurities in the MSS powders was 300-500ppm, which was 2-3 times higher than in the CMO powders. This may be due to the substitution of $Na^+$ and $K^+$ for $Pb^{2+}$.

Figure 2 (a) and (b) show the variation of linear shrinkage and apparent density in PFN ceramics as a function of sintering temperature, respectively. The linear

shrinkage increased with increasing the flux weight ratio to raw materials(W). According to the reports by Onoda and Messing,[10] for binary powder mixtures, as the fraction of large particle increases, the small particles tend to fill some of the interstitial sites within the large particle matrix. That is, the shrinkage is initially controlled by sintering of the small particles until the large particles come into contact and control further shrinkage. Therefore, in this experiments, the specimens prepared using the initial particles with more portion of fine particles have the large linear shrinkage. The density shows the trends similar to the variation of the linear shrinkage. The slight decrease of density may be caused by the PbO loss, which is similar to the reports of Kassarijian et al. about the PFN-$Pb(Zn_{1/3}Nb_{2/3})O_3$-$Pb(Fe_{2/3}W_{1/3})O_3$ system.[11]

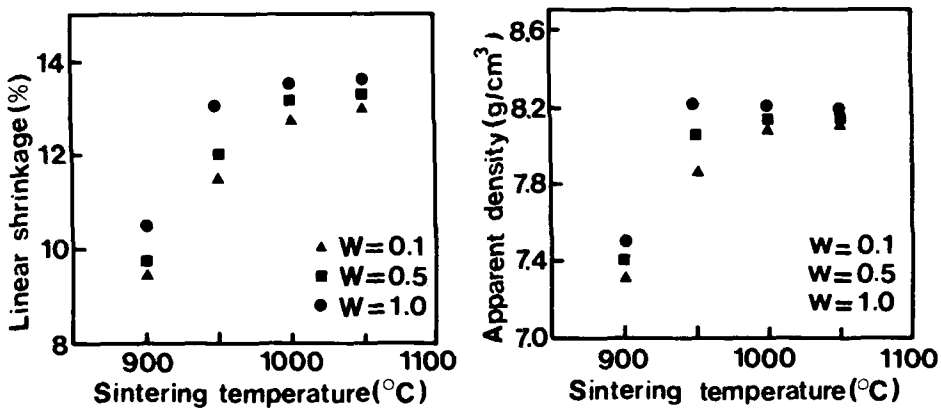


FIGURE 2 (a) Linear shrinkage and (b) apparent density vs. sintering temperature in PFN ceramics prepared with different flux weight ratio(W)

Figure 3 shows the SEM photographs of sintered specimens prepared at 950°C with various flux amounts. The grain size in specimens with W=1.0 was larger than other specimens. This can be explained as the promotion effect of densification rate in the specimens with smaller particles.

Figure 4 shows typical temperature dependence of dielectric constant and dielectric loss for the PFN ceramics sintered at 950°C. Dielectric constant increased with increasing weight ratio of flux to raw materials. In general,

FIGURE 3 SEM photographs of PFN ceramics sintered at 950°C with different flux weight ratio(W) ;(a)W=0.1, (b)W=0.5 and (c)W=1.0 (bar=1μm).

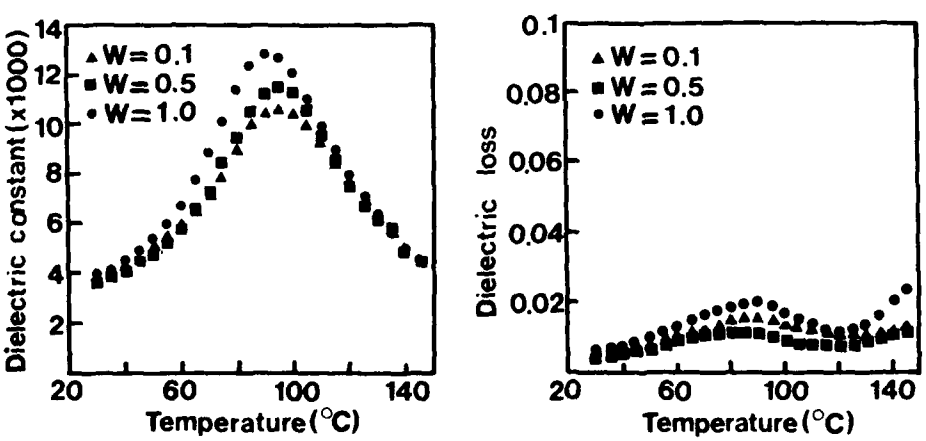


FIGURE 4 (a) Dielectric constant and (b) dielectric loss of PFN ceramics prepared with different flux weight ratio(W).

dielectric constant has a dependence on grain size and sintered density. In this work, the specimens with W=1.0 have a large dielectric constant due to larger density as well as large grains. Dielectric loss showed a minimum value in the specimens with W=0.5. The reason for this result may be not clear, but it may be the effect of porosity and the substitution of $Na^+$ and $K^+$.

## CONCLUSIONS

1) As the weight ratio of the NaCl-KCl flux to raw materials increased, the average particle size decreased and the particle size distribution tended to narrow due to the uniform reaction.

2) The linear shrinkage and density increased with decreasing the initial particle size due to the promotion of densification.

3) The dielectric constant increased with decreasing the initial particle size resulting from the increase of density and grain size.

## ACKNOWLEDGEMENT

This work was supported by the Korea Science and Engineering Foundation.

## REFERENCES

1. I.B.Cutler, Ceramic Processing before Firing, Ed. G.Y.Onoda and L.L. Hench, pp22, John Wiley & Sons (1978)
2. W.D.Kingery, H.K.Bowen and D.R.Uhlman, Introduction to Ceramics, pp381 John Wiley & Sons (1976)
3. M.F.Yan, Advances in Powder Technology, Ed. Y.Chin, pp101, ASFM(1980)
4. R.H.Arendt, J.H.Rosolowski and J.W. Szymazek, Mat. Res. Bull., 14 (5) 703 (1979)
5. T. Kimura and Y. Yamaguchi, Advances in Ceramics, Vol 21, Ceramic Powder Science (ed. G.L. Messing, K.S. Mazdiyasni, J.W. Mccauley and R.A. Haber) pp169, Am. Ceram. Soc., (1987)
6. K.H. Yoon, K.Y. Oh and S.O. Yoon, Mat. Res. Bull., 21, 1429 (1986)
7. K.H. Yoon, C.K. Kwak and D.H. Kang, Ferroelectrics, 116, 231 (1991)
8. Annual Book of ASTM Standards, C 20-87 (1987)
9. T. Kimura and T. Yamaguchi, Ceram. Int., 9 (1) 13 (1983)
10. G.Y. Onoda and G.L. Messing, J. Am. Ceram. Soc., 64 (8) 468 (1980)
11. M.P. Kassarijian, R.E. Newnham and J.V. Biggers, Am. Ceram. Soc. Bull., 64 (9) 1245 (1985)

*Ferroelectrics*, 1992, Vol. 133, pp. 289–294
Reprints available directly from the publisher
Photocopying permitted by license only
© 1992 Gordon and Breach Science Publishers S.A.
Printed in the United States of America

**SmP105**

# GROWTH OF RARE-EARTH MOLYBDATE CRYSTALS

BORIS RED'KIN, VLADIMIR KURLOV, IVAN PET'KOV AND SERGEY ROSSOLENKO.
Institute of Solid State Physics Academy of Sciences of Russia, Chernogolovka, Moscow district, RUSSIA.

*Abstract* Growth conditions of high quality rare-earth molybdate crystals by modified Czochralski and Stepanov methods in automated regime are discussed.

## INTRODUCTION

Rare-earth molybdate crystals having the general formula $R_2(MoO_4)_3$ where $R - Gd$, $Tb$, $Sm$ and othes combine ferroelectric and ferroelastic properties[1]. They are ideal materials for the design and manufacture of wide variety of optical, acousto-electric and electromechanical devices, for example see paper[2].

The $R_2(MoO_4)_3$ crystals are usually grown by the conventional Czochralski method. To produce high quality $R_2(MoO_4)_3$ crystals, as has been shown experimentaly, it is required that the pulling rate should be $3 - 8$ mm/h and the rotation rate -80 – 110 rpm. However, the crystals' growth at these conditions is very unstable, the interface often becomes concave instead of the needed flat form and the cross-section of the crystals acquires a complicated form[3]. For these reasons it is difficult to automate the crystal growth of these crystals by the conventional Czochralski method.

The mathematical simulation of evolution of the cross-section of crystals, having a 4-th order rotational symmetry axis, as a function of the angle growth anisotropy and solid-liquid interface confirmed the experimental results[4]. It has been shown it is necessary to support the form of interface as flat or slightly convex and not to permit it to have a concave interface.

This work describes problems of the growth of high quality rare-earth molybdate crystals by different methods and discusses the fundamentals of automation of these methods.

GROWTH OF CRYSTAL BY MODIFIED CZOCHRALSKI METHOD

Rare-early molybdate crystals were grown in an equipment fitted with a system for automatically controlling the weight of growing crystals. The crystals were grown in air from platinum crucibles, 50 – 60 mm in diameter and in height, using MF heating. The growth rates of crystals were 3 – 5 mm/h and 80 – 100 rpm.
The schematic drawing of the modified Czochralski method of crystal growth are presented at figure 1.

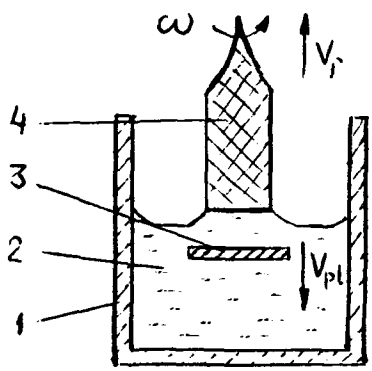


FUGURE 1. Schematic drawing of modified Czochralski method: 1– crucible, 2– melt, 3– plate, 4– crystal; $V_p$– rate of pulling, $\omega$– rate of rotation, $V_{pl}$– plate moving rate.

The present manner is distinguished from standard Czochralsri method by having the platinum plate, which is just under the interface. That plate mostly changes a convective flow of melt in the crucible, which, as it is known, determines the form of interface. The plate gives the opportunity to get interface flat or slightly convex and excludes arising of concave interface. Size, form of plate and distance from it to the interface depends on the size of the crucible and the growing crystal. These magnitudes is determined in the each case experimentally.
In the growth process the distance between the platinum plate and the interface was kept practically constant, as a rule. The moving rate of the plate was equal to the rate of decrease of melt level in the crucible.

It was defined using a system for automatically controlling the weight of the growing crystal.
Rare-earth molybdate crystals grown by the method described were 80 mm in length and 30 × 30 mm in cross-section.

GROWTH OF CRYSTALS BY STEPANOV METHOD

The Stepanov method differs from Czochralski method by a presence of a die. The die limites a value of pertubation a free surface of melt and convection flow in crucible, which takes place during growth of crystals by Czochralski method. There are different variants of the Stepanov method[5]. We used two next methods.

First Method

Rare-earth molybdate crystals is grown by Stepanov method in the same equipment as the Czochralski-grown crystals described above. The growth parameters of crystal in [001] direction were 3 – 8 mm/h and 20 – 100 rpm.
The schematic drawing of this method are shown in figure 2.

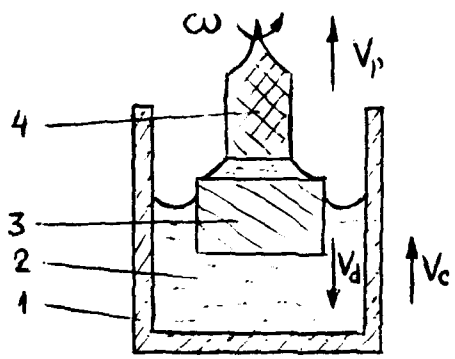


FIGURE 2 Schematic drawing of Stepanov method: 1– crucible, 2– melt, 3– die, 4– crystal; $V_p$– crystal pulling rate, $\omega$– rate of rotation, $V_c$– crucible moving rate, $V_d$– die moving rate.

Scheme of employed platium die presented in fig.3.

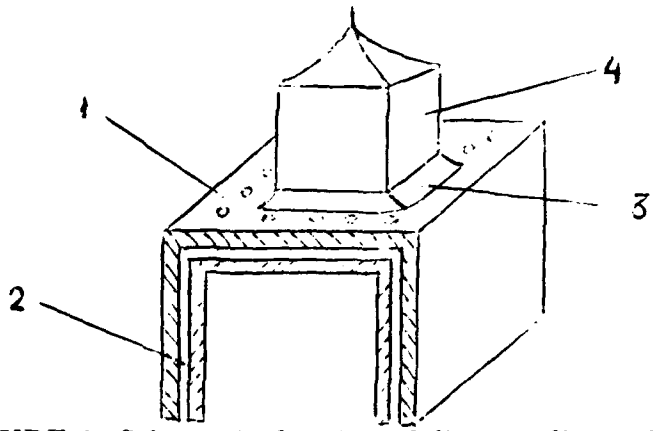


FUGURE 3 Schematic drawing of die: 1– die working surface, 2– capillary channel, 3– melt meniscus, 4– crystal.

During crystal growth the cross-section of the growing crystals did not exceed the cross-section of the working surface of the die. Under such conditions the melt meniscus could move freely along the die working suface and the melt-solid interface was flat.

The problem of capillary stability of movable menisci was examined in paper[6]. It was shown that the capillary stability of the movable meniscus is absent as in the Czochralski method.

To produce high quality $R_2(MoO_4)_3$ by this method, as has been shown exsperimentally, it is required that the pressure in menisci should be constant during the crystal growth. This can be produced by movement of a crucible or a die, and both a crucible and a die simultaneously.

The rate of movement of a crucible or a die was equal to the rate of decreasing of melt level in the crucible and was defined using a system for automatically controllied the weight of growing crystal. At a crucible movement the rate of crystal growth $V_0$ is equal to the rate of pulling $V_p$

$$V_0 = V_p \tag{1}$$

and the rate of crucible movement $V_c$ is equal

$$V_c = \frac{S}{S_c}\frac{\rho_s}{\rho_m}V_p \tag{2}$$

At a movement of die the rate of growth $V_0$ crystals is equal

$$V_0 = \frac{V_p}{1 - \frac{S}{S_c}\frac{\rho_s}{\rho_m}} \tag{3}$$

where $S-$ cross-section of crystal, $S_c-$ cross-section of crucible, $\rho_s-$ density of crystal, $\rho_m-$ density of melt.

From comparison equations (1) with (3) it is seen a change of the rate of crystal growth is taking place with change of crystal cross-section in the case of the die movement, but the rate of crystal growth is constant in the case of crucible movement. This feature is to take into account in the program of crystal growth control. That dependence is just at the crystal growth in the stationary regime. Also the change of menisci height should take into account when growing out of the crystal.

Well-formed $R_2(MoO_4)_3$ crystals grown by this method were 80 mm in lenght and 30 × 30 mm in cross-section.

Second method

The scheme of this method was analogy scheme presented on fig.2. The schematic drawing of employed die is shown in fig.4.

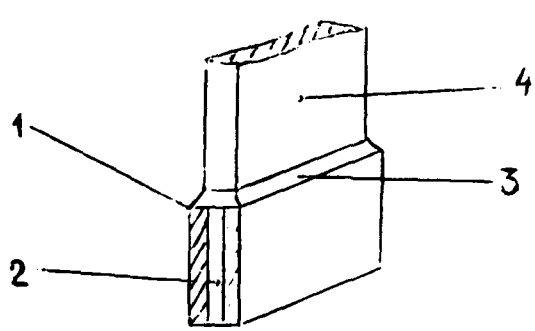


FIGURE 4 Schematic drawing of die: 1– die working surface, 2– capillary channel, 3– melt meniscus, 4– crystal.

In that case the crystals were grown without rotation and theirs cross-section is practically correspondent to the cross-section of the die working suface. Different crystals are grown this method[7] and it is most known as edge-defined film-fed growth (EFG). The main differ of the supposed method is the constant pressure of the melt menisci to be supported during the crystal growth. It is allowed to grow the most quality crystals in compare with the crystals obtained in the condition of constantly falling pressure in the melt menisci.

The shaped crystals producing by this method were 120 – 150 mm in lenght and 20 × 2 mm in cross-section. The pulling rate was 3 – 8 mm/h. The plate crystals were grown in [100] direction and the plate face corresponded (001) face.

ACKNOWLEDGMENT

The authors are grateful to Dr. B.A.Borodin for useful discussions and interest to the work.

REFERENCES

1. L. H. Brixner, J. R. Barkley and W. Jeitschko, in Handbook on the Physics and Chemistry of Rare Earths, edited by K. A. Gschneidner and L. Eyring (North- Holland Publishing Company, Amsterdam, 1979), Chap. 30, pp. 609-654.
2. A. N. Alekseev, Izv. Akad. Nauk SSSR, Ser. Fiz., 53, 1424 (1989).
3. B. S. Red'kin, V. N. Kurlov, I. S. Pet'kov and S. N. Rossolenko, Journal of Crystal Growth, 104, 77 (1990).
4. I. S. Pet'kov and B. S. Red'kin, to be published in Journal of Crystal Growth.
5. V. A. Tatarchenko, Stable Crystal Growth ( Nauka. Moscow, 1988), p. 14.
6. I. S. Pet'kov and B. S. Red'kin, Journal of Crystal Growth, 104, 20 (1990).
7. Shaped crystal growth, edited by G.W.Cullen and T.Surek in collaboration with P.I. Antonov (North-Holland Publishing Company, Amsterdam, 1980).

*Ferroelectrics*, 1992, Vol. 133, pp. 295-300
Reprints available directly from the publisher
Photocopying permitted by license only

© 1992 Gordon and Breach Science Publishers S.A.
Printed in the United States of America

# SmP108

## EFFECT OF SUBSTITUTION $Ba^{2+}$ ION ON SINTERING AND DIELECTRIC PROPERTIES OF CERAMICS IN THE SYSTEM $Pb_{1-x}Ba_x(Cd_{1/3}Nb_{2/3})O_3$

HYUNG-JIN JUNG*, JEONG-HO SOHN*, JONG-GAB BAEK, AND SANG-HEE CHO
Dept. of Inorganic Materials Engineering
Kyungpook National University, Taegu, 702-701 Korea

Abstract Lead-cadmium-niobate ceramics $Pb(Cd_{1/3}Nb_{2/3})O_3$ are difficult to prepare because of the formation of a pyrochlore phase which is detrimental to the dielectric properties. The addition of 0.1 to 0.25 $BaCO_3$ stabilizes the perovskite phase in PCN. Maximum dielectric constant appeared with x=0.1 in $Pb_{1-x}Ba_x(Cd_{1/3}Nb_{2/3})O_3$ system. Curie temperature of these system decreased with increasing amount of substituted $Ba^{2+}$ ions (x).

## INTRODUCTION

Lead-based perovskite compounds of which general formula being $Pb(B_1,B_2)O_3$ have been focused on in recent research. Especially, lead-based ferroelectric relaxors with high dielectric constants(>30000), broad dieletric maxima, and relatively low firing temperatures are now recognized as promising candidate materials for multilayer ceramic capacitors.[1] The compound $Pb(Cd_{1/3}Nb_{2/3})O_3$(herein designated as PCN) was first obtained by Tomashpol'skii et al.[2] in 1965. It shows a plateau of dielectric constant with increasing temperature and is a ferroelectric compound at room temperature which transforms to paraelectric phase at about 270 ℃. Accordingly, its application for a device with good temperature stability could be expected. The synthesis of pure perovskite PCN, however, is difficult. Metastable pyrochlore phases that can be detrimental to the dielectric properties are generally formed in the reaction process. The columbite method proposed by Swartz and Shrout[3] showed that the intermediate pyrochlore phase reaction can be bypassed, but this also fails to yield pure perovskite PCN.

The purpose of this work is to study the effect of $Ba^{2+}$ ion substitution for $Pb^{2+}$ ion on the phase stability and sintering behavior in PCN system. Especially,

* Inorganic Materials Lab., KIST

the elimination of pyrochlore phase through adjusting the tolerance factor and electronegativity difference by this substitution was attempted.

## EXPERIMENTAL

The compositions selected were $Pb_{1-x}Ba_x(Cd_{1/3}Nb_{2/3})O_3$(PBCN) with x being between 0 and 0.75. Raw material powders PbO, $BaCO_3$, CdO, and $Nb_2O_5$ were mixed in stoichiometric ratios, and then calcined. In this study, all the sample preparations were done with the usual solid state reaction process. The weighed powders were homogenized by wet ball-milling in ethanol using a polyethylene pot and zirconia balls for 24 h. The powder mixtures were dried for 24 h at 100 ℃, and then calcined at 750 ℃ for 8 h. The calcined powders were crushed in an agate mortar and pressed into pellets 13 mm in diameter and 2 to 3 mm thick with PVA as a binder. The pellets were then fired between 975 ℃ and 1350 ℃ for 2 h in magnesia and alumina crucibles. To compensate for the PbO loss, a PbO-rich atmosphere was maintained by placing an equimolar powder mixture of PbO and $ZrO_2$ inside the crucible. The phase change and the lattice constants of fired specimens were determined by powder X-ray diffractometry (XRD). The relative amounts of the pyrochlore and perovskite phases were calculated using the X-ray peak intensities of (110) of perovskite and (222) of pyrochlore phase by the following equation:

$$\% \text{ perov} = 100 \times I_{perov} / (I_{perov} + I_{pyro}) \quad (1)$$

The temperature and frequency dependences of dielectric constant and loss were measured between 100 Hz and 10 kHz, with cooling the specimens at a rate of 5 ℃/min. The temperature range of measurement was -30 to 500 ℃.

## RESULTS AND DISCUSSION

### Phase Change and Lattice Constants

Figure 1 shows the change in the relative amount of perovskite phase with the mole fraction of BaO in PBCN system. Considerable improvement in the perovskite formation was observed with increasing amount of $Ba^{2+}$ ion substitution. The origin of the decrease in the pyrochlore phase with increasing amount of $Ba^{2+}$ ion substitution could be attributed to the thermodynamical reason. The stability of several $ABO_3$-type perovskite compounds has been estimated by the Goldschmidt[4] tolerance factor (t) related to the perovskite unit cell size, and the electronegativity difference ($\Delta X$)[5] between cations and anions related to the amount of ionic bonding.

The lead-based relaxor compounds of considerably smaller electronegativity differences and tolerance factors than alkaline-earth titanates such as $BaTiO_3$ are found to be difficult to synthesize in perovskite form. Such compounds tend to form a more covalently bonded pyrochlore structure. Consequently, it is thought that the PBCN compounds with pure perovskite structure obtained have larger tolerance factor and electronegativity difference than PCN. Figure 2 shows changes in the calculated tolerance factor (t) and electronegativity difference ($\triangle X$) with increasing the mole fraction of BaO in PBCN system. Both the tolerance factor and electronegativity difference increase with increasing amount of substituted $Ba^{2+}$ ion, which perhaps contributed to the stabilization of perovskite phase in PBCN. The tolerance factor and electronegativity difference was calculated using Eq.(2) and (3) using ionic radii and electronegativity scale suggested by Pauling.[6]

$$t = \frac{R_A + R_O}{\sqrt{2}\,(R_B + R_O)} \tag{2}$$

$$(X_{A-O} + X_{B-O}) / 2 \tag{3}$$

where $R_A$, $R_B$, and $R_O$ are radii of ions occupying A, B and oxygen sites in perovskite structure, respectively and $X_{A-O}$ and $X_{B-O}$ are the electronegativity differences between A-site cation and oxygen and B-site cation and oxygen, respectively.

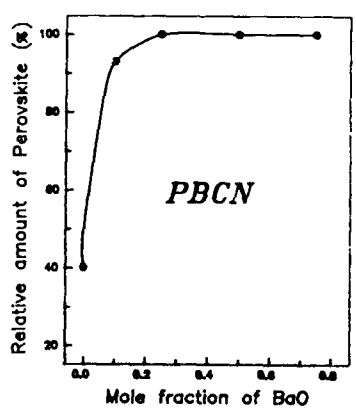


FIGURE 1 Change in relative amounts of perovskite phase with mole fraction of BaO in PBCN system.

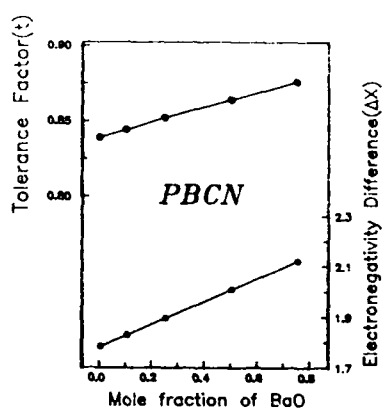


FIGURE 2 Changes in tolerance factor(t) and electronegativity difference($\triangle X$) with mole fraction of BaO in PBCN system.

Figure 3 shows the variation of lattice constant of the perovskite phase with the mole fraction of BaO in PBCN system. The perovskite lattice constant increased by substituting $Pb^{2+}$ with $Ba^{2+}$ ion. This is attributed to the larger ionic radius of

$Ba^{2+}$ ion(1.35 Å) than $Pb^{2+}$ ion(1.20 Å). A clear linearity between lattice constant and the mole fraction of BaO in PBCN system is observed. This result indicates that the $Ba^{2+}$ ions are completely substituted for $Pb^{2+}$ ions in PBCN system. Figure 4 shows change in maximum bulk density ($D_{max}$) with the mole fraction of BaO in PBCN system. Maximum bulk density increased drastically at x=0.1, and then decreased steeply with increasing amount of substituted $Ba^{2+}$ ions. The increase and subsequent decrease in bulk density are mainly due to the removal of pyrochlore phase of lower density than perovskite[7,8] and increment of unit cell volume, respectively.

Dielectric Properties

Temperature dependence of the dielectric constant for PBCN system is showm in Figure 5. All compositions shows a broad maxima of dielectric constant with the variation of temperature. Maximum dielectric constants of C1 and C2 specimens, having x=0.1 and x=0.25 respectively, are larger than that of C0 specimen, which is due to relatively small amount of pyrochlore phase. Maximum dielectric constants of C3 and C4 specimen, having x=0.5 and x=0.75, respectively, however, is much smaller than that of C0 specimen despite having the pure perovskite phase. Figure 6 shows frequency dependence of the dielectric constant and loss for C2 specimen. Increase in Curie temperature ($T_C$) with increasing frequency, typical characteristic of relaxor ferroelectrics, is shown. A corresponding frequency dispersion of the dielectric loss was also observed. The variation of Curie temperature ($T_C$) with the mole fraction of BaO in PBCN system is shown in Figure 7. $T_C$ decreased drastically with increasing BaO up to x=0.5. This result is due to increase in covalent bond energy[9] between A-site ion and oxygen ion in perovskite $ABO_3$ with increasing amount of substituted $Ba^{2+}$ ion in A-site. For ferroelectrics with a diffused phase transition (DPT), the law $1/\varepsilon \propto (T-T_0)^2$ instead of the normal Curie Weiss law is known to conform over a wide temperature range.[10] If the local Curie temperature has Gaussian distribution, the reciprocal permittivity can be written in the form

$$\frac{1}{\varepsilon} = \frac{1}{\varepsilon_m} + \frac{(T-T_0)^2}{2\varepsilon_m\delta^2} \tag{4}$$

where $\delta$ and $\varepsilon_m$ are diffuseness coefficient and maximum dielectric constant, respectively. The values of $\delta$ could be calculated for PBCN system from the slope of plots of $1/\varepsilon$ vs $(T-T_0)^2$. Plots of diffuseness coefficient ($\delta$) and maximum dielectric constant ($\varepsilon_m$) with the mole fraction of BaO for PBCN system is shown in Figure 8. The value of $\delta$ shows an increase with increasing mole fraction of BaO, indicating a broadened phase transition for PBCN system. Maximum dielectric constant decreased in accordance with the increase in $\delta$, which shows correlation between them through Gaussian distribution.

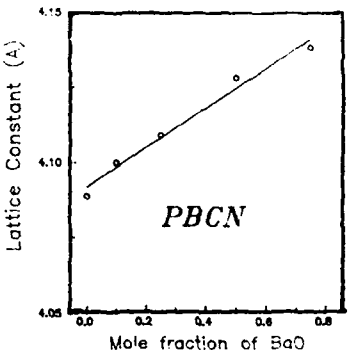


FIGURE 3 Variations of lattice constant with mole fraction of BaO in PBCN system.

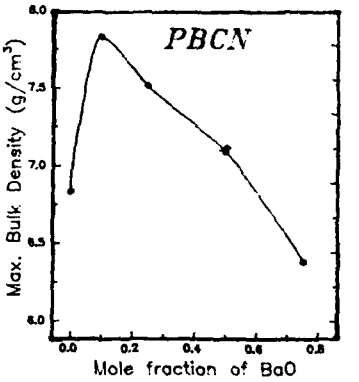


FIGURE 4 Maximum bulk density(Dmax) with mole fraction of BaO in PBCN system.

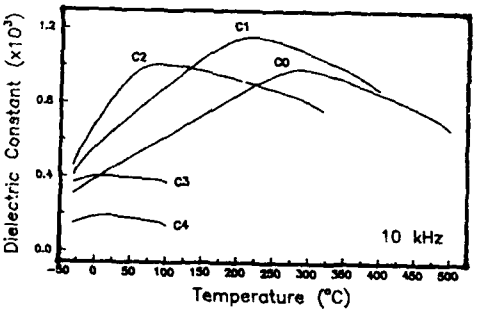


FIGURE 5 Temperature dependence of the dielectric constant at 10 kHz for PBCN system.

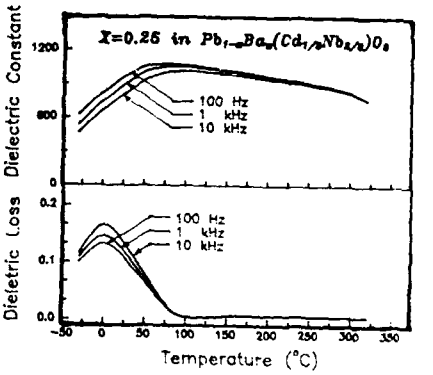


FIGURE 6 Frequency dependence of the dielectric constant and loss for C2 specimen.

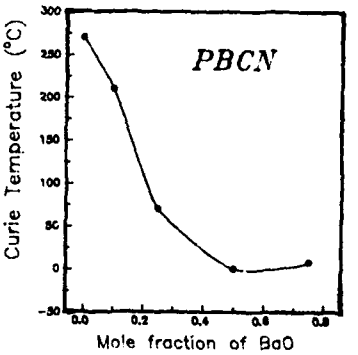


FIGURE 7 Variation of Curie temperature with mole fraction of BaO in PBCN system.

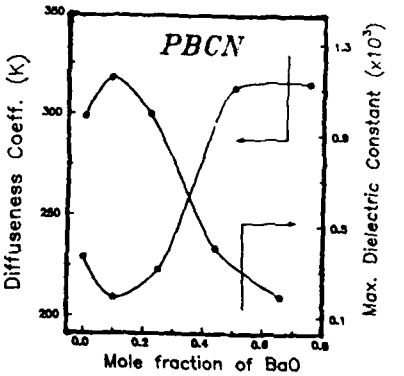


FIGURE 8 Changes in diffuseness coefficient ($\delta$) and maximum dielectric constant($K_{max}$) with mole fraction of BaO for PBCN system.

## CONCLUSION

The effects of substitution $Ba^{2+}$ ions on the perovskite formation, sintering, and dielectric properties of ceramics in the system $Pb_{1-x}Ba_x(Cd_{1/3}Nb_{2/3})O_3$ were studied. The amount x of substitution $Ba^{2+}$ ions in stoichiometric composition $Pb_{1-x}Ba_x(Cd_{1/3}Nb_{2/3})O_3$ was between 0 and 0.75, and the substitution was done by firing compacts of mixed oxides up to 1350 ℃. Considerable improvement in the sinterability and perovskite formation was observed with increasing amount of substitution $Ba^{2+}$ ions and sintering temperature in PBCN system. Maximum dielectric constant appeared with x=0.1 of $Ba^{2+}$ ions in PCN. Curie temperature of these systems decreased with increasing amount of substituted $Ba^{2+}$ ions. The diffuseness coefficient and the maximum dielectric constant of these typical DPT dielectrics increased and decreased with increasing amount of substitution $Ba^{2+}$ ions, and thus showed correlation between them.

## ACKNOWLEDGEMENTS

This work was made possible by the financial support from the Ministry of Education Research Fund Advanced of Materials (1990)

## REFERENCES

1. T. R. Shrout and A. Halliyal, Am. Ceram. Soc. Bull., 66 (4) 704-11 (1987).
2. Y. Y. Tomashpol'skii and Y. N. Venevtsev, Sov. Phys.-Solid State. 7 (2) 412 (1965).
3. S. L. Swartz and T. R. Shrout, Mater. Res. Bull., 17 1245-50 (1982).
4. V. M. Goldschmidt, Geochmische Verteilungsgesetze der Elemente I-IX, Skrift, Norske, Vid. Akad., Oslo, I. Mater.- Naturv. Kl.
5. A. Halliyal, U. Kumar, R. E. Newnham and L. E. Cross, Am. Ceram. Soc. Bull., 66 (4) 671-76 (1987)
6. F. S. Galasso, "Structure and Properties of Inorganic Solids", Pergamon Press, 8-11 (1970)
7. T. R. Shrout and S. L. Swartz, Mat. Res. Bull., 18 663-667 (1983).
8. Y. Matsuo, H. Sasaki, S. Hayakawa, F. Kanamura and M. Koizumi:Proc. 2nd Int. Meet. Ferroelectricity, Kyoto, 1969, J. Phys. Soc. Jpn., 28 Suppl. p.410 (1970).
9. K. Igarashi, K. Koumoto and H. Yanagida, Yogyo-Kyokai-Shi 95 (7) (1987).
10. K. Uchino, S. Nomura, L. E. Cross, S. J. Jang and R. E. Newnhan, J. Appl. Phys., 51 (2) 1142 (1980).

*Ferroelectrics*, 1992, Vol. 133, pp. 301-306
Reprints available directly from the publisher
Photocopying permitted by license only
© 1992 Gordon and Breach Science Publishers S.A.
Printed in the United States of America

# SmP109

## STUDY ON THE PREPARATION OF PZT CERAMIC MATERIAL FOR MEDIUM HIGH FREQUENCY SAW DEVICES BY LOW VACUUM ATMOSPHERE SINTERING

MING MING WEI FENG GU WEI YI XIE
Department of Materials Shanghai University of Science & Technology
Jiading Shanghai, 201800
People's Republic of China

Abstract Ternary PZT-PNM* ceramics is prepared by low vacuum atmosphere($5x10^{-2}$bar) sintering technique to improve the microstructure,density, polished surface smoothness, as well as the piezoelectric properties. The grain growth has been restrained by doping small amount of $CeO_2$. At the same time. The density up to 7.97g/$cm^3$ and grain size less than 2um have also been obtained. The size of pits on the polished surface is less than 0.5um. It is suitable for manufacturing SAW devices in medium high frequency of 10 to 40 MHz.

## INTRODUCTION

At present, the prefered substrate materials for surface acoustic wave(SAW) device are made of single crystals, such as $LiNbO_3$ and $LiTaO_3$. Besides these single crystals, ceramic materials also can be employed in this field but their surface smoothness must be improved.

According to design demand for device and manufacturing, when using PZT Ceramics for 38MHz SAW device, in order to avoid breaking of interdigital electrode, the biggest hole size must be less than 1.5um. The size of pore in conventional PZT ceramics is about 5-10um. To satisfy the above mentioned demand the density and the pore must be improved further.

PNM ceramics exhibit suitable electrical properties for SAW devices. This paper investigates on how to improve densification and piezoeletric properties of PNM ceramics with vacuum sintering and $CeO_2$ doping, so that we can obtain ceramics which can be used

---

* PNM is $Pb[(Mn_{1/3}Nb_{2/3})_xZr_yTi_{1-x-y}]O_3$

for SAW device in medium high frequency ranging from 10 to 40MHz.

## EXPERIMENTAL PROCEDURE AND RESULTS

The chemical composition of the ceramics was prepared according to the following chemical formula: $Pb[(Mn_{1/3}Nb_{2/3})_xZr_yTi_{1-x-y}]O_3$, where x=0.05, y in different PNM sample is as following:

| PNM sample | I | II | III | IV |
|---|---|---|---|---|
| y | 0.45 | 0.49 | 0.55 | 0.60 |

The raw materials used were 99.9% pure $TiO_2$, PbO, $ZrO_2$, $Nb_2O_5$, $CeO_2$ and $MnO_2$. These samples are fabricated with conventional ceramic procedure but with two different sintering conditions---in low vacuum atmosphere($5x10^{-2}$bar) and in conventional atmosphere sintering. The synthesis process is completed at 850°c for two hours and it is sintered at 1220°c for one hour. Table I shows the properties in two different sintering conditions for PNM sample I to IV.

TABLE I Influence of different sintering conditions on properties

| Sintering Condition | Sintered in atmosphere (1220°c/1h) | | | | Sintered in Vacuum ($5x10^{-2}$ bar 1220°c/1h) | | | |
|---|---|---|---|---|---|---|---|---|
| Samples | I | II | III | IV | I | II | III | IV |
| Dielectric constant $\varepsilon_{33}^T$ | 290 | 630 | 330 | 330 | 280 | 610 | 310 | 310 |
| Electromechanical coupling Coefficient Kp | 0.29 | 0.48 | 0.30 | 0.23 | 0.35 | 0.52 | 0.36 | 0.33 |
| Electromechanical coupling Coefficient Kt | 0.20 | 0.25 | 0.32 | 0.26 | 0.22 | 0.27 | 0.36 | 0.40 |
| Mechanical Quality factor Qm | 3140 | 1040 | 2340 | 2440 | 3500 | 2710 | 3000 | 3000 |
| Density p(g/cm$^3$) | 7.79 | 7.75 | 7.86 | 7.84 | 7.93 | 7.92 | 7.95 | 7.95 |
| Porosity % | 3.50 | 5.16 | 3.10 | 3.16 | 1.74 | 1.75 | 1.70 | 1.69 |
| Average grain size D(μm) | 7.8 | 2.5 | / | 2 | 10 | 6 | / | 4.5 |

It shows that nearly all the properties of the samples in low vacuum atmosphere condition are superior to those samples sintered in conventional atmosphere, especially the density is raised greatly, except the property of $\varepsilon_{33}^T$ which is almost the same in two conditions. The grain size of sample sintered in low vacuum atmosphere is nearly twice of that sintered in conventional atmosphere as shown in detail by the Fig.1, which shows the SEM of microstructure for

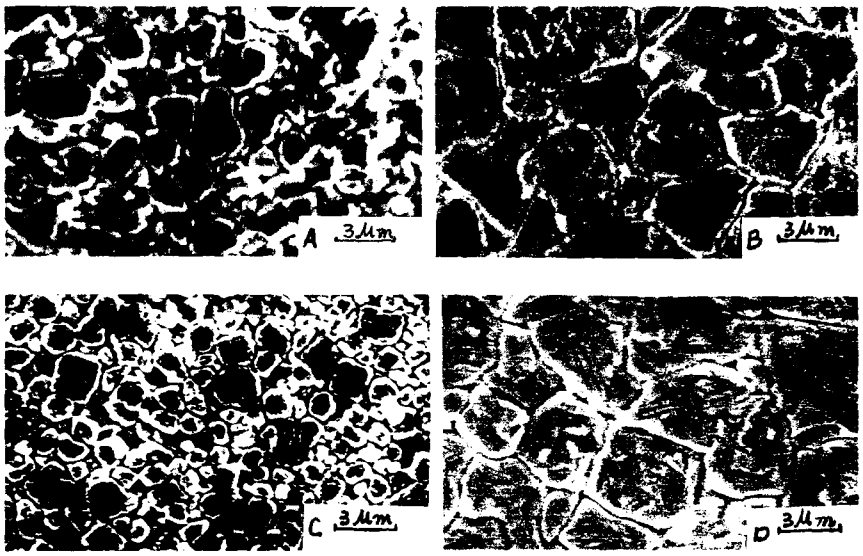


Fig. 1. SEM of the microstructure for samples sintered in different conditions at 1220°c
A.C. Sintered in conventional atmosphere
B.D. Sintered in low vacuum atmosphere ($5x10^{-2}$ bar)
A.B--PNM II; C.D--PNM IV

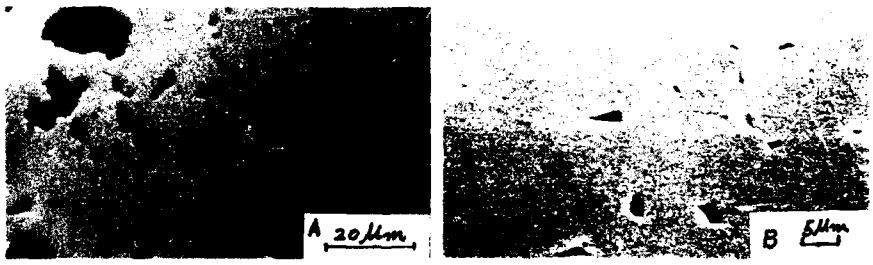


Fig. 2. Polished surface morphology of samples PNM IV sintered in different conditions at 1220°c
A Sintered in conventional atmosphere
B Sintered in low vacuum atmosphere ($5x10^{-2}$ bar)

samples II. IV. Simultaneously the polished surface of sample is improved as shown in Fig.2. In low vacuum atmosphere sintering both the hole size and number of holes are reduced compared with convention-

al atmosphere sintering.
Because a large grain size will increase the SAW propagation loss[1], therefore, improved density as well as reduced grain size are necessary. Small amount of dopant $CeO_2$ is used to restrain grain growth. The grain size is reduced from 4.5μm to 1.5um and the value of Kp, Kt and Qm remain the same while the density is raised further more as shown in table 2. Fig.3,A shows the effectiveness of dopant $CeO_2$ on grain growth in microstructure SEM. Fig.3.B shows the SEM of polished surface smoothness of sample with dopant $CeO_2$, the biggest pits size on the surface is decreased from 5μm to 0.5μm.

TABLE 2. Influence of dopant $CeO_2$ on properties of sample PNM IV

| Sample | Dopant wt% | $\varepsilon_{33}^{T}$ | Kp | Kt | Qm | p g/cm$^3$ | D μm |
|---|---|---|---|---|---|---|---|
| PNM IV | 0.4 $CeO_2$ | 330 | 0.33 | 0.46 | 3500 | 7.97 | 1.5 |

The following composition is suitable for manufacturing medium high frequency SAW filter substrate

$$Pb[(Mn_{1/3}Nb_{2/3})_xZr_yTi_{1-x-y}]O_3+zwt\%CeO_2$$

Where 1>x>0.04; 0.80>y>0.35; 0.60>z>0.20. Its properties is shown in table 3. Using the above mentioned material, SAW filters of 10.7MHz and 38MHz has been fabricated by Shanghai First Radio Factory. Their frequency response diagram is shown in fig.4 and explaining data is shown table 4.

Fig.3. The microstructure and polished surface morphology of sample PNM IV doped with $CeO_2$ sintered at 1220°c
A. Microstructure
B. Polished surface morphology

TABLE 3 Properties of substrate material(PNM ceramics) of 10.7MHz and 38MHz SAW filter

| p g/cm$^3$ | D μm | Surface pits size μm | $\varepsilon_{33}^T$ | Qm | Kp | Kt | Vs m/s | Ks |
|---|---|---|---|---|---|---|---|---|
| 7.97 | 1.5 | 0.5 | 345 | 3500 | 0.34 | 0.46 | 2340 | 0.16 |

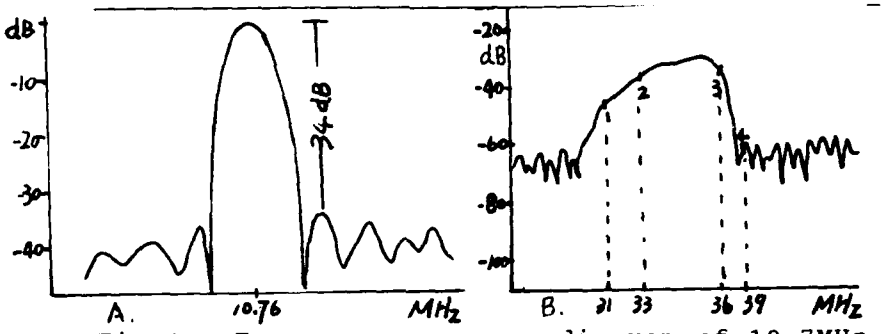


Fig.4 Frequency response diagram of 10.7MHz and 38MHz SAW filter
A. 10.7MHz SAW filter
B. 38MHz SAW filter

TABLE 4. Properties of 10.7MHz and 38MHz SAW filter measured by HP 8753A network analyzer
A. 10.7MHz SAW filter

| Center frequency MHz | 3dB band width KHz | Insertion loss dB |
|---|---|---|
| 10.76 | 310 | 17 |

B. 38MHz SAW filter

| Insertion loss dB | Vision carrier dB | Color carrier dB | Sound carrier dB | Adjacent vision trap dB | Adjacent sound trap dB | Lower side lobe dB | Supper side lob dB |
|---|---|---|---|---|---|---|---|
| 30.0+1 | 4.5+2 | 5.0+2 | 15+3 | >3.5 | >30 | >30 | >25 |

## DISCUSSIONS

1.High speed of heating is used to minimize the volatilization of PbO in low vacuum atmosphere sintering and cooling in normal air atmosphere is applied to decrease oxygen vacancy produced in low

vacuum atmosphere sintering. In the specimen obtained by this procedure, there are only tiny pore in bulk and the pinning effect from the pore is reduced, as a result, it promotes sintering. Consequently, ceramics with high density and bigger grain size are obtained.
2. The density of samples sintered in low vacuum atmosphere condition is increased, so the combination force among the grains is also increased and the spalling phenomena during the polishing is decreased. Consequently,samples sintered in low vacuum atmosphere have only tiny pits on the polished surface.
3.Dopant $CeO_2$ can restrain grain growing, it is possible that the $Ce^{4+}$ exists on the grain boundary to restrain the migration of grain boundary during the sintering and the fine grain microstructures are obtained.
4.Manganous ions exist in air with various valencies (2+,3+,4+,6+,7+), when the temperature reaches above 800°c, the established equilibrium of partial pressures varies with the temperature increasing between the manganous and oxygen, making the manganous ions become $Mn^{2+}$ and $Mn^{3+}$ [2]. In low vacuum atmosphere sintering, low oxygen partial pressure restrains the transforming of $Mn^{2+}$ into $Mn^{3+}$, consequently it is advantageous to the existing for $Pb(Mn_{1/3}Nb_{2/3})O_3$ and enhances piezoelectric properties greatly[3]. With the low vacuum sintering, the material density is improved greatly and the piezelectric property Kt and Qm are increased appropriately.

## CONCLUSIONS

1. Sintering PNM ceramics in low vacuum atmosphere can enhances density and piezoelectric properties and it is an easy procedure for manufacturing SAW substrate material.
2. Adding dopant $CeO_2$ into PNM system can produce fine grains. It is beneficial to improving polished surface smoothness as well as enhancing piezoelectric properties.

## REFERENCES

1. Shigeru Jyomura, KaznyuKi Nagatsuma and Hiroshi Takeuchi, J.Appl. phys., Vol.52, No.7 (1981) 4472.
2. E.M.Levin, C.R.Robbins and H.F.McMurdie,Phase Diagram for Ceramics, p.39,2nd ed. Edited by M.K.Reser. The Amer. Ceram. Soc.(1969).
3. M.Takahashi, N.Tsubouchi, M.Yonezawa, T.Ohno, T.Akashi. J.Japan Soc. of Powder and Powder Metallurrgy 20(8)(1974) p.274.

*Ferroelectrics*, 1992, Vol. 133, pp. 307–311
Reprints available directly from the publisher
Photocopying permitted by license only

© 1992 Gordon and Breach Science Publishers S.A.
Printed in the United States of America

# SmP110

## SYNTHESIS OF ELECTRONIC CERAMICS BY USING $CO_2$ LASER

SUNAO SUGIHARA AND TOSHIE FUKUYAMA
Shonan Institute of Technology, Fujisawa, Japan

Abstract A new method is discussed for synthesis of $Pb(Zr,Ti)O_3$ ceramics using $CO_2$ laser irradiation. There are two kinds of the system. One is a compact of mixed powder of $PbTiO_3$ and $Bi_2(ZrO_3)_3$ and the other is a compact of $Pb_3O_4$, $ZrO_2$ and $TiO_2$ powders as the starting materials. The green pellets of oxides are irradiated by $CO_2$ laser at the power of 143, 286 and 1430 $W/cm^2$ in a flow rate of 350 cc/min. of 20% $O_2/Ar$ ($10^5$ Pa). The latter system is better for synthesis of $Pb(Zr,Ti)O_3$ than the former one with the lower power. The former system, however, can work to take Zr into $PbTiO_3$ matrix as well. The $CO_2$ laser treatment will be efficient for the sintering and introducing certain elements into a matrix.

## INTRODUCTION

Piezoelectric ceramics, $Pb(Zr,Ti)O_3$ have been usually fabricated by the solid state sintering; PbO(or $Pb_3O_4$), $ZrO_2$ and $TiO_2$ are mixed using a ball mill for several hours, then pressed at 2 ton/$cm^2$ followed by pre-sintering at 800°C and final sintering at a temperature of 1230°C for one hour. Sometimes $MO_x$(M:metal) are added for the certain purposes.

The $CO_2$ laser treatment as the heat source can be used for welding, cutting, coating and others and the technique has several merits such as cleanliness, large input power and short process time. There have been many studies on crystal growth [1,2,3], fabrication of ultra fine powders [4] and film coating by a laser or a laser CVD method. However, there have not been many studies on sintering of ceramics by $CO_2$ laser as the heat source, although the laser irradiation on

$ZrO_2$-$HfO_2$ and $ZrO_2$-$Y_2O_3$-$HfO_2$ were reported for instance[5-6]. Also there has been few studies about synthesis of electronic ceramics in bulk by $CO_2$ laser irradiation. In this report, the preliminary study on $CO_2$ laser treatment was applied to synthesis the piezoelectric ceramics, $Pb(Zr,Ti)O_3$ (hereafter, PZT) and the starting materials are; (1) $PbTiO_3$/$Bi_2(ZrO_3)_3$ mixture and (2) $Pb_3O_4$/$ZrO_2$/$TiO_2$ mixture.

## EXPERIMENTS

The $CO_2$ laser treatment system is shown in Fig.1. The beam on a specimen is a 0.3 mm spot at a focusing distance of 38.1 mm with a continuous mode. The induced angle of the laser beam is at 15 degrees to the specimen, and the laser power is 143,286 and 1430 W/cm$^2$. The atmosphere in the laser treatment chamber is a mixture of gases of 20% $O_2$/Ar at $10^5$ Pa with a flow rate of 350cc/min. The specimen sizes for both cases are a disk with 10 mm in diameter and 0.3 mm in thickness. In the mixture of $PbTiO_3$(hereafter,PT) and $Bi_2(ZrO_3)_3$ (hereafter,BZ), the powders are mixed manually and pressed at 1 ton/cm$^2$ and the other specimen is a green comact of $Pb_3O_4$/$ZrO_2$/$TiO_2$ pressed at the same pressures as PT/BZ system. The purities of $TiO_2$, $ZrO_2$ and $Pb_3O_4$ are 98.51%,99.77 % and 97.72%, respectively (Fuji Titanium Co.Ltd.). The specimen is put on an alumina plate in the chamber and heated at 350 C to avoid thermal shock, and the specimen is covered by alumina powder(99.9% purity)in order to get an uniform heat distribution by the laser irradiation since alumina can absorb laser energy by more than 80%,and

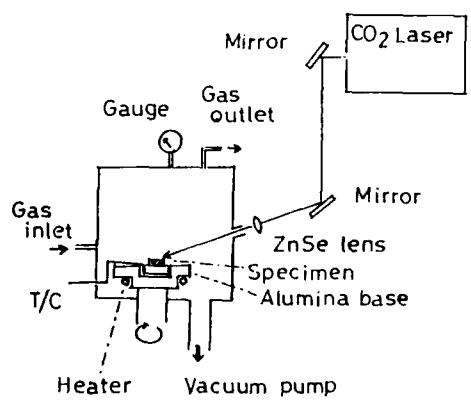


**FIGURE 1 Schematic of a $CO_2$ laser irradiation system.**

the thermal conductivity is $3X10^{-3}$ W/cm·C. Furthermore, a specimen is manually movable from outside the chamber. The temperatures during irradiation were measured on the alumina base near the specimen(about 5 mm)with thermocouples(Pt-PtRh 13%). The changes of temperatures are shown in Fig.2. After the laser treatment,the specimens are examined by an XRD, a SEM and an EPMA.

## RESULT AND DISCUSSION

A small amount of Bi is usually added to the matrix such as $BaTiO_3$or $PbTiO_3$. In this report, however, $Bi_2(ZrO_3)_3$ can be considered as one of materials for providing Zr to make PZT with PT. In the reaction of PT with BZ by $CO_2$ laser,BZ will be expected to decompose, then to dissolve into PT lattice

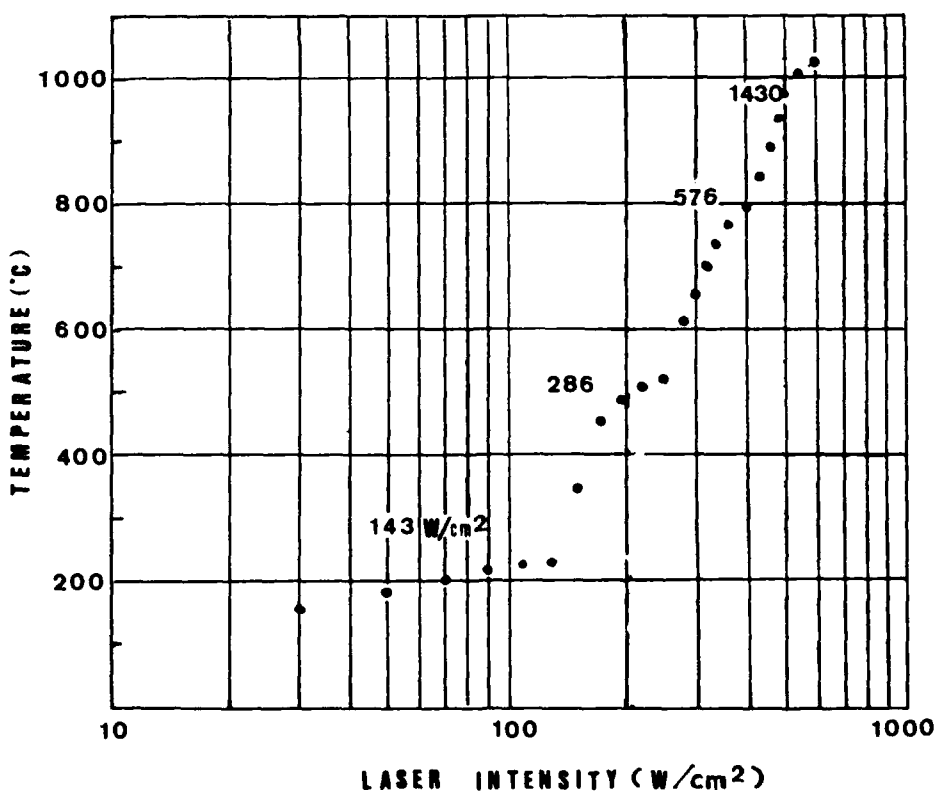


**FIGURE 2 Changes of temperature with laser intensity.**

resulting PZT ceramics.Only small amount of PZT were recognized when treated at a laser intensity of 1430 $W/cm^2$ with an XRD,and Bi in the specimen after irradiation was found in trace by an EPMA, although it was not determined whether Bi formed $Bi_2O_3$ or the oxide decomposed, since it is unstable at more than 800°C. The mixture of $Pb_3O_4$,$TiO_2$ and $ZrO_2$ are more popular for making PZT ceramics.After laser treatment at 286 $W/cm^2$,PZT lines were found, although the starting materials remained in high concentrations as shown in Fig.3. Figure 4(a) presented the microstructure of a pellet after irradiation at 286 $W/cm^2$. It reveals that neckings between particles have much developed than those of a presintered pellet as shown in Fig.4(b). Generally,in the sintering of ternary system of oxides here, solid state reactions are completed around 800°C, then the sintered density is raised at about 1200°C [7].Therefore,pre-sintering at 800°C is suggested to fabricate PZT ceramics followed by a sintering at 1230°C in the usual method.The sintering by a laser irradiation,however,could be achieved at lower temperatures since the neckings appeared at 500-600°C.

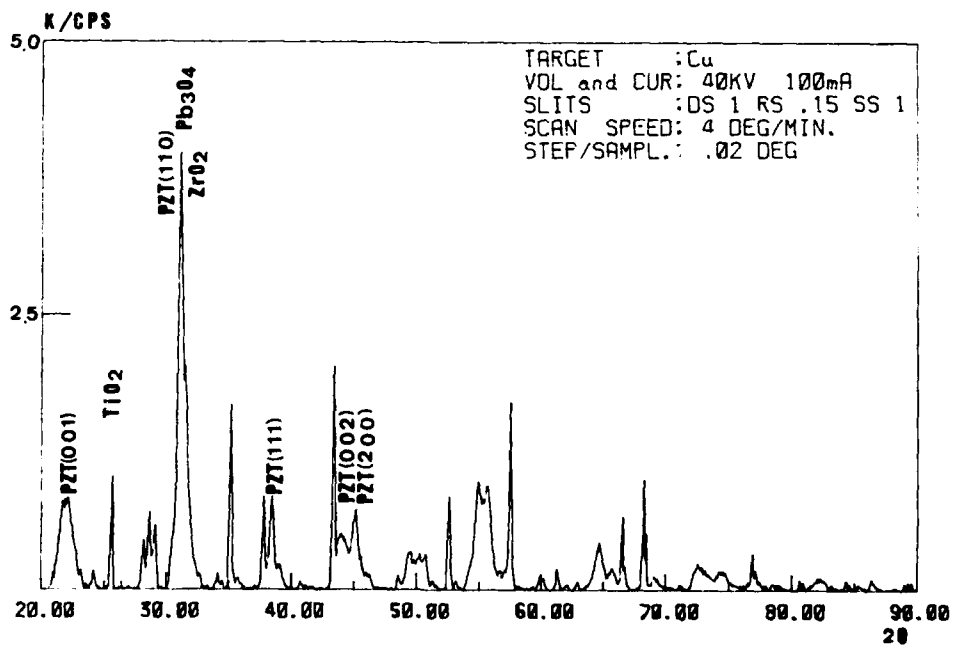


**FIGURE 3 XRD analysis after laser irradiation at 286 $W/cm^2$.**

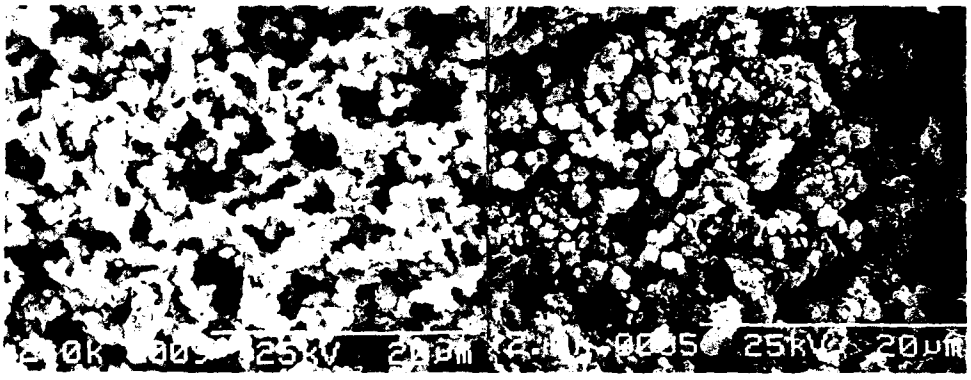

(a) (b)

**FIGURE 4 SEM photographs of pellets ; (a) $CO_2$ laser treatment (b) pre-sintering.**

## CONCLUSION

It was recognized that PZT ceramics can be synthesized from the mixture of $Pb_3O_4$, $ZrO_2$ and $TiO_2$ by the laser irradiation at a relatively small intensity. It is better that the specimen's thickness is supposed to be less than 1 mm. The preliminary study concludes that the laser treatment is capable of synthesizing other electronic ceramics in a bulk state.

As the next step, synthesis of electronic ceramics by $CO_2$ laser irradiation will be followed by investigation to make a complete solid solution of PZT from the ternary oxides, then to evaluate piezoelectric properties and comparisons of them among other fabrication method.

## REFERENCES

1. B.Cockayne and D.B.Gasson, J.Mater.Sci.,5,837(1970).
2. J.G.Bednorz and H.Arend, J.Crystal Growth,67,660(1984).
3. K.Takagi and M.Ishii, J.Mater.Sci.,12,517(1977).
4. W.R.Cannon,S.C.Danforth,J.S.Haggerty and R.H.Marra, J.Ame.Ceram. Soc.,65[7],330(1982).
5. M.Okutomi,J.High Temperature Soc.,12[3],109(1986)[Japanese].
6. M.Okutomi,M.Kasamatsu,K.Tsukamoto,S.Shiratori and F.Uchiyama, Appl.·Phys.Lett.,44[12],1132(1984).
7. K.Okazaki,Ceramic Engineering for Dielectrics (Gakkensha, Tokyo, 1983)P.213 and P.343[Japanese].

*Ferroelectrics*, 1992, Vol. 133, pp. i–iii
Reprints available directly from the publisher
Photocopying permitted by license only

© 1992 Gordon and Breach Science Publishers S.A.
Printed in the United States of America

# AUTHOR INDEX

## Proceedings of the Second European Conference on the Application of Polar Dielectrics

## Volumes 133–134

Abdi, F., *DiP223*, 175; *EoC21*, 313
Adams, D. A., *TdI18*, 61
Afonikova, N., *MsP145*, 229
Aillerie, M., *DiP223*, 175; *EoC21*, 313
Albareda, A., *PdP131*, 411
Alemany, C., *PcP123*, 389
Al-Jassim, M., *TfC17*, 615
Alquie, C., *PvP129*, 553
Arlt, G., *DiP219*, 163; *DoP234*, 223; *PtP240*, 565
Auciollo, A., *TfX2*, 3
Austin, M., *TdI18*, 61
Azough, F., *DiC12*, 127; *DiP224*, 181
Azuma, M., *TdI10*, 47

Baek, J.-G., *SmP108*, 295
Balzer, G., *EoP202*, 329
Banys, J., *DiP229*, 199
Bak, W., *TrP140*, 241
Baptista, J. L., *DiC12*, 127
Bdikin, I., *MsP145*, 229
Bell, A., *DiP230*, 205
Bell, A. J., *DiC7*, 115; *TfC13*, 597
Benadero, L., *PdP131*, 411
Biermann, A., *PtP240*, 565
Böttger, U., *PtP240*, 565
Brabant, P., *TdI18*, 61
Briot, R., *PmP114*, 475
Bruchhaus, R., *TdI9*, 73
Budzier, H., *PyI12*, 41
Buhay, H., *TdI18*, 61
Bune, A. V., *EoC21a*, 319

Carmona, F., *PcP123*, 389
Chadney, J. E., *TfP259*, 661
Cho, S.-H., *SmP108*, 295
Changshui, F., *PyC18*, 507
Chen, C.-C., *EoP254*, 347
Chen, P.-O., *EoP254*, 347
Chu, F., *DiC7*, 115
Chung, J. H., *SmC11*, 277
Chupis, I. E., *TfP255*, 649
Close, J. A., *PmP262*, 493
Colla, E. L., *DiP256*, 217
Costa, B. V., *PvP150*, 559
Cross, L. E., *PdX4*, 11

Daglish, M., *DiC7*, 115
Das-Gupta, D. K., *PcC15b*, 383
Dexter, K. F., *TfI8*, 85; *TfP259*, 661
Dmytrow, D., *DiC9*, 121
Dorogovtsev, S. N., *PtP251*, 577
Dzimianski, J., *TdI18*, 61

Eyraud, L., *PcC2*, 371; *PdC13*, 405
Eyraud, P., *PcC2*, 371
Echer, C., *TfC17*, 615

Ferreira, V. M., *DiC12*, 127
Fontana, M. D., *DiP223*, 175; *EoC21*, 313
Freer, R., *DiC12*, 127; *DiP224*, 181
Fridkin, V. M., *EoC21a*, 319
Fujimoto, S., *DiP233*, 211
Fujiu, T., *PmC4*, 445
Fukuyama, T., *SmP110*, 307
Fukushima, Y., *EoP203*, 335

Garabedian, C., *PdC13*, 405
Gealy, F. D., *TfC17*, 615
Gleeson, H. F., *EoI13*, 15
Glissa, N., *PmP114*, 475
Goel, T. C., *PyP247*, 529
Godefroy, G., *DiP223*, 175; *EoC21*, 313
Gonnard, P., *PdC13*, 405; *PmP116*, 481
Gorbatenko, V. V., *PmP154*, 365
Gorri, J. A., *PdP131*, 411
Govindan, A., *PyP247*, 529
Grange, G., *PcC2*, 371
Gridnev, S. A., *PmP154*, 365
Grigas, J., *DiP229*, 199
Gu, F., *SmP109*, 301
Guillemot-Amadei, M. M., *PmP116*, 481
Gunter, P., *EoX1*, 1
Gutmann, R., *TfC14*, 603

Hafid, M., *DiC9*, 121
Hamaji, Y., *DiC14a*, 133
Handerek, J., *DiC9*, 121
Heinecke, R. A., *TfI8*, 85
Hirakata, K., *DiC15a*, 139
Hofmann, G., *PyI12*, 41; *PyP214*, 513
Hongsheng, Z., *PyC18*, 507

Hsieh, K. Y., *TfX2*, 3
Huang, Y., *TfC13*, 597
Huffman, M., *TfC17*, 615
Hulliger, J., *TfC14*, 603
Hwang, S.-J., *EoP261*, 353

Ilchenko, M. E., *PyP216*, 519
Imai, A., *PmP111*, 463
Ishida, T., *TfP205*, 631
Ito, Y., *TfP210*, 637

Jiménez, B., *PcP123*, 389; *PmP113*, 469
Jimenez-Morales, F., *PyP217*, 525
Jung, H.-J., *SmP108*, 295

Kajtoch, C., *DiP228*, 193
Kamba, S., *DiP230*, 205
Kammerdiner, L., *TfC17*, 615
Kanai, K., *DiP233*, 211
Kanda, H., *TfP210*, 637
Kandušer, A., *PyP261*, 535
Kang, D. H., *SmC11*, 277
Kanno, M., *PdC1*, 395
Kano, G., *TdI10*, 47
Karpinsky, D., *ThP152*, 265
Kato, T., *PmP111*, 463
Kawamura, Y., *PdP136*, 433
Kim, E. S., *DiP227*, 187
Kimura, S., *TfP205*, 631
Kingon, A. I., *TfX2*, 3
Klee, M., *TfI14*, 91
Kobialka, T., *EoP202*, 329
Korzunova, L., *PmP118*, 487
Kosaka, Y., *DiC15a*, 139
Kosec, M., *PyP261*, 535
Kozlov, G. V., *DiP230*, 205
Krzywanek, K., *TrP140*, 241
Kugel, G. E., *DiC9*, 121
Kugel, V., *TrP142*, 253
Kurlov, V., *SmP105*, 289
Kuś, C., *TrP140*, 241
Kushida, K., *TfP210*, 637

Laburthe Tolra, C., *PvP129*, 553
Lampe, D. R., *TdI18*, 61
Lane, R., *PdC4a*, 401
Lang, S. B., *TrP142*, 253
Larsen, P. K., *TfI14*, 91
Lavrenčič, B. B., *PyP261*, 535
Lee, W.-Y., *EoP254*, 347; *EoP261*, 353
Legrand, J. F., *EoC21a*, 319
Lemanov, V. V., *PmC6*, 451
Lewiner, J., *PvP129*, 553
Lewis, K. L., *TfI8*, 85; *TfP259*, 661
Liang, J.-J., *EoP254*, 347; *EoP261*, 353
Lichtenwalner, D., *TfX2*, 3
Lin, G.-S., *EoP254*, 347
Liu, Y. M., *TdI18*, 61
Llewellyn, I. P., *TfI8*, 85
Lobo, R. P. S. M., *DiP222*, 169
Lubitz, K., *PcI2*, 21

Maksimov, A. Yu., *PmC6*, 451
Mandrino, D., *PyP261*, 535
Marat-Mendes, J. N., *PvP127*, 541; *PvP128*, 547
Matsumoto, Kozo, *PdP136*, 433
McGettrick, B. P., *DiC16b*, 151
McMillan, L. D., *TdI10*, 47
Mihara, T., *TdI10*, 47; *TfP205*, 631
Millar, C. E., *SmC5*, 271
Min, W., *PyC18*, 507
Mochizuki, S., *TfP205*, 631
Mohallem, N. D. S., *DiP222*, 169
Moreira, R. L., *DiP222*, 169; *PvP150*, 559
Mukherjee, B. K., *PcC3*, 377; *PdP135*, 423
Muramatsu, K., *PmC4*, 445
Murphy, C. E., *PcP151*, 501
Myasnikova, A., *TrP141*, 247

Neumann, N., *PyI12*, 41; *PyP214*, 513
Nir, D., *TrP142*, 253
Nishiyama, T., *DiC14a*, 133
Novitskii, E. Z., *SwP218*, 259

Obhi, H. S., *TfC16*, 609
Okabe, H., *PdC1*, 395
Okada, M., *TfI7*, 79
Ohanessian, H., *PdC13*, 405
Ono, T., *TfI7*, 79
Onozato, H., *TfP210*, 637
Orlova, E. V., *TdP213*, 677
Osbond, P. C., *DiC17*, 159

Pan, W., *TfI15*, 97
Panjan, P., *PyP261*, 535
Pardo, L., *PcP123*, 389
Parinov, I., *ThP152*, 265
Parinova, L., *ThP152*, 265
Park, K. B., *SmP104*, 283
Patel, A., *PyI11*, 35; *TfP258*, 655
Pavlova, N. G., *PmP154*, 365
Paz de Araujo, C. A., *TdI10*, 47
Pedersen, L., *SmC5*, 271
Pereverzeva, L. P., *PyP216*, 519
Pérez, R., *PdP131*, 411
Pet'kov, I., *SmP105*, 289
Petrovsky, V. I., *TdP213*, 677
Petzelt, J., *DiP230*, 205
Pevtsov, E. F., *TdP213*, 677
Pillai, P. K. C., *PyP247*, 529
Polinsky, M., *TdI18*, 61
Poplavko, Yu. M., *PyP216*, 519
Poprawski, R., *FgP244*, 583
Prasad, S. E., *PcC3*, 377
Prieto, C., *EoP264*, 359
Preu, G., *PcI2*, 21
Ptak, W. S., *TrP140*, 241

Qingwu, W., *PyC18*, 507

Raposo, M., *PvP127*, 541; *PvP128*, 547
Reaney, I. M., *DiP256*, 217; *TfC13*, 597

Red'kin, B., *SmP105*, 289
Ribeiro, P. A., *PvP127*, 541, *PvP128*, 547
Richard, C., *PcC2*, 371
Richard, M. Ms., *PcC2*, 371
Richardson, T., *PcP151*, 501
Robels, U., *DiP219*, 163; *DoP234*, 223
Roberts, G. G., *PcP151*, 501
Rosenman, G., *TrC10*, 235; *TrP142*, 253
Rossetti, Jr., G. A., *ThI3*, 103
Rossolenko, S., *SmP105*, 289
Rushin, S., *TrP142*, 253

Sakabe, Y., *DiC14a*, 133
Sakano, S., *PdC1*, 395
Sakashita, Y., *TfI7*, 79
Salloway, A. J., *PdC4a*, 401
San Emeterio Prieto, J. L., *PdP133*, 417
Sato, S.-I., *DiC15a*, 139
Savchenko, V. V., *PtP242*, 571
Sawamura, K., *DiC15a*, 139
Schneider-Störmann, L., *DoP234*, 223
Schöner, H.-P., *PdI1*, 27
Schulmeyer, B., *PcI2*, 21
Scott, J. F., *TdI10*, 47
Segawa, H., *TfI7*, 79
Setter, N., *DiP230*, 205; *DiP256*, 217
Sharma, H. D., *PyP247*, 529
Sherrit, S., *PcC3*, 377; *PdP135*, 423
Shmyt'ko, I., *MsP145*, 229
shorrocks, N., *PyI11*, 35; *TfP258*, 655
Shorrocks, N. M., *TfC16*, 609
Shuren, Z., *PcC15b*, 383
Shuvalov, L. A., *PmP154*, 365
Sigov, A. S., *TdP213*, 677
Sinharoy, S., *TdI18*, 61
Smirnova, E. P., *PmC6*, 451
Smith, A., *DiC16a*, 145
Smith, C. W., *DiC16a*, 145
Smith, W. A., *PmC6a*, 457
Smyth, D. M., *DeI6*, 13
Sobiestianskas, R., *DiP229*, 199
Sohn, J.-H., *SmP108*, 295
Sotnikov, A. V., *PmC6*, 451
Sternberg, A., *EoP250*, 341
Stevens, R., *PmP262*, 493
Stoll, R., *PcI2*, 21
Sugawara, K., *TfP210*, 637
Sugihara, S., *SmP110*, 307
Sun, S., *TfI15*, 97

Takenaka, T., *PmC4*, 445
Takeuchi, H., *TfP210*, 637
Tarakanov, E. A., *PmC6*, 451
Thakoor, S., *TdC20*, 667
Tilley, D. R., *TfC23*, 625
Tolstikov, I. G., *SwP218*, 259
Tominaga, K., *TfI7*, 79
Tomiyasu, H., *EoP203*, 335
Tossell, D. A., *TfC16*, 609
Toyoda, S., *EoP203*, 335
Tresanchez, M., *PdP131*, 411
Tripathi, A. K., *PyP247*, 529
Troccaz, M., *PmP114*, 475; *PmP116*, 481
Trubitsyn, M. P., *PtP242*, 571
Tschudi, T., *EoP202*, 329
Twiney, R. C., *PdC4a*, 401

Ueda, D., *TdI10*, 47
Ueda, T., *TdI10*, 47
Uesu, Y., *EoP203*, 335
Ujma, Z., *DiC9*, 121
Uchikoba, F., *DiC15a*, 139

Verkhovskaya, K. A., *EoC21a*, 319
Vest, R. W., *TfP253*, 643
Vicente, J. M., *PmP113*, 469
Vij, J. K., *DiC16b*, 151
Villar, J. L., *PdP131*, 411
Volkov, A. A., *DiP230*, 205
Vorotilov, K. A., *TdP213*, 677

Wang, H.-M., *EoP261*, 353
Waser, R., *TrI4*, 109
Watanabe, H., *TdI10*, 47
Watton, R., *PyX3*, 5
Wei, M. M., *SmP109*, 301
Whatmore, R., *PyI11*, 35; *TfP258*, 655
Whatmore, R. W., *DiC17*, 159; *PdC4a*, 401; *TfC16*, 609
Wiederick, H. D., *PcC3*, 377; *PdP135*, 423
Winfield, G., *DiP224*, 181
Wolff, A., *PcI2*, 21
Wolny, W. W., *SmC5*, 271
Wüest, H., *TfC14*, 603

Xie, W. Y., *SmP109*, 301

Yamada, N., *PmP111*, 463
Yoon, K. H., *DiP227*, 187; *SmC11*, 277; *SmP104*, 283
Yoshimori, H., *TdI10*, 47
Yue, C.-F., *TfI15*, 97
Yushin, N. K., *PmC6*, 451; *PtP251*, 577

Zadon, Ch., *DiP219*, 163
Zaldo, C., *EoP264*, 359
Zeks, B., *TfC23*, 625
Zelenka, J., *PdP152*, 439
Zhu, J. G., *TfC17*, 615
Zhu, W., *TfP253*, 643
Zurcher, P., *TfC17*, 615
Zurmühlen, R., *DiP230*, 205

# Special Issue on Piezoelectric and Electrostrictive Actuators

A special issue of the international journal *Ferroelectrics* is scheduled for 1992 on the subject "Piezoelectric and Electrostrictive Actuators."

Recent developments in piezoelectric and electrostrictive ceramics are remarkable, especially in the field of optics and precision machinery. Camera shutters, dot-matrix printers, and air valves have been widely commercialized. Ultrasonic motors will partially replace conventional electromagnetic motors in the future.

This special issue will cover the fundamental studies of ceramic actuators and applications:

1. Ceramic actuator materials — piezoelectrics, electrostrictors, phase transition — related ceramics
2. Fabrication processes — powders, tape casting
3. Micro/macrostructure — grain size dependence, monomorph, electrode configuration
4. Control technique — polarization control, pulse drive method
5. Applications — deformable mirrors, positioners, pulse drive motors
6. Ultrasonic motors

Invited and contributed papers are welcome. All manuscripts will be reviewed. Manuscripts should be prepared according to the instructions on the inside back cover of "Ferroelectrics."

Authors are cordially invited to submit their papers to the Guest Editors below:

Professor Kenji Uchino
Department of Physics
Sophia University
Kioi-cho 7-1, Chiyoda-ku
Tokyo 102, Japan
or
Materials Research Laboratory
The Pennsylvania State University
University Park, PA 16802, USA
(July 1-September 30)

Professor L. Eric Cross
Materials Research Laboratory
The Pennsylvania State University
University Park, PA 16802

For further information, please feel free to contact the Guest Editors.

*First Announcement*

# The Eighth
# INTERNATIONAL MEETING OF FERROELECTRICITY

**8–13 August 1993**
**National Institute of Standards and Technology**
**Gaithersburg, Maryland USA**

The scope of the conference will be similar to that of the preceding IMFs. Both invited and contributed papers will be presented on fundamental and applied research on ferroelectrics, including but not limited to:

Phase transitions and critical phenomena
Electronic structure, quantum effects
Lattice dynamics, lattice instabilities, and soft modes
First principles calculations
Low-temperature properties
Superconductivity in oxides
Charge density waves, polarization fluctuations
Structure and crystal growth
X-ray and neutron scattering
Acoustic and ferroelastic properties
Dielectric, piezoelectric, and pyroelectric properties
Optical properties and phase conjugation
Modulated and incommensurate systems
Disordered and glassy systems
Domains, domain boundaries, and imperfections
Raman, Brillouin, IR, and submillimeter spectroscopy
NMR, ESR, PAC, and other types of spectroscopy
Electron microscopy
High-pressure effects
Polymers and liquid crystals
Ceramics and composite materials
Sensors, actuators, and transducers
Thin films and surfaces
Ferroelectric/semiconductor integration

| | | |
|---|---|---|
| Wallace A. Smith | L. Eric Cross | George W. Taylor |
| Office of Naval Research | Pennsylvania State University | Princeton Resources |
| IMF8 Chairman | IMF8 Vice Chairman | IMF8 Vice Chairman |

To receive future announcements, send your name and address to:

Ms. Kathy Kilmer, IMF8 Conference Manager
National Institute of Standards and Technology
Administration Building, Room A917
Gaithersburg, MD 20899
TEL (301) 975-2776; FAX (301) 926-1630

Title and Name _____
Institution _____
Department _____
Street _____
City/State/Zip _____
Country _____
Phone _____
FAX _____

❒ I will present a paper entitled: _____

❒ I will be accompanied by _____ guests.

❒ I will attend, but will not present a paper.

❒ I will not attend, but would like to be kept informed.

第４回強誘電性液晶国際会議
（日本学術振興会 主催）

# FOURTH INTERNATIONAL CONFERENCE ON FERROELECTRIC LIQUID CRYSTALS

SEPT. 28 - OCT. 1
1993

TOKYO, JAPAN

FIRST ANNOUNCEMENT

こまばエミナース，東京
KOMABA EMINENCE, TOKYO

FLC 93 TOKYO, to be held Sept. 28 - Oct. 1, 1993, at Komaba Eminence under the auspices of JSPS (Japan Society for the Promotion of Science), is the fourth in the series of biennial international meetings on ferroelectric liquid crystals begun in Arcachon (1987) and continued in Göteborg (1989) and Boulder (1991).

Scientists with interests in the basic and applied aspects of ferroelectric liquid crystals are welcome to participate in this meeting. The program will consist of single sessions of invited lectures, contributed oral and poster presentations.

To receive further information, please fill out and return by mail or FAX the attached preregistration form by Oct. 1, 1992. Preregistrants will be sent the second circular, including details of abstract submission and meeting arrangements, by the end of 1992.

Comments and questions on FLC 93 TOKYO are welcome and should be directed to the conference organizers:

Atsuo FUKUDA (FLC 93 TOKYO)
Tokyo Institute of Technology
Faculty of Engineering
Department of Organic & Polymeric Materials
O-okayama, Meguro-ku, Tokyo 152, JAPAN

FAX : +81-3-3748-5369
TEL : (03) 3726-1111 Ext. 2437
E-mail: ytakanis@cc.titech.ac.jp

Mail to:

Atsuo FUKUDA (FLC 93 TOKYO)
Tokyo Institute of Technology
Faculty of Engineering
Department of Organic & Polymeric Materials
O-okayama, Meguro-ku, Tokyo152, JAPAN

## Preregistration Form

Name & Title:

Affiliation:

Address:

FAX:

E-Mail:

Telex:

(over)

Area of FLC Interest:

- Dynamics
- Physics
- New Materials
- Phase Behavior & Microscopy
- Device Technology
- Polymer FLC's
- Chiral Systems
- Antiferroelectrics
- Optics
- Interfaces
- Theory
- Others (

Tentative Title of Your Contribution:

ORGANIZING COMITTEE:

Atsuo Fukuda: Chair
Hideo Takezoe
Naoyuki Koide
Ichiro Tsunoda
Hirokazu Toriumi
Dietrich Demus

INTERNATIONAL ADVISORY BOARD:

| | |
|---|---|
| L. Bata | U. Finkenzeller |
| R. Blinc | J. Fousek |
| L. M. Blinov | J. W. Goodby |
| E. Chiellini | G. Heppke |
| N. A. Clark | S. T. Lagerwall |
| H. Coles | R. B. Meyer |
| C. Destrade | J. Prost |
| G. Durand | M. Schadt |
| C. Escher | |

142 COMMITEE of JSPS:

M. Takeda: Chair
K. Okano
H. Sasabe
H. Kokado

Komaba Eminence, where the scientific meeting will take place, is located within walking distance from the University of Tokyo, Komaba Campus, and is close to one of the downtown area, Shibuya. The days fixed for FLC 93 TOKYO are Sept. 28 - Oct.1, 1993; just after the Conference, Oct. 5 - 9, the 1993 Electronic Show will be held at Makuhari Messe near Tokyo. The participants will surely enjoy not only the scientific meeting of FLC 93 TOKYO but also exhibitions of devices and equipment, particularly of liquid crystal displays, in the 1993 Electronic Show.

*First Announcement*

# Magnetoelectric Interaction Phenomena in Crystals

2nd International Conference
September 13–18, 1993

Centro Stefano Franscini, Monte Verità
Ascona (Ticino), Switzerland

## GENERAL INFORMATION

### Conference Site

The conference will be held at the Centro Stefano Franscini, Monte Verità, Ascona, on the banks of Lago Maggiore in the Italian-speaking part of Switzerland.

### Accommodation

The possibilities of getting suitable accommodation are limited. Lodging facilities are available at the Centro itself for about 60 participants. For the others, hotels in nearby Ascona are foreseen, but it cannot be guaranteed that accommodation can be found for all participants. Moreover the lecture room available also limits the total number of participants.

### Second Circular

A second circular with a call for papers and more detailed information will be sent in December 1992 to all those returning the attached form to:

**Mme Odile Hirth/MEIPIC**
Secrétariat de Chimie appliquée
Université de Genève, Sciences II
30, Quai Ernest Ansermet

**CH-1211 Genève 4**
Suisse/Switzerland

E-mail: MEIPIC@sc2a.unige.ch
Phone: (+41)22-702-6408(Hirth)
-6419 (Rivera)
-6418 (Ye)
-6111 (Exchange)
Fax: (+41) 22-329-6102
Telex: 421.159 SIAD

### Organization

Organized by the Department of Mineral, Analytical and Applied Chemistry of the University of Geneva, in collaboration with the Laboratory for Neutron Scattering at the Paul Scherrer Institute, Würenlingen and Villigen, Switzerland and with the Institute for Theoretical Physics, University of Nijmegen, The Netherlands.

### Financial support

Swiss Federal Institute of Technology, Zürich.

### Motivation

The magnetoelectric effect foreseen by Landau and Lifshitz in 1956 has been predicted to occur in chromiumoxyde $Cr_2O_3$ by Dzyaloshinskii (1960). It is characterized by the appearance of an electric polarization on applying a magnetic field and a magnetization on applying an electric field. The experimental observation of the effect in $Cr_2O_3$ followed rapidly (Astrov 1960, 1961; Folen, Rado and Stalder 1961). Thereafter the effect was observed and studied in many more materials.

The status of theoretical understanding and experimental work after the first decade of research in magnetoelectricity is well reflected by the book *The Electrodynamics of Magneto-Electric Media* of O'Dell (1970) and the proceedings of the conference *Magnetoelectric Interaction Phenomena in Crystals* held in 1973 (Freeman and Schmid 1975). During the following two decades of research more theoretical and experimental know-how has been accumulated, but many problems

still remain unsolved. It has become clear, however, that the magnetoelectric effect is an invaluable tool for studying materials, for example the magnetic symmetry and phase transitions of magnetically ordered phases. These facts are to a great extent still ignored by the scientific community working in solid state physics.

**Organizing Committee**

H. Schmid (chairman),
A. Janner, H. Grimmer, J.-P. Rivera,
Z.-G. Ye.

**International Advisory Board**

**Czechoslovakia**: V. Janovec.
**France:** F. Bertaut, M. Clin, P. Tolédano
**Germany:** H. G. Kahle
**Great Britain**: G. Gehring, D. Tilley
**Israel:** S. Shtrikman, R. M. Hornreich
**Japan:** J. Kobayashi, K. Kohn, K. Siratori
**The Netherlands:** T. Janssen
**Poland:** J. Barnas
**Russia:** M. I. Bichurin,
A. S. Borovik-Romanov,
R. V. Pisarev,
Yu. Venevtsev
**Switzerland:** E. Ascher, P. Fischer,
P. Günter
**Ukraine:** I. E. Chupis
**USA:** I. Dzyaloshinskii, G. T. Rado,
J. F. Scott

## SCIENTIFIC PROGRAM

**Fields and Special Topics**

- Linear and higher order magnetoelectric, piezomagnetoelectric and other magnetoelectrically related effects.
- Relation between symmetry and magnetoelectric properties (tensorial, crystallographic, relativistic).
- Phenomenological and microscopic theories (Landau theory of phase transitions, exchange effects).
- Frontier fields (toroidal moments, kinetoelectric and kinetomagnetic effects, problems of magnetoelectricity and related symmetry phenomena in quantum magnets, e.g. anyonic systems and chiral phases).
- Synthesis, structural and physical properties of magnetoelectric materials (single crystals, ceramics, composites): ordinary magnetoelectrics and complex ones, such as ferromagnetic, ferrimagnetic or antiferromagnetic ferroelectrics, antiferroelectrics and ferroelastics ("Seignettomagnetics").
- Magnetoelectric effect in incommensurate crystals (modulated, intergrowth and quasicrystals).
- Magnetoelectrically monitored magnetic phases and phase transitions.
- Field induced effects. Static magnetic field induced polarization, electric field induced magnetization, quasistatic, pulsed, dynamic and high frequency.
- Optical properties (crystal optics of magnetoelectric materials in transmission and reflection: magnetoelectrically generated non-linear optical effects).
- Domains and domain walls (switching, symmetry aspects, coupling with applied fields, stress, etc.).
- Elementary excitations in magnetoelectric materials.
- Inhomogeneity and defect induced magnetoelectric effects.
- Measuring techniques.
- Applications.

**Contributions and Proceedings**

Plenary sessions of tutorial expositions and invited lectures selected among the contributed papers are foreseen, as well as posters. Conference proceedings are planned to be published. Invited lecturers and contributing participants are asked to have their manuscripts available at the beginning of the conference.
All papers will be refereed.

# 5th International Symposium on Integrated Ferroelectrics

April 19, 20, 21, 1993

*Antlers Doubletree Hotel*
*Colorado Springs, Colorado*

Chairman: Prof. C. A. Paz de Araujo
Co-chairman: Prof. R. Panholzer
General Technical Program Coordinator:
Prof. J. F. Scott

**Symposium Sponsors**

Office of Naval Research
Defense Advanced Research Projects Agency
Naval Postgraduate School
University of Colorado at Colorado Springs

## Call for Papers

**Deadline for abstracts—**
**September 30, 1992**

This is the 5th Annual International Symposium dedicated to ferroelectric thin-film materials integrated with semiconductor circuits.

Over the past few years, interest in this field of integrated ferroelectrics has grown beyond all expectation and the 1993 symposium should attract an even larger number of participants.

Authors are invited to submit a 300-word abstract by *September 30, 1992*. Topics include but are not limited to:

- ferroelectric memories
- ferroelectric and pyroelectric CCDs
- high dielectric constant materials for integrated circuits (64 Mbit DRAM, etc.)
- ferroelectric and pyroelectric sensors
- integrated optics
- optical storage
- radiation-related subjects, such as radiation hardness
- fundamental properties
- process and substrates
- process integration
- new devices and architecture
- device modeling
- materials processing and integration
- supporting circuitry and applications
- ferroelectric ASICs
- smart tags
- RF identification
- neural networks
- bypass capacitors

Abstracts should be submitted on 8½ × 11 paper with the title centered in upper case, leaving two line spaces, then the author's name and affiliation, centered. Up to two pages of pictures or figures of supporting data may be included.

Abstracts will be juried and authors will be informed of acceptance at a later date.

## Deadline for Abstracts

**September 30, 1992**

**Registration Fee**

| | Before April 5 | After April 5 |
|---|---|---|
| General | $275.00 | $350.00 |
| Government | $225.00 | $300.00 |
| All students | $ 40.00 | $ 60.00 |

One copy of the Symposium Proceedings is covered by the registration fee. Additional copies will be available at $55.00 each.

**Hotel Accommodations**

Antlers Doubletree Hotel

| | Single | Double |
|---|---|---|
| General | $72.00 | $82.00 |
| Government | $51.00 | $71.00 |

Please make hotel reservations for the Symposium *before* April 5, 1993 *directly with*:

Antlers Doubletree Hotel
4 South Cascade Avenue
Colorado Springs, Colorado 80903
(719) 473-5600

Send check or money order made payable to Antlers Doubletree Hotel or guarantee your reservation with a major credit card.

A limited number of economy accommodations are available in the proximity of the Antlers Doubletree Hotel.

**Mail Abstracts to:**

Alona S. Miller, Symposium Coordinator
University of Colorado at Colorado Springs
1420 Austin Bluffs Parkway
P.O. Box 7150
Colorado Springs, Colorado 80933
Phone: 719-593-3488
FAX: 719-594-4257

# FERROELECTRICS
## and related materials

### NOTES FOR CONTRIBUTORS

Manuscripts should be typewritten with double-spacing and submitted in triplicate. Authors are requested to forward their manuscripts to either the Editor:

**G. W. Taylor**
**Princeton Resources,**
**P.O. Box 211,**
**Princeton, New Jersey 08540, USA**

or one of the Associate Editors:

**Peter Günter**
**Institut für Quantenelektronik**
**ETH**
**CH 8093 Zürich**
**Switzerland**

**Sidney B. Lang**
**Department of Chemical Engineering**
**Ben Gurion University of the Negev**
**Beer Sheva 84120, Israel**

**Koichi Toyoda**
**Research Institute of Electronics**
**Shizuoka University**
**Hamamatsu 432**
**Japan**

Submission of a paper to *Ferroelectrics* will be taken to imply that it represents original work not previously published, that it is not being considered for publication elsewhere, and that if accepted it will not be published elsewhere in the same form, in any language, without the consent of the editors.

It is a condition of the acceptance by the editor of a typescript for publication that the publishers acquire automatically the copyright in the typescript throughout the world.

*Manuscript length:* The maximum length preferred is 35 units, where a unit is a double-spaced typewritten page or one figure. Longer papers, or papers not following the prescribed editorial format, cannot be guaranteed prompt publication.

*Abstracts and Key Words:* Each manuscript should contain a leading abstract of approximately 100–150 words and be accompanied by up to six key words which characterize the contents of the paper.

*Figures* should be given numbers and captions, and should be referred to in the text. Captions should be collected on a separate sheet. Please label each figure with the figure number and the name of the author. *Line drawings of high enough quality for reproduction should be prepared in India ink on white* paper or on tracing cloth; coordinate lettering should be included. Figures should be planned so that they reduce to a 6¼ cm column width. The *preferred* width of submitted figures is 12 to 15 cm, with lettering 4 mm high, for reduction by one-half. Photographs intended for halftone reproduction should be good, original glossy prints, at roughly twice the desired size. Redrawing, and author's alterations in excess of 10%, will be charged.

*Color Plates:* Whenever the use of color is an integral part of the research, or where the work is generated in color, the journal will publish the color illustrations without charge to authors. Reprints in color will carry a surcharge. Please write to the Editor for details.

*Equations* should be typewritten wherever possible, with subscripts and superscripts clearly indicated. It is helpful to identify unusual symbols in the margin.

*Units.* Acceptable abbreviations will be found in the *Style Manual* of the American Institute of Physics and similar manuals. Metric units are preferred.

*References and Notes* are indicated in the text by superior numbers; the full list should be collected and typed on a separate page at the end of the paper. Listed references are arranged as follows:

1. J. C. Slater, *J. Chem. Phys.* **9**, 16 (1941).
2. F. Jona and G. Shirane, *Ferroelectric Crystals* (Pergamon Press, Oxford, 1962), pp. 186–7.

*Proofs:* Page proofs, including figures, will be forwarded by air mail to authors for checking.

*Reprints:* Reprints may be purchased; a reprint order form will be sent with page proofs.

There are no page charges to authors or to institutions.